Hydromagnetic waves in Earth's core and their influence on geomagnetic secular variation

Christopher Charles Finlay

Submitted in accordance with the requirements for the degree of PhD

The University of Leeds

School of Earth and Environment

May 2005

Abstract

In this thesis east-west motions of Earth's magnetic field on time scales of centuries to millennia and associated patterns of field evolution at the core surface are studied. The hypothesis that hydromagnetic waves in Earth's core contribute to such changes is investigated by comparing analysis of historical and archeomagnetic observations with predictions from analytical and numerical wave models.

Geomagnetic field models are analysed in order to quantify the characteristics of radial magnetic field (B_r) evolution at the core surface. In the historical model *gufm1*, spatially and temporally coherent (wave-like) patterns are identified in B_r. Particularly striking is a low latitude signal with azimuthal wavenumber m=5 that travels westwards at $\sim$17 km yr^{-1}. Studying the archeomagnetic model CALS7K.1, episodes of both eastward and westward motion of wave-like patterns in B_r are observed. Analysis of the evolution of fields and underlying flows from geodynamo simulations is used to illustrate that inability to resolve the smallest length scales of the field makes quantitative inferences concerning the flow difficult, unless the flow is large scale. Furthermore, it is found azimuthal motions of patterns in B_r can be produced by hydromagnetic waves in the simulations. The remainder of the thesis addresses whether hydromagnetic waves in the core could be the origin of azimuthal geomagnetic secular variation.

Magneto-Rossby waves driven by convection (with a dynamical balance between magnetic forces, latitude-dependent Coriolis forces, and buoyancy forces) are proposed as a suitable candidate for hydromagnetic waves in the core. When driven by thermal convection, such waves propagate on the thermal diffusion time scale. Convection-driven magneto-Rossby waves are found to exhibit dispersive behaviour and a dependence of propagation speed on latitude. It is shown that such hydromagnetic waves in the core could produce wave-like patterns in B_r in two ways. One mechanism involves the distortion of toroidal magnetic field within the core by wave flows producing new, spatially periodic and azimuthally drifting, concentrations of B_r. This mechanism is investigated using a 3D, linear, dynamical model with spherical geometry and an imposed toroidal magnetic field. When this toroidal magnetic field is equatorially symmetric, wave-like patterns in B_r centred on the equator are obtained. Wave flows are found to consist of alternating regions of flow convergence and divergence close to the outer boundary. A second mechanism whereby hydromagnetic waves can produce spatially and temporally coherent patterns in B_r involves advection of existing B_r by the wave flows. This mechanism is studied using a 1D, diffusionless, analytical model and a 2D numerical model on a spherical surface including limited magnetic diffusion. It is found that propagating concentrations in B_r are produced that pulsate in amplitude if the wave propagation speed is faster than the fluid motions within the wave. Both mechanisms could feasibly be involved in producing the wave-like patterns in B_r identified at the core surface.

The wave modelling results are used as a guide to indicate whether azimuthal motions of the spatially periodic patterns in B_r at the core surface are a result of wave propagation or advection by azimuthal flows. The propagation speeds of convection-driven magneto-Rossby waves are found to be too slow to account for observed field motions. Furthermore, no evidence for dispersive behaviour or for systematic latitudinal trends in azimuthal speeds associated with magneto-Rossby wave propagation are found during analysis of geomagnetic field models. It is therefore suggested that advection by azimuthal flows, perhaps driven by thermal or magnetic winds, could be responsible for the observed azimuthal magnetic field motions.

In summary, a scenario consistent with both observations and theoretical modelling is proposed. Hydromagnetic waves driven by convection exist in Earth's core and produce spatially periodic patterns in B_r by distorting toroidal magnetic fields into new B_r and concentrating existing B_r at points of flow convergence. These patterns move either westwards or eastwards producing geomagnetic secular variation primarily as a result of advection by azimuthal flow in the core.

Contents

List of Figures

List of Tables

Notation, physical constants, abbreviations and conventions

Notation for symbols

α	Coefficient of volume expansion
β	Linear rate of change of Coriolis force in northward direction
β'	Magntitude of the background temperature gradient
β^*	Upper boundary slope in QG model (see non-dimensional control parameters)
γ	Magnitude of gravitational acceleration
$\gamma_l^{mc/s}$	Secular variation coefficients
Δ	Differential operator that is the angular part of $r^2\nabla^2$
ΔT	Temperature difference across spherical shell in dynamo model
$\Delta\theta$	Grid spacing in latitude
$\Delta\phi$	Grid spacing in longitude
Δt	Grid spacing in time
$\delta\lambda$	Difference between eigenvalues at two choices of trunctation
ϵ	Heat per unit mass in the Boussinesq thermal equation
Θ	Perturbation temperature field
$\widehat{\boldsymbol{\theta}}$	Unit vector in the meridional (north-south) direction
θ	Spherical polar co-latitude (angle south from North pole for Earth)
η	Magnetic diffusivity ($1/\mu\sigma$)
κ	Thermal diffusivity of the fluid
Λ	Elsasser number (see non-dimensional control parameters)
Λ_c	Critical Elasser number for the onset of magnetic instability
λ	Complex eigenvalue in magnetoconvection problem
λ_{lat}	Latitude
λ_{lat}^*	Fixed latitude studied in β-plane model
λ_{in}	Eigenvalue of the inertial wave problem
λ_S	Spatial damping factor used to regularise field model
λ_T	Temporal damping factor used to regularise field model
μ	Magnetic permeability
μ_0	Magnetic permeability of non-permanently magnetised material
ν	Kinematic viscosity of the fluid
∇	Gradient operator
∇_H	Horizontal component of the gradient operator
ρ	Fluid density
ρ_0	Constant density of incompressible fluid, used in Boussinesq approx.
Φ	Objective function minimised during inversion for field model

$\widehat{\boldsymbol{\phi}}$	Unit vector in the eastward direction in spherical geometry
	Also denotes eastward component when appears as a subscript
ϕ	Spherical polar longitude (angle east from Greenwich meridion for Earth)
ϕ'	Longitude co-ordinate in reference frame drifting along with 2D wave flow
Ψ	Streamfunction of kinematically prescribed, simple wave flow
ψ	Spatial co-ordinate in frame drifting along with 1D wave flow
σ	Electrical conductivity
τ_η	Magnetic diffusion time (D^2/η)
τ_ν	Viscous diffusion time (D^2/ν)
$\boldsymbol{\Omega}$	Angular rotation rate of system
$\widehat{\boldsymbol{\Omega}}$	Unit vector in the direction of the angular rotation rate vector
Ω	Magnitude of the angular rotation rate of system
ω	Angular frequency of wave or signal
ω_M	Angular frequency of simple hydromagnetic (Alfven) wave
ω_A	Angular frequency of internal gravity wave
ω_C	Angular frequency of inertial wave
ω_{MC}	Angular frequency of slow Magnetic-Coriolis (MC) wave
ω_c	Angular frequency of wave at the onset of instability
χ	Streamfunction of flow in Quasi-Geostrophic annulus model
	Also the normalised misfit of data to field model
Υ	Accumlated drift rate of reference frame drifting along with wave flow
ζ	Component of fluid vorticity along the rotation axis in QG model

$\boldsymbol{\mathcal{A}}$	Matrix of terms without time dependence in magnetoconvection problem
A_{ijk}	Array linking components of secular variation, magnetic field and flow
$\boldsymbol{\mathcal{B}}$	Matrix of terms with time dependence in magnetoconvection problem
$\boldsymbol{B}$	Vector magnetic field (strictly referred to as magnetic flux density)
$\boldsymbol{B}_0$	Background magnetic field linearised around
$\widehat{\boldsymbol{B}_0}$	Unit vector in the direction of the background magnetic field
B_0	Magnitude of background (imposed) magnetic field
B_{0x}	Component of background magnetic field in the cartesian x direction
B_{0y}	Component of background magnetic field in the cartesian y direction
B_{0z}	Component of background magnetic field in the cartesian z direction
B_r	Magntitude of magnetic field in the radial direction
$\bar{B}_r$	Time-averaged, axisymmetric, part of radial magnetic field
$\widetilde{B_r}$	(B_r-$\bar{B}_r$), high pass filtered with cut-off period t_c
$\widetilde{B}_r^{rec}$	Reconstruction of particular modes of B_r after mask-FK filtering $\widetilde{B_r}$
B_{r0}	Background radial magnetic field
B_r'	Perturbation radial magnetic field
B_r^{NAD}	Non-axial dipole part of radial magnetic field
B_θ	Amplitude of magnetic field in the southward direction
B_ϕ	Amplitude of magnetic field in the eastward direction
$\mathcal{B}$	Typical order of magnitude of magnetic field, used in scaling arguments
$\boldsymbol{b'}$	Perturbation magnetic field
$\boldsymbol{b}$	Perturbation magnetic field after dropping of '

$\boldsymbol{b}_T$	Toroidal component of magnetic field perturbation
$\boldsymbol{b}_P$	Poloidal component of magnetic field perturbation
b_x	Perturbation magnetic field component in the cartesian x direction
b_y	Perturbation magnetic field component in the cartesian y direction
b_z	Perturbation magnetic field component in the cartesian z direction
$b_l^{mc/s}$	Spherical harmonic coefficients for magnetic field
$b_l^{mc/s'}$	Spherical harmonic coefficients for magnetic field in drifting frame
$\mathbf{C_e}$	Covariance matrix for observations of the geomagnetic field
$\mathbf{C_m}$	Covariance matrix for geomagnetic field model
C	Correction factor applied to Radon transform to remove directional bias
C_p	Specific heat capacity at constant pressure
c_{az}	Azimuthal speed of field features
c_{ph}	Phase speed of wave
c	Radius of outer spherical shell in models, r_{cmb} for Earth
D	Declination: angle between the magnetic field and the northward direction
	Also the spherical shell thickness for dynamo models
	Also gap between cylinders for Quasi-Geostrophic annulus model
$\mathcal{D}$	Linear operator arising under double curl of momentum and induction eqns
$\mathbf{d}$	Vector of observations (data)
d_0	Length scale of system under study
E	Ekman number (see non-dimensional control parameters)
E^S	Equatorially symmetric
E^A	Equatorially anti-symmetric
e	Toroidal scalar for the velocity field
F	Magnitude of magnetic field vector, known as total intensity
F_w	Function determining time-dependent field morphology produced by wave flow
F_C	Coriolis force
F_H	Frequency domain representation of high pass filter used on $H - \bar{H}$ to obtain $\widetilde{H}$
F_I	Inertial force
F_L	Lorentz force
$\mathcal{F}$	Ohmic heating norm minimised during construction of field model
$\mathbf{f}$	Functional relating data to model in inversion of field model
f	Frequency (Fourier transform partner with time t)
	Also poloidal scalar for the velocity field in spherical geometry
f_c	Coriolis parameter ($2\,\Omega \sin \lambda_{lat}$) in plane models
f_{c0}	Constant Coriolis parameter in β-plane model ($2\,\Omega \sin \lambda^*_{lat}$)
G_v	Summed absolute deviation of H from $\widehat{H}$
$\boldsymbol{g}$	Vector gravitational acceleration
$\widehat{\boldsymbol{g}}$	Unit vector in the direction of the gravitational acceleration
g	toroidal scalar for the perturbation magnetic field
g_l^m	Cosine Gauss coefficients
H	Generic time-dependent scalar field on a spherical surface
$\mathcal{H}$	Fourier transform of generic scalar field H
$\mathcal{H}_R$	Radon transform of generic scalar field H
$\bar{H}$	Time-averaged, axisymmetric part of H
$\widetilde{H}$	H with time-averaged axisymmetric part removed and high pass filtered

$\widehat{H}$	Time-averaged H
$\widehat{\widetilde{H}}$	Time-averaged $\widetilde{H}$
H^{rec}	Reconstruction of H after mask filtering in the FK domain
H_{slope}	Difference in height btw inner and outer cylinders in QG model
h	Poloidal scalar for the perturbation magnetic field
h_l^m	Sine Gauss coefficients
I	Inclination: angle between the magnetic field and the horizontal plane
I_0	Zeroth-order spherical Bessel function
i	$\sqrt{-1}$, used with imaginary numbers
$\boldsymbol{J}$	Electrical current density
J_H	Internal heating rate per unit volume
j	Axial component of the perturbation electrical current
$\mathbf{k}$	Wavevector in direction of wave propagation
k_x	Component of wavevector in the cartesian x direction
k_y	Component of wavevector in the cartesian y direction
k_z	Component of wavevector in the cartesian z direction
k	Wavenumber (Fourier transform partner with x)
	Also wavenumber of disturbance ($\frac{2\pi}{L_\lambda}$)
L	Number of spherical harmonic degrees used in representation of variables
L_{MC}	Typical length scale of MC wave disturbance in the field and flow
L_{SV}	Maximium spherical harmonic degree of secular variation
L_U	Maximium spherical harmonic degree used in expansiosn of flow scalars
L_λ	Wavelength of a general disturbance
$\mathcal{L}_1$	Linear operator premultiplying ($\widehat{\boldsymbol{z}} \times \boldsymbol{u}$) in Malkus model of hydromagnetic waves
$\mathcal{L}_2$	Linear operator premultiplying $\boldsymbol{u}$ in Malkus model of hydromagnetic waves
$\mathcal{L}^2$	Angular momentum operator (angular part of Laplacian)
l	Spherical harmonic degree
M_n	Fourth order B-spline basis functions
$\mathbf{m}$	Field model obtained by inverting observations
m	Azimuthal wavenumber (Fourier transform partner with ϕ)
	Also index for discrete points on z axis in Radon transform
	Also order of associated Legendre function P_l^m
m_c	Azimuthal wavenumber of wave at the onset of instability
N	Number of Chebyshev modes used in representation of variables
N_t	Number of discete time sample points in a time series under study
N_ϕ	Number of discete spatial sample points in a region under study
n	In context of Radon transform, is an index for discrete angles of q
$\mathcal{O}$	Order of magnitude
P	Combined mechanical and centrifugal pressures
P_0	Background pressure
P'	Perturbation pressure field
P_v	Percentage ratio of R_v to G_v, each summed over all locations
Pr	Prandtl number (see non-dimensional control parameters)
Pr_m	Magnetic Prandtl number (see non-dimensional control parameters)
P_l^m	Associated Legendre function of degree l and order m
$\mathcal{Q}$	Operator arising from double curl of momentum and induction eqns

q	Angle used in definition of Radon transform (see figure 2.4)
	Also used to represent discrete time-steps in time-stepping algorithm
R_v	Summed absolute deviations of $\widetilde{H}$ from $\widehat{\widetilde{H}}$
Ra	Rayleigh number (see non-dimensional control parameters)
Ra_c	Critical Rayleigh number marking the onset of convection
Ra_m	Modified Rayleigh number (see non-dimensional control parameters)
R_m	Magnetic Reynolds number (see non-dimensional control parameters)
R_m^{cl}	Magnetic Reynolds number used by Clark (1965)
$\widehat{\boldsymbol{r}}$	Unit vector in the radial direction in spherical geometry
r	Displacement in the radial direction
	Also denotes radial component when appears as a subscript
r_{cmb}	Core-mantle boundary radius
r_i	Inner radius of spherical shell under study
r_0	Outer radius of spherical shell under study
$\mathbf{S}$	Covariance matrix for spatial norm used in inversion for field model
S	Distribution of square of Radon transform amplitudes summed along z
s	Cylindrical radius
	Also used in method of characteristics to define position on characteristic
	Also surface poloidal scalar for flow on a spherical surface
SL	Array containing S (see previous entry) for all latitudes
$\mathbf{T}$	Covariance matrix for temporal norm used in inversion for field model
T	Temperature field
	Also flow toroidal scalar, for flow on a spherical surface
T_0	Background temperature field linearised around
∇T_0	Vector background temperature gradient
$\widehat{\nabla T_0}$	Unit vector along the background temperature gradient
T_H	Time domain representation of high pass filter used on $H - \bar{H}$ to obtain $\widetilde{H}$
T_{MC}	Typical time scale of MC wave disturbance in the field and flow
T_k	Chebyschev polynomial of degree k
t	Time
t_c	Threshold period for high-pass filter; signals slower than this are removed
$\boldsymbol{U}_0$	Background velocity field
U	Maximum amplitude of flow within prescribed wave flow
U_{rms}	Root mean square flow speed
U_{zhang}	Form of inertial wave flows on spherical boundary from Zhang et al. (2000)
$\mathcal{U}$	Typical order of fluid flow (velocity), used in scaling arguments
$\boldsymbol{u}$	Vector flow field (velocity field)
	Also perturbation to flow field after re-labelling
$\boldsymbol{u}'$	Flow perturbation
	Also flow in reference frame moving with the flow
$\boldsymbol{u}_T$	Toroidal component of flow
$\boldsymbol{u}_P$	Poloidal component of flow
u_r	Flow magntiude in the radial direction
u_θ	Flow magntiude in the meridional (southward) direction
u_ϕ	Flow magntiude in the zonal/azimuthal (eastward) direction
u_x	Flow magntitude in cartesian x direction

u_y	Flow magntitude in cartesian y direction
u_z	Flow magntitude in cartesian z direction
V	Magnetic potential
v_n	Array of azimuthal speeds derived using the Radon transform method
X	Amplitude of magnetic field in the northwards direction
$\boldsymbol{x}$	Vector of unknown expansion coefficients in magnetoconvection problem
$\widehat{\boldsymbol{x}}$	Unit vector in the direction of the cartesian x-axis
x	Spatial displacement (distance) along cartesian x-axis
	Also displacement in the eastward direction in β-plane models
Y	Amplitude of magnetic field in the eastwards direction
	Also represents spherical harmonic functions
$\widehat{\boldsymbol{y}}$	Unit vector in the direction of the cartesian y-axis
y	Spatial displacement (distance) along cartesian y-axis
Z	Amplitude of magnetic field in the radially inwards direction
$\widehat{\boldsymbol{z}}$	Unit vector in the direction of the cartesian z-axis
z	Spatial displacement along the cartesian y-axis
	Also x axis rotated by angle q when referring to the Radon transform

Non-dimensional control parameters

$E = \frac{\nu}{2\Omega d_0^2}$	Ekman number
$Pr = \frac{\nu}{\kappa}$	Prandtl Number
$Pr_m = \frac{\nu}{\eta}$	Magnetic Prandtl number
$Ra = \frac{\lvert\boldsymbol{g}\rvert \alpha \lvert\nabla T_0\rvert d_0^4}{\kappa\nu}$	Rayleigh number
$Ra_m = \frac{ERa}{Pr}$	Modified Rayleigh number
$R_m = \frac{U_{rms} d_0}{\eta}$	Magnetic Reynolds number
$R_m = \frac{U}{k\eta}$	Magnetic Reynolds number of Clark (1965)
$\Lambda = \frac{B_0^2}{2\Omega\mu\rho_0\eta}$	Elsasser number
$\beta^* = \tan\frac{H_{slope}}{D}$	Angle of sloping upper boundary in QG model

Values adopted for physical constants, relevant to Earth's core

α=1.3 $\times$ 10^{-5} K^{-1}
η=1.6 $\mathrm{m}^2\,\mathrm{s}^{-1}$
κ=8.6$\times 10^{-6}$ $\mathrm{m}^2\,\mathrm{s}^{-1}$
ν=10^{-6} $\mathrm{m}^2\,\mathrm{s}^{-1}$
ρ_0=1$\times 10^4$ $\mathrm{kg\,m}^{-3}$
μ_0=4π $\times$ 10^{-7} $\mathrm{H\,m}^{-1}$
Ω=7.29 $\times$ 10^{-5} s^{-1}
$B_0 \sim 1\times 10^{-3}$ T
$d_0 = r_{cmb} - r_i$=3485 km - 1215 km=2260 km
γ=9.8 s^{-2}
$|\nabla T_0| \sim 0.1$ $\mathrm{K\,km}^{-1}$ (superadiabatic)
(values taken from Gubbins (2000))

Abbreviations and model names

A.D.	Anno Domini (denotes year after 0 in the Christian calender)
BACK	Synthetic field evolution model derived from spectrally smoothing *gufm1*
B.C.	Before Christ (denotes years prior to 0 in the Christian calender)
CALS7K.1	Geomagnetic field model of Korte and Constable (2005): 5000B.C.—1950A.D.
CHAMP	CHAllenging Minisatellite Payload (German Earth-observing satellite)
FK	Frequency-wavenumber; refers to frequency-wavenumber power spectra
gufm1	Geomagnetic field model of Jackson et al. (2000): 1590—1990A.D.
HEMI	HEMINB with realistic background field BACK added
HEMINB	Hemispherically confined wave-like synthetic field evolution model
IGRF	International Geomagnetic reference Field
LAS	Latitude-azimuthal speed; refers to latitude-azimuthal speed power plots
MAC	Magnetic-Archimedes-Coriolis, Archimedes means buoyancy
MC	Magnetic-Coriolis
SAC-C	Scientific Applications Satellite - C (Argentine)
SPOT	Synthetic field model of drifting spot plus background field
SPOTNB	Synthetic field model of drifting spot without a background field
TL	Time-longitude; refers to time-longitude plots
WAVE	Synthetic field model of a wave plus background field
WAVENB	Synthetic field model of a wave without a background field

Conventions

S.I. units are employed throughout this thesis
Blue-Orange colour scale is used to represent radial magnetic fields
Blue-White-Red colour scale is used to represent temperature fields
Blue-Green-Red colour scale is used to represent radial and azimuthal flows

Acknowledgements

I would like first to express my gratitude to Andrew Jackson for supervising my research over the past four years. This thesis owes much to his suggestions for fruitful research ideas. During our many discussions I have benefited immensely from his deep knowledge of geomagnetism and received sound advice on a wide range of practical matters. His willingness in allowing me to pursue my own ideas and to provide constructive criticism have been particularly appreciated.

The geomagnetism group in Leeds has provided an extremely stimulating work environment during my time as a PhD student. I have learnt a great deal in discussions with David Gubbins who has always been generous with his time and been a constant source of challenging and provocative ideas. Philip Livermore's help and advice on how to survive as a research student were invaluable in my first few years. Ashley Willis has provided useful advice on numerics and dynamo related matters. Discussions with Nick Teanby and Nicola Pressling have improved my understanding of palaeomagnetism, and conversations with James While have helped illuminate the subtleties of spectral analysis. During the final six months of this thesis the advice and encouragement of Mathieu Dumberry and Nicolas Gillet have been a great help. Their efforts in proof reading are particularly appreciated. I am also indebted to Stuart Borthwick and Nick Barber for running the geophysics computer system and to the secretarial staff for administrative support.

I have benefited greatly from the generosity of those who provided me with data, models and code. Andrew Jackson provided the historical geomagnetic field model *gufm1* that was used in chapter 3 and the core flow codes that were modified in chapter 8. Monika Korte provided the archeomagnetic field model CALS7K.1 that was analysed in chapter 4. Johannes Wicht provided output from the geodynamo model MAGIC that was analysed in chapter 5. Christopher Jones and Steven Worland provided the basis of the linear magnetoconvection code that was used in chapter 7. I would also like to acknowledge the insight of Stanislav Braginsky and Raymond Hide who first suggested that waves in Earth's core might contribute to geomagnetic secular variation.

I am indebted to Emmanuel Dormy for hosting me during a three month stay in Paris during which my understanding of hydromagnetic instabilities greatly improved. The warm welcome given by Vincent Morin, Aude Chambodut and Arnaud Chulliat as well as the friendship of Ingo Wardinski during this time was much appreciated.

Financially I must acknowledge the NERC for the studentship that supported me for the first three years of my study and the EU for the Marie-Curie fellowship which funded my time in Paris.

I should also like to thank all my friends in the Earth Sciences department who have made the past four years so enjoyable. In particular I would like to mention Kristof, Lindsey, Trudi, David Green, James Wookey, James Hammond, Andy C., Dan, Bryony, Andy G., Lucy, Siska, Steve, Laura, Carlos, Simon, Tung, as well as Murray, Andy B., Dave B., Cathal, Nathan, James Cleverley and all the other regulars at the Eldon. I am especially grateful to Ian Bastow, who has shared both an office and the strains of writing up with me during the past year and somehow always managed to keep smiling.

Special thanks are due to my parents for their continuing support, and to Edith for her unfailing love and positivity.

Chapter 1

Introduction

1.1 Overview

Earth possesses a global magnetic field that shields the planet from the effects of the solar wind (Jacobs, 1974; Kivelson and Russell, 1995; Langel and Hinze, 1998). This geomagnetic field is not static, but fluctuates on a wide range of time scales from seconds to millions of years (Bloxham, 1995). Changes occurring over decades to millennia are known as geomagnetic secular variation and have their origin in motions of liquid metal in Earth's core. This thesis focuses on the mechanism behind east-west motions of the geomagnetic field and on the hypothesis that this involves hydromagnetic wave motions in the core.

In this introductory chapter the background to the thesis is given. The observed nature of Earth's magnetic field and its origin in the outer core are described. Possible core dynamics governing magnetic field evolution are discussed, with particular attention given to the wave hypothesis of geomagnetic secular variation. Finally the aims of the thesis are set out and an outline of its structure is given.

1.2 Earth's magnetic field

1.2.1 Observations of the geomagnetic field

The presence and structure of a magnetic field can be deduced by measuring the force it exerts on moving charged particles and how this varies with location. The geomagnetic field is today measured by high precision vector and scalar magnetometers (see, for examples, Forbes (1987)) in a worldwide network of geomagnetic observatories as well as by the Earth observing satellites Ørsted, CHAMP and SAC-C. The vector geomagnetic field $\mathbf{B}$ can be described by its strength in particular directions (northwards ($X = -B_\theta$), eastwards ($Y = B_\phi$) and radially inwards ($Z = -B_r$)), or by the angle between its orientation in the horizontal plane and the northward direction (declination D), the

angle between its orientation and the horizontal plane at Earth's surface (inclination I), and the total intensity of the field ($F = |\mathbf{B}| = (X^2+Y^2+Z^2)^{1/2}$). Measurements of these components made at different locations are collected and used to produce geomagnetic field models (see, for example, Langel (1987)). An example of the D and F components of the IGRF (International Geomagnetic Reference field) at Earth's surface for the year 2000 A.D. (Mandea and Macmillan, 2000) is presented in figure 1.1.

(a) Declination *D* **(b) Total intensity *F***

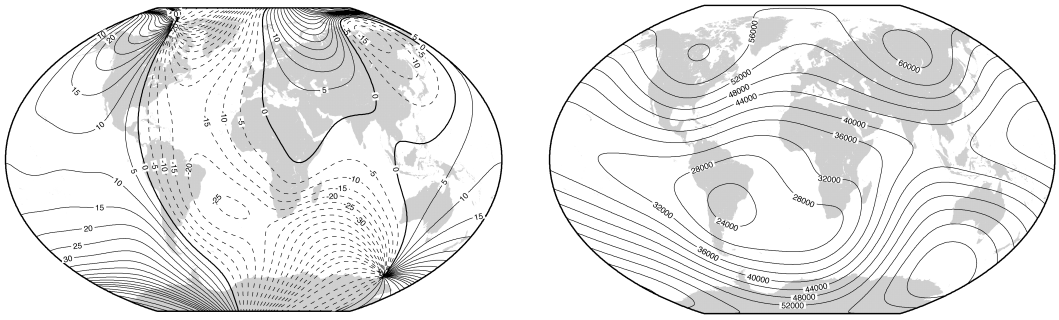

Figure 1.1: The geomagnetic field at Earth's surface in 2000 A.D.
The declination D in (a) and the total intensity F in (b) of the geomagnetic field at Earth's surface in 2000 A.D. from the eighth generation IGRF (Mandea and Macmillan, 2000). Contours of D are in degrees with dashed lines indicating negative values (magnetic north to the east of true north means positive D) while in (b) the contours of F are in nano-Tesla (nT). Plots are in Winkel's Tripel projection.

The positions of convergence of contours of D in figure 1.1a are the magnetic north and south poles indicated by navigational compasses. The high amplitude of F at high latitudes and its low amplitude at low latitudes in figure 1.1b shows the predominantly dipolar structure of the field at Earth surface. A consequence of the low F observed at South America is that solar radiation affects satellites most severely above this position. Understanding the structure of the geomagnetic field and its changes is therefore important not just from the standpoint of scientific curiosity, but also to telecommunication and other industries reliant on the operation of near-Earth satellites.

In the past 1000 years humans have made direct measurements of the geomagnetic field using a variety of techniques. The first known observations of the direction of the geomagnetic field were made by the Chinese scholar Shen Kua in 1088 A.D. (Needham, 1962) but only isolated observations were made before the 16th century when use of compasses for long maritime voyages became widespread. Carl-Fredrich Gauss (1777 A.D.— 1855 A.D.) devised a method for measuring the intensity of the geomagnetic field, stimulating the establishment of a global network of geomagnetic observatories by 1840 A.D.. Magnetic surveys of remote parts of the globe provided valuable additional measurements before true global coverage was achieved in the satellite era, most notably using vector field measurements made during the Magsat mission in 1980. Jackson et al. (2000) have constructed a time-dependent geomagnetic field model for the interval 1590

A.D. to 1990 A.D. using all suitable observations from this interval (see appendix A).

The geomagnetic field is also recorded indirectly in magnetised rocks (both igneous and sedimentary) as they form, and in pottery and ceramics as these are fired (see, for example, McElhinny and McFadden (2000)). Such paleomagnetic and archeomagnetic observations allow the behaviour of Earth's magnetic field to be studied over time scales of thousands to millions of years. Unfortunately, these sources can usually only provide information on the gross features of the geomagnetic field, because of the small numbers of records that exist at any particular time and the large uncertainties inherent in the measurements. Such observations do however indicate that Earth's global magnetic field has been present for at least the past 3.5 billion years (Hale, 1987; Layer et al., 1996) and that it has been predominantly dipolar for much of that time.

1.2.2 Geomagnetic secular variation

The geomagnetic field varies on wide range of time scales. At the highest frequency end of the spectrum are changes over seconds to days caused by the dynamic interaction between the geomagnetic field and the solar wind far above Earth's surface. These rapid external variations take place about a relatively slowly varying main (internal) field that is the focus of attention in this thesis.

On time scales of about a year, abrupt changes in the second time derivative of the field are observed in geomagnetic observatory records. These geomagnetic secular variation impulses or jerks (Courtillot et al., 1978; Courtillot and Le Mouël, 1984) are of global extent (Alexandrescu et al., 1996), and have been shown to have their origin inside the Earth (Malin and Hodder, 1982). Geomagnetic jerks are correlated with changes in the length of day (Holme and deViron, 2005) and can be explained as a superposition of rigid, axisymmetric motions of the fluid outer core known as torsional oscillations (Bloxham et al., 2002).

On time scales of centuries to millennia, undoubtedly the most obvious change in the geomagnetic field is an east-west (azimuthal) motion of contours of D. This aspect of geomagnetic secular variation is commonly referred to as 'the westward drift' because the azimuthal motion observed since the advent of systematic observations has been in the westward direction. The westward drift was noted by Halley (1692) who felt it provided evidence for motions deep within the Earth. Later this drift was quantified by Bullard et al. (1950) and Vestine and Kahle (1968) who estimated its speed to be ~ 0.2 degrees longitude per year. Bloxham et al. (1989) showed that the westward drift is not globally uniform, but is instead associated with the motion of particular field concentrations found primarily in the Atlantic hemisphere. Wardinski (2005) has recently shown that from 1980 A.D. to 2000 A.D. the westward drift had an average value of 0.11 $^\circ\mathrm{yr}^{-1}$, being significantly faster at low latitudes ($0.22^\circ\mathrm{yr}^{-1}$). The westward drift is most easily

seen by comparing maps of the declination D at Earth's surface from different epochs. Such maps from 1600 A.D. and 350 years later in 1950 A.D., constructed using the model *gufm1* of Jackson et al. (2000), are presented in figure 1.2. The agonic[1] line at the boundary between positive D (blue) and negative D (orange) has moved from the tip of South Africa in 1600 A.D. westward to South America by 1950 A.D. This azimuthal motion is a first order property of Earth's magnetic field and its origin is the subject of this thesis.

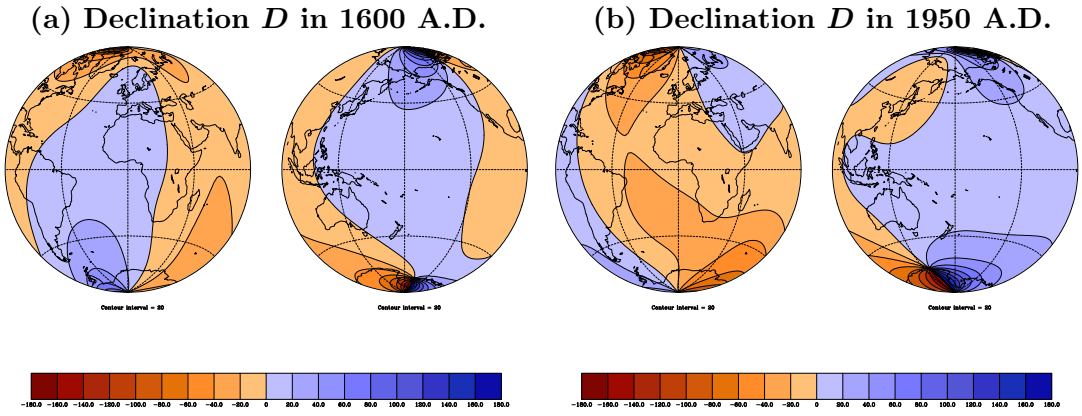

Figure 1.2: Westward drift of the geomagnetic field from 1600 to 1950 A.D. Declination D at Earth's surface in 1600 A.D. and 1950 A.D. at Earth's surface from the model *gufm1* of Jackson et al. (2000) showing the westward azimuthal motion of the geomagnetic field over a 350 year time interval. Plots are in Lambert equal area projections of the Atlantic and Pacific hemispheres.

As well as changes in the direction of the geomagnetic field, there have been striking changes in its intensity since instrumental records of the full vector field began 150 years ago. Over this time the axial dipole field strength has decreased by about 10 % at an average rate of 16nTyr^{-1} (Gubbins, 1987; Bloxham et al., 1989). The origin of this change is uncertain, but it is consistent with fluctuations in field intensity (and direction) observed in indirect archeomagnetic and paleomagnetic observations over the past 2 million years (see, for example, Valet (2003), Valet et al. (2005)). These observations suggest that the geomagnetic field is fundamentally rather unstable (Gubbins, 1999).

The most dramatic fluctuations of Earth's magnetic field are the irregular polarity reversals that have punctuated its history. During such events the axial dipole component of the geomagnetic field changes sign and the field intensity drops by up to 75 % (see, for example, Merrill and McFadden (1999)). Reversals are thought to take around 5000 to 10000 years to occur[2], which though slow on human time scales is very rapid in geological terms. The longest time scale variations associated with the geomagnetic field are modulations in the rate at which reversals occur (McFadden and Merrill, 1984; Jacobs, 1994). The most striking instance of this modulation is the existence of very long

[1] where $D = 0°$.

[2] though the time can be as short as 2000 years at low latitudes (Clement, 2004).

intervals when no polarity reversals occurred, such as the Cretaceous superchron from 120 to 83 million years ago. The link between the mechanisms producing polarity reversals and geomagnetic secular variation (including westward drift) remains unclear, but it seems likely that the underlying causes are in some way coupled (Gubbins, 1987; 1994). Studying changes in the magnetic field over the past 400 years should therefore lead to an improved understanding of the mechanisms producing field evolution over longer time scales.

1.3 Origin of the geomagnetic field in Earth's outer core

1.3.1 Internal source of the geomagnetic field

Using Gauss's mathematical theory of a magnetic field in a source free region (i.e. with no moving charged particles or electrical currents) it is possible to separate the magnetic field at Earth's surface into internal and external parts (see, for example, Langel (1987)). When this separation is carried out it is found that (except during times of geomagnetic storms induced by solar disturbances) over 97 % of the field has an internal origin (Sabaka et al., 2002; 2004). One commonly used method for finding the depth of internal field sources is to determine where the spatial power spectrum of the magnetic field ($|\mathbf{B}|^2$ versus spherical harmonic degree l) becomes flat[3]. For the large scale field this occurs at the depth when Earth's convecting, liquid outer core is reached[4]. Figure 1.3 shows the gross structure of the interior of the Earth as inferred by seismologists.

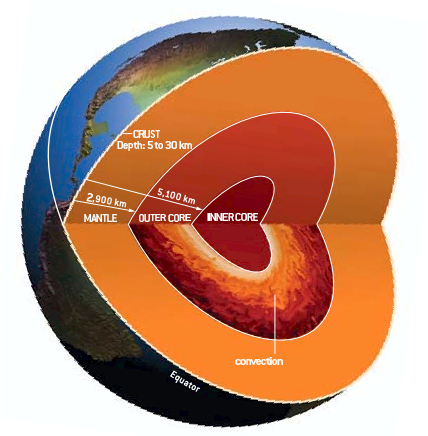

Figure 1.3: Structure of Earth's interior inferred from seismology.
Schematic picture of the interior of the Earth, showing the crust, mantle, fluid outer core and inner core. The radius of the Earth is 6123 km, the outer core begins at a radius of approximately 3485 km. Adapted from Glatzmaier and Olson (2005).

[3]The power spectrum for spherical harmonic degrees $l > 13$ is flat at Earth's surface because on length scales $<$ 3000km magnetised rocks in the lithosphere dominate the magnetic field observed there.

[4]Studies of seismic waves travelling through the solid Earth suggest the fluid outer core begins at a radius of ∼3485km from the centre of the planet (Dziewonski and Anderson, 1981).

The origin of the geomagnetic field in Earth's liquid core has been confirmed by the elegant study of Hide and Malin (1981). They were able to estimate the radius of the internal source region using geomagnetic secular variation observations. Their result agreed very well with the seismologically determined outer core radius. This study also suggested that Earth's mantle must be a rather good electrical insulator, providing justification for considering Earth's magnetic field in the mantle as a potential field. Further evidence suggesting that the mantle is a good electrical insulator comes high pressure mineral physics experiments which imply that the electrical conductivity is likely to be less than $10\,\mathrm{Sm}^{-1}$ (Shankland et al., 1993) above the mineralogically distinct D'' layer present at the base of the mantle.

Adopting this assumption that the mantle is to first order an electrical insulator, it is possible (with suitable regularisation; for a discussion of this concept see Parker (1994)) to downward continue the geomagnetic field to the edge of its generation region at the core surface. Figure 1.4 shows a contour map of the radial magnetic field B_r at the core surface in 2000 A.D. obtained by downward continuing a model constrained by observations made by the Ørsted satellite. Red colours represent regions where radial magnetic field exits the core, blue colours represent regions where radial magnetic field enters the core; the intensity of the colour indicates the concentration of field lines.

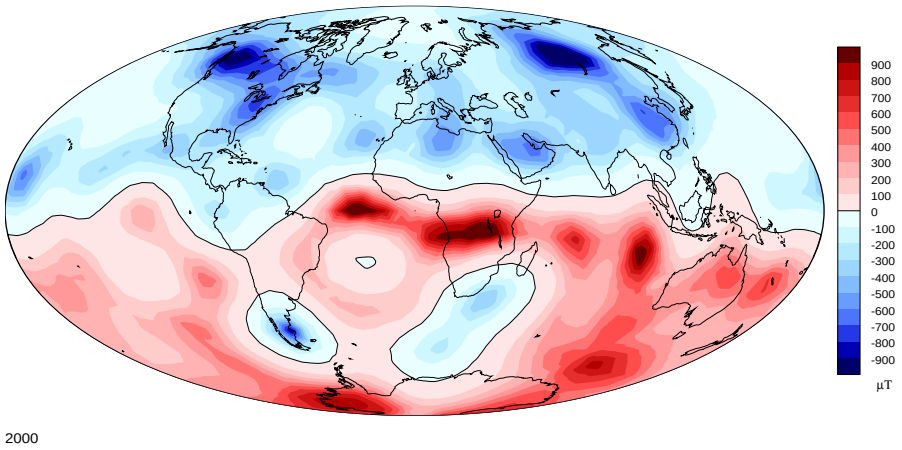

Figure 1.4: Radial magnetic field B_r at the core surface in 2000 A.D.
Using data from the Ørsted satellite, Jackson (2003) constructed this high resolution image of B_r at the core surface using a maximum entropy norm as regularisation when inverting to find a geomagnetic field model at the core surface. The map projection is Aitoff equal-area projection and the scale is in μT.

The magnetic field at the core surface is considerably more complicated than that at Earth's surface, with more small scale structure visible and the field amplitude varying between $\pm 1 \times 10^6$nT compared to $\pm$ 55000nT at Earth's surface. At high latitudes in both hemispheres (under Canada, Siberia and under the antipodal sites close to Antarctica) high amplitude field concentrations are observed. Close to the geographical equator a series of high amplitude positive B_r features are observed stretching from under the

Indian ocean through Africa and the Atlantic ocean towards South America. A similar series of high amplitude negative B_r features are found around 20°N. A pair of features whose field lines are in the opposite direction to the surrounding field (reversed flux features) are also present in the southern hemisphere, with one feature under the tip of South America being particularly prominent.

Similar maps of the magnetic field at the core surface can be constructed using historical observations from the past 400 years (the *gufm1* model of Jackson et al., 2000) and also at lower resolution using archeomagnetic, lava and lake sediment data from the past 7000 years (the CALS7K.1 model of Korte and Constable, 2005). These models show that many core surface field features are not static. This field evolution is the signature at the core surface of the geomagnetic secular variation observed at Earth's surface. At low latitudes and particularly in the Atlantic hemisphere many field features are observed to move azimuthally westwards causing the westward drift of the magnetic field observed at the surface (Bloxham et al., 1989). Equator to pole motion of reversed flux features and their simultaneous intensification is also observed, and appears to be correlated with the decay of the axial dipole moment observed at Earth's surface (Gubbins, 1987). Having mapped the magnetic field and its changes at the core surface one is led to wonder what is happening in Earth's core to generate the global magnetic field and cause the observed patterns of field evolution.

1.3.2 Physical properties of the outer core

Earth's core is the most inaccessible part of the planet. It can only be probed remotely using seismology, gravity and magnetic fields, and using inferences from its rotational properties. Geochemists attempt to determine its composition by comparing chondritic meteorite compositions to the known compositions of the crust and mantle (the core being the missing link), while mineral physicists perform high pressure, high temperature, experiments and quantum mechanical calculations to determine the likely properties of materials located there. From these various approaches a consistent picture of conditions in Earth's core is beginning to emerge.

The outer core is believed to consist primarily of liquid iron (or perhaps an iron-nickel alloy) with approximately 10 % of its composition being due to light elements (Birch, 1964; Masters and Shearer, 1990). The light elements are thought to be either silicon, sulphur, or oxygen (Allègre et al., 1995). Carbon, hydrogen and potassium may also be present in smaller quantities (McDonough and Sun, 1995). The pressure at the boundary between the inner and outer core is estimated to be approximately 330GPa and the temperature there is thought to be approximately 5600K (Alfé et al., 2002). Under these conditions the liquid iron in the outer core is expected to have a low viscosity comparable to that of water at room pressure and temperature (Poirier, 1994; de Wijs et al., 1998) and to be an excellent electrical conductor (Secco and Schloessin, 1989;

Poirier, 1994).

1.3.3 Energy sources and core motions

The liquid iron in Earth's core is thought to be undergoing vigorous motion. On short time scales of hours to days disturbances driven by core-mantle coupling and tidal forcing will produce a broad spectrum of internal gravity and inertial waves (Aldridge, 2003). It has been suggested that precessional and tidal strains could produce instabilities leading to large amplitude flows in the core (Malkus, 1994). On longer time scales the presence of a variety of energy sources suggests that convection is occurring in the outer core. These energy sources include secular cooling of the core in the aftermath of planetary formation, release of latent heat and buoyant light material at the inner-core boundary as the inner core solidifies, and radioactive heating (see, for example, Gubbins et al. (2003; 2004); Roberts et al. (2003)).

Due to the very low viscosity of liquid iron in the core, vigorous convective motions are expected to be dominated by the influence of the Coriolis forces (a consequence of planetary rotation) and the strong magnetic fields present there. Nonlinear interactions between flow, magnetic and buoyancy fields will produce complex, time-dependent flow patterns. The presence of magnetic fields in an electrically conducting fluid also permits a class of fluid motions known as hydromagnetic waves. These arise because the distortion of magnetic fields by fluid motion produces a magnetic (Lorentz) force opposing that distortion. In combination with fluid inertia this magnetic restoring force leads to transverse wave motions (Alfvén, 1942). The form of these hydromagnetic waves will be strongly influenced by rapid rotation (Lehnert, 1954), unstable stratification (Braginsky, 1964), and spherical geometry (Hide, 1966) all of which are thought to be important in Earth's outer core.

1.3.4 The geodynamo mechanism

The generation of the geomagnetic field in Earth's core is now fairly well understood thanks in particular to recent advances in computational modelling (see, for example, Roberts and Glatzmaier (2000a)). The high temperatures in the core and the time-dependence of the observed field rule out an explanation in terms of permanent magnetism. Instead, a mechanism producing a rapidly evolving, self-sustaining, magnetic field is required. A dynamo explanation is the only reasonable candidate for such a mechanism (see, for example, Gubbins and Masters (1979)). A dynamo is a system that converts kinetic energy into magnetic energy by motional induction given some initial seed magnetic field (Roberts, 1994). Motions of electrically conducting fluid in Earth's core moving through a weak pre-existing magnetic field (e.g. the inter-planetary magnetic field) will generate electrical currents. These electrical currents produce magnetic

fields and, if the fluid flows are in a suitable configuration, these will reinforce the existing magnetic field leading eventually to a much stronger field. Fluid motions in Earth's core that will be strongly affected by rotation appear ideally suited to act as a dynamo, in what is referred to as the geodynamo mechanism. In the next few paragraphs the history of attempts to model the geodynamo will be outlined.

Larmor (1919) was the first to propose the idea that a self-exciting dynamo mechanism could be responsible for Earth's magnetic field. Cowling (1934) dealt the proposal a blow by proving that purely axisymmetric magnetic fields could not act as a dynamo, but Elsasser (1946) and Bullard (1949) showed that Earth's magnetic field could evade Cowling's theorem by virtue of its observed non-axisymmetry. Bullard and Gellman (1954) developed a formalism for solving the equations of magnetic induction which proved useful for numerical computation and which permitted the demonstration of whether specified flows would produce dynamo action (kinematic dynamo theory). The existence of dynamo action in a sphere was finally proven by Herzenberg (1958) and Backus (1958), though both employed rather unrealistic flows. Kinematic dynamo theory has become a useful tool in efforts to understand magnetic field generation and reversal mechanisms. Recent work has focused on flows likely to arise from convection. Systematic parameter regime investigations of 3D kinematic dynamos have now been carried out (see, for example, Gubbins et al. (2000)).

The first numerical models of the geodynamo to self-consistently incorporate buoyancy driven flows and magnetic field generation taking into account all couplings and feedbacks in a 3D spherical geometry were independently produced by Glatzmaier and Roberts (1995) and Kageyama et al. (1995). Various groups have since developed similar models (Christensen et al., 2001). These models have been remarkably successful in reproducing Earth-like magnetic field features such as dipole domination, reasonable field intensity, drifting field concentrations at the core surface and even reversals. Unfortunately, these models are operating in a dynamical regime remote from that expected in the core — their rotation rates are too slow and turbulent effects are often included in a rather ad-hoc manner (Jones, 2000). It is therefore difficult to judge if the success of such models is merely a coincidence, or whether Earth-like behaviour becomes inevitable once there is the correct representation of spherical shell geometry, convection and the size ordering of the forces (magnetic, buoyancy and Coriolis similar magnitude, inertial and viscous weaker). To evaluate the success of these models and to decide which of the various methods is to be preferred, quantitative comparisons to both geomagnetic and paleomagnetic observations are of paramount importance (see, for example, Dormy et al. (2000) or Kono and Roberts (2003)).

One weakness of such computationally demanding numerical dynamo models is that they are extremely complex. Whilst they produce Earth-like behaviour, so many processes are interacting that it becomes hard to isolate the basic mechanisms of interest. It is therefore

important that investigations of simpler models of particular aspects of magnetic field generation and evolution are carried out as was advocated by Hide (2000).

1.3.5 Causes of geomagnetic secular variation, flow at the core surface and changes in the length of day

Within the framework of the geodynamo mechanism, core motions and magnetic diffusion are the origin of the slow changes observed in Earth's magnetic field. The patterns of B_r observed at the core surface can be altered by core motions both when new B_r is produced by the distortion of toroidal magnetic field lines (those contained entirely within the core), or when motions close to the core surface rearrange pre-existing B_r.

Most recent quantitative attempts to interpret geomagnetic secular variation have focused on the latter process. Following Roberts and Scott (1965) it can be assumed that, on time scales much shorter than the magnetic diffusion time scale, field evolution is entirely a result of frozen flux advection (for an introduction to this assumption see Moffatt, (1978) or Davidson, (2001) while Love, (1999) discusses its limitations). Adopting the frozen-flux approximation along with an additional dynamical constraint one can invert from geomagnetic secular variation to obtain a regularised solution for the flow at the core surface that is capable of rearranging B_r to produce the observed changes in B_r. Various dynamical constraints have been used for this purpose including steady flow (Voorhies and Backus, 1985), steady flow in a drifting reference frame (Holme and Whaler, 2001), tangentially geostrophic flow[5](LeMouël, 1984) and toroidal flow[6] (Lloyd and Gubbins, 1990). An example of the result of a time dependent core flow inversion over the interval 1840 A.D. to 1990 A.D. (using a tangential geostrophy dynamical constraint) from Jackson (1997) is presented in figure 1.5.

Noteworthy features include the circulations under the southern Atlantic ocean, the weak eastward flow under the Indian ocean, oscillatory motions at low latitudes especially under Indonesia, and the predominantly westward flow near the equator under the Atlantic ocean. Interpretations of geomagnetic secular variation based on core flow inversions ascribe the westward motion of magnetic field features in the Atlantic hemisphere to advection by these low latitude flows (see, for example, (Bloxham and Jackson, 1991)).

Evidence for the reliability of the time-dependent, axisymmetric part of the flows obtained by inverting geomagnetic secular variation comes from changes in the rotation rate of Earth (referred to as changes in the length of day). Jault et al. (1988) and Jackson et al. (1993) demonstrated that changes in the length of day in the 20th century could be accounted for by considering the conservation of angular momentum of the

[5]when magnetic forces are neglected to first order and the tangential component of the Coriolis force balances tangential pressure gradients at the core surface.

[6]when fluid motions are purely tangential and there is no fluid upwelling or downwelling.

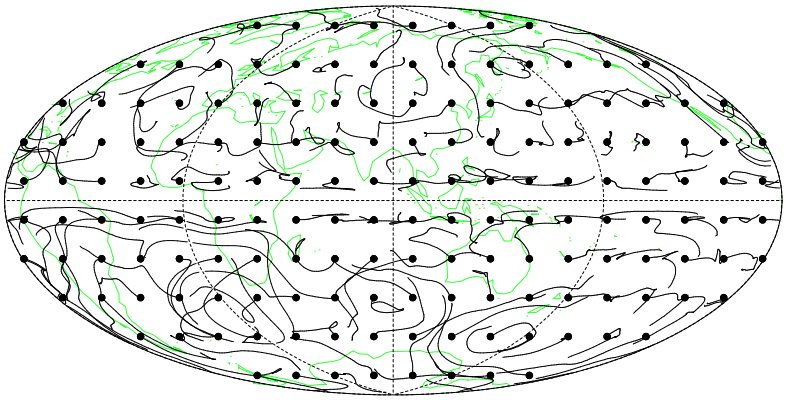

Figure 1.5: Flow at the core surface from 1840 to 1990 A.D.
Result from Jackson (1997) of a time-dependent, tangentially geostrophic, weakly regularised core flow inversion covering the interval 1840 A.D. to 1990 A.D.. The dots show initial positions of fluid particles in 1840 A.D. and the lines the subsequent motion of these particles over the next 150 years.

core-mantle system. Core angular momentum was calculated from the time-dependent, axisymmetric component of tangentially geostrophic core flow inversions, assuming that these flows were invariant on cylindrical surfaces within the core[7].

The dynamical mechanism underlying the coupling between the core and the mantle has proven difficult to pin down. Topographic features (bumps) at the core-mantle boundary would produce pressure gradients that could produce the required coupling (Hide, 1967; 1989; Jault and LeMouël, 1989) though this remains controversial (Kuang and Bloxham, 1993; Kuang and Chao, 2001). Electromagnetic core-mantle coupling could produce the required torque provided that a thin, highly electrical conducting layer exists at the base of the mantle (Holme, 1998a;b; 2000). Alternatively, gravitational coupling between the mantle and the inner core (Buffett, 1996a;b; Buffett and Glatzmaier, 2000) could be the important mechanism provided that the viscosity of the inner core is not too low (Buffett, 1997). Recent studies (Mound and Buffett, 2003; 2005) suggest that a combination of gravitational coupling along with electromagnetic coupling is the most plausible scenario, though there have also been indications that viscous coupling could be important (Brito et al., 2004) due to the turbulent nature of flow in the core.

Despite the success of correlations between the time-dependent axisymmetric component of the inferred core flows and changes in the length of the day, doubts remain about whether such inversions also successfully model the origin of other components of geomagnetic secular variation. By studying inversion of known flows in geodynamo models,

[7]Normal modes of such rigid, almost geostrophic, time-dependent, axisymmetric flows called torsional oscillations were first described by Braginsky (1970). Dynamical considerations suggest torsional oscillations should exist in Earth's core (Taylor, 1963; Bloxham, 1998) and they are capable of explaining geomagnetic jerks (Bloxham et al., 2002).

Rau et al. (2000) have demonstrated that the retrieved flows can contain spurious features, especially at low latitudes where wave propagation can be incorrectly interpreted as intense azimuthal flow. The role and extent of field evolution mechanisms involving expulsion and magnetic diffusion (Allan and Bullard, 1966; Bloxham, 1986; Gubbins, 1996) is difficult to quantify, but such processes seem likely to be important for explaining episodes of growth and decay of field features at the core surface (Bloxham and Gubbins, 1986; Gubbins, 1987).

Most importantly for this thesis, interpretations of geomagnetic secular variation based on core surface inversions do not take into account the role that hydromagnetic waves could play in producing drifting patterns of B_r at the core surface. In order to place any confidence in the results of core flow inversions (particularly at low latitudes) the influence of hydromagnetic waves in Earth's core on geomagnetic secular variation must be understood.

1.4 Hydromagnetic waves in the core and geomagnetic secular variation

1.4.1 An example of a hydromagnetic wave in the core and its possible effects

Hydromagnetic waves are propagating disturbances that exist in electrically conducting fluids permeated by magnetic fields as a result of the elasticity endowed to the fluid by the presence of a strong magnetic field[8]. In a rapidly rotating fluid these waves can operate on very slow time scales if the Coriolis force acts to balance the magnetic restoring force. In Earth's core such waves could arise either as a free oscillation in response to perturbation (for example by boundary topography) or as a manifestation of instability either in the flow, in the magnetic field or in the density field.

The magnetic field in Earth's core is thought to have a strong azimuthal component (Roberts, 1978). Hydromagnetic waves would result from the distortion of this field. The flow pattern associated with these waves would probably be columnar in structure because of the influence of strong Coriolis forces on fluid motions. The wave and its signature, a spatially coherent pattern of disturbance in the magnetic field and in the flow, would propagate azimuthally following the magnetic field line[9]. Figure 1.6 is a schematic depiction of the form such a hydromagnetic wave might take in Earth's core.

The distortion of the magnetic field inside the core will have a radial component that will be visible as a regular perturbation of B_r at the core surface. The wave flow pattern will also rearrange pre-existing B_r at the core surface. These spatially coherent patterns of B_r will then move along with the wave in the core generating geomagnetic secular

[8] In this thesis, the term 'hydromagnetic wave' is used to describe a wave mechanism involving both fluid motions and magnetic fields. The mechanism underlying hydromagnetic waves in Earth's core may also involve the effects of rotation, buoyancy forces, and spherical geometry (see chapter 6).

[9] Hydromagnetic waves can arise due to the distortion of a magnetic field line of any orientation, so are not in general restricted to travel azimuthally.

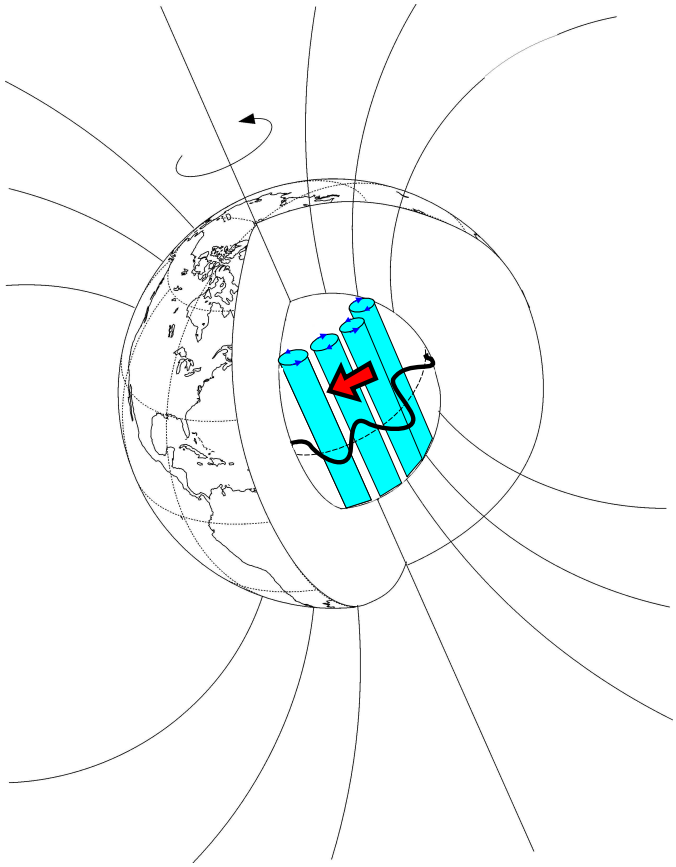

Figure 1.6: A possible hydromagnetic wave in Earth's core.
Thin black lines represent the observed magnetic field lines outside Earth's core, the thick black line represents a distorted azimuthal magnetic field line in the core, with the blue columns representing the concomitant hydromagnetic wave flow. The red arrow shows a possible propagation direction for the hydromagnetic wave.

variation which would be observed at Earth's surface.

This hypothetical, qualitative, scenario suggests that the idea of hydromagnetic waves in Earth's core producing changes in Earth's magnetic field merits further investigation.

1.4.2 Previous studies linking hydromagnetic waves and geomagnetic secular variation

The hypothesis that hydromagnetic waves in Earth's core might influence the geomagnetic field is not new. Braginsky (1964) was the first to suggest a link between hydromagnetic waves and geomagnetic secular variation, while Hide (1966) made a similar suggestion but also including the effect of spherical geometry on such waves. Both Hide and later Braginsky attempted to compare the predictions of simple hydromagnetic wave theories to available observations of geomagnetic secular variation.

Hide (1966) identified three major factors in favour of the wave hypothesis: (i) hydromagnetic waves modified by rotation could have periods comparable with the time scale

of geomagnetic secular variation; (ii) such waves could have dispersion times comparable with the time scale of geomagnetic secular variation; (iii) such waves could have dispersion characteristics (shorter wavelengths travelling faster) compatible with geomagnetic secular variation. His observational analysis was based on the mean westward drift rates of spherical harmonics up to degree 4 (from seven previous publications spanning 135 years from 1830 to 1965). Despite the failure of detailed comparisons between the predicted and observed drift rates for individual spherical harmonics, Hide's study was instrumental in persuading many geophysicists that a hydromagnetic wave origin for geomagnetic secular variation was a viable proposition.

Braginsky (1967;1972;1974) sought to confirm the wave hypothesis by comparing his own theoretical predictions of the spectrum of diffusionless, convection-driven hydromagnetic waves in a rapidly rotating fluid (he called these MAC or Magnetic Archimedes Coriolis waves) to an observationally inferred spectrum of geomagnetic secular variation. The observational spectrum was determined by fitting a superposition of stationary fields and azimuthally travelling waves to time series of geomagnetic field spherical harmonic coefficients up to degree and order 2, inferred from a selection of historical and archeomagnetic data covering the past 2000 years. A reasonable fit of the model to the data was found to be possible using travelling waves with periods of 1560, 1040, 780, and 520 years. Unfortunately, the reliability and internal consistency of the observations used in these studies is questionable, as was the strategy of determining model parameters by simple least squares fitting to incomplete data with large (and uncertain) errors. However, given the poor quality of data available in the early 1970's, Braginsky's efforts were important in demonstrating that the hydromagnetic wave hypothesis was compatible with observations.

Since the studies of Hide and Braginsky there has been no concerted effort to re-evaluate the worth of the wave hypothesis of geomagnetic secular variation. The past 30 years has seen significant advances in observational knowledge of Earth's magnetic field and its evolution, as well as in the ability to model the geodynamo and core dynamics including hydromagnetic waves. This thesis attempts to utilise these advances to provide a contemporary perspective on the issue of hydromagnetic waves as a source of geomagnetic secular variation. This study therefore has implications for both our understanding of azimuthal motions of the geomagnetic field and for core dynamics on time scales of centuries to millennia.

1.5 Thesis aims and structure

The aim of this thesis is to answer in as rigorous a manner as possible the following questions regarding hydromagnetic waves in Earth's core and their influence on geomagnetic secular variation.

(i) Can hydromagnetic waves exist in Earth's outer core?

(ii) What would be the properties of hydromagnetic waves in Earth's core?

(iii) How would hydromagnetic waves in the core influence the evolution of B_r at the core surface and hence geomagnetic secular variation?

(iv) Is there any evidence supporting the existence of hydromagnetic waves in Earth's outer core?

(v) Can study of such wave motions shed any light on the origin of apparent hemispherical differences in secular variation?

The structure of this thesis does not follow the logical sequence suggested by these questions. The rationale behind this decision is that in geophysics observations are the fundamental knowledge which are subsequently interpreted from a theoretical standpoint. The first half of the thesis is therefore devoted to analysis of models of the evolution of the geomagnetic field derived from observations and to the analysis of similar results from dynamo simulations. Having established the observational facts and their possible limitations, the second half of the thesis concentrates on theoretical models of hydromagnetic waves and investigates how these could influence the evolution of B_r at the core surface. Each chapter focuses on a particular issue and is designed to address this in a rigorous manner.

The thesis begins in chapter 2 by describing the development and testing of a suite of techniques for analysing the evolution of scalar fields on a spherical surface. These methods are applied to the historical geomagnetic field model *gufm1* in chapter 3, to the archeomagnetic field model CALS7K.1 in chapter 4 and to output from two convection-driven geodynamo models in chapter 5. In chapter 6 a review of previous theoretical studies of hydromagnetic waves in a rapidly rotating fluid is presented. Chapter 7 documents the parameter dependence of simple, convection-driven, hydromagnetic waves in a sphere and chapter 8 investigates the possible effects of wave flows on B_r at the core surface. In chapter 9 a scenario is proposed which is consistent with both theory and observations. On this basis answers to the questions posed in this introduction are given. The work carried out and major conclusions of the thesis are summarised, and finally proposals for possible future tests of this scenario are suggested.

Chapter 2

A space-time processing and spectral analysis methodology

2.1 Overview

The traditional approach to characterising the spatial and temporal evolution of Earth's magnetic field has been to study the time dependence of the coefficients of the spherical harmonic representation of the field (see, for example, Langel, 1987, Yokoyama and Yukutake, 1991 and Backus et al., 1996). For construction of instantaneous models of the magnetic field at the planet's surface a spherical harmonic representation is both mathematically expedient and physically sensible, allowing an efficient representation of a potential field satisfying Laplace's equation in spherical geometry (see appendix A). Unfortunately, the fluid motions in Earth's core and the concomitant patterns of change produced in the magnetic field at the core surface do not satisfy Laplace's equation. It is therefore unlikely that an analysis of field evolution based on a spherical harmonic representation will be the best method to gain insight into the mechanisms producing geomagnetic secular variation.

This thesis is concerned with determining whether changes in Earth's magnetic field could be caused by hydromagnetic wave propagation in the outer core. Waves in other planetary scale rotating fluids, especially the atmosphere and the ocean, have been intensively studied for many years (see, for example, the recent studies by Chelton and Schlax, (1996); Wheeler and Kiladis, (1999); Hill et al., (2000)). Successful identification and characterisation of wave motions has been achieved by studying the space-time properties of tracer fields on geographically localised grids. This method is a useful alternative to analysis based on global expansion coefficients. It has the advantage of not requiring the summation of many modes in order to represent geographically localised wave motions.

In this chapter space-time processing and spectral analysis techniques used extensively in later chapters are described in detail and tested on synthetic models. The construction

and interpretation of time-longitude plots, frequency-wavenumber power spectra, and of Radon transform methods is described. The use of such methods in meteorology and oceanography is discussed in order to illustrate how they can aid identification of wave motions in tracer fields. Removal of the time averaged axisymmetric and very long period field components is described and justified. Finally use of these tools to investigate geographic variations in the azimuthal speed of field features and the use of frequency-wavenumber filtering to isolate signals of interest is described and illustrated on the synthetic models.

2.2 Visualisation and analysis techniques

2.2.1 Griding models in space and time

The starting point for all the analysis techniques is the generation of a discrete, regular grid of scalar field values (a generic scalar field called H is used as the basis for the discussions in this chapter). Grid points are located over the entire spherical surface (from 0 to 360 degrees longitude and from -90 to +90 degrees latitude). The data set is then sampled at discrete times at each of these grid points. The grid spacing is chosen to be 2 degrees in latitude and longitude, while the spacing in time depends on the temporal resolution and time scale of dynamics of interest (for example, it is chosen to be 2 years when studying the historical geomagnetic field model *gufm1*). Although this form of spatial griding is not optimal at high latitudes, it is suitable for studying field motions at low to mid-latitudes. Models of the scalar field studied typically initially consist of time-dependent spherical harmonic coefficients that are substituted into spherical harmonic expansions to generate the scalar field $H(\theta_i, \phi_j, t_k)$ at the required grid points.

2.2.2 Construction and interpretation of time-longitude (TL) plots

The longitude, latitude, time dataset that results from the regular griding procedure can be thought of as a data cuboid. This cuboid can be sectioned and processed in whatever manner leads to the clearest, most insightful, visualisation of H. Latitude-longitude maps at a particular epoch are one example of a section through the data cuboid. Another section, previously rather neglected by geomagnetists (though see Kono et al. (2000)), is a time-longitude (TL) section at a particular latitude. Construction of a TL plot from maps of a scalar field H on a spherical surface is illustrated schematically in figure 2.1.

Examination of the evolution of the radial magnetic field B_r at the core surface and of the evolution of magnetic fields and flows in geodynamo models close to the outer boundary indicates that many non-axisymmetric features often move approximately azimuthally perpendicular to the rotation axis. A consequence of the dominance of azimuthal motions is that TL sections can be used to characterise accurately the evolution

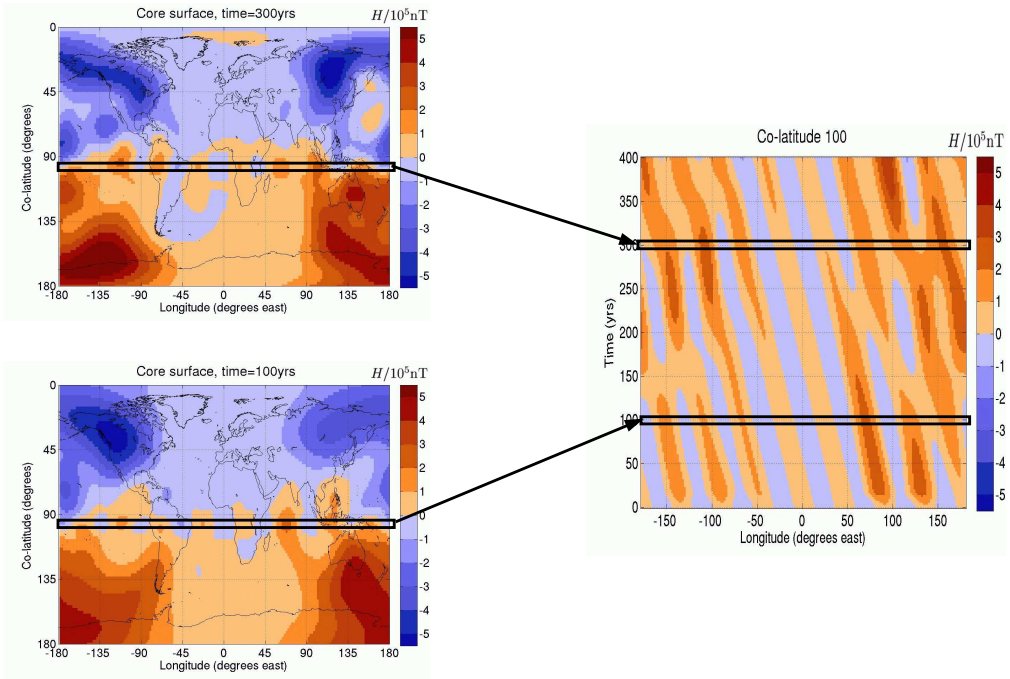

Figure 2.1: Relation of latitude-longitude maps to time-longitude(TL) plots. Field values at all gridded longitudes at a chosen latitude (10°S here) are taken from latitude-longitude maps at each discrete time interval to construct time-longitude plots at the chosen latitude (the equator in this example).

of non-axisymmetric field features.

Hovmöller (1949) was the first to employ the technique of using TL plots to study wave motions in a planetary scale rotating fluid. He considered the height of the 500 mb pressure level as a tracer field of atmospheric motions. The resulting TL plot is reproduced in figure 2.2a. He visually determined the azimuthal phase speed of field motions by following the position of crests and troughs[1] (see, for example, the dashed lines in figure 2.2a). He inferred an azimuthal group speed by following the path of transmission of energy (proportional to squared field amplitude) by identifying paths along which field maxima and minima are consistently observed (see the solid lines in figure 2.2a). He used these observations to test whether the motions were consistent with Rossby's theory of planetary waves[2] in the atmosphere (Rossby, 1939), concluding this was the case.

[1] A more sophisticated way to determine phase speeds, especially useful when energy is present over a range of frequencies and wavenumbers, is to filter so that only a single frequency component or wavenumber component remains. The azimuthal speed of these features is then the azimuthal phase speed associated with that frequency. By performing this procedure over a range of frequencies or wavenumbers, the dispersion (frequency versus wavenumber) characteristics of the field motion can be determined. Azimuthal group speeds associated with the speed of transmission of energy are often determined by following peaks of the square of the field amplitude.

[2] Planetary (or Rossby) waves are large scale, slowly propagating, waves found in rotating fluids. Their existence is a consequence of the restoring force that arises due to the variation of the Coriolis force with latitude. Readers unfamiliar with these waves should consult Andrews (2000) for an accessible introductory account.

(a) TL plot from Hovmöller (1949) showing field motions indicative of waves in the 500mb pressure level of geopotential height

(b) TL plot from Chelton et al. (2003) showing field motions indicative of waves in filtered sea surface height anomalies

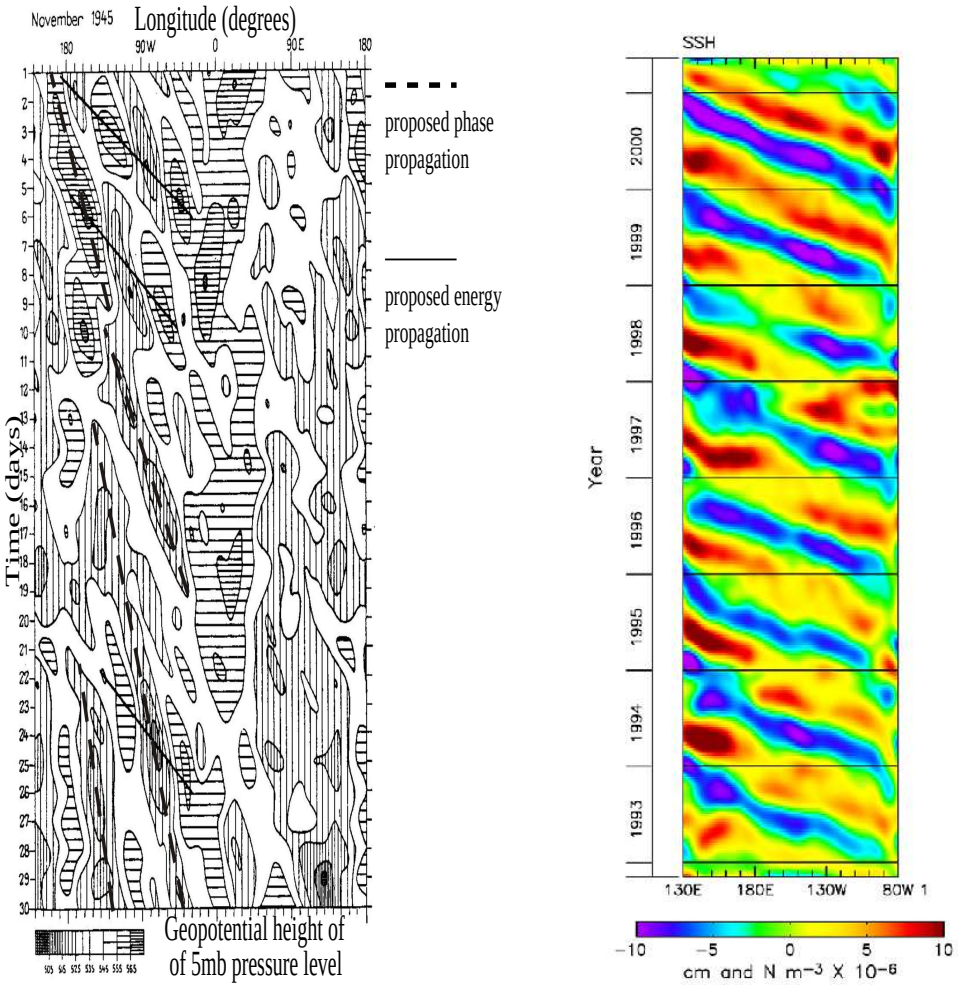

Figure 2.2: Time-longitude (TL) plots from meteorology and oceanography. (a) Shows the first published time-longitude (TL) plot from Hovmöller (1949) where contours of the geopotential height (the work required to raise a unit mass from sea level to a certain height, divided by the global average of gravity at sea level) of the 500mb pressure level averaged over latitudes 35 to 55°N were plotted for all longitudes during November 1945. Following the motion of crests and troughs (dashed lines), the azimuthal phase speeds were estimated while following the path of energy transmission (solid lines) enabled the azimuthal group velocity to be estimated. (b) Shows a recent identification by Chelton et al. (2003) of oceanic Rossby waves in a time-longitude (TL) plot of sea surface height anomalies at latitude 5.5°N and longitudes 130°E to 80°W (Pacific basin). The data were derived from 8.5 years (1992 to 2001) of observations collected by the TOPEX/POSEIDON satellite and high pass filtered to remove long term trends.

The era of global satellite observation has stimulated similar studies of planetary Rossby waves in oceanography. Examples of the use of TL plots to infer the presence of azimuthally travelling oceanic Rossby waves can be found in studies of sea surface height anomalies (Boulanger and Menkes, 1999; Chelton and Schlax, 1996; Chelton et al., 2003; Cipollini et al., 1997); sea surface temperatures (Cipollini et al., 1997; Hill et al., 2000; Sutton and Allen, 1997); and even ocean colour (chlorophyll concentrations can be enhanced or weakened by the Rossby waves causing meridional displacements of water across chlorophyll gradients (Cipollini et al., 2001; Mete Uz et al., 2001; Quartly et al., 2003)). A TL plot of sea surface height (SSH) anomalies showing the spatially and temporally coherent azimuthal motions indicative of oceanic Rossby waves from Chelton et al.(2003) is reproduced in figure 2.2b.

It is important to emphasise that sequences of azimuthally travelling field anomalies in TL plots are not a unique signature of wave propagation. Any mechanism that generates a series of spatially coherent highs and lows in a tracer field and is subsequently azimuthally advected in a temporally coherent way is an equally consistent explanation of the observations. However, in circumstances where azimuthal flows are unlikely, a wave explanation is the simplest and most parsimonious explanation.

2.2.3 Construction and interpretation of frequency-wavenumber (FK) power spectra

Frequency-wavenumber (FK) power spectra of TL plots are an indispensable tool for quantifying properties of azimuthal field motions. In this section, the construction of FK power spectra, their previous use by meteorologists and the interpretation of such spectra is discussed. An example of how FK power spectra can aid comparison to theory is shown in figure 2.3. This example comes from the recent study by Wheeler and Kiladis (1999) of wave motions of the equatorial troposphere observed in long wavelength radiation measurements.

Space-time spectral studies were pioneered in the meteorological literature, motivated by a desire to test the predictions of analytical wave theory against high quality observations and results from numerical simulations. The techniques were developed in studies of high resolution space-time data generated by early general circulation models (Hayashi, 1974), and later in studies of models including assimilated observational data (Hayashi, 1974; Hayashi and Golder, 1986; 1994). More recently, the availability of high quality satellite data with global coverage has made it possible to perform such analyses directly on observational data (Wheeler and Kiladis, 1999). In all such studies the approach is to identify prominent peaks in the FK power spectrum and then to associate these peaks with particular mechanisms of azimuthal field evolution.

Practically, constructing FK power spectra involves computing the two dimensional, discrete Fourier transform of an array of time-longitude data taken from a scalar field

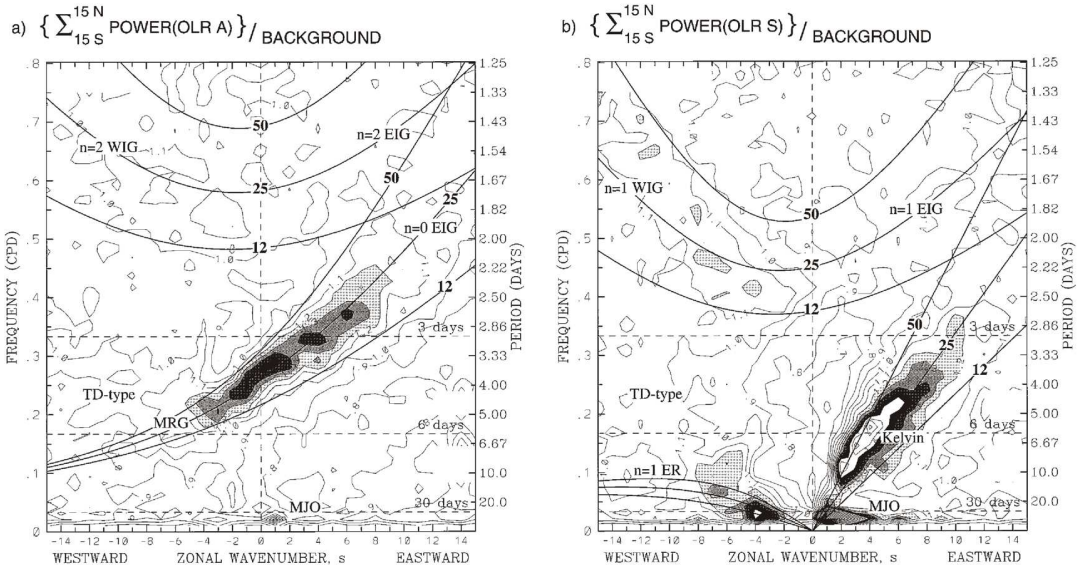

Figure 2.3: Example of frequency-wavenumber (FK) power spectra. Observations from satellite long wavelength radiation measurements are re-gridded into TL plots, and separated into motions symmetric and anti-symmetric about the equator. A 2D FFT is used to transform to FK space and spectra are stacked from 15°N to 15°S, then divided by a smoothed background spectrum. Contours of the resulting power are plotted. Superimposed are the dispersion curves for modes of equatorial waves with three three layer depths of 12, 25 and 50 metres. Equatorially axisymmetric power is plotted in (a), while symmetric power is plotted in (b). (from Wheeler and Kiladis, 1999)

model evaluated at a particular latitude on a specified spherical surface. First, the one dimensional FFT (Fast Fourier Transform) is taken of columns of the data array where each column contains a time series of the field at a sampled longitude. The resulting array is then subjected to a second FFT, this time across the rows where each row contains a longitude section at a particular time. Considerable care must be taken to keep track of the index transformations involved in the FFT (for more details see Press et al. (1992)). Having computed from the field $H(x,t)$ the two dimensional Fourier spectrum $\mathcal{H}(k,f)$, the magnitude of the Fourier coefficients defines the Fourier amplitude spectrum, while the magnitude squared ($|\mathcal{H}|^2$) defines the Fourier power spectra.

In order to prevent ringing effects (where sharp edges at the start and end of the original time series cannot be accurately represented by a finite number of Fourier coefficients so spectral power leaks into coefficients that would otherwise be zero) both the start and end of the time series are tapered using a cosine function, typically over a length of 10 sample points. This degrades the information at the start and end of the time series, but makes the spectral representation more accurate[3].

[3]In principle this degradation can be minimised by use of multi-taper methods (Percival and Walden, 1993), though application of such techniques to two dimensional data is non-trivial (Simons et al., 2005).

The resolution limit of any discrete Fourier spectra arises because of the finite length of the data series being analysed (see, for example, Priestley (1981)). In two dimensions this means that frequency resolution is fundamentally limited to $\Delta f = 1/N_t\Delta t$ where $N_t\Delta t$ is the total timespan of the record while wavenumber resolution is limited to $\Delta k = 1/N_\phi\Delta\phi$ where $N_\phi\Delta\phi$ is the total longitude sampled. So for example, with a time series of length 400 years, frequency space is sampled every 0.0025 cycles per year and it is difficult to extract reliable information concerning signals that have power between for 0 and 0.0025 cycles per year. Similarly for the full span of 360 degrees of longitude, sampling in wavenumber space will be 1/360 or 0.00277 degrees^{-1}. This corresponds to a resolution in azimuthal wavenumber of $\Delta m = \frac{360}{\Delta k}$=1) indicating (as expected) that only information concerning integer angular wavenumbers is possible.

Fortunately, the interpretation of spectra can be aided by artificially increasing the number of sample points in the record by adding zeros to the start and end of the record. This method of zero-padding does not add any new information, but permits interpolation of an originally coarsely discretized spectra greatly aiding interpretation (Gubbins, 2004). In the present application, the 2D gridded data are zero-padded in time but not in space. This is because the longitude representation is periodic (start and end points represent the same point in physical space)and adding zeros simply destroys this desirable periodicity. Interpretation is in practise carried out using interpolated contour plots of the zero-padded FK power spectra. These permit visual identification of prominent spectral peaks.

The FK spectra presented in this thesis display both positive and negative wavenumbers corresponding to signals travelling eastwards ($+k$) and westwards ($-k$) respectively. The 2D FFT returns the spectral coefficients for both positive and negative wavenumbers (k) and frequencies (f), but because the signal we are studying is real there is a symmetry between signals at (k, f) and ($-k$,$-f$), so all the information is present in the $+f$ half-plane that is plotted.

When interpreting FK power spectra it is useful to recall the FK signatures produced by particular patterns of interest in real space. Isolated, azimuthally moving field features in TL plots that move at an azimuthal speed c_{az} will produce a series of peaks in the FK power spectra along the line $f = c_{az}k$. This is because an isolated azimuthally moving field feature in real space can only be constructed from a sum over many wavenumbers and frequencies. In contrast, an idealised monochromatic wave consisting of a spatially coherent wave-like pattern of field anomalies travelling azimuthally at a constant speed has a single, well defined frequency and wavenumber and will therefore appear as a single, sharp peak at (f, k) in the FK power spectra. Thus the presence of sharp peaks in FK power spectra is indicative of wave patterns in real space. These points are illustrated clearly in discussions of the analysis of the synthetic models WAVENB and SPOTNB (see §2.3).

In dealing with the FK power spectra of observed geomagnetic field evolution an unfortunate complication is non-stationarity. This arises both from the changes in the spatial and temporal resolution of geomagnetic field models (see, for example, Bloxham et al. (1989)) but also from the fundamentally unsteady nature of the geodynamo (Gubbins, 1999). This non-stationarity means that definitive statements concerning the space-time spectral content of geomagnetic field evolution calculated from field models with finite time spans are rather limited. What can be reported is the average spectral content over a specified interval of time. If the period studied is short compared to the time scales of field evolution, then the spectral content reported should not be considered definitive. Nonetheless, the spectral signature of specific field evolution episodes provides invaluable information on the generic mechanisms causing field evolution. This pragmatic philosophy is adopted in this thesis when FK power spectra are interpreted.

2.2.4 Construction and interpretation of latitude-azimuthal speed (LAS) power plots, using a Radon transform technique

FK power spectra provide valuable quantitative information and are useful in assisting in the qualitative interpretation of field evolution, but only provide indirect estimates of the azimuthal speeds of field features. An alternative approach, based on the automation of the visual procedure of estimating azimuthal speeds by determining the gradient of a field feature in TL plots, is described in this section. This method will be used extensively in later chapters to determine the azimuthal speeds of field features as a function of latitude.

The visual estimation of azimuthal speeds of field features in TL plots is rather subjective and time consuming to apply to a large number of (not always clearly delineated) field features. A more objective technique, based on use of the Radon transform (Deans, 1988), has been developed to do this. Radon transform methods are widely used in seismology (where it is referred to as a slant-stack or τ-p transform (Pawlowski, 1997)), in medical tomography (Shepp and Kruskal, 1978), and more relevantly in oceanography (Chelton and Schlax, 1996; Cipollini et al., 1997; Hill et al., 2000) where it has been used to analyse the speeds of azimuthally travelling features in TL plots of sea surface height and temperature anomalies. These oceanographic applications provided the stimulus to develop of the present technique.

The Radon transform of a two dimensional image (defined by an angle q) is the projection of the image along the direction normal to a line defined by q. Mathematically it is expressed as (Deans, 1988)

$$\mathcal{H}_R(q,z) = \int_u H(x,t)\Big|_{\substack{x=z\cos q-u\sin q \\ t=z\sin q+u\cos q}} du \tag{2.1}$$

where $\mathcal{H}_R(q,z)$ denotes the Radon transform of a field $H(x,t)$, $(x,\ t)$ are the original

co-ordinate axes, and (z, u) are the new co-ordinates axes after rotation clockwise by an angle q. The action of the Radon transform on a TL plot is shown schematically in figure 2.4.

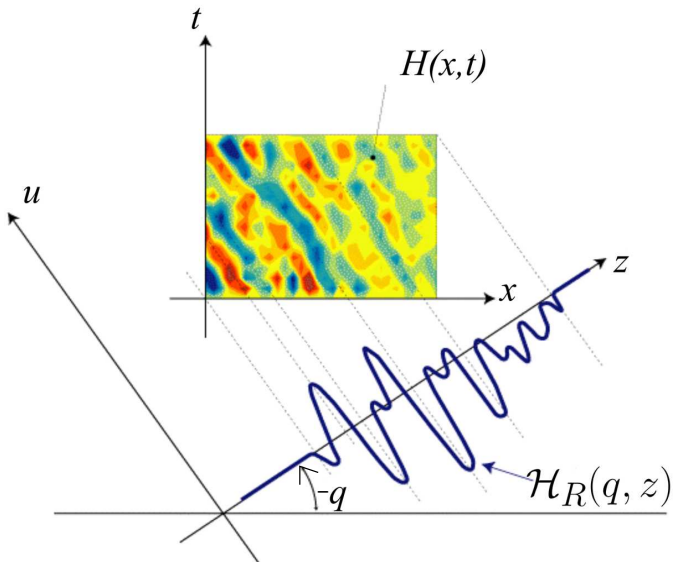

Figure 2.4: Radon transform of a time-longitude plot.
The Radon transform $\mathcal{H}_R(q,z)$ of an image $H(x,t)$ takes the projection of the field in the direction normal to the line defined by an angle q, with z measuring position along the projected image (after Cipollini et al. (2004)).

Since the TL plot consists of an array of discrete values, a discrete version of the Radon transform which finds an array of transformed values $\mathcal{H}_R(q_n, z_m)$ is employed. This implementation of the Radon transform has the origin of its coordinate axes in the centre of the image being transformed and measures q clockwise from the x axis up to $\pm 90°$. The discretisation of q_n is in steps of 2 degrees from -90 degrees to 90 degrees. The discretisation of z_m is more complex and is arranged such that when q_n=0 it matches that in the x direction and when $q_n = \pm 90°$ it matches that in the t direction. Figure 2.5 shows an example of the application of this discrete Radon transform to a synthetic model of field evolution on a spherical surface consisting of a wave pattern travelling westward at 17 kmyr^{-1} at latitude 10°S. In Figure 2.5, (a) shows a snapshot of the signal on the spherical surface (100 years into the model); (b) shows the example TL plot at 10°S and (c) shows the result following the application of the discrete Radon transform.

Having computed $\mathcal{H}_R(q_n, z_m)$ each value in the array $\mathcal{H}_R(q_n, z_m)$ is squared, and summed over all m (along the z direction) to give a discrete measure of $\int |\mathcal{H}_R|^2 \mathrm{d}z$. It is then necessary to divide by a normalised correction factor $C(q_n)$ that accounts for the fact that with a rectangular array, different numbers of grid points will be summed over for different q_m (for further details see the analytic solution for the Radon transform for a rectangle region of constant amplitude on p.63 of Deans (1988)). If all points in a TL plot have the same constant value then taking the discrete Radon transform, squaring

and summing over z_m produces a distribution $C(q_n)$ with a peak at $q_n = 0$ rather than a flat distribution (see figure 2.5c). The directional bias can therefore be corrected if one divides $\sum_m |\mathcal{H}_R(q_n, z_m)|^2$ by $C(q_n)$ so that

$$S(q_n) = \frac{1}{C(q_n)} \sum_m |\mathcal{H}_R(q_n, z_m)|^2. \tag{2.2}$$

The resulting distribution $S(q_n)$ is a directionally unbiased representation of the power travelling per 2 degrees of angular gradient of the image (e.g. a TL plot of H) and will have units of $(\mathrm{nT})^2$ if for example H is a field measured in nT. An example of $S(q_n)$, for the simple synthetic signal shown in figure 2.5a,b is displayed in figure 2.5e with the strong peak at $q_n \sim -15^\circ$ corresponding to the angle the dominant signal makes to the t axis (or that the line normal to the signal makes to the x axis, measured with a clockwise positive convention for q).

$S(q_n)$ from TL plots at each gridded colatitude θ_i are combined into a single array $SL(q_n, \theta_i)$ (see figure 2.5f). The angles q_n defining the directions associated with entries in SL are then converted into azimuthal speeds ($SL(q_n, \theta_i) \rightarrow SL(v_n, \theta_i)$) using the relation

$$v_n = \frac{2\pi c}{360} \cdot \sin\theta_i \cdot \tan q_n \cdot \frac{\Delta\phi}{\Delta t} \quad \mathrm{km\,yr^{-1}}, \tag{2.3}$$

where c_{az} is the azimuthal speed in kilometres per year, $\Delta\phi$, Δt are the longitude and time grid spacings in the TL plot in degrees and years respectively, c is the radius of the spherical surface under study in kilometres (the core surface here) and q_n is the angle under consideration that varies between -90° and +90° in steps of 2°. Note the resolution in velocity space is primarily determined by the values $\tan q_n$, so is best for small q_n (slow moving signals) and worst for q_n close to $\pm 90^\circ$ (rapidly moving signals). The transformation breaks down for very fast angular velocities because $\tan q_n$ diverges close to $\pm 90^\circ$. To avoid this issue the array SL is cropped, and only angles up to $\pm 70^\circ$ are retained. The effect of decreasing the temporal resolution (increasing Δt) is to decrease the maximum velocity that can be reliably estimated.

It is also found that the present method of determining the azimuthal speed of field features breaks down at high latitudes (at latitudes above $\pm 70^\circ$) where even small angular field features spread over many longitude grid-points and can be mistakenly interpreted as very fast moving field features. This problem is avoided by restricting $SL(v_n, \theta_i)$ to latitudes $-70^\circ \leq \theta_i \leq 70^\circ$. Finally, the $SL(v_n, \theta_i)$ array is re-gridded using a cubic interpolation method to be equally spaced in azimuthal speed making the determination of speeds of field features possible by looking for the position of elements with largest amplitude in the array. Latitude-azimuthal speed (LAS) plots of $SL(v_n, \theta_i)$ thus show the distribution of the power ($\int |\mathcal{H}_R|^2 \mathrm{d}z$) as a function of latitude and azimuthal speed, measured in units of $(\mathrm{nT})^2$ if H is a field measured in nT (see figure 2.5g). It is important for interpretation purposes to note that this method implicitly averages over all longitudes and times within a TL plot, but that the peaks could be due to features

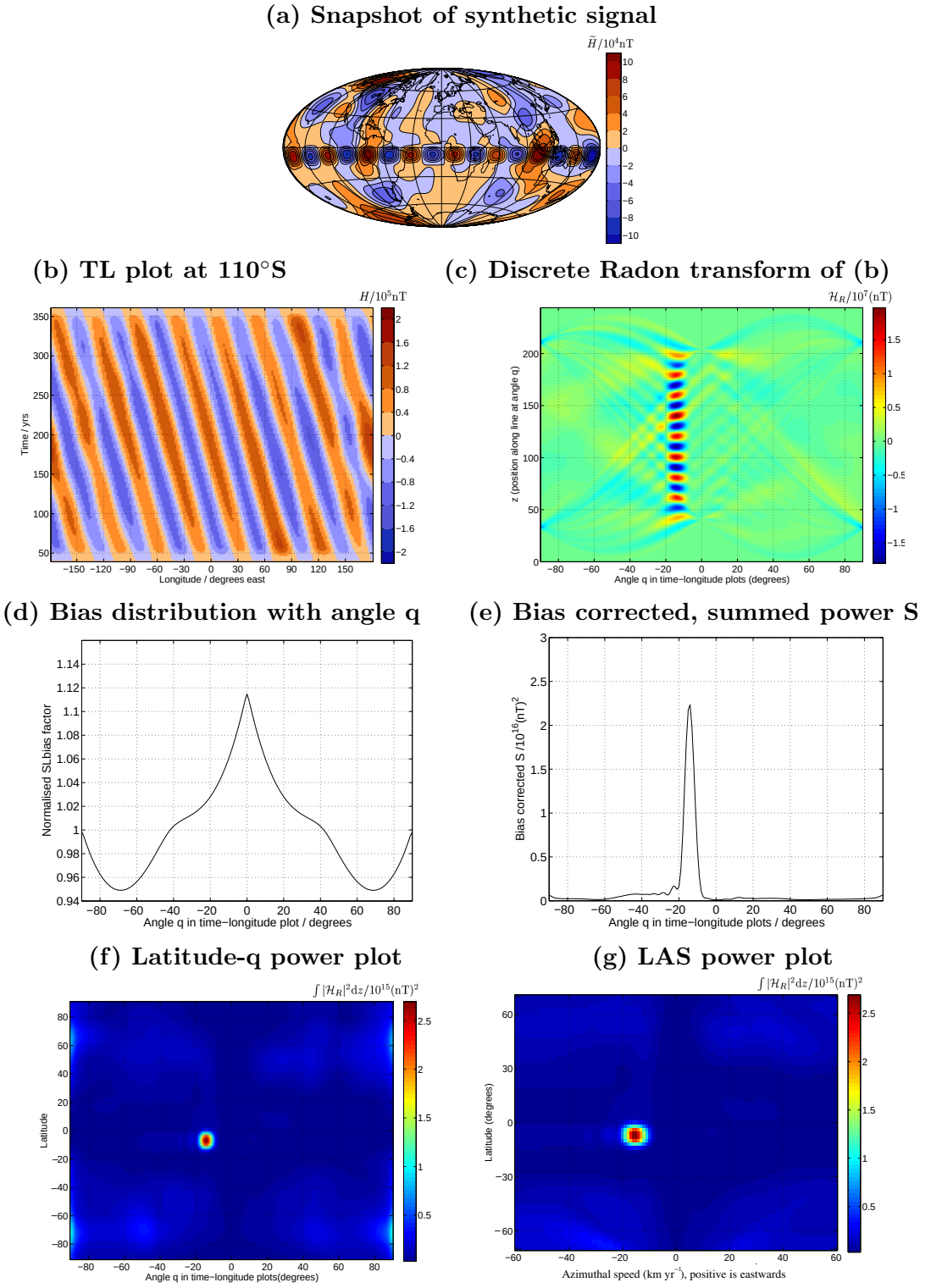

Figure 2.5: Construction of latitude-azimuthal speed (LAS) power plots. (a) is a snapshot (in Hammer-Aitoff equal area map projection) of a synthetic model H of a wave at 10°S, (b) shows a TL plot at 10 °S, (c) shows the result of taking the discrete Radon transform $\mathcal{H}_R(q_n, z_m)$ of (b). (d) is a plot of the bias of the power at different q_n due to the rectangular shape of the time-longitude plots (obtained by performing the analysis on a TL plot of constant value), (e) is the bias corrected power $S(q_n)$ at each q_n from (b). (f) is a collection of plots similar to (e) for all latitudes, (g) is (f) cropped and re-gridded to display linear velocity on a spherical surface.

confined to a particular subset of longitude or sub-interval of time. It is only through the application of this latitude-azimuthal speed power plot method to smaller moving TL sub-windows (see §2.6 and §2.7) that this issue can be properly addressed.

2.3 Synthetic field models used for methodology testing

In order to develop, test and illustrate the operation of space-time spectral analysis techniques (including TL plots, FK power spectra, LAS power plots, and various field processing strategies) 4 synthetic datasets of scalar field evolution on a spherical surface have been constructed. Two types of signal are studied: (i) a model of a wave motion (WAVENB) with a spatially coherent pattern of field anomalies (of alternating signs) that evolves in a temporally coherent manner at constant azimuthal speed; (ii) a model of an isolated field anomaly (SPOTNB) that also moves in a temporally coherent manner at a constant azimuthal speed. The suffix NB in each case indicates that no background field (noise) has been added to the signals of interest. The properties of models SPOTNB and WAVENB are displayed in figure 2.6 where snapshots of the scalar field on the spherical surface, the TL plot at 10°S, the FK power spectra at 10°S, and the LAS power plots are shown.

SPOTNB was chosen to be an isolated field feature of size 24 degrees latitude, 32 degrees longitude, centred at latitude 10 degrees south and moving westward at a speed of 15 $\mathrm{km\,yr^{-1}}$. WAVENB was chosen to be a model of a azimuthally moving wave pattern, with wavenumber m=8, azimuthal speed of 15 $\mathrm{km\,yr^{-1}}$ westward, also of width 24 degrees latitude and centred at latitude 10 degrees south. The motivation behind these choices of synthetic field evolution models was to determine whether the perfectly known speeds, frequencies and wavenumbers could be correctly retrieved after space-time processing, and to see which indicators might be used to distinguish between wave motions and drift of isolated field features. The properties of the field evolution models without any background field added (SPOTNB and WAVENB) are displayed in figure 2.6.

Of course, the real signals that will be investigated in later chapters consist of background noise as well as the signals of interest. To include this effect a model called BACK was developed of the background low frequency (long period) geomagnetic field variations[4]. These signals tend to obscure the decade to millennial time scale signals of interest. The method adopted to derive this realistic background noise model was that proposed by Wheeler and Kiladis (1999). It involves taking the field that will later be studied (B_r at the core surface from *gufm1* over the interval 1590 A.D. to 1990 A.D.), and smoothing it in the spectral domain to remove any periodic or quasi-periodic signals.

Smoothing was carried out in the spectral domain as follows. B_r from *gufm1* was gridded at the core surface and TL plots constructed of the field evolution at each latitude. The

[4]referred to as a red noise in this context.

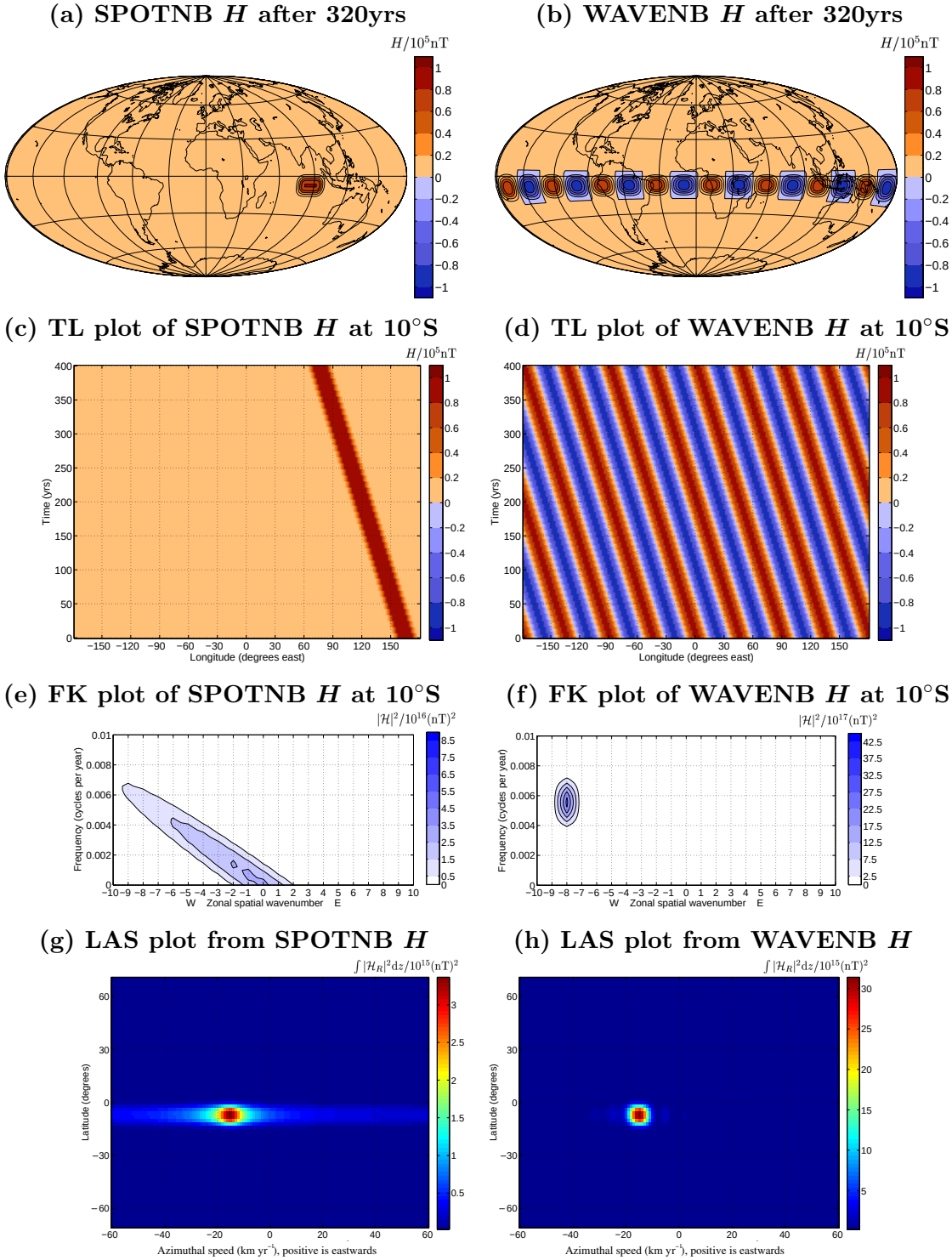

Figure 2.6: Analysis of H from SPOTNB and WAVENB field models. SPOTNB contains an isolated drifting field feature and WAVENB contains a $m = 8$ azimuthally propagating wave. Plots (a) and (b) show H at the core surface after 320years (these and all subsequent snapshots in this chapter are in Hammer-Aitoff map projection), (c) and (d) show time-longitude (TL) plots of the evolution of H at 10°S and (e), (f) the frequency-wavenumber (FK) power spectra $|\mathcal{H}|^2$ at this latitude. (g) and (h) show the latitude-azimuthal speed (LAS) power plots of $\int |\mathcal{H}_R|^2 \mathrm{d}z$.

TL plots were both tapered and zero-padded in time[5] and 2D FFT's were taken. The resulting FK amplitude spectra were then smoothed in both frequency (f) and wavenumber (k) directions by convolution with a 1-2-1 filter[6], before being inverse transformed back in to the space-time domain. Finally the smoothed TL plots at each latitude were collected to yield a complete synthetic space-time model of a background field evolution (BACK) from which all strong periodic and quasi-periodic signals have been weakened. The properties of the resulting background field (red noise) model is shown in figure 2.7 as a plot of the field on the core surface in 1910 (after 320 years), a TL plot and the associated FK power spectra at 10°S and a LAS power plot.

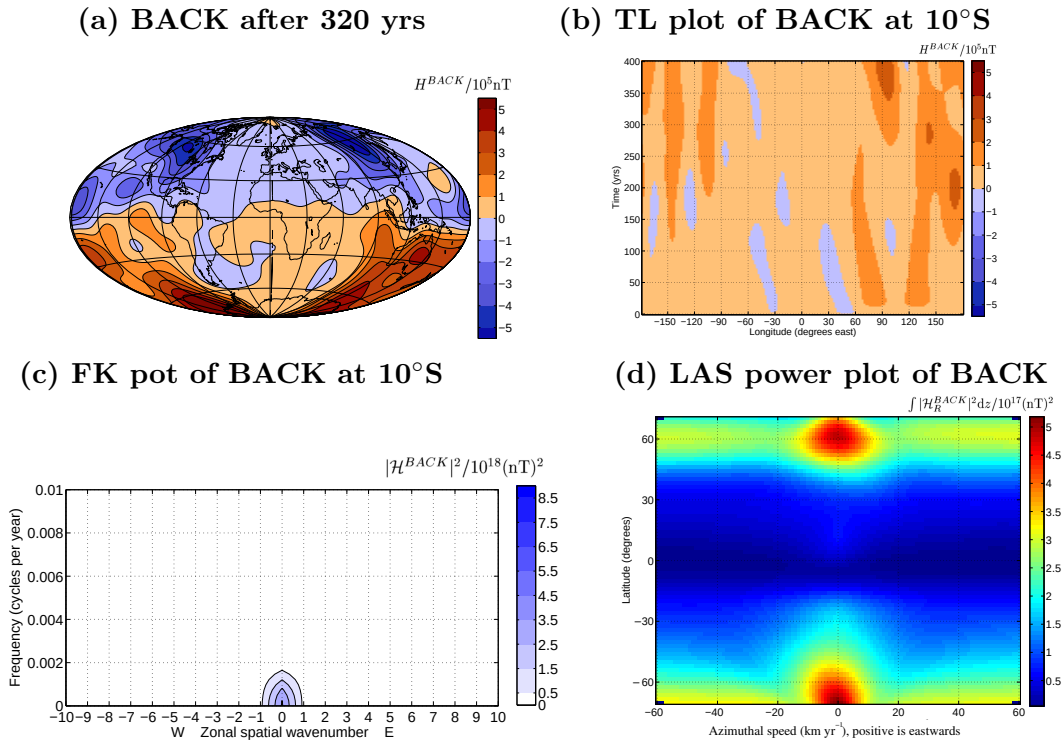

Figure 2.7: Analysis of background field evolution model (BACK).
The synthetic field model BACK is derived by smoothing the spectrum of *gufm1* in frequency-wavenumber space. (a) shows a snapshot of BACK at the core surface after 320years, (b) shows a TL plot of the field evolution at 10°S and (c) the associated frequency-wavenumber (FK) power spectra. (d) shows the latitude-azimuthal speed (LAS) power plot, of BACK.

It is noteworthy that snapshots of B_r from BACK at the core surface are dipole dominated and include the well known, stationary high latitude flux lobes described by Bloxham and Gubbins (1985). Additionally the snapshots show low field amplitude with little variation in the Atlantic hemisphere: the rapid changes found here in *gufm1* have been removed by smoothing of the frequency-wavenumber amplitude spectrum. This

[5]See, for example, Gubbins (2004) for a discussion of these pre-Fourier transforming signal processing techniques.

[6]This involves each point in the 2D Fourier amplitude spectra being replaced by (0.25 times its two nearest neighbours (in either the F or K direction) plus 0.5 times itself).

suggests that geomagnetic secular variation in the Atlantic hemisphere can be associated with quasi-periodic or periodic effects, that are removed by spectral smoothing. In contrast, high amplitude field features are observed in the Pacific hemisphere, suggesting that almost stationary field features are more prominent there.

BACK consists of the field one wished to remove in order to study field evolution mechanisms with time scales of centuries and shorter in *gufm1*. This model is therefore added to the idealised signals SPOTNB (generating a model called SPOT) and WAVENB (generating a model called WAVE) to produce synthetic models that contain both synthetic signals of interest as well as a realistic background field (simulated noise). SPOT and WAVE will be used in order to test space-time field processing methodologies in the remainder of this chapter.

The properties of the synthetic models SPOT and WAVE are presented in figure 2.8, showing snapshots of H at the core surface after 320 years, TL plots of field evolution at 10°S, FK power spectra, and LAS power plots. Note that in these plots, neither of the field evolution signals from SPOTNB or WAVENB are very prominent in snapshots of H at the core surface, though both (and especially WAVENB) can be distinguished by spatially and temporally coherent motions in the TL plots. The FK power spectra for both plots are dominated by power at low frequency and wavenumbers, though the WAVENB signal is also observed in WAVE. Neither signatures of WAVENB or SPOTNB are visible in the LAS plots that are dominated by motions almost stationary over the 400 year timespan considered.

2.4 Removal of the time-averaged axisymmetric field

In the remainder of this chapter the processing techniques that are deployed in space-time spectral analysis to isolate field evolution mechanisms of interest will be described, and their effect demonstrated using the synthetic models SPOTNB, WAVENB, SPOT and WAVE.

The first processing step towards isolating the field evolution processes of interest is the removal of the time-averaged axisymmetric field. This is equivalent to subtracting the arithmetic mean of the field in each TL plot; this procedure is a necessary precursor to spectral analysis. The time-averaged axisymmetric field is unlikely to be directly involved in the evolution of the non-axisymmetric field features that have dominated geomagnetic secular variation at the core surface over the past four hundred years, so can be subtracted without sacrificing information regarding the field evolution processes of interest.

Formally, the calculation of the time-averaged axisymmetric field at a particular latitude involves taking the arithmetic mean of all the gridded values in the TL plot, so for a scalar field $H(\theta_i, \phi_j, t_k)$ at a latitude θ_i, where j refers to the longitude index running

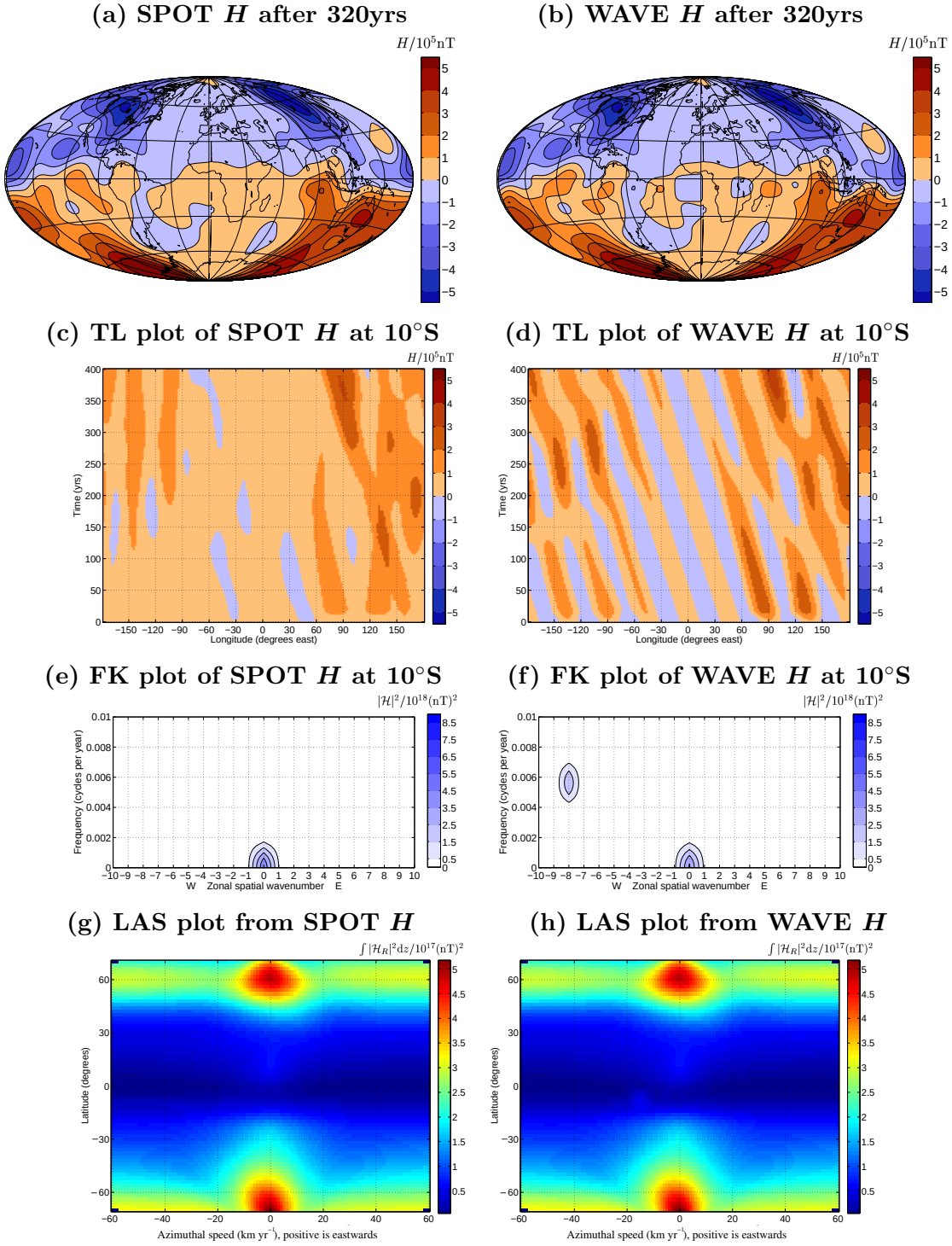

Figure 2.8: Properties of field H from synthetic models SPOT and WAVE. Both consist of a background field derived from *gufm1*, SPOT also contains a moving field feature and WAVE contains a $m = 8$ zonally propagating wave. (a) and (b) show H at the core surface after 320years, (c) and (d) show time-longitude (TL) plots of the field evolution at 10°S and (e), (f) the frequency-wavenumber(FK) amplitude power spectra at this latitude. (g) and (h) show the latitude-azimuthal speed (LAS) power plots.

from 1 to N_ϕ (longitude spacing of $360/N_\phi$) and k refers to the time index running from 1 to N_t (time spacing of $360/N_t$) then the time-averaged axisymmetric field $\bar{H}$ is

$$\bar{H}(\theta_i) = \frac{1}{N_\phi N_t} \sum_{j=1}^{N_\phi} \sum_{k=1}^{N_t} H(\theta_i, \phi_j, t_k). \tag{2.4}$$

Examples of $\bar{H}(\theta_i)$ generated by applying this procedure to the synthetic models SPOT and WAVE are shown in figure 2.9. $\bar{H}$ can also be found if only the $m = 0$ terms in the spherical harmonic representation of the field are retained, and time averaging carried out. However, it is important to note that the m=0, time-averaged axisymmetric field and the time-averaged axial dipole field are not identical. An axial dipole model contains only the l=1, m=0 term from the spherical harmonic representation of the field, while an axisymmetric field contains all the m=0 spherical harmonics. As seen in figure 2.9 the major difference between $\bar{H}$ from SPOT and WAVE (very similar because both contain BACK) and an axial dipole field is the lower field strength near the north pole that would not be present for an axial dipole field.

(a) Time-averaged axisymmetric axisymmetric field $\bar{H}$ from SPOT

(b) Time-averaged axisymmetric axisymmetric field $\bar{H}$ from WAVE

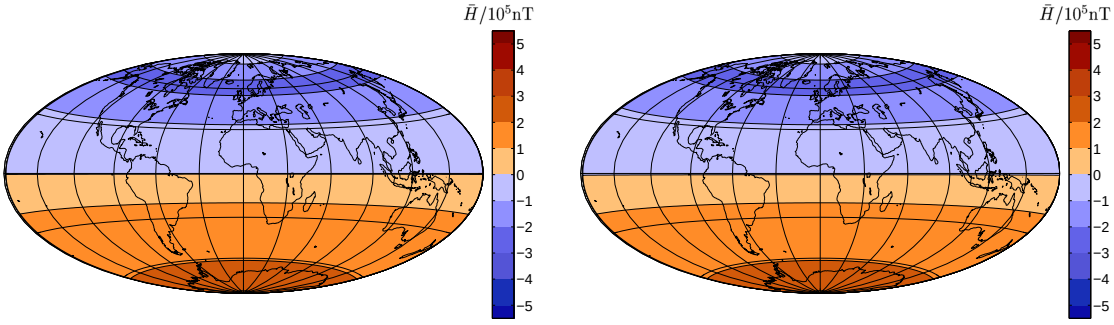

Figure 2.9: Time-averaged, axisymmetric fields $\bar{H}$ from SPOT and WAVE. Averaging the field H azimuthally and over time to obtain $\bar{H}$, in the synthetic models SPOT and WAVE. These models are derived from the large scale, long period background field of *gufm1* plus a isolated drifting field feature (SPOTNB) and a propagating wave in the field (WAVENB) respectively.

The properties of the field evolution after the removal of the time-averaged axisymmetric field (H-$\bar{H}$) is displayed in figure 2.10. The field evolution patterns SPOTNB and WAVENB are definitely more visible in snapshots and TL plots than H, and the dominant m=0 peak has been eliminated from the FK power spectra. However, a sizable m=1 signal with a very long period (almost stationary for this 400 year record) is still present as shown in figure 2.10e, f. Again the field evolution signal in WAVE is more readily seen in all plots and is easily distinguished from the motion of an isolated field feature in the TL plot. The LAS power plots are still dominated by quasi-stationary features at high latitudes. To make further progress in focusing on the field evolution signals SPOTNB and WAVENB contained within SPOT and WAVE it is necessary to filter in order to to remove more of the unwanted background field variation.

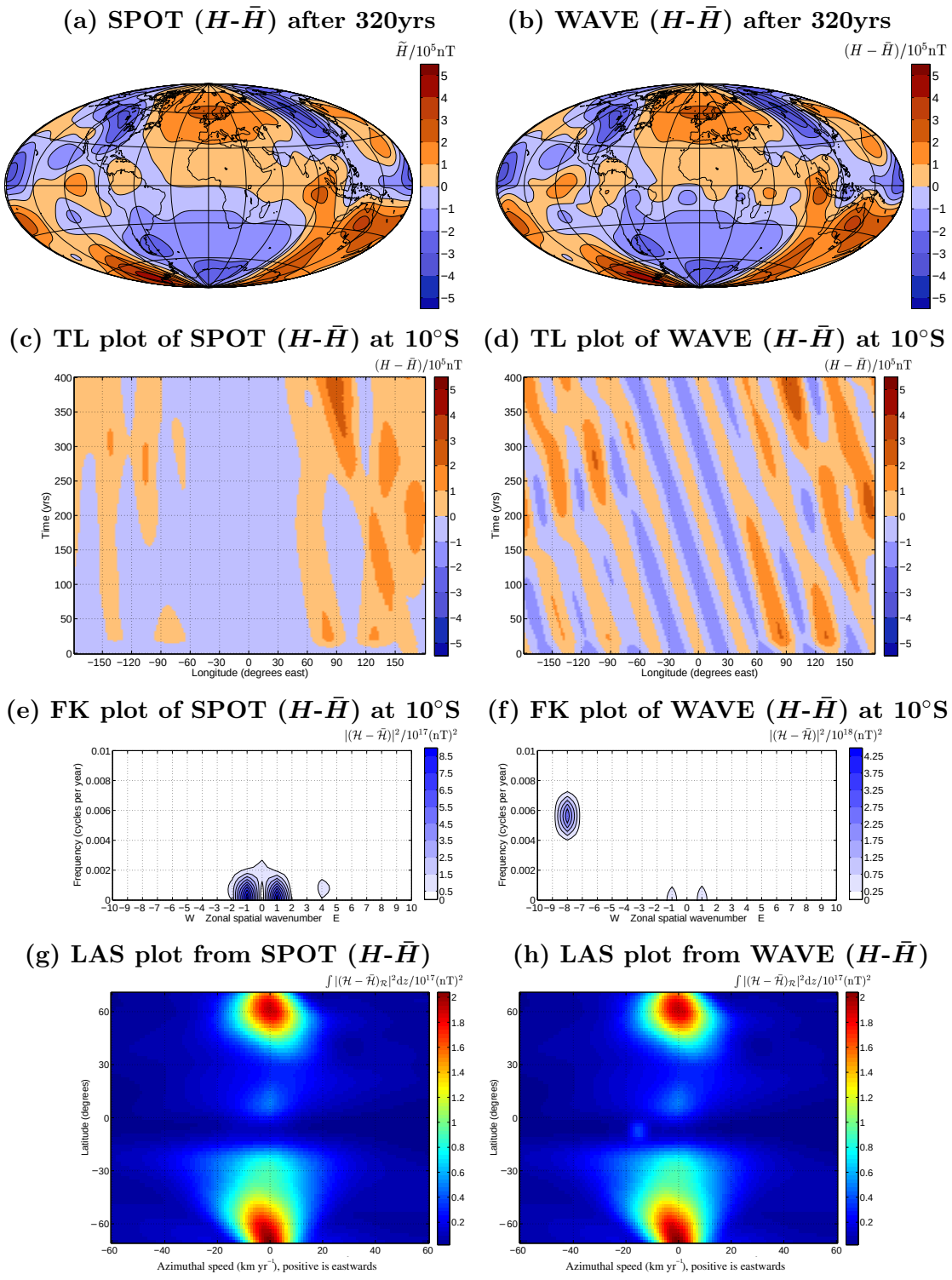

Figure 2.10: SPOT and WAVE (H-$\bar{H}$) field models.
Both consist of BACK, but SPOT also contains an isolated drifting field feature and WAVE contains a $m = 8$ azimuthally propagating wave. The time-averaged axisymmetric field has also been removed here. Plots (a) and (b) show the field at the core surface after 320 years, plots (c) and (d) show time-longitude (TL) plots at 10°S and (e), (f) the frequency-wavenumber (FK) power spectra at this latitude. (g) and (h) show the latitude-azimuthal speed (LAS) power plots.

2.5 High-pass filtering

2.5.1 Motivation for high-pass temporal filtering of field models

In geophysical signal processing applications, observations are routinely filtered to focus on particular component of interest (see, for example, Buttkus (2000)). This approach is often feasible because the physical mechanism being investigated operates within a limited frequency band. By decomposing the signal into its Fourier components, retaining only components within the frequency range of interest, and inverse transforming back to the time domain, the signal of interest can be isolated. In this spirit, geomagnetic field models can be filtered to isolate field evolution signals of interest.

The major problem in studying the evolution of geomagnetic field models at the core surface on time scales of decades to millennia is not high frequency, high wavenumber noise[7] but rather low frequency, long period signals that tend to overwhelm the more rapid field evolution patterns. In order to remove this red noise background signal a high pass filter in time can be applied. In the remainder of this section the high pass filtering used in later chapters is described and tested on the synthetic models SPOT and WAVE.

2.5.2 Filter specification and implementation

High-pass temporal filtering was applied to the time series of field evolution $(H - \bar{H})(t_k)$ associated with each gridded latitude-longitude (θ_p, ϕ_q) location to yield the field $\widetilde{H}(\theta_p, \phi_q, t_k)$. Filtering was carried out in the time domain with a two pass procedure to guarantee that no time shifts were introduced (zero-phase filtering). The processing involved convolving the filter T_H with the time series, time reversing the result, convolving with T_H again and returning the time ordering to that of the original signal. In the frequency domain this is equivalent to multiplying the Fourier representation of the time series by $|F_H|^2$, where F_H is the Fourier representation of the filter T_H. The amplitude response of $|F_H|^2$ is shown in figure 2.11.

The filter employed is a third order Butterworth filter. A discussion of why this is a reasonable choice can be found in §2.5.3 and §2.5.4. The amplitude response in the frequency domain for this filter is

$$|F_H(f)| = 1 - \frac{1}{\left[1 + \left(\frac{f}{f_c}\right)^6\right]^{1/2}}, \tag{2.5}$$

where $f_c = \frac{1}{t_c}$ where t_c is the period of the filter cut-off. In a Butterworth filter of order n, $\left(\frac{f}{f_c}\right)$ appears to the power $2n$, and thus in a 3rd order filter appears to the power 6.

[7] The field models have been constructed from observations using regularisation constraints as described in appendix A, which smooths out high frequency, high wavenumber signals.

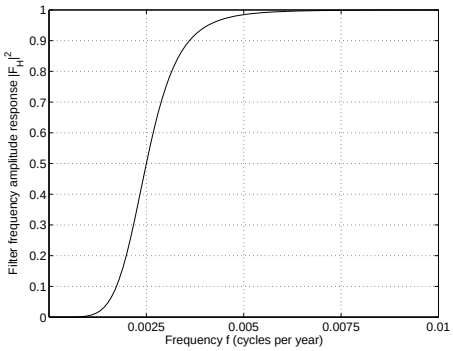

Figure 2.11: Amplitude response of filter $|F_H|^2$ in the frequency domain. Amplitude response in the frequency domain of a 3rd order, Butterworth, high pass filter with f_c=0.0025 (t_c=400yrs). This an example of the form of the filter used to remove unwanted long period signals during the construction of $\widetilde{H}$.

2.5.3 Filter warm-up effects and choice of filter order.

In figure 2.12 the results of TL plots of $\widetilde{H}$ from the synthetic models SPOT and WAVE, obtained using different choices of filter order are presented. Only minor differences are observed in the form of $\widetilde{H}$, suggesting that the precise choice of filter order is not crucial in order to correctly capture the field evolution signal of interest.

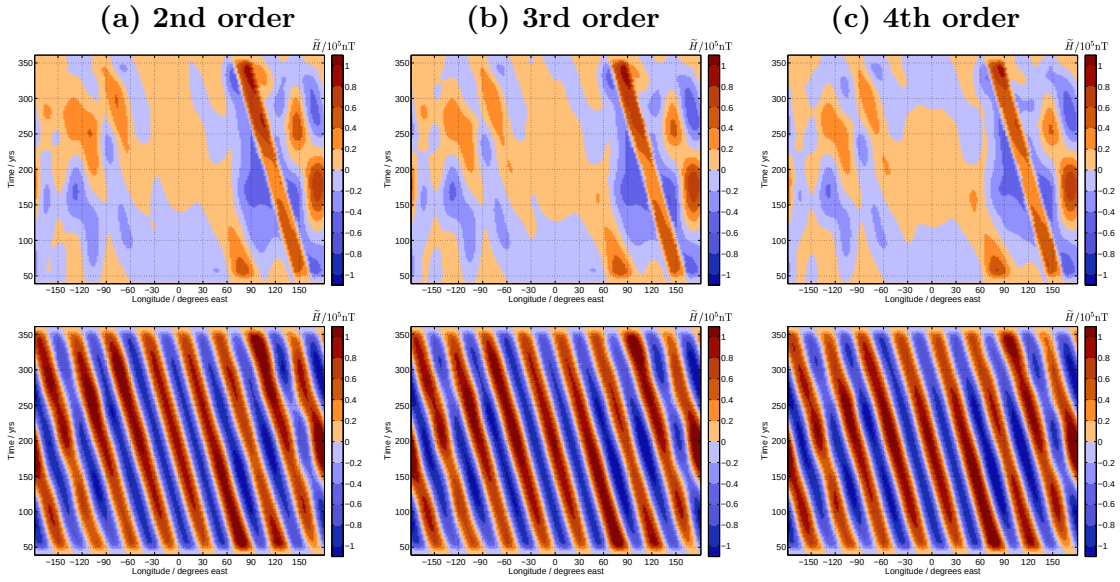

Figure 2.12: Trials with 2nd, 3rd and 4th order Butterworth filters. To test if the order of the filter effects the form of $\widetilde{H}$ SPOT (top row) and WAVE (bottom row) were high pass filtered using 2nd order (column (a)), 3rd order (column (b)) and 4th order (column (c)) Butterworth filters, all with $t_c = \frac{1}{f_c} = 400$ yrs.

The filter order determines how sharp the cut-off of the filter is in the frequency domain (high order means a sharp cut-off). It also determines the length of the filter in the time domain (high order means long filter) which in turn determines the time span of the

filter warm-up interval[8]. A 3rd order filter was chosen because this is short in the time domain (so warm-up problems only affect short regions at the start and end of the time series) whilst also having a fairly sharp threshold in the frequency domain.

Applying a 3rd order Butterworth filter with $t_c = 400$ years to a record of length 400 years sampled every 2 years, it was found to be necessary to discard the first and last 40 years of the record. An important consequence of this is that the filtered time series obtained from the historical geomagnetic field model *gufm1* studied in chapter 3 are only of length 320 years.

2.5.4 Influence of filter type on processed field

Another important issue is whether the choice of a Butterworth filter, rather than some other type of filter significantly affects the form of $\widetilde{H}$. To test this, high pass filtering was carried out with 3rd order Elliptic, Chebyshev and Butterworth filters[9] all with cut-off periods of 400 years, and the resulting TL plots compared in in figure 2.13. The important characteristics (especially the positions and motions of field features) of $\widetilde{H}$ were found to be independent of the particular type of filter used. A Butterworth filter was therefore implemented for all subsequent analysis because of its simplicity.

(a) Butterworth filter **(b) Chebyshev filter** **(c) Elliptic filter**

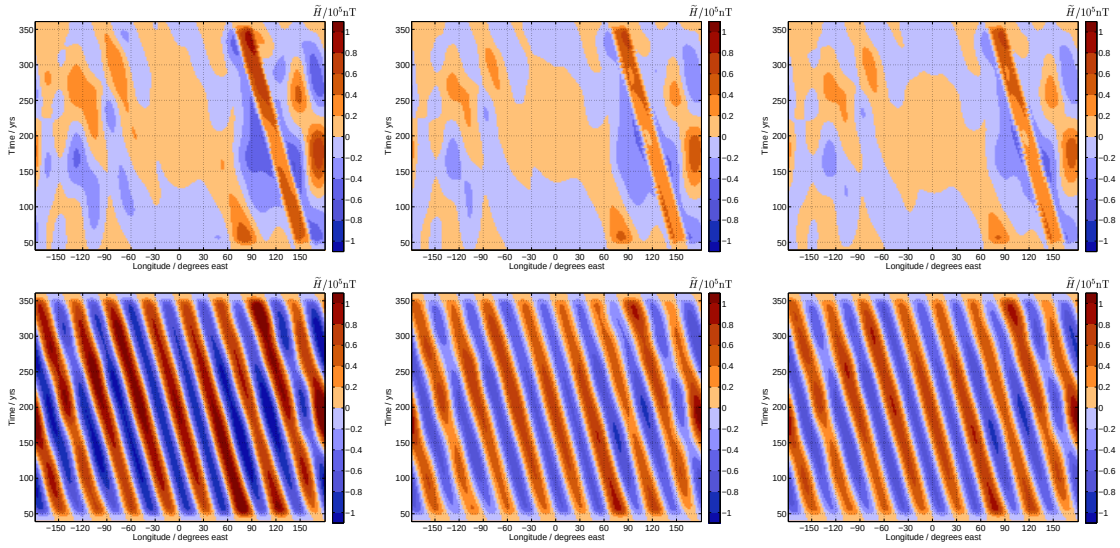

Figure 2.13: Trials with Butterworth, Chebyshev and Elliptic types of filters High pass filtering SPOT (top row) and WAVE (bottom row) using 3rd order Butterworth (1st column), Chebyshev (2nd column) and Elliptic (3rd column) filters.

[8]Filter warm-up occurs due to convolution of the filter with the time-series and results in regions at the start and end of the filtered series being anomalously large and oscillatory in amplitude. By keeping the filter length in the time domain short the warm-up interval is minimised.

[9]For a discussion of the relative merits of these filters, see for example Smith (1997).

2.5.5 Criteria for choice of filter cut-off period t_c

The choice of filter cut-off frequency $f_c = \frac{1}{t_c}$ is a key step in the filter specification. The choice of filter cut-off can be justified on the basis of trying, as best as possible, to satisfy the following three criteria:

(i) Isolation of the signature of a physical mechanism — historical geomagnetic field evolution occurs on decade to millennial time scales so changes occurring on much longer time scales should be removed by filtering.

(ii) Length of the time series — properties of processes occurring on timescales much longer than the length of the time series are unlikely to be robust. Consequently attention should be focused on processes with timescales shorter than the length of the time series, and filtering used to remove signals with longer periods.

(iii) Frequency content of the model — the cut-off frequency must be such that there is significant signal left to be interpreted.

The specific choice of high pass cut-off frequency used to filter each field model investigated, and the amount of variation in the original signal accounted for in the processed signal varies between models. This will be discussed in detail prior to the presentation of results in later chapters.

2.5.6 Measuring field variations captured as a function of t_c

In this section, a measure of the severity of the high pass filtering in terms of the amount of variability in the original signal captured (P_v, see definition in equation (2.6)) is developed. Information on how this quantity varies with t_c is needed in order to choose an optimal t_c. How P_v varies with t_c will be studied for each of the fields investigated in this thesis.

The percentage of field variations in the original signal H captured by the processed signal $\widetilde{H}$, averaged over a spherical surface, may be measured by the quantity P_v defined as

$$P_v = \frac{\sum_{i,j} R_v(\theta_i, \phi_j)}{\sum_{i,j} G_v(\theta_i, \phi_j)} * 100\%, \tag{2.6}$$

$$\text{where} \quad R_v(\theta_i, \phi_j) = \sum_k \left| \widetilde{H}(\theta_i, \phi_j, t_k) - \widehat{\widetilde{H}}(\theta_i, \phi_j) \right|, \tag{2.7}$$

$$G_v(\theta_i, \phi_j) = \sum_k \left| H(\theta_i, \phi_j, t_k) - \widehat{H}(\theta_i, \phi_j) \right|, \tag{2.8}$$

$$\widehat{\widetilde{H}} = \frac{1}{N_t} \sum_k \widetilde{H}(\theta_i, \phi_j, t_k), \tag{2.9}$$

$$\text{and} \quad \widehat{H} = \frac{1}{N_t} \sum_k H(\theta_i, \phi_j, t_k), \tag{2.10}$$

where the index i runs over all sampled latitudes θ_i, j runs over all sampled longitudes ϕ_j and k over all sampled times t_k, excluding times effected by filter warm-up periods (see discussion in §2.5.3). $\widehat{H}(\theta_i, \phi_j)$ and $\widehat{\widetilde{H}}(\theta_i, \phi_j)$ are respectively the time-averaged field values of the original field H and the processed field $\widetilde{H}$ at each latitude-longitude location on the spherical surface. $R_v(\theta_i, \phi_j)$ at each location is the sum of the absolute deviations of $\widetilde{H}$ from $\widehat{\widetilde{H}}$, and $G_v(\theta_i, \phi_j)$ at each location is the summed absolute deviation of H from $\widehat{H}$. P_v represents the percentage ratio of the sum of R_v over all locations to the sum of G_v over all locations. In the limit when $t_c \to \infty$ P_v be equal to 100 % because $\widetilde{H}$ captures all the variation in H. In the opposite limit when $t_c \to 0$ P_v tends to zero because $\widetilde{H}$ captures very little of the variation present in H. It was found that looking at P_v as a function of filter-cut off t_c was an effective way to study the amount of the variation in the original model captured by the processed model. The effect on P_v of varying t_c for the synthetic models SPOTNB, SPOT and WAVENB, WAVE is shown in detail in figure 2.14.

(a) Field variation captured as a function of cut-off period for WAVE

(b) Field variation captured as a function of cut-off period for SPOT

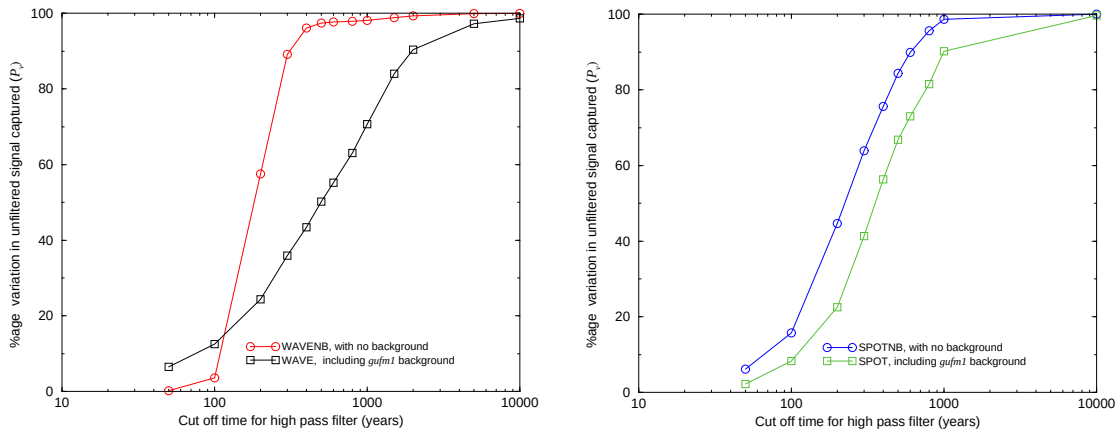

Figure 2.14: Field variations captured as a function of filter cut-off period. The percentage of the original field variation captured by the processed field (P_v), as defined in equation (2.6), is plotted as a function of the high pass filter cut-off period (t_c) for the synthetic field models WAVENB and WAVE in (a) and for SPOTNB and SPOT in (b).

In figure 2.14a considering the model WAVENB, when t_c is less than 200 years, P_v is close to zero. On the other hand, when t_c is more than 200 years P_v is close to 100 %. The sharp transition at around 200 years is because this is the period of the WAVENB signal. Therefore, in order to capture the field evolution pattern in this example, a filter cut-off period must be chosen to be greater than 200 years.

When BACK is added to WAVENB to give WAVE other longer period variations are also present, but over 40% of the original variation can nonetheless captured by filtering with t_c=400 years. Studying $\widetilde{H}$ with t_c=400 years therefore captures a large proportion

of the field change seen in H, including the field evolution mechanism of interest.

Considering SPOTNB and SPOT in figure 2.14b the situation is similar except that even with no noise added SPOTNB does not display a sharp transition, because it arises from a superposition of power over a range of frequencies. The addition of BACK further increases the amount of power at long periods. A filter cut-off of 400 years (suggested by the record length criteria) turns out to be sufficient to retrieve the SPOTNB motion field evolution (especially its motion) adequately.

2.5.7 Discussion of properties of form of processed field for a range of filter cut-off periods

If results obtained on the basis of analysis of $\widetilde{H}$ are to be trusted, then its form should be robust to changes in the choice of the filter cut-off threshold t_c. To illustrate that this is indeed the case, snapshots, TL plots, FK power spectra and LAS power plots of $\widetilde{H}$ are displayed for the synthetic models SPOT and WAVE with cut-off periods of 200 years in figure 2.15, 400 years in figure 2.16 and 600 years in figure 2.17. The success of the processing and analysis techniques may be judged by comparing the noise-free field evolution patterns of SPOTNB and WAVENB displayed in figure 2.6 to the results shown figures 2.15, 2.16 and 2.17.

The field evolution patterns of both SPOTNB and the WAVENB can clearly be seen in the TL plots of $\widetilde{H}$ from the SPOT and WAVE models at 10°S regardless of whether a 200, 400 or 600 year cut-off period is chosen, giving confidence that the field evolution patterns in $\widetilde{H}$ are indeed robust to changes in the cut-off periods. The FK power spectra in all cases picked out the correct frequency (f=0.005cpy) and wavenumber (m=8) of the WAVENB signal. Furthermore the LAS power plot technique correctly identifies both SPOTNB and WAVENB field evolution patterns as having speed 15 $\mathrm{km\,yr^{-1}}$ andas being located at 10°S.

Unfortunately, the FK power spectra of $\widetilde{H}$ from the pattern of field evolution SPOTNB are difficult to retrieve accurately because they contain power along a line of constant f/k, and filtering has removes power close to the origin that lies on this line. Nonetheless, power is certainly spread over a wider range of frequencies and wavenumbers compared with models containing the WAVENB field evolution pattern.

Choosing a cut-off period lower than suggested by criteria (i) of §2.5.5 (i.e. a 200 year cut-off that is too close to the time scale of the field evolution mechanism WAVE and much shorter than the record length), it is observed that in TL plots and snapshots of SPOT, much of the power required to reproduce SPOTNB has been lost. Consequently the isolated, drifting field feature is no longer seen as a single, high amplitude, field feature. Instead it is flanked by spurious anomalies. On the other hand, when the filter cut-off period is 600 years (longer than would be preferred on the basis of criteria (ii))

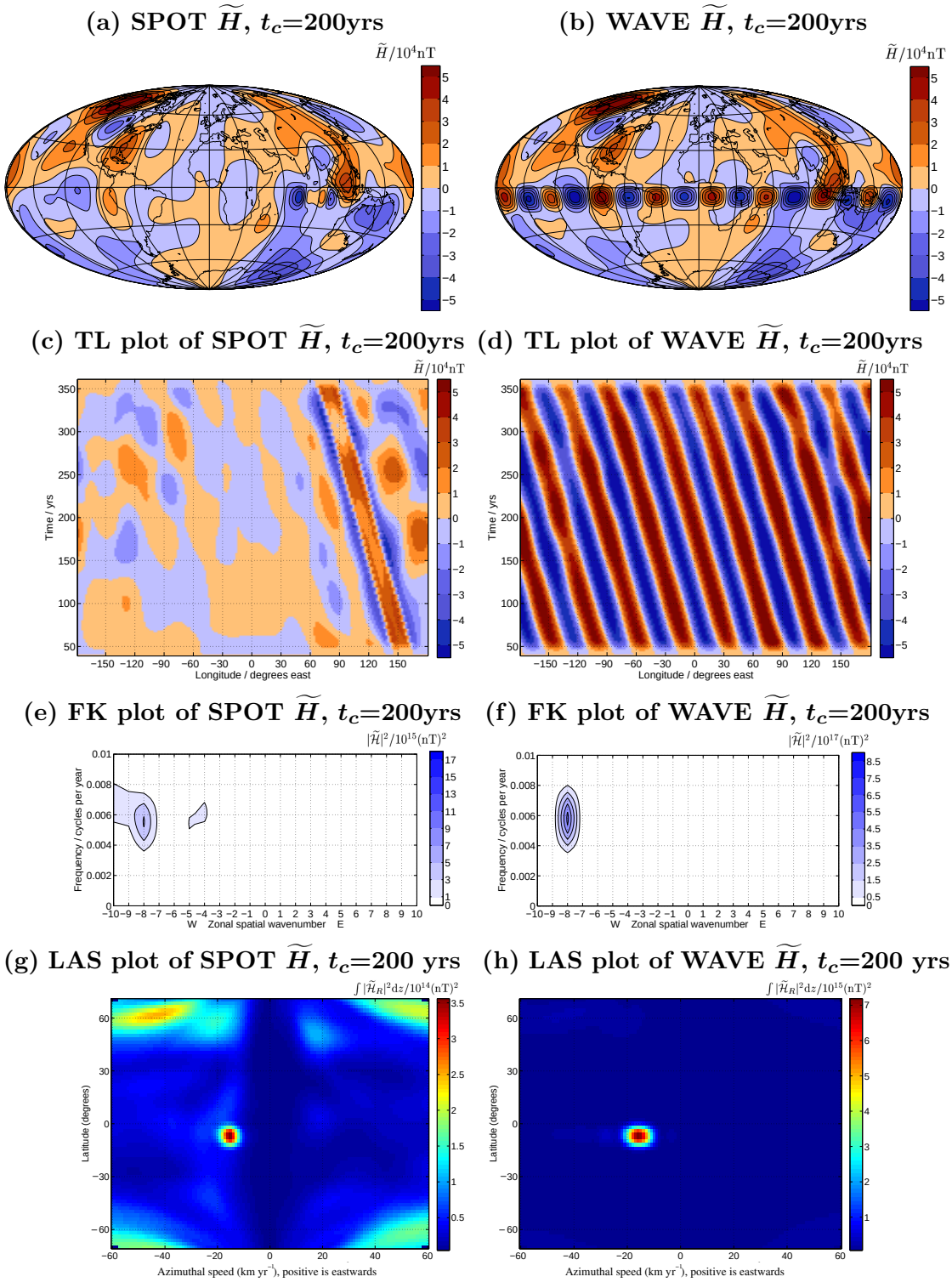

Figure 2.15: SPOT and WAVE $\widetilde{H}$, high pass filtered with t_c=200yrs. Synthetic field models SPOT (left column) and WAVE (right column) with the time-averaged axisymmetric field removed and high pass filtered with $t_c = 200$yrs. In (a) and (b) fields on the spherical surface after 320years are plotted. (c) and (d) show time-longitude (TL) plots at 10°S and in (e) and (f) the frequency-wavenumber (FK) power spectra at this latitude. (g) and (h) show latitude-azimuthal speed (LAS) power plots.

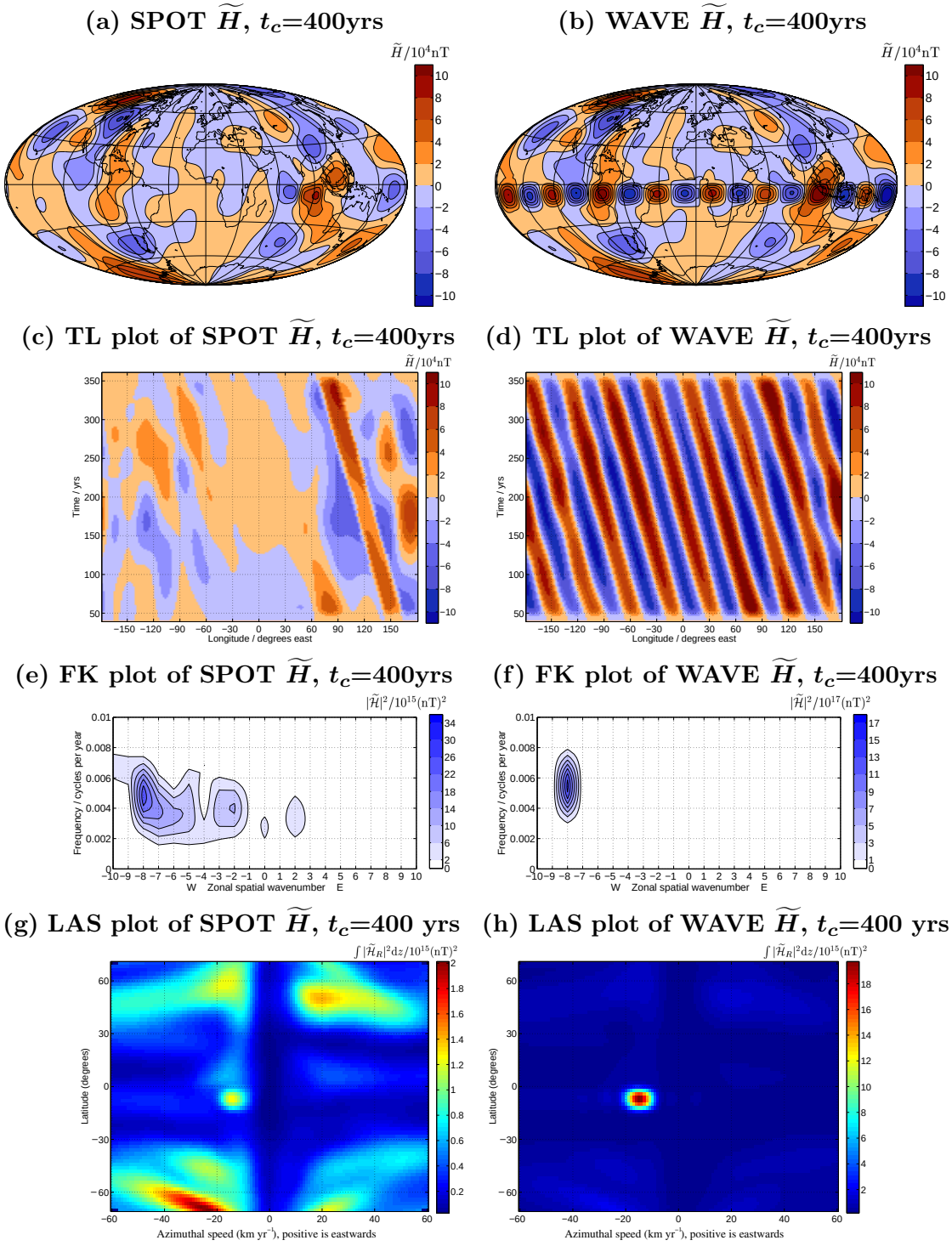

Figure 2.16: SPOT and WAVE $\widetilde{H}$, high pass filtered with t_c=400yrs. Synthetic field models SPOT (left column) and WAVE (right column) with the time-averaged axisymmetric field removed and high pass filtered with t_c = 400yrs. In (a) and (b) fields on the spherical surface after 320years are plotted, (c) and (d) show time-longitude (TL) plots at 10°S and in(e) and (f) the frequency-wavenumber (FK) power spectra at this latitude. (g) and (h) show latitude-azimuthal speed (LAS) power plots.

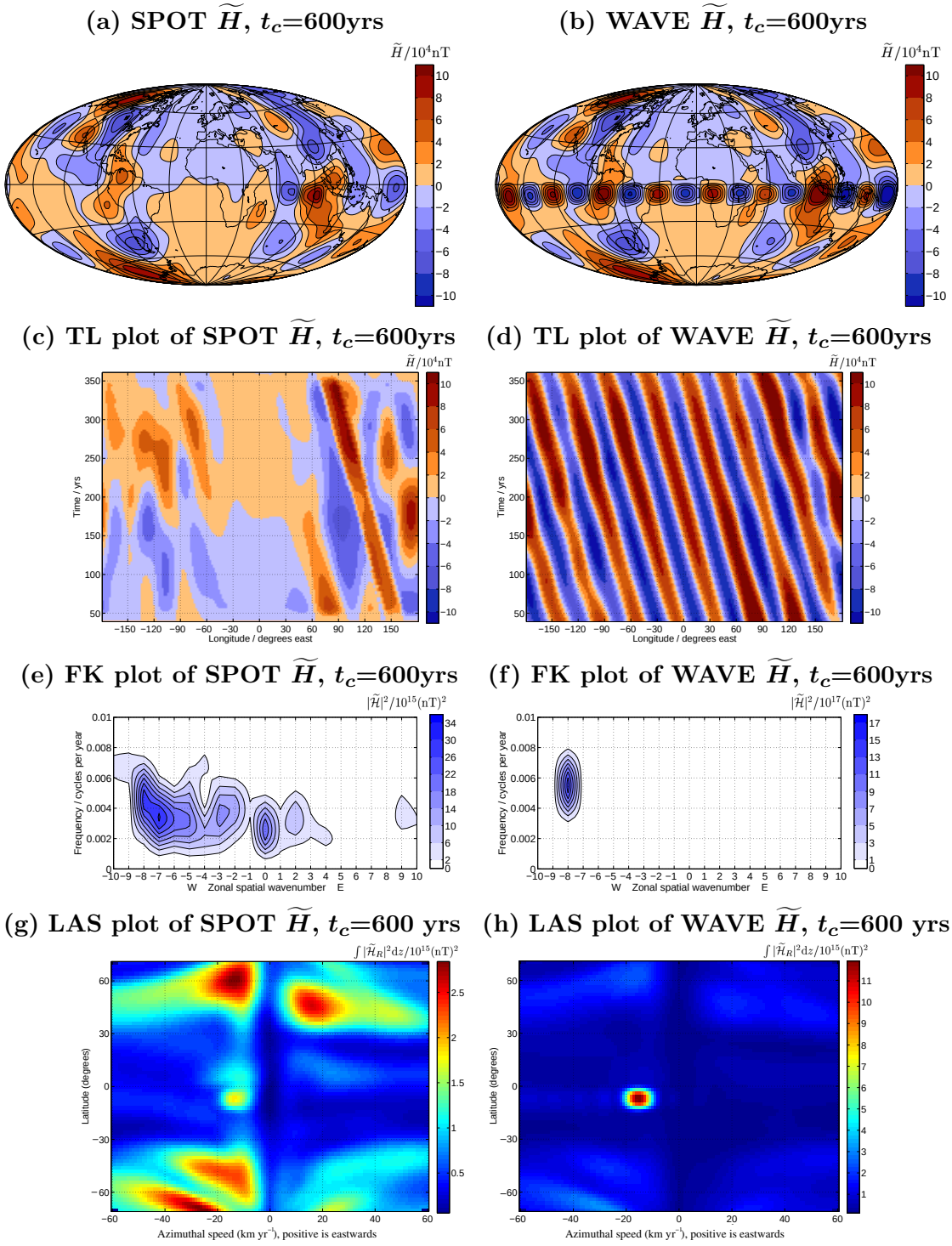

Figure 2.17: SPOT and WAVE $\widetilde{H}$, high pass filtered with t_c=600yrs. Synthetic field models SPOT (left column) and WAVE (right column) with the time-averaged axisymmetric field removed and high pass filtered with t_c = 600yrs. In (a) and (b) fields on the spherical surface after 320years are plotted, (c) and (d) show time-longitude (TL) plots at 10°S and in (e) and (f) the frequency-wavenumber (FK) power spectra at this latitude. (g) and (h) show latitude-azimuthal speed (LAS) power plots.

it is more difficult to pick out the signature of SPOTNB in the LAS power plots.

Clearer results are obtained when observing whether WAVENB patterns are retrieved in $\widetilde{H}$ from WAVE for the 200, 400 and 600 year cut-offs. A very clear signal of a spatially and temporally coherent series of propagating highs and lows are seen in TL plots while localised peaks are found in both the FK power spectra and the LAS power plots. It can be concluded that the choice of t_c=400 years seems, in these examples where the signal of interest has a time scale of 200 years, to be a suitable choice for the filter cut-off threshold.

2.6 Geographical distribution of azimuthal speeds of field features

The variation in the azimuthal speeds of field features with geographical position is an observable that allows theoretical ideas on field change mechanisms to be tested. In the context of oceanography, plotting the variation of azimuthal speed of field features with latitude allowed a test of the prediction that long Rossby waves travel with a speed that depends on the cosine of latitude (so field features travel fastest near the equator). This dependence has been observed (Chelton and Schlax, 1996), and second-order trends found in the observations have stimulated improved theoretical models of Rossby waves (Killworth et al., 1997).

Azimuthal speeds at a particular latitude and longitude can be determined using the Radon transform method of determining azimuthal speeds (see §2.2.4), but applying it to longitudinally confined sub-windows of TL plots centred on the particular longitude of interest. Sub-windows were chosen to be of width 80° longitude[10] and the centre of the longitude windows was moved in steps of 20°. From each TL sub-window, the azimuthal speed corresponding to the q that maximises $S(q_n)$ (see equation (2.2)) is assigned to be the speed for that latitude and the central longitude of the sub-window. To ensure that only clear signatures of spatially and temporally coherent azimuthally moving field features are recorded, a speed is only assigned if the maximum of $|S(q_n)| > \frac{4\sum_n S(q_n)}{N_q}$. The pre-factor 4 is a free parameter that is chosen as a compromise between the desire to include all possible signals and the desire to exclude unwanted, non-coherent field variations.

The methodology was again tested using the synthetic models SPOTNB, WAVENB, SPOT and WAVE. The results from these trials are shown in figure 2.18. Both the magnitude and directions of the azimuthal speeds and the latitude and longitude of the synthetic field motions were correctly identified in all the models. These tests permit confidence that this method will be able to successfully retrieve any geographical trends in the speeds of of azimuthally moving field features.

[10] large enough so that propagating features with $m > 4$ can be analysed.

(a) Geographical distribution of azimuthal speeds in SPOTNB $\widetilde{H}$

(b) Geographical distribution of azimuthal speeds in WAVENB $\widetilde{H}$

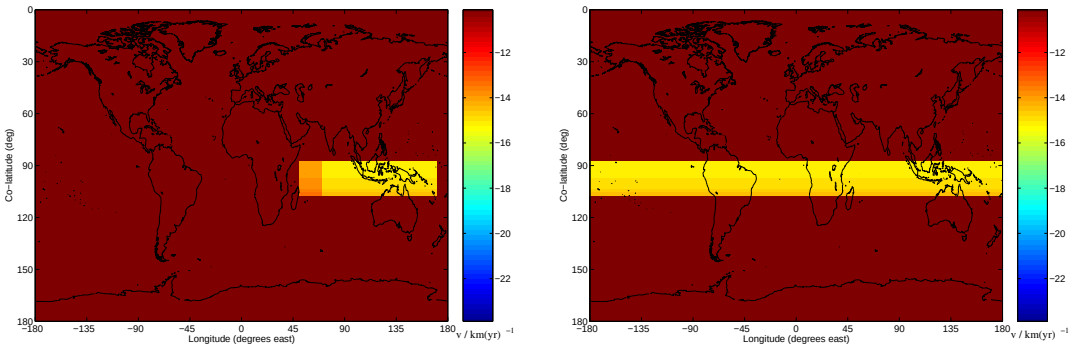

(c) Geographical distribution of velocity variation in SPOT $\widetilde{H}$

(d) Geographical distribution of velocity variation in WAVE $\widetilde{H}$

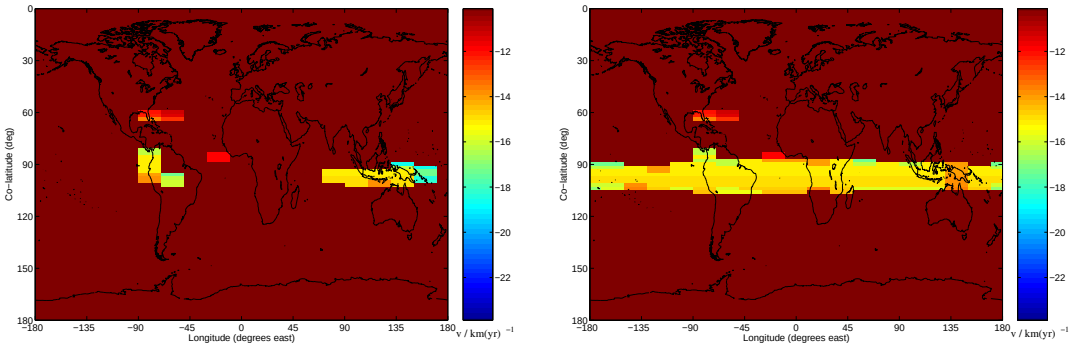

Figure 2.18: Geographical distribution and speeds of field features. Variation in azimuthal speeds of field features with geographical position, calculated using the Radon transform technique and a sliding window in longitude.

2.7 Temporal variations in latitude-azimuthal speed (LAS) power plots

The information on field evolution mechanisms provided by LAS power plots is a temporal average over the entire span of the TL plot analysed. It is of interest to see whether features identified in LAS plots are stationary or vary in strength and position with time. To do this, sub-windows in time (rather than the sub-windows in space that were discussed in the previous section) can analysed using the Radon transform methods described in §2.2.4.

The temporal sub-windows were chosen to be 1/5 of the full timespan (i.e. 80 years for a 400 year record) and were moved steps of size 1/20 of the timespan (i.e. 20 years for a 400 year record). A series of LAS power plots (one for each temporal sub-window) were constructed each of which describes an average over the span of the sub-window. However, shorter windows in time mean that each discrete angle q_n in the TL-sub window corresponds to a larger range of azimuthal speeds, so the resolution in speed determination is decreased.

The technique was once again tested on the synthetic models SPOTNB, WAVENB, SPOT and WAVE. The resulting LAS power plots are shown for the 80 year sub-window centred on 200 years after the start of the models in figure 2.19. The degradation of azimuthal speed resolution is apparent, but encouragingly the maxima of the power is still located at the correct speed (15 km yr^{-1} westward) and latitude (10°S) for all the models. However, as shown in the LAS plot if figure 2.19c, the signal of interest is not the dominant signal observed when SPOT is analysed. This demonstrates that coherent signals of interest can be difficult to pick out when short time windows are used.

(a) Snapshot of LAS plot from SPOTNB $\widetilde{H}$ at 200yrs

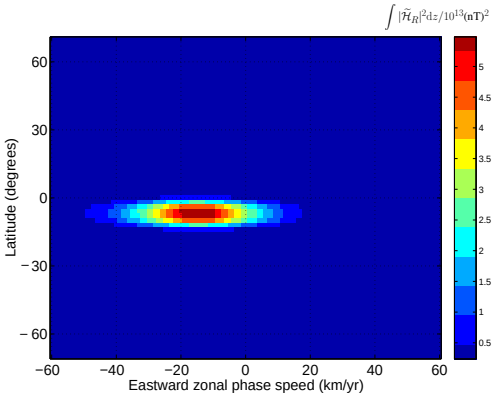

(b) Snapshot of LAS plot from WAVENB $\widetilde{H}$ at 200yrs

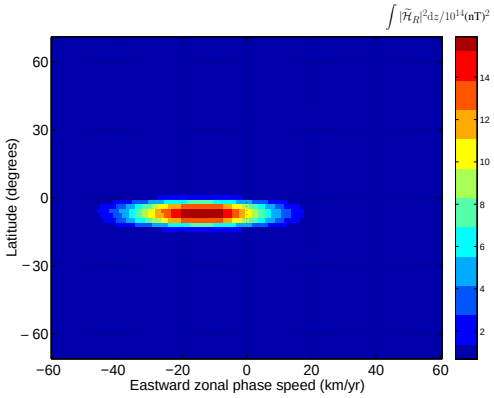

(c) Snapshot of LAS plot from SPOT $\widetilde{H}$ at 200yrs

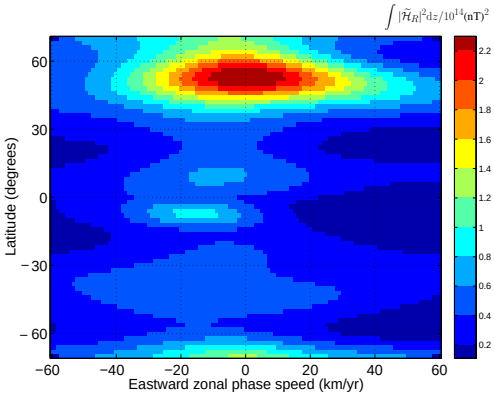

(d) Snapshot of LAS plot from WAVE $\widetilde{H}$ at 200yrs

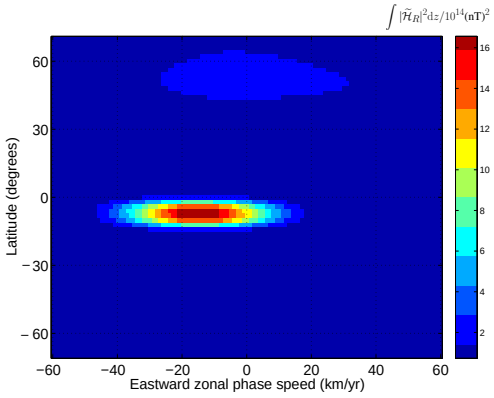

Figure 2.19: Temporal changes in latitude-azimuthal speed power plots. LAS power plots from temporal sub-windows covering the interval 160yrs to 240 yrs, for the synthetic models SPOTNB in (a), WAVENB in (b), SPOT in (c) and WAVE in (d).

2.8 Analysis of hemispherically confined signals

Previous studies of geomagnetic field evolution at Earth's core surface (see, for example, Bloxham et al. (1989), Bloxham and Jackson (1992) and Jackson et al. (2000)) indicate persistent asymmetry between the Atlantic and Pacific hemispheres. The Atlantic

hemisphere is consistently found to possess high amplitude, westward travelling field features. In contrast, in the Pacific hemisphere, the field amplitude is generally lower and no coherent patterns of field evolution are easily observed. When the question of the hemispherical symmetry of field evolution patterns isolated using space-time spectral processing techniques is considered in later chapters, it will be of important to know whether observed signals in one hemisphere could be a by-product of the processing techniques. In particular, it is of interest to determine whether a hemispherically confined signal remains confined after the removal of its time-averaged axisymmetric part and after high-pass filtering has eliminated slow field variations.

This issue is addressed in this section through the analysis of two synthetic models consisting of hemispherically confined patterns of magnetic field evolution called HEMINB and HEMI. HEMINB is derived from the WAVENB model, with field amplitudes in longitudes 180°W to 90°W and 90°E to 180°E (the Pacific hemisphere) set to zero and a constant field of 0.5×10^5 nT added to all locations. It represents a clean, idealised, example of a hemispherically confined signal that can clearly demonstrate whether spatial aliasing between hemispheres is a side-effect of the field processing. Results from the analysis of HEMINB are presented in figure 2.20. A second synthetic model called HEMI consisting of a realistic background signal (BACK) along with the hemispherically confined wave signal HEMINB is also studied. This more realistic model is designed to show whether a strong signal in one hemisphere and a weaker signal in the other hemisphere can both be reliably analysed following field processing. The results from the analysis of HEMI are presented in figure 2.21.

Figure 2.20 demonstrates that the space-time spectral analysis techniques employed in this thesis do not cause signals that are confined to the Atlantic hemisphere to be mapped into the Pacific hemisphere. Both snapshots(figure 2.20 a,b) and time-longitude (TL) plots (figure 2.20 c,d) of the processed signal retain the hemispherical asymmetry present in the unprocessed models. This result can readily be understood by noting that no direct alteration of the spatial spectrum is carried out during the processing (except the removal of the time-averaged m=0 part of the signal) so no spatial aliasing that might produce a spurious signal in the Pacific hemisphere arises. The FK spectra of both the filtered and unfiltered signal (see figure 2.20 e,f) have strong peaks at the expected wavenumber for the signal (m=8) despite the fact that the signal has been removed in one hemisphere. Furthermore, the latitude-azimuthal speed (LAS) power plot of both the filtered and unfiltered signal correctly captures the azimuthal speed of the WAVENB signal. The conclusion from this synthetic test is therefore that if any signal is observed in a particular hemisphere in $\widetilde{H}$, then it must actually be present in that hemisphere and can not have been mapped there as a result of the processing procedure.

The more realistic scenario illustrated in the model HEMI and presented in figure 2.21 demonstrates that given a strong signal in one hemisphere and a weaker signal in the

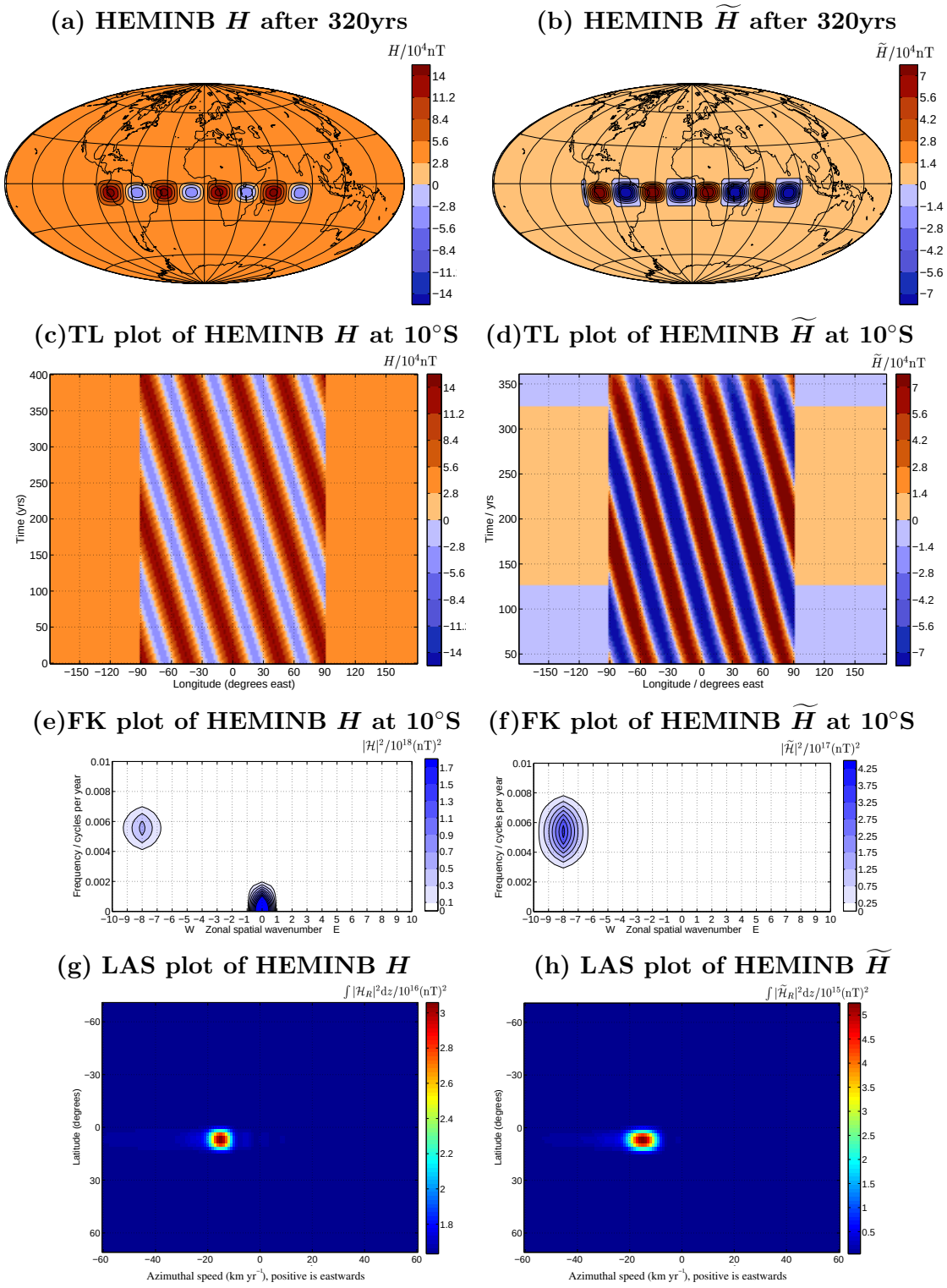

Figure 2.20: Analysis of a hemispherically confined wave.
Synthetic model HEMINB of a hemispherically confined wave with a constant background field added. The unprocessed field H is shown in (a), (c), (e), and (g) while the processed field with time-averaged axisymmetric part removed and high pass filtered with t_c=400 years ($\widetilde{H}$) is shown in (b), (d), (f) and (h). (a) and (b) show snapshots at the core surface after 320 years, (c) and (d) show time-longitude (TL) plots at 10°S and (e) and (f) the frequency-wavenumber (FK) spectra at this latitude, while (g) and (h) show the latitude-azimuthal speed (LAS) plots.

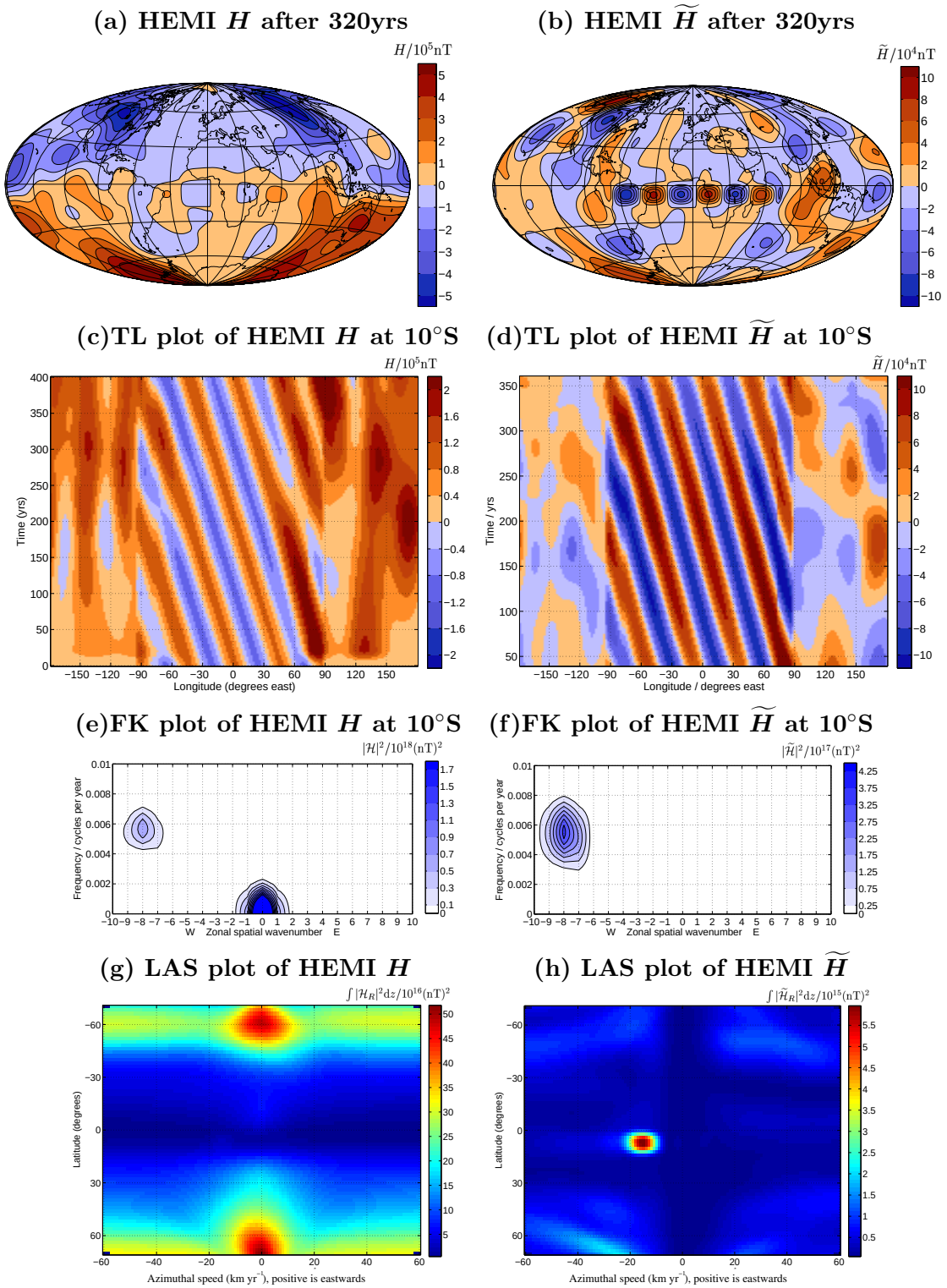

Figure 2.21: Analysis of hemispherically confined wave and background field. Synthetic model HEMI of a hemispherically confined wave with an additional background field (BACK) added. The unprocessed field H is shown in (a), (c), (e), and (g) while the processed field with time-averaged axisymmetric part removed and high pass filtered with t_c=400 years ($\widetilde{H}$) is shown in (b), (d), (f) and (h). (a) and (b) show snapshots at the core surface after 320 years, (c) and (d) show time-longitude (TL) plots at 10°S and (e) and (f) the frequency-wavenumber (FK) spectra at this latitude, while (g) and (h) show the latitude-azimuthal speed (LAS) plots.

other hemisphere, then the processed field retains that asymmetry. It also demonstrates that the presence of a strong signal in a particular hemisphere does not preclude one from observing weak signals in the other hemisphere. In HEMI, some weak signals are observed in the Pacific hemisphere. These were present in the model BACK (derived from a spectrally smoothed version of *gufm1* — see §2.3) and continue to be observed in the Pacific hemisphere even when a strong signal is present in the Atlantic hemisphere. The findings of these synthetic tests will prove useful later when *gufm1* and CALS7K.1 are analysed in chapters 3 and 4 respectively.

2.9 Frequency-wavenumber filtering techniques

In studies of fluid motions in the oceans and atmosphere it is common to filter observed signals in spectral space, so that only the power associated with a evolution pattern of interest remains, and then to inverse transform back to the space-time domain where comparisons to theory can be easily made. Such FK-filtering techniques can obviously be also applied in the present contact, and are of particular interest when attempting to determine the structure of possible wave-like features in geomagnetic field models. In this section the synthetic models SPOTNB, WAVENB, SPOT and WAVE are FK-filtered to isolate a spectral feature of interest and this feature is then reconstructed in the space-time domain. Performing this procedure when the underlying signal is known provides insight in the possible errors which could result from this procedure.

A simple FK-filtering technique was developed to allow signals of interest to be studied in this manner. The starting field H is first processed as described in §2.4 and §2.5 to give $\widetilde{H}$. The FK amplitude spectra of $\widetilde{H}$ is then calculated from TL plots at each latitude. A peak of interest is identified and a 2D mask filter constructed that is zero everywhere except within the region occupied by the spectral peak, where it has value 1. The sharp edges of the mask filter are then tapered to minimise power leakage. The mask filter is then multiplied with the FK amplitude spectra to yield a modified FK amplitude spectra that contains only information within the desired region of spectral space. A 2D inverse Fourier transform is then applied to the new FK amplitude spectra (the phase spectrum is assumed to be unchanged) to obtain a new TL plot. The same procedure is repeated at all latitudes. When TL plots have been reconstructed for all latitudes they can be combined to give a complete space-time model (H^{rec}). This can be analysed in the same way as any other field model, so latitude-longitude snapshots can be taken to view the field structure on a spherical surface, TL plots used to view the field evolution in the azimuthal direction, the FK power spectra calculated to check the consistency of the filtering and the LAS power plots signature of peaks in FK space determined.

Following the now familiar procedure, the methodology was tested using the models

SPOTNB, WAVENB, SPOT and WAVE. A filter mask running from wavenumbers -7 to -9 and frequencies 0.003 to 0.008 cycles per year (periods from 125 to 330 years) was chosen to illustrate the analysis. Such a mask is expected to capture exactly the motion of the synthetic field evolution pattern in the WAVENB model so, if the method is functioning correctly, the field evolution seen in figure 2.6a,b should be retrieved from analysis of WAVENB and WAVE. It is found that the FK filtering does indeed do a good job of retrieving the WAVENB patterns of field evolution, whether or not a background field in present (see figures 2.22b,d,f,h and 2.23b,d,f,h).

This mask is, however, certainly not optimised for capturing the linear shape of the FK power spectra of the isolated drifting flux feature in SPOTNB. It might even be expected that such a mask-filter could map the field evolution of SPOTNB and SPOT into a wave-like form. Results shown in figures 2.22a,c,e,g and 2.23a,c,e,g show that although SPOTNB is not well captured, the field evolution is much more localised than for WAVENB and no spurious strong global wave patterns have been produced.

Clearly care is needed in interpreting the results of FK filtering in term of modes of field evolution. A simple circular mask should only applied when unambiguous, isolated peaks in spectral space are present. However, this approach does provide a way of finding out more about the space-time signatures of possible modes of field evolution (in particular their latitudinal extent) that might be present in geomagnetic field models.

2.10 Discussion

The synthetic models used in this chapter were chosen to mimic two distinct end member forms of field evolution: a monochromatic, spatially and temporally coherent, wave pattern moving at a constant azimuthal speed and an isolated spot of intense field also moving at a constant azimuthal speed. It was found that both types of field evolution could be accurately characterised, though results were most striking for the wave patterns. Several possible ways to distinguish between spatially coherent (wave-like) patterns of field evolution and isolated drifting field features have become evident in the investigations in this chapter.

The most direct indicator is that in TL plots of $\widetilde{H}$ where the time-averaged axisymmetric and long period variations have been removed, wave patterns can be easily seen as a spatially and temporally coherent pattern of field anomalies of alternating signs. In contrast, analysis of an isolated drifting field feature yields no spatially extended wave-like pattern. Instead the processed field is characterised by a single strong feature often flanked by weak anomalies of the opposite sign (see for example figure 2.16c,d giving the appearance of a series of three propagating anomalies, even though only one field feature is present).

Furthermore, in both FK power spectra and LAS power plots, azimuthally moving wave

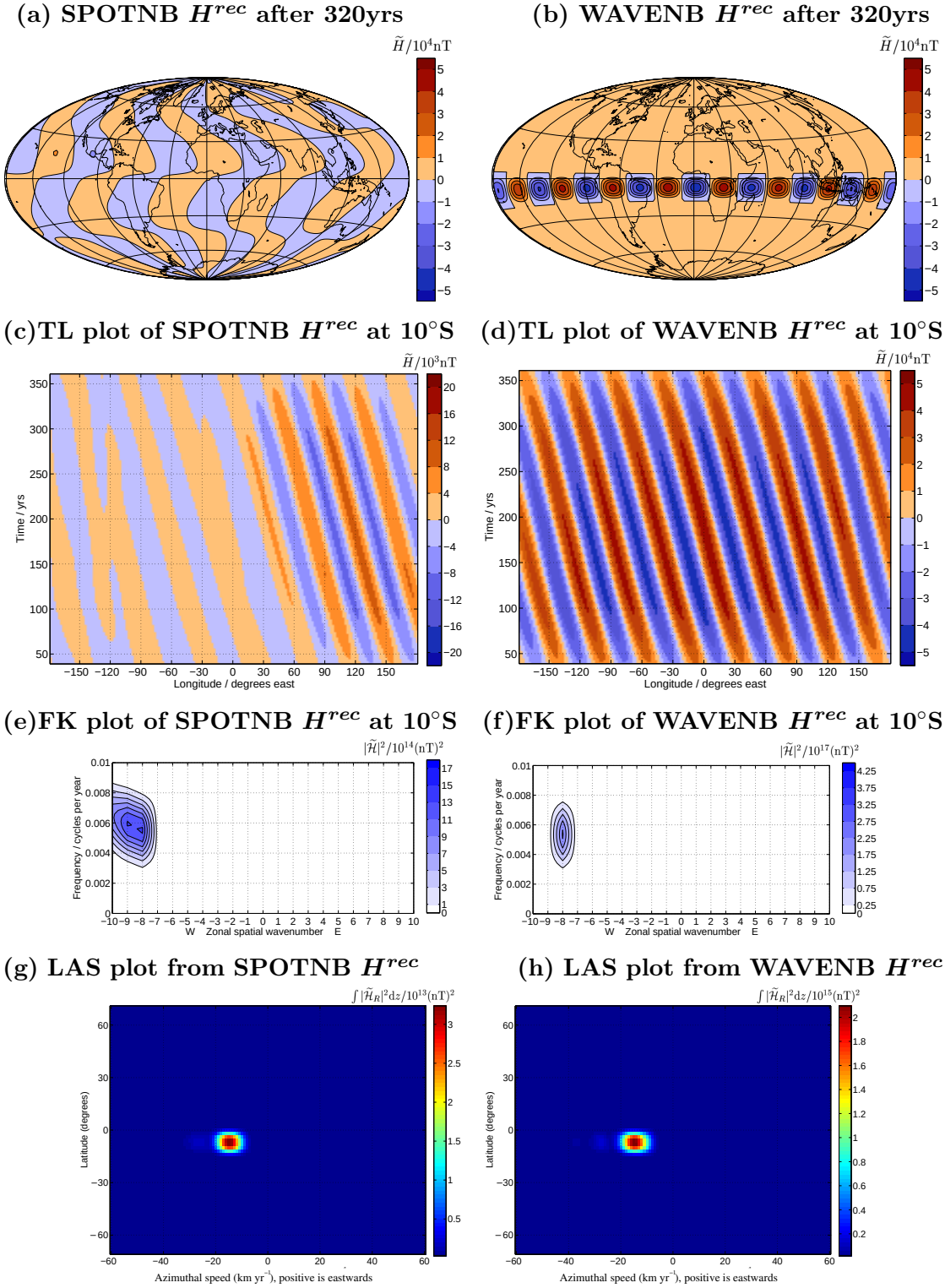

Figure 2.22: FK-filtered, reconstructed SPOTNB and WAVENB models. FK filtering models SPOTNB and WAVENB so that only frequencies 0.003 to 0.008cpy and wavenumbers 7 to 9 remain. Plots (a) and (b) show the radial part of the magnetic field at the core surface after 320 years, plots (c) and (d) show time-longitude (TL) plots of the field evolution at 10°S and in (e) and (f) the frequency-wavenumber(FK) spectra at this latitude. (g) and (h) show the latitude-azimuthal speed (LAS) power plots.

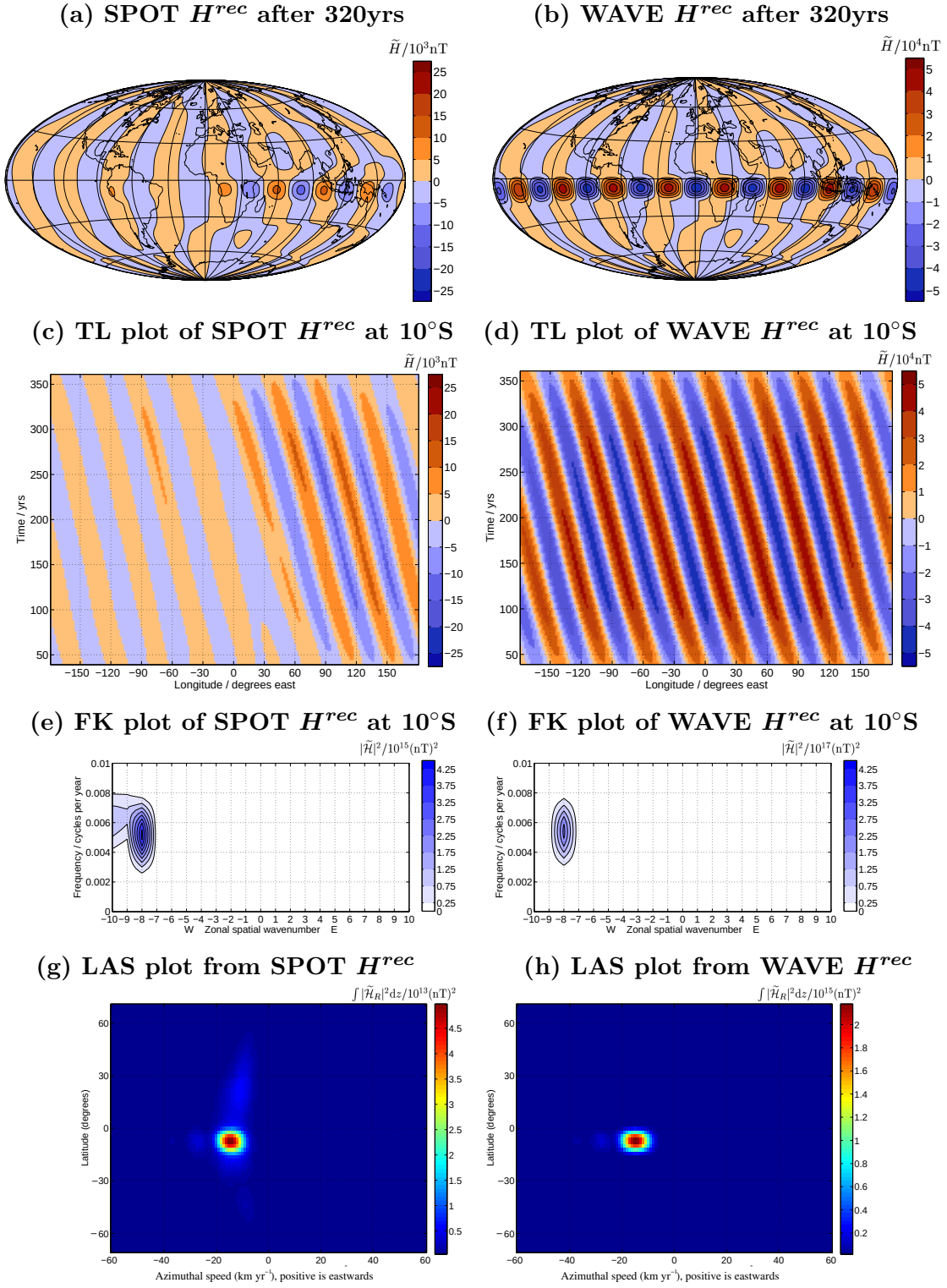

Figure 2.23: FK-filtered, reconstructed SPOT and WAVE field models. FK filtering models SPOT and WAVE so that only frequencies 0.003 to 0.008cpy and wavenumbers 7 to 9 remain. Plots (a) and (b) show the radial part of the magnetic field at the core surface after 320 years, plots (c) and (d) show time-longitude (TL) plots of the field evolution at 10°S and in (e) and (f) the frequency-wavenumber(FK) spectra at this latitude. (g) and (h) show the latitude-azimuthal speed (LAS) power plots.

patterns yields much larger amplitude peaks than isolated drifting features. This is essentially because the spatially and temporally coherent energy in wave patterns is present over all longitudes, and maps into a single point FK space and to a well defined azimuthal speed in LAS space. In contrast, considering a single field anomaly moving over only a subset of longitudes the power is mapped into a range of frequencies and wavenumbers. Therefore very strong peaks in FK power spectra and the LAS power plots are further evidence in favour of wave-like patterns of field evolution.

In real observations, wave patterns of field evolution are likely to be much less spatially and temporally coherent than in WAVENB since the wave will respond to changes in its local environment as it travels. Therefore signatures of wave type field evolution will certainly not be as clear as those seen for WAVENB.

The major assumption implicit in the methodology of this chapter, that should be borne in mind during interpretation, is the focus of the analysis on purely azimuthal motions of field features. If persistent field features do not move azimuthally, they will appear only as short lived features in TL plots and will not contribute significant power to FK power spectra at particular latitudes or show up clearly in LAS power plots. Fortunately, the motions of the geomagnetic field features of interest in this thesis are observed to move approximately azimuthally suggesting the methods developed in this section will be of use. It will be possible to justify this assumption retrospectively, since strong signals in TL plots, FK power spectra and LAS plots are only possible if a significant amount of azimuthal motion of non-axisymmetric field features is present.

2.11 Summary

In this chapter a space-time processing and spectral analysis methodology has been introduced. The origins of the techniques in the study of wave motions in meteorology and oceanography have been described. The practical implementation of the processing and analysis techniques have been discussed and tested on synthetic field models. The tests demonstrate that the methodology is capable of capturing the characteristics (including hemispherical asymmetry) of plausible patterns of field evolution, giving confidence that meaningful interpretations can be made when real data is analysed. The tools developed here will be applied in later chapters to geomagnetic field and archeomagnetic models and field models obtained from a geodynamo model in order to characterise the mechanisms of field evolution.

Chapter 3

Application of the space-time spectral analysis technique to the historical geomagnetic field model *gufm1*

3.1 Introduction

In this chapter results of the application of the space-time spectral analysis technique described in chapter 2 to the historical field model *gufm1* (Jackson et al., 2000) are presented. Details of the observations and field modelling methods used in the construction of *gufm1* can be found in appendix A. The analysis of this chapter follows previous studies of the magnetic field at the core surface and focuses on the radial component B_r. This component is studied because it is continuous across the core-mantle boundary (so provides a direct link to fluid motions close to the core surface) and because the other components contain no additional information under the assumption that the magnetic field at the core surface is a potential field.

The properties of the unprocessed radial magnetic field B_r, the radial magnetic field with the time-averaged axisymmetric part removed ($B_r - \bar{B}_r$) and the radial field with the time-averaged axisymmetric part removed and high pass filtered $\widetilde{B_r}$ are first described in detail. Dominant modes of field evolution in the azimuthal direction are then identified and reconstructed using FK filtering.

An attempt to determine dispersion in patterns of geomagnetic field evolution over the past 400 years is described and problems in making such determinations are discussed. Geographical variations in azimuthal speeds of field features are mapped and resulting implications discussed. Hemispherical similarities and differences in the patterns of field evolution are described and possible interpretions in terms of core-mantle interactions suggested. The time dependence of field evolution processes are also documented. Finally, implications for mechanisms of geomagnetic secular variation (including whether the results favour a wave or flow origin for azimuthal field motion) are discussed.

3.2 Description of field evolution processes in the azimuthal direction

3.2.1 Unprocessed radial magnetic field (B_r)

The field features observed in B_r at the core surface in *gufm1* are qualitatively the same as those observed in earlier historical field models (see Bloxham and Gubbins (1985), Bloxham et al. (1989) and Bloxham and Jackson (1992)). Maps of B_r at the core surface from *gufm1* in 1650, 1710, 1770, 1830, 1890 and 1950 are displayed in figure 3.1.

Non-axisymmetric field features can be classified as either static or drifting over the historical observation interval from 1590 to 1990. Almost stationary, high amplitude, field features are observed under Canada and Siberia in the northern hemisphere and at antipodal sites below Antarctica. Rapidly drifting field features are observed especially in the Atlantic hemisphere and most move westward. It is not easy to follow these spots by comparing maps at different epochs, but they are readily followed in animations of the time-dependent field model (see animation A2.1, consult appendix F for details). The most prominent drifting feature is a positive field anomaly first seen in 1590 near the longitude of India, at latitude 15°S. It can be followed westward and finishes under the mid-Atlantic ocean in 1990 and undergoing an interval of reduced amplitude between 1780 and 1830.

In figure 3.2 time-longitude (TL) plots and their associated frequency-wavenumber (FK) power spectra are presented for latitudes 60°N, 20°N, the equator and 40°S. It is in general rather difficult to visually identify azimuthally moving field anomalies. Both the TL plots and the FK power spectra are dominated by the almost stationary axisymmetric field. The only exception is at the equator where the axial dipole component of the field is weak. Here there is some indication of westward moving field features, although the dominance of stationary, non-axisymmetric, field features now makes the determination of the characteristics of the field evolution mechanisms impossible.

The latitude-azimuthal speed (LAS) power plot for unprocessed B_r is shown in figure 3.3. Unfortunately it too yields little information because it too is dominated by stationary field features, particularly at high latitudes. When interpreting the LAS power plots shown throughout this chapter it should be remembered that peaks of power represent the latitudinal position and azimuthal speed of spatially and temporally coherent field evolution patterns, averaged over time and longitude. The spread of power around the dominant peaks (for example the full width at half maximum) can be considered as a measure of the variability in the field evolution mechanisms that can be used to give approximate bounds on the azimuthal speed and latitudinal positions. Unfortunately in figure 3.3 no clear dominant peaks are found in the LAS plot indicating that further processing of the field is required to isolate field evolution mechanisms of interest.

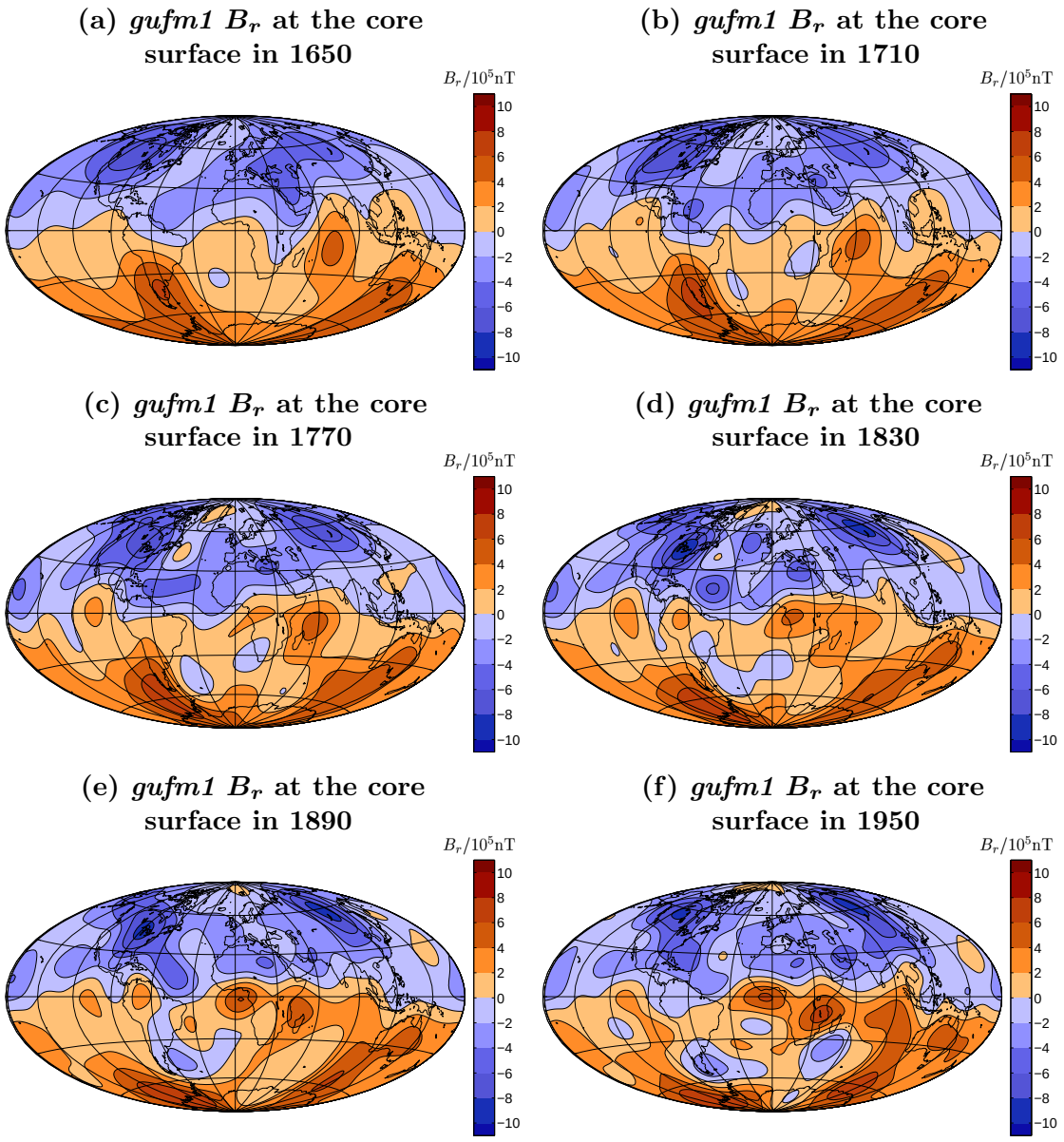

Figure 3.1: Snapshots of B_r from *gufm1* at the core surface.
Unfiltered radial magnetic field (B_r) from the model *gufm1* is presented in a series of snapshots from the years (a) 1650, (b) 1710, (c) 1770, (d) 1830, (e) 1890, (f) 1950. These and all subsequent snapshots in this chapter are in Hammer-Aitoff equal area map projection.

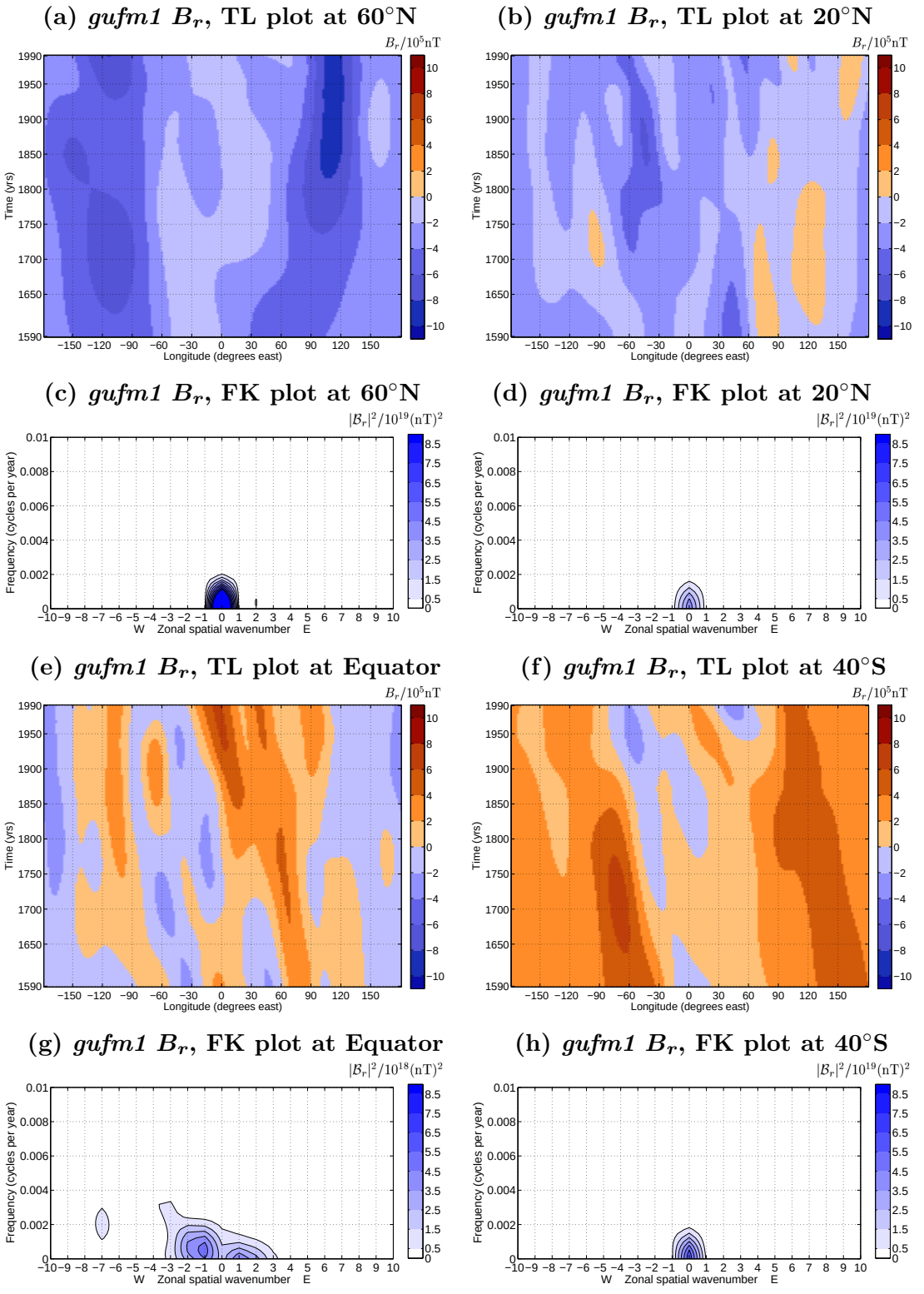

Figure 3.2: TL plots and FK power spectra of B_r from *gufm1*.
Time-longitude (TL) plots of the unprocessed radial magnetic field B_r from the field model *gufm1* at latitudes 60°N in (a), at 20°N in (b), at the Equator in (e) and at the 40°S in (f). The associated frequency-wavenumber (FK) power spectra are found in (c), (d), (g) and (h).

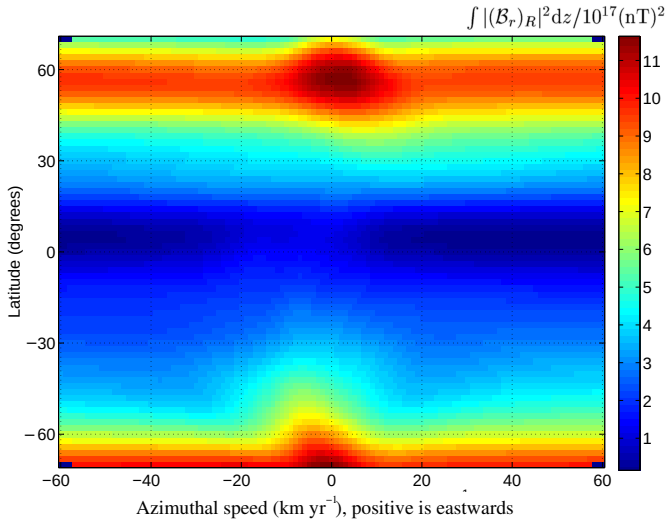

Figure 3.3: Latitude-azimuthal speed (LAS) power plot of B_r from *gufm1*. Power distribution as a function of latitude and azimuthal speed in a latitude-azimuthal speed (LAS) power plot of the unprocessed radial magnetic field B_r from the field model *gufm1*, constructed using the Radon transform method described in §2.2.4.

3.2.2 Radial magnetic field without time-averaged axisymmetric part $(B_r - \bar{B}_r)$

Following the strategies outlined in chapter 2, the radial field from *gufm1* is next progressively processed in an attempt to isolate field evolution modes of interest. The first step is to remove the time-averaged axisymmetric field $\bar{B}_r$, leaving $(B_r - \bar{B}_r)$. Snapshots of $(B_r - \bar{B}_r)$ in 1650, 1710, 1770, 1830, 1890 and 1950 are presented in figure 3.4. In these snapshots, the largest amplitude deviations from the time averaged axisymmetric field are often located at low latitudes. An animation of the evolution of $(B_r - \bar{B}_r)$ (see animation A2.2, consult appendix F for details) illustrates that this field is qualitatively similar to that of B_r, but with the latitudinal bias of the dipolar field removed.

TL plots and associated FK power spectra of $(B_r - \bar{B}_r)$ at 60°N, 20°N, the equator and 40°S are presented in figure 3.5. The m=0 dominant peak has been removed from the FK power spectra, allowing an improved identification of non-axisymmetric field anomalies. Clear azimuthally moving field features are obvious at the equator and at 40°S. The FK power spectra are unfortunately still dominated by large scale (particularly m=1) almost stationary features.

The associated LAS power plot is shown in figure 3.6. It remains dominated by almost stationary field features (now non-axisymmetric) at higher latitudes particularly in the northern hemisphere, though there are indications of a field feature moving westwards at approximately 8kmyr^{-1} near 40°S. A faint equatorial signal can just be distinguished.

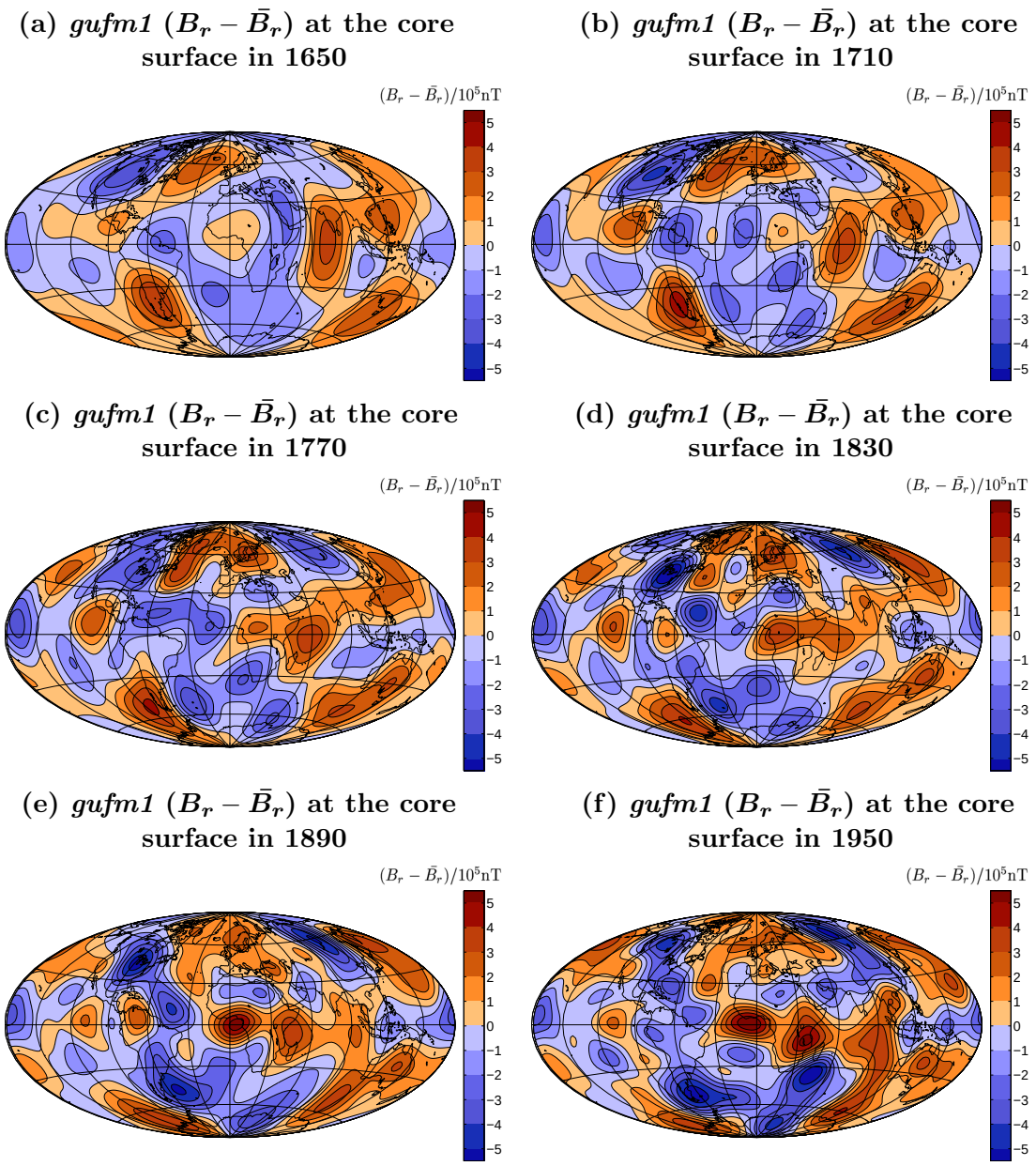

Figure 3.4: Snapshots of $(B_r - \bar{B}_r)$ from *gufm1* at the core surface.
Radial magnetic field at the core surface from *gufm1*, with the time averaged, axisymmetric part removed $(B_r - \bar{B}_r)$, is presented in a series of snapshots from (a) 1650, (b) 1710, (c) 1770, (d) 1830, (e) 1890, (f) 1950.

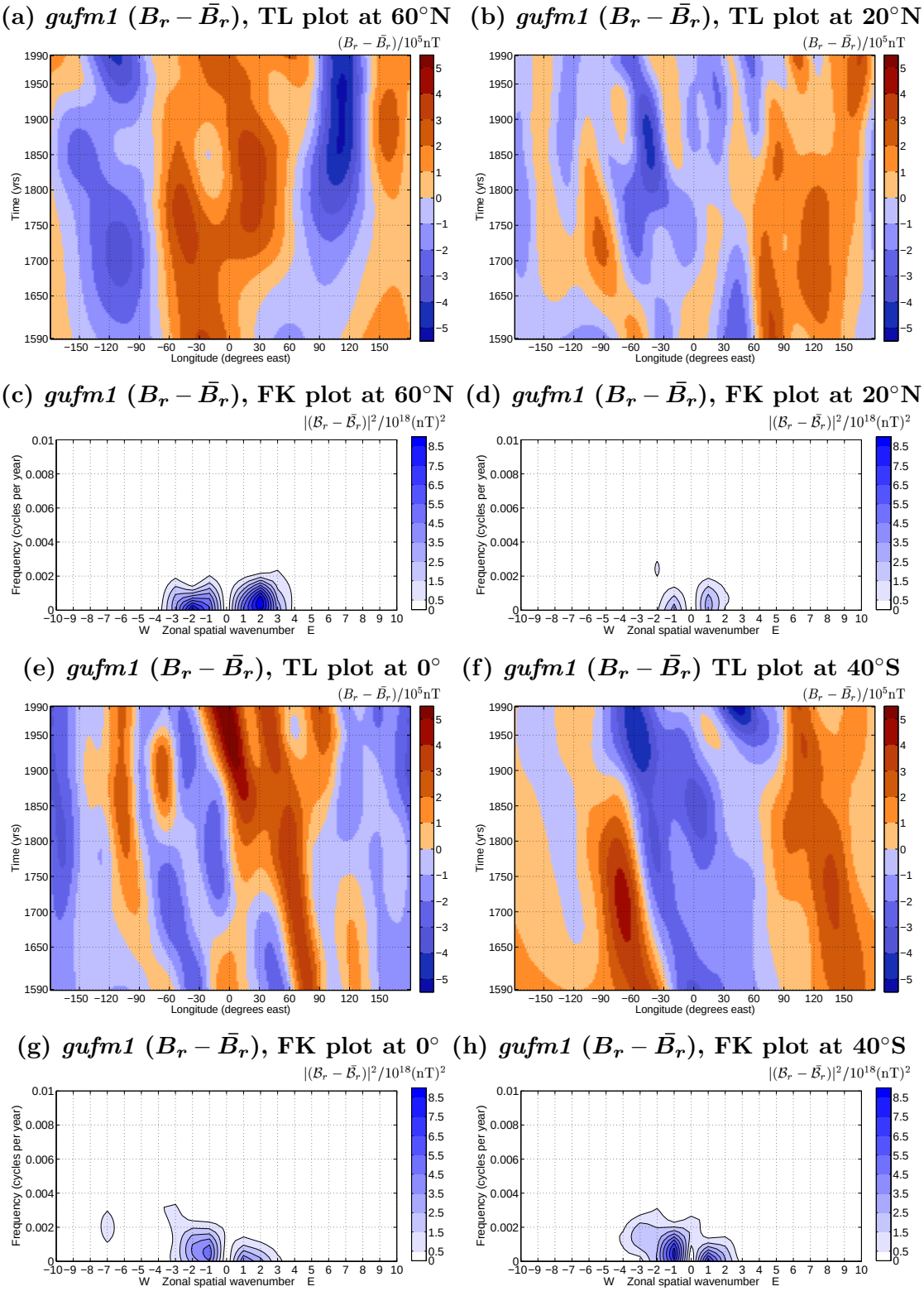

Figure 3.5: TL plots and FK power spectra of $(B_r - \bar{B}_r)$ from *gufm1*. Time-longitude (TL) plots of the radial magnetic field with time averaged axisymmetric component subtracted $(B_r - \bar{B}_r)$ from the field model *gufm1* at latitudes 60°N in (a), at 20°N in (b), at the equator (e) and at 40°S in (f). The associated frequency-wavenumber (FK) power spectra are found in (c), (d), (g) and (h).

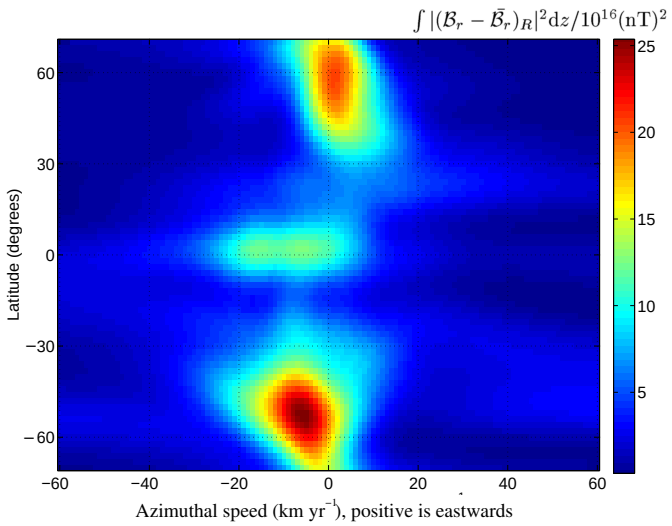

Figure 3.6: Latitude-azimuthal speed power plot of $(B_r - \bar{B}_r)$ from *gufm1*. Power distribution as a function of latitude and azimuthal speed in a latitude-azimuthal speed (LAS) power plot of the radial magnetic field with the time averaged axisymmetric field subtracted $(B_r - \bar{B}_r)$ from the field model *gufm1*, constructed using the Radon transform method described in §2.2.4.

3.2.3 Radial magnetic field with time averaged axisymmetric component removed and high pass filtered ($\widetilde{B_r}$)

The next processing step is to high-pass filter to remove field features evolving on long time scales. As for the synthetic examples in chapter 2, a range of cut-off periods were investigated. A filter cut-off choice of 400 years was chosen for further analysis because it removed field changes on time scales much longer than the record length that are difficult to rigorously investigate, yet succeeded in capturing 43 % of the original field variability as illustrated in figure 3.7.

The snapshots of $\widetilde{B_r}$ in 1650, 1710, 1770, 1830, 1890 and 1950 are presented in figure 3.8 and the time-dependent animation of $\widetilde{B_r}$ (see animation A3.3, consult appendix F for details) illustrates that removing the slowly evolving part of the field has dramatically altered the familiar picture of B_r evolution at the core surface.

The remaining field is dominated by westward moving field features, particularly at low latitudes (within 30° of the equator). There is also evidence for field features moving north-south into and out of the equatorial region, especially migrating towards the equator under Asia and away from the equator under the Atlantic and under North and South America. Field features generally emanate from the region under the eastern Pacific ocean and move westward, intensifying as they move over Africa, then splitting to move north and south under central America before they reach the Pacific region. Larger wavelength features are evident (particularly in the 20th century) at latitude 40°S. There are also weaker indications of a higher wavenumber disturbance in the northern hemisphere

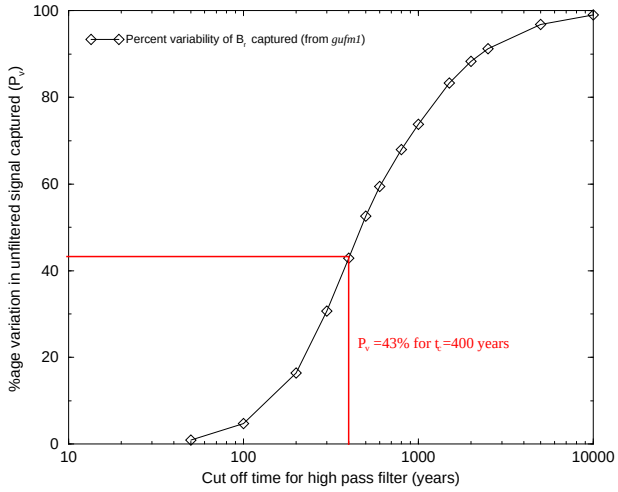

Figure 3.7: B_r variations captured by $\widetilde{B}_r$.
Graph showing the percentage of the original field variation P_v, as defined in equation (2.6), captured by $\widetilde{B}_r$ as the choice of filter cut-off is varied.

around 20 to 30°N. To further characterise this preliminary picture of the azimuthal field evolution, space-time spectral analysis was carried out.

In figure 3.9 the TL plots and FK power spectra for latitudes 60°N, 20°N, the equator and 40°S are presented. At 60°N there is evidence of a strong m=3 signal, with period of approximately 250 years, while at 20°N there is evidence for an m=7 signal with a period of approximately 220 years. At mid-latitudes in the southern hemisphere, for example at 40°S, m=2, 3 westward signals as well as a m=5 signal are observed.

The most striking observation is the presence of a series of alternating positive and negative westward moving field anomalies at the equator, under the Atlantic hemisphere. Six spatially and temporally coherent, westward drifting field anomalies are evident in the TL plot at the equator (figure 3.9e). The FK spectrum for this TL plot (figure 3.9g) has a dominant peak at $m = 5$ westward. This wave-like pattern of field anomalies could be a consequence of the influence of a hydromagnetic wave in Earth's core on B_r (Finlay and Jackson, 2003). This possibility is explored further using a range of theoretical and numerical models in chapters 6, 7 and 8.

The LAS power plot for $\widetilde{B}_r$ is found in figure 3.10. It provides further evidence for the presence of spatially and temporally coherent, azimuthally drifting, field features during the past 400 years. The strong equatorial maxima emphasises that the clearest coherent azimuthal field motion on time scales shorter than 400 years occurs at low latitudes. The peak of power suggests an azimuthal speed of $17\pm7\,\mathrm{kmyr}^{-1}$ westward[1]. The signal is centred at 2°N though there is a spread of power over latitudes from 15°N to 15°S. Weaker signals are also observed at high latitudes in the northern hemisphere at 50°N

[1]Estimates of the variability in the azimiuthal speeds come from the full width at half maximum amplitude of the peaks in the LAS power plot.

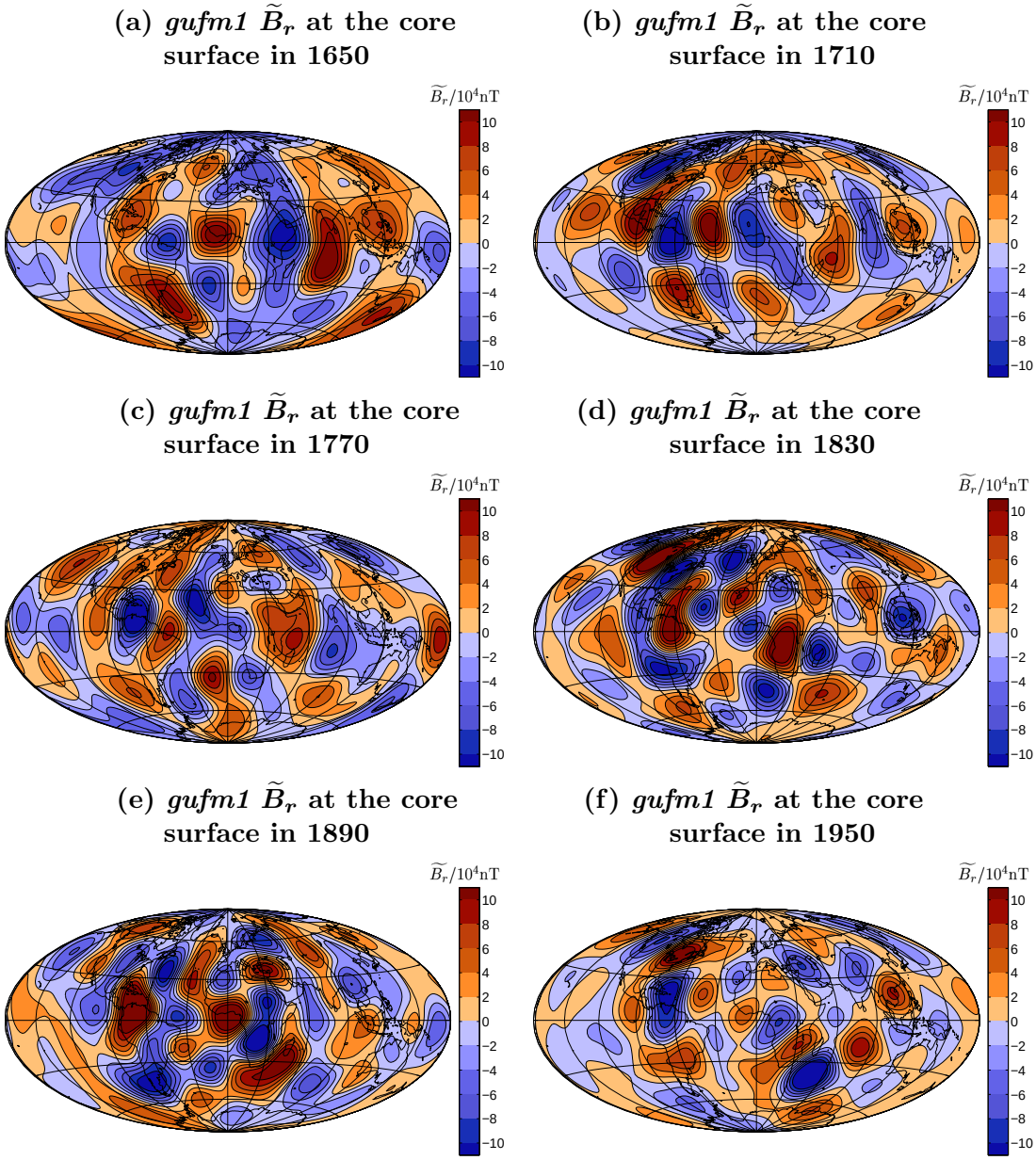

Figure 3.8: Snapshots of $\widetilde{B}_r$ from *gufm1* at the core surface.
Processed radial magnetic field $\widetilde{B}_r$ at the core surface, with the time averaged, axisymmetric part removed and high pass filtered with cut-off period 400 years, from the model *gufm1* is presented in a series of snapshots from (a) 1650, (b) 1710, (c) 1770, (d) 1830, (e) 1890, (f) 1950.

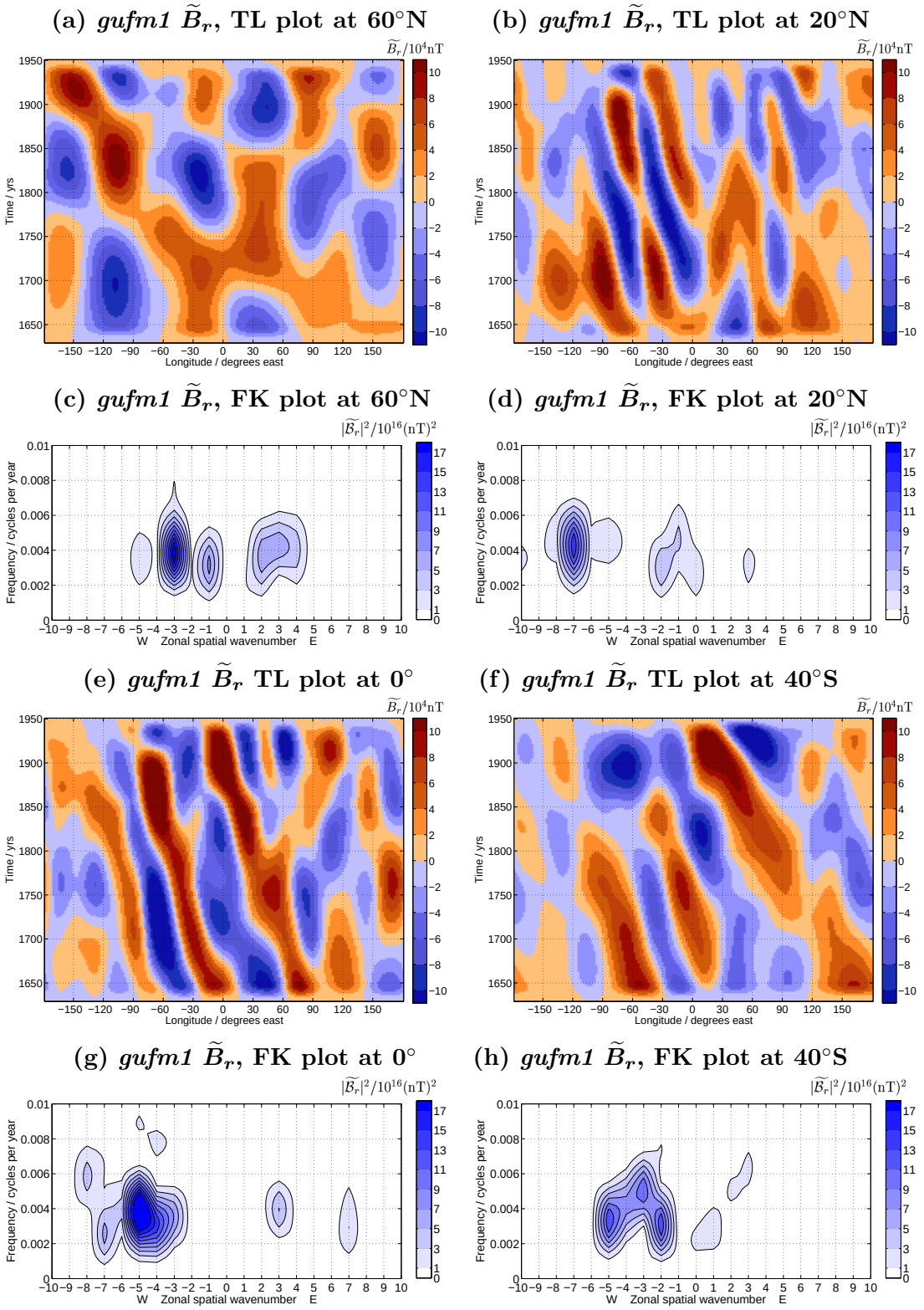

Figure 3.9: TL plots and FK power spectra of $\widetilde{B}_r$.
Time-longitude (TL) plots of the processed radial magnetic field $\widetilde{B}_r$ with time averaged axisymmetric component subtracted and high pass filtered with cut-off period 400 years, from the field model *gufm1* at latitudes 60°N in (a), at 20°N in (b), at the equator in (e) and at 40°S in (f). The associated frequency-wavenumber (FK) power spectra are found in (c), (d), (g) and (h).

to 60°N with maximum power at a speed of 16 kmyr^{-1} westward and in the southern hemisphere at 35°S to 50°S with maximum power at a speed of ∼30 kmyr^{-1} westward.

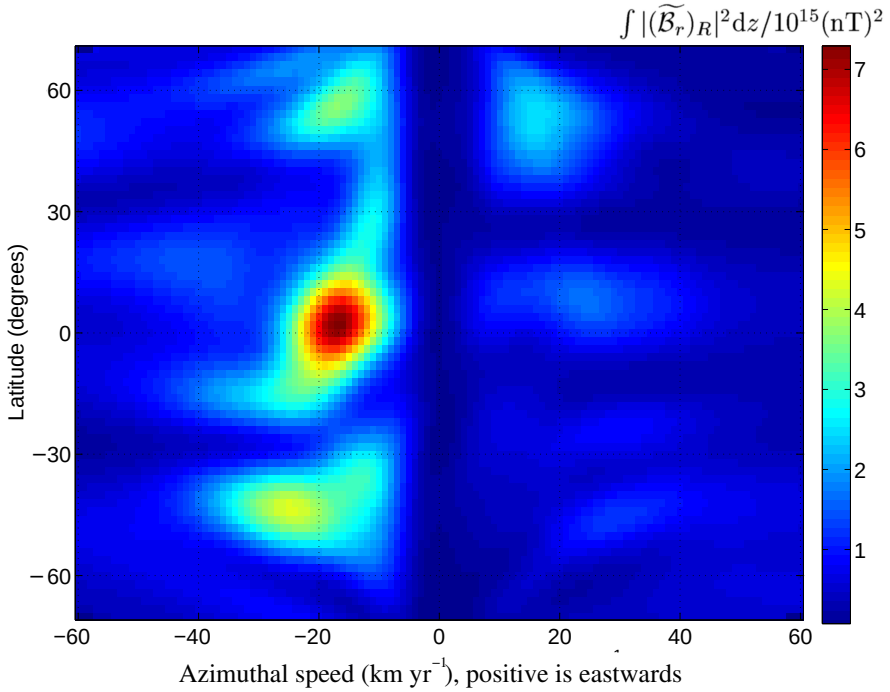

Figure 3.10: Latitude-azimuthal speed (LAS) power plot of $\widetilde{B}_r$ from *gufm1*. Power distribution as a function of latitude and azimuthal speed in a latitude-azimuthal speed (LAS) power plot of the processed radial magnetic field $\widetilde{B_r}$ with the time averaged axisymmetric field subtracted and filtered with a cut-off threshold of 400 years, from the field model *gufm1*, constructed using the Radon transform methodology of §2.2.4.

3.2.4 Comparison of $\widetilde{B_r}$ when filtering threshold is 400 years and 600 years

In order to be confident when interpreting $\widetilde{B_r}$, one must be satisfied that the features it shows are robust and not artifacts introduced by the processing. This question has already been partly addressed by considering synthetic models in chapter 2. There it was found that the form of $\widetilde{B_r}$ was insensitive to the small changes in filter parameters and that a signal with a 200 year period could be accurately recovered when a high pass filter threshold of 400 years was used. Here these finding are extended by comparing the form of $\widetilde{B_r}$ from *gufm1* with two choices of high pass filter threshold (400 and 600 years). Figure 3.11 shows the resulting snapshots, TL plots and FK power spectra at the equator and the LAS power plots. The evolution of $\widetilde{B_r}$ with t_c=600 years can also be seen in animation A3.4 (see appendix F for further details): it is morphologically very similar to animation A3.3 that documents the evolution of $\widetilde{B_r}$ when t_c=400 years. The TL plots and FK power spectra in the two cases are also very similar in form, but the m=7 signal appears to have more power when the cut-off is 600 years.

The peaks in the LAS power plot for t_c=400 years are all also present when t_c=600

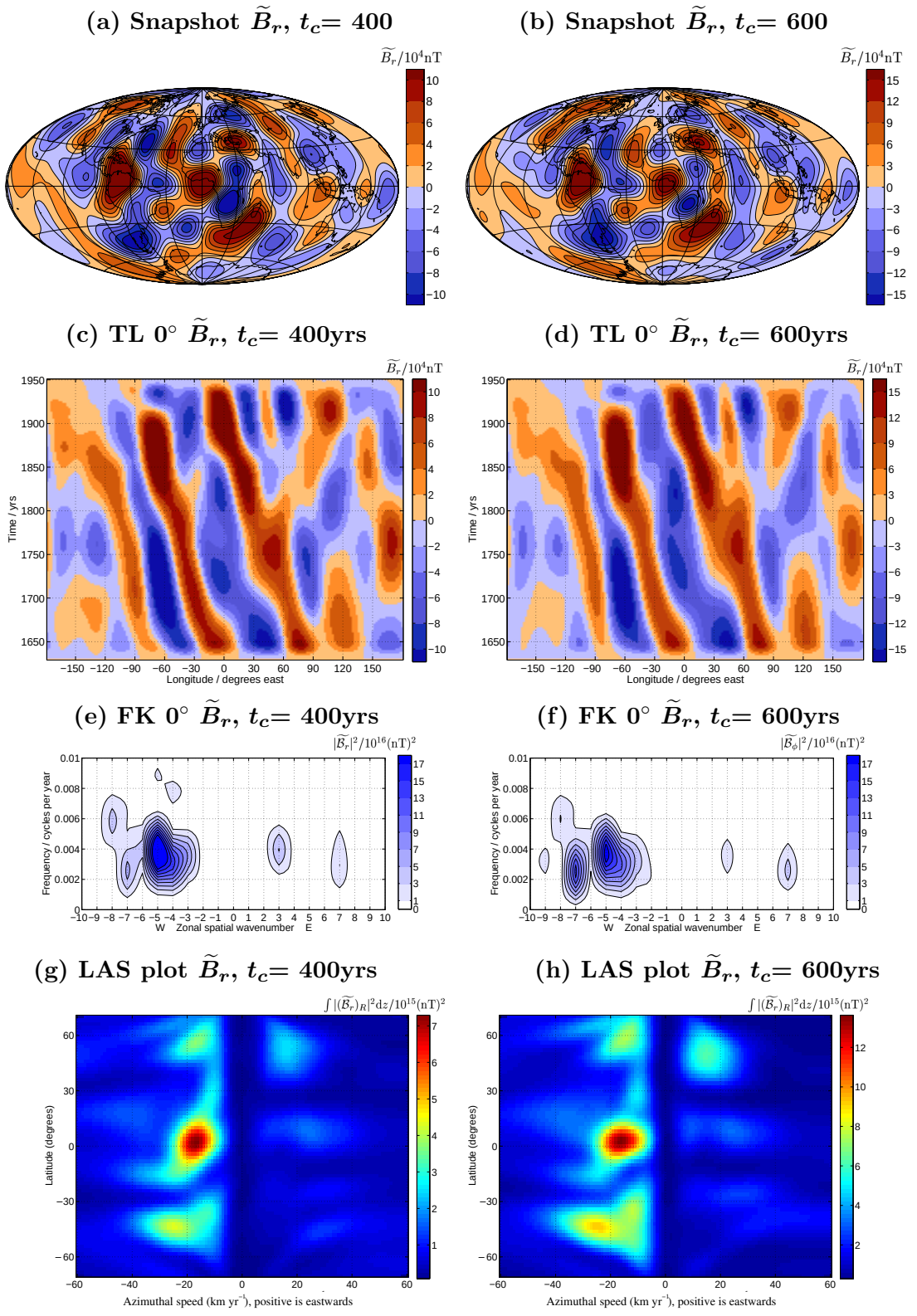

Figure 3.11: $\widetilde{B}_r$ from *gufm1* for filter cut-offs of t_c=400yrs and 600yrs. Processed radial magnetic field with time averaged axisymmetric field removed and high pass filtered with cut-off period t_c of 400 years and 600 years, from *gufm1*. (a), (b) show snapshots of the field at the core surface in 1890; (c), (d) show time-longitude (TL) plots of the field evolution at the equator and (e),(f) the associated frequency-wavenumber (FK) power spectra; (g), (h) show the latitude-azimuthal speed (LAS) power plots.

years. This means that the features interpreted in the previous section are robust and not artifacts. With a 600 year cut-off the higher latitude peaks have larger amplitude suggesting the field evolution mechanisms associated with them operate on time scales longer than the record length. The 400 year cut-off results have been presented in detail in this chapter rather than the 600 year results because it is difficult to rigorously justify the interpretion of field changes on time scales longer than the 400 year length of *gufm1*.

3.2.5 Spherical harmonic power spectrum for $\widetilde{B_r}$

Rather than processing space-time grids of a geomagnetic field model, it is also possible to construct $\widetilde{B_r}$ by processing the spherical harmonic model coefficients sampled at discrete time intervals. In this case the equivalent processing involves first subtracting the time average of each m=0 spherical harmonic (removing the time-averaged axisymmetric field). Secondly, discrete time series for each spherical harmonic coefficient must be high pass filtered (the filter cut-off threshold is chosen as before to be 400 years).

This alternative field processing method is instructive for two reasons. First it provides a check that $\widetilde{B_r}$ has been constructed correctly in the space-time griding method[2] and secondly it enables the effect of processing on the time-averaged spherical harmonic power spectra to be determined (see figure 3.12).

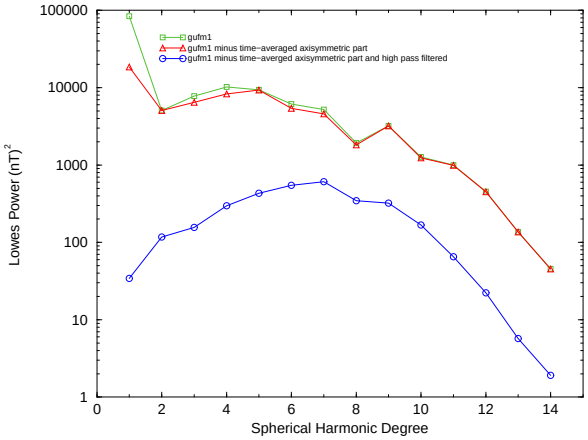

Figure 3.12: Spherical harmonic power spectra of B_r,B_r-$\bar{B}_r$),$\widetilde{B}_r$ from *gufm1*. The time-averaged spherical harmonic power spectra (Lowes, 1974) defined by the expression $R_l = (\frac{a}{c})^{2l+4}(l+1)\sum_{m=0}^{L}[(g_l^m)^2+(h_l^m)^2]$, where L is the degree of model truncation, g_l^m, h_l^m are the spherical harmonic coefficients, a is the radius of Earth's surface and c is the core radius. The green squares and line show the time-averaged power spectra of the unprocessed field model *gufm1*, the red triangles and line show the power spectra of the time-averaged axisymmetric (m=0) component and the blue circles and lines show the time-averaged power spectra after the $m = 0$ component has been removed and the times series for each spherical harmonic have been high pass filtered with t_c=400 yrs.

[2] $\widetilde{B_r}$ from processing model coefficients was identical to that found from the space-time grids.

The model associated with $\widetilde{B_r}$ has considerably less power at all degrees, due to the removal of the m=0 time-averaged components and the high pass filtering. It exhibits a shallow peak over degrees 4 to 10 in contrast to the spectra for the unprocessed field model that is dominated by low degree spherical harmonics. This illustrates that looking at $\widetilde{B_r}$ involves focusing on smaller spatial scales than those that dominate the original field model, even though no explicit spatial filtering has been carried out.

3.3 Isolation and description of field evolution modes in $\widetilde{B_r}$

In this section frequency-wavenumber filtering (see §2.9) is carried out to isolate the space-time signatures of strong spectral peaks found in the analysis of $\widetilde{B_r}$ shown in figure 3.9. It was decided to investigate the m=3 signal that dominates in figure 3.9c, the m=7 signal that dominates in figure 3.9d and the m=5 signal that dominates in figure 3.9g. For each wavenumber investigated, only frequencies of 0.003 to 0.008 cycles per year (periods between 125 years and 333 years) are retained. In figure 3.13 snapshots of the field at the core surface in 1890 and the LAS power plots associated with the reconstruction of m=7, m=5, and m = 3 are presented. Animations of the field evolution at the core surface from 1630 to 1950 associated with the modes can be found in animations A3.5 (m=7), A3.6 (m=5) and A3.7 (m=3) respectively (see appendix F for further details).

The m=7 mode in figure 3.13a,b is observed to have most power at mid-latitudes in the northern hemisphere from 10°N to 50°N, centred around 30°N. It is initially located at low latitudes, but moves slightly northwards as time progresses, until in the 20th century it is centred at 30°N. It is noteworthy that the position of this m=7 mode in the 20th century is coincident with previous identifications of wave features in B_r at the core surface during that period. In particular, it is consistent with the mid-latitude polar wave discussed by Bloxham et al. (1989) (see their figure 28) that was tentatively identified as being of wavenumber between m=5 and m=8; it is also consistent with the northern hemisphere part of the approximately m=8 patterns recently reported in high resolution images constrained by satellite data and linked to wave motions by Jackson (2003). The lack of any southern hemisphere signal associated with this mode means it cannot be definitively classified as either equatorially symmetric (E^S) or equatorially antisymmetric (E^A).

The reconstruction of the m=5 mode in the space-time domain and its LAS power plot in figure 3.13c,d confirms this mode as the source of the high amplitude equatorial signal seen in figure 3.10 that was earlier reported by Finlay and Jackson (2003). This low latitude m=5 mode is clearly observed to be symmetric about the equator (E^S). It is present throughout the interval from 1630 A.D. to 1950 A.D., but in the animation A3.6 it appears to weaken in the 20th century. There also seems to be a strong m=5 signal at between latitudes 40° to 50° north and south. The phase of these higher latitude signals

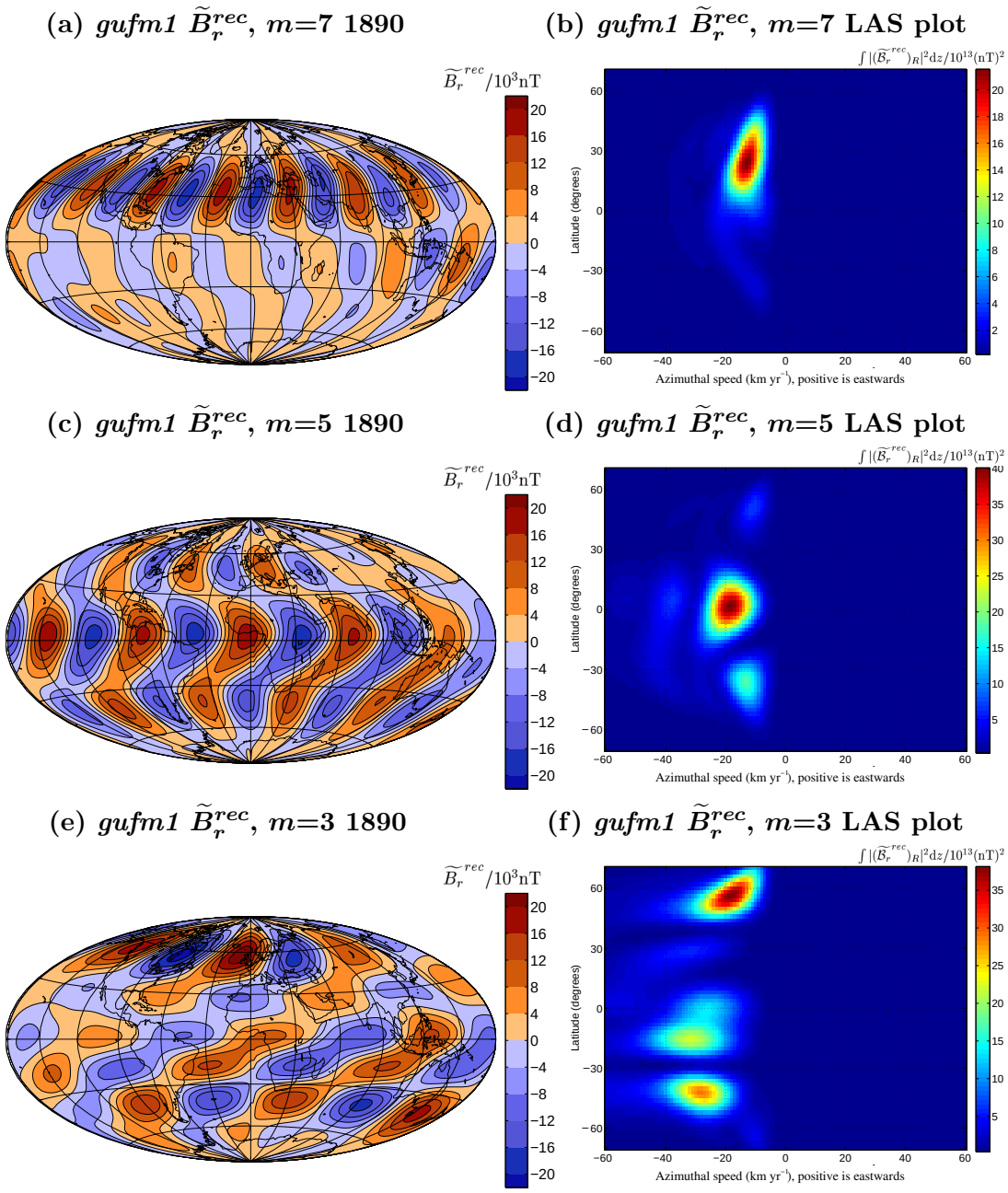

Figure 3.13: Snapshots and LAS plots of $\widetilde{B}_r^{rec}$ from *gufm1*; m= 7, 5 and 3. By FK-filtering, motions with wavenumbers m= 7, 5 and 3 and periods between 125 and 333 years were isolated. Snapshots of the recovered field at the core surface in 1890 are shown in (a) for m=7, in (c) for m=5, in (d) for m=3, while the latitude-azimuthal speed (LAS) power plots are shown in (b) for m=7, in (d) for m=5, in (e) for m=3.

is not fixed compared with that of the equatorial signal.

Results from the FK-filtering reconstruction of the m=3 westward mode are shown in figure 3.13e,f and its evolution at the core surface can be followed in animation A3.7. Most power is found at higher latitudes, particular in the northern hemisphere at 60°N, travelling westward at an average speed of approximately 18 km yr^{-1}. The signal in the

southern hemisphere is at 40°S, so no clear equatorial symmetry exists for this mode.

Care should be taken when interpreting the results of FK-filtering discussed above. Experiments with synthetic models illustrated that this processing can map a single drifting field feature into a wave-like group, with maximum amplitude where the drifting feature was in the original. Especially at latitudes where a range of wavenumbers are present in $\widetilde{B}_r$, inferences concerning properties associated with a single wavenumber should be treated with caution. However, at latitudes where $\widetilde{B}_r$ is dominated by a single wavenumber (such as at the equator) and where global wave patterns are seen before spatial filtering, inferences concerning the mode properties should be considered reliable.

3.4 Geographical trends in azimuthal speeds of field features

The use of spatial sub-windows as described in §2.6 permits the determination of variations in the azimuthal speeds of spatially and temporally coherently field features (time-averaged over the observation interval) as a function of position on the core surface. This technique was applied to $\widetilde{B}_r$ constructed using a high pass filter with cut-off period of 400 years from *gufm1*. The results are displayed in figure 3.14.

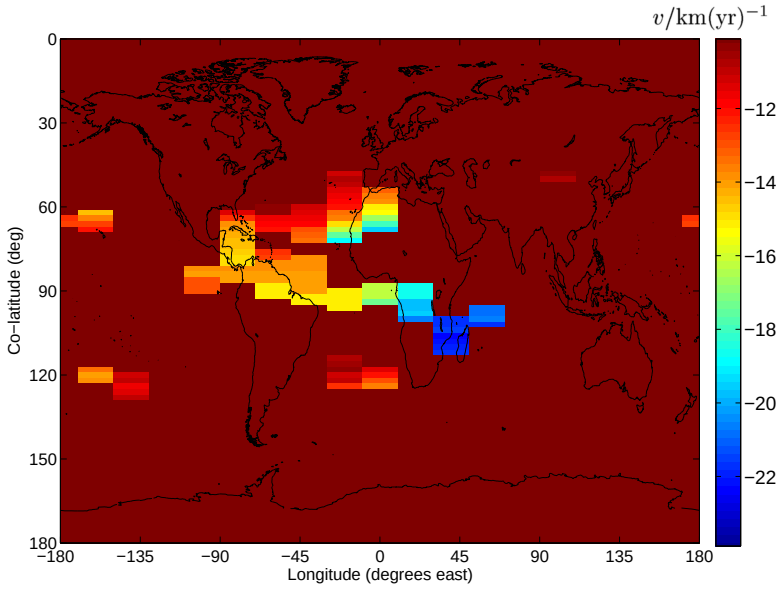

Figure 3.14: Geographical variations in azimuthal speeds of $\widetilde{B}_r$ from *gufm1*. Using longitudinal windows of width 80 degrees, moving in steps of 20 degrees the variations in azimuthal speed as a function of both latitude and longitude can be determined using the Radon transform methodology described in §2.2.4 and §2.6. Only the peak with most power is utilised in each sub-LAS power plot, and that peak must be greater than 4 times the average power in the plot for it to be displayed, otherwise a speed of 0 km yr^{-1} is assigned to the location.

Low latitudes in the Atlantic hemisphere is the region with most high amplitude, spatially

and temporally coherent, azimuthally moving features, consistent with animations of $\widetilde{B_r}$. There does not seem to be any obvious trend in the azimuthal speeds of field anomalies as a function of latitude. Features move fastest (around 22 $\mathrm{km\,yr^{-1}}$) under south-western Africa and slowest (around 12 $\mathrm{km\,yr^{-1}}$) at mid-latitudes under the Atlantic ocean. The fast speeds under South-western Africa are consistent with the m=3 mode discussed in §3.3, the slower speeds at mid-latitudes under the northern Atlantic are consistent with the m=7 mode. The features seen under Venezuela and the Caribbean are consistent with the speeds and location of the m=5 mode.

Similar studies of geographical variations in the azimuthal speed of oceanic motions (e.g. Chelton and Schlax (1996)) showed clear latitudinal trends. These helped to diagnose the presence of oceanic Rossby waves and enabled theoretical predictions of their propagation speeds to be tested. The lack of any clear latitudinal trends in the present study suggests that there is no evidence for the propagation of waves whose phase speed varies in a simple manner with latitude, for example as a result of the β-effect (the variation in the Coriolis force with latitude).

3.5 Hemispherical differences in field evolution processes

Whether Earth's magnetic field and its evolution are fundamentally different in the Pacific hemisphere has been discussed since the time of the Carnegie Institution's magnetic surveys of the oceans in the early 20th century (Fisk, 1931) when anomalously low secular variation was observed there. Whitham (1958) suggested that there was no convincing evidence for westward drift of non-dipole field features into the Pacific hemisphere while Vestine and Kahle (1966) proposed that the lack of secular variation in the Pacific was linked to low main field amplitude and gradients there (also consult Walker and Backus (1996) for a demonstration of the statistical difference in the average value of B_r^2 between the Pacific and Atlantic hemispheres).

Doell and Cox (1965; 1971) used evidence from paleomagnetic records in Hawaiian lavas to propose that secular variation in the Pacific has been anomalously low there over the past million years, suggesting that this might be a signature of a heterogeneous lower mantle influencing convection in the core. Recently Bloxham (2002), Christensen and Olson (2003) and Gubbins and Gibbons (2004) have provided quantitative support for this proposal by modelling how hemispherical differences in core flow patterns (and hence secular variation) could be produced by variations in heat flux at the core surface. In order to further evaluate such proposals it is necessary to compare predicted patterns of field evolution to the patterns found in geomagnetic field models. The analysis of *gufm1* carried out in this chapter is suitable for this purpose.

In figure 3.15 time-longitude (TL) plots for the Pacific and Atlantic hemispheres from *gufm1* are presented separately in order that the properties of the field evolution in the

east-west direction in the two hemispheres can be compared and contrasted. These plots illustrate that the strongest spatial and temporally coherent field evolution is found in the Atlantic hemisphere. However, there also appear to be weaker westward moving field anomalies in the Pacific hemisphere, particularly at 40 °S (see figure 3.15e). This demonstrates that westward drift of field features in the historical era is not confined the Atlantic hemisphere. The synthetic tests of §2.8 demonstrated that signals in the Pacific hemisphere could not result from aliasing of a strong Atlantic hemisphere signal which gives confidence in the reality of the Pacific signal observed here. Furthermore, the wavenumber and speeds of the azimuthally moving field features in the Pacific and Atlantic hemispheres are similar. This appears to be an indication that the core motions inducing wave-like patterns of secular variation are global in extent and not confined to the Atlantic hemisphere. The signal may be weaker in the Pacific hemisphere because the field amplitude and gradients acted on by core motions are smaller there (Vestine and Kahle, 1966). This hypothesis is investigated further in chapter 8 where the forward problem of global wave flows acting on a historical magnetic field configuration is studied. The explanations of Christensen and Olson (2003) and Gubbins and Gibbons (2004) whereby inhomogeneous thermal boundary conditions produce very different forms of flow in the Pacific and Atlantic hemispheres predicts different field evolution patterns in the two hemispheres; this seems incompatible with the results of the present study.

The question of whether the Pacific hemisphere has always experienced weak secular variation, and if so why low field amplitude and gradients should be localised there cannot be answered using *gufm1*. These issues are discussed further when the archeomagnetic model CALS7K.1 is analysed in chapter 4.

3.6 Temporal variations in field evolution processes

A shortcoming of LAS power plots calculated from the whole timespan of data is their inability to distinguish between short intervals of high amplitude, spatially and temporally correlated field motions, and weaker less coherent field motion over a longer interval. This is a consequence of the implicit averaging over the entire timespan that is involved in taking the Radon transform of an entire TL plot.

This issue can be addressed (at the expense of resolution of the azimuthal speed of field features — see §2.7) by calculating LAS power plots for sub-windows of time. After synthetic trials (see §2.7), window widths of 80 years were chosen and the windows moved through the record in steps of 10 years. The results for windows centred on 1670, 1700, 1750, 1800, 1850 and 1910 are shown in figure 3.16.

The strong equatorial feature is present throughout the record, though is most prominent before 1800 and appears to weaken after 1900. Evidence for a higher latitude (around 60°N) spatially and temporally coherent field evolution process is seen in the northern

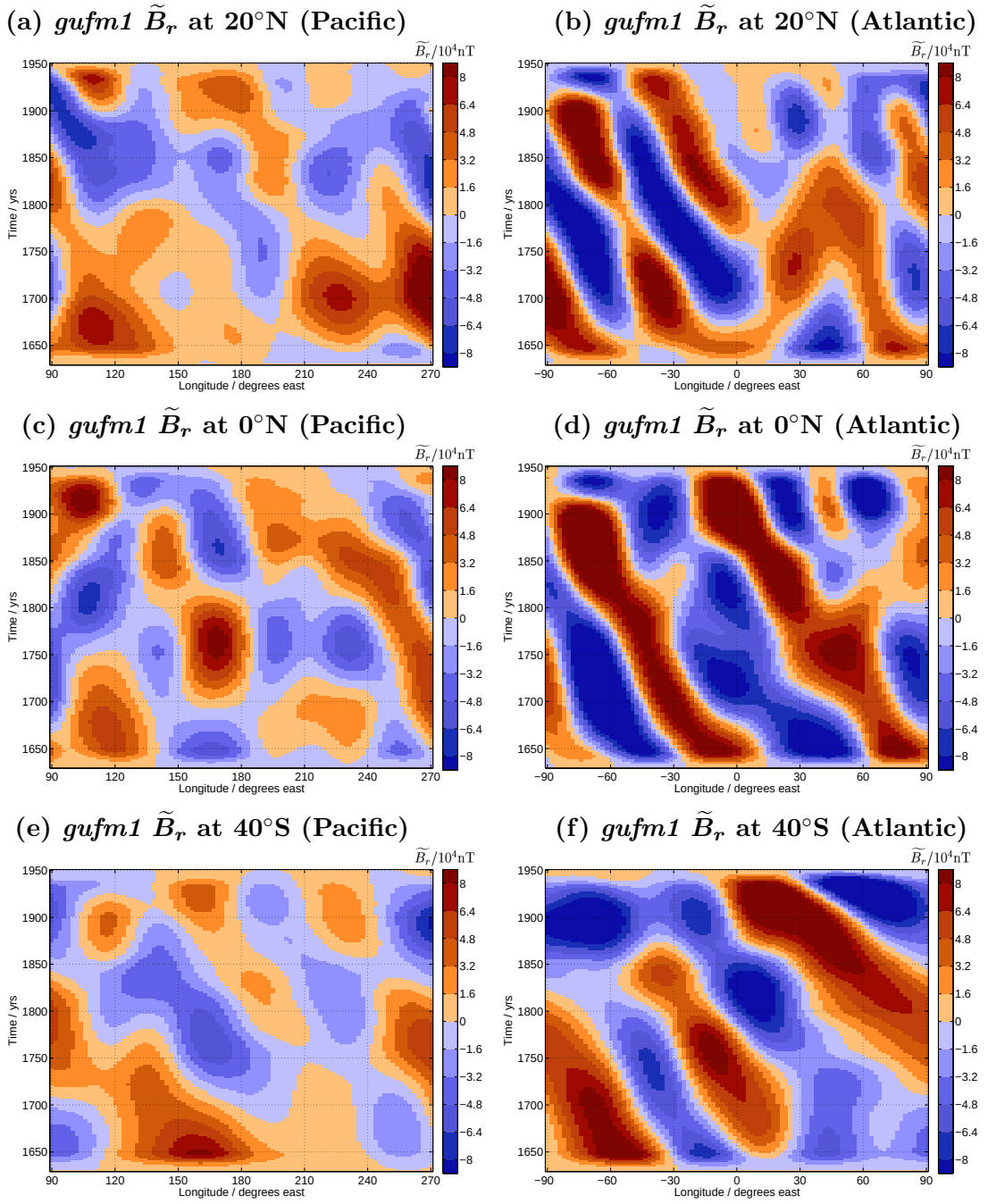

Figure 3.15: Hemispherical differences in field evolution in *gufm1*.
Time-longitude (TL) plots of the evolution in the east-west direction of processed radial magnetic field, with time-averaged axisymmetric field removed and high pass filtered with cut-off period of $t_c = 400$ years ($\widetilde{B}_r$), separated into the Pacific and Atlantic hemispheres. (a), (c), (e) show the evolution in the Pacific hemisphere at 20°N, 0°N, and 40°S respectively. (b), (d), (f) show the evolution in the Atlantic hemisphere at 20°N, 0°N, and 40°S respectively.

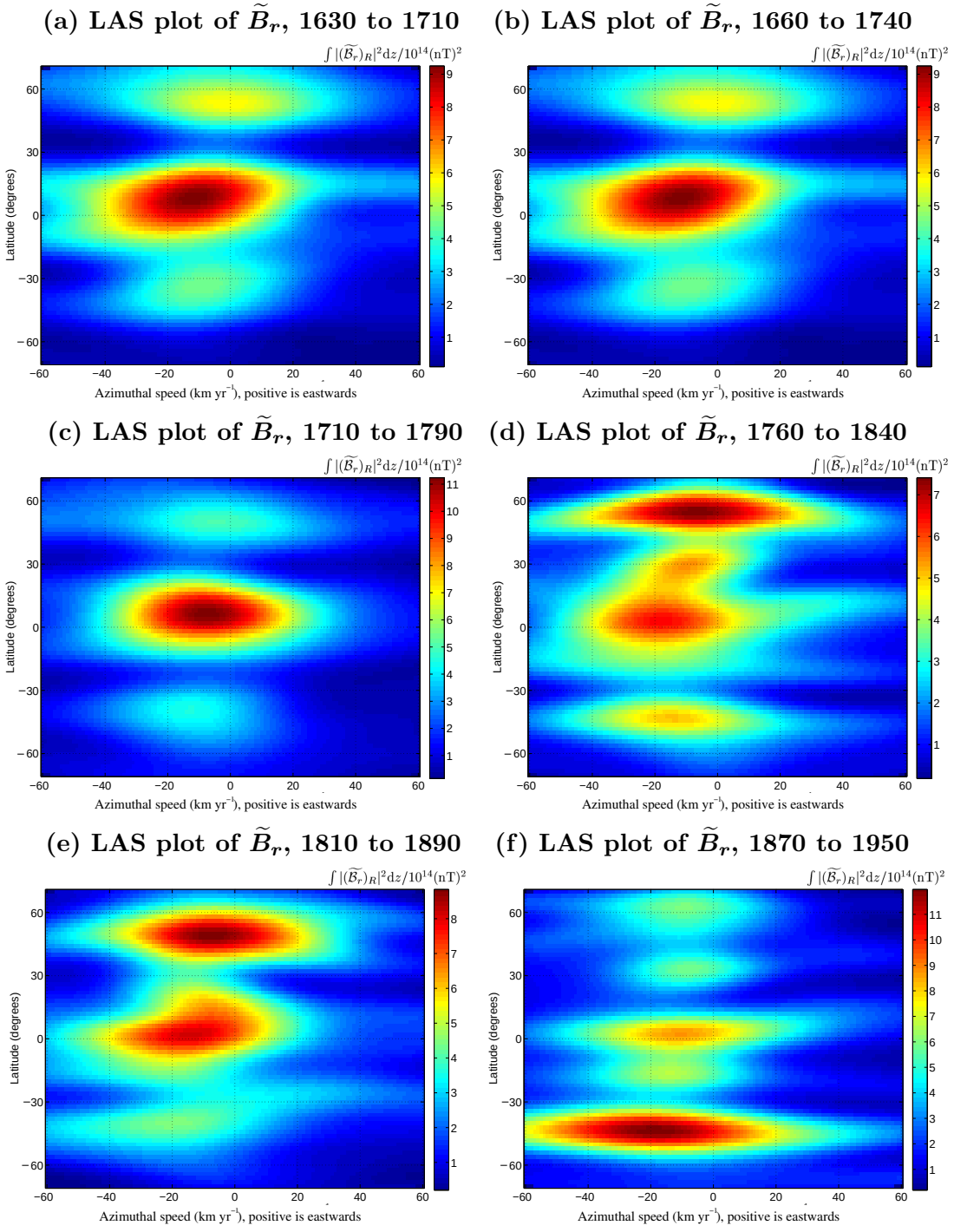

Figure 3.16: Temporal evolution of LAS plots of $\widetilde{B}_r$ from *gufm1*.
Using sub-windows in time of length 80 years, the evolution of the latitude-azimuthal speed (LAS) power plot is followed, and the permanence of features seen in the average LAS plot constructed from the full record (See figure (3.10)) can be assessed. (a) shows a time sub-window centred on 1670, (b) a window centred on 1700, (c) a window centred on 1750, (d) a window centred on 1800, (e) a window centred on 1850 and (f) a window centred on 1910.

hemisphere especially from 1760 to 1890, consistent with the m=3 FK-reconstructed signal discussed in §3.3. From 1860 until the end of the record, at latitude 40°S a strong signal is seen consistent with the southern hemisphere m=3 FK-reconstructed mode. There is also a weaker feature at 30°N in the northern hemisphere in the 20th century, that seems likely to be linked with the m=7 FK-reconstructed signal.

All of the field evolution modes, identified in §3.3 as being associated with peaks in the LV plot for $\widetilde{B_r}$ in figure 3.10, therefore appear to be rather transitory phenomenon. They have not been steady in amplitude, position or speed over the past 400 years. This should be borne in mind when seeking to make inferences concerning the time-independent spectral content of field evolution mechanisms, and when making comparisons to geodynamo model output or when comparing to predictions from simple theoretical models.

3.7 Determination of dispersion by wavenumber filtering $\widetilde{B_r}$ from *gufm1*

Dispersion is the phenomenon whereby the speed at which a signal is transmitted depends on its frequency and hence its wavelength (see, for example, the discussion in Feynman et al. (1963)). By measuring dispersion from observations of a propagating disturbance and calculating the best (least squares, regularised) fit obtained to theoretical models of wave propagation, it is possible to assess the viability of the different models as an explanation for the propagating disturbance. Furthermore, if a model can be found that produces a good fit to the observations, it may be possible to infer bounds on previously undetermined physical properties associated with the propagation mechanism. The use of observations of dispersion in seismic surface waves to infer the structure of Earth's crust and mantle (see, for example Shearer (2001) and Romanowicz (2002); Shearer (2001)) is one example of a geophysical application of such ideas.

Now consider drifting geomagnetic field features at Earth's core surface. If the dispersion of such features could be accurately determined it would be possible to test proposed models for the origin of the drift, such as hydromagnetic wave propagation or advection. If a satisfactory model could be found, the range of acceptable model parameters could be used to place bounds on core dynamics. The first step in this scheme is to determine whether or not there is any evidence for dispersion in current geomagnetic field models. Here an attempt to do just that was made using *gufm1*.

The field $(B_r - \bar{B}_r)$ was filtered so that only a single wavenumber remained, but without restriction in frequency. An estimate of the equatorial azimuthal speed corresponding to this wavenumber was then obtained by constructing a LAS power plot and finding the speed corresponding to maximum power at the equator. The LAS power plots used to infer the azimuthal phase speeds for different wavenumbers are presented in figure 3.17.

Considering all latitudes, strong signals can be found over a wider range of wavenumbers, but it seems likely that different field evolution mechanisms might operate at different

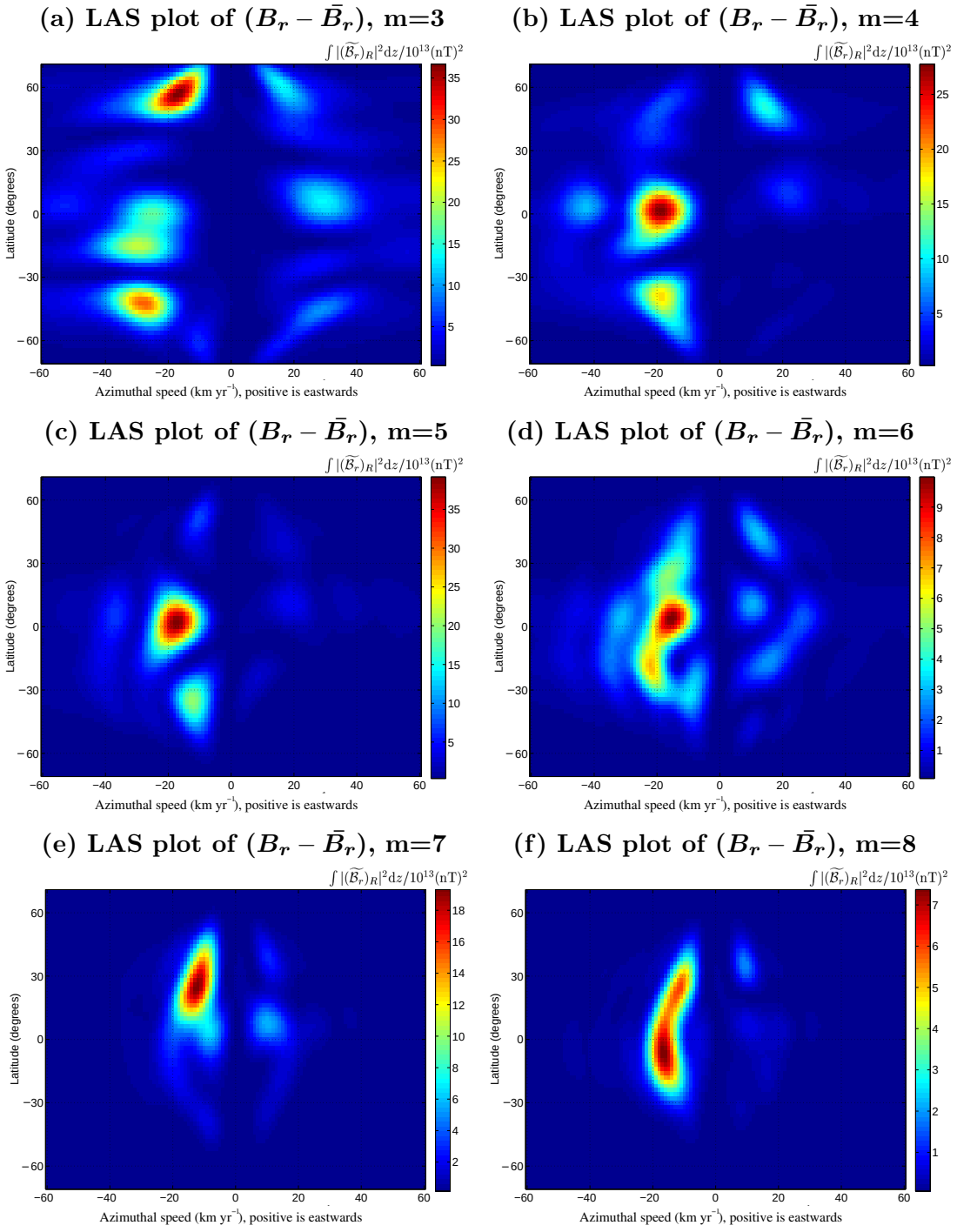

Figure 3.17: LAS plots from *gufm1* of $(B_r - \bar{B}_r)$ filtered by wavenumber. Latitude-azimuthal speed (LAS) plots of $(B_r - \bar{B}_r)$ from *gufm1* filtered only by wavenumber and retaining all frequencies. (a) shows wavenumber m=3, (b) m=4, (c) m=5, (d) m=6, (e) m=7 and (f) m=8.

latitudes. Therefore only a single latitude (the equator) where the clearest signal was located was investigated. Unfortunately, the FK power at the equator contains power at only a small range of wavenumbers (between m=3 and m=8), with most of the power associated with the m=5 signal. This makes it rather difficult to measure dispersion.

In figure 3.18 the equatorial azimuthal speeds of anomalies in $(B_r - \bar{B}_r)$ estimated from the LAS power plots in figure 3.17 (with bounds indicating the full width at half maximum (FWHM) of the peaks in the LAS plots) are presented as a function of wavenumber. Even over the small range of wavenumbers available, the m=3, 7 modes in figure 3.17 are rather weak at the equator and must therefore be regarded with suspicion.

Two possible interpretations of the variation of the azimuthal speed of field features with wavenumber are suggested in figure 3.17. Considering only m=4, 5, 6, 8 as robust, then the least squares best fit line shows only a very weak gradient; infact a best fit line with zero gradient would also lie well within the FWHM limits. Therefore, the most robust data can be said to be consistent with the hypothesis of no dispersion in azimuthal geomagnetic secular variation at the equator.

A second interpretation is possible if one is willing to accept the weak m=3,7 signals as reliable. In this case, the least squares best fit line and any best fit lines compatible with the error bounds require that smaller wavenumbers (longer wavelengths) travel faster azimuthally than larger wavenumbers (shorter wavelengths). In this case azimuthal geomagnetic secular variation at the equator would be interpreted as having an inverse dispersive character.

The almost monochromatic nature of the strong equatorial signal indicates that the mechanism generating the field evolution may not be a free oscillation process suitable for study via wave dispersion techniques, but instead the signature of a forced instability as a result of which only a small range of wavenumbers are excited. The caveat that only a single wavenumber is observed because of the short record length should also be noted. Higher resolution observations over a longer period are (as usual) the only way to definitively resolve this issue.

The most cautious and rigorous interpretation of the results of this investigation is that there is no evidence of dispersive behaviour in the geomagnetic secular variation captured by *gufm1*. Since dispersive behaviour is expected for hydromagnetic waves in a rapidly rotating fluids (see chapter 6) this result favours advection rather than wave propagation as the source of the azimuthal motion of wave-like patterns observed in $\widetilde{B}_r$ in figure 3.10.

3.8 Summary

In this chapter the azimuthal evolution of B_r at the core surface over the past 400 years as captured by the model *gufm1* has been studied in detail. Space-time spectral analysis has

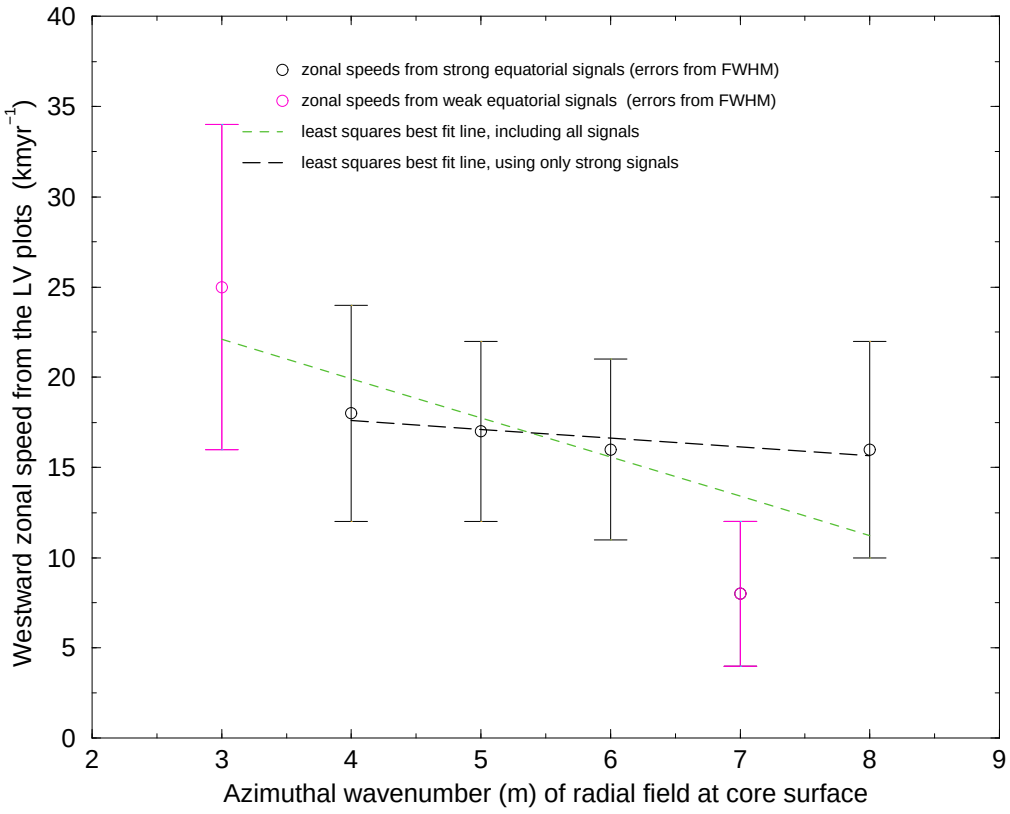

Figure 3.18: Wavenumber versus azimuthal speed of $(B_r - \bar{B}_r)$ at 0°N. Azimuthal (zonal) speeds of field features of $(B_r - \bar{B}_r)$ from *gufm1* determined from LAS plots after the field has been filtered so only single wavenumbers remain. The black line shows the best least squares fit to m=4, 5, 6, 8 observed speeds. The observations for m=3, 7 may not be robust because there is little power seen in the LAS plots at the equator for these wavenumbers.

been carried out on $\widetilde{B_r}$ after the removal of the time-averaged axisymmetric component as well as the part of the field changing on time scales longer than 400 years. Spatially and temporally coherent, azimuthally drifting, wave-like patterns in B_r have been identified. Hemispherical differences in field evolution processes have been discussed. Geographical and temporal variations in the azimuthal speeds of field evolution mechanisms have been investigated. The dependence of azimuthal speed on wavenumber (dispersion) has also been studied.

The most striking result of this investigation is the identification of a mode of magnetic field evolution at low latitudes dominated by a single wavenumber (m=5). This mode has a frequency f=0.004 cpyr (corresponding to a period of around 250 years) and moves westward at an average speed of 17 km yr^{-1}. It is equatorially symmetric (E^S) and is present throughout the historical record, though appears to have weakened in the 20th century. It is observed most clearly under the Atlantic hemisphere from 100°E to 100°W. Its properties are insensitive to the high pass filter threshold used in the analysis. There are no known systematic errors introduced by the spectral analysis, field modelling or

measurement methods that would produce such a spatially and temporally coherent signal on these long time scales, implying that this must be a genuine mode of magnetic field evolution at the core surface.

Other signals identified in $\widetilde{B_r}$ include a weaker m=7 signal found at low to mid latitudes in the northern hemisphere and a m=2, 3 signal that is strongest at mid latitudes in the southern hemisphere. The m=7 signal is observed most clearly near to latitude 30°N in the 20th century though it is initially located at lower latitudes and slowly drifts northward. It has frequency f=0.004 cpyr (a period of around 250 years) and moves westward at an average speed of around 12 km yr^{-1}. The m=2, 3 signal is observed most clearly between 20°S and 40°S and has a frequency of 0.0042 cpyr (a period of 235 years) and moves rapidly westward at an average speed of 30 km yr^{-1}. It is strongest towards the end of the historical record (especially after 1800), and at longitudes 150°E to 90°W. It was further found that although the highest amplitude, spatially and temporally coherent patterns of field evolution were located in the Atlantic hemisphere, weaker patterns with similar form were also present in the Pacific hemisphere.

It was not possible to detect either dispersive behaviour or any systematic geographic trends in azimuthal speeds of field features. These are properties associated with hydromagnetic wave propagation mechanisms in rapidly rotating fluids (see chapter 6). The negative results obtained therefore suggest that the azimuthal motion of the wave-like patterns in B_r may be more consistent with advection by azimuthal flow than with hydromagnetic wave propagation in the core. Wave propagation as a mechanism for azimuthal magnetic field motion cannot be ruled out on the basis of the results of this chapter, but there is no strong evidence in its favour.

Chapter 4

Application of the space-time spectral analysis technique to the archeomagnetic field model CALS7K.1

4.1 Introduction

In this chapter results of the application of the space-time spectral analysis methods to a continuous archeomagnetic and lake sediment geomagnetic field model spanning the interval 5000 B.C. to 1950 A.D. (CALS7K.1 — see appendix B for a description of the model) are presented.

The most serious shortcoming of an analysis of geomagnetic secular variation based on *gufm1* is that this model spans only 400 years. This is unfortunately not long enough for rigorous and statistically significant conclusions to be drawn concerning field evolution mechanisms with time scales of centuries to millennia. A possible resolution of this difficulty involves using indirect measurements of Earth's magnetic field. Constructing global field models and testing hypotheses concerning geomagnetic secular variation requires a density of spatial and temporal coverage of observations that exist only in the past few millennia, so attention will focus on this time interval.

Over the past decade a continuous geomagnetic field model derived from indirect measurements from the past seven millennia has been developed by Cathy Constable and co-workers as described in Johnson and Constable (1998), Constable et al. (2000), Korte and Constable (2003), Korte et al. (2005) and Korte and Constable (2005). Their latest model is known as CALS7K.1 (Continuous Archeomagnetic and Lake Sediment model of the past 7000 years, Version 1) and is the best current source of information concerning the evolution of the geomagnetic field at the core surface on millennial time scales.

In this chapter an attempt is made to assess the reliability of CALS7K.1 by comparing a subsection of the model from 1600 A.D. to 1950 A.D. (referred to as CALS7K.1h)

to a version of the historical geomagnetic field model *gufm1* (referred to as *gufm1d*) processed so that its spatial power spectra matches that of CALS7K.1h. Having gained insight into the limitations of CALS7K.1, the full span of model CALS7K.1 is analysed using time-longitude methods developed in chapter 2 to search for episodes of spatially and temporally coherent azimuthal motion of B_r at the core surface. Finally the results of the investigations are summarised and the implications for understanding mechanisms of geomagnetic secular variation are discussed.

4.2 Comparison of CALS7K.1h to *gufm1d*

In this section a subset of the field model CALS7K.1, covering the interval 1600 A.D. to 1950 A.D., and referred to as CALS7K.1h is analysed in detail and compared to a version of the historical model *gufm1* (referred to as *gufm1d*) processed to mimic the power spectra of CALS7K.1h (but of course derived using higher quality data). Comparison between these models permits the reliability of CALS7K.1h (and hence that of CALS7K.1) to be assessed. It allows identification of where and on what time scales spurious features should be expected. This should help to guard against erroneous interpretations of CALS7K.1 later in the chapter.

4.2.1 Creation of *gufm1d* and spherical harmonic power spectra

The model called *gufm1d* was created by multiplying the coefficients for each degree in *gufm1* by a modulation factor $\sqrt{\frac{R_l^{CALS7K.1h}}{R_l^{gufm1}}}$ to force the power spectra of the result (*gufm1d*) to be identical to that of CALS7K.1h. The time-averaged power spectra of CALS7K.1h (also that of *gufm1d*) is compared to the time averaged power spectra of *gufm1* in figure 4.1. The power in CALS7K.1h is always lower than that in *gufm1*, but they are of comparable magnitude up to spherical harmonic degree 5. At high spherical harmonic degree the power in CALS7K.1h drops off much faster than the power in *gufm1*. *gufm1d* was created to determine whether a model with the same spatial power characteristics as CALS7K.1 can capture the major field evolution processes noticed in the study of *gufm1* in chapter 3, and to isolate the effects of data errors and problems due to the sparse geographical spread of observations compared to the effect strong damping of field coefficients in CALS7K.1h.

4.2.2 Comparison of unprocessed radial magnetic field (B_r)

Snapshots from CALS7K.1h and *gufm1d* in 1650 A.D., 1830 A.D. and 1950 A.D. are displayed in figure 4.2, while animations A4.1 and A4.2 show the continuous evolution of CALS7K.1h and *gufm1d* respectively over the interval 1600 A.D. to 1950 A.D. Figure 3.1 and animation A4.1 should be consulted in order to compare CALS7K.1 and *gufm1d* with

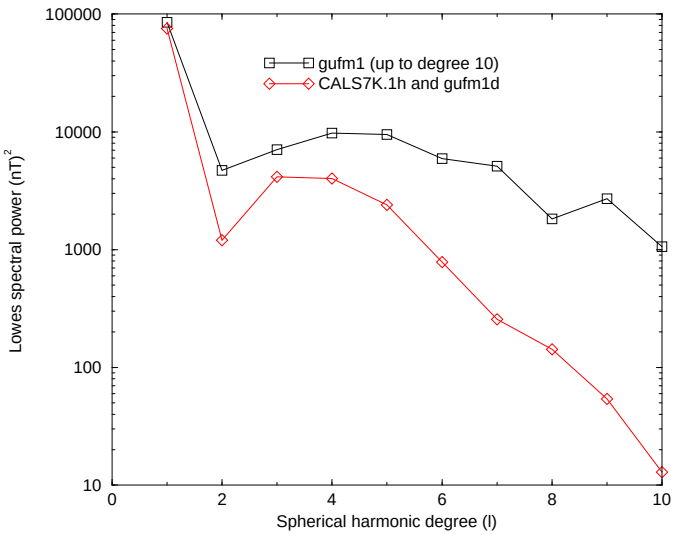

Figure 4.1: Spectra from *gufm1* compared to CALS7K.1h and *gufm1d*. The time-averaged spherical harmonic power spectra (Lowes, 1974) defined by the expression $R_l = (\frac{a}{c})^{2l+4}(l+1)\sum_{m=0}^{L}[(g_l^m)^2+(h_l^m)^2]$, where L is the degree of model truncation, g_l^m, h_l^m are the spherical harmonic coefficients, a is the radius of Earth's surface and c is the core radius. The black squares and line show the power spectra of *gufm1* up to spherical harmonic degree 10, while the red diamonds and line show the power spectra of CALS7K.1h and *gufm1d*, in which each spherical harmonic degree in *gufm1* has been scaled in order to obtain the same power spectra as CALS7K.1h.

gufm1. *gufm1d* does a surprisingly good job of capturing field evolution patterns seen in B_r at the core surface in *gufm1*, except that high amplitude, small length scale features are smoothed out. In the subsequent discussions it shall therefore be assumed that *gufm1d* accurately represents the large scale field evolution that CALS7K.1 should ideally reproduce, given more accurate data and a better global distribution of observations.

Both CALS7K.1h and *gufm1d* are dipole dominated, with high latitude field concentrations in the northern hemisphere, have westward moving undulations of the geomagnetic equator and have lows in B_r amplitude under the northern Atlantic. These similarities are remarkable given differences in both data type and the spatial distributions of observations. However, differences in positions of field concentrations and their time evolution in these two models are certainly present. For example the B_r concentration initially observed below the Indian ocean and moving westward is very prominent in *gufm1d* but not seen in CALS7K.1h; under Africa in CALS7K.1h there is a region where the magnetic equator is almost north-south, this is not observed in *gufm1d*; concentrations of B_r are observed at high latitudes in the southern hemisphere in *gufm1d* but not in CALS7K.1h; there is a reversed flux patch observed in the Northern Atlantic after 1850 in CALS7K.1h that is only a low amplitude field feature in *gufm1d*.

The absence of B_r features known to be present in historical models constructed with higher accuracy data indicates that CALS7K.1h accurately captures only certain aspects

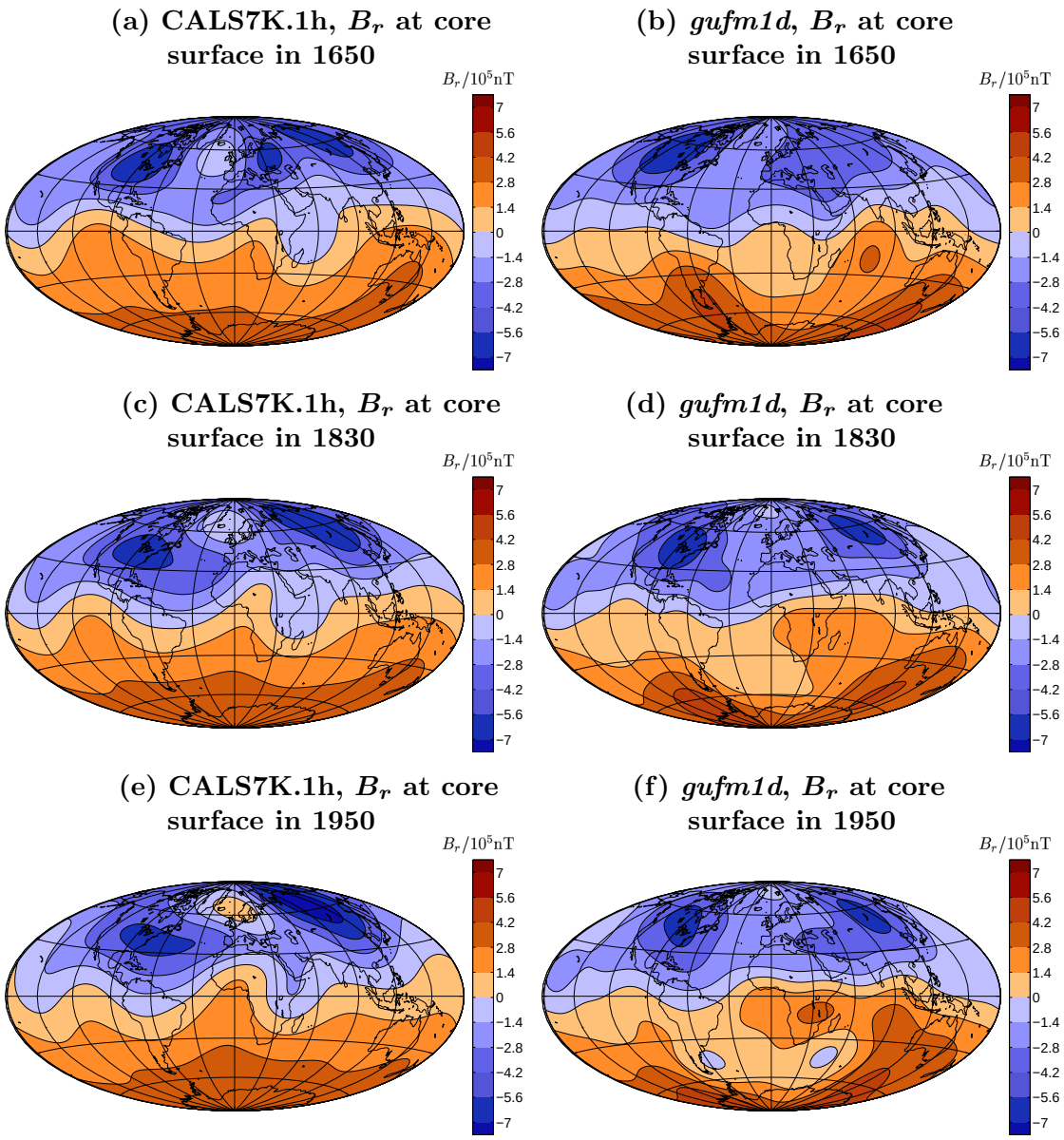

Figure 4.2: Comparison of snapshots of B_r from CALS7K.1h and *gufm1d*. Unfiltered radial magnetic field (B_r) at the core surface from the models CALS7K.1h and *gufm1d* are presented for comparison in snapshots from 1650 A.D. in (a), (b), from 1830 A.D. in (c), (d) and from 1950 A.D. in (e), (f). These and all subsequent snapshots in this chapter are in Hammer-Aitoff equal area map projection.

of the geomagnetic field evolution. The presence of features in CALS7K.1h not seen in *gufm1* raises the dilemma that interpretation of CALS7K.1 without thought could lead to erroneous conclusions regarding field evolution mechanisms. These problems are illustrated in more detail in figure 4.3 where time-longitude (TL) plots of the unprocessed B_r from CALS7K.1 and *gufm1d* are presented. These should also be compared and contrasted with the TL plots of *gufm1* in figure 3.2.

At 60°N, two nearly stationary, high amplitude features are found in both *gufm1d* and in CALS7K.1h though the space-time paths are slightly different. A reverse flux feature at 0°E is prominent in CALS7K.1h, but it is only observed as a low amplitude feature in *gufm1d*. At 20°N, features from 0°E to 180°E exist after 1800 A.D. in CALS7K.1h that are not as striking in *gufm1d*. At the equator, CALS7K.1 fails to correctly capture positions and speeds of the most rapidly azimuthally moving features seen in *gufm1d*: the feature moving from 90°E in 1600 A.D. to 60°E in 1800 A.D. in *gufm1d* is not present in CALS7K.1h . The problems with degraded information in CALS7K.1h compared to *gufm1d* are most serious in the southern hemisphere; for example at 40°S no field features at all are observed in the western hemisphere in CALS7K.1h, while structures are certainly present in *gufm1d*. Despite these shortcomings, some reliable information is obtained from CALS7K.1h: the direction of motion of field features in *gufm1d* and CALS7K.1h is found to agree well. For example the feature at 20°N moving from 30°W in 1600A.D. to 60°W in 1950A.D. is present in both models. It can certainly be concluded that CALS7K.1h will not show spatially and temporally coherent, westward moving, field features in TL plots unless they are also present in *gufm1d*.

4.2.3 High pass filtering and the variability captured by *gufm1d* and CALS7K.1h

When attempting to characterise the evolution of B_r in *gufm1* it was found to be useful to remove the time-averaged axisymmetric field and to high pass filter to remove stationary and very slow moving field features. Ideally, one would like to carry out the same procedure to CALS7K.1. However, as has already become evident, it seems unlikely that CALS7K.1 will have the spatial or temporal resolution to capture all the processes of interest observed in *gufm1*. Nevertheless it is important to attempt such procedures, in order to determine the precise shortcomings of CALS7K.1 and to aid future development of similar millennial time scale field models, that will undoubtedly eventually become valuable research tools.

The percentage variability captured compared to the unfiltered case (P_v, see equation (2.6)) in CALS7K.1h and *gufm1d* between 1600A.D. and 1950A.D. compared to that of *gufm1* is shown in figure 4.4 for a range of high pass filter thresholds. Models *gufm1* and *gufm1d* show almost identical variations with 42 % of field change remaining when changes longer than 400 years are removed. In contrast, CALS7K.1h is dominated by slower field change mechanisms, with only 18 % of field changes remaining when the

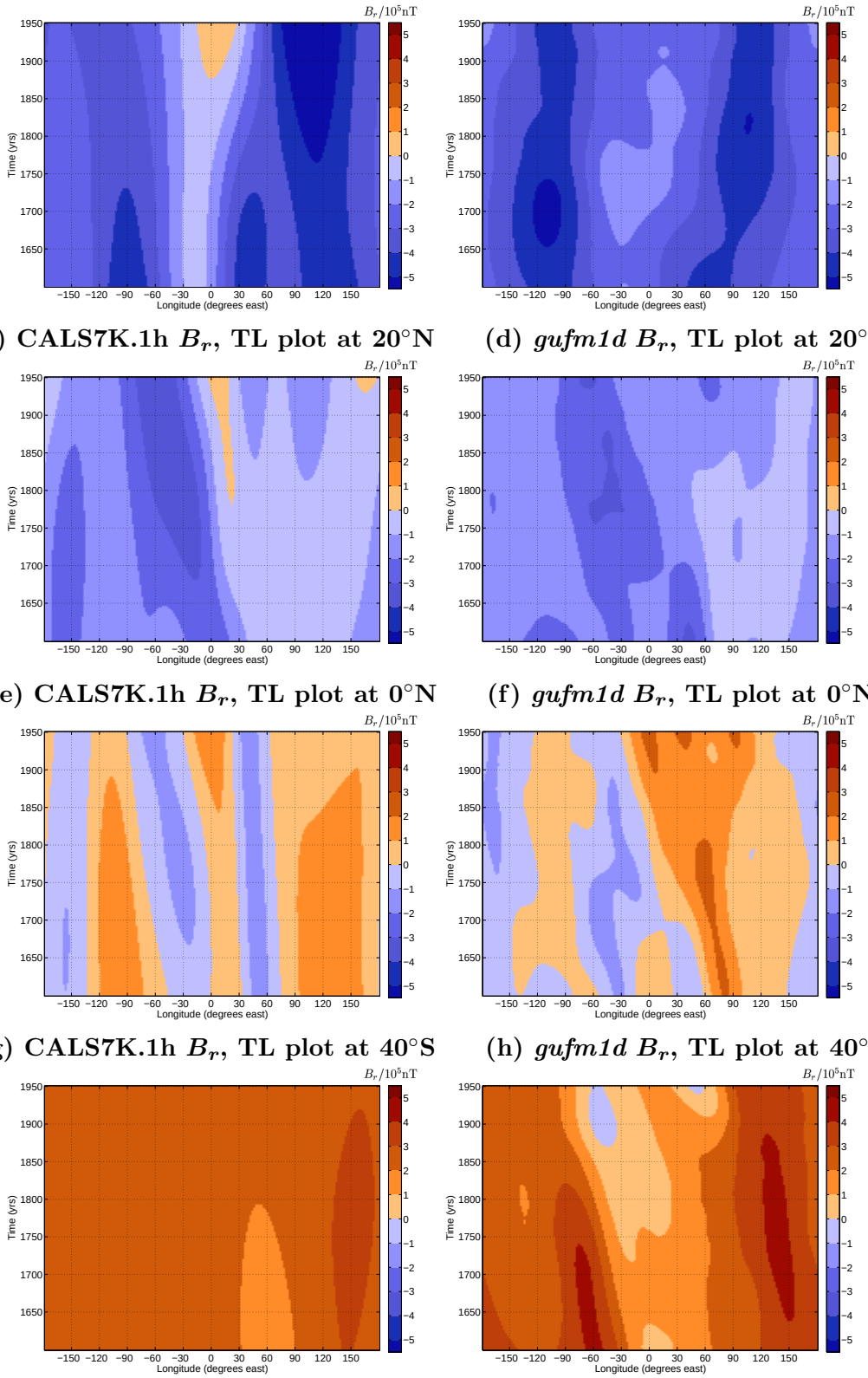

Figure 4.3: TL plots of B_r from CALS7K.1h and *gufm1d*.
Time-longitude (TL) plots of the unprocessed radial magnetic field (B_r) from the field models CALS7K.1h and *gufm1d* from 1600A.D. to 1950A.D. at latitudes 60°N in (a), (b); at 20°N in (c), (d); at the Equator in (e), (f) and at the 40°S in (g), (h).

filtering threshold is 400 years. Unfortunately, this 18 % is the most poorly constrained component of CALS7K.1h, given the large errors associated with dating indirect records of the magnetic field in the past. It is clearly not sensible to filter CALS7K.1h with a threshold of 400 years, but it may be reasonable to filter it with a longer threshold of a few thousand years in which a significant percentage of the original variability in the unprocessed model is captured.

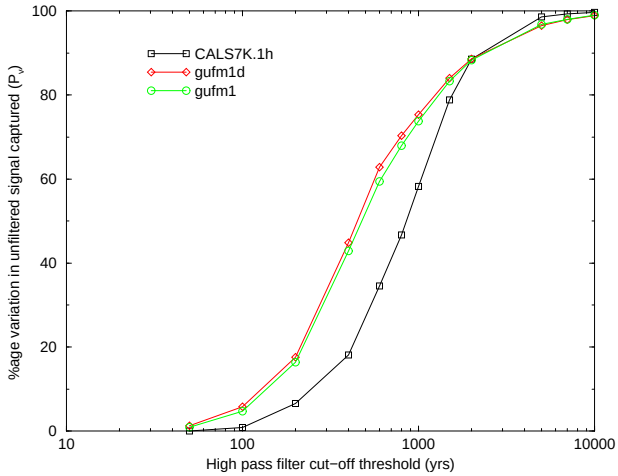

Figure 4.4: Variation in CALS7K.1h compared to *gufm1d* and *gufm1*. Graphs showing the percentage of the original field variation P_v, as defined in equation (2.6), captured by $\widetilde{B_r}$ as the choice of filter cut-off is varied in CALS7K.1h, *gufm1d* and *gufm1*, over the interval 1600A.D. to 1950A.D.

Figure 4.5 gives further insight into the fidelity with which field evolution processes are captured. It documents changes in latitude-azimuthal speed (LAS) power plots for CALS7K.1h and *gufm1d* as the filter-cut off threshold is varied. When only the time-averaged axisymmetric field is removed, but no filtering is carried out the LAS power plots for the two model show some similarities. A slow eastward moving field feature is dominant at mid to high latitudes in the northern hemisphere (at approximately 60°N) and a westward moving feature is observed at mid to low latitudes in the northern hemisphere. However, the strong southern hemisphere feature seen at 50°S in *gufm1d* is absent from CALS7K.1h, emphasising the incomplete coverage in data coverage in the southern hemisphere in CALS7K.1 during this time interval.

For a filter threshold of 2500 years, the strong southern hemisphere signal in *gufm1d* is still not captured, but a strong westward signal is found for both models at low to mid latitudes in the northern hemisphere, with an azimuthal speed of approximately 20 $\mathrm{km\,yr^{-1}}$, but with a much larger spread of power in CALS7K.1h. When the filter threshold is decreased further to 800 years an eastward signal at 45°N is seen in both models, and both still show a low latitude signal in the northern hemisphere. Finally when the filter threshold is 400 years,the two models both have signals in the northern hemisphere (at round 50°N) that were interpreted in the previous chapter as being the

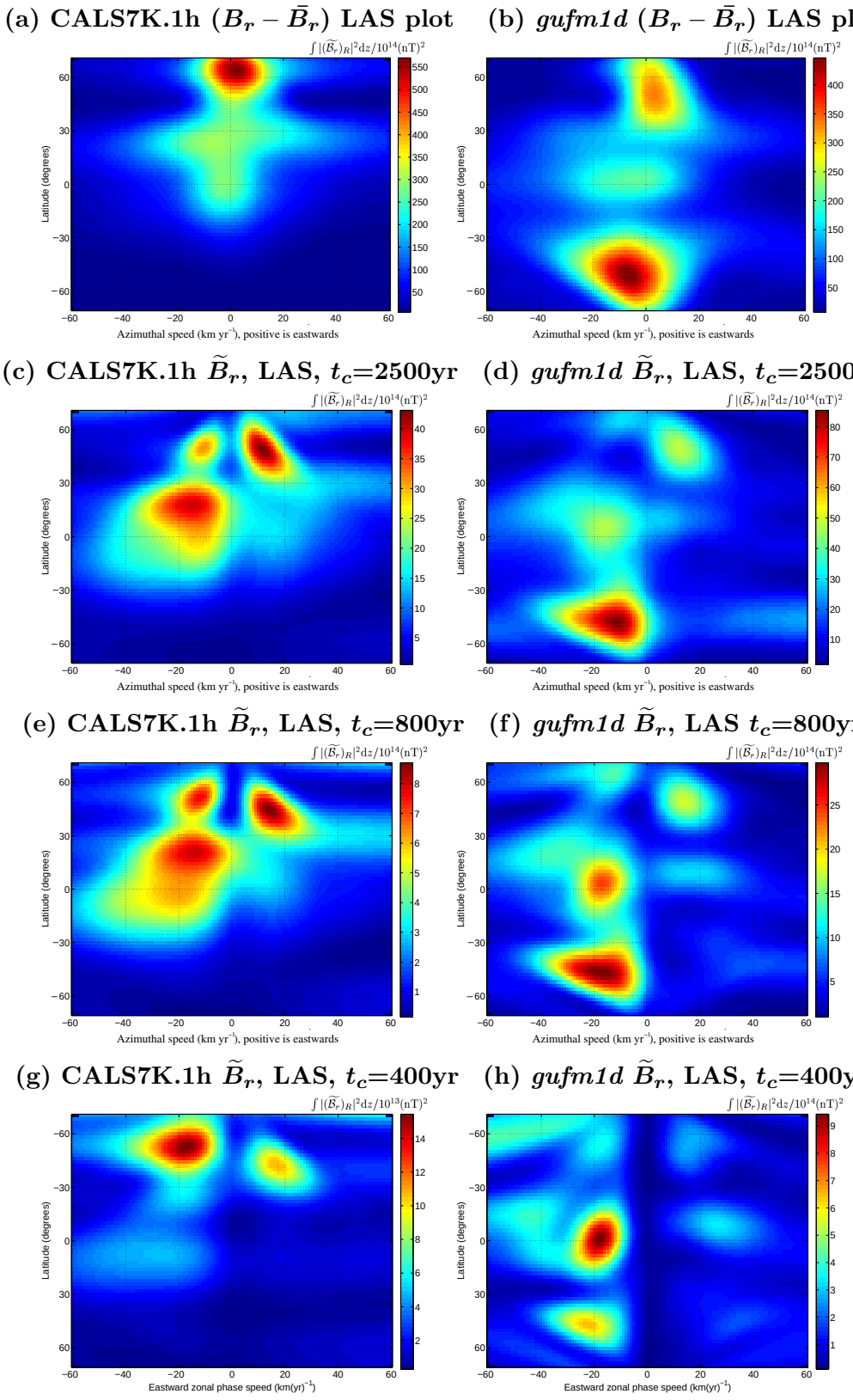

Figure 4.5: LAS power plots of $\widetilde{B}_r$ from CALS7K.1h and *gufm1d*. Latitude-azimuthal speed (LAS) power plots of radial magnetic field with time-averaged axisymmetric field removed and high pass filtered ($\widetilde{B}_r$) from CALS7K.1 and *gufm1d* from 1630A.D. to 1910A.D. with no filtering in (a) and (b) and a high pass filter threshold of 2500 yrs in (c), (d); 800 years in (e), (f) and 400 years in (g), (h).

result of an m= 2 or 3 features travelling in both eastward and westward directions. However, it must be emphasised that CALS7K.1h fails to capture the strong equatorial or southern hemisphere signals on these time scales.

The conclusion from the comparison of CALS7K.1h and *gufm1d* is that *gufm1d* with its truncated power spectra captures the field changes in *gufm1* surprisingly well but that CALS7K.1h has more difficulty. CALS7K.1h does, however, yield useful information on long wavelength field changes at mid to high latitudes in the northern hemisphere on time scales longer than around 800 years. In particular, it can determine whether the predominant azimuthal motion of field features at a particular latitude is either eastward or westward. If only short time scales shorter than 800 years are retained, spurious features dependent on the heterogeneous data distribution arise. In appears that the data coverage in much of the southern and Pacific hemispheres is then insufficient to capture even large scale, slow field evolution processes.

4.3 Space-time analysis of CALS7K.1

In this section the space-time spectral analysis method is applied to B_r at the core surface for the full span of CALS7K.1. The interval from 2000B.C. to 1700A.D. is then focused on and results presented after its time-averaged axisymmetric part and the component evolving on time scales longer than 2500 years have been removed. Choosing a much longer high pass filter threshold compared to that used when studying *gufm1* is reasonable in this case because the timespan of the model is much longer. This choice also lessens the problems associated with focusing on field changes happening on time scales faster than 800 years, for which the model was found to be unreliable in the previous section.

4.3.1 Analysis of unprocessed radial magnetic field (B_r) for full span of CALS7K.1

Snapshots of B_r at the core surface from CALS7K.1 in 5000 B.C., 3650 B.C., 2300 B.C., 950 B.C, 400 A.D. and 1750 A.D. in figure 4.6 show how the field morphology has varied over the past 7000 years. An animation showing the continuous evolution of B_r over this interval can be found in animation A4.3.

Motions of B_r field concentrations are observed both in east-west and in north-south directions in CALS7K.1. There is no concerted westward motion of the field, though episodes of both eastward (for example from 2750B.C. to 2200 B.C. near 45°N) and westward motion (for example at near 20°S from 200 B.C. to 500 B.C.) are observed. The TL plots in figure 4.7 give more precise information concerning azimuthal field motion.

Slow eastward and westward motions are discernible at 60°N in figure 4.7a, especially after 1500B.C. At 40°N the westward motion of a succession of perturbations in B_r is

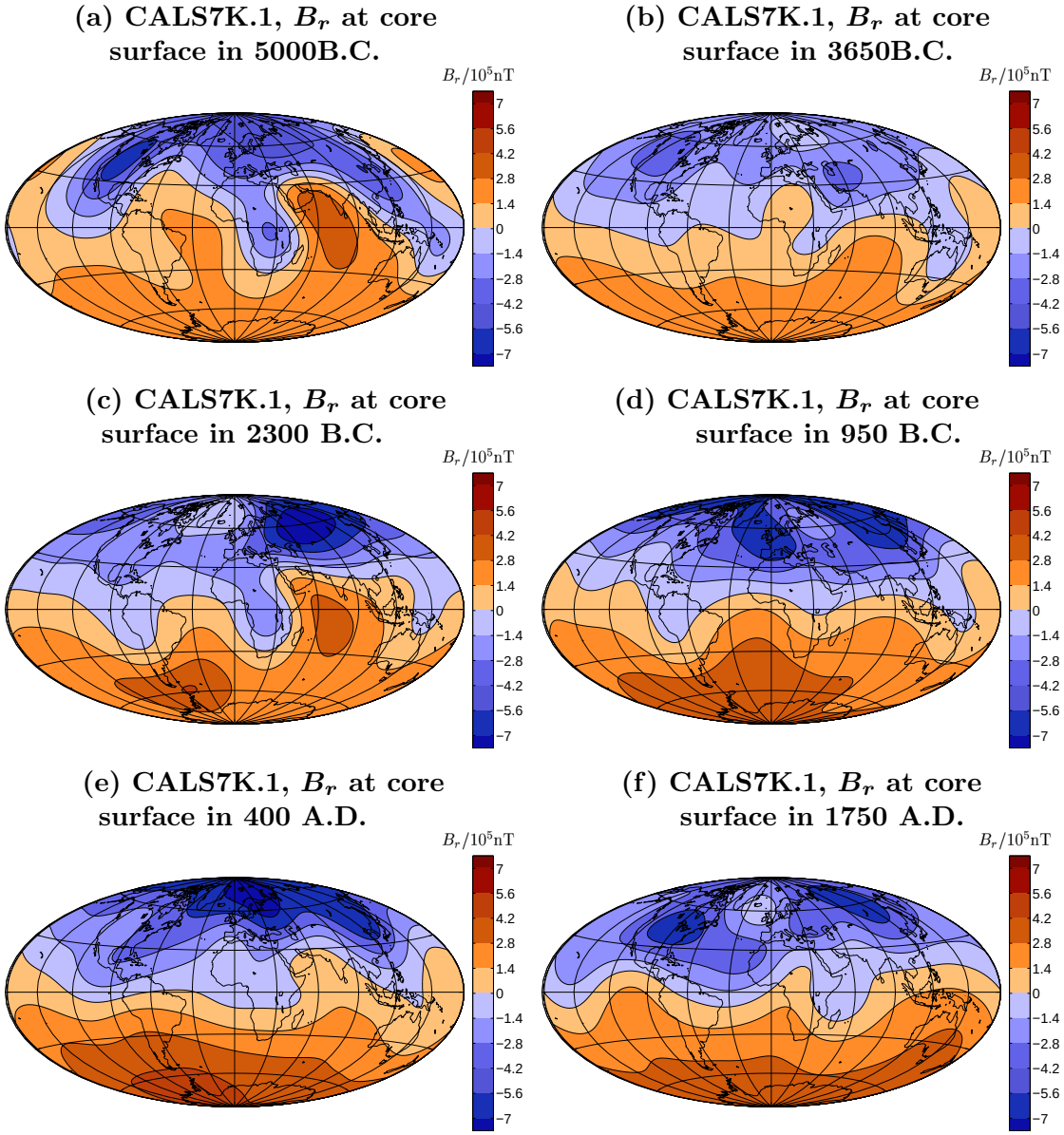

Figure 4.6: Snapshots of B_r from CALS7K.1 from 5000B.C. to 1750A.D. Unfiltered radial magnetic field (B_r) at the core surface from the model CALS7K.1 presented in snapshots from 5000 B.C. in (a); 3650 B.C. in (b); 2300 B.C. in (c), 950 B.C.; in (d) 400 A.D. in (e) and 1750 A.D. in (f).

(a) CALS7K.1, TL plot of B_r, 60°N

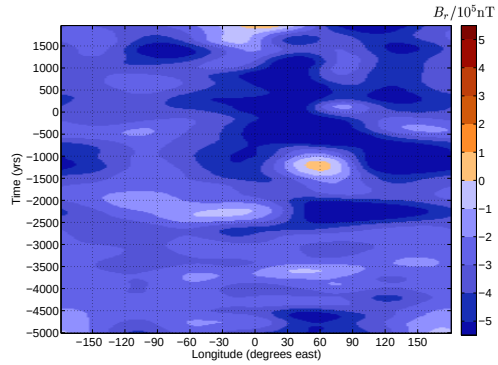

(b) CALS7K.1, TL plot of B_r, 40°N

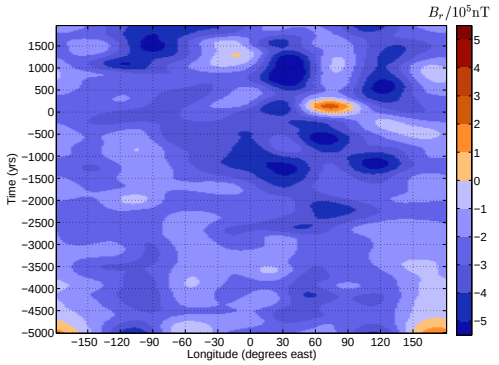

(c) CALS7K.1, TL plot of B_r, 20°N

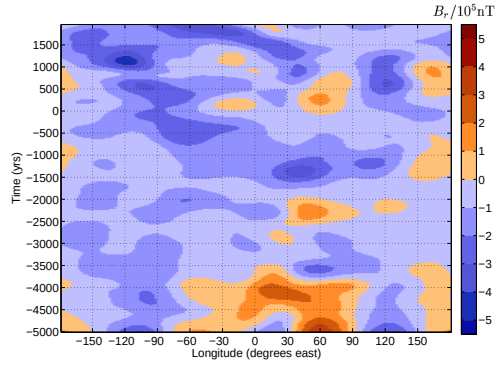

(d) CALS7K.1, TL plot of B_r, 0°N

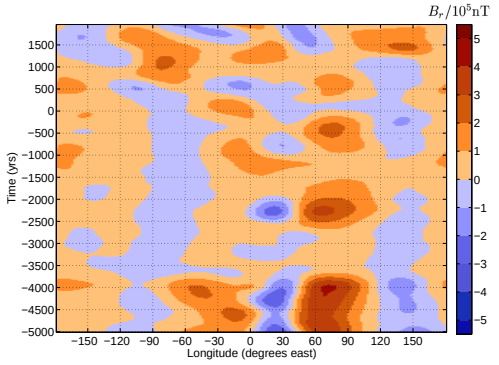

(e) CALS7K.1, TL plot of B_r, 10°S

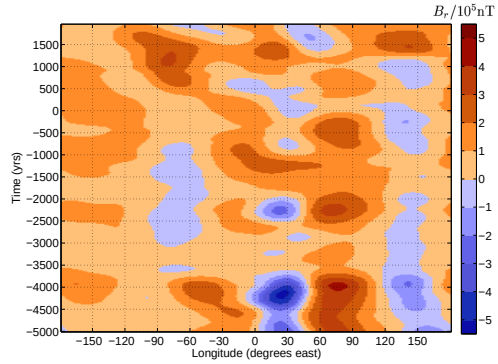

(f) CALS7K.1, TL plot of B_r, 20°S

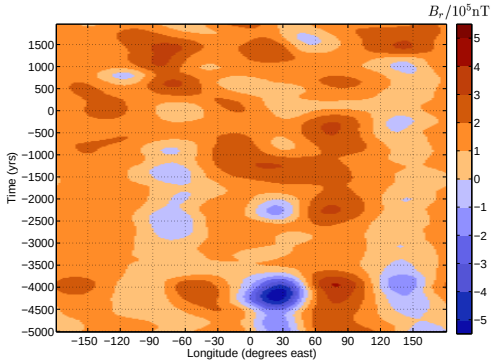

(g) CALS7K.1, TL plot of B_r, 40°S

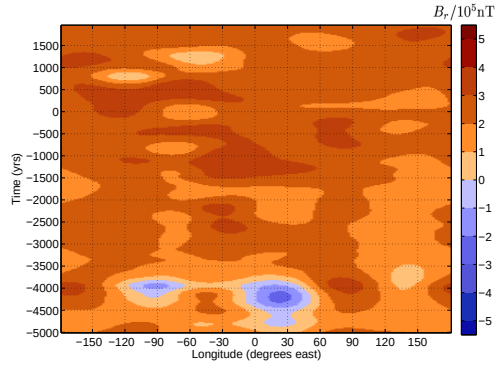

(h) CALS7K.1, TL plot of B_r, 60°S

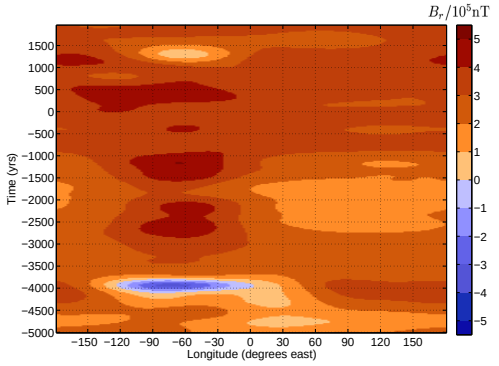

Figure 4.7: TL plots of B_r from CALS7K.1.
Unfiltered B_r at the core surface from the model CALS7K.1 in time-longitude plots at latitudes (a) 60°N, (b) 40°N, (c) 20°N, (d) 0°N, (e) 10°S, (f) 20°S, (g) 40°S and (h) 50°S.

particularly prominent between 1500 B.C to 500 A.D from 150°E around 500 B.C. to 60°E in 250 B.C., with slow eastward motion of field features observed close to 120°E from 500 A.D. to 1500 A.D.. At low latitudes, there are some weak signals of field features drifting (usually westwards) between 1500 A.D. and 1950 A.D. (see previous section for a discussion on how these are similar too but don't quite correctly capture the motions seen in *gufm1* during the interval 1600 A.D. to 1950A.D.).

At 40°S and at higher latitudes in the southern hemisphere there is no evidence for either eastward or westward motions of field concentrations: it seems likely that this is primarily because of data limitations (the sparsity of measurements in the southern hemisphere) rather than the operation of any different physical mechanisms in this region. Prior to 2000 B.C. no evidence is found at any latitude in unprocessed TL plots of azimuthally moving field features in B_r. Instead, the field in this early part of CALS7K.1, is dominated by stationary field features some of which slowly change amplitude on millennial time scales.

4.3.2 Analysis of $\widetilde{B_r}$ from 2000 B.C. to 1700 A.D.

The TL plots of unprocessed B_r from CALS7K.1 suggest that a number of azimuthally moving field features may be present during the interval 2000 B.C. to 1700 A.D., suggesting that this interval should be studied more closely, focusing on the millennial time scale for which CALS7K.1 contains reasonable power. As a preliminary step in this process, the amount of field change captured when different high pass filter thresholds were applied to the CALS7K.1 model was studied to facilitate the choice of a sensible filter threshold. The results of this investigation are shown in figure 4.8.

Long term variations dominate the field evolution in CALS7K.1, with around 20 % of field changes not accounted for when changes on time scales longer than 10000 years are removed. Only 25 % of field changes are captured when the threshold is 1000 years, while just over 50 % are captured when the threshold is 2500 years. The field changes occurring on this 1000 to 2500 year time scale are likely to be of interest, so 2500 years was chosen as the high pass filter threshold. In this investigation, CALS7K.1 was gridded at the core surface at intervals of 2 years, to allow the finer details of the field evolution to be observed and in order to achieve the best possible resolution in the latitude-azimuthal speed (LAS) power plots.

The evolution of $\widetilde{B_r}$ at the core surface from CALS7K.1 from 2000 B.C. to 1700 A.D. (after the time-averaged axisymmetric field and field changes with periods longer than 2500 years have been removed) can be followed in animation A4.4. The strongest field features are located at mid to high latitudes under Eurasia where episodes of both eastward and westward motion are observed. These episodes do not appear to consist of simple periodic oscillations but are highly time-dependent. The presence of rapid

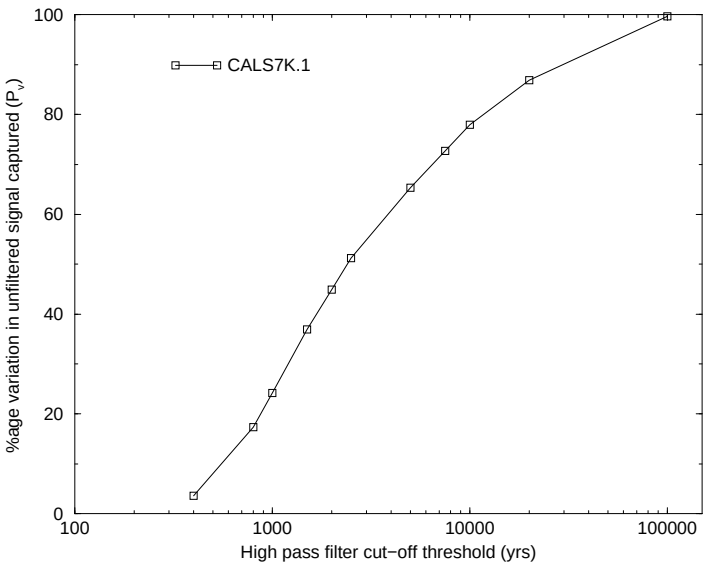

Figure 4.8: Variation in CALS7K.1 as a function of filter threshold period. Graph showing the percentage of original field variation P_v, as defined in equation (2.6), captured by $\widetilde{B_r}$ as the choice of high pass filter threshold is varied for CALS7K.1 over its full span from 5000B.C. to 1950A.D..

motions of field concentrations at low latitudes is intriguing and invites speculation that they could be the ill-resolved signature of the equatorial field evolution processes similar to those observed during the historical interval. TL plots of the processed magnetic field from 2000B.C. to 1700A.D. and associated FK power spectra are presented in figure 4.9.

At 60°N, high amplitude, m=1 and m=2 westward moving field features with period around 1400 years (and azimuthal speeds $\sim$ 5 km yr^{-1}) are seen at eastern longitudes from 2000 B.C. to 1000 A.D. At westward longitudes after 500A.D. weaker m=2 eastward moving field features are found (for example that moving from 90°W in 700 A.D. to 30°E in 1400 A.D at an average speed of also around 5 km yr^{-1} at the core surface). At 40°N co-existing eastward and westward moving field features are observed. These seem to converging in Λ shaped features, (for example the features moving from eastwards from 105°W in 200 B.C. and westwards from 180°E in 0 A.D. to meet at 15°E in 700 A.D.). The eastward moving field concentrations are observed to be weaker and of smaller length scale (m=4 rather than m = 3) while both eastwards and westwards moving features have similar azimuthal speeds of $\sim$7 km yr^{-1}.

The clearest evidence of spatially and temporally coherent motion of radial magnetic field anomalies is found at low latitudes (at the equator and especially at 20°S) where m=2, 3 features with characteristic periods of approximately 1250 years are observed. The most striking example is a feature at 20°S that moves from 90°E in 1200B.C. to -60°E in 200A.D. (average speed of approximately 0.11°yr^{-1}, or 7 km yr^{-1} at the core surface).

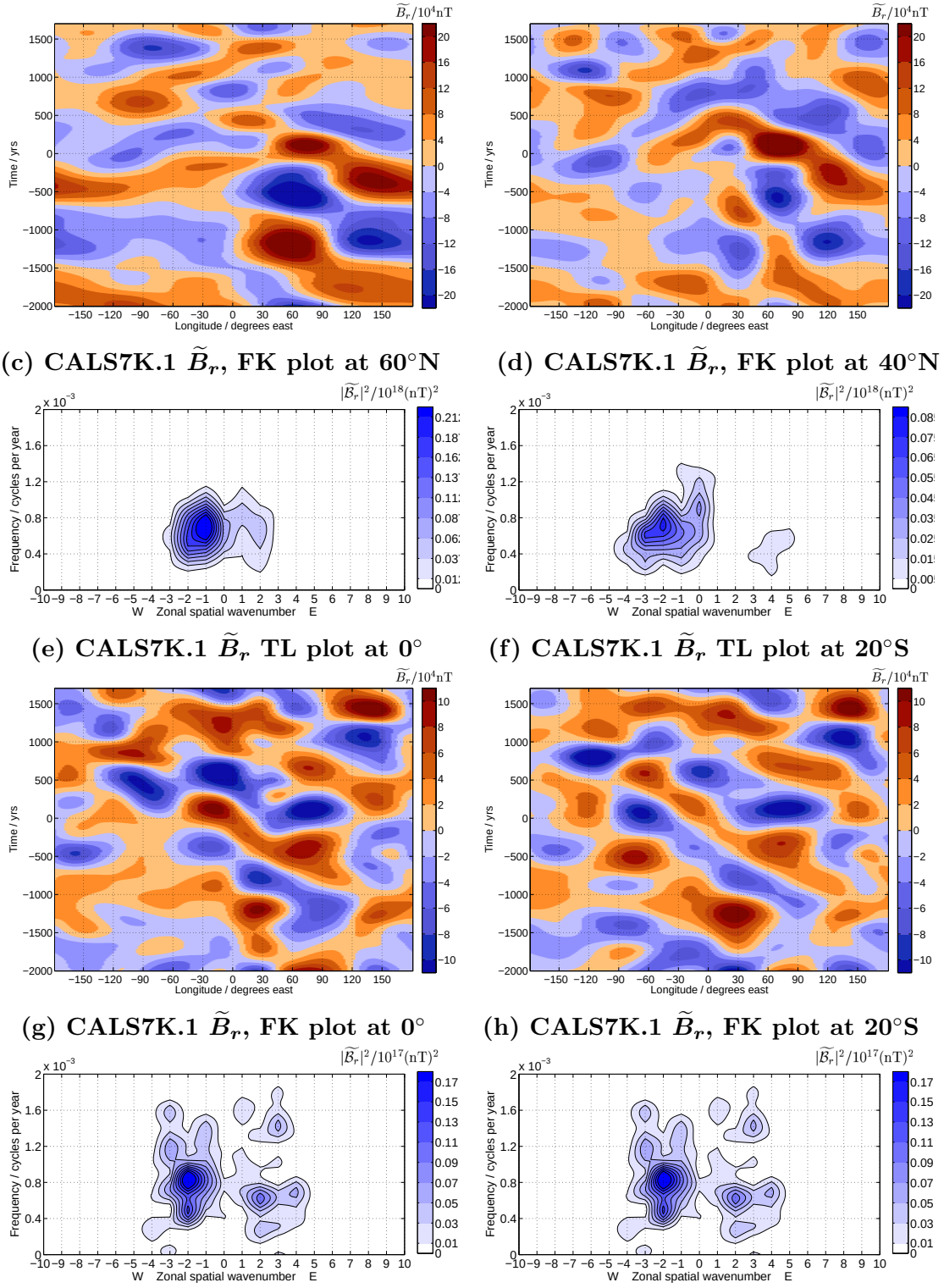

Figure 4.9: TL and FK plots of $\widetilde{B}_r$ from CALS7K.1 2000B.C to 1700A.D. Time-longitude (TL) plots of the processed radial magnetic field $\widetilde{B}_r$ with time averaged axisymmetric component subtracted and high pass filtered with threshold of 2500 years, from the field model CALS7K.1 from 2000B.C to 1700A.D. at latitudes 60°N in (a), at 40°N in (b), at the equator in (e) and at 20°S (f). The associated frequency-wavenumber (FK) power spectra found in (c), (d), (g) and (h).

In figure 4.10 the latitude-azimuthal speed (LAS) power plots of $\widetilde{B_r}$ from CALS7K.1 (2000B.C to 1700A.D.), with no high pass filtering applied and a high pass filter threshold of 2500 years are presented. The unfiltered LAS plot shows the strongest signals in the record during this interval appear at high latitudes in the northern hemisphere.

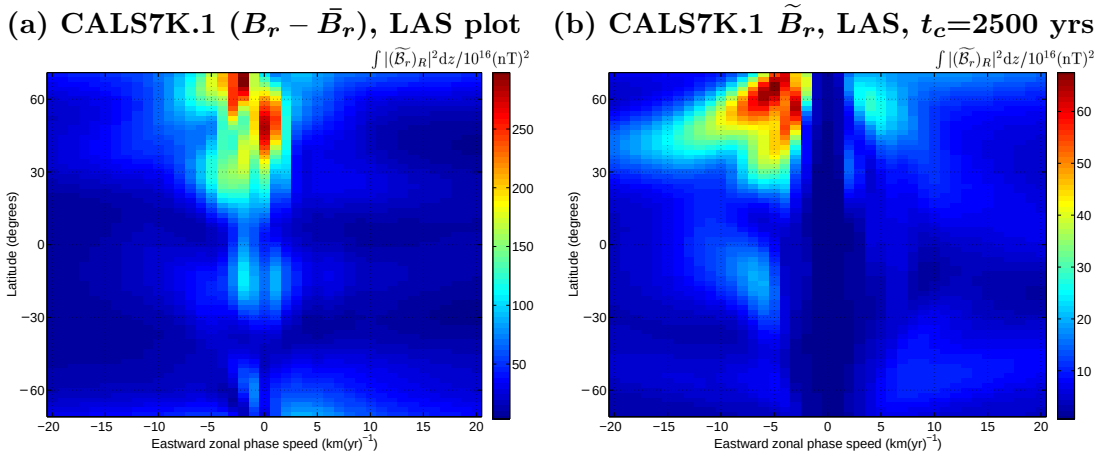

Figure 4.10: LAS plots of $\widetilde{B}_r$ of CALS7K.1 from 2000B.C to 1700A.D. Latitude-azimuthal speed (LAS) power plots of the processed radial magnetic field $\widetilde{B_r}$ with time averaged axisymmetric component subtracted and high pass filtered with cut-off period 2500 years, of the field models CALS7K.1 from 2000B.C to 1700A.D..

When high pass filtering is used to eliminate signals with time scales longer than 2500 years (the case dealt with in the TL plots and FK power spectra of figure 4.9), the LAS power plot of 4.10b shows that the strongest remaining signals are slow ($\sim$ 5 km yr^{-1}) and westwards at high latitudes ($\sim$ 60°N), though similar but weaker eastward signals are also present. Signals indicating both some eastward but predominantly westward field motions at latitudes $\sim$60°N were also found when *gufm1* was studied in chapter 3 (see, for example, figure 3.10).

There are also weak indications in figure 4.10 of a lower amplitude, faster moving, signal between 20°S and the equator, though this is an order of magnitude weaker than the high latitude signal (note also the difference between the amplitudes of the high latitude and low latitude signals in the TL plots in figure 4.9). This suggests that CALS7K.1 does show indications of spatially and temporally coherent signals at low latitudes, but that using filter cut-off of 2500 years they are much weaker than the higher latitude signals. This was also the case for *gufm1* when this was studied with a 2500 year filter threshold. A caveat to these observations is that the low latitude signal might be only poorly resolved because of the lack of coverage of CALS7K.1 in the southern hemisphere (see appendix B).

4.3.3 Hemispherical differences in field evolution processes

As was discussed in §3.5 the issue of whether there are systematic differences in the evolution of the geomagnetic field in the Atlantic and Pacific hemispheres has been debated for many years. CALS7K.1 is a suitable tool for investigating whether any such difference has persisted for several millennia, or whether it is simply a peculiarity of the structure of the geomagnetic field over the historical era.

Time-longitude (TL) plots of CALS7K.1, with the time-averaged axisymmetric field and fields evolving on time scales longer than 2500 years removed, are presented for the Pacific and Atlantic hemispheres in figure 4.11. These illustrate that the strongest, spatially and temporally coherent, patterns of field evolution are predominantly found in the Atlantic hemisphere, particularly at low latitudes. However, there are indications of similar patterns of field evolution in the Pacific hemisphere, especially at mid-latitudes in the northern hemisphere where data coverage at Earth's surface is best. At lower latitudes and in the southern hemisphere the field evolution under the Pacific is lower in amplitude and less convincingly wave-like, though the limitations of the data used to constrain the field in these regions should be borne in mind.

On the basis of CALS7K.1, the tentative conclusion therefore appears to be that azimuthally drifting magnetic field concentrations at the core surface have in the past been present the Pacific hemisphere, especially at northern mid-latitudes. At lower latitudes and in the southern hemisphere, the resolution of the model does not appear to be good enough for any definitive statements to be made, but it does seem that field features evolving on time scales shorter than 2500 years are of lower amplitude in the Pacific hemisphere.

These results suggest that the field structure has been consistently different (lower in amplitude and with weaker gradients) at low and southern latitudes in the Pacific hemisphere over the past 3000 years. This does not seem to have been the case at mid-latitudes in the northern hemisphere. Possible explanations for this behaviour are discussed further in chapter 8.

4.3.4 Discussion

The analysis of CALS7K.1 certainly provides evidence that azimuthally moving (both eastward and westward) concentrations of B_r are present at the core surface in CALS7K.1 on millennial time scales. However, whether the models are accurately characterising the patterns of field evolution (recall the results of the comparison between CALS7K.1h and *gufm1*) remains questionable. To reiterate these problems, in figure 4.12 TL plots, FK plots and LAS plots of $\widetilde{B_r}$ from CALS7K.1 and *gufm1* (not *gufm1d*) from 1630 A.D. to 1910 A.D are presented. In both cases the time-averaged field and changes on time scales longer than 2500 years have been removed.

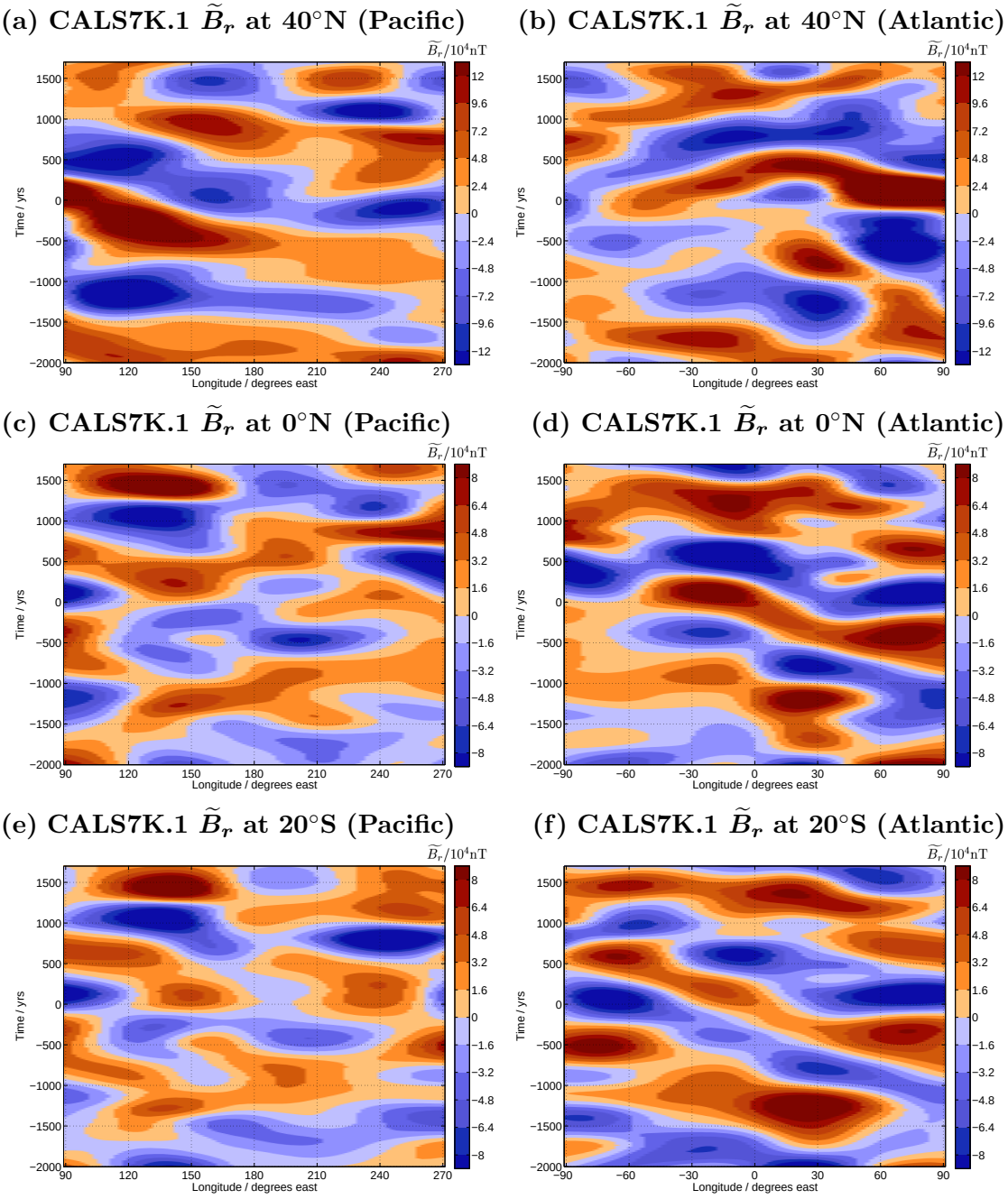

Figure 4.11: Hemispherical differences in field evolution in CALS7K.1. Time-longitude (TL) plots of the evolution in the east-west direction of processed radial magnetic field from CALS7K.1 between 2000B.C and 1700A.D., with time averaged axisymmetric field removed and high pass filtered with cut-off period t_c of 2500 years ($\widetilde{B_r}$), separated into the Pacific and Atlantic hemispheres. (a), (c), (e) show the evolution in the Pacific hemisphere at 20°N, 0°N, and 40°S respectively. (b), (d), (f) show the evolution in the Atlantic hemisphere at 20°N, 0°N, and 40°S respectively.

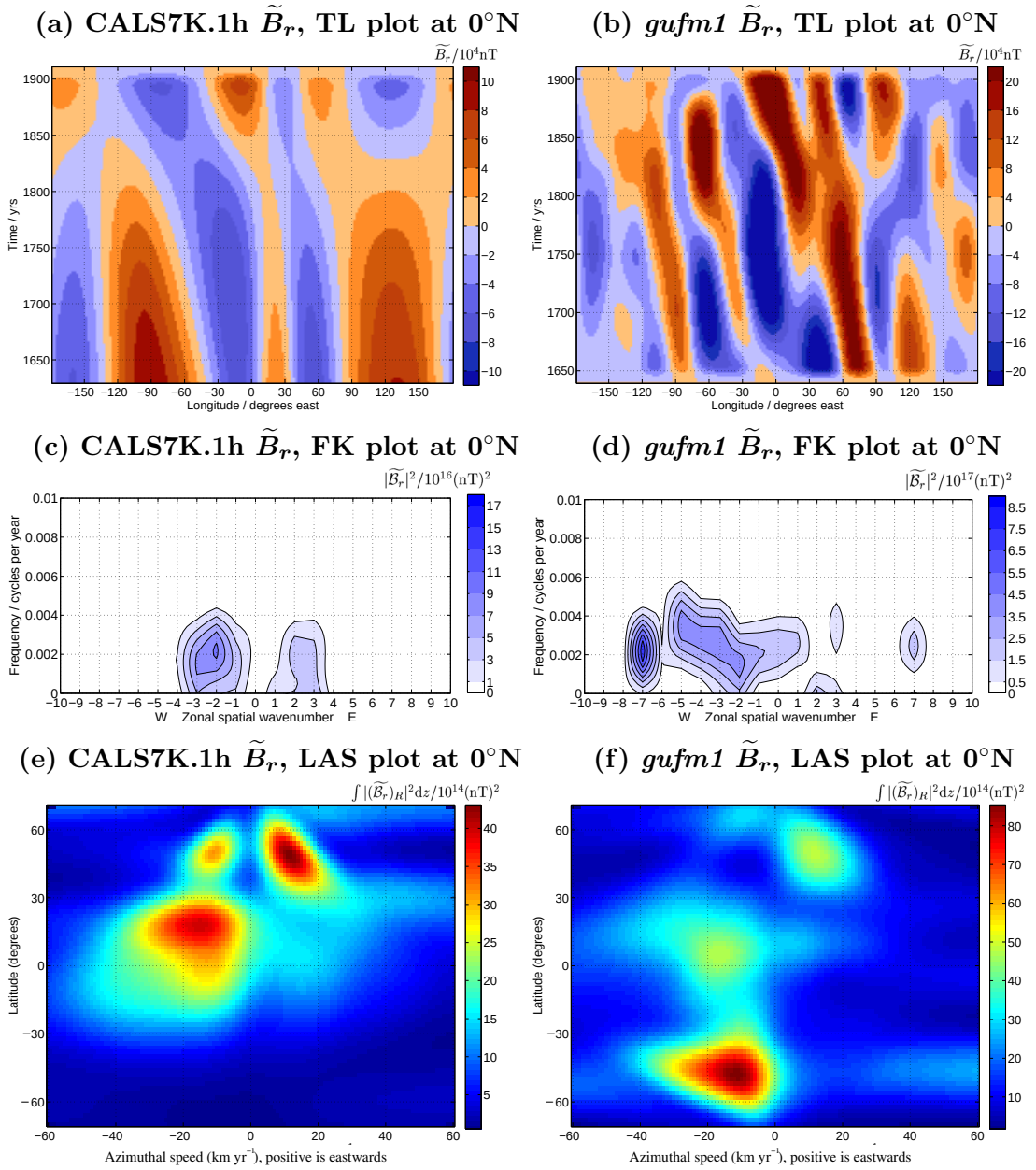

Figure 4.12: TL, FK and LAS plots plots from CALS7K.1 and *gufm1*. Time-longitude (TL) plots and frequency-wavenumber (FK) power spectra from the equator and latitude-azimuthal speed (LAS) plots of the processed radial magnetic field $\widetilde{B}_r$ with time averaged axisymmetric component subtracted and high pass filtered with cut-off period 2500 years, from the field models CALS7K.1 and *gufm1* from 1630B.C to 1910A.D.

Figure 4.12a,b illustrates that CALS7K.1 correctly registers the presence of westward moving field features during the historical interval, but because it cannot image the shorter length scale features reliably (see figure 4.12c,d) the space-time paths of the field concentrations are not accurately captured. Nonetheless, the azimuthal direction of motion, approximate latitude and the azimuthal speed of the strongest LAS plot signals in northern hemisphere (an eastward signal at 45°N and a faster westward signal at around 5°N) are also found in CALS7K.1. It should in addition be noted that this comparison is not without limitations because field variations on millennial time scales included in these plots are not reliably captured by *gufm1* because of its comparatively short timespan.

4.4 Summary of application of space-time spectral analysis to CALS7K.1

In this chapter the space-time evolution of B_r at the core surface over the past 7000 years as captured in CALS7K.1 has been discussed. Comparison of field evolution in *gufm1d* and CALS7K.1 during the interval 1600 A.D. to 1950 A.D. has shown that CALS7K.1 is not sufficiently accurate to precisely characterise field evolution processes with azimuthal wavenumbers greater than 5 or with periods shorter than 1000 years, and that this results in the mapping of power into larger length scales (smaller wavenumbers). Comparison of *gufm1* with *gufm1d* demonstrated that this loss of resolution was primarily a result of the data errors and limitations in the data distribution, rather than being a consequence of the limited spherical harmonic resolution (heavy damping) of the model.

On millennial time scales, both eastward and westward motions of spatially and temporally coherent field anomalies are observed in CALS7K.1. This suggests that the westward drift of the geomagnetic field may not be a defining feature of geomagnetic secular variation as has previously been believed on the basis of observations from the past 400 years. Instead episodes of azimuthal motion in both eastward and westward directions seem to occur, particularly at mid-latitudes and on millennial time scales.

Chapter 5

Application of the space-time spectral analysis technique to output from a convection-driven geodynamo model

5.1 Introduction

In the past decade, self consistent numerical models of the generation and evolution of a magnetic field resulting from convection-driven fluid motions in a 3D spherical shell geometry (including all coupling and feedback mechanisms) has demonstrated the feasibility of the geodynamo mechanism in Earth's core as the source of Earth's magnetic field (Dormy et al., 2000; Roberts and Glatzmaier, 2000a; Kono and Roberts, 2003). In such numerical models, the mechanisms producing changes in the magnetic field at the outer boundary can be determined directly because the magnetic, velocity and temperature fields are known at all points in time and space inside the model domain, and the applied boundary conditions are known. This scenario is in striking contrast to the case for Earth's core where only the magnetic field at the outer boundary is known, and then only to limited resolution.

Although present models operate in a parameter regime far from that estimated for the Earth (See appendix C) they do succeed in getting the ordering of the magnitude of terms in the governing equations correct and in generating a predominantly dipolar magnetic field (see, for example, Christensen et al. (1999)). Some workers have even suggested that present models can accurately simulate aspects of the morphology and evolution of the historical geomagnetic field (Christensen et al., 1998; Kuang and Bloxham, 1998), though this assertion remains contentious because of differences in time scales between the models and the Earth (see Jones (2000), Dumberry and Bloxham (2003) and the discussion in appendix C).

In this chapter, links between patterns of magnetic field evolution at the outer surface and patterns of flow evolution within the convecting region of two examples of geodynamo

models are investigated using the space-time spectral analysis techniques developed in chapter 2 with three primary objectives in mind:

(i) To determine whether patterns of field evolution at the outer surface bear any systematic resemblance to historical (Jackson et al., 2000) or millennial (Korte and Constable, 2005) time scale changes observed in the geomagnetic field. Attention will focus on whether azimuthally moving radial field concentrations are found at low latitudes and whether field concentrations move consistently westwards (as in *gufm1*), or in both eastward and westward directions (as observed in CALS7K.1—see chapter 4).

(ii) To determine whether the mechanism producing azimuthally moving concentrations of radial magnetic field found at low latitudes in many geodynamo models (Glatzmaier and Roberts, 1997; Olson et al., 1999; Kono et al., 2000) can be consistently classified as either bulk advection or wave propagation.

(iii) To determine the limitations of viewing a truncated representation of the radial magnetic field at the outer boundary (see, for example, Rau et al. (2000)) and investigating how this might affect attempts to infer information regarding core flow motions causing the observed field evolution.

Geodynamo model output in two different parameter regimes generated using the MAGIC code of Wicht (2002) are used as the data sets in this chapter. The two runs investigated are (i) a very simple dynamo illustrating mechanisms of field evolution in an easily comprehensible manner but with parameters far from Earth's regime (DYN1) and (ii) a much more complex dynamo with parameters as close as is currently numerically possible to Earth's parameter regime (DYN2). Appendix C summarises the modelling strategies adopted in MAGIC, lists the non-dimensional parameters defining DYN1 and DYN2 and discusses how best to scale geodynamo model output to the Earth.

5.2 DYN1: (E=2×10^{-2}, Pr=1, Pr_m=10, $Ra/Ra_c \sim 3$, $R_m \sim 100$)

The rationale behind studying DYN1 is twofold. The primary reason is its convection-driven flow is large scale, so its dynamics are not too complicated and the underlying mechanisms can be easily grasped. It is however also possible that at very low Ekman number in Earth's core, the length scale of flows will be large due to a leading order balance between Coriolis and Lorentz forces (see, for example, Zhang and Schubert (2000)). In this case DYN1 might yield some useful inferences on the relationship between large scale convection-driven flows and magnetic field evolution processes.

5.2.1 Radial magnetic field (B_r) from DYN1

In figure 5.1 snapshots of the radial magnetic field B_r at the outer boundary from DYN1 are presented. An animation of snapshots can be found in animation A5.1. The field morphology is less dipole dominated than for B_r at the core surface in *gufm1* or CALS7K.1. Field features are predominantly large scale and none are stationary throughout the run (1 magnetic diffusion time $\tau_\eta \sim 1.22 \times 10^5$years, this run lasts $0.106\tau_\eta \sim 13 \times 10^3$ years, much longer than the interval covered by *gufm1* and about twice as long as the interval covered by CALS7K.1).

The most prominent B_r concentrations fall into two classes. Firstly there are high latitude (40 — 60°N or S) normal polarity flux concentrations that are essentially equatorially antisymmetric (E^A) in B_r (as would be produced by an equatorially symmetric (E^S) feature in the velocity field — see appendix E for a description of equatorial symmetries). An example of this type of feature can be seen in figure 5.1f near 120°W and 45°N and S (the map projections are centred at 0°E).

The second obvious mechanism of field evolution consists of a westward drifting pair of low latitude flux concentrations as is seen clearly in figure 5.1c,d,e. An example of such a feature is seen forming after $t = 0.04\tau_\eta$ near 15°W. The field concentrations move, then move coherently for about 50° longitude ($0.87r_0$ where r_0 is the radius of the outer boundary or 3040 km scaling to the Earth) by $t = 0.1\tau_\eta$ (scaling using the magnetic diffusion time this equates to an interval of 5000yrs). Their average drift speed is thus $\sim 17\ r_0\tau_\eta^{-1}$ or 0.6 km yr^{-1}. This is considerably slower than the low latitude flux features discussed in chapters 3 and 4, though there are problems with relating time scales in dynamo models to time scales in Earth's core (see appendix C for a discussion).

The azimuthal evolution of B_r is shown in figure 5.2. The time-longitude (TL) plots at high latitude show intervals of slow eastward and westward motions; unfortunately, the associated frequency-wavenumber (FK) plots are dominated by m=0 axisymmetric field fluctuations. On the other hand, at low latitudes, azimuthal motions of reversed field features are clearly observed even without any field processing in figure 5.2b,e. Since the TL plots show motion of isolated flux features, the resulting FK power spectra consist of linear shaped maxima passing through the origin with gradient corresponding to the azimuthal speed of the field feature, reminiscent of the results from the analysis of the synthetic model SPOT in chapter 2.

Processed radial magnetic field from DYN1 ($\widetilde{B_r}$)

To obtain further information concerning the azimuthal evolution of B_r in DYN1, following the procedures outlined in chapter 2. The time-averaged axisymmetric field was removed and the time series of the remaining (B_r-$\bar{B}_r$) were high-pass filtered using a range of filter thresholds. In figure 5.3 the percentage of the variation in B_r captured

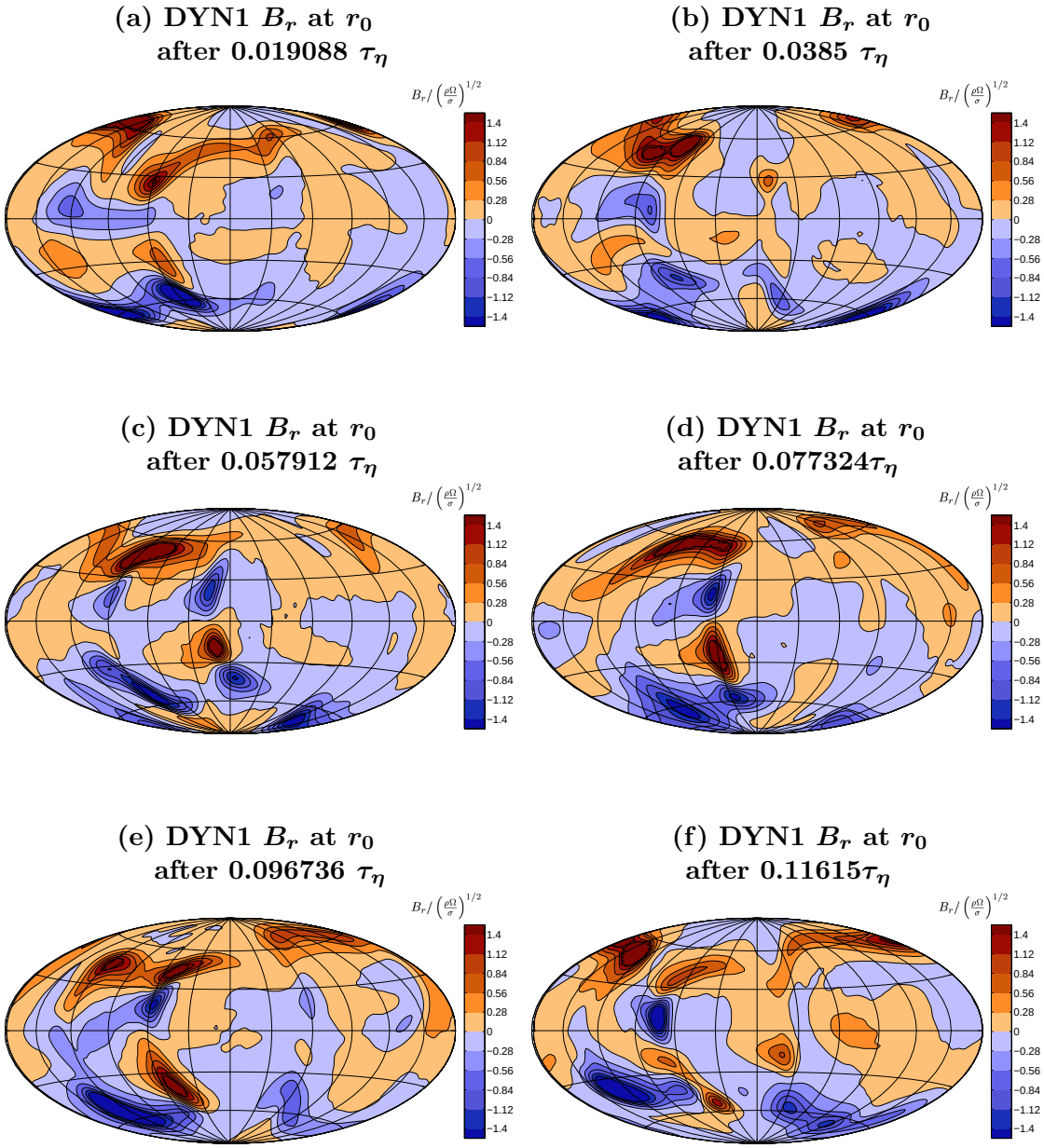

Figure 5.1: Snapshots of B_r from DYN1 at r_0.
Unfiltered radial magnetic field (B_r) from the model DYN1 is presented in a series of snapshots after (a) 0.019088 τ_η, (b) 0.0385 τ_η, (c) 0.057912 τ_η, (d) 0.077324 τ_η, (e) 0.096736 τ_η, (f) 0.077324 τ_η. These and all subsequent snapshots in this chapter are in Hammer-Aitoff equal area map projection.

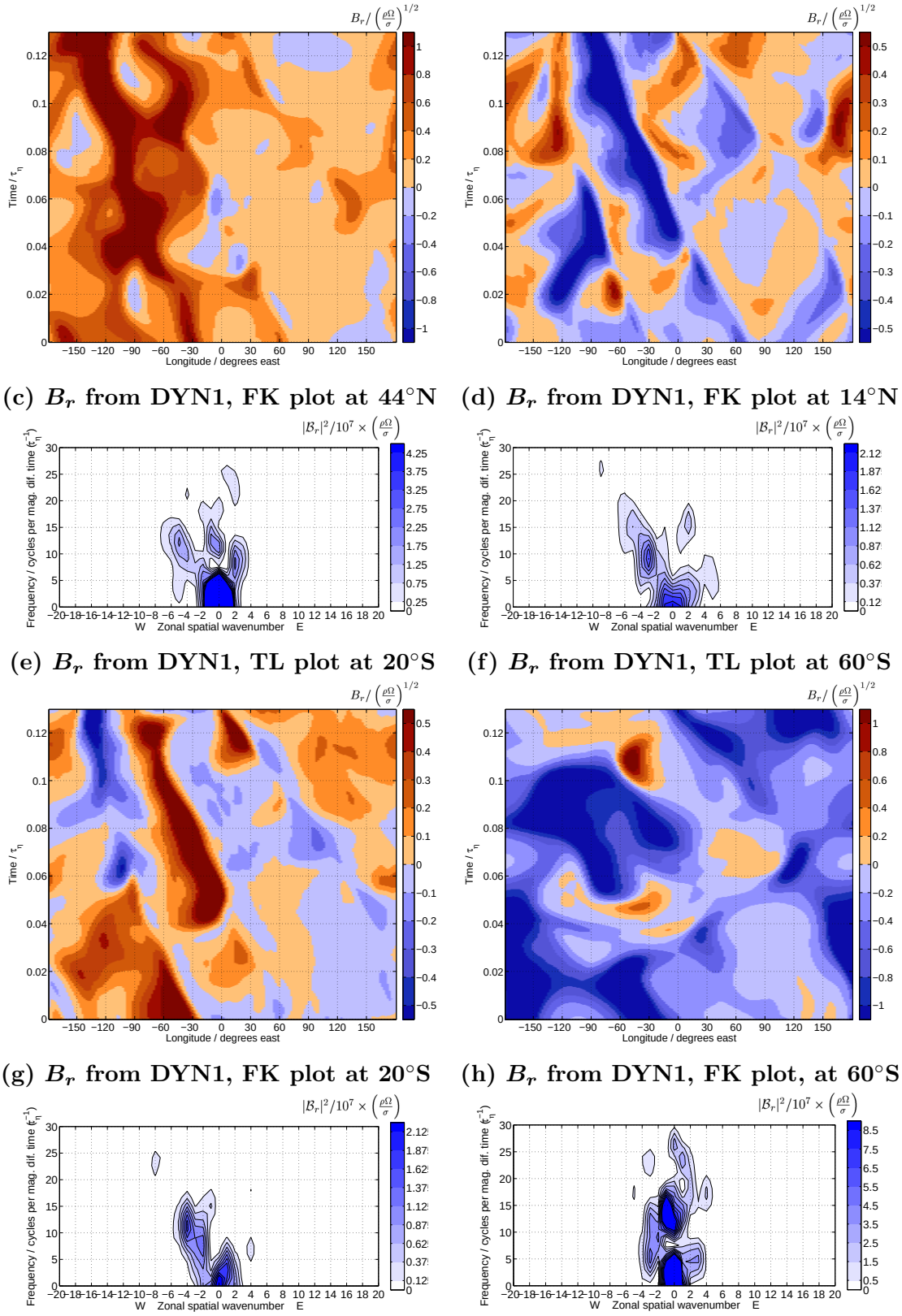

Figure 5.2: TL plots and FK power spectra of B_r from DYN1.
Time-longitude (TL) plots of the radial magnetic field B_r from DYN1 at latitudes 44°N in (a), at 14°N in (b), at 20°S in (e) and 60°S in (f). The associated frequency-wavenumber (FK) power spectra are found in (c), (d), (g) and (h).

by $\widetilde{B_r}$ (P_v as defined in equation (2.6)) is plotted against the high-pass filter threshold period in units of the magnetic diffusion time τ_η. In DYN1, 99 % of the original variation is captured when only field changes longer than 1 magnetic diffusion time are excluded, while 50 % of the field change can be captured when the threshold is $0.065\tau_\eta$.

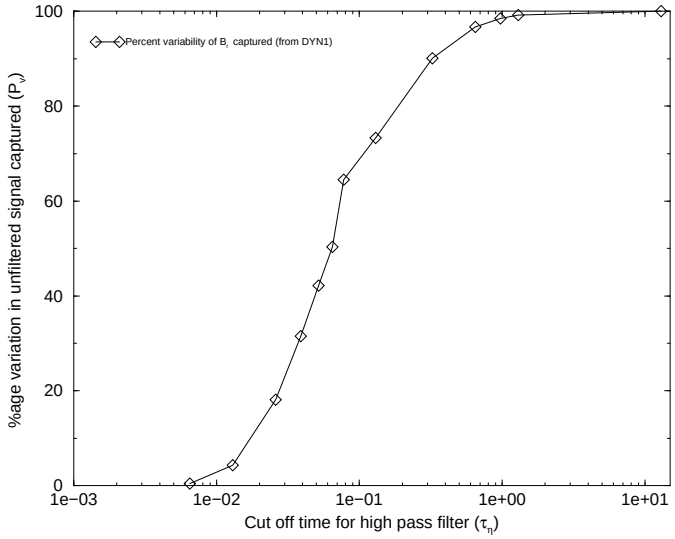

Figure 5.3: B_r variation captured by $\widetilde{B}_r$ in DYN1 as function of filter cut-off. Graph showing the percentage of the original field variation captured by $\widetilde{B}_r$ (P_v, as defined in equation (2.6)), as the choice of high pass filter cut-off is varied.

In figure 5.4 latitude-azimuthal speed (LAS) power plots are displayed for a range of high-pass filter thresholds. Without any high pass filtering (figure 5.4a) the highest amplitude signal involves slow, high latitude field motions, though there is also an indication of a signal at low latitudes[1]. Low latitude field motions are seen most clearly when the high pass filter threshold is around $0.0649\tau_\eta$, at latitudes of 20°N and S, with azimuthal speed of $15\pm3\ r_0\tau_\eta^{-1}$ in agreement with earlier visual estimates[2]. The low latitude features are still present when the threshold is below $0.02\tau_\eta$, but are then much weaker.

Snapshots of $\widetilde{B_r}$ from DYN1 constructed using a filter cut-off threshold of 0.06485 τ_η are presented in figure 5.5. The high latitude, slowly drifting field concentrations are now seen only via the transient wobbles in their position, while low latitude azimuthally moving features are well recovered, especially in figure 5.5b,c,d.

In figure 5.6, the TL plots and FK power spectra for $\widetilde{B_r}$ from DYN1 constructed using a filter cut-off threshold of $0.06485\tau_\eta$ are shown. The low latitude features are now very prominent, and are flanked by weaker anomalies of the opposite sign, that are a consequence of the filtering process. The single drifting spot nature of this mechanism is evident in the linear features found in the FK power spectra in figures 5.6d,g.

[1] since at low latitudes in DYN1 only a single, high amplitude, moving field concentration is present, the signal in the LAS power plots is not as dominant as the coherent the wave-trains observed in *gufm1*.

[2] The estimated bounds on the azimuthal speeds come from the full width at half maximum of the peak in the LAS power plots being interpreted.

(a) LAS plot of DYN1, no filtering

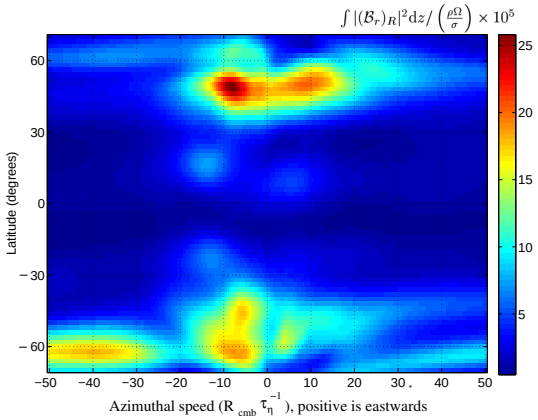

(b) LAS plot of DYN1, t_c= 0.6485τ_η

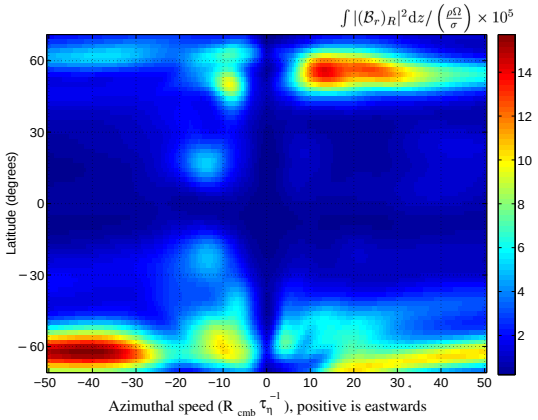

(c) LAS plot of DYN1,t_c= 0.1297τ_η

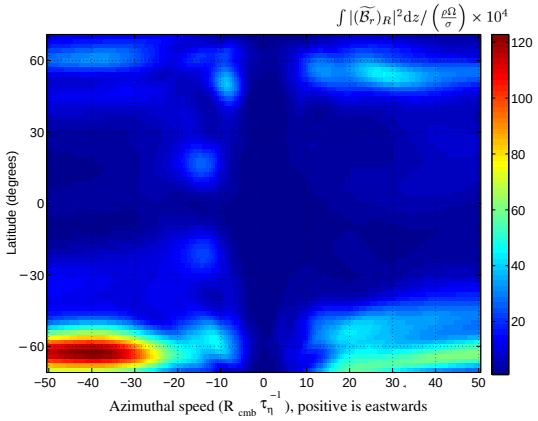

(d) LAS plot of DYN1, t_c= 0.06485τ_η

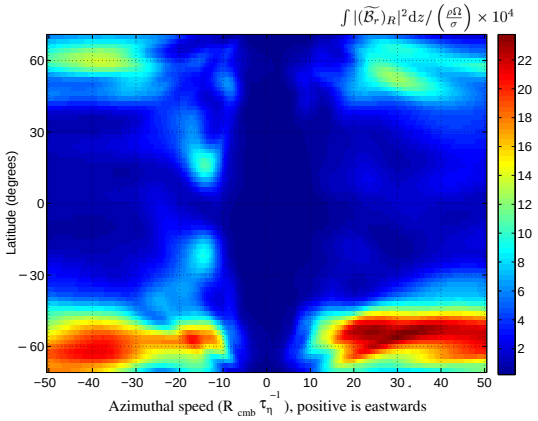

(e) LAS plot of DYN1, t_c= 0.03891τ_η

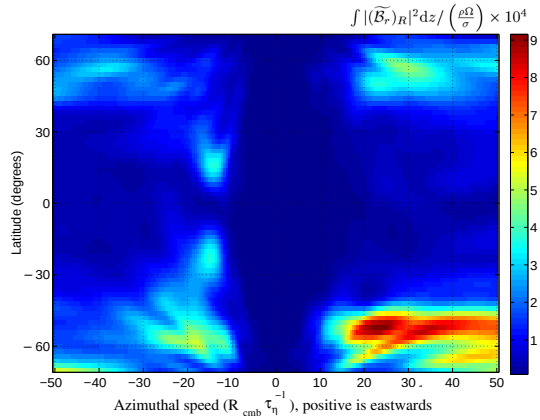

(f) LAS plot of DYN1, t_c= 0.01297τ_η

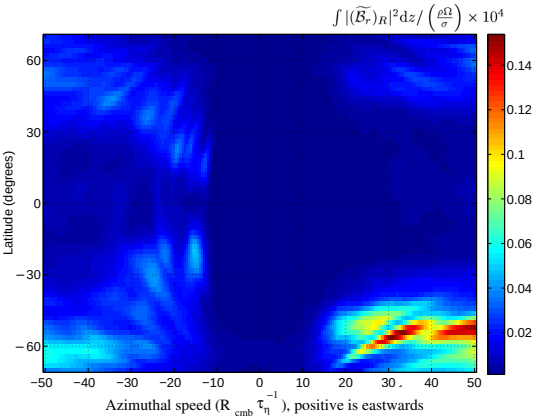

Figure 5.4: LAS plots of $\widetilde{B}_r$ from DYN1 of for a range of filter thresholds. Latitude-azimuthal speed (LAS) power plots of $\widetilde{B}_r$ from DYN1 with time-averaged axisymmetric field removed and high pass filtered with a threshold of (a) infinity (no filtering), (b) 0.6485 τ_η , (c) 0.1297 τ_η, (d) 0.06485 τ_η, (e) 0.03891 τ_η and (f) 0.01297 τ_η. Note the change in the scale of the power as the filter cut-off threshold period is varied.

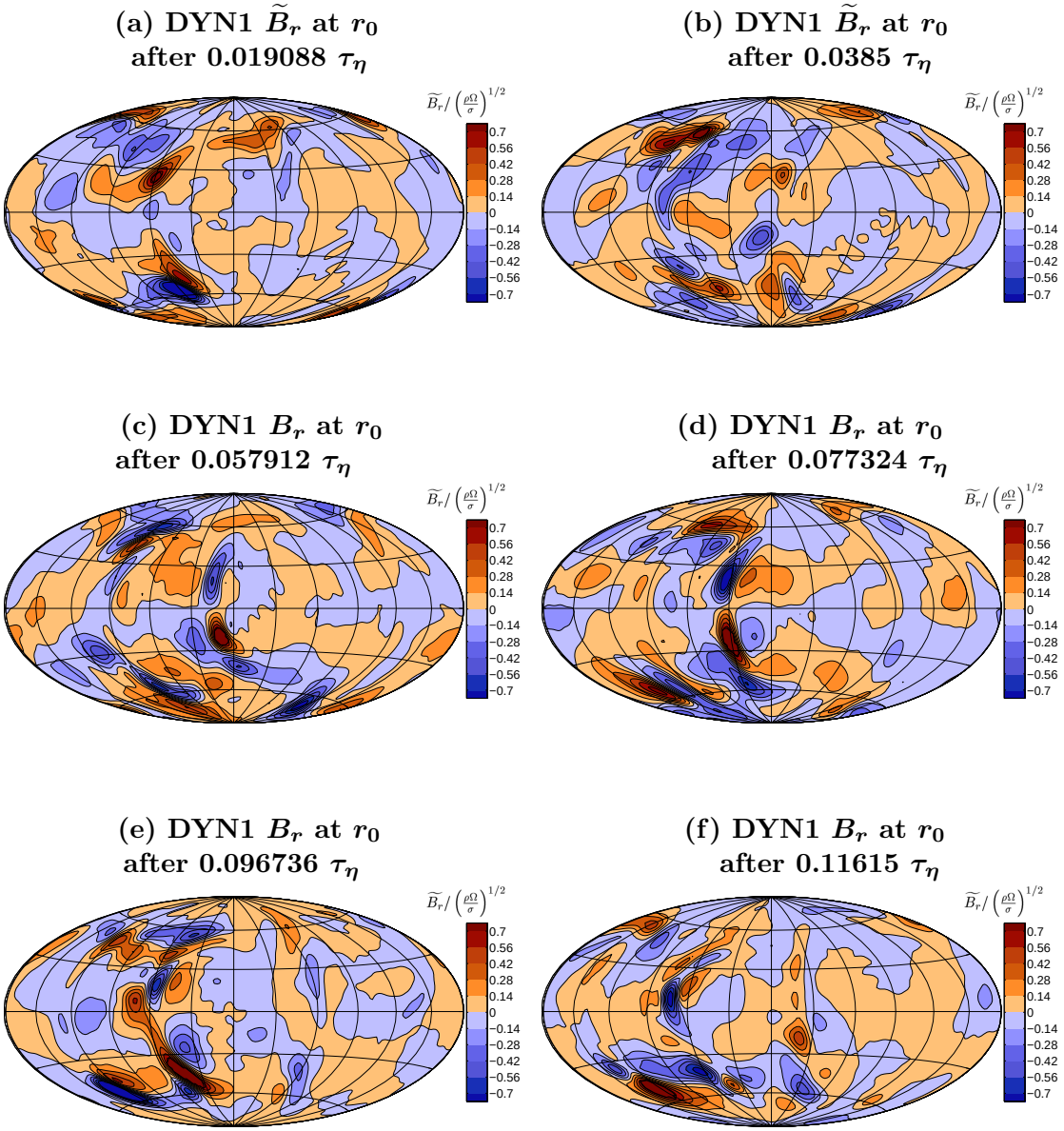

Figure 5.5: Snapshots of $\widetilde{B}_r$ from DYN1 at r_0.
Radial magnetic field with time-averaged axisymmetric part removed and high pass filtered with a threshold period of 0.0649 τ_η ($\widetilde{B}_r$) from the model DYN1 is presented in a series of snapshots after (a) 0.019088 τ_η , (b) 0.0385 τ_η , (c) 0.057912 τ_η, (d) 0.077324 τ_η , (e) 0.096736 τ_η, (f) 0.11615 τ_η.

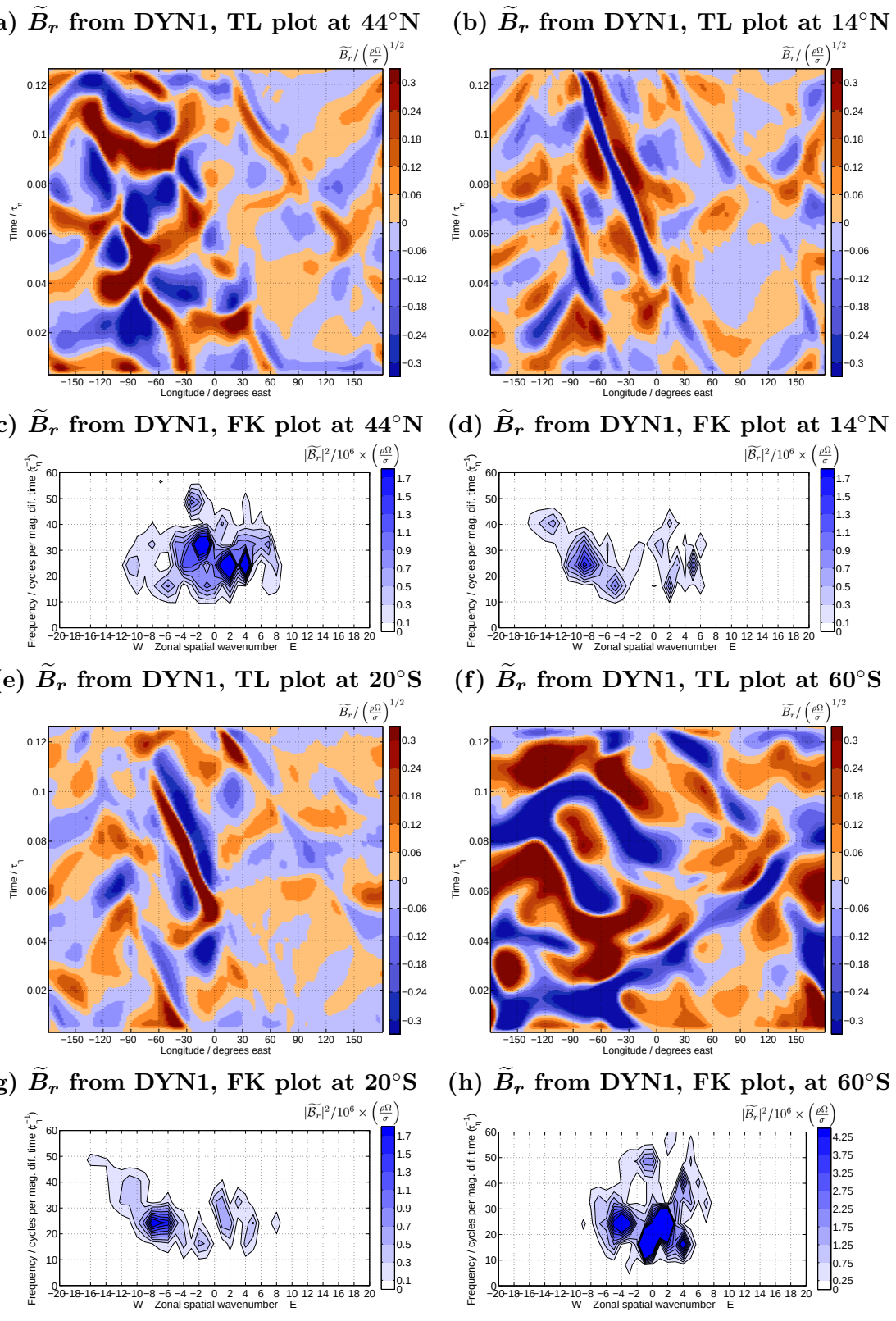

Figure 5.6: TL plots and FK power spectra of $\widetilde{B}_r$ from DYN1.
Time-longitude (TL) plots of the radial magnetic field with time averaged axisymmetric part removed and high pass filtered with threshold 0.0649 τ_η ($\widetilde{B}_r$) from DYN1 at latitudes (a) 44°N (b) 14°N, (e) 20°S (f) 60°S with the associated frequency-wavenumber (FK) power spectra in (c), (d), (g) and (h).

Having analysed the evolution of B_r, the radial velocity field u_r from DYN1 can also be studied to determine whether low latitude B_r concentrations have any relation to flow upwelling or downwelling, while the eastward component of the velocity field u_ϕ can be used to infer whether flow convergence is important in producing concentrations in B_r and in determining whether their motion is due to a azimuthal flow or caused by wave propagation of the velocity field.

5.2.2 Velocity field from DYN1

In the model DYN1, preliminary visual analysis by Johannes Wicht (personal communication August 2004) suggested that the primary flow pattern was travelling westward in a wave-like manner in the absence of any strong mean azimuthal flow and that the westward motion of the low latitude concentrations in B_r at outer boundary appeared to be a consequence of this phenomenon. The present analysis was designed to investigate this suggestion that magnetic field evolution in geodynamo models can be caused in part by hydromagnetic wave propagation.

The space-time spectral analysis methodology described in chapter 2 can be applied to any scalar field. In this section it is applied to u_r and u_ϕ from DYN1. The scalar components of the velocity field are examined on a spherical surface of radius $r = 0.96r_0$, close to the outer boundary but below the viscous Ekman boundary layer.

The wave flow pattern observed in DYN1 was found to be sufficiently striking that additional processing (such as removal of the time-averaged axisymmetric field or high pass filtering) was unnecessary before carrying out the space-time spectral analysis.

Radial velocity field (u_r)

The evolution of the u_r at $r = 0.96r_0$ is documented as a series of snapshots in figure 5.7 and also in the animation A5.2 (see appendix F for details). The most striking aspect of the evolution is the westward motion of a m=3 pattern of equatorially symmetric (E^S) high amplitude upwellings and weaker, extended downwellings. There are several other processes occurring, for example involving meridional motion of upwellings and downwellings and modulations in their amplitude. The similarity of the morphology of u_r to that found in linear models of convection-driven hydromagnetic waves in spherical geometry (see chapter 7) is striking especially given that model is fully non-linear and has a dynamo generated rather than imposed magnetic field[3].

The azimuthal evolution of flow upwellings and downwellings were considered in more detail at latitudes where azimuthal motion of B_r concentrations was observed at the outer

[3]In the future it is planned to examine these similarities in more detail, with the aim of definitively identifying the particular hydromagnetic wave mechanism operating in the dynamo model (see chapter 6 for a discussion of different possible hydromagnetic wave mechanisms).

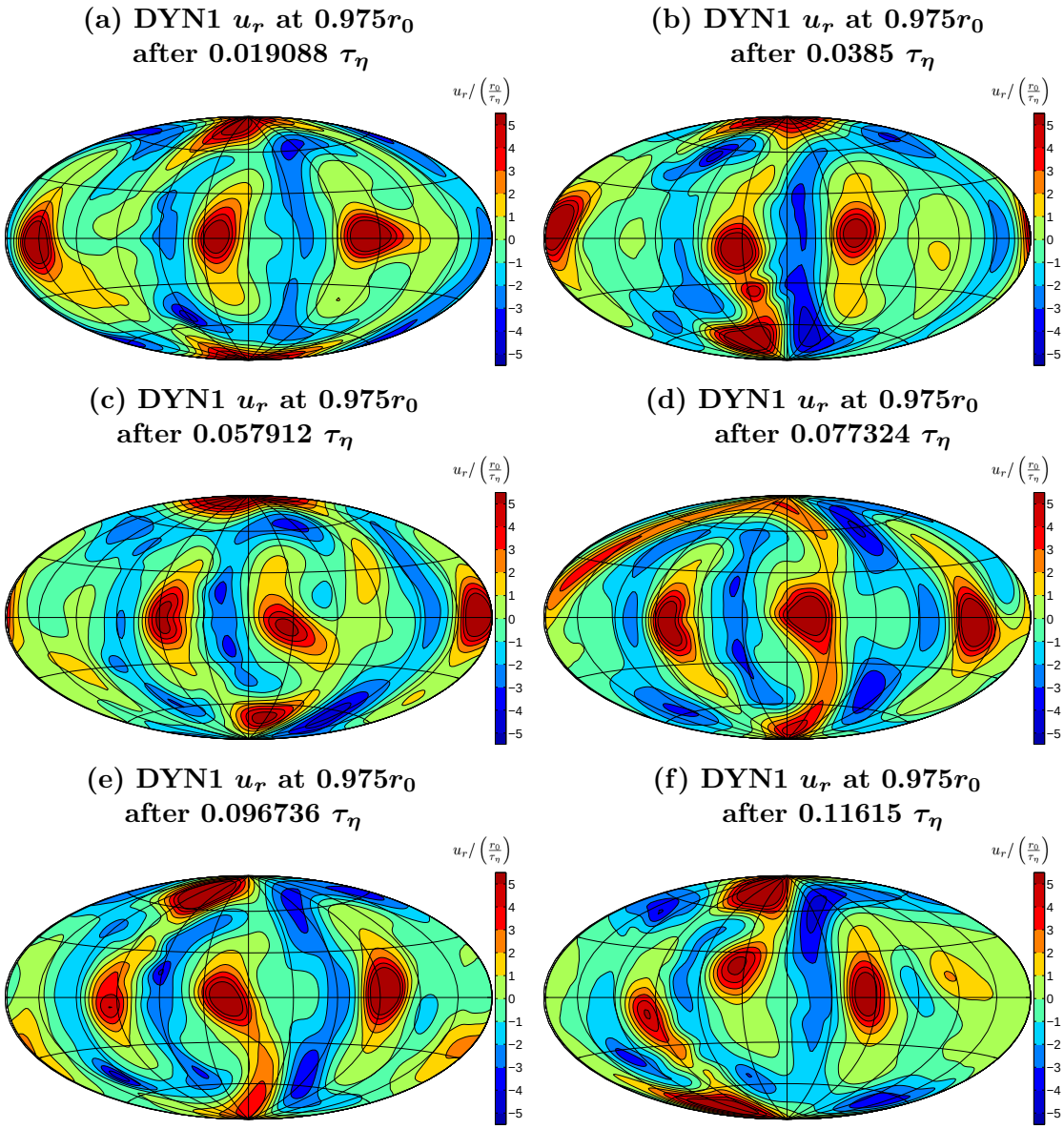

Figure 5.7: Snapshots of u_r from DYN1 at $0.975r_0$.
Unfiltered radial velocity field (u_r) from the model DYN1 is presented in a series of snapshots after (a) 0.019088 τ_η, (b) 0.0385 τ_η, (c) 0.057912 τ_η, (d) 0.077324 τ_η, (e) 0.096736 τ_η, (f) 0.11615 τ_η.

boundary, to determine whether there was any link between these two phenomenon. TL plots of u_r at radius $0.96r_0$, along with associated FK power spectra for latitudes 14°N and 20°S and LAS power plots (all without any processing) are presented in figure 5.8.

(a) u_r from DYN1, TL plot at 14°N **(b) u_r from DYN1, TL plot at 20°S**

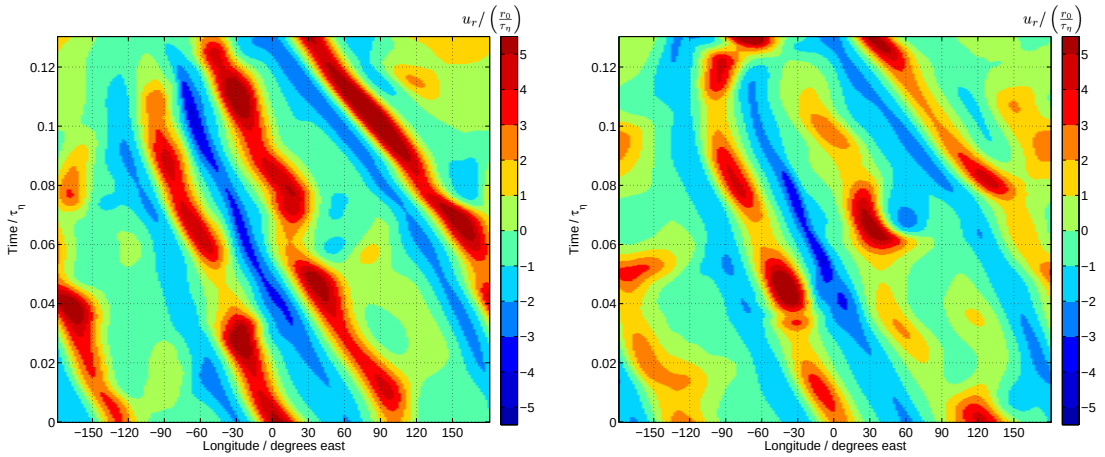

(c) u_r from DYN1, FK plot at 14°N **(d) u_r from DYN1, FK plot at 20°S**

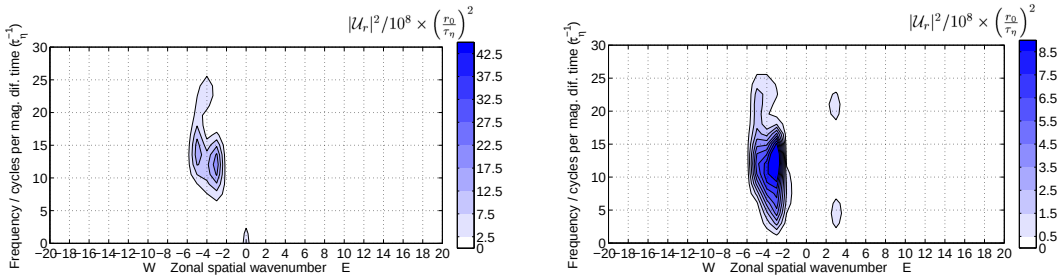

(e) u_r from DYN1, LAS power plot

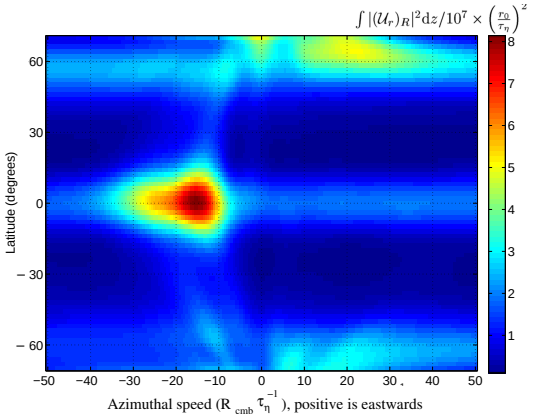

Figure 5.8: TL plots, FK power spectra and LAS plot of u_r from DYN1. Time-longitude (TL) plots of the unprocessed radial velocity field u_r from DYN1 at $0.96r_0$ at latitudes 14°N in (a), at 20°S in (b) with the associated frequency-wavenumber (FK) power spectra in (c), (d). The latitude-azimuthal speed (LAS) power plot for u_r is shown in (e), with azimuthal speeds mapped out to r_0 to facilitate comparison to the speed of magnetic field changes.

The spatially and temporally coherent motion of a succession of upwellings and downwellings is unmistakable in the TL plots and leads to strong individual peaks (at m=3,

$T = \frac{1}{f} = 0.08\tau_\eta$) in the FK power spectra and causes a strong peak in the LAS power plot. This evidence points towards an almost monochromatic wave as the major cause of the evolution of u_r observed at low latitudes. From the LAS power plot it can be inferred that upwellings and downwellings travel westward with an average azimuthal speed[4] of 16±5 $r_0\tau_\eta^{-1}$.

Comparing the TL plots of u_r and $\widetilde{B_r}$ at 14°N and 20°S it is found that the drifting concentrations of B_r are often correlated with azimuthally moving downwellings. For example, comparing figure 5.6b and figure 5.8a of the TL plots at 14°N, the strong negative field feature running from 0° longitude at $0.0475\tau_\eta$ to 75°W at $0.12\tau_\eta$ follows the same time-longitude path as the strongest downwelling feature also moving from 0° longitude at $0.0475\tau_\eta$ to 75°W at $0.12\tau_\eta$. Other weaker downwelling features in u_r also appear to be correlated with hints of weaker azimuthally moving features present in $\widetilde{B_r}$, for example from -60°E at $0.035\tau_\eta$ to -90°E at $0.06\tau_\eta$. At 20°S, the highest amplitude drifting features in $\widetilde{B_r}$ again appear to follow the same space-time path as the highest amplitude drifting downwellings in u_r at $r = 0.96r_0$. It is noticeable in both cases that downwelling patterns are larger scale (more extended in longitude) than the magnetic field concentrations.

The presence of an azimuthally drifting downwelling is apparently not a sufficient condition for producing a moving concentration of B_r. Whether or not a concentration of B_r is formed and then moves with a downwelling appears to depend on the configuration of B_r on which the flow pattern acts[5]. Even if the initial magnetic field configuration is favourable, and if B_r becomes concentrated at a downwelling, the field concentration does not continue to move azimuthally indefinitely but soon disperses, either because the downwelling flow becomes disrupted or because of the effects of the magnetic diffusion that are rather strong in DYN1 (see appendix C). Such issues concerning how a wave flow can influence a radial magnetic field are explored further with simple kinematic models in chapter 8.

Comparison of FK power spectra of u_r, B_r and $\widetilde{B_r}$, at 14°N and 20°S show that these have rather different character. Considering u_r, the FK power spectra clearly indicates a m=3, westward moving disturbance. Some indications of power at m=3 is also found in the FK power spectra of B_r, particularly at 14°N. However, there is also significant power at higher f and k (but same ratio of $\frac{f}{k}$ so moving at same phase speed). These higher 'harmonics' of the field occur because the m=3 flow can produce sharp field concentrations that require higher harmonics to be presented in a Fourier expansion. The FK power spectra of $\widetilde{B_r}$ predominantly picks up these higher 'harmonics' because the strong m=3 signal is partially removed by the high-pass filtering.

[4]mapped from $r = 0.96r_0$ to r_0 to permit easy comparison with the speeds of magnetic field features at the outer boundary.

[5]The toroidal magnetic field and its distortion by the wave flow has not been examined here: this is planned as future work. The configuration of this toroidal field could also be important in determining whether concentrations of B_r are obtained at the outer boundary.

The observed concentrations of B_r are equatorially anti-symmetric (E^A) as is expected from an equatorially symmetric (E^S) flow acting on an initially E^A magnetic field close to the outer boundary (see appendix E for details of those symmetries of field and flow that are consistent with each other). The source of the inverse polarity of the propagating field features is rather unclear, but following their formation in animation A5.1 it seems that low concentrations of inverse field were present as the initial configuration of the B_r that was subsequently concentrated at the positions of downwelling in the flow.

Eastward velocity field (u_ϕ)

The eastward velocity field u_ϕ at $r = 0.96r_0$ was studied to determine whether wave propagation or advection by a mean azimuthal flow was responsible for the motion of low latitude concentrations of B_r. The presence of a drifting pattern of alternating regions convergence and divergence in u_ϕ is often indicative of a wave mechanism (see, for example, chapter 7). On the other hand, the presence of a mean zonal flow at the latitude of moving B_r with the same magnitude as the speed of movement of field features would suggests this as the origin of azimuthal field motion.

In figure 5.9 snapshots of u_ϕ at $r = 0.96r_0$ are displayed; animation A5.3 shows the continuous pattern of evolution. The dominant feature is an m=3, westward moving, wave pattern that consists of alternating foci of eastward and westward flow. It is notable that the westward flow anomalies are slightly more intense than the eastward flow anomalies at low latitudes, suggesting a weak mean zonal flow is present there.

In figure 5.10, the TL plots, FK power spectra and LAS power plots for u_ϕ are presented. In close agreement with figure 5.8 for u_r these show definitive evidence for m=3 wave motion, with highest amplitudes at low latitudes and a characteristic period of approximately 0.08 τ_η. Comparison of TL plots for u_r and u_ϕ shows that the maxima of westward flow lags behind the downwellings that are correlated with magnetic field concentrations. The phase difference between the fields is about $\frac{\pi}{2}$ or $\frac{1}{4}$ of a cycle, so that the magnetic field concentrations are correlated with convergent neutral points (associated with downwellings) of approximately zero azimuthal flow (see for example at -60°E and 0.1 τ_η). The lack of any strong m=0 signal in u_ϕ at the latitude of moving B_r features (see figure 5.10c,d) suggests that simple advection by azimuthal flows is unlikely to be the dominant field evolution mechanism.

Figure 5.10f shows that time and zonal averaging indicates a weak, westward, mean zonal flow at low latitudes. However, considering this mean flow at latitudes where azimuthal motion of B_r was observed (-2 $r_0\,\tau_\eta^{-1}$ at 14°N and -4 $r_0\,\tau_\eta^{-1}$ at 20°S) reveals it to be too slow to explain the observed field motions (which have azimuthal speeds of $\sim -15 r_0\,\tau_\eta^{-1}$). It is therefore concluded that the wave flow pattern and associated magnetic field concentrations move azimuthally primarily by a wave propagation mechanism. It

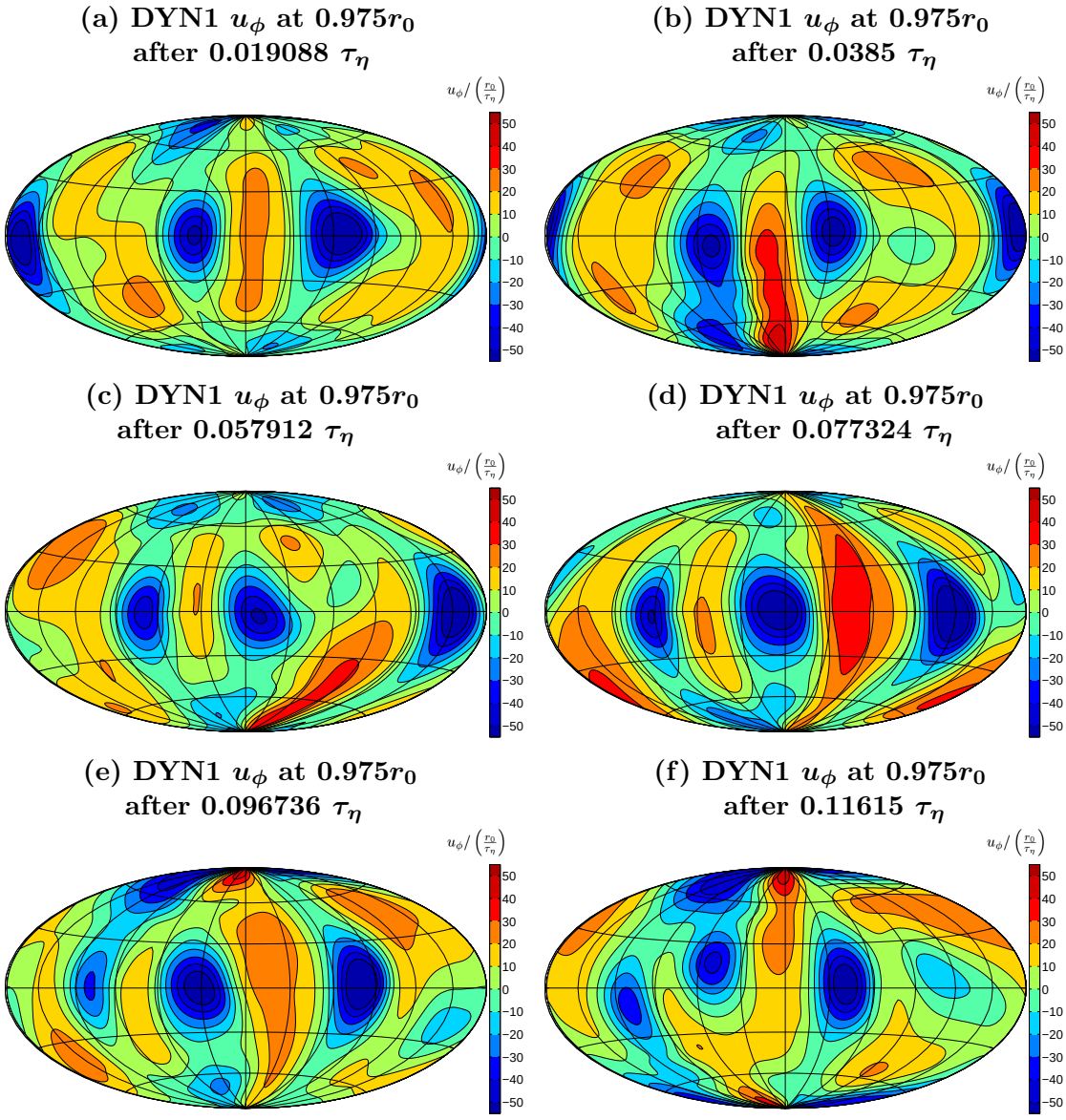

Figure 5.9: Snapshots of u_ϕ from DYN1 at $0.975r_0$.
Unfiltered radial velocity field (u_r) from the model DYN1 at $0.96r_0$ is presented in a series of snapshots after (a) 0.019088 τ_η , (b) 0.0385 τ_η, (c) 0.057912 τ_η, (d) 0.077324 τ_η, (e) 0.096736 τ_η, (f) 0.11615 τ_η.

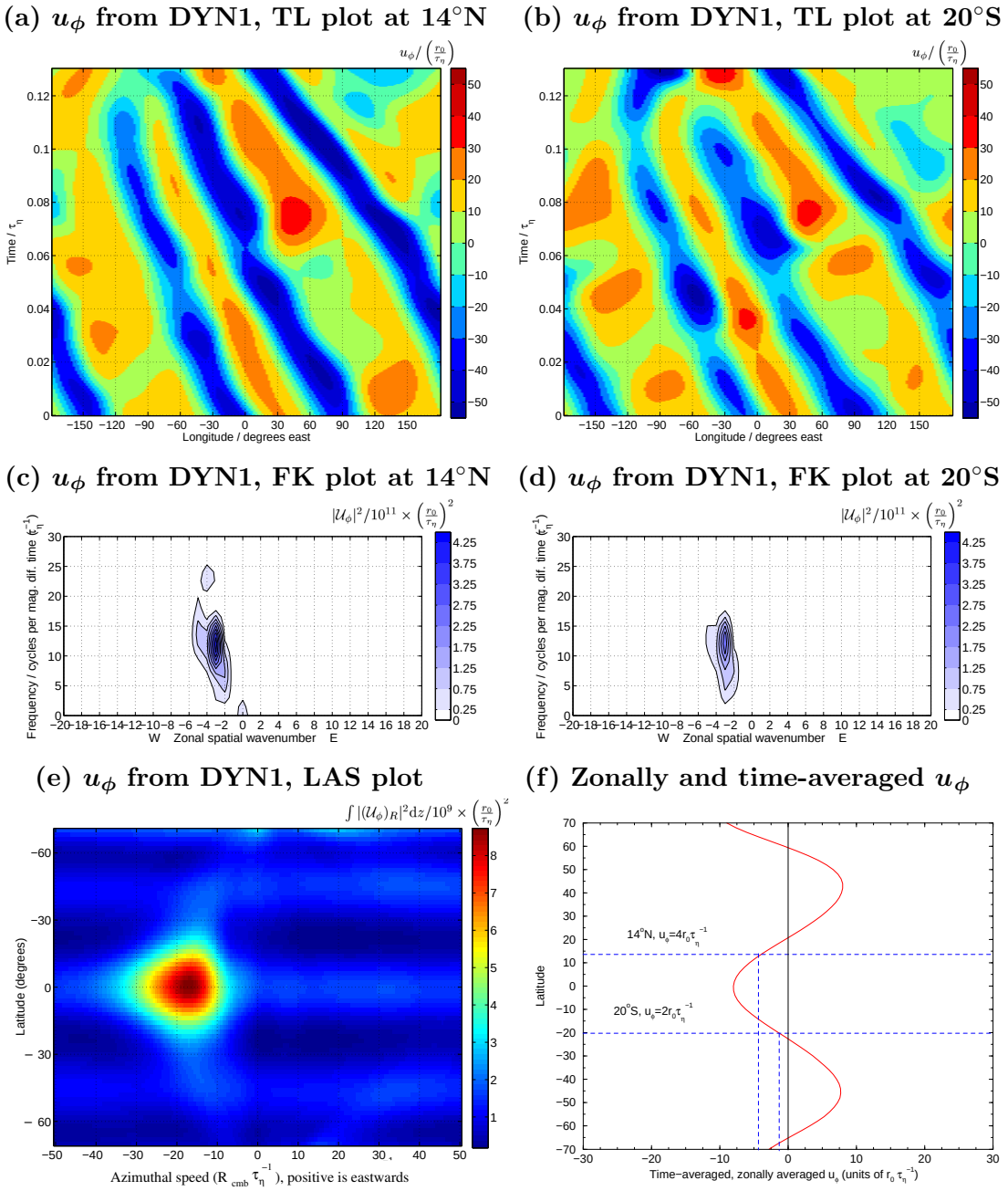

Figure 5.10: TL plots, FK plot and LAS plot of u_ϕ from DYN1.
Time-longitude (TL) plots of the unprocessed eastward velocity field u_ϕ from DYN1 at $0.96r_0$ at latitude 14°N in (a), at 20°S in (b) with the associated frequency-wavenumber (FK) power spectra in (c), (d). The LAS power plot for u_ϕ with azimuthal speeds extrapolated out to r_0 is shown in (e). Time-averaged, zonally averaged u_ϕ as a function of latitude is plotted for comparison in (f) with blue dash lines indicating latitudes of moving field concentrations.

should however be noted that this example may not be Earth-like because its mean zonal flows are rather weak since convection is only marginally supercritical and because it has no-slip boundary conditions at a relatively large Ekman number so viscous suppression of zonal flows will be significant. It should finally be noted that (i) the magnitude of u_ϕ within the wave flow is considerable larger than the azimuthal speed at which the pattern is moving and (ii) the magnetic field concentrations moving with the wave do not pulsate in amplitude. This is consistent with the predictions of the kinematic analysis of the effects of wave flows on a magnetic field presented in chapter 8.

5.2.3 Discussion of results from DYN1

Comparing the evolution of B_r at the outer boundary in DYN1 to that observed at the core surface in *gufm1*, the most obvious similarity is the presence of concentrations of B_r at low latitudes that drift westward. There are however several rather important differences. First, there is only a single pair of drifting B_r concentrations in DYN1, while a coherent pattern of concentrations is observed in *gufm1*. Secondly, in DYN1 the perturbation in B_r is E^A while that observed in *gufm1* is E^S. Thirdly, the B_r concentrations in DYN1 are reversed flux patches, while those seen in *gufm1* are the same polarity as the dominant (dipolar) field in that hemisphere.

None of these differences appears to be insurmountable. Considering the first problem, there are (at least weak) indications of concentrations in $\widetilde{B_r}$ associated with the paths of all downwellings observed in figure 5.6b. Considering the second problem, if an E^S flow of the type suggested by DYN1 is the origin of azimuthally moving concentrations in B_r and it acts on an E^S background magnetic field at low latitudes (rather than the E^A fields present in DYN1) then E^S perturbations in B_r could be produced as seen in geomagnetic field models. Regarding the third problem, since the mechanism of formation of magnetic field concentrations seems to involve focusing of magnetic field lines by convergence at downwellings, the reversed polarity is likely a consequence of the polarity of the initial B_r (see animation A5.1). If the wave flow acted on normal initial B_r then the resulting field concentrations would be of normal polarity (as is observed in DYN2) rather than the observed reversed polarity, so this difference does not appear to be crucial.

Regarding the hemispherical confinement of field evolution patterns, it is interesting to note that the azimuthally moving field features found in DYN1 were most prominent in one hemisphere than the other, even though the underlying wave flow was global. This appears to have been because the background field was more suitable for creating field concentrations in one hemisphere. The breakdown of the azimuthally moving field concentrations appears to have been the result of nonlinear interactions between the wave flow and other flow structures, as well as due to the effects of magnetic diffusion.

The simple mechanism causing azimuthal motion of B_r concentrations identified in DYN1 consists of concentrations forming at and moving along with positions of flow convergence at downwellings that are part of a global wave flow. Such a mechanism could perhaps account for the patterns of azimuthally drifting field concentrations of B_r observed in *gufm1*, this possibility is investigated in more detail in chapter 8. It should however be noted that the flow in Earth's core may not be as simple as that in DYN1. To address this issue a more complicated dynamo model (DYN2) was next considered.

5.3 DYN2: (E=3×10^{-4}, Pr=1, Pr_m=3, $Ra/Ra_c \sim 32$, $R_m \sim 500$)

The rationale behind studying DYN2 is primarily that its control parameters were as close as is numerically feasible to Earth's (see appendix C). However, the legitimate question 'is the parameter regime of DYN2 close enough to that in Earth's core for the model to be in the correct dynamic regime?' is rather difficult to answer. On the one hand hydromagnetic wave theory and magnetoconvection modelling considering steady imposed magnetic fields (see Chapters 6 and 7) indicates that at the very low Ekman number the leading order force balance will be between magnetic (Lorentz) and Coriolis forces, producing flows with large length scales (see, for example, Zhang and Schubert (2000)). On the other hand, no convection-driven spherical dynamo model has yet yielded the anticipated large length scales at low Ekman number; instead length scales have been observed to continue decreasing as the Ekman number is reduced, suggesting that the change-over to large scale convection is delayed when the magnetic field is not stationary (Zhang and Gubbins, 2002)[6]. If the length scale of convection remains small as the Ekman number is decreased further to Earth-like values then model DYN2 will likely be a good approximation of the dynamical regime in the core. On the other hand, if at smaller Ekman number the length scale of convection increases, the dynamical regime of DYN2 will be a poor approximation to the dynamical regime in Earth's core.

In the absence of any firm knowledge of the likely length scales of convection in the core, it is important to consider not only a dynamo model with large length scale flows (DYN1) but also a dynamo model with smaller length scale flows (DYN2). In the later case it is also important to address whether any accurate inferences concerning the nature of the underlying flow can be made by studying a truncated magnetic field at the outer boundary (DYN2d) that mimics the geophysical process of crustal filtering.

[6]Note, however, that an increase in the dominant length scale has been observed in convection-driven rotating plane layer dynamos at Ekman number smaller than is currently achieved in spherical dynamos (Rotvig and Jones, 2002; Stellmach and Hansen, 2004).

5.3.1 Undamped radial magnetic field (B_r) from DYN2

In figure 5.11 snapshots of B_r at the outer boundary ($r = r_0$) from the model run DYN2 with the full resolution of the model retained (up to spherical harmonic degree 85) are presented; animation A5.4 shows the continuous evolution of B_r at $r = r_0$. The concentrations of B_r observed in DYN2 have much smaller length scale than those in DYN1 because the convection patterns generating the field are much smaller scale; this is a consequence of the lower Ekman number. Even worse (given the desire to make interpretations in terms of simple mechanisms causing field change) is that the solution in DYN2 is much more chaotic because the Rayleigh number is more super critical than was the case for DYN1.

Nonetheless, a few general statements concerning the evolution of B_r at $r = r_0$ can be made. The highest amplitude concentrations of B_r are typically observed at high latitudes (near 60°N or S) and are not stationary but tend to move azimuthally, splitting into smaller features and merging with other field concentrations. Field evolution is punctuated by events involving rapid meridional movements of concentrations of B_r, while the polar regions are especially active sites of birth and decay of field concentrations. At lower latitudes, both E^S (for example in figure 5.11e at 45°W) and E^A (for example in figure 5.11d at 120°E) field concentrations that drift either westward or eastward are observed. These features often merge with other low latitude field concentrations and drift coherently for only short intervals $\sim 0.1\tau_\eta$.

Further insight into the azimuthal space-time evolution of B_r is obtained by considering the TL plots and their FK power spectra found in figure 5.12. At high latitudes (60°N and S) in figure 5.12a,f, a general trend of slow westward motion of field concentrations is seen superimposed upon smaller scale fluctuations. The FK power spectra suggest this is due to an m=2 disturbance with period of approximately 0.025 τ_η. The high latitude field disturbances have E^A symmetry, consistent with E^S core motions acting on E^A background fields.

The situation at lower latitudes is more complicated. The majority of azimuthally moving concentrations in B_r are rather short lived ($\sim 0.01-0.02\tau_\eta$). For example, at the equator in figure 5.12b a blue (negative anomaly) feature moves from from 60°W at $0.09\tau_\eta$ to 45°W at $0.1\tau_\eta$ and at 20°S in figure 5.12e where another blue feature moves from 165°W at $0.016\tau_\eta$ to 90°W at $0.038\tau_\eta$. There are also indications of a smaller number of more slowly moving, longer-lived magnetic field concentrations. These are distinct from the concentrations observed in DYN1 because as time goes on other field concentrations merge into them, causing changes in their amplitude speed and even in the sign of the anomaly. An example of such a feature is found in figure 5.12e where an initially orange feature (positive anomaly) moves from 75°W at $0.032\tau_\eta$ to 165°W at $0.11\tau_\eta$. The result of many rapidly moving features merging with slower moving features (not necessarily moving in the same direction) is the dendritic character evident in TL plots such as

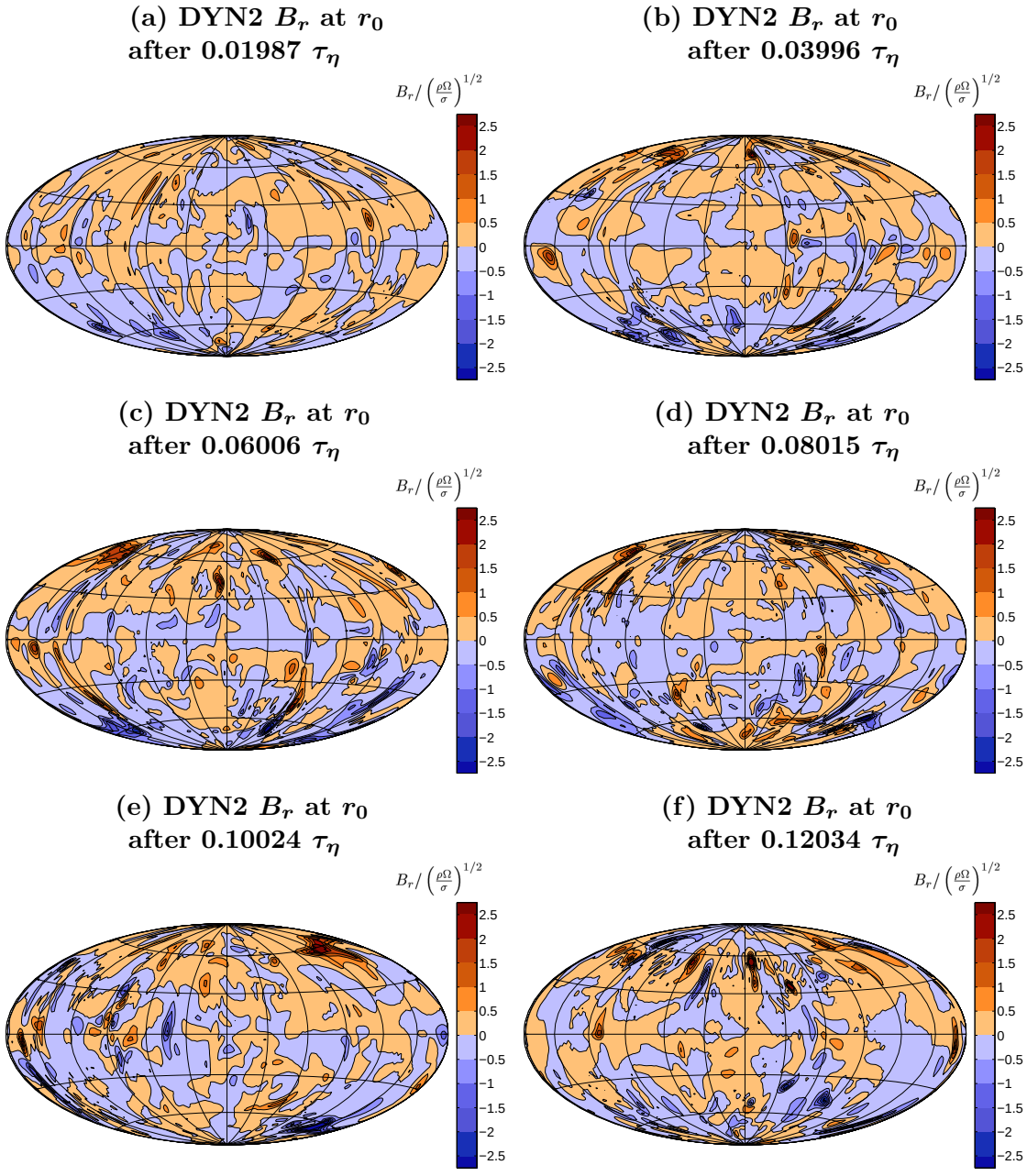

Figure 5.11: Snapshots of B_r from DYN2 at r_0.
Unfiltered radial magnetic field (B_r) from the model DYN2 is presented in a series of snapshots after (a) 0.01987 τ_η, (b) 0.03996 τ_η, (c) 0.060056 τ_η, (d) 0.08015 τ_η, (e) 0.10024τ_η, (f) 0.12034 τ_η.

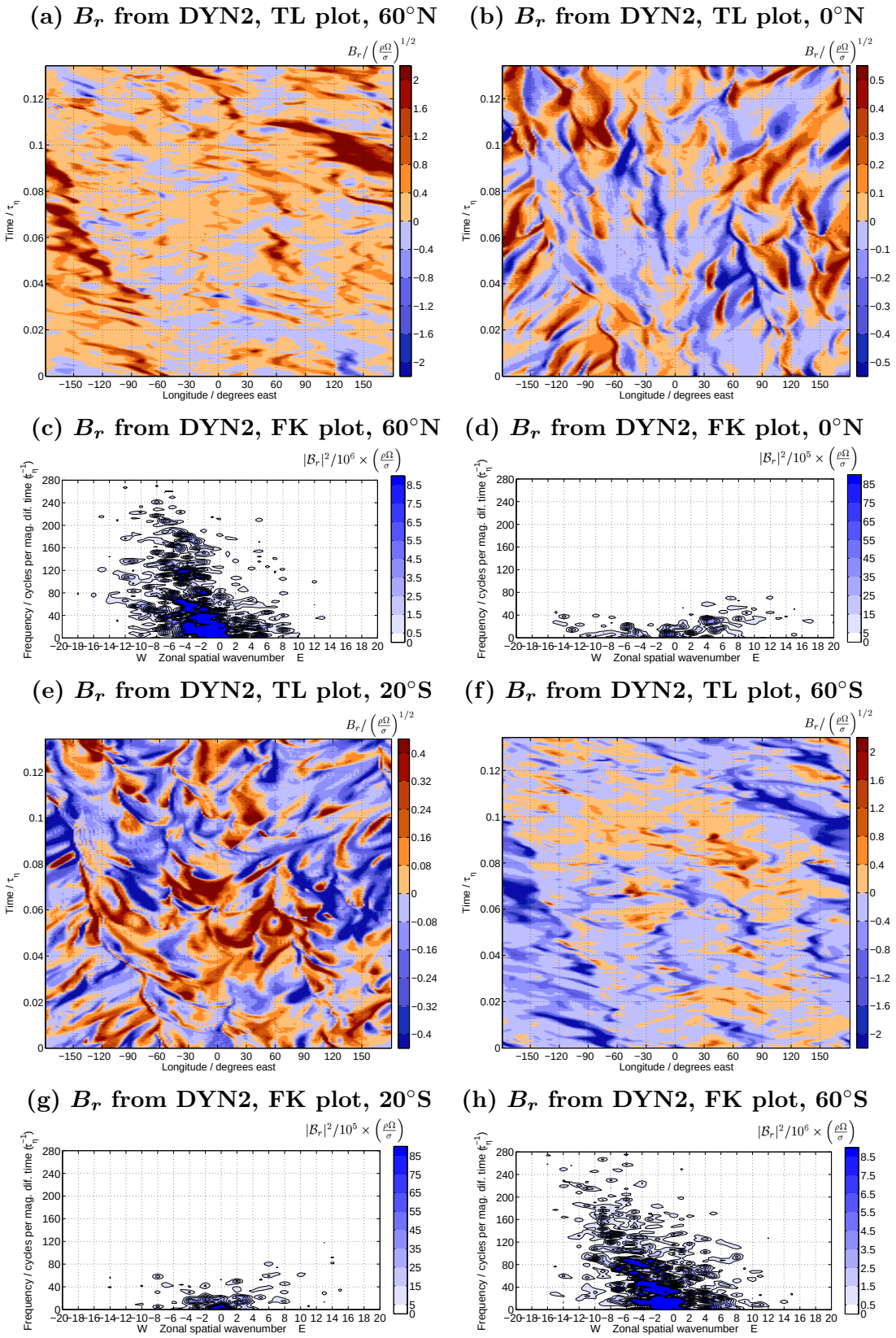

Figure 5.12: TL plots and FK power spectra of B_r from DYN2.
Time-longitude (TL) plots of radial magnetic field B_r from the model DYN2 at latitudes 60°N in (a), at 0°N in (b), at 20°S (e) and 60°S in (f). The associated frequency-wavenumber (FK) power spectra are found in (c), (d), (g) and (h).

figure 5.12e. The FK power spectra at low latitudes of DYN2 are very complicated, and it is hard to identify any dominant wavenumbers and frequencies.

Considering the amount of variability in B_r from DYN2 captured as the high pass filter threshold is varied leads to figure 5.13. Compared to DYN1 (figure 5.3) there is more variability at periods shorter than $0.05\tau_\eta$ in DYN2. For example with a filter cut-off of $0.01\tau_\eta$ 52 % of the variability is captured in DYN2, while only 3 percent is captured in DYN1.

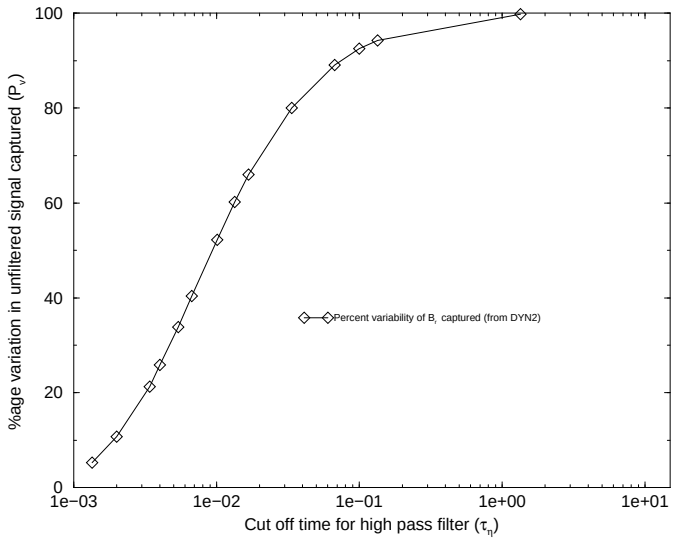

Figure 5.13: B_r variation captured by $\widetilde{B}_r$ in DYN2.
Graph showing the percentage of variation in B_r captured by $\widetilde{B}_r$ (P_v, as defined in equation (2.6)) in DYN2, as the choice of filter cut-off is varied.

In an effort to focus on the faster azimuthally moving field concentrations present at low latitudes, a filter threshold of $0.01\tau_\eta$ was chosen for further investigations. The TL plots and FK power spectra obtained after the time-averaged axisymmetric field has been removed and high-pass filtering has been carried out are shown in figure 5.14.

The trend of slow eastward or westward motion has been removed from the TL plots at high latitudes, leaving only transient behaviour. At low latitudes the slowly moving field concentrations have been removed, revealing episodes of spatially and temporally coherent rapid azimuthal motion of field concentrations, FK power spectra reveal these to be dominated by disturbances with wavenumbers $m \sim 14$ and periods of $\mathrm{T} \sim 0.0083\tau_\eta$. The FK power spectra for $\widetilde{B_r}$ are found to correctly capture the higher wavenumber and frequency peaks that are barely visible in the FK spectra of B_r. It should however be remembered that FK spectra of $\widetilde{B_r}$ give no information on the lower wavenumber and frequency signals (which could give information on large length scale core motions) that have been filtered out.

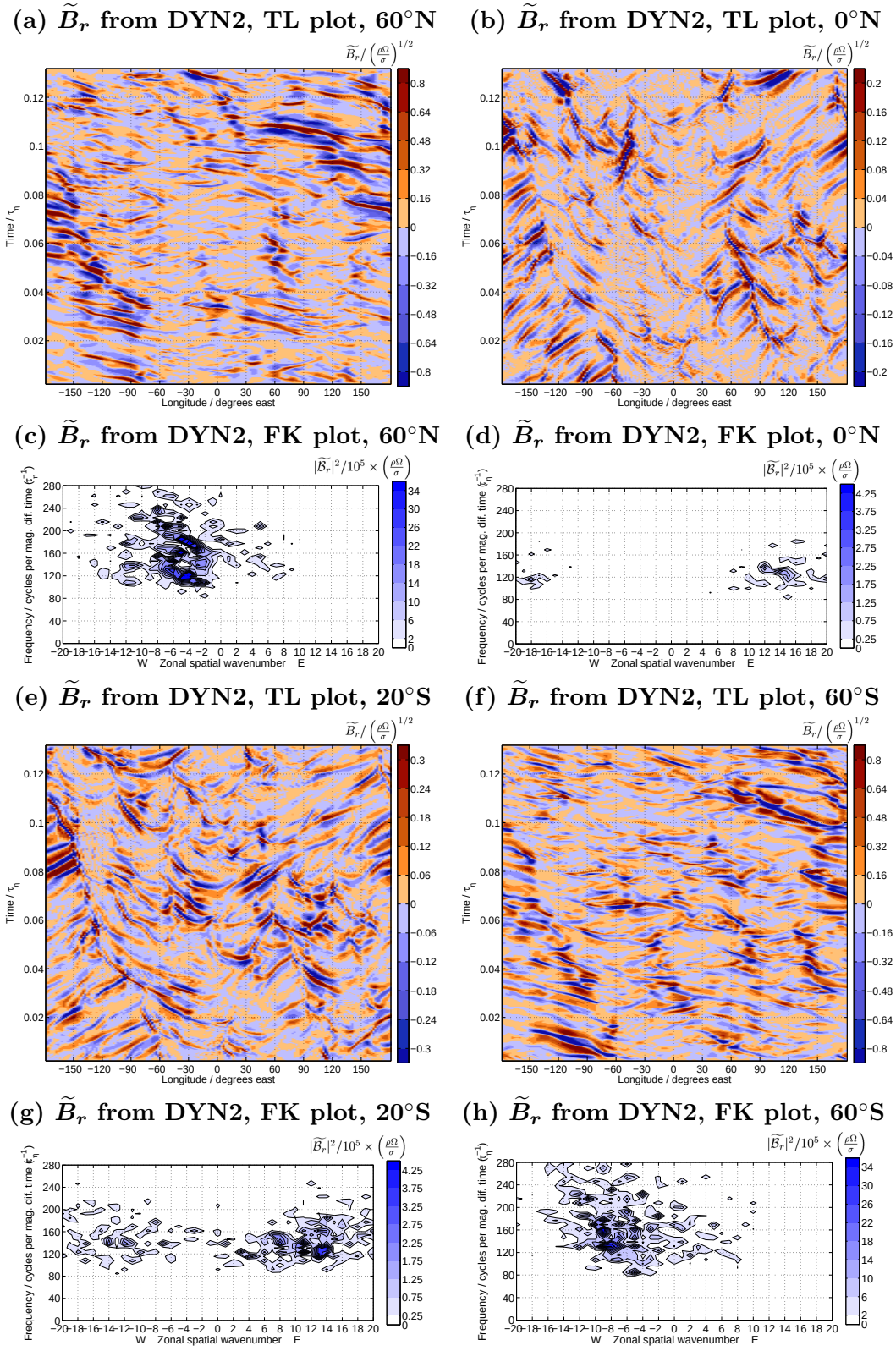

Figure 5.14: TL plots and FK power spectra of $\widetilde{B}_r$ from DYN2.
Time-longitude (TL) plots of $\widetilde{B}_r$ from the model DYN2 with filter threshold $0.01\tau_\eta$ at latitudes 60°N in (a), at 0°N in (b), at 20°S (e) and 60°S in (f). The associated frequency-wavenumber (FK) power spectra are found in (c), (d), (g) and (h).

5.3.2 Radial magnetic field from DYN2 (B_r) with $l > 10$ damped

Even if B_r at the core surface were as complicated as B_r at $r = r_0$ from DYN2, features with small length scales represented by spherical harmonic degrees greater than $l = 14$ would not be observed. This unfortunate circumstance arises because for $l > 14$ the contribution of the unknown crustal field (a source of error when seeking to determine the field at the core surface (see, for example, Langel (1987)) dominates in measurements made at Earth's surface. In the absence of an effective method of removing the crustal field, the influence of this truncation on our observations of core dynamics must be accounted for. In the present context this can be done by repeating the foregoing analysis with the same model but modifying the amplitude of the spherical harmonics with l=10 to 14 so they are damped[7] and also setting those with l >14 to zero. The model resulting when this procedure is applied to DYN2 (referred to as DYN2d) will be analysed in this section.

In figure 5.15 a series of snapshots of B_r from DYN2d at $r = r_0$ are displayed while animation A5.5 shows the associated time-dependent field evolution. Compared to the DYN2, DYN2d does a reasonable job of getting B_r concentrations of the correct polarity and relative amplitude in approximately the correct geographical positions. However, the amplitude of the strongest field concentrations in DYN2d is much lower than those found in DYN2 (by a factor of 5) and the smallest length scale intense features in DYN2 are smeared into lower amplitude, larger length scale features in DYN2d. Good illustrations of such effects can be seen by comparing the low latitude field concentrations focused on in the previous section (the E^S) feature in figures 5.15e and 5.11e at 45°W and the E^A feature in figures 5.11d and 5.15d at 120°E).

In figure 5.16, TL plots and FK power spectra of unprocessed B_r from DYN2d at latitudes 60°N, 0°N, 10°S and 60°S are presented for comparison with figure 5.12. The large scale, slow trends in the positions of field concentrations at high latitudes are well captured by DYN2d. At lower latitudes the larger scale, fast azimuthally moving field features are also well captured (for example in figure 5.16b and 5.12b from 165°W at $0.016\tau_\eta$ to 90°W at $0.038\tau_\eta$), but the slower, smaller length scale features (for example that found in figure (5.12b) running from 75°W at $0.032\tau_\eta$ to 165°W at $0.11\tau_\eta$) are no longer seen clearly in DYN2d.

In figure 5.17 the percentage variability in B_r captured by the high pass filtered field ($\widetilde{B}_r$) (i.e. P_v as defined in equation (2.6)) is plotted against the choice of the filter threshold for DYN2d. Compared with DYN2 (figure 5.13), there is less variability at very short periods because rapid field changes are associated with the shortest length scales that

[7]The tapering/synthetic damping prescription used is that from l=10 to l=14 the field is multiplied by a factor $\frac{1}{2}\left[1 - \sin\left(\frac{\pi(l-12)}{4}\right)\right]$ (Wicht, personal communication, April 2005). It should be noted that this taper is rather ad-hoc; a more realistic taper for simulating regularised field modelling is described in §8.3.6.

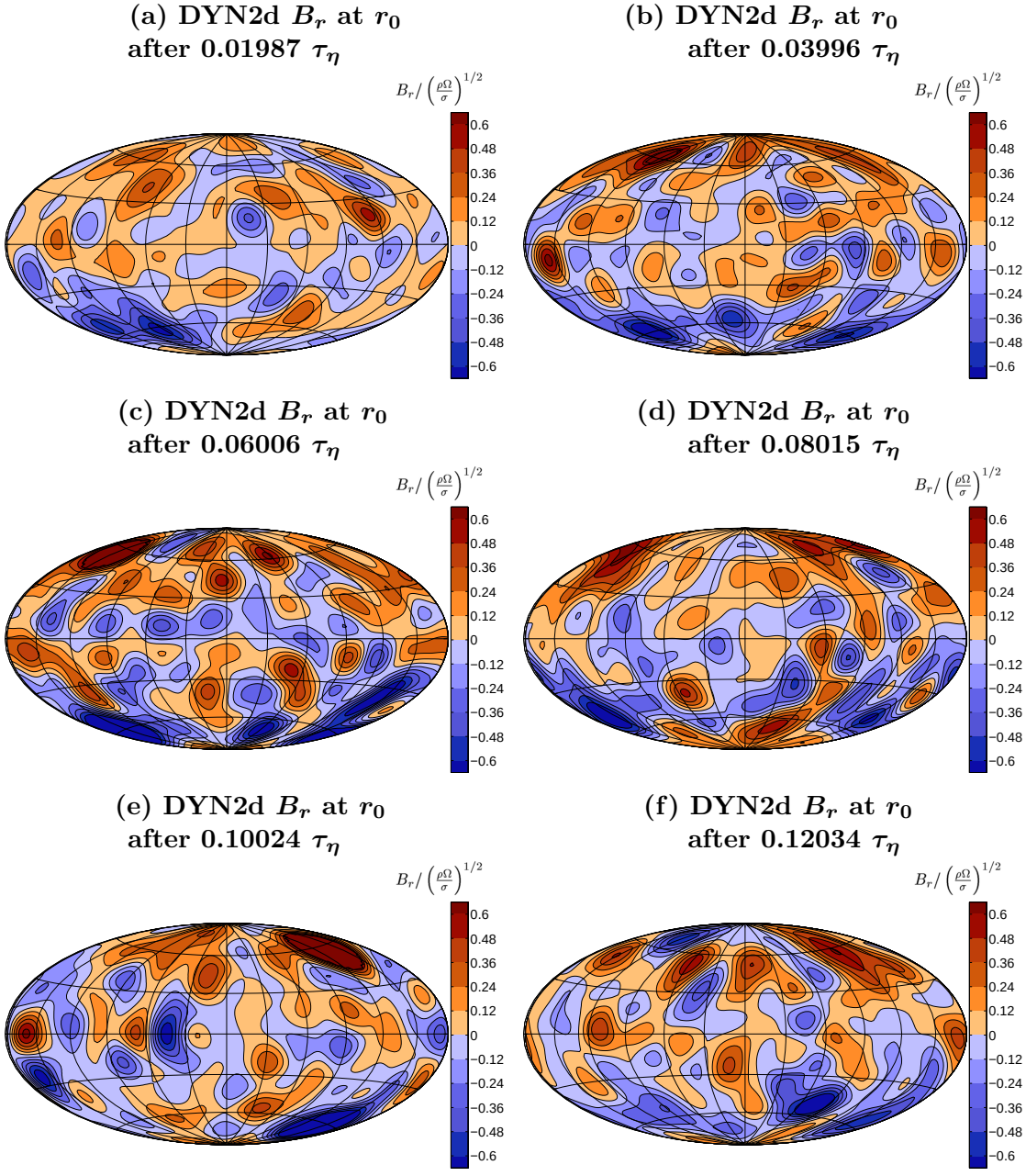

Figure 5.15: Snapshots of B_r from DYN2d at r_0.
Unfiltered radial magnetic field (B_r) from the truncated model DYN2d is presented in a series of snapshots after (a) 0.01987 τ_η , (b) 0.03996 τ_η , (c) 0.060056 τ_η, (d) 0.08015 τ_η , (e) 0.10024τ_η, (f) 0.12034 τ_η.

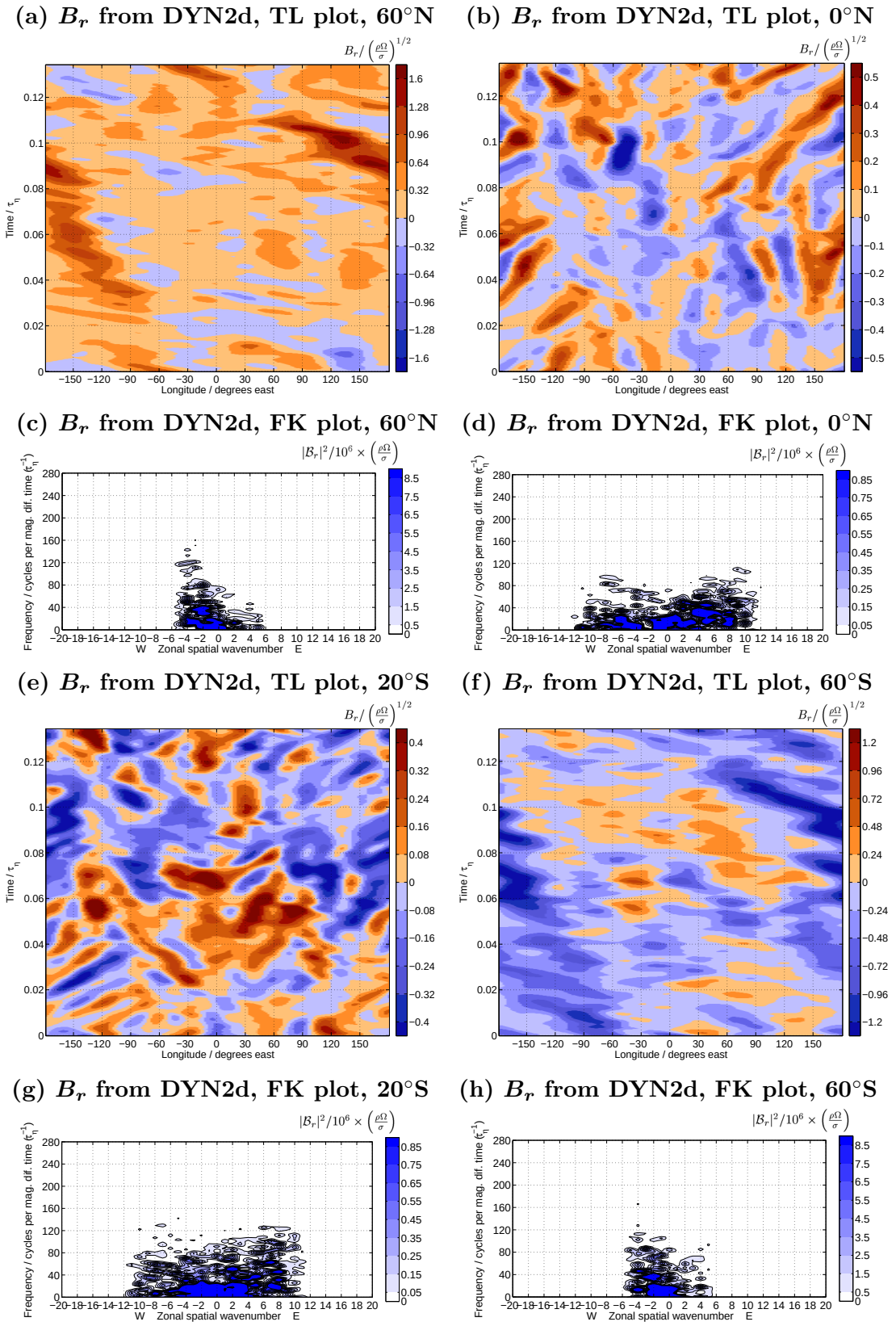

Figure 5.16: TL plots and FK power spectra of B_r from DYN2d.
Time-longitude (TL) plots of the radial magnetic field B_r from DYN2d at latitudes 60°N in (a), at 0°N in (b), at 20° (e) and 60°S in (f). The associated frequency-wavenumber (FK) power spectra are found in (c), (d), (g) and (h).

are not captured by DYN2.

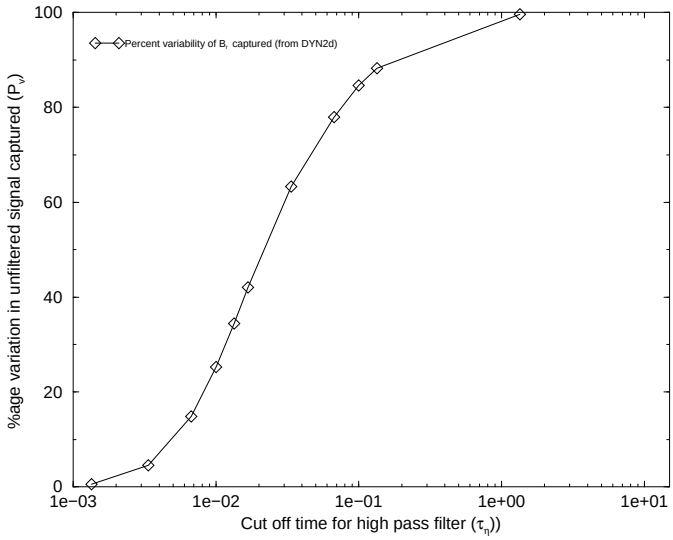

Figure 5.17: B_r variation captured by $\widetilde{B}_r$ in DYN2d, changing filter cut-off. Graph showing the percentage of the original field variation (P_v, as defined in equation (2.6)) captured by $\widetilde{B}_r$ as the choice of high pass filter cut-off is varied for the model DYN2d.

TL plots and FK power spectra for DYN2d after the time-averaged axisymmetric field has been removed and high pass filtering (threshold $0.01\tau_\eta$) applied are shown in figure 5.18. Compared to the results from DYN2 in figure 5.14, there are some obvious discrepancies. In particular, the azimuthally moving field concentrations are generally of larger spatial scale in DYN2d compared to DYN2. This lack of resolution can also mean that the azimuthal speed of the field features can be incorrectly inferred in DYN2d, if small length scale field features become merged. For example, a negative (blue) B_r anomaly at the equator in DYN2 moves from 60°W at $0.09\tau_\eta$ to 45°W at $0.1\tau_\eta$ (see figure 5.12). However, in DYN2d it moves from 60°W at $0.095\tau_\eta$ to 45°W at $0.1\tau_\eta$ (see figure 5.16). It should also be noted that the wavenumbers of high amplitude, large length scale (low wavenumber) features in DYN2 are correctly captured by DYN2d. An example of this can be found by considering the FK power spectra of $\widetilde{B_r}$ in DYN2 and DYN2d in figure 5.12c and figure 5.18c: both display a clear spectral peaks at $m = 4$W and $f = 120\tau_\eta^{-1}$.

5.3.3 Velocity field from DYN2

Radial velocity field (u_r) from DYN2

In an effort to understand the mechanisms causing the existence and motion of B_r concentrations observed at $r = r_0$, the untruncated velocity field from DYN2 was studied at a radius of $0.975r_0$. In figure 5.19 a sequence of snapshots of u_r at $0.975r_0$ are shown; an animation of the field at this radius can be seen in animation A5.6. The evolution of the velocity field in DYN2 is also very complex. Noteworthy features include

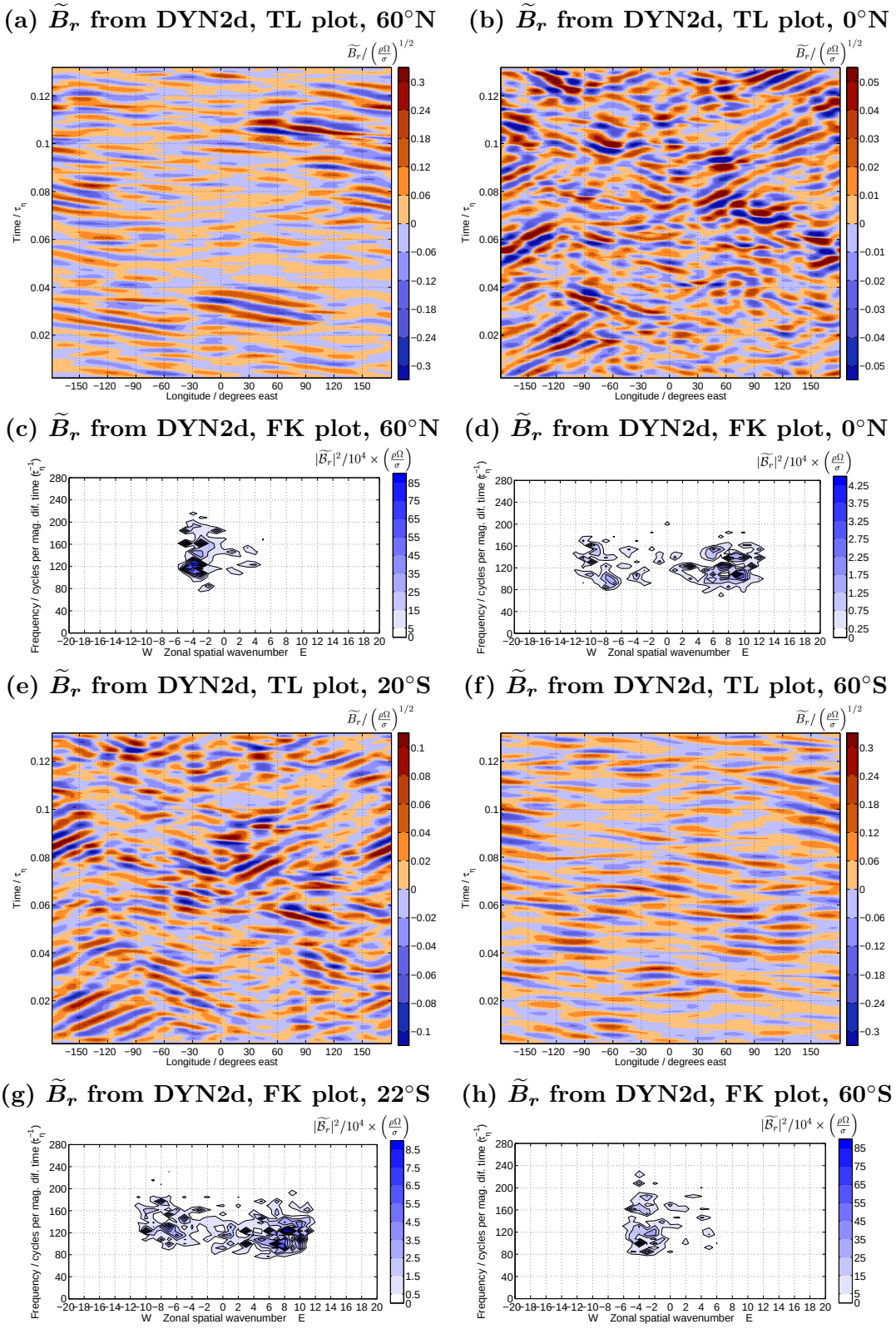

Figure 5.18: TL plots and FK power spectra of $\widetilde{B}_r$ from DYN2d.
Time-longitude (TL) plots of radial magnetic field $\widetilde{B}_r$ with filter threshold $0.01\tau_\eta$ from DYN2d at latitudes 60°N in (a), at 0°N in (b), at 20°S (e) and 60°S in (f). The associated frequency-wavenumber (FK) power spectra are found in (c), (d), (g) and (h).

intense activity inside the tangent cylinder inscribing around the inner core, bursts of meridional migration of intense upwelling and downwellings, and episodes of azimuthally drifting upwellings and downwellings at low latitudes. Often the regions of upwelling and downwelling are not latitudinally localised, but have large north-south extent. These are always E^S but have relatively small azimuthal length scale as expected for thermal convection at low Ekman number (Busse, 1970; Roberts, 1968). Isolated, azimuthally drifting, upwellings and downwellings often seem to occur very close together (within 5° of longitude of each other).

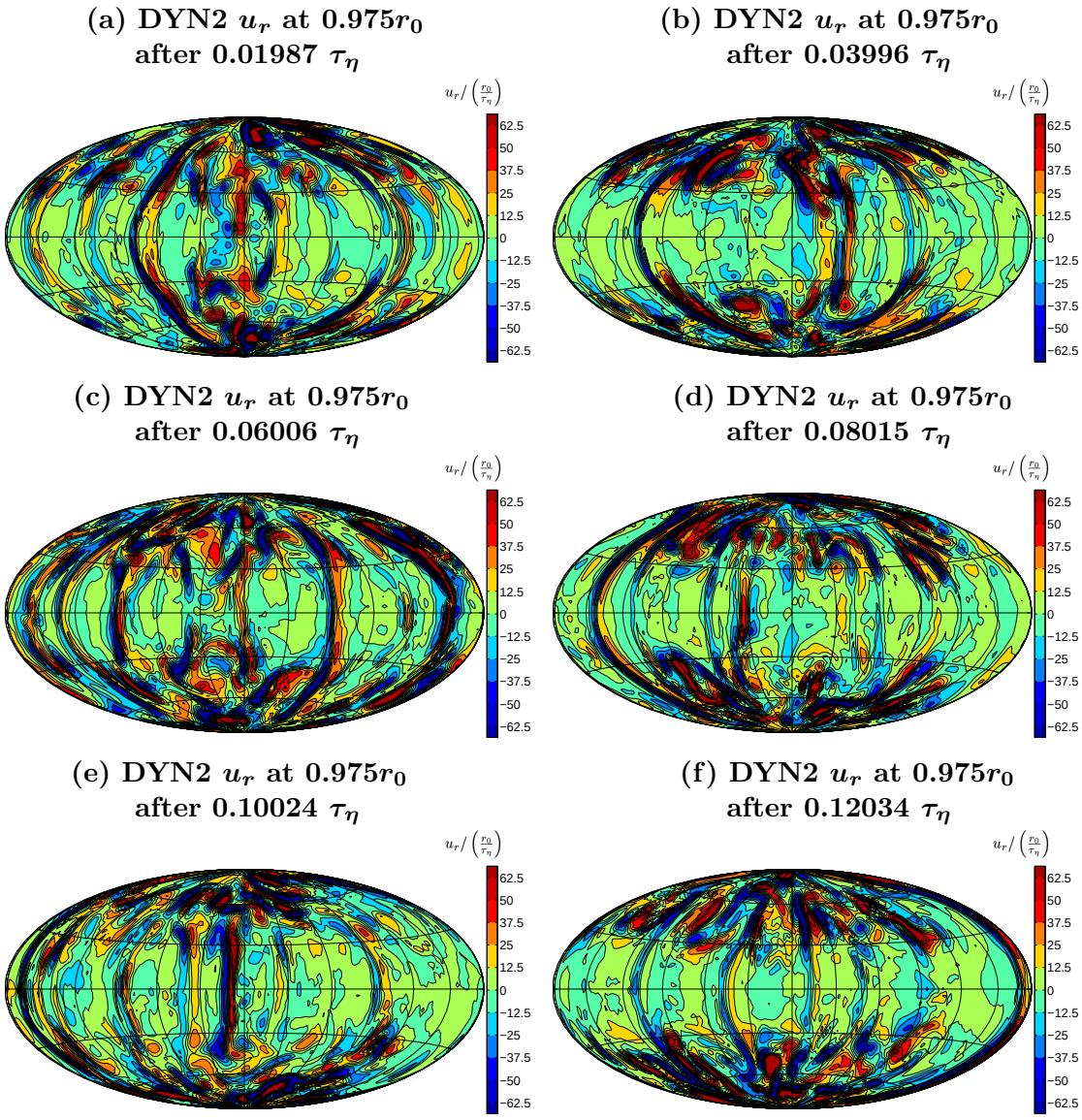

Figure 5.19: Snapshots of u_r from DYN2 at $0.975r_0$.
Unprocessed radial velocity field (u_r) at $r = 0.975r_0$ from the model DYN2 is presented in a series of snapshots after (a) $0.01987\tau_\eta$, (b) $0.03996\tau_\eta$, (c) $0.060056\tau_\eta$, (d) $0.08015\tau_\eta$, (e) $0.10024\tau_\eta$, (f) $0.12034\ \tau_\eta$.

TL plots and associated FK power spectra of u_r (without any processing) are presented in figure 5.20. At high latitudes, a slow background westward drift was observed, as was

also the case for B_r. At lower latitudes, the dendritic evolution patterns mentioned in the discussion of the B_r are very striking with rapidly moving, spatially and temporally coherent patterns of upwellings and downwellings merging into slower, higher amplitude features that appear to be instrumental in organising the flow evolution on longer time scales. The FK power spectra illustrate that motions are larger scale (m=2 to 6) and primarily westward at high latitudes, while at lower latitudes, the highest amplitude peaks are found at m=12 to 16 and are likely to be the result of the slow moving, high amplitude pairs of upwellings and downwelling being fed by the weaker, faster moving features.

Eastward velocity field (u_ϕ) from DYN2

Finally, the eastward velocity field u_ϕ from DYN2 was investigated to ascertain whether any persistent azimuthal flows were present that might enable an advection mechanism to explain observed motions of concentrations of B_r observed at the outer boundary. Snapshots of u_ϕ on a spherical shell of radius $0.975r_0$ are presented in figure 5.21, and the evolution can be seen in animation A5.7. The evolution of u_ϕ has very similar characteristics to u_r, but generally has larger spatial scales and fewer very intense, sharp features. Most motion of foci of u_ϕ occurs at mid to high latitudes, with occasional episodes of activity at lower latitudes. The E^S feature identified in B_r at the equator at 45°W at $0.10024\tau_\eta$ is found to be correlated with a convergence of eastward and westward flow, while the E^A low latitude feature at 120°E at $0.08015\tau_\eta$ occurs in an extended region of weak eastward azimuthal flow.

Considering the TL plots and FK power spectra of u_ϕ at 60°N and S, at the equator and at 20°S in figure 5.22 it is observed that at high latitudes a background m=2 pattern of u_ϕ moves slowly to the west. Superimposed on this large scale pattern are more rapid, transient motions of smaller length scales that complicate the picture. At lower latitudes (0°N and 20°S), the most striking feature is the dichotomy between eastward and westward flow, with the zero of eastward flow (actually a point of zonal flow convergence) occurring at the locations of the downwelling features observed in figure 5.20.

5.3.4 Discussion of results from DYN2 and DYN2d

Comparing truncated B_r at the outer boundary (DYN2d) to the geomagnetic field at the core surface over the past 400 years (*gufm1*), the morphology of the fields are on first impressions rather similar, though DYN2d is less dipole dominated. Both have intense, large scale, slowly moving, high latitude field concentrations and transient episodes of azimuthal motions of field features at low latitudes. Both E^S and E^A symmetry features are observed at low latitudes in DYN2d; which symmetry is present appears to depend

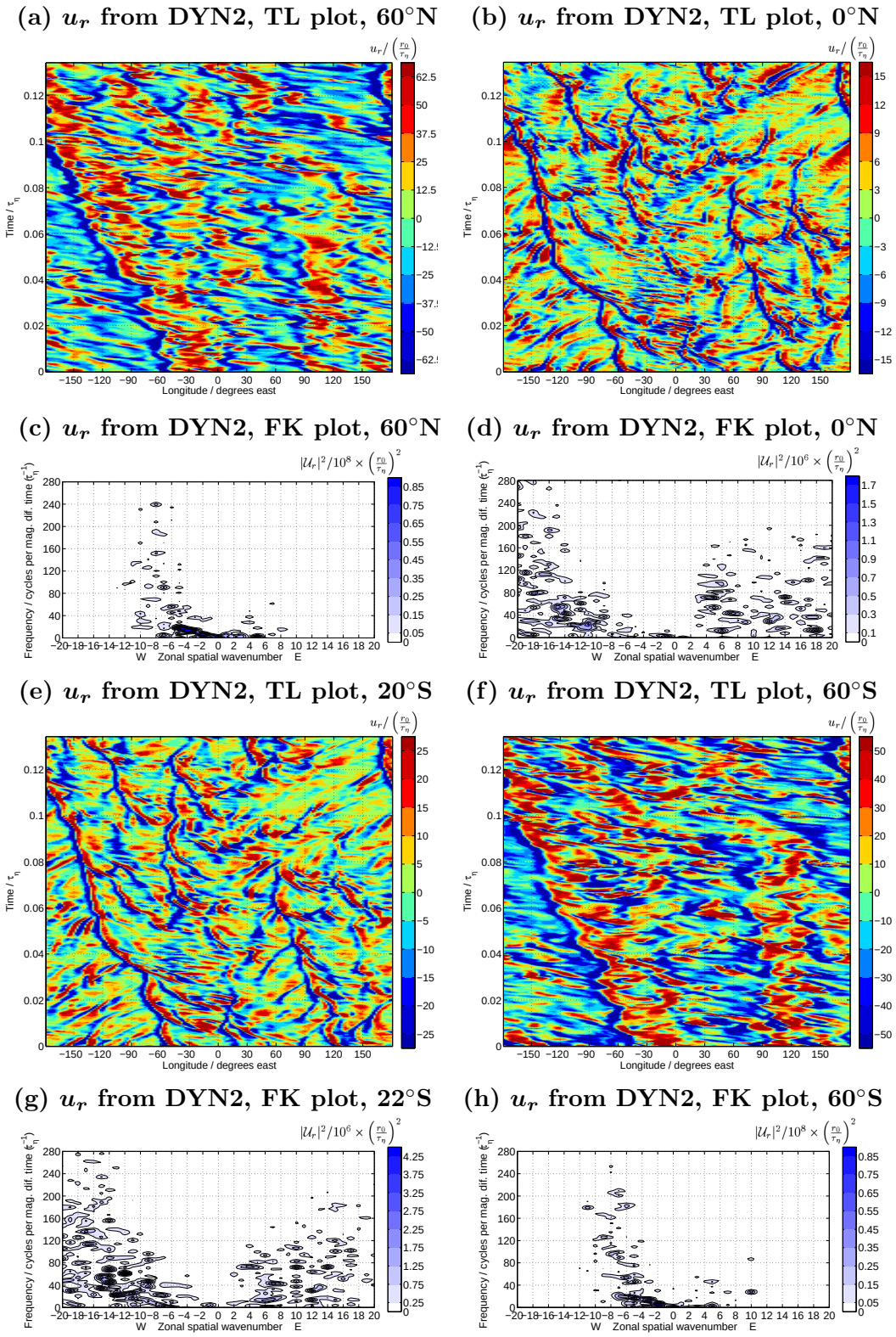

Figure 5.20: TL plots and FK power spectra of u_r from DYN2.
Time-longitude (TL) plots of unprocessed radial velocity field u_r from the model DYN2 at $r = 0.975r_0$, at latitudes 60°N in (a), at 10°N in (b), at 20° (e) and 60°S in (f). The associated frequency-wavenumber (FK) power spectra are found in (c), (d), (g) and (h).

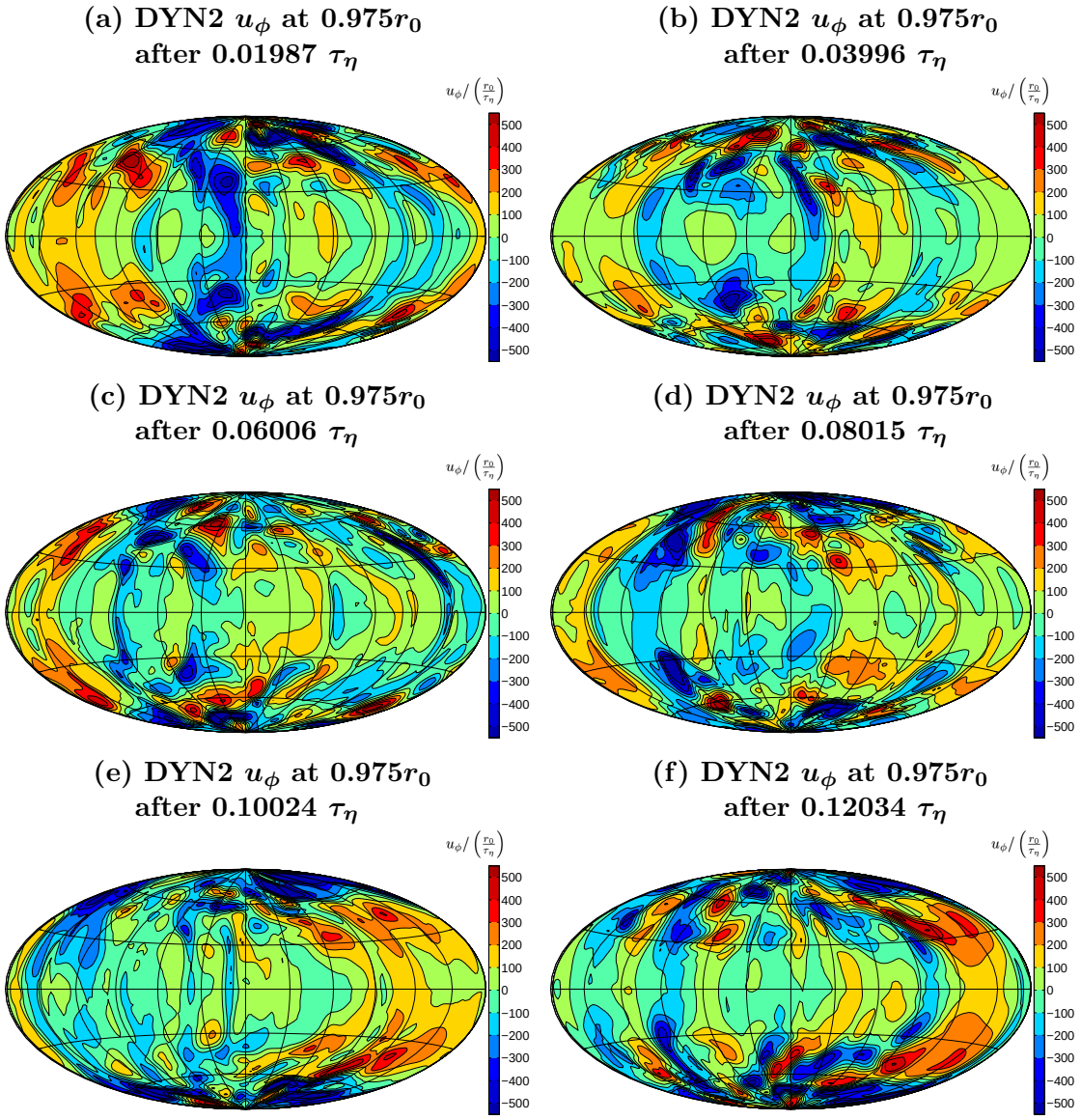

Figure 5.21: Snapshots of u_ϕ from DYN2 at $0.975r_0$.
Eastward velocity field (u_ϕ) at $r = 0.975r_0$ from the model DYN2 is presented in a series of snapshots after (a) 0.01987 τ_η , (b) 0.03996 τ_η, (c) 0.060056 τ_η, (d) 0.08015 τ_η , (e) $0.10024\tau_\eta$, (f) 0.12034 τ_η.

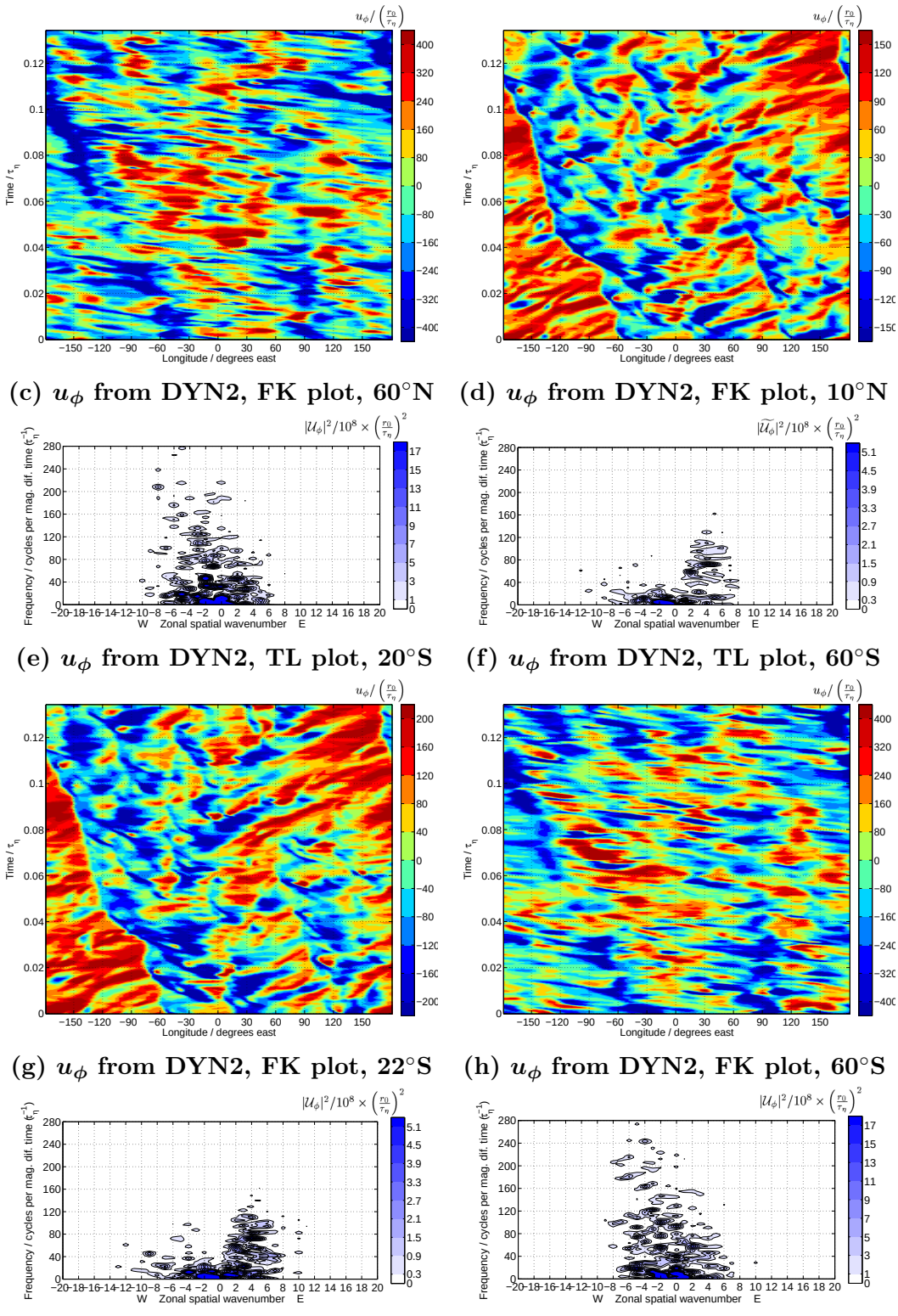

Figure 5.22: TL plots and FK power spectra of u_ϕ from DYN2.
Time-longitude (TL) plots of radial magnetic field u_ϕ from the model DYN2 (undamped) at $r = 0.975r_0$ without filtering at latitudes 60°N in (a), at 10°N in (b), at 20° (e) and 60°S in (f). The associated frequency-wavenumber (FK) power spectra are found in (c), (d), (g) and (h).

to a large extent on the symmetry of the initial (and local) B_r acted upon by the wave flow. In DYN2d there are also many more reversed polarity features than are observed in *gufm1*; this may be because DYN2 is not sufficiently dipole dominated.

Intervals of both eastward and westward motion of concentrations of B_r are observed in both DYN2 and DYN2d, as was the case when the archeomagnetic field model CALSK7.1 analysed in chapter 4. This result suggests that there is unlikely to be any fundamental reason for azimuthal motions of field features to be only westward at the core surface, as is the case in historical geomagnetic field model *gufm1*. By this reasoning, it seems more plausible that the westward drift of field features in *gufm1* is a transient episode of westward motion. Several episodes of such azimuthal motion (both eastward or westward) are observed in CALS7K.1 where they last between 500 and 2000 years, and also in both the magnetic and velocity fields of DYN2, where episodes typically last around 0.01 τ_η.

The analysis of DYN2 supports earlier findings from the study of DYN1 that azimuthally moving concentrations of B_r at low latitudes in some circumstances move along with the locations of flow convergence (where there is no net azimuthal flow) at positions of flow downwelling. The motion of such concentrations of B_r can sometimes not be explained by advection alone, and must involve wave propagation. The diagnosis is, however, much more difficult in DYN2 than DYN1 because of the smaller length scales involved and the more complicated (super-critical) nature of the evolution of the velocity field. Furthermore, in DYN2 there are additional instances of azimuthal motion (both eastwards and westwards) of concentrations of B_r at low latitudes that are not associated with any downwelling in the flow field. Their azimuthal motion appears to be caused by material advection along with the fluid rather than by wave propagation. In highly supercritical convection, it seems that both wave propagation and advection by zonal flows will contribute to azimuthal motion of magnetic field features.

The spectrally limited (damped) B_r studied in DYN2d was found to accurately capture the motions of the large length scale field features seen in DYN2, but unfortunately small length scale features are lost, leading to inaccuracies in the inferred azimuthal speeds. Nonetheless, the equatorial symmetry and direction of motion of features in (damped) B_r were found to be accurate diagnosis tools. It should be noted that limitations in the utility of B_r introduced by damping are only of relevance if the underlying fluid flow is dominated by small length scales.

5.4 Summary

In this chapter the utility of space-time spectral analysis techniques in analysing output from geodynamo models has been demonstrated. The methodology facilitates the comparison of the evolution of dynamo magnetic field at the outer boundary to the observed

characteristics of geomagnetic field evolution. It also enables the concomitant changes in velocity fields (and if necessary temperature fields) within the generation region to be studied giving insights into possible mechanisms of geomagnetic secular variation.

In both DYN1 and DYN2 evidence for radial magnetic field evolution associated with wave propagation was found. Under favourable conditions it was found that magnetic field concentrations could form at regions where flow converged at downwellings and moved along with these downwellings, interacting with other field concentrations to change amplitude and speed before eventually dispersing. Simple, large scale wave motions were observed in DYN1, and propagating flow features with much smaller length scales and more complicated nonlinear interactions were also observed in DYN2. The truncation of the magnetic field at the outer boundary in DYN2d was found to make it difficult to accurately infer the properties of the smallest scale fluid motions producing magnetic field change. Despite this, the azimuthal direction of field motions and equatorial symmetry of the underlying flow features could be accurately determined, regardless of spectral damping.

The models analysed in this chapter have succeeded in demonstrating that hydromagnetic waves can arise even if the background toroidal magnetic field is not steady, but is dynamo generated and constantly evolving. The evolution of the background field does however seem to ensure that the spatially coherent waves have finite lifetimes and soon break down. The existence of hydromagnetic waves in convection-driven dynamos in this chapter provides support for the hypothesis that they could exist in Earth's outer core.

Chapter 6

Theory of hydromagnetic waves in rapidly rotating fluids

6.1 Introduction

Hydromagnetic waves are propagating disturbances found in electrically conducting fluids permeated by magnetic fields. They exist as a result of the restoring force provided by magnetic tension that arises when fluid parcels move across field lines. Hydromagnetic waves are the natural response of a hydromagnetic system to perturbation, but can also occur as a manifestation of instability in the magnetic field or flow. It would therefore be very surprising if such waves were not present in Earth's outer core. In this chapter a review of the theory of hydromagnetic waves in rapidly rotating fluids is presented; the emphasis of this exposition will be on the different types of waves that could exist in Earth's core and the factors determining their properties. In the absence of diffusive processes, the dimensional equations of linear, Boussinesq rotating magnetoconvection (see appendix D, equations (D.13) to (D.15)) will be the basis for the mathematical development, while when diffusion is included, a viscous non-dimensionalisation (see appendix D, equations (D.19) to (D.21)) will be employed to facilitate comparison to non-magnetic studies.

Following a brief survey of the extensive literature in this area, the force balance responsible for the existence of hydromagnetic waves in rapidly rotating fluids will be discussed and fundamental time scales associated with their propagation identified. Using the Boussinesq, equations for rotating magnetoconvection described in appendix D, dispersion relations for diffusionless hydromagnetic waves in the presence of rotation and convection are derived. The influence of diffusion, spherical geometry, imposed magnetic field morphology, presence of an inner core, nonlinear feedbacks and fluid stratification on the waves are described, using previously published studies as a guide. Finally, possible types of hydromagnetic waves that could exist in Earth's core are discussed.

6.2 Survey of hydromagnetic wave literature

Study of hydromagnetic waves, with a focus on geophysical applications has a rich history and has captured the attention of some of the finest applied mathematicians and theoretical geophysicists over the past 50 years. Alfvén (1942) initiated the study of hydromagnetic waves, investigating the simplest possible scenario where a balance of magnetic tension and inertia gives rise to waves, which became known as Alfvén waves in his honour. Lehnert (1954) deduced that rapid rotation of a hydromagnetic system would lead to the splitting of plane Alfvén waves into two possible circularly polarised, transverse waves. One type of wave was found to have a period similar to inertial waves (found in all rotating fluid systems due to their intrinsic stability– see Stewartson (1978) for a description) while the other type of wave had a much longer period. The later represents a new, fundamental time scale in rotating hydromagnetic systems, which shall be referred to as the magnetic-Coriolis (MC) time scale. Chandrasekhar (1961) studied the effects of buoyancy on rotating hydromagnetic systems in detail, though he focused primarily on axisymmetric motions. Braginsky (1964; 1967) realised the importance of non-axisymmetric disturbances and showed that if magnetic, buoyancy and Coriolis forces were equally important, fast inertial waves as well as slower hydromagnetic waves are again obtained, but with periods dependent on the strength of stratification. He christened these slow waves, that were dependent on magnetic, buoyancy (Archimedes) and Coriolis forces, as MAC waves.

Hide (1966) was the first to consider the influence of spherical geometry on two dimensional hydromagnetic waves. He studied the effects of a linear variation of the Coriolis force with position, mimicking the effect of the variation in the Coriolis force with latitude in a spherical shell (known as the β effect in meteorology and oceanography). He showed that the resulting slow hydromagnetic waves (known as MC Rossby waves, because like Rossby waves in the atmosphere and ocean their restoring force relies on the variation of the Coriolis force with position (Gill, 1982; Pedlosky, 1987)) had the correct time scale to account for some parts of the geomagnetic secular variation, particularly the westward drift described by Bullard et al. (1950). Malkus (1967) studied MC waves in a full sphere for the special case of a background field increasing in strength with distance from the rotation axis. Stewartson (1967) developed an analytic theory of such MC waves in a thin spherical shell.

Eltayeb (1972), Roberts and Stewartson (1974), Soward (1979b) Roberts and Loper (1979) and more recently Roberts and Jones (2000) have illustrated the importance of including magnetic and thermal diffusion in models of hydromagnetic waves, showing that the most unstable waves in plane layer systems often occur on diffusive time scales. Eltayeb and Kumar (1977) and Fearn (1979b) carried out the first numerical studies of hydromagnetic waves to include the effects of both buoyancy and diffusion in a rotating, spherical geometry. Fearn and Proctor (1983) went on to consider the effect of

more geophysically plausible background magnetic fields satisfying electrically insulating boundary conditions at the outer boundary and with non-zero mean background flows. They found that the imposed background field had little influence on the properties of hydromagnetic waves, but that the background azimuthal flow could determine both the drift speed and latitudinal position of the waves. Most recently, Zhang and Fearn (1994), Zhang (1995) and Zhang and Gubbins (2002) have discussed the properties of MC and MAC waves in a spherical shell geometry, considering a variety of imposed magnetic field configurations.

The overviews by Hide and Stewartson (1973) and Braginsky (1989) provide concise introductions to the theory of hydromagnetic waves in rapidly rotating systems. The textbooks by Moffatt (1978), Melchoir (1986), Davidson (2001) and Rüdiger and Hollerbach (2004) contain summaries of hydromagnetic wave theory in the context of more general surveys of magnetohydrodynamics. More focused, technical reviews of the subject can found in Roberts and Soward (1972), Acheson and Hide (1973), Eltayeb (1981), Gubbins and Roberts (1987), Fearn et al. (1988), Proctor (1994) and Zhang and Schubert (2000).

6.3 Leading order force balance associated with hydromagnetic waves in rapidly rotating fluids

A physical understanding of MC waves can be achieved through consideration of the force balance in a rotating, electrically conducting, inviscid fluid which involves inertia, magnetic forces, and Coriolis forces. Inertia is the resistance to changes in the state of motion that all matter (including fluids) exhibit. Magnetic forces always act so as to oppose motions that cause distortions in magnetic field lines (Lenz's law). Understanding of the influence of Coriolis forces on fluid motions requires a little more thought. Coriolis forces are well known for causing circulating eddies in fluids (for example, hurricanes in the atmosphere) and exist in rotating reference frames because inertial motions follow curved trajectories rather than straight lines in such reference frames. Acting at right angles to direction of motion, the Coriolis force results in circular motions of fluid elements, which periodically return to their initial position. Such a fluid is said to possess intrinsic stability (Batchelor, 1967; Tritton, 1987). An intuitive understanding of this stability may be gained by thinking in terms of vortex lines which, by analogy to magnetic field lines, point in the direction of the local vorticity (Lighthill, 1966). Vortex lines resulting from the Coriolis force are initially parallel to the rotation vector for a homogeneous fluid in solid body rotation and like magnetic field lines impart an effective elasticity to the fluid by resisting fluid motions that distort them (Lighthill, 1978). Propagation of waves in rapidly rotating hydromagnetic fluids therefore depends on fluid motions distorting either the undisturbed parallel vortex lines, or the undisturbed magnetic field lines, or a combination of both.

In rapidly rotating hydromagnetic fluid systems, four possible force balances are conceivable; the first three require rapid fluid motions while the final is only possible for slow fluid motions[1]:

(i) When magnetic forces are much stronger than Coriolis forces, magnetic tension alone is capable of balancing inertia and disturbances are communicated by **Alfvén waves** where the magnetic restoring force acts to return magnetic field lines to their initial configuration (see figure 6.1b).

(ii) When Coriolis forces are much stronger than magnetic forces, vortex line tension is capable of balancing inertia and disturbances are communicated by **inertial waves** (see figure 6.1c).

(iii) When magnetic and Coriolis forces are of similar strength, the sum of of magnetic field tension and vortex tension can balance inertia and disturbances are communicated by **inertial magnetic-Coriolis (inertial-MC) waves** (see figure 6.1d).

(iv) When fluid motions are slow so that inertia is unimportant in the leading order force balance but magnetic and Coriolis forces are of similar strength, then magnetic and vortex tension are capable of balancing each other and disturbances are communicated by **magnetic-Coriolis (MC) waves**. In this case time-dependency arises through changes in the magnetic field, so that changes in the magnetic field configuration produce fluid motions through the action of the Lorentz force; these motions are then opposed by vortex line tension, resulting in oscillations and wave motion (see figure 6.1e).

Balance (iv) permits the existence of a new class of slow wave in rotating hydromagnetic systems, which cannot exist without the presence of both magnetic fields and rotation.

An estimate of the MC time scale can be obtained by performing a scale analysis of the important terms in the equations for conservation of momentum and induction. In the momentum equation (D.1), assuming a balance between Coriolis and magnetic (Lorentz) forces, $2\Omega\mathcal{U} = \frac{\mathcal{B}^2}{\rho_0 \mu L_{MC}}$, where Ω is the angular rotation rate, $\mathcal{U}$ is a typical velocity scale, $\mathcal{B}$ is a typical magnetic field strength, L_{MC} is a typical length scale over which changes associated with MC waves occur, ρ_0 is the density of the fluid and μ is the fluid's magnetic permeability. For a highly electrically conducting fluid, changes in the magnetic field come primarily from advection so scale analysis of the induction equation ignoring diffusion yields $\frac{\mathcal{B}}{T_{MC}} = \frac{\mathcal{U}\mathcal{B}}{L_{MC}}$, where T_{MC} is a typical time scale over which changes associated with MC waves occur. Substituting this expression for $\mathcal{U}$ into the expression for the force balance leads to the relation $T_{MC} = \frac{2\Omega L_{MC}^2 \rho_0 \mu}{\mathcal{B}^2}$. The quantity $v_A = \frac{\mathcal{B}}{(\rho_0 \mu)^{1/2}}$ has units of velocity and is the propagation speed of Alfvén

[1]The presence of the pressure gradient in the force balance is not explicitly discussed because it plays a passive role in incompressible fluids.

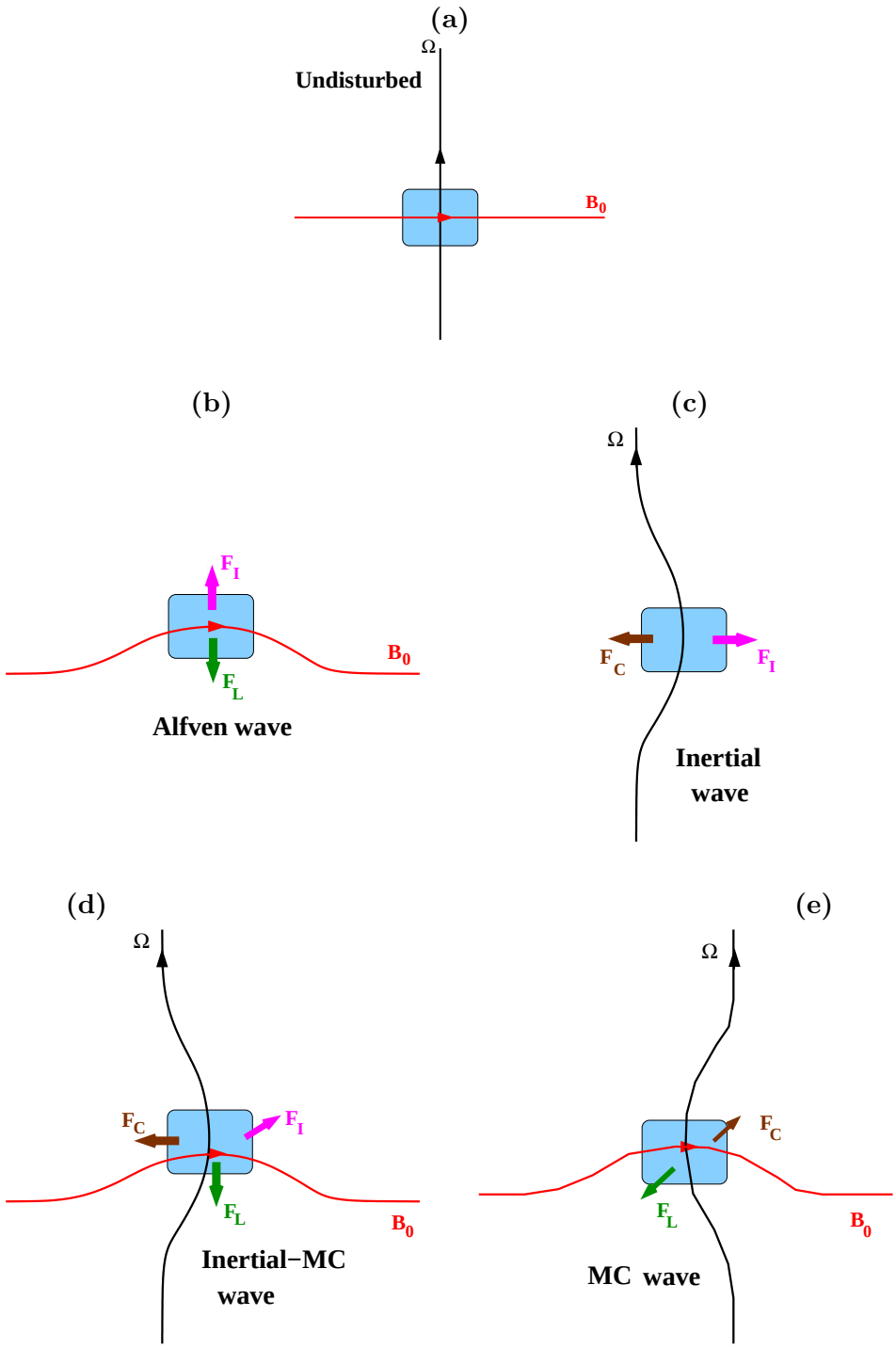

Figure 6.1: Hydromagnetic wave mechanisms in a rapidly rotating fluid. Possible hydromagnetic wave mechanisms. Black lines are vortex lines due to rotation, red lines are the imposed magnetic field and the light blue region is a fluid parcel. The green arrow represents the action of the Lorentz force on the fluid parcel, the brown arrow the action of the Coriolis force and the magenta arrow inertial acceleration. In (a) the undisplaced fluid parcel is shown, in (b) inertia and Lorentz force give rise to Alfvén waves, in (c) inertia and Coriolis force produce inertial waves, in (d) inertia is counteracted by the combination of Lorentz and Coriolis forces to give rise to inertial-MC waves while in (e) inertia is negligible and the Lorentz force caused by changes in the form of magnetic field lines is counteracted by the Coriolis force, producing MC waves.

waves (see, for example, Davidson (2001)). Estimates for these quantities in Earth's core are $\Omega = 7.3 \times 10^{-5} s^{-1}$, $\rho_0 = 1 \times 10^4 \mathrm{kgm}^{-3}$, $\mu = 4\pi \times 10^{-7} \mathrm{T}^2 \mathrm{mkg}^{-1} \mathrm{s}^2$, so that $T_{MC} \sim \frac{10^{-6} L_{MC}^2}{\mathcal{B}^2}$. Neither the magnetic field strength or the length scale associated with its variation in Earth's core are well known. Taking $\mathcal{B} = 5 \times 10^{-4} \mathrm{T}$, as suggested by models of the field at the core surface constrained by models at Earth's surface, and $L_{MC} = 3.5 \times 10^6 \mathrm{m}$, the core radius, yields $T_{MC} \sim 1.5 \times 10^6$ years. Equally plausibly, considering a wave with azimuthal wavenumber m=8, and assuming that the field inside the outer core is 10 times the inferred core surface field strength leads to an estimate of $T_{MC} \sim 250$ years. The coincidence between this time scale and that of geomagnetic secular variation motivates attempts to link the two phenomena.

6.4 Hydromagnetic waves driven by convection, in a rotating plane layer

In this section, the mathematical analysis of the generalisation of MC waves to the case when buoyancy forces are present (MAC waves) is presented. The starting point is the set of dimensional equations of linearised, Boussinesq rotating magnetoconvection (equations (D.13) — (D.17)). These equations express the principles of conservation of mass, momentum, energy and electromagnetic induction. In this particular model the equations are simplified by assuming that the imposed magnetic field $\boldsymbol{B_0}$ is uniform (so $(\boldsymbol{b} \cdot \nabla)\boldsymbol{B_0} = 0$) and that viscous, magnetic and thermal diffusion are negligible ($\nu = \eta = \kappa = 0$).

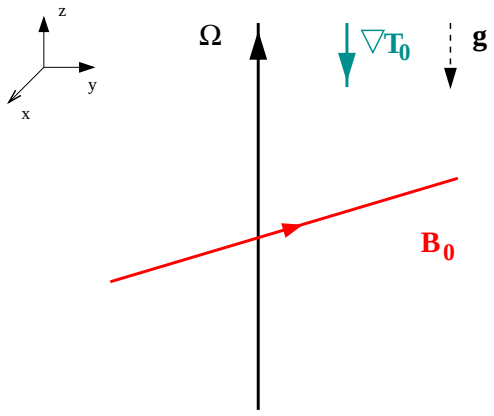

Figure 6.2: Geometry of plane layer model of diffusionless MAC waves . Geometry of background state in model of MC/MAC waves in an infinite rotating layer. The fluid rotates uniformly about the $\widehat{\boldsymbol{z}}$ axis, the imposed magnetic field is uniform, but in an arbitrary direction. The imposed temperature gradient and gravity act in the -$\widehat{\boldsymbol{z}}$ direction.

Working in Cartesian co-ordinates $(\widehat{\boldsymbol{x}}, \widehat{\boldsymbol{y}}, \widehat{\boldsymbol{z}})$ the axis of rotation is chosen to be along $\widehat{\boldsymbol{z}}$, the imposed magnetic field is chosen to be uniform but in an arbitrary direction, so $\boldsymbol{B_0} = (B_{0x}\widehat{\boldsymbol{x}} + B_{0y}\widehat{\boldsymbol{y}} + B_{0z}\widehat{\boldsymbol{z}})$, and the uniform background temperature gradient is $\nabla T_0 = -\beta'\widehat{\boldsymbol{z}}$. In a gravity field $\boldsymbol{g} = -\gamma\widehat{\boldsymbol{z}}$, the buoyancy force is therefore $\rho_0 g\alpha\Theta$ in the $\widehat{\boldsymbol{z}}$ direction, where $T = T_0 + \Theta$. Attention is focused on the slow motions, so the inertial term $\rho_0\frac{\partial \mathbf{u}}{\partial t}$ is neglected. The linearised governing equations are then

$$2\boldsymbol{\Omega}\times\boldsymbol{u} = -\frac{1}{\rho_0}\nabla P + \frac{1}{\mu\rho_0}\left(\mathbf{B_0}\cdot\nabla\right)\boldsymbol{b} + \gamma\alpha\Theta\widehat{\boldsymbol{z}}, \tag{6.1}$$

$$\frac{\partial \boldsymbol{b}}{\partial t} = \left(\mathbf{B_0}\cdot\nabla\right)\boldsymbol{u}, \tag{6.2}$$

$$\frac{\partial \Theta}{\partial t} = \beta'\left(\widehat{\boldsymbol{z}}\cdot\boldsymbol{u}\right). \tag{6.3}$$

Taking $\frac{\partial}{\partial t}\nabla\times$ the momentum equation (6.1) to eliminate pressure gives

$$2(\boldsymbol{\Omega}\cdot\nabla)\frac{\partial \boldsymbol{u}}{\partial t} = \frac{(\mathbf{B_0}\cdot\nabla)}{\mu\rho_0}\frac{\partial}{\partial t}(\nabla\times\boldsymbol{b}) + \gamma\alpha\frac{\partial}{\partial t}(\nabla\times\Theta\widehat{\boldsymbol{z}}), \tag{6.4}$$

while taking the curl $(\nabla\times)$ of the magnetic induction equation (6.2) yields

$$\frac{\partial}{\partial t}(\nabla\times\boldsymbol{b}) = \left(\mathbf{B_0}\cdot\nabla\right)(\nabla\times\boldsymbol{u}). \tag{6.5}$$

Substituting from equation (6.5) into equation (6.4) for $\frac{\partial}{\partial t}(\nabla\times\boldsymbol{b})$ gives a vorticity equation quantifying the MAC balance with terms arising from Coriolis forces on the left hand side and terms arising from the magnetic and buoyancy forces on the right hand side

$$2(\boldsymbol{\Omega}\cdot\nabla)\frac{\partial \boldsymbol{u}}{\partial t} = \frac{\left(\mathbf{B_0}\cdot\nabla\right)^2}{\mu\rho_0}(\nabla\times\boldsymbol{u}) + \gamma\alpha\frac{\partial}{\partial t}(\nabla\times\Theta\widehat{\boldsymbol{z}}). \tag{6.6}$$

Operating on equation (6.6) with $\frac{(\mathbf{B_0}\cdot\nabla)^2}{\mu\rho_0}\nabla\times$ gives

$$2(\boldsymbol{\Omega}\cdot\nabla)\frac{\partial}{\partial t}\frac{\left(\mathbf{B_0}\cdot\nabla\right)^2}{\mu\rho_0}(\nabla\times\boldsymbol{u}) = \left[\frac{\left(\mathbf{B_0}\cdot\nabla\right)^2}{\mu\rho_0}\right]^2(\nabla\times(\nabla\times\boldsymbol{u})) + \gamma\alpha\frac{\left(\mathbf{B_0}\cdot\nabla\right)^2}{\mu\rho_0}\frac{\partial}{\partial t}(\nabla\times(\nabla\times\Theta\widehat{\boldsymbol{z}})). \tag{6.7}$$

This can be simplified by noting that $\frac{(\mathbf{B_0}\cdot\nabla)^2}{\mu\rho_0}(\nabla\times\boldsymbol{u})$ can be eliminated by using equation (6.6) again, and remembering that for an incompressible fluid $\nabla\times(\nabla\times\boldsymbol{u}) = -\nabla^2\boldsymbol{u}$. Then taking the dot product of equation (6.7) with $\widehat{\boldsymbol{z}}$ and recognising that $\widehat{\boldsymbol{z}}\cdot(\nabla\times\Theta\widehat{\boldsymbol{z}}) = 0$ and $\widehat{\boldsymbol{z}}\cdot(\nabla\times(\nabla\times\Theta\widehat{\boldsymbol{z}})) = -(\frac{\partial^2}{\partial x^2} + \frac{\partial^2}{\partial y^2})\Theta = -\nabla_H^2\Theta$ leaves

$$4(\boldsymbol{\Omega}\cdot\nabla)^2\frac{\partial^2}{\partial t^2}u_z = -\left[\frac{\left(\mathbf{B_0}\cdot\nabla\right)^2}{\mu\rho_0}\right]^2\nabla u_z - \gamma\alpha\frac{\left(\mathbf{B_0}\cdot\nabla\right)^2}{\mu\rho_0}\nabla_H^2\frac{\partial\Theta}{\partial t}.$$

Finally, making use of the linearised heat equation (6.3) to eliminate $\frac{\partial\Theta}{\partial t}$, a sixth order equation in u_z is obtained. This is the diffusionless MAC wave equation

$$\left(4(\boldsymbol{\Omega}\cdot\nabla)^2\frac{\partial^2}{\partial t^2} + \left[\frac{\left(\mathbf{B_0}\cdot\nabla\right)^2}{\mu\rho_0}\right]^2\nabla^2 - \gamma\alpha\beta'\frac{\left(\mathbf{B_0}\cdot\nabla\right)^2}{\mu\rho_0}\nabla_H^2\right)u_z = 0.$$

Properties of diffusionless MAC waves can now be deduced by substitution of plane travelling wave solutions of the form $u_z = Re\{\widehat{u_z}e^{i(\mathbf{k}\cdot\mathbf{r}-\omega\mathbf{t})}\}$, where $\mathbf{k}$ is the wavevector and ω is the angular frequency, yielding

$$4(\boldsymbol{\Omega}\cdot\boldsymbol{k})^2\omega^2 - \left[\frac{(\mathbf{B_0}\cdot\boldsymbol{k})^2}{\mu\rho_0}\right]^2 k^2 - \frac{(\mathbf{B_0}\cdot\boldsymbol{k})^2}{\mu\rho_0}\gamma\alpha\beta'(k_x^2+k_y^2) = 0. \tag{6.8}$$

This expression can be written more concisely by observing that terms in it correspond to characteristic natural angular frequencies for hydromagnetic waves in the absence of rotation (Alfvén waves — see Davidson (2001)), internal gravity waves in a thermally stratified fluid and simple inertial waves in a rotating fluid (see Stewartson (1978) or Tritton (1987)), respectively defined as

$$\omega_M^2 = \frac{(\mathbf{B_0}\cdot\boldsymbol{k})^2}{\mu\rho_0}, \qquad \omega_A^2 = \frac{\gamma\alpha\beta'(k_x^2+k_y^2)}{k^2}, \qquad \omega_C^2 = \frac{4(\boldsymbol{\Omega}\cdot\boldsymbol{k})^2}{k^2}, \tag{6.9}$$

so equation (6.8) simplifies to

$$\omega_C^2\omega^2 - \omega_M^4 - \omega_M^2\omega_A^2 = 0. \tag{6.10}$$

Solving for ω gives the necessary condition (or dispersion relation) which must be satisfied by the angular frequency and wavevectors of plane MAC waves (Braginsky, 1964; 1967; Moffatt, 1978; Soward, 1979a; Soward and Dormy, 2005)

$$\omega = \pm\frac{\omega_M^2}{\omega_C}\left(1+\frac{\omega_A^2}{\omega_M^2}\right)^{1/2} = \pm\frac{k\,(\mathbf{B_0}\cdot\boldsymbol{k})^2}{2\rho_0\mu(\boldsymbol{\Omega}\cdot\boldsymbol{k})}\left(1+\frac{\gamma\alpha\beta'\rho_0\mu(k_x^2+k_y^2)}{k^2\,(\mathbf{B_0}\cdot\boldsymbol{k})^2}\right)^{1/2}. \tag{6.11}$$

Note that this is singular if $\mathbf{B_0}\cdot\boldsymbol{k} = \mathbf{0}$ or if $\boldsymbol{\Omega}\cdot\boldsymbol{k} = 0$, so diffusionless MAC waves cannot propagate normal to magnetic field lines or the rotation axis (though they can propagate across field lines and vortex lines unlike simple Alfvén waves and inertial waves). Their frequency depends strongly on their wavelength (i.e., they are highly dispersive) and on their direction (i.e., they are anisotropic). In the special case when the background magnetic field and the direction of the rotation axis are parallel to the direction of wave propagation, and when buoyancy forces are absent ($\alpha = 0$), the dispersion relation simplifies to $\omega = \frac{B_0^2k^2}{2\Omega\rho_0\mu}$ or $T_{MC} = \frac{2\Omega\rho_0\mu L_{MC}}{B_0^2}$ as was deduced from scaling arguments for MC waves in the previous section. The phase speed of the waves is then $c_{ph} = \omega/k = \frac{B_0^2k}{2\Omega\rho_0\mu}$ so that waves with shorter wavelengths travel faster.

The presence of a magnetic field strong enough to balance the effects of the Coriolis force is a necessary condition for the existence of the MC waves which are much slower than either inertial waves or Alfvén waves. It is worth noting that ω_{MC} is proportional to the square of the magnetic field strength, so that the magnetic field strength increases the phase speed of the MC waves also increases.

6.4.1 Effect of diffusion on hydromagnetic waves

Thus far the influence of any source of dissipation (viscous, magnetic or thermal diffusion) has been neglected in order to simplify both the mathematical analysis and the

physical picture. In this section these effects are re-introduced. Naively, the presence of dissipation might be expected to merely damp disturbances and irreversibly transform energy to an unusable form. Although such processes undoubtedly occur, the presence of diffusion has other more unexpected influences. Perhaps most importantly diffusion adds extra degrees of freedom to the system and facilitates the destabilisation of waves that were stable in the absence of diffusion (see Roberts (1977), Roberts and Loper (1979) and Acheson (1980)). This rather counter-intuitive effect means that instability of MAC/MC waves can occur for smaller unstable density gradients compared with when no diffusion is present and it has been found that instability can even occur in the presence of a stable density gradient.

The diffusive instability mechanism works most effectively when the oscillation frequency matches the rate of diffusion, so the time scale of the most unstable waves will be that of the diffusion process which is facilitating the instability (Acheson, 1980). Diffusion thus introduces new preferred time scales in the MAC wave problem: that of thermal diffusion for thermally driven waves, and that of magnetic diffusion for magnetically driven waves.

To include diffusion in the mathematical description of MAC waves, it is necessary to replace the operator $\frac{\partial}{\partial t}$ by $\left(\frac{\partial}{\partial t} - \nu\nabla^2\right)$ in the momentum equation, $\left(\frac{\partial}{\partial t} - \eta\nabla^2\right)$ in the induction equation, and $\left(\frac{\partial}{\partial t} - \kappa\nabla^2\right)$ in the heat equation. Retaining the acceleration term in the momentum equation and including the Laplacian (diffusion) terms before the substitution of plane wave solutions results in a rather more complicated dispersion relation for diffusive MAC waves (Moffatt, 1978; Soward, 1979a; Soward and Dormy, 2005),

$$\begin{aligned}\Big(\omega_C^2(\omega+i\eta k^2)^2 - \left[(\omega+i\nu k^2)(\omega+i\eta k^2)-\omega_M^2\right]^2\Big)\,(\omega+i\kappa k^2)\\ +\omega_A^2(\omega+i\eta k^2)\left[(\omega+i\nu k^2)(\omega+i\eta k^2)-\omega_M^2\right]=0.\end{aligned} \tag{6.12}$$

Restricting attention to the conditions thought to exist in Earth's outer core, where ohmic diffusion is expected to dominate viscous and thermal diffusion ($\eta \gg \nu, \kappa$) and where inertial acceleration can be neglected when considering slow oscillations, this expression simplifies to,

$$\left(\omega_C^2(\omega+i\eta k^2)^2-\omega_M^4\right)\,\omega \;-\; \omega_M^2\omega_A^2(\omega+i\eta k^2)=0. \tag{6.13}$$

The link to diffusionless MC waves becomes apparent if buoyancy forces are negligible ($\omega_A = 0$) when equation (6.13) reduces to,

$$\omega = \frac{\omega_M^2}{\omega_c} - i\eta k^2. \tag{6.14}$$

Here the classical damping role of magnetic diffusion is obvious, causing MC waves with shorter wavelengths to decay in amplitude more quickly than MC waves with longer wavelengths. More detail on diffusive MC waves with and without the inclusion of inertia, and their unwanted impact on geodynamo simulations can be found in Walker et al. (1998) and Hollerbach (2003).

6.5 Influence of spherical geometry on hydromagnetic waves

Earth's outer core is not an infinite plane layer, but a thick spherical shell with inner core radius approximately one third of its outer core radius. How does a spherical shell geometry influence the propagation properties, the stability and the planform of hydromagnetic waves? It appears that when the magnetic field is strong, so that the Lorentz force plays a dominant role in the momentum equation, the influence of spherical boundaries is a secondary effect (Fearn, 1979b; Soward, 1979b). On the other hand, when the magnetic field is weaker, the influence of the Coriolis force and its latitudinal variations due to spherical geometry[2] are dominant. In this section some simplified models that have been used to study the influence of spherical geometry on hydromagnetic waves are discussed.

6.5.1 Variation of Coriolis force with latitude: Hide's β-plane model

Hide (1966) developed a simple analytical model of MC waves in a spherical shell. He assumed that the waves would have a two dimensional form, being to a first approximation invariant parallel to the rotation axis. He was therefore able to focus on local motions of fluid columns in the eastward and northward directions on a spherical surface. Rather than a constant Coriolis force (as for a plane layer) or a Coriolis force depending on the sine of latitude ($\sin\lambda_{lat}$) as in a full spherical geometry, he followed Rossby (1939) and let the Coriolis force vary linearly in the north-south direction about a fixed latitude λ^*_{lat}. The linearised Coriolis force is then $-f_c u_y$ in the eastward direction and $f_c u_x$ in the northward direction, where $f_c = 2\Omega \sin\lambda^*_{lat} + \frac{2\Omega\cos\lambda^*_{lat}}{c} y = f_{c0} + \beta y$ and c is the outer radius of the spherical shell. Though $\beta = \frac{2\Omega\cos\lambda^*_{lat}}{c}$ in thin spherical shell, Hide argued that it should take the opposite sign ($\beta = -\frac{2\Omega\cos\lambda^*_{lat}}{c}$) in thick spherical shells (see discussion below). The 'β' in β-plane thus refers to the constant defining the linear rate of change of the Coriolis force in the north-south direction in this simplified model. The geometry of the local coordinate system used in this β-plane model (Gill, 1982; Pedlosky, 1987; Andrews, 2000) is presented in figure 6.3.

The imposed magnetic field $\boldsymbol{B_0}$ was chosen to be uniform but inclined at an angle to the eastward direction; for simplicity the results of the model are reported here for the case when $\boldsymbol{B_0}$ is entirely eastwards. The background velocity field is assumed to be zero for

[2]The Coriolis force in a spherical geometry imparts stability to a rapidly rotating fluid in two ways. Firstly, the rotation of the fluid gives it an intrinsic stability whereby perturbations lead to circular particle motions (this is the elasticity imparted by vortex lines) and is the mechanism underlying fast inertial waves which can propagate in both eastwards and westwards directions (Malkus, 1967; Stewartson, 1978; Zhang, 1993). Additionally however, slow motions tend to be invariant parallel to the rotation axis and have a columnar structure; in a spherical geometry, if these columns move latitudinally they change their height and by conservation of mass their vorticity alters to oppose the change in latitude. This provides a stability to latitudinal motions and is the basis for uni-directional Rossby waves propagating westwards in thin shells and eastwards in thick shells. Greenspan (1968) and Zhang et al. (2000) discuss how, because rotation is the basis for this second mechanism, Rossby waves can be considered as special, very low frequency inertial waves.

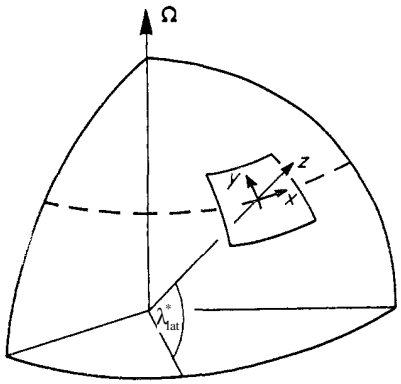

Figure 6.3: The β-plane geometry employed by Hide (1966).
The local coordinate system at latitude λ^*_{lat}, employed in the β-plane model of Rossby (1939) and Hide (1966) (diagram adapted from Acheson and Hide (1973)).

simplicity. Magnetic and viscous diffusion and all thermal and stratification effects were neglected in the model. The linearised equations governing the evolution of the velocity field and magnetic field disturbances $(\boldsymbol{u}, \boldsymbol{b})$ on the β-plane, after the subtraction of the leading order geostrophic balance between pressure and the constant part of the Coriolis force $(f_{c0} = 2\Omega \sin \lambda^*_{lat})$, are then

$$\frac{\partial u_x}{\partial t} - \beta y u_y = -\frac{1}{\rho_0}\frac{\partial P}{\partial x}, \tag{6.15}$$

$$\frac{\partial u_y}{\partial t} + \beta y\, u_x = -\frac{1}{\rho_0}\frac{\partial P}{\partial y} + \frac{B_0}{\rho_0 \mu_0}\left(\frac{\partial b_y}{\partial x} - \frac{\partial b_x}{\partial y}\right), \tag{6.16}$$

$$\frac{\partial b_x}{\partial t} = B_0 \frac{\partial u_x}{\partial x}, \tag{6.17}$$

$$\frac{\partial b_y}{\partial t} = B_0 \frac{\partial u_y}{\partial x}. \tag{6.18}$$

where B_0 is the strength of the background magnetic field. The component equations on the β-plane rather than the usual vector equations are presented because it is awkward to write the β-plane Coriolis term in vector notation. There is no Lorentz force term in equation (6.15) because $\boldsymbol{B_0}$ is uniform and purely in the x direction.

Taking the curl of the momentum equations ($\frac{\partial}{\partial y}$ of equation (6.15) minus $\frac{\partial}{\partial x}$ of equation (6.16)) yields the z component of the vorticity equation

$$\frac{\partial \zeta}{\partial t} + \beta u_y = \frac{B_0}{\rho_0 \mu_0}\frac{\partial}{\partial x}\left(\frac{\partial b_y}{\partial x} - \frac{\partial b_x}{\partial y}\right), \tag{6.19}$$

where $\zeta = \left(\frac{\partial u_x}{\partial y} - \frac{\partial u_y}{\partial x}\right)$ is the z component of vorticity. Taking the time derivative of this, substituting from $\frac{\partial}{\partial y}$ (equation (6.17)) and $\frac{\partial}{\partial x}$ (equation (6.18)) and operating with $\nabla^2_H = \left(\frac{\partial}{\partial x^2} + \frac{\partial}{\partial y^2}\right)$ to eliminate u_y, an equation for the evolution of ζ on a β plane is obtained

$$\left(\frac{\partial^2}{\partial t^2} - \frac{B_0^2}{\rho_0 \mu_0}\frac{\partial^2}{\partial x^2}\right)\nabla^2_H \zeta + \beta \frac{\partial}{\partial t}\left(\frac{\partial \zeta}{\partial x}\right) = 0. \tag{6.20}$$

Plane wave solutions of the form $\zeta = \hat{\zeta} e^{i(kx+ky-\omega t)}$, where k is $\frac{2\pi}{L_\lambda}$, L_λ is the wavelength of the disturbance (for simplicity assumed to be the same in the northward and eastward directions), and ω is the angular frequency of the waves, can now be considered. Substituting the plane wave solutions into (6.20) yields the dispersion relation

$$\omega^2 + \frac{\beta\omega}{k} - \frac{B_0^2 k^2}{\rho_0 \mu_0} = 0. \tag{6.21}$$

This quadratic equation can be solved to give an expression for ω in terms of k,

$$\omega = -\frac{\beta}{2k} \pm \frac{\beta}{2k}\left(1 + \frac{4B_0^2 k^4}{\rho_0 \mu_0 \beta^2}\right)^{1/2} \tag{6.22}$$

For long wavelength disturbances in a rapidly rotating fluid $\left(\frac{4B_0 k^4}{\rho_0 \mu_0 \beta^2}\right)$ will be small and a Taylor expansion in this small parameter shows that two values for ω are possible,

$$\omega_r = -\frac{\beta}{k} \qquad \text{and} \qquad \omega_m = \frac{B_0^2 k^3}{\mu_0 \rho_0 \beta}. \tag{6.23}$$

The mode ω_r is recognisable as a Rossby wave on a β-plane (Rossby, 1939; Dickinson, 1978; Gill, 1982; Pedlosky, 1987). Rossby waves are the special low-frequency, unidirectional inertial waves that arise because of the latitudinal variation of the Coriolis force in spherical shell geometry (Longuet-Higgins, 1964; Greenspan, 1968; Zhang et al., 2000). ω_m on the other hand corresponds to a wave very similar in form to the MC wave found in a rotating plane layer, but inversely proportional to $\beta = \frac{2\Omega \cos \lambda^*_{lat}}{c}$ rather than 2Ω. It is conventionally referred to as either Hide's wave or as a MC Rossby wave and is a result of a leading order balance between magnetic forces and the latitudinally varying Coriolis force responsible for Rossby waves.

The key to understanding the mechanism underlying both Rossby waves and Hide's MC-Rossby waves is the meaning ascribed to the β parameter — this is best seen by considering the thin and thick spherical shell geometries displayed in figure 6.4. Hide (1966) argued that when considering slow motions in a rapidly rotating spherical shell of homogeneous fluid, the most relevant fluid elements are columns of fluid aligned with the rotation axis. This is a natural consequence of the Proudman-Taylor theorem that slow, steady motions in a rapidly rotating fluid will be invariant in the direction parallel to the rotation axis. Following Rossby (1939), Hide argued that the fundamental quantity which must be conserved in the motion of such columns is their linearised potential vorticity $(\frac{\zeta+2\Omega}{L_{col}})$, where L_{col} is the length of the fluid column (see James (1994) or McIntyre (2000) for an introduction to the concept of potential vorticity and its utility). Changes in the latitude of a fluid column are accompanied by changes in L_{col}: in order to conserve potential vorticity this will induce a change in ζ that acts to return the fluid column to its original position. This mechanism has long been recognised as the origin of Rossby waves (Rossby, 1939; Andrews, 2000). Rossby took this effect into account in his simplified β-plane theory by replacing the Coriolis force with the β-effect (see discussion of governing equations above).

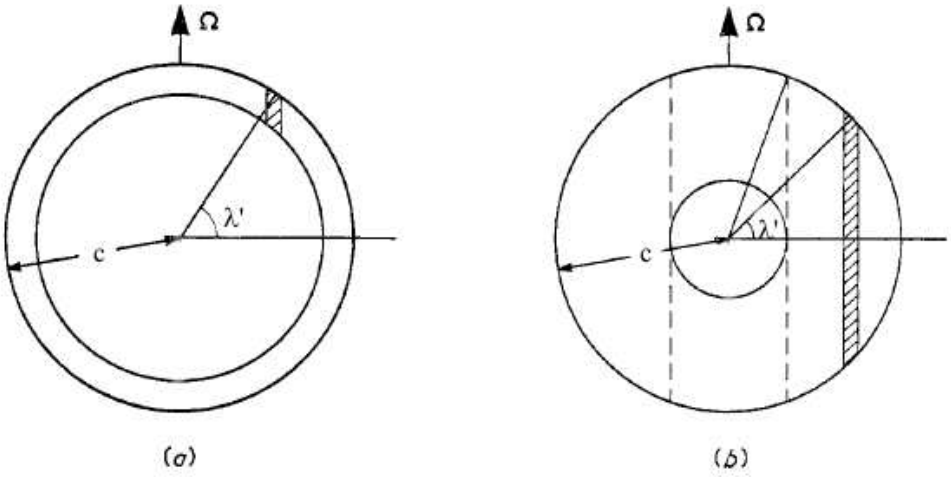

Figure 6.4: Movement of fluid columns in thin and thick spherical shells. Examples of (a) a thin spherical shell and (b) a thick spherical shell, showing a fluid column in each case. Notice that outside the tangent cylinder denoted by the dotted lines in (b) columns get shorter as they approach the equator, while in the thin shell case shown in (a) they get longer. Hide (1966) argued that the variation in Coriolis force with latitude (as measured by the β parameter) would therefore be positive for thin shells, but negative for thick shells (adapted from Acheson and Hide (1973)).

Hide (1966) and later Acheson and Hide (1973) used geometrical arguments to show that a general expression for the β parameter, considering changes in L_{col} with distance from the rotating axis, is $\beta = \sin^2 \lambda' \left(\frac{2\Omega}{L_{col}} \frac{dL_{col}}{ds} \right)$ where s is the distance from the rotation axis. In a thin spherical shell, the length of fluid columns increases towards the equator and this expression simplifies to $\beta = \frac{2\Omega \cos \lambda^*_{lat}}{c}$ as earlier inferred by Rossby. In contrast, for thick spherical shells outside the tangent cylinder, the length of columns decreases towards the equator and $\beta = -\frac{2\Omega \cos \lambda^*_{lat}}{c}$ has the opposite sign. This argument indicated that Rossby waves should propagate in opposite directions in thick and thin spherical shells as has since been confirmed in numerical models (Yano et al., 2003). The argument also predicts that MC-Rossby waves should propagate westwards, though it is only valid so long as fluid motions remain columnar, which may not be true if magnetic forces dominate the effects of rotation. The idea of modelling columnar motions in thick shells using a β-plane has proved very influential, inspiring a series of related quasi-geostrophic (QG) models (Busse, 1970; Busse and Or, 1986; Cardin and Olson, 1994; Aubert, Gillet and Cardin, 2003).

The problem of finding mathematically precise analytical solutions for MC-Rossby waves in a spherical shell problem was addressed by Stewartson (1967). He was able to obtain rigorous solutions in thin spherical shells that were compatible with Hide's β-plane analysis, but was unable to make progress analytically in the thick shell case, even in the absence of a magnetic field (Stewartson and Rickard, 1969).

6.5.2 Full spherical geometry: the special case of the Malkus field

The role of spherical geometry in determining the properties of MC waves was further illuminated in the seminal study of Malkus (1967). In an ingenious piece of analysis, Malkus demonstrated that, if the background magnetic field is that due to a uniform electrical current density (with magnetic field strength increasing linearly with distance from the rotation axis), then the hydromagnetic wave problem in a sphere reduces to the inertial wave problem in a sphere. The solutions have identical eigenfunctions and systematically modified eigenvalues (wave frequencies). His analysis is outlined here because the Malkus field has been the basis of many subsequent models.

Malkus's background magnetic field is purely toroidal and azimuthal with the mathematical form $\boldsymbol{B_0} = \frac{B_0 r \sin\theta}{c}\widehat{\boldsymbol{\phi}}$ where θ is the co-latitude, c is the radius of the outer spherical boundary and B_0 is the maximum magnitude of the imposed field at the outer boundary in the equatorial plane. This field is invariant on cylindrical surfaces aligned with the rotation axis, and increases in strength linearly with distance from the rotation axis. This field is force free ($\nabla \times (\nabla \times \boldsymbol{B_0}) = 0$), so $\boldsymbol{U}_0 = 0$ is a consistent choice for the background flow. The dimensional, linearised, governing equations D.13 to D.15, if one ignores all thermal and diffusive processes and defines the rotating axis to be along $\widehat{\boldsymbol{z}}$, reduce to

$$\rho_0 \frac{\partial \boldsymbol{u}}{\partial t} + 2\rho_0 \Omega (\widehat{\boldsymbol{z}} \times \boldsymbol{u}) = -\nabla P + \frac{1}{\mu_0}\left[(\boldsymbol{B_0}\cdot\nabla)\boldsymbol{b} + (\boldsymbol{b}\cdot\nabla)\boldsymbol{B_0}\right], \tag{6.24}$$

$$\frac{\partial \boldsymbol{b}}{\partial t} = \nabla \times (\boldsymbol{u} \times \boldsymbol{B_0}). \tag{6.25}$$

The major difference here compared to studies of uniform imposed magnetic fields is in the inclusion of the final term in the momentum equation $(\boldsymbol{b}\cdot\nabla)\boldsymbol{B_0}$ resulting from the non-zero spatial gradient in $\boldsymbol{B_0}$. Soward (1979b) refers to this as the magnetic hoop stress term. For Malkus's special choice of $\boldsymbol{B_0}$ it turns out that both terms in the Lorentz force and the advection term in the induction equation have very simple forms. Recognising that the advection term can be rewritten $\nabla \times (\boldsymbol{u} \times \boldsymbol{B_0}) = (\boldsymbol{B_0}\cdot\nabla)\boldsymbol{u} - (\boldsymbol{u}\cdot\nabla)\boldsymbol{B_0}$ and making use of the following relations that hold for the Malkus field

$$(\boldsymbol{b}\cdot\nabla)\boldsymbol{B_0} = \frac{B_0}{c}(\widehat{\boldsymbol{z}} \times \boldsymbol{b}) \tag{6.26}$$

$$(\boldsymbol{B_0}\cdot\nabla)\boldsymbol{b} = \frac{B_0}{c}\left(\frac{\partial \boldsymbol{b}}{\partial \phi} + \widehat{\boldsymbol{z}} \times \boldsymbol{b}\right) \tag{6.27}$$

$$(\boldsymbol{B_0}\cdot\nabla)\boldsymbol{u} = \frac{B_0}{c}\left(\frac{\partial \boldsymbol{u}}{\partial \phi} + \widehat{\boldsymbol{z}} \times \boldsymbol{u}\right) \tag{6.28}$$

$$(\boldsymbol{u}\cdot\nabla)\boldsymbol{B_0} = \frac{B_0}{c}(\widehat{\boldsymbol{z}} \times \boldsymbol{u}) \tag{6.29}$$

the governing equations become

$$\rho_0 \frac{\partial \boldsymbol{u}}{\partial t} + 2\rho_0 \Omega (\widehat{\boldsymbol{z}} \times \boldsymbol{u}) = -\nabla P + \frac{B_0}{c\mu_0}\left[\frac{\partial \boldsymbol{b}}{\partial \phi} + 2\widehat{\boldsymbol{z}} \times \boldsymbol{b}\right], \tag{6.30}$$

$$\frac{\partial \boldsymbol{b}}{\partial t} = \frac{B_0}{c}\left(\frac{\partial \boldsymbol{u}}{\partial \phi}\right). \tag{6.31}$$

Substituting in azimuthally travelling wave solutions of the form

$$(\boldsymbol{u}, \boldsymbol{b}) = (\hat{\boldsymbol{u}}(s,z)e^{i(m\phi-\omega t)}, \hat{\boldsymbol{b}}(s,z)e^{i(m\phi-\omega t)}), \tag{6.32}$$

where m is the azimuthal wavenumber of the wave, and ω is its angular frequency leads to the relations

$$-i\omega\rho_0\boldsymbol{u} + 2\omega\rho_0(\widehat{\boldsymbol{z}}\times\boldsymbol{u}) = -\nabla P + \frac{B_0}{\mu c}\left(im\boldsymbol{b} + 2(\widehat{\boldsymbol{z}}\times\boldsymbol{b})\right), \tag{6.33}$$

$$-i\omega\boldsymbol{b} = \frac{imB_0}{c}\boldsymbol{u}. \tag{6.34}$$

Substituting from equation (6.34) into equation (6.33) for $\boldsymbol{b}$ and collecting like terms yields a single equation

$$\mathcal{L}_1(\widehat{\boldsymbol{z}}\times\boldsymbol{u}) + \mathcal{L}_2\boldsymbol{u} + \nabla P = 0, \tag{6.35}$$

$$\text{where} \qquad \mathcal{L}_1 = 2\left(\Omega\rho_0 + \frac{B_0^2 m}{\mu_0\omega c}\right) \qquad \mathcal{L}_2 = \left(-i\omega\rho_0 + i\frac{B_0^2 m^2}{\mu_0\omega c^2}\right). \tag{6.36}$$

This has the same form as the momentum equation governing the evolution of inertial waves (Melchoir, 1986; Zhang et al., 2000), but with $\mathcal{L}_2$ rather than simply $-i\omega\rho_0$ and $\mathcal{L}_1$ rather than $2\rho_0\Omega$. The consequence of the presence of the Malkus background magnetic field is therefore that only that the strength of the latitude-dependent Coriolis force and the time scale of the inertial response of the fluid have been changed.

Equation (6.35) can be re-written in terms of pressure only (for details of this manipulation consult Malkus (1967)) as

$$\left(\mathcal{L}_2^2\nabla^2 + \mathcal{L}_1^2\frac{\partial}{\partial z}\right) P = 0. \tag{6.37}$$

The appropriate rigid spherical boundary condition ($\boldsymbol{u}\cdot\hat{\boldsymbol{n}} = 0|_{r=c}$ where $\hat{\boldsymbol{n}}$ is a normal to the spherical surface), in a form applicable to pressure can be obtained using the link between $\boldsymbol{u}$ and P in (6.35) and is

$$\left(\mathcal{L}_2^2 s\frac{\partial}{\partial s} + (\mathcal{L}_1^2 + \mathcal{L}_2^2)z\frac{\partial}{\partial z} + i\mathcal{L}_1\mathcal{L}_2\right) P = 0, \tag{6.38}$$

where $s = r\sin\theta$ is the cylindrical radius. By choosing

$$\lambda_{in} = \frac{2\mathcal{L}_2}{i\mathcal{L}_1} \qquad \text{so that} \qquad -\lambda_{in}^2 = \frac{4\mathcal{L}_2^2}{\mathcal{L}_1^2} \tag{6.39}$$

the governing equations in P are transformed into the standard form of the Poincaré equation for inertial waves in a sphere (see, for example, Zhang (1993))

$$\left(\nabla^2 - \frac{4}{\lambda_{in}^2}\frac{\partial}{\partial z}\right) P = 0, \tag{6.40}$$

and the associated boundary condition

$$\left(s\frac{\partial}{\partial s} + \frac{2m}{\lambda_{in}} - \frac{4}{\lambda_{in}^2}z\frac{\partial}{\partial z}\right) P = 0 \qquad \text{on} \qquad s^2 + z^2 = c^2. \tag{6.41}$$

The solution to the inertial wave problem in the sphere involves finding eigenvalues[3] λ_{in} and associated eigenvectors which satisfy equation (6.40) and equation (6.41). The solutions are very complicated in general and have only recently been written down explicitly by Zhang et al. (2000), though Malkus (1967) and Zhang (1993) had earlier studied some simple cases.

Regarding λ_{in} as known, the angular frequencies ω of the solutions to the hydromagnetic wave problem in a sphere in the presence of the Malkus magnetic field are defined. By substituting expressions for $\mathcal{L}_1$, $\mathcal{L}_2$ into equation (6.39) the relation between λ_{in} and ω is

$$\lambda_{in} = \frac{2\left(-\omega\rho_0 + \frac{B_0^2 m^2}{c^2\mu_0\omega}\right)}{2\left(\Omega\rho_0 + \frac{B_0^2 m}{c^2\mu_0\omega}\right)}, \tag{6.42}$$

which gives the quadratic equation,

$$\omega^2 + \Omega\lambda_{in}\omega + \frac{B_0^2 m}{c^2\rho_0\mu_0}(\lambda_{in} - m) = 0, \tag{6.43}$$

that has solutions

$$\omega = \frac{\Omega\lambda_{in}}{2}\left[-1 \pm \left(1 - \frac{4B_0^2 m(\lambda_{in} - m)}{c^2\Omega^2\lambda_{in}^2\rho_0\mu_0}\right)^{1/2}\right]. \tag{6.44}$$

In the case of large wavelength disturbances (small m) in a rapidly rotating fluid when $\frac{4B_0^2 m}{\Omega^2\lambda_{in}^2\rho_0\mu_0}$ is small, a Taylor series expansion shows that the two possible solutions are (Malkus, 1967)

$$\omega_i \sim -\Omega\lambda_{in} \qquad \text{and} \qquad \omega_m \sim \frac{B_0^2}{c^2\Omega\rho_0\mu_0}\frac{m(m - \lambda_{in})}{\lambda_{in}}. \tag{6.45}$$

ω_i is essentially an inertial wave, that can travel both eastward and westward depending on the sign of λ_{in}, while ω_m is an MC wave where the inertial term is unimportant and the Lorentz and Coriolis forces balance each other to leading order. As noted by Jackson (2003), regarding the case when m=8, for the choice of eigenvalue λ_{in}=-0.57, $B_0 = 4.3 \cdot 10^{-3}$T, ρ_0 =10^4kg, Ω =7.29×10^{-5}s^{-1} and $c = 3485 \times 10^3$m, then $\frac{2\pi}{\omega_m} \sim 1000$ years, suggesting such a wave might be capable of explaining some drifting field features that are part of geomagnetic secular variation. The relation between Malkus' MC wave and Hide's MC-Rossby waves becomes clear if one considers a λ_{in} corresponding to a quasi-geostrophic inertial wave (QGIW) of very low frequency as discussed by Zhang et al. (2000) and Zhang and Liao (2004). Such QGIWs are unidirectional (always travel eastward because λ_{in} is < 0 always), and show little variation in structure parallel to the rotation axis: they are simply Rossby waves in a thick spherical shell. For such Rossby waves with $\lambda_{in} < 0$, an MC waves (MC-Rossby waves) will travel westward as predicted by Hide's analysis.

[3]The notation λ_{in} used for eigenvalues bears no relation to the latitude λ_{lat} that was discussed in the β-plane model in §6.5.1, but rather denote solutions to the inertial wave eigenvalue problem.

Malkus's imposed magnetic field is rather special in a number of ways. The combination of its cylindrical symmetry, its purely azimuthal form and its linear increase with distance from the rotation axis means the associated Lorentz force affects fluid motions in a manner very similar to the Coriolis force in a sphere. This physical similarity results in a formal mapping to the inertial wave problem that permits analytically tractable solutions to this special case of the spherical MC wave problem. The Malkus field therefore provides a very clear demonstration of the wave mechanism associated with MC balance. It is also somewhat atypical from an energetic point of view. It is stable to magnetic field gradient instabilities (see next section) so is useful for filtering out most waves driven by this mechanism and for focusing on waves driven by thermal instability. Unfortunately, it also fails to naturally satisfy electrically insulating boundary conditions. When electrically insulating boundary conditions are imposed in its presence a dynamically active magnetic boundary layer arises that can induce magnetic instability for m=1 wave (Roberts and Loper, 1979; Zhang and Busse, 1995). Such m=1 instabilities are often filtered out when focusing on thermal instability by considering only modes with $m > 1$ (see, for example chapter 7).

6.6 Instability mechanisms for hydromagnetic waves

The energy source exciting hydromagnetic wave motion in Earth's outer core is not known. If the source were impulsive (for example, due to perturbations caused by a large earthquake or sharp change in the rotation rate of the mantle) the resulting waves would be free oscillations. It has been demonstrated in §6.4 and §6.5 that free MC/MAC waves in a spherical shell are highly dispersive, and no evidence for dispersive behaviour has been found in observations of magnetic field evolution (see §3.7) which are dominated by a single wavenumber disturbances (see §3.3). Rather than being free oscillations it therefore appears more likely that hydromagnetic waves of a small group of wavenumbers are being excited by some instability mechanism.

Waves resulting from instability are only energetically possible if a basic state stores sufficient energy to enable a suitable perturbation to grow, overcoming dissipation effects (see, for example, Drazin (2002)). The classical example of this process is thermal convective instability (see, for example, Chandrasekhar (1961)) when the exchange of heavier fluid with initially underlying lighter fluid releases gravitational potential energy. If the thermally induced density gradient is large enough that sufficient gravitational potential energy is available to overcome viscous and thermal diffusion, and if perturbations of the form required to release the required energy are dynamically possible then convective perturbations will grow. Different length scales of perturbation will release different amounts of energy; the dynamically conceivable perturbation releasing the most energy will define the length scale (wavenumber) of the onset of convection. Many other examples of suitable instability mechanisms can be imagined:

(i) Topographic forcing (see, for example, Hide (1967) or Bell and Soward (1996)) caused by topography at the core-mantle boundary.

(ii) Inhomogeneous boundary heat flux forcing (see, for example, Bloxham and Gubbins (1987), Gubbins (1994), Zhang and Gubbins (1994), or Christensen and Olson (2003)).

(iii) Tidally or precessionally forced instability (see, for example, Kerswell (1994)).

(iv) Shear instability of the background flow in the core (see, for example, Fearn (1989)).

(v) Instability of the background magnetic field (see, for example, Acheson (1972) or Fearn (1993)).

(vi) Convection-driven instability, usually modelled as thermal instability (see, for example, Braginsky (1964), Fearn (1979b) or the review of Zhang and Schubert (2000)).

Although other mechanisms cannot be ruled out, in this section a review of waves driven only by the last two instability mechanisms is given. The focus on these mechanisms is because these seem the most likely to arise and have proved to be the easiest to model in detail.

6.6.1 Magnetically-driven instabilities in a rapidly rotating fluid

Magnetic instabilities result from the rearrangement of a background magnetic field into a lower energy configuration yielding a release of energy. If the energy supplied to the perturbation in the magnetic and velocity fields is sufficient to overcome diffusive processes, it will grow until saturated by nonlinear mechanisms. This rearrangement of the field lines can occur by two distinct mechanisms. In an ideal ($\eta \to 0$) magnetic field instability (Acheson, 1972; 1973; 1983; Fearn, 1983; 1988) the rearrangement of magnetic field lines occurs without reconnection of field lines; in a resistive instability (Fearn, 1984; 1988) the rearrangement of magnetic field lines involves reconnection of the field lines which requires finite magnetic diffusivity. There are therefore two necessary conditions which must be fulfilled if magnetic instability is to occur; (1) sufficient energy must be available from the unstable background magnetic field to overcome diffusive effects and (2) the magnetic field morphology must be such that either an ideal or resistive reorganisation of field lines is possible.

The first condition can be stated in terms of the time scales of the energy transfer process. It requires that dissipation processes occur more slowly than the time scale of the perturbations (more precisely that the magnetic diffusion time scale be sufficiently longer than the MC time scale of the perturbations) in order for growth to occur. The

non-dimensional parameter called the Elsasser number (see appendix D, equation (D.22)) is a measure of this ratio

$$\Lambda = \frac{B_0^2}{2\Omega\mu_0\rho_0\eta} = \frac{\text{Magnetic diffusion time scale}}{\text{MC time scale}}. \tag{6.46}$$

Condition (1) can therefore be restated as

$$\Lambda > \Lambda_c, \tag{6.47}$$

where Λ_c is the critical value of the ratio of the magnetic diffusion time scale to the MC time scale needed for growth of magnetic instabilities[4]. Λ_c depends in general on both the geometry of the container and the morphology of the background magnetic state. Numerous studies have been carried out for different choices of container geometry and field morphology. A series of studies have been carried out in spherical geometry with the equatorially-antisymmetric imposed toroidal and poloidal magnetic fields expected to be appropriate to the situation in Earth's core (Zhang, 1995; Zhang and Fearn, 1993; 1994; 1995; Zhang and Gubbins, 2000a;b; 2002). They found that $\Lambda_c \sim 10$ for a purely toroidal field while for purely poloidal magnetic fields $\Lambda_c \sim 20$. Since Λ is also the ratio of the strength of the Lorentz force to the strength of the Coriolis force, this means that very strong magnetic fields that will dominate the fluid dynamics are required to obtain such magnetic instabilities.

Condition (2) depends on the precise mechanism of magnetic field rearrangement. At least four mechanisms have been discussed in the literature (Fearn, 1993). The first, most extensively studied mechanism, is that of the ideal magnetic field gradient instability. This was discovered and analytically investigated by Acheson (1972; 1973; 1978) in a simplified cylindrical annulus geometry where the fluid was in uniform solid body rotation and in the presence of a purely azimuthal background magnetic field ($\boldsymbol{B_0} = B_0(s)\widehat{\boldsymbol{\phi}}$, where s is the cylindrical radius). He showed that in order for the magnetic field configuration to be unstable to an ideal rearrangement of magnetic field lines then

$$\frac{s^3}{B_0^2}\frac{d}{ds}\left(\frac{B_0^2(s)}{s^2}\right) > m^2, \tag{6.48}$$

where m is the azimuthal wavenumber of the disturbance. Physically this means that the magnetic field strength must increase with s somewhere faster than $s^{3/2}$ for the most unstable $m = 1$ mode to be obtained. This result has since been extended and numerically tested for cases where $B_0(s, z)$ and where the fluid is differentially rotating (Fearn, 1983; 1988). Acheson (1972) also demonstrated that waves resulting from ideal magnetic field gradient instabilities can only propagate in the retrograde (westward) direction.

The second widely studied mechanism of rearrangement of magnetic field lines involves reconnection and hence requires the presence of magnetic diffusion (the resistive instability). This mechanism requires the existence of critical points in the background magnetic

[4]This in analogous to the existence of a critical Rayleigh number for thermal instability which measures the ratio of the stokes rise time for a buoyant flow parcel to the thermal diffusion time.

field where $\boldsymbol{k} \cdot \boldsymbol{B_0} = \boldsymbol{0}$ [5]; for purely azimuthal fields this reduces to the condition that $\boldsymbol{B_0} = \boldsymbol{0}$. Magnetic field perturbations resulting from this instability tend to be localised at the latitudes of such critical points, but do not appear to have any preferred direction of propagation (both westward and eastward are possible). The recent study of Zhang and Gubbins (2002) showed that in spherical geometry poloidal magnetic can fields become unstable to eastward propagating waves, suggesting an origin in resistive instability, rather than ideal instability for which westward propagation is expected.

Two other possible magnetic field instability mechanisms have been discussed in the literature. The 'exceptional' case described by Roberts and Loper (1979), Fearn (1988) and Acheson (1980) involves stable density stratification catalyses magnetic instability by weakening the rotational constraint on motion. The remaining possibility is dynamic instability (Malkus, 1967; Zhang et al., 2003), for which the stabilising influence of the rotation is insufficient to prevent the azimuthal magnetic field from becoming unstable to axisymmetric disturbances. However, neither of these mechanisms appear to be relevant to Earth's core because they require very large $\Lambda_c > 10^3$.

It seems likely that condition (2) is satisfied somewhere in Earth's core, either through the field gradient condition or the resistive instability condition being satisfied. It is, however, unclear whether the condition $\Lambda > \Lambda_c$ is ever satisfied even locally. Furthermore, it seems unlikely that an unstable background magnetic field configuration would persist and continue to supply energy indefinitely. Magnetic instability therefore seems unlikely to be the origin of coherent wave-like patterns seen in geomagnetic secular variation over the historical and archeomagnetic intervals. In chapter 7, and in the next section, attention therefore focuses on the $m > 1$ perturbations of the Malkus background field which filters out waves produced by magnetic instability (Roberts and Loper, 1979), allowing attention to focus on waves generated by thermal instability.

6.6.2 Convection-driven instabilities in the presence of a magnetic field and rapid rotation

Convection-driven by buoyancy, either thermal or compositional, is likely to be the major driving mechanism producing the geodynamo in Earth's outer core (Braginsky, 1964; Gubbins and Masters, 1979; Roberts et al., 2003). Only thermal driving is considered for simplicity in the discussion here. The form of convection will be strongly influenced by both the rapid rotation of the fluid and the presence of a magnetic field. Both these forces impart stability to the fluid, so convection often takes the form of hydromagnetic waves. By studying the onset of rotating magnetoconvection, one can therefore investigate the properties and mechanisms underlying the most unstable convection-driven hydromagnetic waves, for a given set of physical parameters. The findings of such studies are reviewed in this section.

[5] where $\boldsymbol{k}$ is the wavevector of the disturbance.

Quasi-geostrophic (QG) annulus model, including β-effect

Many of the important mechanisms associated with convection-driven hydromagnetic waves in a spherical shell are captured in a QG[6] cylindrical annulus model with constantly sloping lid (producing a β-effect). A uniform azimuthal magnetic field is imposed and viscous, thermal and magnetic diffusion are included. A radial thermal gradient due to internal heating and radial gravity gives rise to radial buoyancy forces. Such an arrangement, assuming the gap D between the inner and outer cylinders is small compared to the height of the annulus L, makes it possible to work in a local Cartesian co-ordinate system (Busse, 1986) as shown in figure 6.5. This model was first developed by Busse (1976) and later analysed in detail by Soward (1979a). It will be analysed in detail here because it illustrates the possible types of convection-driven hydromagnetic waves that will arise in more complicated, realistic models.

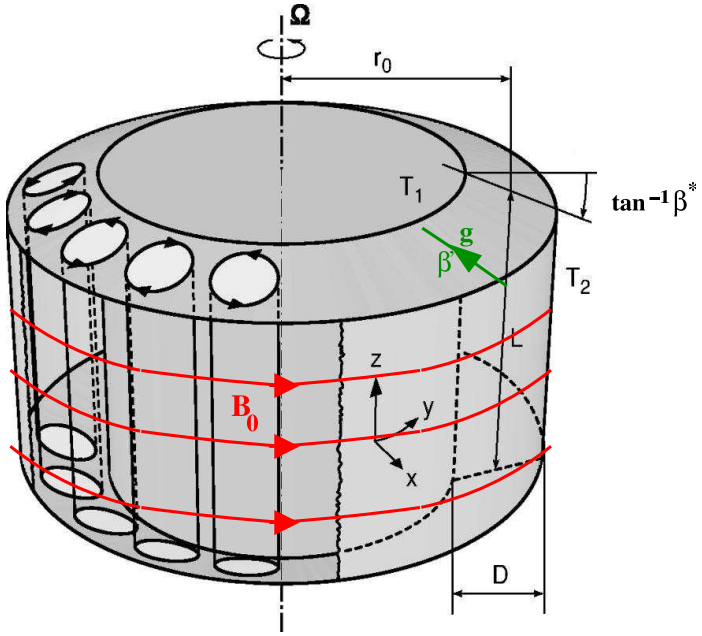

Figure 6.5: Quasi-geostrophic (QG) annulus model geometry.
Geometry of the quasi-geostrophic (QG) annulus model for studying convection-driven hydromagnetic waves as developed by Busse (1976) and Soward (1979a). The fluid rotates uniformly about the $\widehat{\boldsymbol{z}}$ direction, a uniform azimuthal magnetic field $\boldsymbol{B_0}$ is imposed in the $\widehat{\boldsymbol{y}}$ direction and both gravity and the imposed temperature gradient are in the $-\widehat{\boldsymbol{x}}$ direction. The top boundary has a angle of slope $\tan^{-1}\beta^*$. This figure has been adapted from Busse (2002).

The appropriate governing equations are the linear rotating magnetoconvection equations in the viscous non-dimensionalisation (see appendix D, equations (D.19) to (D.21)), with

[6]The term 'Quasi-Geostrophic' (or QG) refers to the physical state where the horizontal components of long period motions in a rotating fluid are to leading order in a state of geostrophic balance i.e. pressure forces are balanced by the Coriolis forces (Dickinson, 1978). It does however permit departures from geostrophy, particularly those associated with boundary conditions. This state is often associated with columnar fluid motions in thick shells where latitudinal variation in the Coriolis force producing Rossby waves are important. More formal conditions for its validity can be found in Gill (1982).

the length scale being the maximum height of the annulus L. The analysis here closely follows that of Soward (1979a). For the geometry of background states in figure 6.5, $\widehat{\boldsymbol{\Omega}} = \widehat{\boldsymbol{z}}$, $\widehat{\boldsymbol{g}} = -\widehat{\boldsymbol{x}}$ and $\widehat{\nabla T_0} = -\widehat{\boldsymbol{x}}$ so that $(\boldsymbol{u}\cdot\nabla)T_0 = -\beta' u_x$ while $\boldsymbol{B_0} = B_0\widehat{\boldsymbol{y}}$ means $(\boldsymbol{b}\cdot\nabla)\widehat{\boldsymbol{B_0}} = 0$, $(\widehat{\boldsymbol{B_0}}\cdot\nabla)\boldsymbol{b} = \frac{\partial \mathbf{b}}{\partial y}$ and $\nabla\times(\boldsymbol{u}\times\widehat{\boldsymbol{B_0}}) = \frac{\partial \mathbf{u}}{\partial y}$ so equations (D.19) to (D.21) simplify to

$$E\left(\frac{\partial}{\partial t} - \nabla^2\right)\boldsymbol{u} + (\widehat{\boldsymbol{z}}\times\boldsymbol{u}) = -\nabla P + ERa\Theta\widehat{\boldsymbol{x}} + \Lambda\frac{\partial \boldsymbol{b}}{\partial y}, \tag{6.49}$$

$$\left(\nabla^2 - Pr\frac{\partial}{\partial t}\right)\Theta = u_x, \tag{6.50}$$

$$\left(\nabla^2 - Pr_m\frac{\partial}{\partial t}\right)\boldsymbol{b} = \frac{\partial \boldsymbol{u}}{\partial y}, \tag{6.51}$$

where the definitions and physical meanings of Λ, E, Ra, Pr and Pr_m can be found in appendix D, equations (D.22) to (D.26). Taking the $\widehat{\boldsymbol{z}}$ component of the curl of equations (6.49) and (6.51) while defining the axial component of perturbation vorticity as $\zeta = \widehat{\boldsymbol{z}}\cdot(\nabla\times\boldsymbol{u})$ and the axial component of the perturbation electric current density as $j = \widehat{\boldsymbol{z}}\cdot(\nabla\times\boldsymbol{b})$ gives

$$E\left(\frac{\partial}{\partial t} - \nabla^2\right)\zeta + \frac{\partial u_z}{\partial z} = -ERa\frac{\partial\Theta}{\partial y} + \Lambda\frac{\partial j}{\partial y}, \tag{6.52}$$

$$\left(\nabla^2 - Pr_m\frac{\partial}{\partial t}\right)j = \frac{\partial\zeta}{\partial y}. \tag{6.53}$$

Now the assumption of quasi-geostrophy (QG) is implemented: Integrating equations (6.52), (6.50) and (6.53) with respect to z and dividing by the depth of the fluid, ζ, j, and Θ can be re-interpreted as the vertically averaged perturbations in axial vorticity, axial electrical current and temperature respectively. This is possible because geostrophy (z independence) holds to leading order when the slope of the top boundary is small (see, for example, Busse and Or (1986) for the formal development of the QG model). However, because of the presence of the sloping boundary, the term $\frac{\partial u_z}{\partial z}$ associated with the Coriolis force cannot be z independent. It can however be evaluated using the conservation of mass of an incompressible fluid ($\nabla\cdot\boldsymbol{u} = 0$) which at the boundary implies that $u_z = -\beta^* u_x$[7],

$$\int_0^1 \frac{\partial u_z}{\partial z}dz = [u_z]_0^1 = -\beta^* u_x, \tag{6.54}$$

where the non-dimensional parameter β^* measures the slope of the upper boundary and is related to the dimensional thick shell β-plane parameter discussed in §6.5.1 by $\beta = \frac{2\Omega\beta^*}{L}$. To leading order, the velocity fields in the QG approximation are 2D so can be represented by a stream function χ where $u_x = \frac{\partial\chi}{\partial y}$ and $u_y = -\frac{\partial\chi}{\partial x}$ so $\zeta = -\nabla\chi$. The equations for the QG system in terms of χ, j and Θ are then,

$$-E\left(\frac{\partial}{\partial t} - \nabla^2\right)\nabla^2\chi + \beta^*\frac{\partial\chi}{\partial y} = -ERa\frac{\partial\Theta}{\partial y} + \Lambda\frac{\partial j}{\partial y}, \tag{6.55}$$

[7]This expression ignores the influence of viscous boundary layers and associated Ekman pumping. It only rigorously applies when free slip boundary conditions are implemented, but provides a reasonable leading order approximation for the present linear problem.

$$\left(\nabla^2 - Pr\frac{\partial}{\partial t}\right)\Theta = -\frac{\partial \chi}{\partial y}, \tag{6.56}$$

$$\left(\nabla^2 - Pr_m\frac{\partial}{\partial t}\right) j = -\frac{\partial}{\partial y}\nabla^2\chi. \tag{6.57}$$

Plane wave solutions for χ, j and Θ proportional to $e^{i(kx+ky-\omega t)}$ (invariant in the $\widehat{\boldsymbol{z}}$ direction and taking k to be an estimate of the wavenumber in both the x and y directions for simplicity) can then be substituted into equations (6.55) to (6.57). This yield relations between j and χ, and between Θ and χ

$$\Theta = \frac{-ik\chi}{-k^2 + iPr\omega} \qquad \text{and} \qquad j = \frac{ik^3\chi}{-k^2 + iPr_m\,\omega}, \tag{6.58}$$

which when substituted into equation (6.55) give a dispersion relation in the complex frequency ω,

$$E(-i\omega + k^2) + \frac{i\beta^*}{k} = \frac{ERa}{-iPr\,\omega + k^2} - \frac{\Lambda k^2}{-iPr_m\omega + k^2}. \tag{6.59}$$

The first term comes from the inertial and viscous forces, the second term comes from the variable Coriolis force, the third term represents thermal (convective) forcing, and the fourth term the influence of the uniform magnetic field. This dispersion relation is key to understanding and predicting the properties of hydromagnetic wave driven by convection and is also capable of recovering the dispersion relations for free waves deduced by Hide (1966) if convective forcing and diffusion are ignored. By neglecting terms in equation (6.59), simple explicit solutions can be found for ω which give insight into the types of wave motion possible in this system:

(i) **Rossby waves.**

Ignoring thermal driving and the influence of magnetic fields leaving inertia, viscosity and the β-effect in balance,

$$E(-i\omega + k^2) = -\frac{i\beta^*}{k} \qquad => \qquad \omega = \frac{\beta^*}{Ek} - i\frac{k^2}{E}. \tag{6.60}$$

This is the viscous non-dimensionalisation dispersion relation expected for free Rossby waves, damped by viscous diffusion effects and travelling in the prograde (eastward) direction in the annulus geometry which mimics the scenario outside the tangent cylinder in a thick spherical shell.

(ii) **Hide's MC-Rossby waves.**

Ignoring viscosity, inertia, thermal driving and magnetic diffusion, the β-effect is balanced by the effect of changes in the magnetic field,

$$\frac{i\beta^*}{k} = \frac{\Lambda k^2}{-iPr_m\omega} \qquad => \qquad \omega = -\frac{\Lambda k^3}{\beta^* Pr_m}. \tag{6.61}$$

This is the dispersion relation expected for Hide's unforced MC-Rossby waves, travelling in the retrograde (westward) direction with frequency inversely proportional to the β-effect and proportional to the square of the magnetic field strength.

(iii) **Thermal Rossby waves and magnetically-modified thermal Rossby waves.**

Including the magnetic field but ignoring its time changes, (as is reasonable when $Pr_m \to 0$ as is the case for liquid metals), but retaining thermal driving, the appropriate dispersion relation is

$$E(-i\omega + k^2) + \frac{i\beta^*}{k} = \frac{ERa}{-iPr\,\omega + k^2} - \Lambda. \tag{6.62}$$

Eliminating Ra from the imaginary part of this equation and using the expression for Ra obtained from the real part leads to the dispersion relation,

$$\omega = \frac{\frac{\beta^* k}{EPr}}{(1 + Pr^{-1})k^2 + \frac{\Lambda}{E}}, \tag{6.63}$$

and an expression for the critical Ra above which thermal instability will occur,

$$Ra = k^4 + \frac{\Lambda k^2}{E} + \frac{\left(k^2 + \frac{\Lambda}{E}\right)\frac{\beta^*}{E^2}}{\left[(1 + Pr^{-1})k^2 + \frac{\Lambda}{E}\right]^2}. \tag{6.64}$$

Considering equation (6.63), when Λ is very small the dispersion relation reduces to that for thermal Rossby waves ($\omega = \frac{\beta^*}{Ek}\frac{1}{1+Pr}$). For a weak magnetic field when Λ is small, the character of disturbances remains essentially that of the thermal Rossby waves, but slowed as increasing Λ decreases the magnitude of ω.

For larger Λ, the frequency of disturbances takes the form $\omega = \frac{\beta^* k}{\Lambda Pr}$. This mode is fundamentally different from thermal Rossby waves, and relies crucially on the magnetic field for its existence: it is not just a small correction (Busse, 1976; Fearn, 1979a; Soward, 1979b). This mode is therefore called the thermal magneto-Rossby wave and involves a leading order force balance between thermal driving, the β-effect and the Lorentz force due to a steady magnetic field, with inertia and viscous effects being negligible. These waves also become slower as the magnetic field strength is increased.

(iv) **Thermal magneto-Rossby waves and thermal MC-Rossby waves.**

If inertia and viscosity are neglected, and changes in the magnetic field taken into consideration, the appropriate dispersion relation is

$$\frac{i\beta^*}{k} = \frac{ERa}{-iPr\,\omega + k^2} - \frac{\Lambda k^2}{-iPr_m\omega + k^2}. \tag{6.65}$$

Substituting between the expressions for the real and imaginary parts leads to a quadratic dispersion relation,

$$\omega^2 - \frac{\Lambda k^3(Pr - Pr_m)}{\beta^* Pr_m^2}\omega + \frac{k^4}{Pr_m^2} = 0. \tag{6.66}$$

For very slow waves when ω^2 can be neglected, and when Pr is not equal to Pr_m, this reduces to

$$\omega = \frac{k\beta^*}{\Lambda(Pr - Pr_m)}. \tag{6.67}$$

When magnetic field changes are ignored (i.e. when Pr_m is negligible) this is identical to the large Λ limit of equation (6.63) illustrating that this is again the thermal magneto-Rossby wave. Note that this wave is very slow, propagating on the thermal diffusion time scale; it is dispersive with higher wavenumbers expected to travel faster and the waves associated with it will be largest where β^* is largest (anticipated to be at the equator in spherical geometry). These properties will prove to be very important when looking for evidence for the existence of this wave in Earth's core by analysing geomagnetic observations. The expression for the critical Rayleigh number of these waves is

$$Ra = \frac{Pr^2\beta^{*2}}{E\Lambda(Pr - Pr_m)} + \frac{\Lambda k^2}{E}. \tag{6.68}$$

Ignoring the term $\frac{k^4}{Pr_m^2}$ (that arises due to the presence of magnetic diffusion and is negligible when $\eta \to 0$ and $Pr_m \to \infty$) and retaining ω^2 with its associated magnetic field changes in equation (6.66), a new wave type that was filtered out in equation (6.62) is obtained with the dispersion relation,

$$\omega = \frac{\Lambda k^3 \left(Pr - Pr_m\right)}{\beta^* Pr_m^2} \tag{6.69}$$

This wave arises from a balance between the β-effect and frozen-flux magnetic effects and is thermally driven, so is referred to as the thermal MC Rossby wave. This balance is only likely to come about when Pr_m is much greater than 1, which is unlikely to the case in Earth's liquid metal core. The expression for the critical Rayleigh number of these modes takes the form,

$$Ra = \frac{\Lambda}{E}\left(\frac{k^2 Pr^2}{Pr_m^2} + \frac{\beta^{*2}}{k^2\left(\frac{Pr}{Pr_m} - 1\right)^2}\right) \tag{6.70}$$

Since both terms are proportional to Λ, thermal MC Rossby waves are much harder to thermally excite than thermal magneto-Rossby waves, unless Pr_m is very large.

In summary, the QG model demonstrates the existence of three distinct types of thermal excited hydromagnetic wave: magnetically modified thermal Rossby waves, thermal magneto-Rossby waves and thermal MC-Rossby waves. It is also capable of supporting thermal Rossby waves in the absence of a magnetic field and Rossby and MC-Rossby waves in the absence of thermal driving. For Earth's core which has strong magnetic fields and convective driving present, this model suggests that convection-driven magneto-Rossby waves will be the most relevant type of convection-driven hydromagnetic wave. The limitations of this model should be remembered: (i) when motions are no longer quasi-geostrophic, for example when very strong magnetic fields ($\Lambda >> 1$) are present, this model is invalid; (ii) formally the β effect approach is only valid for small slopes (small β^*) and will break down in the equatorial region for a thick spherical shell; (iii) a

uniform background magnetic field profile was assumed: when this is not the case, extra terms will be present and other force balances possible.

Analytic studies in the presence of strong, non-uniform magnetic fields

Soward (1979b) has analytically studied the rotating magnetoconvection problem in a plane layer geometry, including thermal and magnetic diffusion and the presence of an imposed non-uniform Malkus magnetic field. This model is not limited to weak magnetic field strengths which was a drawback of the QG model. He found that the non-uniform magnetic field gives rise to an additional term in the dispersion relation (he calls this the magnetic hoop stress term) that controls the direction of propagation of thermal MAC waves when the field strength is strong enough, and can cause wave propagation in a retrograde (westward) direction. He suggests that thermal MAC waves will be present regardless of the confining geometry when the magnetic field is sufficiently strong and that the magnetic hoop stress effect could help to explain westward motions of waves found for strong magnetic fields in a spherical geometry.

Asymptotic studies in spherical geometry

Building on the landmark asymptotic studies of the onset of thermal convection in a rapidly rotating sphere in the double limit $E << 1$ and $\frac{Pr}{E} >> 1$ of Roberts (1968) and Busse (1970), Fearn (1979a) carried out a similar study of local stability with a weak imposed Malkus ($\boldsymbol{B_0} = B_0 r \sin\theta \widehat{\boldsymbol{\phi}}$) magnetic field. This study essentially confirmed the picture found in the QG annulus model described in the previous section: when the field is very weak the critical modes are essentially thermal Rossby waves perturbed slightly by the magnetic field. As the field strength increases (so that magnetic and Coriolis forces come to balance each other to leading order) the preferred modes become the thermal magneto-Rossby waves, whose direction of travel depends on the ratio $\frac{Pr_m}{Pr}$. Both waves were found to be non-axisymmetric, equatorially symmetric and columnar in structure. All these analyses rely on the scaling assumptions that $\frac{1}{s}\frac{\partial}{\partial\phi} \sim \mathcal{O}(E^{-1/3})$, $\frac{\partial}{\partial z} \sim 1$ and $\frac{\partial}{\partial t} \sim \mathcal{O}(E^{-2/3})$ in the limit $E << 1$. Such scalings imply that $k \sim \mathcal{O}(E^{-1/3})$ and $\omega \sim \mathcal{O}(E^{-2/3})$ and will also be relevant in the QG model. Substituting these into the expression for Λ in terms of k and ω obtained by balancing the imaginary parts of the β-effect and magnetic force terms in equation (6.59) gives

$$\Lambda = Pr_m \beta \frac{\omega}{k^3} \sim Pr_m \beta \frac{\mathcal{O}(E^{-2/3})}{(\mathcal{O}(E^{-1/3}))^3} \sim \mathcal{O}(E^{1/3}) \tag{6.71}$$

This $\Lambda \sim \mathcal{O}(E^{1/3})$ scaling for the threshold Λ is that which occurs when the Lorentz force is just able to balance the β-effect and it is expected to mark the transition from magnetically-modified thermal Rossby waves to the thermal magneto-Rossby waves (Fearn, 1979a).

More recently, Jones et al. (2000) and Dormy et al. (2004) have extended the non-magnetic theories of the onset of thermal instability in sphere and spherical shell geome-

tries to rigorous global stability analyses. They deduced that the appropriate cylindrical radial asymptotic scaling for the columnar modes was $\frac{\partial}{\partial s} = \mathcal{O}(E^{-1/3})$. Jones et al. (2003) have carried out the related global stability analysis with a weak Malkus field including boundary layer and other first order corrections. This theory was successfully compared with results from a numerical solution of the full eigenvalue problem (where no scaling assumptions were made) at small E and large $\frac{Pr}{E}$. The scaling assumptions of small radial extent made in all these asymptotic theories break down for low Pr and large Λ.

Zhang (1994a,b) has developed an asymptotic theory of the onset of thermal convection in a sphere in the distinct limit of $E << 1$ and $\frac{Pr}{E} << 1$, that is based on the perturbation analysis of inertial wave solutions. Zhang (1995) and Zhang and Busse (1995) have applied this theory to the spherical rotating magnetoconvection problem, in the presence of an imposed Malkus field. There is no restriction on the applied field strength in this case because, as shown in §6.5.2, the special properties of the Malkus magnetic field means the magnetic problem is simply the non-magnetic problem with modified eigenvalues. Unfortunately the restriction to $\frac{Pr}{E} << 1$ limits the applicability of the results of this theory to rather lower Pr than is anticipated to be the case in Earth's core.

In an important recent development Zhang and Liao (2004) have shown the compatibility of Zhang's thermal-inertial convection theory with the Roberts-Busse thermal Rossby wave theory of convection. They have developed a new asymptotic theory, valid for all $\frac{Pr}{E}$, in which the columnar thermal Rossby waves can be represented by a sum over a small number of the QG inertial wave modes derived by Zhang et al. (2000). It will be exciting to see how this theory will be extended in the future to include the effects of imposed magnetic fields.

When considering the regime relevant to Earth's core ($0.1 < \Lambda < 10$, $E < 10^{-5}$, $0.01 < Pr < 10$, $10^{-5} < Pr_m < 1$) the only feasible option at present is to numerically solve numerically the full governing equations. Such studies are reviewed in the next section.

Numerical studies in spherical geometry

Studies using the Malkus field

The first study to fully incorporate the effect of spherical geometry and also consider strong magnetic fields along with convective driving was that of Eltayeb and Kumar (1977) who employed the Malkus field ($\boldsymbol{B_0} = B_0 r \sin\theta \widehat{\boldsymbol{\phi}}$). They formulated an eigenvalue problem, and used an iterative method to locate the important eigenvalues, starting with initial values for Ra and ω from the non-magnetic convection problem. Increasing the field strength from zero, they noted that the critical Rayleigh number for the onset of convection (Ra_c) initially increased (suggesting that the magnetic field was stabilising the fluid) and that disturbances drifted eastwards as expected for magnetically-modified

thermal Rossby waves. Increasing the strength of the magnetic field further, Ra_c was observed to fall (magnetic field facilitating instability) and the length scales of the disturbance increased. The resulting waves were again z independent, drifting slowly to the east if $\frac{Pr_m}{Pr} << 1$ and to the west if $\frac{Pr_m}{Pr} >> 1$ as expected for thermal magneto-Rossby waves. For stronger field strengths they noted that convection filled the whole sphere and that all waves drifted westwards. Unfortunately, given the nature of computational resources in the mid 1970's when this study was carried out, there was doubt over the convergence of some of the results reported.

Fearn (1979b) carried out a similar, but more accurate numerical study again using the Malkus field but concentrating on the case when the Roberts number $q = \frac{Pr_m}{Pr}$ approached zero. He considered the regime ($0.1 \leq \Lambda \leq 100$) and documented marginally stable modes at the onset of thermal convection. He definitively identified magnetically modified thermal Rossby waves at low Λ, and observed a transition to thermal magneto-Rossby waves at $\Lambda \sim O(E^{1/3})$ as predicted by his analytical work (Fearn, 1979a). At $\Lambda \sim O(1)$, the propagation direction of the most unstable modes changed from eastwards to westwards. It was suggested this indicated a transition to thermal MAC modes for which magnetic hoop stress was more important than the β-effect in determining the wave propagation direction (see Soward (1979b) for further details). As Λ was increased further, Fearn observed that Ra_c began to increase again, as the magnetic field (rather than rotation) began to inhibit convection. For $\Lambda > 20$ magnetically driven MAC waves were found when stable thermal stratification ($Ra \leq 0$) was present (this is the exceptional mode of magnetic instability described in §6.6.1). The stability diagram from Fearn (1979b) is presented in figure 6.6. For $Ra > 0$, the diagram summarises our current understanding of the different types of convection-driven hydromagnetic waves possible in a rapidly rotating fluid sphere, as a function of magnetic field strength.

Jones et al. (2003) and Worland (2004) recently completed a comprehensive investigation (both analytical and numerical) of the properties of linear magnetoconvection in a rapidly rotating sphere, when the imposed magnetic field is weak $\Lambda << 1$, and of the Malkus type, with $E < 10^{-6}$. They identified the magnetically-modified thermal Rossby wave and thermal magneto-Rossby waves to high accuracy, verifying the scenario proposed by Fearn (1979a;b) and described the effects of varying Λ, Pr and Pr_m on the structure of the wave solutions. Increasing Λ was found to lower the azimuthal wavenumber of the solution and straighten out the spiralling convection characteristic of thermal Rossby waves at low Pr (Zhang, 1992). As Pr decreased, cells were found to spiral more, with azimuthal wavenumber decreasing and the position of the transition between the two types of waves moving to higher Λ. As Pr_m increased, the effects associated with the transition were delayed until larger Λ. The localisation of the waves moved outwards towards the region of higher field strength following the transition from magnetically-modified thermal Rossby wave (when magnetic field inhibits convection) to the thermal magneto-Rossby wave (when the magnetic field facilitates convection). The transition

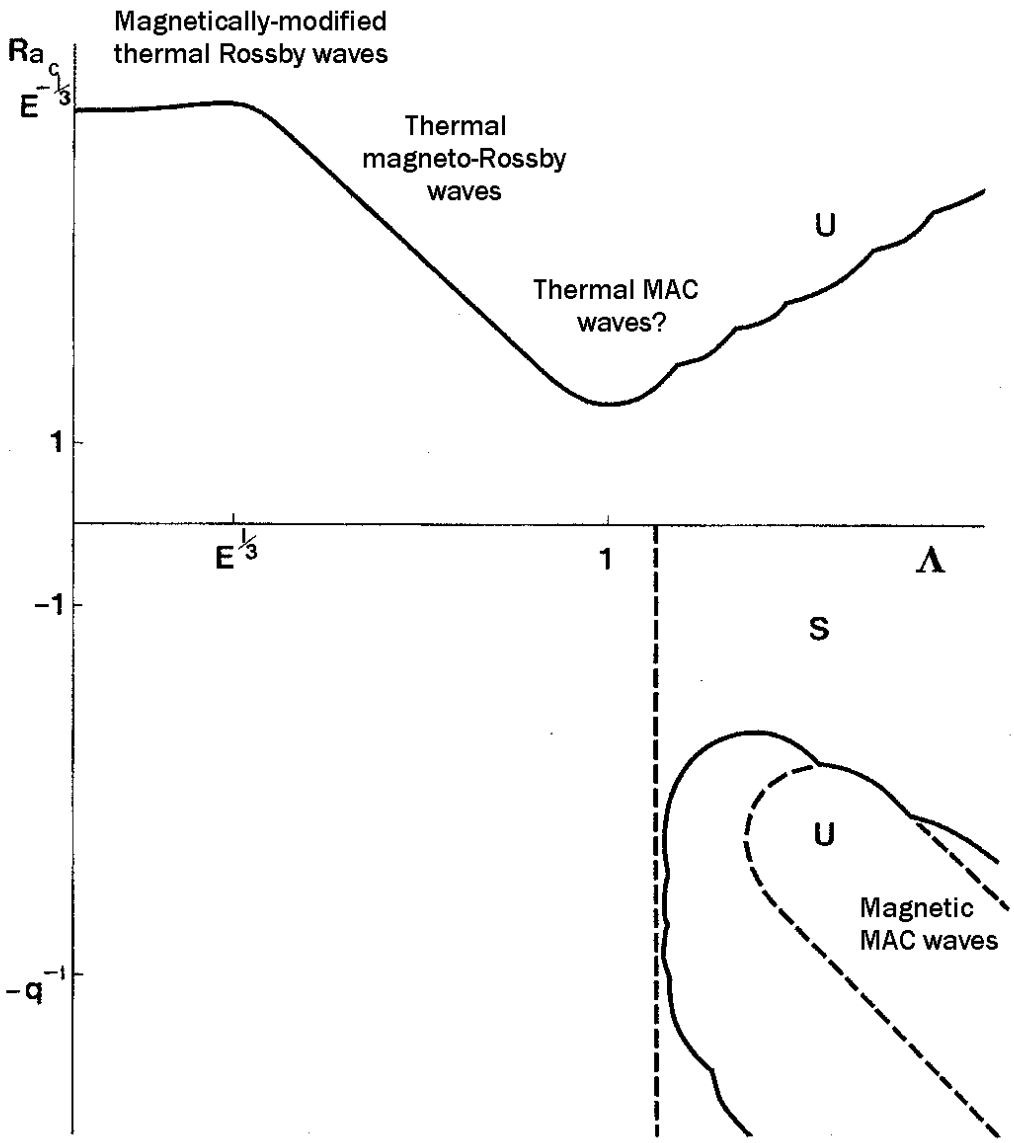

Figure 6.6: Stability diagram from Fearn (1979b).
Stability diagram for convection-driven hydromagnetic waves in a sphere with a Malkus background magnetic field. Elsasser number Λ (a measure of magnetic field strength) is plotted against critical Rayleigh number Ra_c (a measure of the strength of thermal driving). The solid line is the boundary between stable waves (S region) and unstable waves (U region) inferred from numerical calculations. For weak magnetic fields (low Λ) Ra_c increases with Λ as expected for the magnetically-modified thermal Rossby waves. For $\Lambda > \mathcal{O}(E^{1/3})$, Ra_c falls indicating a transition to thermal magneto-Rossby waves. For $\Lambda > 1$ convection fills the whole sphere and waves travel westward, suggesting the dominance of thermal MAC waves. For negative Ra_c (stable stratification) magnetic MAC waves, driven by magnetic instability catalysed by thermal stratification are observed. This diagram adapted from Fearn (1979b).

between these modes was found to be continuous at large Pr_m but discontinuous at small Pr_m. This study did not document changes in the form of the thermally driven hydromagnetic waves for $\Lambda \sim 1$: this regime is studied in chapter 7.

Effect of more realistic background magnetic fields and flows

Fearn and Proctor (1983) took an important step towards geophysical realism by studying both more realistic background fields and flows. They chose an axisymmetric, toroidal magnetic field $\boldsymbol{B_0} = 8r^2(1-r^2)\sin\theta\cos\theta\,\widehat{\boldsymbol{\phi}}$. This vanishes on the outer boundary without the need for any magnetic boundary layer and is equatorially anti-symmetric (E^A) as required to generate the observed E^A dipole symmetry poloidal field by differential rotation (the ω-effect, see for example, Roberts (1994)). Initially they neglected the background flow to isolate the effect of an E^A imposed field on convection-driven hydromagnetic waves. Little qualitative difference in Ra_c and ω was then observed compared to studies involving the Malkus field, though magnetically driven MAC waves were observed for lower Λ and without stable stratification. Eltayeb (1992) came to similar conclusions when considering the effect of a range of weak imposed magnetic fields in a spherical shell geometry, finding that the form of the field was only important in determining latitudinal location of the wave, but not the type of wave excited or its drift speed.

Fearn and Proctor (1983) also considered the effect of axisymmetric background flows involving differential rotation on convection-driven hydromagnetic waves, when an E^A toroidal magnetic field was imposed. Toroidal magnetic fields with E^A symmetry that satisfy insulating boundary conditions cannot be z independent and therefore have an associated Lorentz force that drives azimuthal flow (see Braginsky (1980) and Fearn et al. (1988) for a discussion of this magnetic wind phenomenon). It is therefore important to include background azimuthal flows in order to study the influence of E^A imposed fields in a self consistent manner. Fearn and Proctor (1983) found that including such a background azimuthal flows leads to major changes in the properties of convection-driven hydromagnetic waves. The critical Ra is increased as the amplitude of the flow increases, waves become localised at the latitude of extrema in the flow with the speed of the waves approaching the fluid speed at that point. Since azimuthal flows associated with both magnetic and thermal winds are probable in Earth's core (see, for example, Dumberry and Bloxham (2005)), the fact that they crucially influence the properties of hydromagnetic waves (Braginsky, 1980; Fearn and Proctor, 1983) implies they must be taken into account if one is to accurately predict the properties of hydromagnetic waves in Earth's outer core.

Zhang (1995) studied the parameter dependence of the structure of convection-driven hydromagnetic waves in a spherical shell, with an E^A imposed toroidal magnetic field but no self-consistent background flow at $E = 10^{-4}$ and Pr_m=1. The imposed magnetic field was chosen to be the axisymmetric toroidal decay mode of the lowest order having

E^A symmetry and satisfying electrically insulting boundary conditions. A mathematical description of all such decay modes resulting from the solution to the magnetic diffusion problem in a spherical shell can be found in Zhang and Fearn (1994). Zhang (1995) demonstrated convincingly that with E^A imposed fields there is no minimum in Ra_c as a function of Λ because above $\Lambda \sim O(1)$ the imposed magnetic field supplies the energy required for convection through magnetic instability. This is in contrast to the scenario for the Malkus field where the magnetic field only facilitates thermal convection and stable stratification is required in order for magnetic instability to occur. Zhang also noted that as $\frac{Pr_m}{Pr}$ becomes small, the limit between convection-driven and magnetically-driven waves is discontinuous for any particular wavenumber. Zhang and Jones (1996) have investigated this troublesome transition in detail and conclude that there is no physical difficulty because as $\frac{Pr_m}{Pr}$ tends to zero, the critical thermal and magnetic modes with the same Ra_c always have different wavenumbers.

Decreasing Pr from 1 towards 0, Zhang observed that hydromagnetic waves display the spiralling structure familiar from non-magnetic convection (Zhang, 1992), but the Lorentz force can cause spiralling in the westward rather than eastward direction. At very low Pr a transition is observed to waves with similar form to thermal-inertial waves (Zhang, 1994a;b; Zhang and Busse, 1987), with structure localised close to the outer boundary. At very low Pr, fluid inertia is capable of balancing the Coriolis force, so thermal forcing drives inertial waves rather than Rossby waves and with a weak magnetic field strength present, magnetically-modified thermal inertial waves are obtained. Little change is observed in the form of these waves as Λ is increased, perhaps because the Lorentz force remains as a weak perturbation since the thermal-inertial wave structure is localised near the outer boundary where the imposed field strength is constrained to be small in order to satisfy the electrically insulating boundary conditions. No thermal MC-inertial waves were found, presumably because they are more difficult to excite.

Longbottom et al. (1995) also studied E^A imposed fields but time-stepped the governing equations (see Hollerbach (2000) for a discussion of this numerical method) at $E = 10^{-4}$ and $\frac{Pr_m}{Pr} = 10^{-6}$. This method has the advantage of not requiring an initial starting guess for the solution. They ignored the influence of inertial effects so were unable to study magnetically-modified thermal Rossby or magnetically-modified thermal-inertial waves. Imposing the same E^A field as Fearn and Proctor (1983) they also found magnetically instabilities for $\Lambda > 10$, and that including a poloidal imposed field made it easier to obtain such instabilities. The influence of a background flow was also investigated and again found to have an important influence if sufficiently strong.

Most recently, attention has focused on the effect of imposing both toroidal and poloidal magnetic fields together. Zhang and Gubbins (2002) studied convection-driven hydromagnetic waves when $E = 10^{-6}$ and Pr=Pr_m=1 with a variety of imposed fields. They found that the poloidal field has less effect on the dynamics than the toroidal magnetic

field because it satisfies electrically insulating boundary conditions with less curvature and therefore less magnetic hoop stress. They observed waves propagating eastward when a poloidal field is dominant and westward when a toroidal field is dominant.

Effect of the presence of an inner core

Zhang (1995) observed that the presence of an insulating inner core did little to change the structure of either convection-driven or magnetically-driven waves, because the preferred waves all had columnar structure and were localised outside the tangent cylinder to the inner core. Longbottom et al. (1995) studied the inclusion of a finitely conducting inner core, with an imposed field that was non-zero inside the inner core, but again found that the presence of the inner core made little difference to the form of the magnetoconvection. Walker and Barenghi (1997) compared their full sphere results to the spherical shell results of Longbottom et al. (1995) and found only very minor differences, that occurred primarily for magnetically-driven instabilities. It can therefore be concluded that the results of models of rotating magnetoconvection in a fluid sphere will be relevant to the case of a spherical shell with only small corrections (see for example Jones et al. (2000)), so results from full sphere models can sensibly be applied when seeking to model hydromagnetic waves in Earth's outer core.

6.7 Nonlinear influences on hydromagnetic waves

The discussion up to now has considered only linear hydromagnetic waves. This approach implicitly assumes (i) waves can be superposed without considering any mutual interaction and (ii) that no feedback occurs between the waves and the rest of the system. This scenario is obviously unphysical because unstable waves can grow without limit, but is nonetheless useful for determining which type of wave will be most easily excited in a particular regime. Early studies by Braginsky (1967), Roberts and Soward (1972) and Braginsky and Roberts (1975), though deriving linear equations for hydromagnetic waves riding on general background states, emphasised the importance of understanding non-linear feedback processes. They noted that wave properties are determined by the background state, but the background state is itself altered by the waves. Furthermore, the possibility of transient growth of eigenmodes due to non-normal structure of the governing equations (see, for example, Farrell and Ioannou (1996) or Livermore (2003)) means placing too much faith in results linear eignvalue calculations alone is dangerous. Therefore, when seeking to interpret geophysical observations indicative of hydromagnetic waves in Earth's core, it should be remembered that linear analysis is only formally valid for small perturbations to an artificial, steady background state and cannot tell us how waves will evolve, saturate, interact with each other or what flow structures might result from nonlinear bifurcations of the waves. Attempts to understand such processes deserves a concerted theoretical and numerical modelling effort in the future.

Some progress in understanding nonlinear hydromagnetic waves has already been made. El Sawi and Eltayeb (1981) and Eltayeb (1981) have derived higher order equations for hydromagnetic waves in a plane layer with a slowly varying background mean flow. Their equations describe the evolution of diffusionless MAC wave amplitude via the conservation of wave action (wave energy divided by wave frequency per unit volume). This conservation law describes how when a wave moves into a region where its frequency is higher (due to changes in the background state), then the increase in wave energy occurs at the expense of a decrease in the energy of the background state.

Ewen and Soward (1994a;b;c) performed a weakly nonlinear analysis of a QG cylindrical annulus model of rotating magnetoconvection in an imposed Malkus-type field. They derived and analysed equations describing the amplitude modulation of thermal magneto-Rossby waves, finding that a geostrophic flow is driven nonlinearly by the Lorentz force resulting from magnetic field perturbations associated with hydromagnetic waves and is linearly damped by Ekman suction at the boundary. They consider stationary pulse, travelling pulse and wavetrain solutions as well as single mode solutions, and find that the nonlinear interaction resulting from the geostrophic flow can redistribute energy amongst the modes.

The 1990's saw the first attempts to study rotating magnetoconvection in 3D spherical geometry in the non-linear regime. Fearn et al. (1994) included only the leading order nonlinearity (the geostrophic flow) and integrated the governing equations in time. They used the same toroidal field as Fearn and Proctor (1983), chose $\frac{Pr_m}{Pr} = 1$ and Λ=5, set E=0 and neglected inertial terms. At low Ra they obtained an equilibrated solution for the geostrophic velocity, but it appeared to be determined by Ekman suction and was clearly not a Taylor state (in which the integral of the azimuthal part of Lorentz force over cylindrical annuli vanishes (Taylor, 1963)) as they had hoped. At higher Ra they found complicated time dependence and no converged steady solutions. Walker and Barenghi (1999) tackled the same problem with rather more success and observed a transition to a Taylor state at higher Ra. They found that the resulting geostrophic flow strongly influenced the frequency and propagation direction of the waves (in agreement with the linear findings of Fearn and Proctor (1983)), causing them to change direction from westward to eastward as Ra is increased.

Olson and Glatzmaier (1995) numerically time-stepped the governing equations starting from a conductive state with random perturbations for a limited region of parameter space ($Pr = 1$, Λ =0.1 or 10, $Pm = 10^{-2}$, $E = 5 \times 10^{-5}$) and Ra highly supercritical. They imposed a magnetic field (with a sin 2θ dependence on co-latitude) at the inner core boundary and specified that the outer boundary be an electrical insulator. When the field was weak, they found fluid motion vigorous and geostrophic outside the tangent cylinder in narrow ($m = 4$) columns parallel to the rotation axis and driven by small, ribbon shaped thermal plumes. There was azimuthal flow driven by Reynolds stresses

due to the tilt of the convective columns, being westward near the tangent cylinder, but eastward further from the axis. With a strong magnetic field they found that most convection occurs inside the tangent cylinder, while outside there was a single, large-scale plume.

Cardin and Olson (1995) used the QG approximation to study fully non-linear magneto-convection for $Pr = 7$, $Pm = 0.1$, $E = 10^{-4}$ with $Ra = 3Ra_c$ and $50Ra_c$, and Λ between 10^{-4} and 2. For weak forcing, they found Reynolds stresses due to the prograde tilt of convective columns drove azimuthal flows, but that a strong magnetic field reduced the wavenumber of convection and suppressed azimuthal flows. For strong forcing, the Reynolds stresses (rather than viscous stresses) appeared to determine the vortex scale with large eddies being formed. Unfortunately, the imposed toroidal field chosen in this study is singular at the origin casting some doubt on the results obtained (Fearn, 1998).

Zhang (1999) studied nonlinear rotating magnetoconvection in a spherical shell, using the same toroidal field as Zhang (1995), but neglecting the inertial terms and studying thermally driven waves at Ra up to 3 times critical, $E = 1 \times 10^{-3}$ and $\Lambda = 10$. Solutions were obtained by integrating the equations numerically over many magnetic diffusion times. He found two bifurcations, the first being the onset of steadily travelling magneto-convective waves with equatorial and azimuthal symmetry, the second being the simultaneously breaking temporal and azimuthal symmetry leading to vacillating magnetoconvection (for further discussion, consult Zhang and Schubert (2000)).

Sakuraba and Kono (2000) studied 3D, fully non-linear, magnetoconvection in a rapidly rotating spherical shell, with an imposed uniform magnetic field parallel to the rotation axis and $E = 2 \times 10^{-5}$. They found a transition from a magnetically-modified thermal Rossby wave to a thermal magneto-Rossby wave at $\Lambda \sim 1$. This transition was associated with an increase in the toroidal magnetic field energy, a decrease in the azimuthal wavenumber of the mode and the confinement of magnetic flux into anti-cyclonic rolls, especially in high amplitude spots in the equatorial region at the outer boundary.

Gillet et al. (2005) have carried out a comprehensive experimental and numerical investigation into the properties of a turbulent flow produced by the nonlinear development of magnetically-modified thermal Rossby waves. This study is limited to weak magnetic fields ($\Lambda << 1$), but addresses the possibility that flow in Earth's outer core may be turbulent. They observe the production of strong azimuthal flows showing the importance of including nonlinear effects in modelling the properties of hydromagnetic waves. Liquid sodium experiments are currently underway and in combination with further nonlinear modelling of magnetoconvection these should help clarify the situation in the more Earth-like regime where $\Lambda \sim \mathcal{O}(1)$.

Theoretical study of nonlinear hydromagnetic waves in rapidly rotating fluids with strong imposed magnetic fields is still in its infancy. Such investigations should be expected to yield important insights enabling a better understanding of observable consequences of

hydromagnetic waves and their interaction with the azimuthal flows in the core.

6.8 Influence of stratification on hydromagnetic waves

There has been some discussion of the possibility of a stratified layer or inner ocean at the top of Earth's outer core (see, for example, Fearn and Loper (1981); Gubbins et al. (1982); Lister and Buffett (1998)) and the hydromagnetic waves that would be supported there (see, for example, Braginsky (1987; 1993; 1999), Drew (1993) and Bergman (1993)). This stratified layer has not yet been observed seismically (Helffrich and Kaneshima, 2004) though its existence seems plausible on thermodynamic grounds with light fluid released during the solidification of the inner core expected to pond below the core-mantle boundary.

The dynamics of a stably stratified layer would be dominated by its thin spherical shell geometry (and the associated β-effect) along with the Brunt-Väisällä frequency (for a discussion of this concept, see Melchoir (1986)) associated with its stable stratification. There would undoubtedly be many similarities with the water ocean on Earth's surface, but with additional complications caused by the presence of magnetic forces. In particular, MC-Rossby waves (relying on the change in the Coriolis force with latitude) would be present within such an ocean though their excitation mechanism remains unclear. Braginsky (1999) has developed models of both axisymmetric and non-axisymmetric disturbances of such a stably stratified layer (including the effects of magnetic diffusion) and claims they can account for oscillations with periods of 65 years and 30 years that he suggests are found in studies of short period geomagnetic secular variation. Unfortunately, hydromagnetic waves in a hidden ocean at the top of the outer core are not the only possible source of periodic geomagnetic secular variation on these decadal time scales — torsional oscillations[8] (Bloxham et al., 2002) are an equally plausible explanation. Until the existence of the hidden ocean of the core can be confirmed, the study of hydromagnetic waves which may exist there will remain of primarily mathematical interest.

6.9 Summary

In this chapter the subject of hydromagnetic waves in rapidly rotating, convecting fluids has been reviewed. The fundamental restoring mechanisms provided by rotation and magnetic fields have been described and dispersion relations have been obtained in a variety of simple cases. Possible excitation mechanisms have been proposed with attention

[8]Torsional oscillations (Braginsky, 1970) are axisymmetric hydromagnetic waves for which pressure gradients completely balance the Coriolis force, so the Lorentz force and inertia constitute the leading order force balance. Oscillations about this state are essentially Alfvén waves involving the magnetic field in the direction perpendicular to the rotation axis.

focusing on waves driven by magnetic and thermal instability. Nonlinear feedback between the waves and azimuthal flows and the effects of stable stratification have also been discussed. Possible types of hydromagnetic wave found in the presence of convection, rapid rotation and imposed magnetic fields are listed in Table 6.1:

Wave type	Time scale	Field strength	Comment
MC-Rossby waves	MC Rossby	$\frac{\lvert\text{Mag. force}\rvert}{\lvert\text{Coriolis force}\rvert} \geq \mathcal{O}(1)$	no diffusion
MC-Inertial waves	rotational	$\frac{\lvert\text{Mag. force}\rvert}{\lvert\text{Coriolis force}\rvert} \geq \mathcal{O}(1)$	no diffusion
MC/MAC waves	MC/MAC	$\frac{\lvert\text{Mag. force}\rvert}{\lvert\text{Coriolis force}\rvert} \geq \mathcal{O}(1)$	no diffusion
Magnetically-modified thermal Rossby waves	thermal diff.	$0 < \Lambda < \mathcal{O}(E^{1/3})$	v. weak B_0
Magnetically-modified thermal inertial waves	rotational	$\Lambda > 0$	v. small Pr
Thermal magneto-Rossby waves	thermal diff.	$\Lambda \geq \mathcal{O}(E^{1/3})$	Earth-like?
Thermal MC-Rossby waves	thermal diff.	$\Lambda \geq \mathcal{O}(E^{1/3})$	v. large Pr_m
Thermal MAC waves	thermal diff.	$\Lambda >> \mathcal{O}(1)$	strong B_0
Magnetic MAC waves	magnetic diff.	$\Lambda >> \mathcal{O}(10)$	v. strong B_0

Table 6.1: Hydromagnetic waves in a rotating, thermally convecting fluid. Summary of types of hydromagnetic wave possible in a rapidly rotating, thermally convecting fluid. Thermal or magnetic in the wave name refers to the type of instability driving the wave, if these are not present the wave is a free wave (natural response of the system to perturbation). The required ratios of the magnetic force to the Coriolis force (or else the range of Λ if diffusion is present) are listed, along with comments on the relevance of each wave to the regime thought to be present in Earth's outer core.

In Earth's core with strong magnetic fields and rapid rotation present ($\Lambda \sim \mathcal{O}(1)$) and with $Pr \sim \mathcal{O}(1)$, $Pr_m << \mathcal{O}(1)$ and with buoyancy forces present, magneto-Rossby waves appear most likely to be excited by convection. These waves are expect to propagate slowly on the thermal diffusion time scale, to exhibit dispersion with higher wavenumbers travelling faster, and to have highest speed when localised at the equator. The parameter dependences of the structure and properties of convection-driven hydromagnetic waves in spherical geometry with a simple Malkus imposed field ($\Lambda \sim \mathcal{O}(1)$) and no background flow present are documented in chapter 7.

It should be emphasised that in order to accurately predict the structure and propagation speeds of hydromagnetic waves in Earth's core, previous studies suggest that realistic representations of both the background toroidal magnetic field and of azimuthal flow in the core should be included in modelling. Further theoretical and numerical studies in this direction are required in the future.

Chapter 7

Convection-driven, linear hydromagnetic waves in a sphere

7.1 Introduction

In this chapter a numerical study of hydromagnetic waves in a rapidly rotating sphere driven by thermal convection in the presence of an imposed azimuthal magnetic field is described. The properties of marginally stable waves are studied as a function of the control parameters. The focus of attention will be the strong magnetic field ($\Lambda \sim 1$) regime that has not previously been documented in detail. The motivation for this chapter is to catalogue the behaviour of waves in this regime that is thought to be relevant to Earth's outer core.

As noted in chapter 6, accurate modelling of the properties of hydromagnetic waves in Earth's core requires taking into account the presence of background flows and nonlinear interactions between waves and these flows. This is a major undertaking, and is not attempted in the present chapter. Instead, attention is focused on understanding the mechanisms responsible for hydromagnetic waves in a simple case that includes the essential ingredients of a rapidly rotating fluid, a magnetic field that strongly influences the dynamics, a spherical geometry and convective driving. The knowledge gained in this study will be of value when attempting to interpret results from more complex and realistic models with either imposed or dynamo generated radial magnetic fields also present (see chapter 5 for an analysis of examples of hydromagnetic waves in dynamo models).

The code forming the basis for numerical investigations in this chapter was kindly provided by Christopher Jones and Steven Worland from the University of Exeter, UK (Jones et al., 2003; Worland, 2004). Their manipulation of the governing equations into a form suitable for numerical solution as an eigenvalue problem and treatment of the boundary conditions are briefly outlined in the first part of this chapter. The numerical solution of the eigenvalue problem is then described, including new extensions

to the numerical method of Jones and Worland (particularly the implementation of an implicitly-started Arnoldi solver (ARPACK) method) allowing solutions to be found even when no reliable starting guesses for the Rayleigh number and wave frequency at the onset of convection are available. Results are reported regarding the parameter dependences of wave properties and their structure. Finally implications of these theoretical investigations for hydromagnetic waves in Earth's core are discussed.

7.2 Manipulation of governing equations into eigenvalue form

7.2.1 Governing equations

The treatment in this section closely follows that of Worland (2004), which contains full details of the extensive algebraic manipulations required; the reader should consult this account if further details are required. As described in appendix D, the linearised equations governing perturbations in the flow, magnetic field and temperature field $(\boldsymbol{u}, \boldsymbol{b}, \Theta)$ associated with hydromagnetic waves in a rapidly rotating, convecting sphere (which is self-gravitating ($\widehat{\boldsymbol{g}} = \gamma \boldsymbol{r}$), where convection is driven by uniform internal heating ($\nabla T_0 = -\beta' \boldsymbol{r}$) and where the rotation axis is in the $\widehat{\boldsymbol{z}}$ direction) in the non-dimensionalisation based on the viscous diffusion time scale are,

$$E\left(\frac{\partial}{\partial t} - \nabla^2\right)\boldsymbol{u} + (\widehat{\boldsymbol{z}} \times \boldsymbol{u}) = -\nabla P + ERa\Theta\boldsymbol{r} + \Lambda\left[(\widehat{\boldsymbol{B}_0} \cdot \nabla)\boldsymbol{b} + (\boldsymbol{b} \cdot \nabla)\widehat{\boldsymbol{B}_0}\right], \tag{7.1}$$

$$\left(\nabla^2 - Pr_m \frac{\partial}{\partial t}\right)\boldsymbol{b} = \nabla \times (\boldsymbol{u} \times \widehat{\boldsymbol{B}_0}), \tag{7.2}$$

$$\left(\nabla^2 - Pr \frac{\partial}{\partial t}\right)\Theta = -\boldsymbol{r} \cdot \boldsymbol{u}, \tag{7.3}$$

$$\nabla \cdot \boldsymbol{u} = 0, \tag{7.4}$$

$$\nabla \cdot \boldsymbol{b} = 0, \tag{7.5}$$

and the the non-dimensional control parameters called the Ekman number E, Rayleigh number Ra, Elsasser number Λ, Prandtl number Pr and magnetic Prandtl number Pr_m are respectively,

$$E = \frac{\nu}{2\Omega {r_0}^2}, \qquad Ra = \frac{\gamma\alpha\beta' {r_0}^6}{\kappa\nu}, \qquad \Lambda = \frac{B_0^2}{2\Omega\mu\rho_0\eta}, \qquad Pr = \frac{\nu}{\kappa}, \qquad Pr_m = \frac{\nu}{\eta}. \tag{7.6}$$

The non-dimensionalised background magnetic field used in this model is

$$\widehat{\boldsymbol{B}_0} = r \sin\theta\, \widehat{\boldsymbol{\phi}}. \tag{7.7}$$

This is the Malkus field that was discussed in §6.5.2 that is useful when one wishes to study simple examples of hydromagnetic waves in spherical geometry. It allows waves driven by magnetic instability (see §6.6.1) to be filtered out, permitting attention to focus on waves driven by thermal instability. It is also force-free ($(\nabla \times \widehat{\boldsymbol{B}_0}) \times \widehat{\boldsymbol{B}_0} = 0$)

so the effect of background azimuthal flows can be neglected in a self-consistent manner because the imposed field does not give rise to a Lorentz force and an associated magnetic wind. It is, however, non-uniform so does incorporate the magnetic hoop stress effect ($(\boldsymbol{b}\cdot\nabla)\widehat{\boldsymbol{B}_0} \neq 0$) that Soward (1979b) suggested plays a role in determining the direction of wave propagation when imposed magnetic fields are strong.

7.2.2 Toroidal-poloidal expansion and equations governing the evolution of the scalar fields

Since $\boldsymbol{u}$ and $\boldsymbol{b}$ are both solenoidal they may be decomposed into toroidal parts ($\boldsymbol{u}_T$, $\boldsymbol{b}_T$) and poloidal parts ($\boldsymbol{u}_P$, $\boldsymbol{b}_P$) as

$$\boldsymbol{u} = \boldsymbol{u}_T + \boldsymbol{u}_P = \nabla \times e\widehat{\boldsymbol{r}} + \nabla \times (\nabla \times f\widehat{\boldsymbol{r}}), \tag{7.8}$$

$$\boldsymbol{b} = \boldsymbol{b}_T + \boldsymbol{b}_P = \nabla \times g\widehat{\boldsymbol{r}} + \nabla \times (\nabla \times h\widehat{\boldsymbol{r}}), \tag{7.9}$$

where e is the toroidal scalar associated with the velocity field, f is the poloidal scalar associated with the velocity field, g is the toroidal scalar associated with the magnetic field, h is the poloidal scalar associated with the magnetic field and $\widehat{\boldsymbol{r}}$ is a unit vector in the radial direction. The toroidal component of a vector lies on spherical surfaces, with the remainder that crosses spherical surfaces being the poloidal component (see, for example, Bullard and Gellman (1954)). Expanding the curl operator in spherical geometry leads to the following expressions for the spherical polar components $(\widehat{\boldsymbol{r}}, \widehat{\boldsymbol{\theta}}, \widehat{\boldsymbol{\phi}})$ of the vector fields in terms of their toroidal and poloidal scalars

$$\boldsymbol{u} = \left[\frac{\mathcal{L}^2 f}{r^2}\right]\widehat{\boldsymbol{r}} + \frac{1}{r}\left[\frac{1}{\sin\theta}\frac{\partial e}{\partial \phi} + \frac{\partial^2 f}{\partial r \partial \theta}\right]\widehat{\boldsymbol{\theta}} + \frac{1}{r}\left[\frac{1}{\sin\theta}\frac{\partial^2 f}{\partial r \partial \phi} - \frac{\partial e}{\partial \theta}\right]\widehat{\boldsymbol{\phi}}, \tag{7.10}$$

$$\boldsymbol{b} = \left[\frac{\mathcal{L}^2 h}{r^2}\right]\widehat{\boldsymbol{r}} + \frac{1}{r}\left[\frac{1}{\sin\theta}\frac{\partial g}{\partial \phi} + \frac{\partial^2 h}{\partial r \partial \theta}\right]\widehat{\boldsymbol{\theta}} + \frac{1}{r}\left[\frac{1}{\sin\theta}\frac{\partial^2 h}{\partial r \partial \phi} - \frac{\partial g}{\partial \theta}\right]\widehat{\boldsymbol{\phi}}, \tag{7.11}$$

where the operator

$$\mathcal{L}^2 = -\frac{1}{\sin\theta}\frac{\partial}{\partial\theta}\left(\sin\theta\frac{\partial}{\partial\theta}\right) - \frac{1}{\sin^2\theta}\frac{\partial^2}{\partial\phi^2}. \tag{7.12}$$

Expressing the vector fields in poloidal-toroidal form means the solenoidal conditions are automatically satisfied and do not have to be explicitly implemented, which would be numerically cumbersome. In poloidal-toroidal form there are now 5 unknowns, so five governing equations are required if solutions are to be found. The required equations are obtained by substituting from equations (7.11), (7.10) and (7.7) into $r^2\widehat{\boldsymbol{r}}\cdot\nabla\times$ equation (7.1), $r^2\widehat{\boldsymbol{r}}\cdot(\nabla\times)^2$ equation (7.1), $r^2\widehat{\boldsymbol{r}}\cdot$ equation (7.2), $r^2\widehat{\boldsymbol{r}}\cdot\nabla\times$ equation (7.2) and equation (7.3) remains unaltered leading to the system (Worland, 2004)

$$E\left(\mathcal{L}^2\frac{\partial e}{\partial t} - \mathcal{L}^2\mathcal{D}^2 e\right) + \mathcal{Q}f - \frac{\partial e}{\partial \phi} = \Lambda\left((\mathcal{L}^2 - 2)\frac{\partial g}{\partial \phi} + 2\mathcal{Q}h\right), \tag{7.13}$$

$$E\left(-\mathcal{L}^2\mathcal{D}^2\frac{\partial f}{\partial t} + \mathcal{L}^2\mathcal{D}^4 f\right) + \mathcal{Q}e + \mathcal{D}^2\frac{\partial f}{\partial \phi} = RaEr\mathcal{L}^2\Theta + \Lambda\left(2\mathcal{Q}g - (\mathcal{L}^2 - 2)\mathcal{D}^2\frac{\partial h}{\partial \phi}\right), \tag{7.14}$$

$$\mathcal{L}^2\mathcal{D}^2 h - Pr_m\mathcal{L}^2\frac{\partial h}{\partial t} = -\mathcal{L}^2\frac{\partial f}{\phi}, \tag{7.15}$$

$$\mathcal{L}^2\mathcal{D}^2 g - Pr_m\mathcal{L}^2\frac{\partial g}{\partial t} = -\mathcal{L}^2\frac{\partial e}{\partial \phi}, \tag{7.16}$$

$$\nabla^2\Theta - Pr\frac{\partial \Theta}{\partial t} = -\frac{\mathcal{L}^2 f}{r}, \tag{7.17}$$

where

$$\mathcal{D}^2 = \nabla^2 - \frac{2}{r^2} - 2\frac{\partial}{\partial r}\frac{1}{r} = \frac{\partial^2}{\partial r^2} - \frac{\mathcal{L}^2}{r^2}, \tag{7.18}$$

and

$$\mathcal{Q} = -\cos\theta\mathcal{L}^2\frac{\partial}{\partial r} - \sin\theta\frac{\partial}{\partial\theta}\frac{\partial}{\partial r} + \frac{\mathcal{L}^2}{r}\left(\sin\theta\frac{\partial}{\partial\theta}\right). \tag{7.19}$$

7.2.3 Assumptions regarding equatorial symmetry of waves

Equatorially symmetric (E^S) rather than equatorially anti-symmetric (E^A) wave flows (see appendix E for a discussion of equatorial symmetry in spherical geometry) are preferentially excited by a uniform distribution of internal heat sources in a sphere during non-magnetic convection (Busse, 1970). This continues to be the case for thermally-driven convection in the presence of an imposed Malkus magnetic field of arbitrary strength (Eltayeb and Kumar, 1977; Fearn, 1979b) and also for waves driven by magnetic instability of an E^A imposed magnetic field (Zhang and Fearn, 1994; 1995). It is therefore both physically reasonable and numerically expedient to restrict calculations of waves to modes with E^S symmetry. Combining such flows with the E^S symmetry of the imposed Malkus magnetic field, the only permitted symmetry of the flow, magnetic field and temperature perturbations are E^S (see appendix E):

$$[u_r, u_\theta, u_\phi](r,\theta,\phi) = [u_r, -u_\theta, u_\phi](r,\pi-\theta,\phi) \tag{7.20}$$

$$[b_r, b_\theta, b_\phi](r,\theta,\phi) = [b_r, -b_\theta, b_\phi](r,\pi-\theta,\phi) \tag{7.21}$$

$$\Theta(r,\theta,\phi) = \Theta(r,\pi-\theta,\phi) \tag{7.22}$$

This restriction is important to consider when developing numerical expansions for the scalar fields, as is described in the next section.

7.2.4 Expansion of scalars into spherical harmonics and Chebyshev polynomials

To transform the system from a set of continuous partial differential equations into a set of simultaneous linear equations that may be solved numerically, the scalar variables are each expressed as the product of a complex spherical harmonic expansion on a spherical surface multiplied by a Chebyshev polynomial series in the radial direction (see, for example, Boyd (2001) for a review of the use of Chebyshev and pseudo-spectral expansions). Regarding the azimuthal wavenumber (spherical harmonic order m) as

fixed, considering only terms contributing to E^S scalar fields and requiring that the radial expansion satisfies the condition of regularity at the origin of the sphere (Kerswell and Davey, 1996; Livermore and Jackson, 2004; Worland, 2004) the expressions for the appropriate expansions of the scalar variables are,

$$e = \sum_{n=1}^{N+1}\sum_{l=0}^{L} e_{ln} r^{k+1} T_{2n-1}(r) P_{2l+m+1}^{m}(\cos\theta) e^{i(m\phi-\omega t)}, \tag{7.23}$$

$$f = \sum_{n=1}^{N+2}\sum_{l=0}^{L} f_{ln} r^{k} T_{2n-1}(r) P_{2l+m}^{m}(\cos\theta) e^{i(m\phi-\omega t)}, \tag{7.24}$$

$$g = \sum_{n=1}^{N+1}\sum_{l=0}^{L} g_{ln} r^{k+1} T_{2n-1}(r) P_{2l+m+1}^{m}(\cos\theta) e^{i(m\phi-\omega t)}, \tag{7.25}$$

$$h = \sum_{n=1}^{N+1}\sum_{l=0}^{L} h_{ln} r^{k} T_{2n-1}(r) P_{2l+m}^{m}(\cos\theta) e^{i(m\phi-\omega t)}, \tag{7.26}$$

$$\Theta = \sum_{n=1}^{N+1}\sum_{l=0}^{L} \Theta_{ln} r^{k-1} T_{2n-1}(r) P_{2l+m}^{m}(\cos\theta) e^{i(m\phi-\omega t)}, \tag{7.27}$$

where e_{ln}, f_{ln}, g_{ln}, f_{ln}, h_{ln} and Θ_{ln} are expansion coefficients corresponding to the lth spherical harmonic mode (which will be of degree $(2l+m+1)$ for e and g but $(2l+m)$ for f, h and Θ to ensure E^S symmetry) and the nth Chebyshev polynomial (which will be of order $2n-1$ to ensure regularity at the origin when multiplied by r^k with k=1 for even m and $k=2$ for odd m). $T_i(r)$ are Chebyshev polynomials of order i and $P_v^u(\cos\theta)$ are associated Legendre polynomials of degree v and order u. Time dependence has been included through analysis into normal modes that are proportional to $e^{i(m\phi-\omega t)}$ (Chandrasekhar, 1961), where ω is a complex number whose real part corresponds to the angular frequency of the mode and whose imaginary part corresponds to the growth rate of the mode. The spherical harmonic expansion is truncated at degree L (so there are $L+1$ spherical harmonic modes in each expansion), and the Chebyshev polynomial series is truncated at degree $N+1$ (and $N+2$ for f), so altogether there are $(5N+6)(L+1)$ unknowns.

7.2.5 Boundary conditions

In addition to the governing equations, in order to find particular solutions, boundary conditions must be implemented on each of the scalar fields. The boundary conditions implemented are documented in this section.

Boundary conditions on the velocity field

The outer boundary is impenetrable ($u_r = 0$ at $r = 1$) and u_r must be regular at the origin (u_r=0 at $r = 0$). Using equation (7.10) $u_r = \frac{\mathcal{L}^2 f}{r^2}$, and these conditions reduce to

the constraint that

$$f = 0 \qquad \text{at } r{=}0 \text{ and } r{=}1 \qquad \text{(origin regularity and impenetrability)} \tag{7.28}$$

At the outer boundary, stress free boundary conditions are imposed. This means that the fluid exerts no tangential force on the impenetrable boundary. Although this scenario is strictly unphysical (the appropriate boundary conditions are really no-slip conditions), Zhang and Jones (1993) have shown that the difference between linear solutions to the rapidly rotating thermal convection problem in a sphere with no-slip and stress free boundary conditions is a second order effect. Their conclusions suggest that the numerical expense of resolving the Ekman boundary layer can be avoided by adopting stress free boundary conditions if one is only interested in linear solutions: this strategy is adopted in the present model. Mathematically, stress free boundary conditions mean that $\frac{\partial}{\partial r}\left(\frac{u_\theta}{r}\right) = \frac{\partial}{\partial r}\left(\frac{u_\phi}{r}\right) = 0$ at $r = 1$. Substituting from equation (7.10) for u_θ and u_ϕ in terms of e and f, and combining the conditions on u_θ and u_ϕ yields a condition on each of e and f,

$$r\frac{\partial^2 f}{\partial r^2} - 2\frac{\partial f}{\partial r} = 0 \qquad \text{and} \qquad r\frac{\partial e}{\partial r} - 2e = 0 \qquad \text{at } r = 1 \qquad \text{(stress free)} \tag{7.29}$$

Boundary conditions on the magnetic field

It is assumed that the outer boundary is an electrical insulator and that the electric current density ($\boldsymbol{J}$) outside the spherical model domain is zero. This is a first approximation to the situation expected at the core-mantle boundary and is also the assumption made in geomagnetic field modelling.

The condition that $\boldsymbol{J} = \boldsymbol{0}$ on the outer boundary means that the perturbation to the electrical current density should also be zero there, so that $\nabla\times\boldsymbol{b}{=}0$ at $r = 1$. Considering only the radial part of this condition and using the fact that $\widehat{\boldsymbol{r}}\cdot(\nabla\times\boldsymbol{b}) = \mathcal{L}^2 g$,

$$\widehat{\boldsymbol{r}}\cdot(\nabla\times\boldsymbol{b}) = \mathcal{L}^2 g = 0 \text{ so } g = 0 \qquad \text{at } r{=}1 \text{ (radial electrical current vanishes)} \tag{7.30}$$

To determine the implications of the horizontal part of the electrical current vanishing, one can note that this implies $\widehat{\boldsymbol{r}}\cdot\nabla\times(\nabla\times\boldsymbol{b}) = 0$ at $r = 1$, but $\widehat{\boldsymbol{r}}\cdot\nabla\times(\nabla\times\boldsymbol{b}) = \mathcal{L}^2\mathcal{D}^2 h$ so $\mathcal{D}^2 h = 0$ or $\frac{\partial^2 h}{\partial r^2} - \frac{\mathcal{L}^2 h}{r^2} = 0$ at $r{=}1$. Assuming $h = H(r)P_l^m(\cos\theta)e^{im\phi}$ this equation can be solved and ensures that for $r \geq 1$ solutions for h take the form $h = \sum_l \frac{h_{lm}}{r^l}P_m^l(\cos\theta)e^{im\phi}$ so that the poloidal magnetic field is a solenoidal potential field.

The other magnetic boundary condition is that the change in the magnetic field should be zero across the outer boundary. Considering the poloidal-toroidal expansion of $\boldsymbol{b}$ in equation (7.11), this will be satisfied if h and $\frac{\partial h}{\partial r}$ are continuous at the boundary. Now the condition that the electrical current vanishes at the boundary has been shown to imply that $h = \sum_l \frac{h_{lm}}{r^l}P_m^l(\cos\theta)e^{im\phi}$ at $r = 1$, so continuity of $\frac{\partial h}{\partial r}$ therefore means that,

$$\frac{\partial h}{\partial r} = -\frac{lh}{r} \qquad \text{at } r{=}1 \qquad \text{(continuity of magnetic field)} \tag{7.31}$$

For further details on the application of electrically insulating boundary conditions in a spherical geometry when using a poloidal-toroidal numerical expansions, the interested reader should consult Worland (2004) or Livermore (2003).

Boundary condition on the temperature field

The temperature at the outer boundary is constrained to be homogeneous, with the temperature perturbation (Θ) there being set to zero.

$$\Theta = 0 \qquad \text{at } r{=}1 \qquad \text{(isothermal outer boundary)} \tag{7.32}$$

This boundary condition is implemented in order to simplify the physics of the model, and is unlikely to be true at the core-mantle boundary. The heterogeneous nature of the lowermost mantle (Lay et al., 1998; Wysession et al., 1998) and the likelihood of structurally complex convection there (Hilst et al., 1998; Tackley, 1998) suggest that the outer boundary of the core will experience thermally inhomogeneous boundary conditions. Discussion of the impact of inhomogeneous thermal boundary conditions on flow within the core can be found, for example, in Zhang and Gubbins (1993), Gibbons and Gubbins (2000), Bloxham (2002) and Christensen and Olson (2003).

7.2.6 Formulation of the eigenvalue problem

Substituting equations (7.23) to (7.27) into equations (7.13) to (7.17) yields a set of linear equations, each specifying the time derivative of each of the modes of e_{nl}, f_{nl}, g_{ln}, h_{nl} and Θ_{nl} in terms of the other coefficients. Such sets of equations are constructed at N collocation points[1] in radius, whose positions are determined by the first N non-trivial zeros of the Chebyshev polynomial T_N. The boundary conditions (excluding those for regularity) are also included in the system providing 6 additional constraint equations.

Noting that because all the modes are proportional to $e^{-i\omega t}$ so that $\frac{\partial}{\partial t} = -i\omega$, the system of equations can be recast in the the form of an complex, generalised eigenvalue problem

$$\lambda \boldsymbol{\mathcal{B}} \boldsymbol{x} = \boldsymbol{\mathcal{A}} \boldsymbol{x} \tag{7.33}$$

where $\lambda = -i\omega$ is a complex eigenvalue, $\boldsymbol{\mathcal{B}}$ is a matrix of the factors pre-multiplying the $\frac{\partial}{\partial t}$ terms in the system of equations and $\boldsymbol{\mathcal{A}}$ is a matrix containing the pre-factors of all the other terms in the governing equations. $\boldsymbol{x}$ is a vector containing the $(5N + 6)(L+1)$ unknown coefficients (the +6 comes from the 6 boundary conditions) arranged sequentially in the order f_{ln}, e_{ln}, Θ_{ln}, g_{ln}, h_{ln}, listing the N Chebyshev modes and the 6 boundary conditions (1 for each scalar except f_{ln} which has 2), before looping over the $(L+1)$ spherical harmonic modes (see Worland (2004) for further details).

[1] consult Boyd (2001) or Canuto et al. (2001) for further details on the collocation method.

Due to the special properties of the Malkus field (see §6.5.2), only the operator $\mathcal{Q}$ (arising from the Coriolis force) couples the evolution equations for a particular spherical harmonic mode to adjacent ($l \pm 1$) spherical harmonic modes (**?**). With appropriate indexing of the matrices and vectors, this means that the matrix $\boldsymbol{\mathcal{B}}$ turns out to be diagonal (with no mode coupling) and the matrix $\boldsymbol{\mathcal{A}}$ is banded (see, for example, Golub and Van Loan (1996) for an explanation of this concept and its numerical advantages).

7.3 Numerical solution of eigenvalue problem

Several techniques exist for solving generalised, complex eigenvalue problems such as equation (7.33). The most widely used (and that employed by Jones et al. (2003) and Worland (2004)) is that of inverse iteration (Press et al., 1992), whereby λ (with Re $\{\lambda\}$ the mode's growth rate and Im$\{\lambda\}$ the mode's angular frequency) can be determined, given some initial guess for λ. Usually the guess Re$\{\lambda\}$=0 is made to enable modes with zero growth rate (marginal modes) to be located; in this case only a guess for the angular frequency of the marginal wave is required in order for the procedure to be carried out.

For a specific choice of the parameters Λ, E, Pr and Pr_m, a particular m is typically considered for a range of Ra. The Ra for which the mode has zero growth rate is found by successive iterations, with Ra varied in a systematic manner, (Numerical Algorithm Group (NAG) routines are available to enable one to do this efficiently). By doing this for all m, the m requiring the lowest Ra for a zero growth rate can be identified. This mode is defined as possessing the critical wavenumber (m_c), critical angular frequency (ω_c) and critical Rayleigh number (Ra_c) for a specific choice of Λ, Pr and Pr_m and E. The successful application of this method was demonstrated by Worland (2004) for $\Lambda < 0.1$ when predictions for m_c, ω_c and Ra_c were available from the global asymptotic theory of Jones et al. (2003). It was unfortunately observed that the numerical results and asymptotic predictions began diverging when $\Lambda \sim 1$, indicating that in the strong field regime the asymptotic theory was no longer useful for supplying the starting guesses required by inverse iteration.

To circumvent the need for a reasonable initial guess for the angular frequency of the solution (and to enable several eigenvalues and their associated eigenvectors to be examined simultaneously) an implicitly-restarted Arnoldi solution method (Golub and Van Loan, 1996) was implemented using ARPACK routines[2] (Lehoucq et al., 1998) appropriate for solving a complex, generalised eigenvalue problem with banded matrices. Instead of solving the eigenvalue problem directly, this method solves a problem with the similar matrices, but with shifted eigenvalues. The largest magnitude eigenvalues found in the shifted problem then correspond to the eigenvalues of the original problem closest

[2]See the website http://www.caam.rice.edu/software/ARPACK; the routine znbdr4.f describing an example of the solution to a generalised eigenvalue problem with banded matrices was the basis for the solution routine implemented in this thesis.

in magnitude to the user chosen shift (see, for example, the discussion in Livermore (2003)). In the context of the linear stability problem, eigenvalues with the largest real part (growth rate) are sought; these will be obtained provided the user chosen real shift is much larger than user chosen imaginary shift. In the present application, because the optimal imaginary shift was unknown, it was varied in regularly spaced steps over a range of conceivable values and the largest (unshifted) eigenvalues were recorded.

7.3.1 Criteria for excepting and rejected eigenvalues

In practise, the implicitly-restarted Arnoldi method described above was implemented (using fairly low truncations) and the 5 eigenvalues with largest real part were found. Next, each of these 5 eigenvalues was found again to higher accuracy using the more efficient inverse iteration method with the initial guess for $\mathrm{Im}\{\lambda\}$ supplied by the result from of the low resolution Arnoldi calculation. The residual $(\boldsymbol{\mathcal{A}}\boldsymbol{x} - \lambda\boldsymbol{\mathcal{B}}\boldsymbol{x})$ and the absolute difference between complex eigenvalues at two different truncation levels ($\delta\lambda = \lambda_{L1N1} - \lambda_{L2N2}$) were calculated. Only eigenvalues with $(\boldsymbol{\mathcal{A}}\boldsymbol{x} - \lambda\boldsymbol{\mathcal{B}}\boldsymbol{x}) < 10^{-12}$ and $\frac{\delta\lambda}{|\lambda|} < 10^{-5}$ were accepted as good eigenvalues[3] (see Boyd (2001) for a discussion of these useful criteria for determining eigenvalues correctly).

All the results reported and discussed in this chapter use a non-dimensional scheme based around the viscous diffusion time scale, but the matrices actually solved in the eigenvalue code employed a different non-dimensionalisation, based on the MC time scale ($\tau_{MC} = \frac{2\Omega r_0^2 \rho_0 \mu_0}{B_0^2}$). There is a one-to-one mapping between the viscous and MC non-dimensionalisations, so this issue has no bearing on the results reported and interpretations made. Numerically, however, for large Λ and small E, the viscous non-dimensionalisation leads to very small matrix elements causing the matrices to be ill-conditioned. The MC non-dimensionalisation was used in order to lessen this problem though it can never be completely avoided.

Graphics routines were written in MATLAB allowing the solutions contained within the eigenvector $\boldsymbol{x}$ to be plotted: u_r, u_θ, u_ϕ, b_r, b_θ, b_ϕ or Θ could be plotted in equatorial sections, meridional sections or in Hammer-Aitoff projections of a spherical surface.

7.3.2 Benchmarking the eigenvalue solver code

Two benchmarking tests were carried out to ensure that the numerical method was functioning correctly. First, the established results of Jones et al. (2003) in the weak field (small Λ) regime were reproduced using the new code (with the ARPACK solver and MC

[3]Optimal truncation parameters were determined in two steps: (i) Performing inverse iteration at high resolution with guesses supplied from the Arnoldi calculations and enforcing selection criteria in order to accurately determine the eigenvalue and (ii) Starting from low truncation values the eigenvalue was recalculated using inverse iteration. The truncation was then increased in small steps until the criteria for good eigenvalues was just satisfied and an eigenvalue identical to 6 significant figures to that found in the high resolution calculation was obtained.

non-dimensionalisation). This demonstrated that these extensions to the original code had not introduced any errors. Secondly, the linear eigenvalue code was benchmarked in the $\Lambda \sim 1$ regime against results from a nonlinear, time-stepping code (the Leeds Spherical Dynamo[4] (LSD) code that was developed by Steve Gibbons and Ashley Willis). Results were kindly provided by A. Willis, personal communication, March 2005. In LSD, the Malkus magnetic field was imposed along with stress free, electrically insulating and isothermal boundary conditions and the spherical shell thickness increased until it was almost a full sphere and only E^S modes included. These conditions were designed to match as closely as possible those in the linear eigenvalue code. Examples of results obtained looking for the onset of convection (over a range of $0.1 \leq \Lambda \leq 10$) using the two codes are plotted for comparison in figure 7.1 and listed in Table 7.1. The two approaches agree well, especially given that the time-stepping code is actually a thick spherical shell, whereas the eigenvalue solver code is a full sphere. This good agreement over at $\Lambda \sim \mathcal{O}(1)$ gives confidence in that results reported in the following sections are correct.

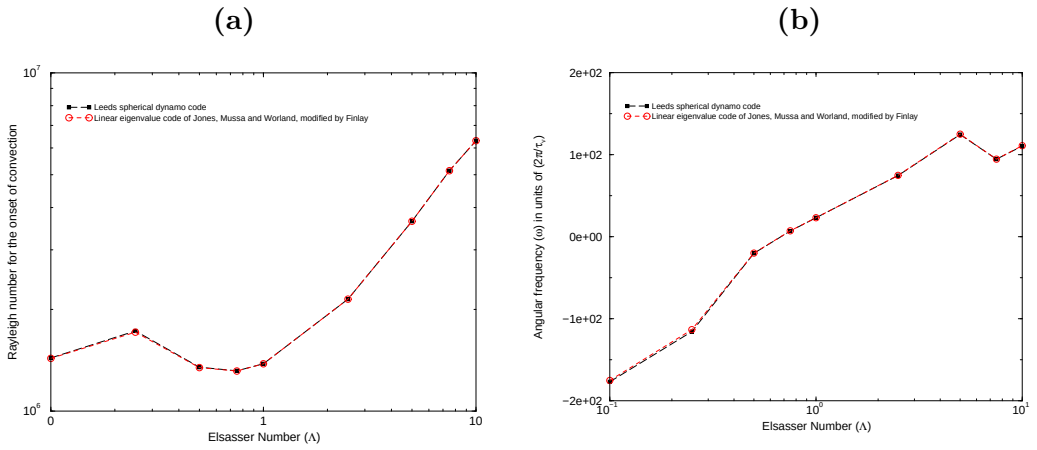

Figure 7.1: Benchmarking of linear Magnetoconvection code.
Comparison of results from the eigensolver code and the LSD code for $E = 10^{-4}$, $Pr = 1$, Pr_m=1 and m=5 and $0.1 \leq \Lambda \leq 10$. Results for the Rayleigh number at the onset of convection are shown in (a) and the corresponding angular frequencies are shown in (b).

7.4 Results

In this section, the results from a parameter survey of the properties of hydromagnetic waves are reported. All the results concern waves that are marginally critical (have zero growth rate), for a particular choice of azimuthal wavenumber m and the non dimensional control parameters: the Ekman number E, Prandtl number Pr, magnetic Prandtl number Pr_m and Elsasser number Λ. The Ra number for zero growth rate and

[4]The LSD code has successfully reproduced the dynamo benchmark (Christensen et al., 2001) and is also capable of performing magnetoconvection studies with an imposed field.

Elsasser Number (Λ)	Ra (eig code)	Ra (time-step code)	ω (eig code)	ω (time-step code)
0.1	0.14367e7	0.14337e7	-0.17679e3	- 0.1752e3
0.25	0.17266e7	0.17123e7	-0.11565e3	-0.1133e3
0.5	0.13494e7	0.13455e7	-0.20176e2	-0.1996e2
0.75	0.13171e7	0.13150e7	0.70652e1	0.7162e1
1.0	0.13819e7	0.13801e7	0.23258e2	0.2325e2
2.5	0.21442e7	0.21433e7	0.74607e2	0.7487e2
5.0	0.3644e7	0.36457e7	0.12471e3	0.1252e3
7.5	0.51401e7	0.51387e7	0.94588e2	0.9471e2
10.0	0.63047e7	0.63059e7	0.11067e3	0.11110e3

Table 7.1: Comparison of results from eigenvalue and time-stepping codes. Results (to 6 S.F.) obtained by the time-stepping code and the eigenvalue code for the same imposed field, boundary conditions and parameters.

the associated angular frequencies ω along with the eigenvectors defining the physical structure of the wave perturbations are calculated by the numerical eigenvalue solver code described in the previous section. By considering the marginal modes for all m, attention is not just focused on the most unstable mode, but other modes that could also be excited during supercritical convection (Zhang, 1999) or by some other excitation mechanism (see §6.6, chapter 6) are also considered. The range of parameters studied is chosen to span likely values in Earth's core as far as computational limitations will permit. The types of waves possible and their different structures are described first as illustrative examples before dependences of wave properties on each of the control parameters is described.

7.4.1 Wave types and their structure

In this section, brief descriptions of defining properties of the structure of different types of thermal (convection) driven hydromagnetic waves are described, so they can be contrasted. The best way to appreciate the wave's structure is of course to consult the figures.

Magnetically-modified thermal Rossby waves

An example of a magnetically-modified thermal Rossby wave is found in figure 7.2 for a case when Λ=0.1, m=8, Pr=1, Pr_m=1, E=10^{-6}. Field perturbations are localised at high latitudes, are almost z independent, have small latitudinal extent and are strongly spiralling. These waves are most easily excited for weak Λ so are unlikely to be of importance in Earth's core (see §7.4.3 for a discussion of their dependence on Λ).

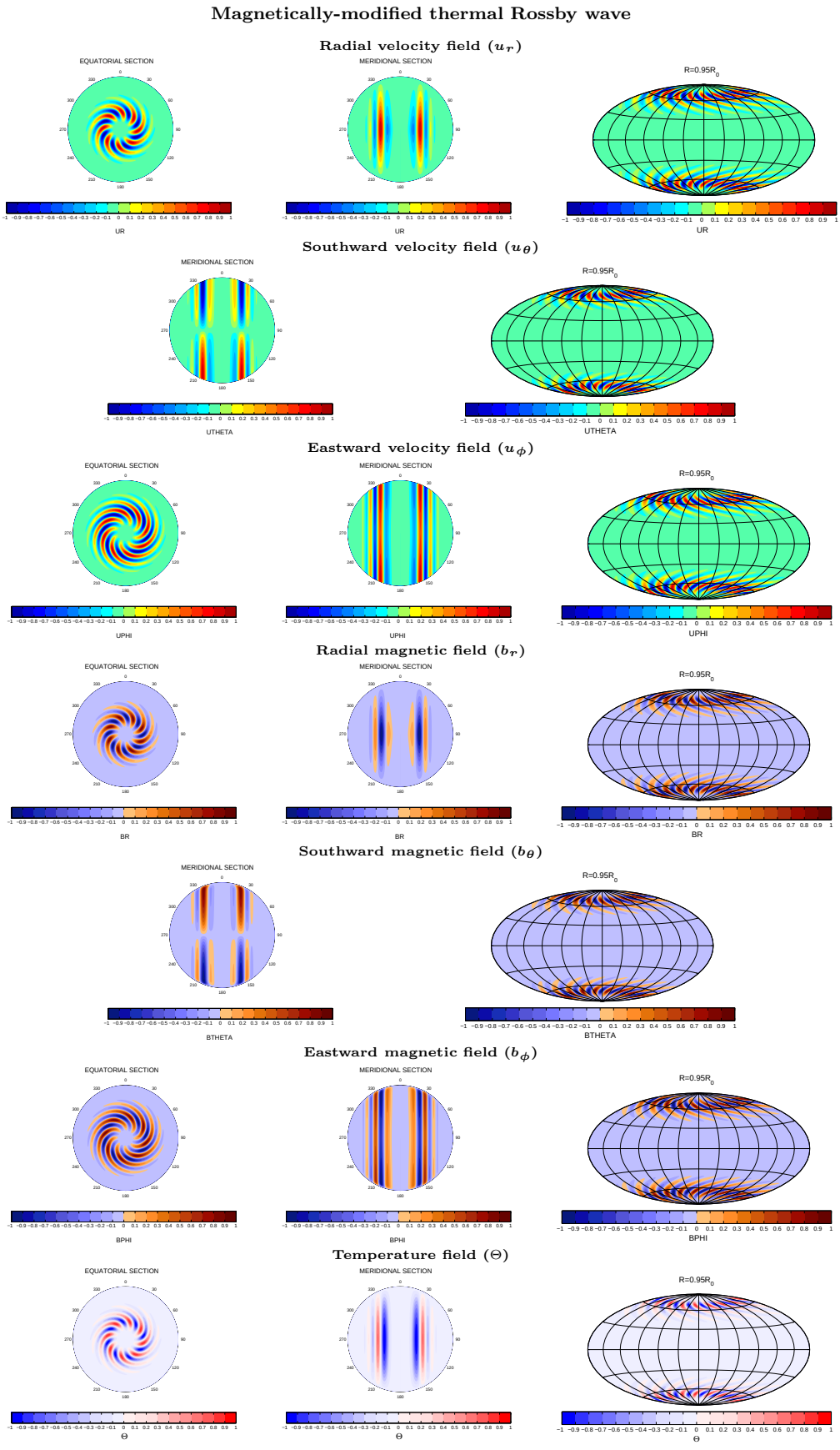

Figure 7.2: Marginal wave with $m = 8$, Λ=0.1, m=8, Pr=1, Pr_m=1 E=10^{-6}.

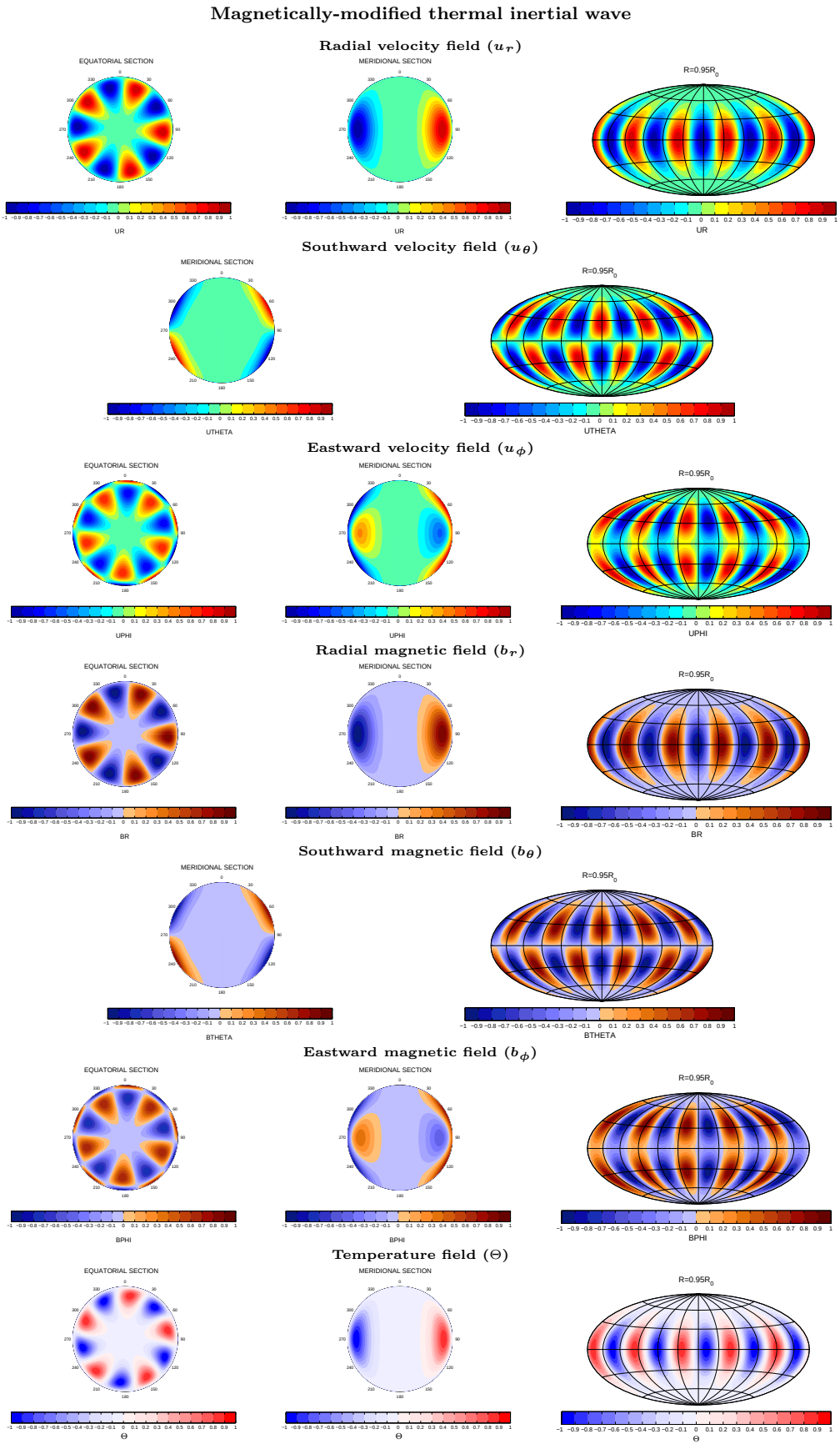

Figure 7.3: Marginal wave for Λ=1, m=5, Pr =10^{-3}, $Pr_m = 1$, E=10^{-6}.

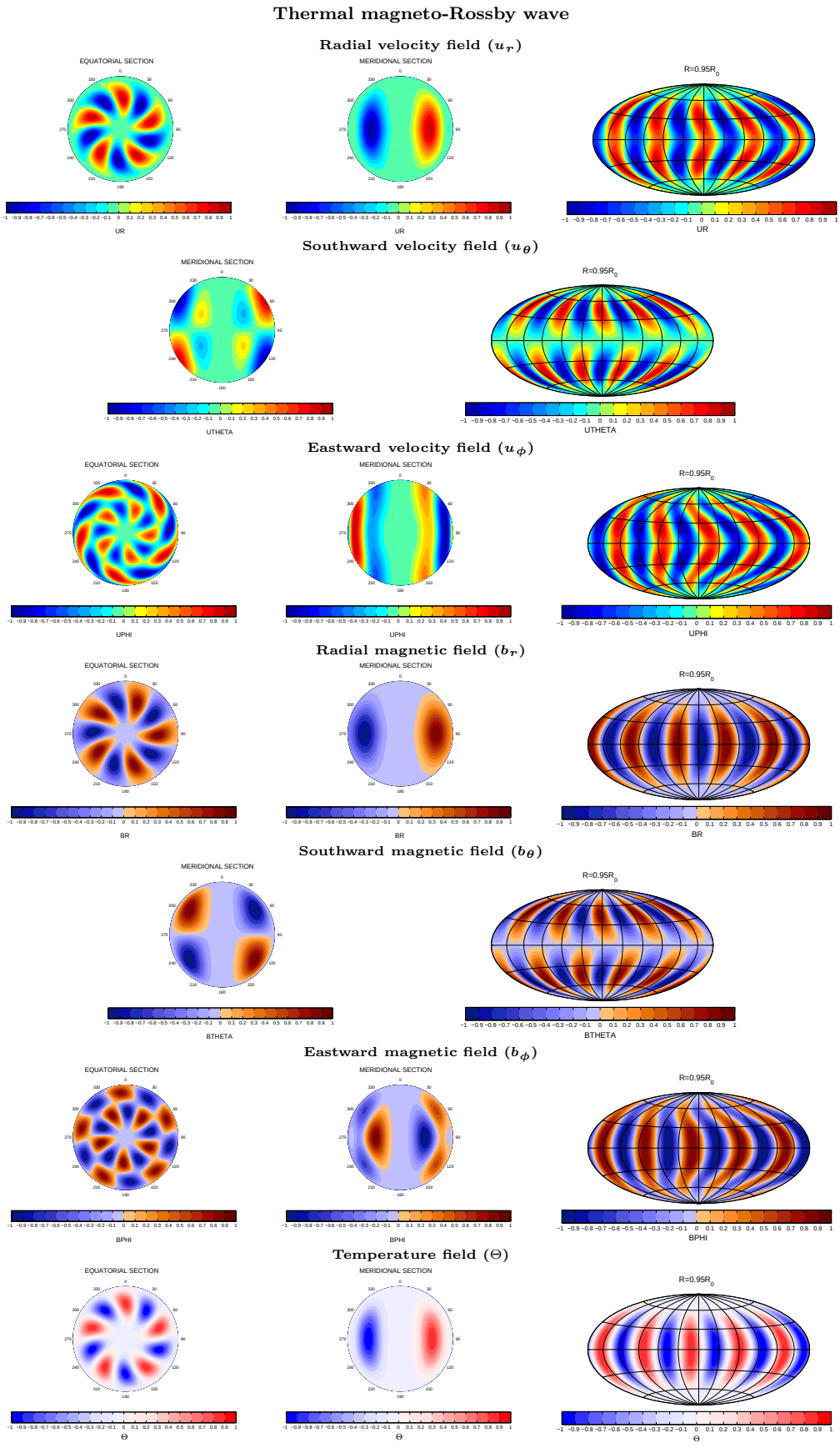

Figure 7.4: Marginal wave for m=5, Λ=1, Pr=0.1, Pr_m=10^{-6},E=10^{-6}.

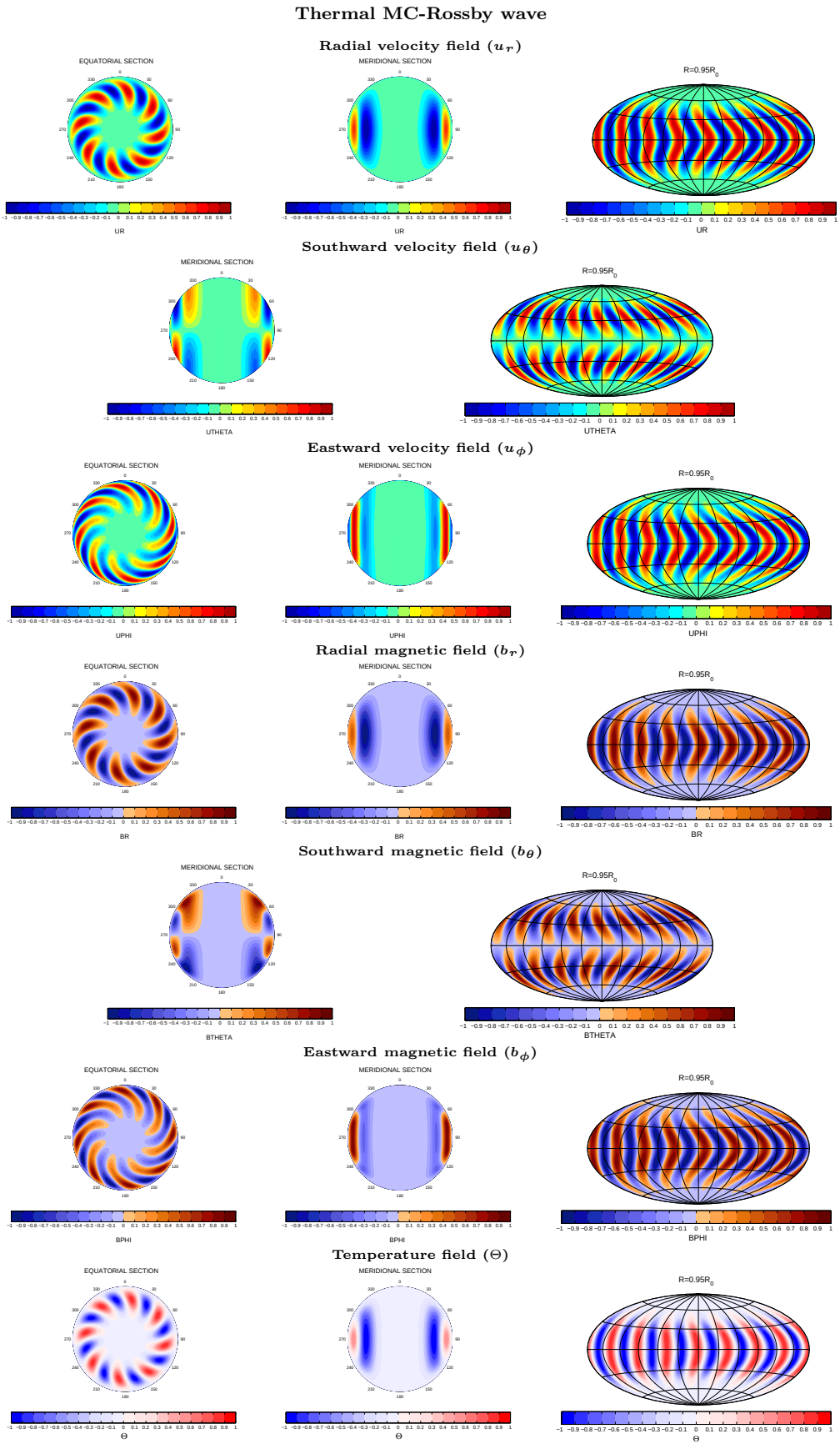

Figure 7.5: Marginal wave with Λ=1, m=8, Pr=1, Pr_m=10^3, E=10^{-6}.

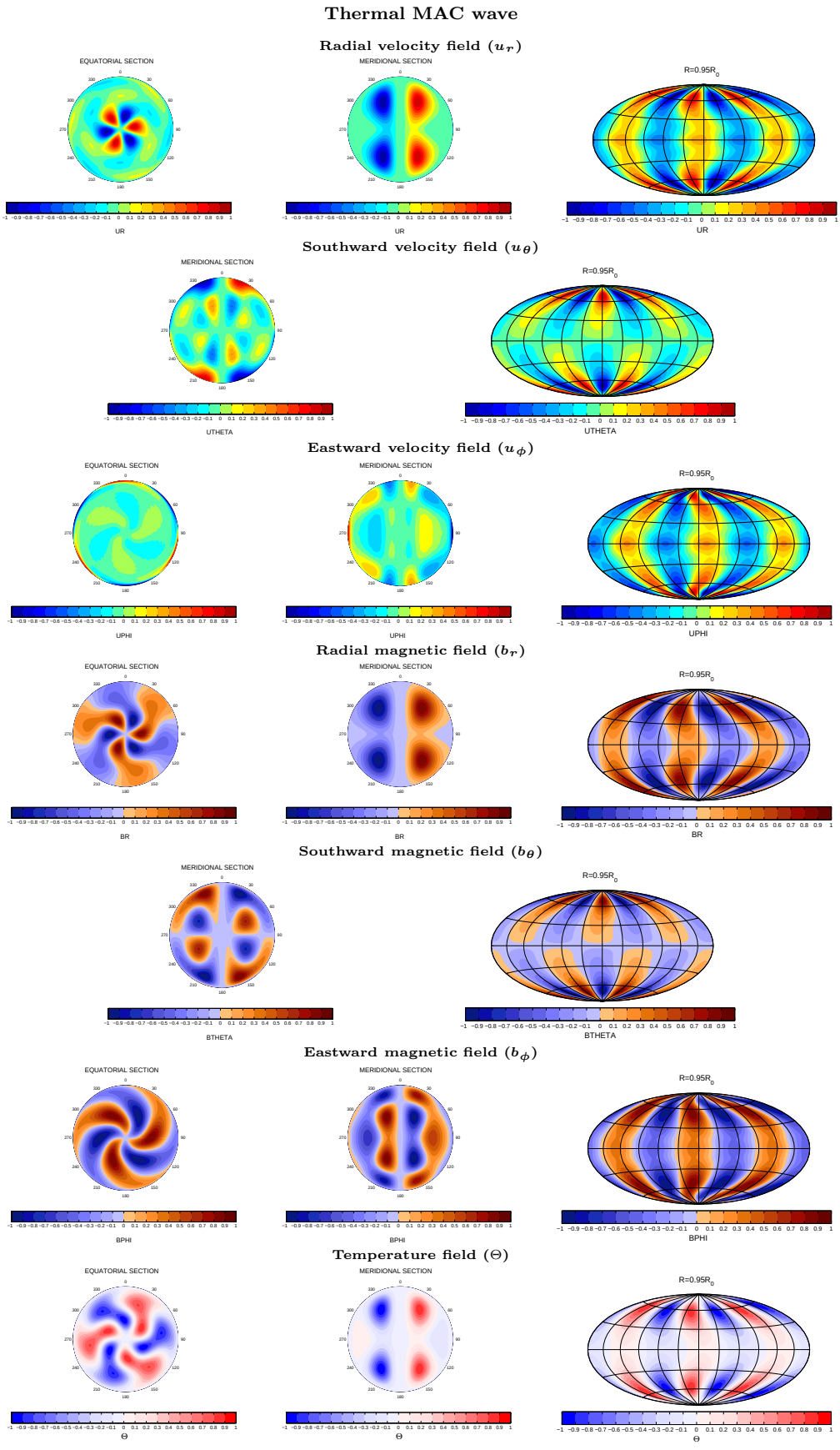

Figure 7.6: Marginal wave for m=3, Λ=10, Pr=1, Pr_m=1, E=10^{-6} .

Magnetically-modified thermal inertial waves

An example of a magnetically-modified thermal inertial wave is found in figure 7.3 for a case when Λ=1, m=5, Pr=10^{-3}, Pr_m=1, E=10^{-6}. Field perturbations are located close to the outer boundary, there is little spiralling and considerable z dependence with disturbances having highest amplitude close to the outer boundary in the equatorial plane. These waves are only easily excited for very low Pr so are also unlikely to be of importance in Earth's core (see §7.4.4 for a discussion of their dependence on Pr).

Thermal magneto-Rossby waves

An example of a thermal magneto-Rossby wave is found in figure 7.4 for a case when Λ=1.0, m=5, Pr=0.1, Pr_m=10^{-6}, E=10^{-6}. Field perturbations are localised at low latitudes close to the outer boundary where the imposed magnetic field is strong, but have large latitudinal extent and are not strongly spiralling. Perturbations are again almost z independent in this case. These waves are very likely to be excited by convection in Earth's core but are characterised by their rather slow propagation speeds (from chapter 6 equation (6.67), $\omega \sim \frac{\beta^* m}{\Lambda(Pr-Pr_m)}$ on the viscous diffusion time scale).

Thermal MC-Rossby waves

An example of a thermal MC-Rossby wave is found in figure 7.5 for a case when Λ=1.0, m=8, Pr=1, Pr_m=10^3, E=10^{-6}. The structure of thermal MC-Rossby waves is rather similar to the thermal magneto-Rossby waves being predominantly z independent, though these waves are more strongly spiralling. These waves are only easily excited for very large Pr_m so are also unlikely to be of importance in Earth's core (see §7.4.5 for a discussion of their dependence on Pr_m).

Thermal MAC waves

An example of a thermal MAC wave is found in figure 7.6 for a case when Λ=10.0, m=3, Pr=1, Pr_m=1, E=10^{-6}. This wave has strong z dependence, with the structure being fully 3D and the disturbance filling the whole sphere. These waves are only easily excited for $\Lambda > 5$ so are probably unlikely to be the important in Earth's core.

Generic conclusions on hydromagnetic wave structure

The perturbations in b_r observed close to the outer boundary can only be caused by a distortion of the imposed azimuthal magnetic field associated with the hydromagnetic wave mechanism. This is therefore a possible mechanism by which hydromagnetic waves could produce an observable wave pattern in B_r at the core surface. It is noticeable

that maxima in b_r produced by this mechanism occur where the perturbation in the azimuthal component of the magnetic field (b_ϕ) is zero (this is especially clear in figure 7.3). This will be a useful diagnostic when studying more realistic models including poloidal imposed fields and attempting to determine the mechanism causing concentrations in B_r at the outer boundary.

The velocity field perturbations associated with the hydromagnetic waves also follow a generic pattern. The waves are associated with a alternating sequence of upwellings and downwellings in u_r close to the outer boundary. Upwellings are found at positions of divergence of the azimuthal flow while downwellings are found at positions of convergence of the azimuthal flow. This generic pattern of flow can be utilised in the construction of simple models of the action of wave flows on B_r (see chapter 8).

7.4.2 Dependence on E

All the results shown so far have been for $E = 10^{-6}$. What impact does varying E have on hydromagnetic wave properties? To address this question the properties of two waves (m=8 and m=5 for Λ=1.0, $Pr = Pr_m = 1$) were studied for E between 10^{-2} and 5×10^{-8}. The results of this investigation are found in figure 7.7.

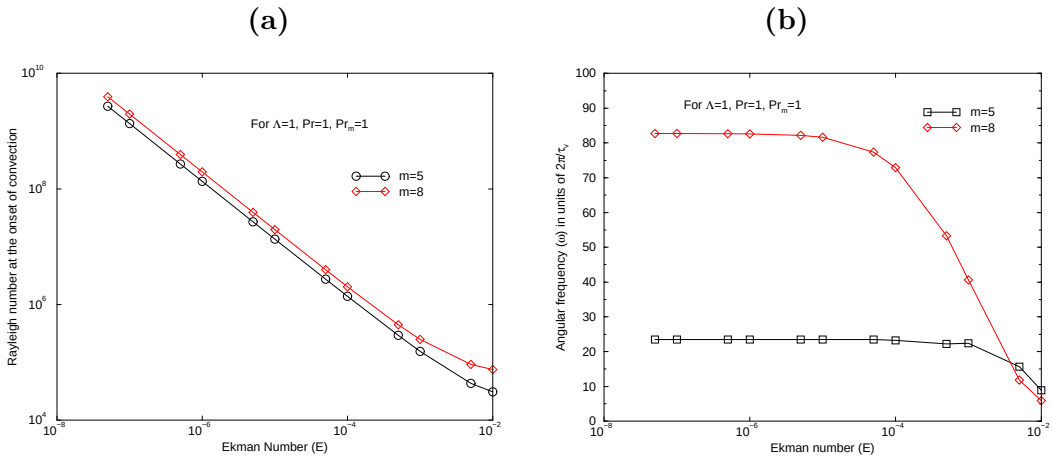

Figure 7.7: Dependence of Ra and ω on E for m=5, 8.
The Rayleigh number Ra for the onset of convection (in the form of thermally-driven hydromagnetic waves) in (a) and the associated angular frequencies ω in (b). For E varied from 10^{-2} to 5×10^{-8} for m=5 and 8. The Prandtl number Pr, the magnetic Prandtl number Pr_m and the Elsasser number Λ are 1 for all cases shown.

It is found that for $E < 10^{-4}$ the results approach an asymptotic low E limit with Ra proportional to E^{-1} for fixed m. This is the dependence expected for Ra at the onset of convection in the form of thermal magneto-Rossby waves (see chapter 6). ω approaches a constant value (measured on the viscous diffusion time scale) as E tends to zero.

These results suggest that when studying linear hydromagnetic waves, $E = 10^{-6}$ is sufficient to be in the low E regime appropriate to Earth's core (where $E \sim 10^{-15}$).

However, this result may not extend to the study of nonlinear hydromagnetic waves where saturation and coupling mechanisms must also be in the low E asymptotic regime.

7.4.3 Dependence on Λ

The most important parameter for determining the mechanism underlying the hydromagnetic waves obtained is the Elsasser number Λ which measures the strength of the imposed magnetic field when the rotation rate is fixed. The value of the Elsasser number in Earth's core is not well known because the toroidal field strength there cannot be directly measured. Using the observed poloidal field strength leads to an estimate $\Lambda \sim 0.1$ which is taken to be the lower limit of the Elsasser numbers investigated here. It is however possible (and perhaps even likely if the dynamo is in a strong field regime (see, for example, Roberts (1978); Hide and Roberts (1979); Zhang and Schubert (2000))) that the toroidal magnetic field is many times stronger than the poloidal field. Zhang and Fearn (1993) have argued that magnetic instability becomes very likely for $\Lambda > 10$ so this provides an upper limit for the time-averaged Λ in Earth's core; this estimate is employed as the upper limit for the range of Λ investigated here.

In figure 7.8 the Rayleigh number Ra for the onset of convection and the angular frequency ω of the associated waves are plotted as a function of Λ for different choices of m between 2 and 9 with $E = 10^{-6}$ and $Pr = Pr_m = 1$. Two distinct behaviours are evident. For low Λ and m=2 to 6, as Λ increases, Ra increases with the angular frequency becoming larger and the propagation direction eastwards. This is the behaviour predicted in chapter 6 for magnetically-modified thermal Rossby waves. For $\Lambda \sim 1$ or greater, waves have smaller angular frequencies (propagate more slowly) and Ra is observed to decrease to a minimum around $\Lambda = 1$ before beginning to increase again. This is behaviour that expected for both thermal magneto-Rossby waves and also for thermal MAC waves[5] that may be present at larger Λ. The behaviour illustrated by the red curve marking the lowest Ra for m between 2 and 9 in figure 7.8a is in agreement with the scenario proposed by Fearn (1979b) (see figure 6.6).

In figure 7.9, Ra and ω are plotted versus m for a range of Λ between 0.1 and 10. Figure 7.9a shows that for low Λ waves are more easily excited when m is large, while for $\Lambda \sim 1$ wavenumbers in the range m= 3 to 6 are most easily excited and at large $\Lambda \sim 10$ the lowest wavenumbers (m=2, 3) are most easily excited. Figure 7.9b and 7.9c illustrate the dispersion (dependence of ω on m) for the various waves. At low Λ, as the wavenumber increases waves travel faster eastwards. For $\Lambda = 1$ lower wavenumbers appear to prefer to travel eastwards, while the higher wavenumbers prefer to travel westwards (all are

[5]It is difficult to make a clear distinction between thermal magneto-Rossby waves and thermal MAC waves looking at Ra and ω, because for a particular m the transition between the modes is continuous. They are best distinguished by considering the wave structures (see figures 7.4 and 7.6). The thermal MAC wave deviate strongly from z invariance, while thermal magneto-Rossby wave structure is primarily z invariant.

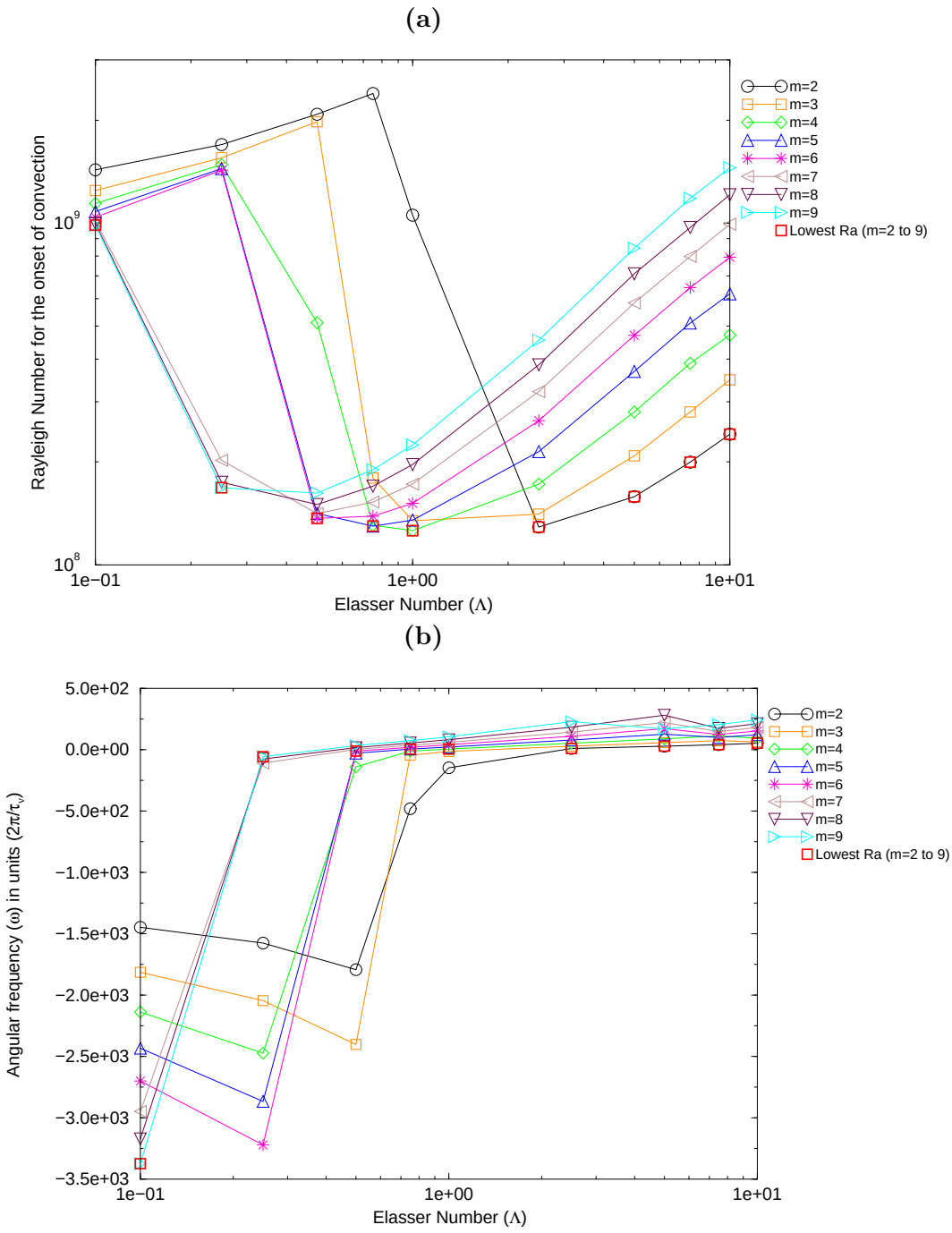

Figure 7.8: Dependence of Ra and ω on Λ for m=2 to 9.
The Rayleigh number Ra for the onset of convection (in the form of thermally-driven hydromagnetic waves) in (a) and the associated angular frequencies ω of the waves (convention negative ω means eastward propagation) in (b), as the Elsasser number is increased from 0.1 to 1.0, for azimuthal wavenumbers m=2 to 9. The red squares mark the trend for the lowest Rayleigh number found over this range of wavenumbers. The Prandtl number Pr and the magnetic Prandtl number Pr_m are 1 in all cases and the Ekman number E is 10^{-6} in all cases.

travelling very slowly on a time scale ~ 0.1 to 0.01 τ_ν where τ_ν is the viscous diffusion time scale. For large Λ modes always appear to travel westwards, with high wavenumbers travelling faster, but being more difficult to excite.

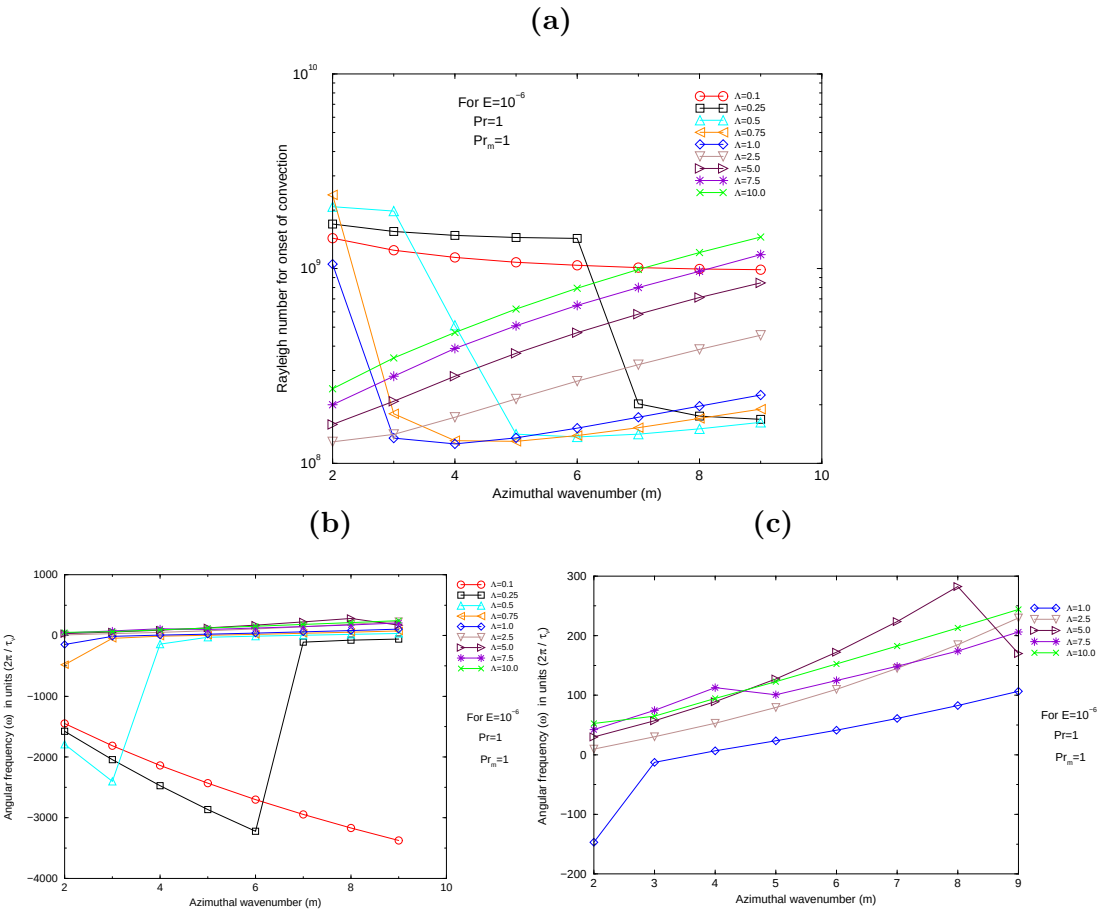

Figure 7.9: Dependence of Ra and ω on m for Λ=0.1 to 10.
Rayleigh number Ra for the onset of convection (in the form of thermally-driven hydromagnetic waves) in (a) and the associated angular frequencies ω plotted against m for Λ=0.1 to 10 in (b). (c) is a magnified version of (b) with only $\Lambda > 1$ plotted. The Prandtl number Pr, the magnetic Prandtl number Pr_m are 1 in all cases and the Ekman number E is always 10^{-6} in the examples plotted.

7.4.4 Dependence on Pr

The Prandtl number Pr defines the ratio of the thermal diffusion time scale to the viscous diffusion time scale. If values for the expected molecular diffusivities in Earth's core are adopted, this will have size ~ 0.1, whilst if turbulent diffusivities are invoked (Roberts and Glatzmaier, 2000a) then it has been argued that $Pr = 1$. A range of values Pr from 10^{-3} to 10^5 was investigated: the results are displayed in figure 7.10.

Two distinct regimes are evident, with a transition region between them close to Pr=1. At large Pr, Ra is independent of Pr, and ω is very small. As Pr is decreased to Pr=1, Ra begins to fall until at very low Pr a different trend for Ra and ω is observed. In this

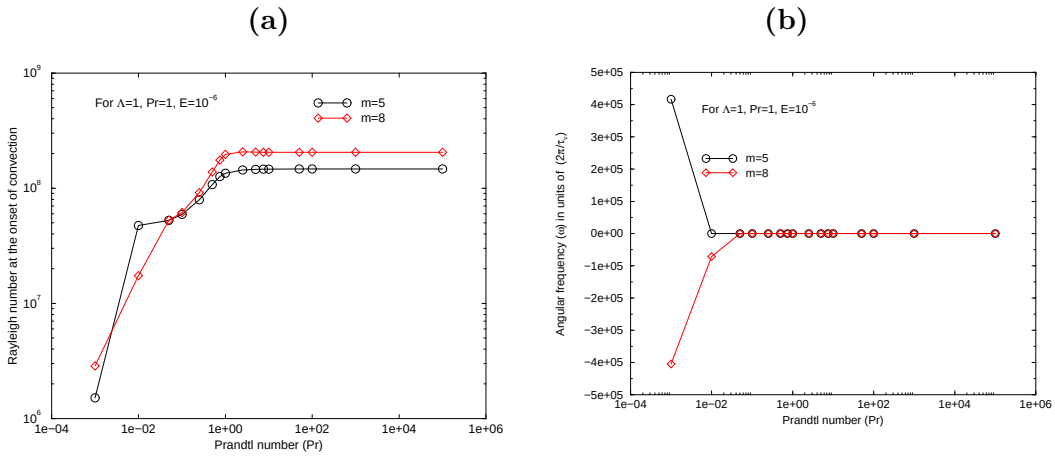

Figure 7.10: Dependence of Ra and ω on Pr for m=5, 8.
The Rayleigh number (Ra) for the onset of convection (in the form of thermally driven hydromagnetic waves) in (a) and the associated angular frequencies (ω) of the waves as plotted as a function of Pr which varies from 10^{-3} to 10^{5} for m=5 and 8. The magnetic Prandtl number Pr_m is 1, the Ekman number E is 10^{-6} and the Elsasser number Λ is 1 in all cases shown.

regime Ra is significantly smaller and ω is much larger with both eastward and westward propagation being possible.

In this low Pr regime, inertial effects are very large and the resulting hydromagnetic waves are the magnetically modified thermal-inertial waves first discussed by Zhang (1995). The structure of these waves is displayed in figure 7.3 and is noteworthy because field perturbations occur close to the outer boundary and considerable z dependence is present. Is is however unlikely that such waves will be of relevance in Earth's core because the Pr below which they are found scales as $E^{1/2}$ so will be many orders of magnitude lower than the value of 0.1 expected in Earth's core (Ardes et al., 1997).

7.4.5 Dependence on Pr_m

The magnetic Prandtl number Pr_m is the ratio of the magnetic diffusion time scale to the viscous diffusion time scale. In Earth's core, taking molecular values this would be $\sim 10^{-6}$ while it would be ~ 1 if one prefers to use turbulent values for diffusivities. Pr_m between 10^{-6} and 10^{2} were investigated for $E = 10^{-6}$, Pr=1, Λ=1 and $m = 5, 8$. The results are displayed in figure 7.11.

Two distinct regimes are evident: one at large Pr_m and the other at small Pr_m with a gradual transition between them close to Pr_m=1. The high Pr_m mode is very slow, propagating in the westward direction and with low Ra and is probably a thermal MC-Rossby wave that occurs when the effects of magnetic diffusion can be neglected (see figure 7.5 for an example of the structure of such a wave). At very low Pr_m waves also travel westwards, but faster and with slightly higher Ra for the onset of convection

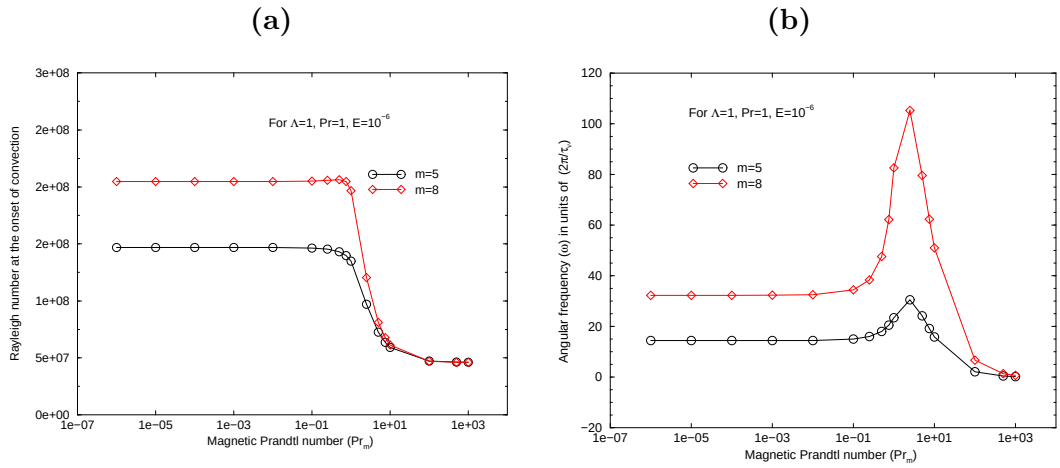

Figure 7.11: Dependence of Ra and ω on Pr_m for m=5, 8.
The Rayleigh number Ra for the onset of convection (in the form of thermally driven hydromagnetic waves) in (a) and the associated angular frequencies ω of the waves are plotted against Pr_m which varies from 10^{-6} to 10^3 for m=5 and 8 in (b). The Prandtl number Pr is 1 the Ekman number E is 10^{-6} and the Elsasser number Λ is 1 in all cases.

than for the thermal MC-Rossby waves. This mode has the properties predicted for the thermal magneto-Rossby wave. The transition between the two types is regular for Ra, but there is a discontinuity in trend for ω, because the thermal MC-Rossby waves frequency varies like Pr_m^{-1} (diverges for small Pr_m), while simple models for thermal magneto-Rossby waves (see §6.6.2) predict that their frequency will tend to a constant for small Pr_m and diverge when $Pr = Pr_m$. In Earth's core it is likely that magnetic diffusion is much more important than viscous diffusion, so Pr_m is anticipated to be much less than 1 and the most relevant waves will be thermal magneto-Rossby waves rather than thermal MC-Rossby waves.

7.5 Discussion of implications for waves in Earth's core

A simple model of hydromagnetic waves has been investigated in this chapter to document the parameter dependence of wave properties in a regime relevant to Earth's core. It would be foolhardy to attempt to link any of the precise details of wave structures and propagation speeds to observations of the geomagnetic field at the core surface given the over-simplified nature of the imposed magnetic field and the lack of any background azimuthal flow. However, several robust conclusions can be made on the basis of the results of this chapter.

In the $\Lambda \sim 1$, $Pr_m << 1$, $Pr \sim 1$, $E \to 0$ regime expected in Earth's core, the most unstable waves driven by thermal instability were found to be of thermal magneto-Rossby type having E^S symmetry and being almost z independent. Wavenumbers m=3 to 6 were found to be most easily excited and the waves propagated either westwards or

eastwards on slow time scales of order 1 to 0.01 τ_ν. The viscous diffusion time scale in Earth's core is not well known, but lies in the range between 10^{10} years (when molecular values for viscosity are adopted) and 10^5 years (when turbulent values for viscosity are adopted). Thus the fastest conceivable time scale for the thermal magneto-Rossby waves studied in this chapter is ~ 1000 years, which is rather slower than the wave-like motions identified in chapter 3 with typical time scales ~ 250 years. This result suggests that propagation of such convection-driven hydromagnetic waves alone may not be a good explanation of the observed azimuthal motions of B_r features at the core surface.

The models in this chapter also convincingly demonstrated that hydromagnetic waves can produce spatially coherent, wave-like patterns in B_r close to the outer boundary of a convecting fluid when a toroidal magnetic field is present. Furthermore, alternating regions of flow convergence and divergence close to the outer boundary are found to be a generic feature associated with such waves. For the E^S thermal magneto-Rossby waves studied in this chapter, with an E^S imposed magnetic field, the magnetic field perturbations at the outer boundary are found to be E^S and centred on the equator. To match with the observations, this suggests that some E^S background magnetic field (either poloidal or toroidal) is required in Earth's core.

7.6 Summary

In this chapter, a numerical investigation of the properties of hydromagnetic waves driven by convection in a spherical geometry with a simple imposed toroidal magnetic field has been carried out. The set of linearised governing equations was solved using an eigenvalue approach and marginally stable modes found. Convection-driven, magneto-Rossby waves were found to be the most likely type of wave to be excited in the regime expected in Earth's core. The E^S waves that were obtained distorted the E^S imposed toroidal field to produce E^S perturbations of B_r close to the outer boundary and were focused on low latitudes. However, their propagation speeds were found to be too slow to account for the azimuthal motions of field features identified in chapter 3 at the core surface. More realistic models including the presence of the background azimuthal flow and imposed magnetic fields compatible with the geodynamo mechanism should be investigated as the next step towards a more rigorous comparison with observations.

Chapter 8

Patterns of magnetic field evolution caused by wave flows

8.1 Introduction

The aim of this chapter is to understand how a propagating wave flow will alter magnetic fields and to determine if such a mechanism can produce spatially and temporally coherent, wave-like, drifting magnetic field patterns. Will propagating concentrations of magnetic field arise? If so what factors govern the amplitude and propagation speed of the field concentrations? Are the resulting patterns of field evolution consistent with observations of magnetic field changes at the core surface? To study these issues purely kinematic models with simple, specified, wave flows are investigated and the evolution of magnetic fields from chosen initial states are determined through the solution of the magnetic induction equation.

Two approaches to the kinematic problem are undertaken. In the first, a simple one dimensional model of a travelling wave flow consisting of a drifting pattern of alternating regions of flow convergence and divergence is solved analytically. This example provides valuable insight regarding mechanisms that could operate in more complex scenarios. Secondly, in a more Earth-like situation, the radial component of the magnetic induction equation at an impenetrable spherical surface is solved for the case of a parameterised spherical wave flow acting on a simple (axial dipole) initial radial magnetic field. A parameter survey is carried out to catalogue changes in field evolution characteristics as the phase speed and the wave flow amplitude are varied.

Finally the effect of wave flows on more complex initial fields is investigated. The 1590 field from *gufm1* is time-stepped forward using different choices of prescribed wave flow and limited magnetic diffusion. The influence of the regularisation applied to field models to eliminate contamination by the crustal field is studied. Hemispherical differences in field evolution patterns are described and their origin discussed. Finally implications for the origins of geomagnetic secular variation and inversions for core flows are discussed.

8.2 1D model of a wave flow acting on a magnetic field

8.2.1 Frozen-flux equation for field evolution

The frozen flux induction equation describes how in the absence of magnetic diffusion magnetic field changes are entirely due to advection of field lines along with the electrically conducting fluid. This can be expressed mathematically as

$$\frac{\partial \boldsymbol{B}}{\partial t} = \nabla \times (\boldsymbol{u} \times \boldsymbol{B}). \tag{8.1}$$

The full magnetic induction equation (see equation (D.3) in appendix D) simplifies to this form when the term $\eta \nabla^2 \boldsymbol{B}$ associated with the effects of magnetic diffusion (Ohmic dissipation) is negligible. The frozen flux assumption is made in the first, simple model presented in this chapter. It is a good first approximation to the scenario being modelled at Earth's core surface when long length scales, and time scales much shorter than the magnetic diffusion time scale are considered. Theoretical arguments in favour of the adoption of the frozen flux assumption can be found in the seminal papers of Roberts and Scott (1965) and Backus (1968) and also in the review of Bloxham and Jackson (1991). The results of numerical experiments suggesting that frozen flux assumption was a useful approximation were reported by Roberts and Glatzmaier (2000b) and Rau et al. (2000). Recently, geomagnetic field models incorporating frozen flux constraints have been developed by Jackson et al. (2005) that are capable of fitting observation within error bounds. The circumstances under which magnetic diffusion should not be neglected have been discussed by Gubbins and Kelly (1996) and Love (1999). The limit of advection-diffusion balance highlighted in the latter papers is discussed further in §8.2.5.

Hydromagnetic wave motions in rotating, spherical containers consist of a propagating sequence of upwellings and downwelling as has been discussed in chapter 7. To study the generic influence of such wave flows on magnetic fields, a simple 2D wave flow is considered here. The idealised wave flow investigated is shown schematically in figure 8.1 and is defined mathematically as

$$\boldsymbol{u} = \begin{pmatrix} u_x(x,z,t)\widehat{\boldsymbol{x}} \\ u_y(x,z,t)\widehat{\boldsymbol{y}} \\ u_z(x,z,t)\widehat{\boldsymbol{z}} \end{pmatrix} = \begin{pmatrix} -U\sin(kx-\omega t)\cos(kz)\widehat{\boldsymbol{x}} \\ 0 \\ U\cos(kx-\omega t)\sin(kz)\widehat{\boldsymbol{z}} \end{pmatrix}, \tag{8.2}$$

where U is maximum magnitude of the flow, $\frac{2\pi}{k}$ is the flow wavelength and $\frac{2\pi}{\omega}$ is the period of the flow. Since this flow is two-dimensional and incompressible, it can be written in terms of a potential function

$$\Psi = \frac{U\sin(kx-\omega t)\sin(kz)}{k}, \tag{8.3}$$

where the flow is then defined to be $\boldsymbol{u} = \nabla \times \Psi \widehat{\boldsymbol{y}} = -\frac{\partial \Psi}{\partial z}\widehat{\boldsymbol{x}} + \frac{\partial \Psi}{\partial x}\widehat{\boldsymbol{z}}$. Contours of Ψ represent instantaneous particle trajectories of the flow and are shown in figure 8.1.

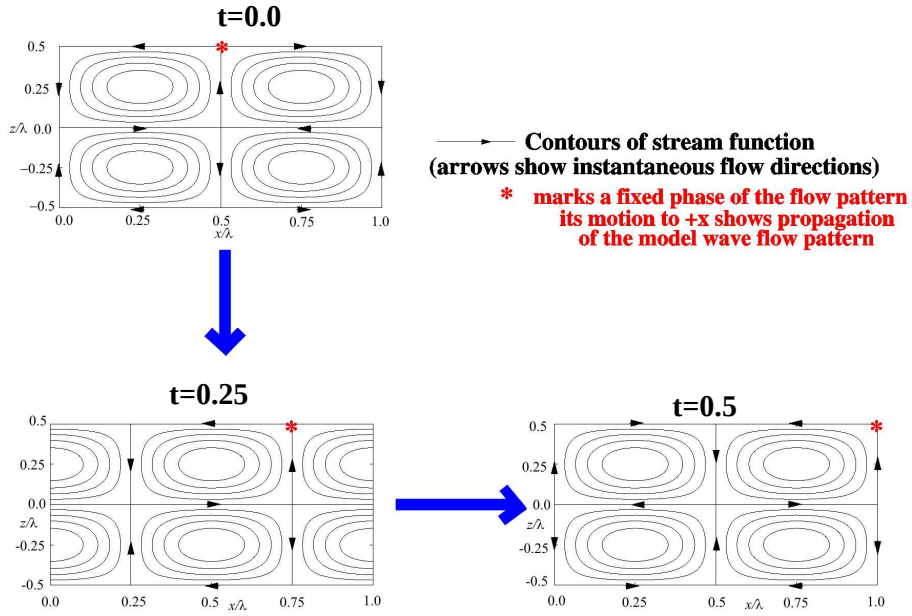

Figure 8.1: Incompressible wave flow used in simple kinematic model. Contours of the stream-function Ψ in the xz plane showing the instantaneous fluid parcel trajectories for the model wave flow as time progresses. The flow pattern always has the same form, but drifts as time progresses towards $+x$. Spatial units in the x and z directions are the flow wavelength ($\lambda = \frac{2\pi}{k}$) and time is measured in units of the flow period ($T = \frac{2\pi}{\omega}$).

Equation (8.2) is a modification of a steady 2D flow that was designed to model convection and has been the subject of several previous kinematic studies by Allan and Bullard (1966), Bloxham (1985; 1986) and Drew (1992). The flow studied here has been altered so the regions of flow convergence and divergence drift towards $+\widehat{\boldsymbol{x}}$ at a constant phase speed ($c_{ph} = \frac{\omega}{k}$) rather than being stationary. Flow convergence and divergence is observed to occur in the $\widehat{\boldsymbol{x}}$ direction at depths $z = \frac{2n\pi}{k}$ where n is any integer (physically this represents the top and bottom edges of the flow cells). Upwelling and downwelling occurs in the z direction, and is a maximum at $z = \frac{(2n+1)\pi}{k}$ at mid-depth in the flow cells.

The magnetic field whose evolution will be determined by the flow (under the frozen flux assumption) can in the most general case be written as

$$\boldsymbol{B} = \begin{pmatrix} B_x(x,y,z,t)\widehat{\boldsymbol{x}} \\ B_y(x,y,z,t)\widehat{\boldsymbol{y}} \\ B_z(x,y,z,t)\widehat{\boldsymbol{z}} \end{pmatrix}. \tag{8.4}$$

Using the conditions for incompressible flow ($\nabla \cdot \boldsymbol{u} = 0$) and solenoidal magnetic fields ($\nabla \cdot \boldsymbol{B} = 0$) and the well known vector identity

$$\nabla \times (\boldsymbol{u} \times \boldsymbol{B}) = (\boldsymbol{B} \cdot \nabla)\boldsymbol{u} - (\boldsymbol{u} \cdot \nabla)\boldsymbol{B} + \boldsymbol{u}(\nabla \cdot \boldsymbol{B}) + \boldsymbol{B}(\nabla \cdot \boldsymbol{u}) \tag{8.5}$$

the frozen-flux induction equation becomes

$$\frac{\partial \boldsymbol{B}}{\partial t} = (\boldsymbol{B}\cdot\nabla)\boldsymbol{u} - (\boldsymbol{u}\cdot\nabla)\boldsymbol{B}. \tag{8.6}$$

The component of this equation in the $\widehat{\boldsymbol{z}}$ direction is then

$$\frac{\partial B_z}{\partial t} = (B_x\frac{\partial u_z}{\partial x} + B_y\frac{\partial u_z}{\partial y} + B_z\frac{\partial u_z}{\partial z}) - (u_x\frac{\partial B_z}{\partial x} + u_y\frac{\partial B_z}{\partial y} + u_z\frac{\partial B_z}{\partial z}) \tag{8.7}$$

For the 2D model wave flow described above, $u_y = 0$ and $\frac{\partial u_z}{\partial y} = 0$ so the governing equation reduces to

$$\frac{\partial B_z}{\partial t} = (B_x\frac{\partial u_z}{\partial x} + B_z\frac{\partial u_z}{\partial z}) - (u_x\frac{\partial B_z}{\partial x} + u_z\frac{\partial B_z}{\partial z}). \tag{8.8}$$

Earth's core-mantle boundary is a solid interface through which no vertical flow occurs. At the top of a flow cell for example at $z = \pi/k$ in equation (8.3) there is also no vertical flow. This similarity means that one can consider the flow defined in equation (8.3) at such a depth to be a crude model that contains the key ingredients of a drifting wave flow adjacent to a rigid boundary such as the core surface. Adopting this assumption, the flow at $z = \pi/k$ is $u_x = U\sin(kx-\omega t)$, $u_z = 0$, $\frac{\partial u_z}{\partial x} = 0$ and $\frac{\partial u_z}{\partial z} = -kU\cos(kx-\omega t)$ so the frozen flux induction equation governing the evolution of B_z becomes

$$\frac{\partial B_z}{\partial t} + U\sin(kx-\omega t)\frac{\partial B_z}{\partial x} + kU\cos(kx-\omega t)B_z = 0. \tag{8.9}$$

It is noteworthy that this is identical to the 1D induction equation without diffusion describing the effects of a compressible wave flow $U\sin(kx-\omega t)\widehat{\boldsymbol{x}}$ acting on a field $B_z\widehat{\boldsymbol{z}}$. This flow consists of alternating regions of flow convergence and divergence. Henceforth the subscript z in $B_z(x,t)$ is dropped and the magnetic field in the $\widehat{\boldsymbol{z}}$ direction is referred to simply as $B(x,t)$ and similarly $U\sin(kx-\omega t)$ is simply denoted by $u(x,t)$.

8.2.2 Changing reference frame to move along with wave flow

The mathematical problem can be simplified by transforming to a frame of reference moving with the phase speed of the wave flow ($c_{ph} = \frac{\omega}{k}$), which for the present flow is a constant. In a frame moving at the phase speed, the wave-pattern is stationary so it is more straightforward to determine the influence of the flow on magnetic field evolution. Similar transformations have been made to aid the determination of core flows from geomagnetic secular variation by Davis and Whaler (1996) and Holme and Whaler (2001).

Following a Galilean transformation to the reference frame drifting with the phase speed of the wave flow, a new variable defining spatial position (ψ) is defined that is related to the original coordinates by $\psi = x - c_{ph}t$. Transforming the flow field u and the magnetic field B to the new co-ordinate system these become

$$u(\psi,t) = \frac{d\psi}{dt} = \frac{dx}{dt} - \frac{d(c_{ph}t)}{dt} = u(x,t) - c_{ph} = U\sin k\psi - c_{ph}, \tag{8.10}$$

and

$$B(\psi, t) = B(x, t). \tag{8.11}$$

The invariance of magnetic fields under Galilean transformation arises because relativistic effects are negligible when considering transformations to frames travelling much slower than the speed of light. This fundamental assumption is implicit in the pre-Maxwell form of the equations of electrodynamics employed in studies of magnetohydrodynamics from which the induction equation is derived (Moffatt, 1978).

Therefore in the new reference frame, equation (8.9) governing the field evolution transforms to

$$\frac{\partial B(\psi,t)}{\partial t} + (U \sin k\psi - c_{ph}) \frac{\partial B(\psi,t)}{\partial \psi} + (Uk \cos k\psi)\, B(\psi,t) = 0, \tag{8.12}$$

or more compactly

$$\frac{\partial B(\psi,t)}{\partial t} = -\frac{\partial}{\partial \psi}[u(\psi,t)B(\psi,t)]. \tag{8.13}$$

A standard mathematical procedure for solving such first order, linear, homogeneous partial differential equations is the method of characteristics (see, for example, Riley et al. (2002) or Ockendon et al. (2003)) which involves simplifying to a set of ordinary differential equations. This method is employed in the next section to find an analytical solution to the problem.

8.2.3 Solution using the method of characteristics

The method of characteristics involves finding a curve in solution space along which the governing partial differential equation (in this case equation (8.12)) is reduced to an ordinary differential equation that can easily be solved. The method consists of two parts, finding appropriate curves in solution space (the characteristic curves) and solving the ordinary differential equation along these characteristic curves.

Position on the characteristic curve can be specified by a single parameter $s = s(\psi, t)$ with derivatives of s, t, ψ related via the chain rule

$$\frac{dB}{ds} = \frac{dt}{ds}\left(\frac{\partial B}{\partial t}\right)_{\psi} + \frac{d\psi}{ds}\left(\frac{\partial B}{\partial \psi}\right)_{t}. \tag{8.14}$$

By choosing the equations of the characteristic curves C to be

$$\frac{dt}{ds} = 1 \qquad \text{and} \qquad \frac{d\psi}{ds} = U \sin k\psi - c_{ph} \qquad \text{so that} \quad \frac{d\psi}{dt} = U \sin k\psi - c_{ph}, \tag{8.15}$$

equation (8.12) simplifies to an ordinary differential equation in s,

$$\frac{dB}{ds} = -kU \cos k\psi\, B. \tag{8.16}$$

Using the relation from equation (8.15) that $ds = \frac{d\psi}{U \sin k\psi - c_{ph}}$, dividing both sides by B and integrating, equation (8.16) can be rewritten as

$$\int_C \frac{dB}{B} = \int_C \frac{-kU \cos k\psi}{U \sin(k\psi) - c_{ph}}\, d\psi, \tag{8.17}$$

so that

$$\ln B \;=\; -\ln\left[\sin k\psi - \frac{c_{ph}}{U}\right] + \ln K, \tag{8.18}$$

or

$$B = \frac{K}{\sin k\psi - \frac{c_{ph}}{U}}, \tag{8.19}$$

where K is a constant that can be determined from the initial state of B. For example, if at t=0, it is known that ψ=ψ_0 and $B(\psi,t)$=$B_0(\psi_0,0)$, then

$$K = B_0(\psi_0,0)\left(\sin k\psi_0 - \frac{c_{ph}}{U}\right). \tag{8.20}$$

So an expression for B in terms of this initial condition is

$$B = \frac{B_0(\psi_0,0)}{\sin k\psi - \frac{c_{ph}}{U}}\left(\sin k\psi_0 - \frac{c_{ph}}{U}\right), \tag{8.21}$$

and recognising that

$$\sin k\psi_0 = \frac{2\tan\frac{k\psi_0}{2}}{1+\tan^2\frac{k\psi_0}{2}}, \tag{8.22}$$

this can be written as

$$B = \frac{B_0(\psi_0,0)}{\sin k\psi - \frac{c_{ph}}{U}}\left(\frac{2\tan\frac{k\psi_0}{2}}{1+\tan^2\frac{k\psi_0}{2}} - \frac{c_{ph}}{U}\right). \tag{8.23}$$

Provided an expression for $\tan\frac{k\psi_0}{2}$ in terms of ψ and t can be found, the development of $B(\psi_0,0)$ is therefore completely known.

Expressions for $\tan\frac{k\psi_0}{2}$ in terms of ψ and t can be derived from the equations of the characteristic curves, though unfortunately this procedure is rather algebraically cumbersome.

Recall that the equation of the characteristic curves from equation (8.15) is

$$\frac{d\psi}{dt} = U\sin k\psi - c_{ph}. \tag{8.24}$$

Letting $z = k\psi$ so that $d\psi = \frac{dz}{k}$ and then separating the variables and integrating

$$\int \frac{dz}{U\sin z - c_{ph}} = \int k\,dt = kt + K_2, \tag{8.25}$$

where K_2 is a constant to be determined. The integral on the left hand side of equation (8.25) is recognisable as a standard integral of elementary transcendental functions (equation (4.3.131) on p.78 of Abramowitz and Stegun (1964)). The solution falls into 3 possible categories depending on relative amplitudes of U and c_{ph}.

When $U^2 > c_{ph}^2$, letting $\Gamma_1 = (U^2 - c_{ph}^2)^{1/2}$

$$\int \frac{dz}{U\sin z - c_{ph}} = \frac{1}{\Gamma_1}\ln\left[\frac{-c_{ph}\tan\frac{z}{2} + U - \Gamma_1}{-c_{ph}\tan\frac{z}{2} + U + \Gamma_1}\right], \tag{8.26}$$

when $U^2 = c_{ph}^2$,

$$\frac{1}{U}\int \frac{dz}{\sin z - 1} = -\frac{1}{U}\tan\left(\frac{\pi}{4} + \frac{z}{2}\right), \tag{8.27}$$

while when $U^2 < c_{ph}^2$, letting $\Gamma_2 = (c_{ph}^2 - U^2)^{1/2}$,

$$\int \frac{dz}{U\sin z - c_{ph}} = \frac{2}{\Gamma_2}\arctan\left[\frac{U - c_{ph}\tan\frac{z}{2}}{\Gamma_2}\right]. \tag{8.28}$$

When t=0 and ψ=ψ_0 so that z=z_0=$k\psi_0$ then equation (8.25) can be used to determine K_2,

$$K_2 = \int \frac{dz_0}{U\sin z_0 - c_{ph}}, \tag{8.29}$$

which has the same solutions as is listed in equations (8.26) to (8.28), but with z replaced by z_0 in each case. All the information required to link $\tan\frac{k\psi_0}{2}$ to ψ and t is now available — the required expressions are obtained by substituting for $\int \frac{dz}{U\sin z - c_{ph}}$ and $K_2 = \int \frac{dz_0}{U\sin z_0 - c_{ph}}$ in equation (8.25) and rearranging.

First considering the case when $U^2 > c_{ph}^2$, defining

$$A = \left[\frac{-c_{ph}\tan\frac{z}{2} + U - \Gamma_1}{-c_{ph}\tan\frac{z}{2} + U + \Gamma_1}\right] = \left[\frac{-c_{ph}\tan\frac{k\psi}{2} + U - \Gamma_1}{-c_{ph}\tan\frac{k\psi}{2} + U + \Gamma_1}\right], \tag{8.30}$$

and

$$X = -c_{ph}\tan\frac{z_0}{2}, \tag{8.31}$$

then equation (8.25) becomes

$$\frac{1}{\Gamma_1}\ln A = kt + \frac{1}{\Gamma_1}\ln\left[\frac{X + U - \Gamma_1}{X + U + \Gamma_1}\right], \tag{8.32}$$

using the laws of logarithms this can be written,

$$-k\Gamma_1 t = \ln\left(\frac{\left[\frac{X+U-\Gamma_1}{X+U+\Gamma_1}\right]}{A}\right), \tag{8.33}$$

so that

$$A = \left[\frac{X + U - \Gamma_1}{X + U + \Gamma_1}\right] e^{k\Gamma_1 t}, \tag{8.34}$$

solving for X gives

$$X = \frac{(U + \Gamma_1)A + (\Gamma_1 - U)e^{k\Gamma_1 t}}{e^{k\Gamma_1 t} - A}, \tag{8.35}$$

and the required expression for $\tan\frac{z_0}{2} = \tan\frac{k\psi_0}{2}$ is therefore

$$\tan\frac{k\psi_0}{2} = \frac{(U + \Gamma_1)A + (\Gamma_1 - U)e^{k\Gamma_1 t}}{c_{ph}(A - e^{k\Gamma_1 t})}. \tag{8.36}$$

When $U^2 = c_{ph}^2$, defining

$$A' = \tan\left(\frac{\pi}{4} + \frac{z}{2}\right) = \tan\left(\frac{\pi}{4} + \frac{k\psi}{2}\right), \tag{8.37}$$

and letting

$$X' = \tan\frac{z_0}{2} = \tan\frac{k\psi_0}{2}, \tag{8.38}$$

then equation (8.25) becomes

$$-\frac{A'}{U} = kt - \frac{1}{U}\tan\left(\frac{\pi}{4} + \frac{z_0}{2}\right), \tag{8.39}$$

but because of the identity

$$\tan(\frac{\pi}{4} + \frac{z_0}{2}) = \frac{1 + \tan\frac{z_0}{2}}{1 - \tan\frac{z_0}{2}} = \frac{1 + X'}{1 - X'}, \tag{8.40}$$

this becomes

$$A' + Ukt = \frac{1 + X'}{1 - X'}, \tag{8.41}$$

which when rearranged to determine $X' = \tan\frac{k\psi_0}{2}$ yields

$$\tan\frac{k\psi_0}{2} = \frac{A' + Ukt - 1}{A' + Ukt + 1}. \tag{8.42}$$

Finally, for the case when $U^2 < c_{ph}^2$, defining

$$A'' = \frac{U - c_{ph}\tan\frac{z}{2}}{\Gamma_2} = \frac{U - c_{ph}\tan\frac{k\psi}{2}}{\Gamma_2}, \tag{8.43}$$

and

$$X'' = \tan\frac{z_0}{2} = \tan\frac{k\psi_0}{2}, \tag{8.44}$$

then equation (8.25) becomes

$$\frac{2}{\Gamma_2}\text{arctan}A'' = kt + \frac{2}{\Gamma_2}\text{arctan}\left[\frac{-c_{ph}X'' + U}{\Gamma_2}\right]. \tag{8.45}$$

Dividing by $\frac{2}{\Gamma_2}$, taking $\frac{1}{2}\Gamma_2 kt$ to the left hand side and then taking the tangent of both sides

$$\tan\left(-\frac{1}{2}\Gamma_2 kt + \text{arctan}A''\right) = \frac{-c_{ph}X'' + U}{\Gamma_2} \tag{8.46}$$

which when rearranged to yield $X'' = \tan\frac{k\psi_0}{2}$ and simplified gives

$$\tan\frac{k\psi_0}{2} = \frac{1}{c_{ph}}\left(U - \frac{1}{\Gamma_2}\left[\frac{A'' - \tan\left(\frac{1}{2}\Gamma_2 kt\right)}{1 - A''\tan\left(\frac{1}{2}\Gamma_2 kt\right)}\right]\right). \tag{8.47}$$

Equation (8.23) together with the expressions for $\tan\frac{k\psi_0}{2}$ in terms of ψ and t for the three cases $U > c_{ph}$ (equation (8.36)), $U = c_{ph}$ (equation (8.42)) and $U < c_{ph}$ (equation (8.47)) constitutes the solution to the problem. For convenient future reference the results are collected in the box below.

$$B(\psi,t) = \frac{B_0(\psi_0,0)}{\sin k\psi - \frac{c_{ph}}{U}}\left(\frac{2\zeta}{1+\zeta^2} - \frac{c_{ph}}{U}\right),$$

$$\text{when} \quad U^2 > c_{ph}^2 \quad \text{then} \quad \zeta = \frac{(U+\Gamma_1)A + (\Gamma_1 - U)e^{k\Gamma_1 t}}{c_{ph}(A - e^{k\Gamma_1 t})},$$

$$\text{when} \quad U^2 = c_{ph}^2 \quad \text{then} \quad \zeta = \frac{A' + Ukt - 1}{A' + Ukt + 1},$$

$$\text{when} \quad U^2 < c_{ph}^2 \quad \text{then} \quad \zeta = \frac{1}{c_{ph}}\left(U - \frac{1}{\Gamma_2}\left[\frac{A'' - \tan\left(\frac{1}{2}\Gamma_2 kt\right)}{1 - A''\tan\left(\frac{1}{2}\Gamma_2 kt\right)}\right]\right),$$

$$\text{where} \quad \Gamma_1 = (U^2 - c_{ph}^2)^{1/2}, \quad \Gamma_2 = (c_{ph}^2 - U^2)^{1/2} \quad \text{and}$$

$$A = \frac{-c_{ph}\tan\frac{k\psi}{2} + U - \Gamma_1}{-c_{ph}\tan\frac{k\psi}{2} + U + \Gamma_1}, \quad A' = \tan\left(\frac{\pi}{4} + \frac{k\psi}{2}\right) \quad \text{and} \quad A'' = \frac{U - c_{ph}\tan\frac{k\psi}{2}}{\Gamma_2}. \tag{8.48}$$

This solution shows that the space-time evolution of any initial magnetic field configuration B_0 is determined by the function

$$F_w = \frac{\left(\frac{2\zeta}{1+\zeta^2} - \frac{c_{ph}}{U}\right)}{\sin k\psi - \frac{c_{ph}}{U}}. \tag{8.49}$$

For simplicity results in the next section are only presented for the case B_0= constant, to emphasise the characteristics of F_w alone rather than the combination of B_0 and F_w. It should however be noted that the framework developed here applies to any initial magnetic field profile. The physical meaning of equation (8.49) and some important limiting cases are discussed in the next section.

8.2.4 Discussion of solutions to 1D frozen flux wave flow problem

In this section the evolution of an initially uniform magnetic field $B_0(x,t) = B_0$ is described for a particular choice of the control parameters U and c_{ph}. For convenience the choice k=1 (corresponding to a flow wavelength of 2π) is fixed, so changing c_{ph} corresponds to changing the frequency ω of the wave flow. The different magnetic field evolution processes occurring in the regimes with $|U| > |c_{ph}|$, $|U| < |c_{ph}|$ and the intermediate case when $|U| \sim |c_{ph}|$ are discussed. The existence of these regimes will have important implications for diagnosing the likely effects of wave flows near to the core surface on radial magnetic fields.

Case when $|U| > |c_{ph}|$: Slowly drifting wave flows

When the wave flow is faster than the drift speed ($|U| > |c_{ph}|$) propagating concentrations of magnetic field are generated as illustrated in figure 8.2. When the flow within the wave is very much faster than the drift speed then to a first approximation the flow can

be considered as stationary and the situation in the drifting and non-drifting reference frames are almost identical. As observed in figure 8.2a,b, magnetic field concentrations become increasingly sharp and develop at the positions of flow convergence (which are associated with flow downwellings in an incompressible flow), where $kx = (2n+1)\pi$ and n is any integer. At positions of flow divergence (associated with flow upwellings) where $kx = 2n\pi$, the magnetic field is found to decrease in amplitude. In future discussions this pattern of field evolution will be referred to as the concentration regime.

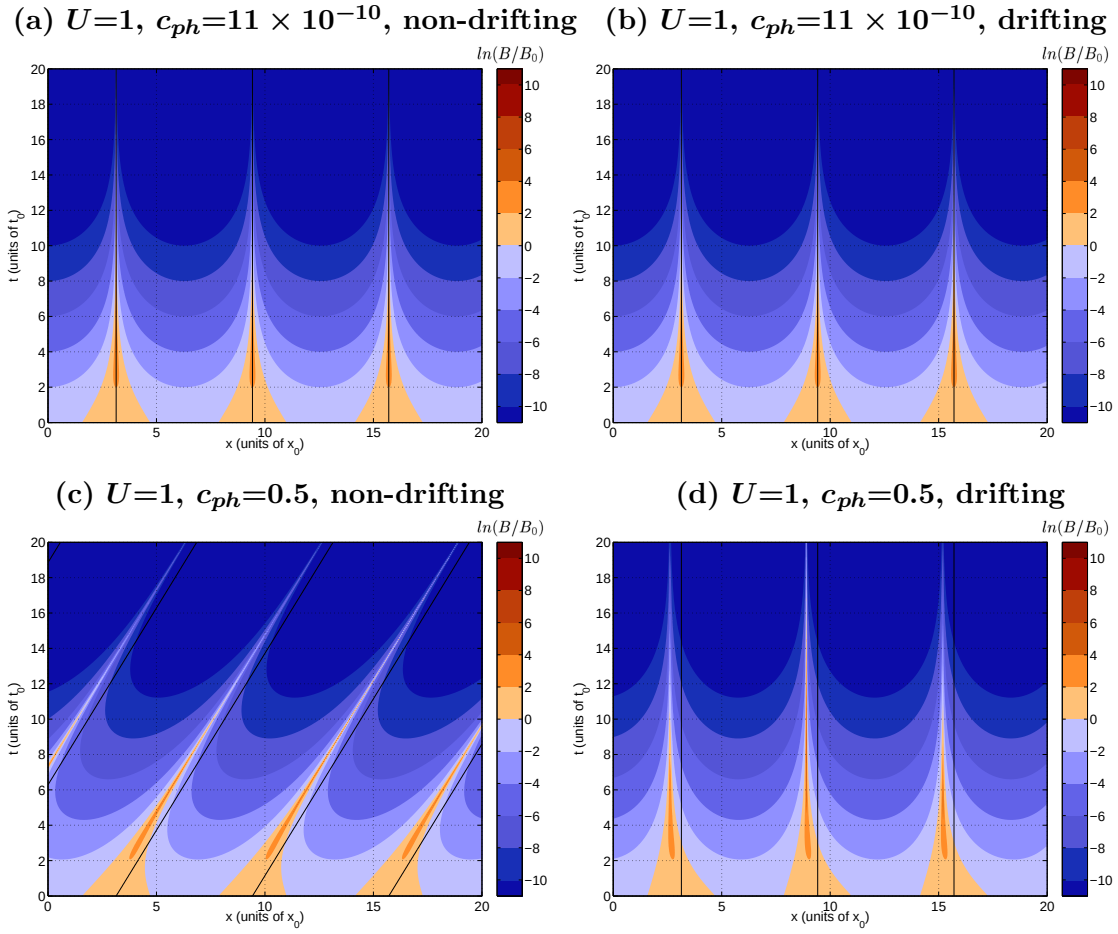

Figure 8.2: Solution for evolution of B in the 1D problem, when $|U| > |c_{ph}|$. Time-distance plots showing the evolution of the magnetic field (displayed as contours of $\log\frac{B}{B_0}$ so orange colours represent field amplification and blue colours represent field weakening) when U=1, $c_{ph} = 1 \times 10^{-10}$ in (a) and when U=1, $c_{ph} = 0.5$ in (c) with the situation in the frame of reference drifting with the flow pattern displayed in (b) and (d). The solid black line tracks the position the of the neutral point of flow convergence in the non-drifting frame. The unit of distance is $x_0 = \frac{1}{k}$ while the unit of time is $t_0 = \frac{1}{\omega}$.

Mathematically, when $\frac{U}{c_{ph}} >> 1$ then $\psi \sim x$, $\Gamma_1 \sim U$, $A \sim \frac{-c_{ph}}{2U}\tan(\frac{kx}{2})$ and $\zeta \sim \tan(\frac{kx}{2})e^{-kUt}$ so that the expression for B simplifies to,

$$B(x,t) = \frac{2B_0}{\sin(kx)}\frac{\tan(\frac{kx}{2})\,e^{-Ukt}}{1+\tan^2(\frac{kx}{2})\,e^{-2Ukt}} = \frac{B_0 e^{-Ukt}}{\cos^2(\frac{kx}{2}) + \sin^2(\frac{kx}{2})e^{-2Ukt}}. \tag{8.50}$$

The solution in this limit was first obtained by Parker (1963) in his model of solar

super-granulation being caused by kinematic concentration of vertical magnetic fields by downwelling flow. That Parker's solution is consistent with equation (8.48) is a useful check on its validity. By examining the form taken by the solution in equation (8.50) along the positions of flow convergence and divergence, further insight may be gained:

(i) Following points of flow divergence and upwelling where $kx = 2n\pi$

Because $\cos^2(n\pi) = 1$ and $\sin^2(n\pi) = 0$, equation 8.50 simplifies to

$$B(\frac{2n\pi}{k}, t) = B_0 e^{-Ukt}. \tag{8.51}$$

The frozen-flux theorem (see Davidson (2001) or Moffatt (1978)) suggests that magnetic field lines will be continuously pulled away from locations of flow divergence and upwelling, providing a physical justification for this field decay.

(ii) Following points of flow convergence and downwelling where $kx = (2n + 1)\pi$

Because $\cos^2((2n + 1)\pi) = 0$ and $\sin^2((2n + 1)\pi) = 1$, equation 8.50 simplifies to

$$B(\frac{2n\pi}{k}, t) = B_0 e^{Ukt}. \tag{8.52}$$

Exponential growth can also be understood physically because at these locations of flow downwelling and convergence, the frozen-flux theorem implies that magnetic field lines will be pulled together, becoming increasingly concentrated.

In figure 8.2c,d where U is only slightly greater than c_{ph}, magnetic field concentrations again develop close to positions of flow convergence (downwellings) and move with the same speed and in the same direction as those locations of convergence. However the field concentrations no longer occur on top of the positions of flow convergence in the non-drifting frame, but lag slightly behind. This unintuitive phenomenon is most easily understood by considering the case shown in figure 8.3 where the maximum magnitude of the flow and the flow drift speed are equal ($|c_{ph}| = |U|$).

Case when $|U| = |c_{ph}|$

When $|U| = |c_{ph}|$ the position of magnetic field concentration lags behind the position of flow convergence in the non-drifting frame by 1/4 of the flow wavelength. This turns out to be the location of the neutral point of flow convergence in the drifting reference frame, where $k\psi = (2n + \frac{1}{2})\pi$. The reason for this requires a moment's consideration. The wave flow in the non-drifting frame is $U \sin(kx - \omega t)$ and is drifting at a phase speed $c_{ph} = \frac{\omega}{k}$. Moving to a frame of reference travelling at this speed where the new position co-ordinate is $\psi = x - c_{ph}t$, the flow becomes $U \sin k\psi - c_{ph}$. It is crucial to understand that this is not the same as $U \sin k\psi$ which would be a simple stationary wave flow. Moving to the new reference frame involves not just changing the drift speed of the wave flow, but also the addition of a new velocity component (equal in magnitude

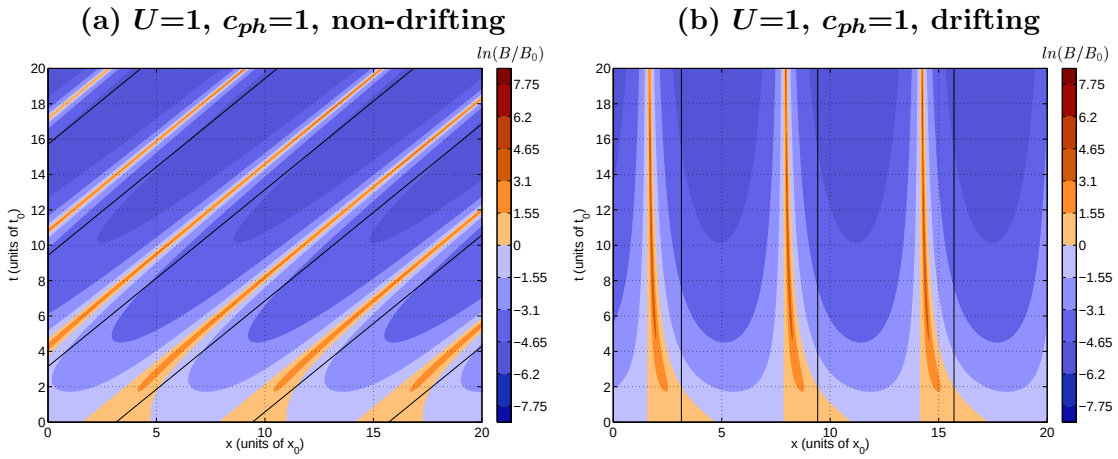

Figure 8.3: Solutions for B in the 1D problem, when $|U| = |c_{ph}|$.
Time-distance plots showing the evolution of the magnetic field (displayed as contours of $\log\frac{B}{B_0}$ so orange colours represent field amplification and blue colours represent field weakening) when U=1, c_{ph}=1 in (a) and with the results in a frame of reference drifting with the flow pattern displayed in (b). The solid black line marks the motion of the centre of flow convergence in the non-drifting frame. The unit of distance is $x_0 = \frac{1}{k}$ while the unit of time is $t_0 = \frac{1}{\omega}$.

and opposite in direction to the motion of the new frame relative to the original frame) to all the fluid parcels in the flow. In the drifting reference frame this means that the positions of flow convergence and divergence are shifted to the zeros of $U \sin k\psi - c_{ph}$ rather than the zeros of $U \sin k\psi$, so when $|U| = |c_{ph}|$, field concentrations are found at $k\psi$=$(2n + \frac{1}{2})\pi$ rather than at $k\psi$=$(2n + 1)\pi$.

In the non-drifting frame there is therefore a continual competition between the ability of the convergent flow to concentrate magnetic field lines and the effects of the movement of the position of flow convergence. As shown in figure 8.3b, in the reference frame drifting with the phase speed of the flow, this becomes a competition between field advection by the wave flow ($U \sin k\psi$) and by the Galilean correction flow ($-c_{ph}$). After a transient interval, magnetic field concentrations become localised at the neutral point of flow convergence in the drifting reference frame, where field advection by the wave flow and by the Galilean correction flow are in balance.

Case when $|U| < |c_{ph}|$: Fast drifting wave flows

The remaining case when $|U| < |c_{ph}|$ is documented in figure 8.4 where (a) and (b) show the case when U is only slightly less than c_{ph} and (c) and (d) show what happens when U is almost negligible compared to c_{ph}. The space-time evolution of the field morphology in the two cases is similar, but the amplitude of the induced field concentrations are very different. In both cases the changes in field amplitude are much smaller than when $|U| \geq |c_{ph}|$; for $U = c_{ph}/2$ field amplitudes less than 3 times greater and smaller than

the original field are produced, while when $U = c_{ph}/10^{10}$ changes in field amplitude are more than 60000 smaller than original field. The amplitude of field changes thus depends rather strongly on the ratio c_{ph}/U.

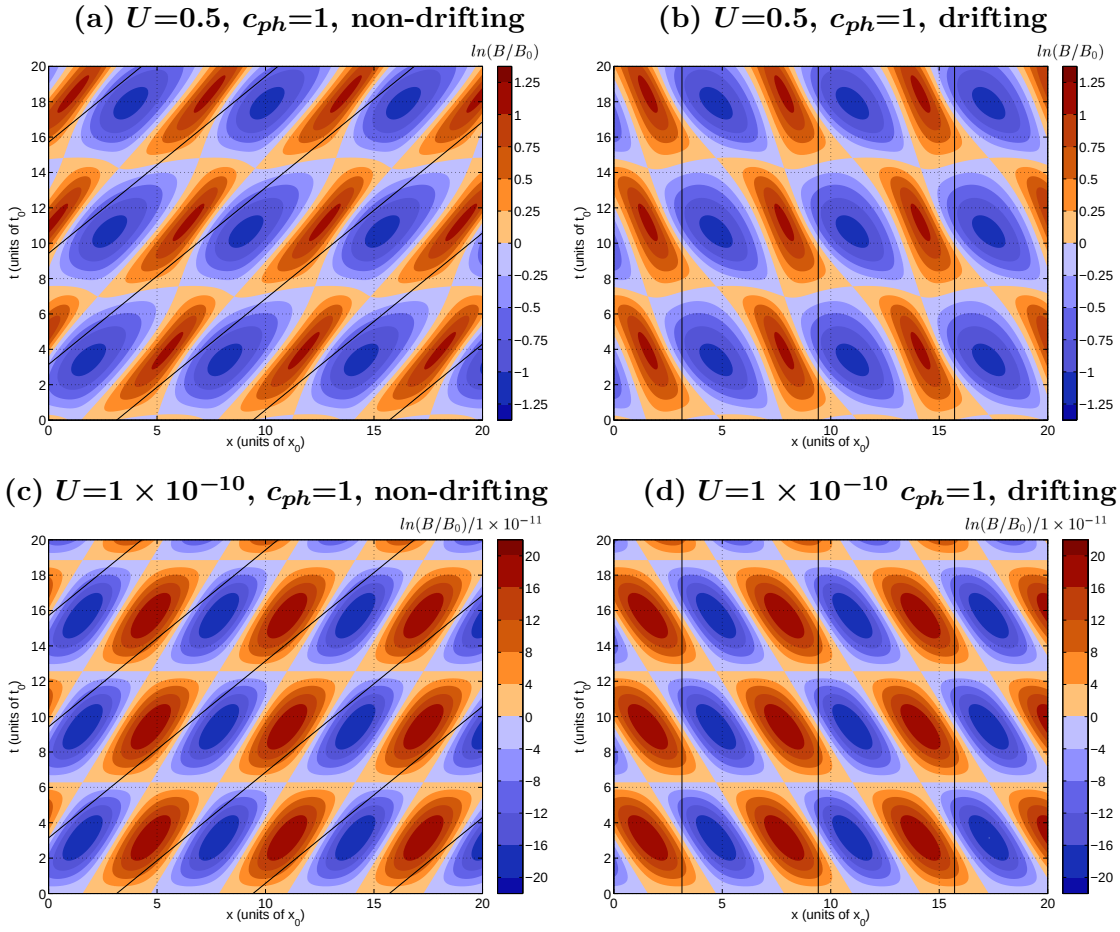

Figure 8.4: Solutions for B in the 1D problem, when $|U| < |c_{ph}|$.
Time-distance plots showing the evolution of the magnetic field (displayed as contours of $\log\frac{B}{B_0}$ so orange colours represent field amplification and blue colours represent field weakening) when U=0.5, c_{ph}=1 in (a) and when $U = 1 \times 10^{-10}$, $c_{ph} = 1$ in (c) with the results in a frame of reference drifting with the flow pattern displayed in (b) and (d). The solid black line marks the motion of the centre of flow convergence in the non-drifting frame. The unit of distance is $x_0 = \frac{1}{k}$ while the unit of time is $t_0 = \frac{1}{\omega}$.

The most striking aspect of the field evolution in this case is the cyclic changes in the amplitude of field concentrations. These changes in amplitude will be referred to as pulsations in future discussions. One pulsation cycle begins with the initially uniform field developing into increasingly intense field concentrations separated by patches of increasingly weak field. The field concentrations eventually reach a maximum amplitude (and the weak field patches reaches their smallest amplitude), before the field amplitudes begin to return toward their original values. Eventually the field returns back to its original uniform morphology and the cycle starts over again. Since there is no dissipation in this model the pulsating behaviour repeats perfectly and indefinitely. The time taken

for one cycle of this oscillation is $T = \frac{2\pi}{\omega} = \frac{2\pi k}{c_{ph}}$ (the time taken for the Galilean correction flow to cover 1 wavelength of the flow pattern) which in the examples shown with k=1 and c_{ph}=1 leads to a period of 2π. In the drifting reference frame, the position where the field maxima are found is the same as where field concentration were observed when $U = c_{ph}$. The position where the weakest field develops similarly occurs where increasingly weak field was found when $U = c_{ph}$. In the non-drifting frame this causes locations of oscillatory field highs and lows that move with the speed c_{ph} of the wave flow pattern.

The reason for the pulsation phenomenon can be understood by considering locations of flow convergence in the drifting reference frame. In this frame the combined wave flow plus the Galilean correction flow ($U \sin k\psi - c_{ph} <$) is always less than zero, so no neutral points can exist. There is thus no location where the wave flow can balance the Galilean correction flow, so field lines are continuously advected across the wave flow pattern rather than ever becoming stuck at a fixed location in the drifting reference frame. The magnetic field is therefore continuously advected by the Galilean flow across the wave flow pattern and experiences consecutively intervals of concentration (when at positions where the wave flow opposes the Galilean flow) and weakening (when at positions where the wave flow helps the Galilean flow). The periodic pulsation of field amplitude is therefore a consequence of the spatially periodic nature of the wave flow and the advection of magnetic field patterns across it, with the period of the oscillations being $\frac{2\pi}{k}/c_{ph}$.

The form of the pulsation is simplest when $|U| << |c_{ph}|$, as seen in figure 8.4c, d with field maxima and minima occurring simultaneously, having the same spatial extent, and temporally bisecting the intervals when uniform field is observed. When U is comparable but less than c_{ph} (as in figure 8.4a, b) the situation is rather more complicated, with the field concentrations being of smaller size than regions of weak field, and the temporal periodicity being longer than the $T = 2\pi$ expected from simple physical reasoning presented above in the case when $|c_{ph}| >> |U|$. The maxima of field concentration and minima of field weakening no longer occur simultaneously with the maxima occurring slightly after the minima. However, even in this case the fundamental pulsation behaviour remains.

The existence of the concentrating and pulsating regimes in this problem does not appear to have been discussed before. It has important consequences concerning whether wave flows are a viable mechanism for producing the spatially coherent, azimuthally moving patterns in B_r that were observed in geomagnetic field models in chapter 3. Before considering more realistic models of this situation, in the next section an attempt is made to understand the amplitude magnetic field concentrations that might be obtained at positions of flow convergence in a wave flow.

8.2.5 Steady state balance between advection and diffusion

When flow within the wave is much faster than the drift speed of the wave pattern ($|U| >> |c_{ph}|$), the solutions from the previous section are unrealistic in the long time limit because magnetic field gradients become so large that magnetic diffusion can no longer be neglected. In this scenario, eventually a steady state balance between advection and diffusion of magnetic field lines will arise, as discussed by Moffatt (1978) and in connection with the scenario at Earth's core surface by Gubbins and Kelly (1996).

In this section, horizontal magnetic diffusion is re-introduced to the model equations in the limit when the wave flow is effectively stationary ($|U| >> |c_{ph}|$)[1]. The solution to this problem when advection and diffusion of magnetic field are in balance provides a useful estimate of the maximum magnetic field amplitude that can be achieved given a particular choice of wave flow and magnetic diffusivity. The analysis in this section closely follows that of Clark (1965) who studied a similar problem when attempting to model solar super granulation.

Assuming $|U| >> |c_{ph}|$, $u_x \sim U \sin kx$ and including horizontal magnetic diffusion η the magnetic induction equation governing field evolution is

$$\frac{\partial B}{\partial t} + U \sin kx \frac{\partial B}{\partial x} + Uk \cos kx B = \eta \left(\frac{\partial^2 B}{\partial x^2} + \frac{\partial^2 B}{\partial z^2} \right). \tag{8.53}$$

To find the steady state amplitude of the magnetic field, two assumptions are made that considerably simplify the analysis:

(i) Steady state assumption ($\frac{\partial B}{\partial t} = 0$): A balance between advection and diffusion of magnetic field is assumed: this is reasonable once sufficiently large gradients of magnetic field have been established.

(ii) Horizontal magnetic diffusion dominates vertical magnetic diffusion: This requires that diffusion of vertical magnetic field B due to field gradients in the $\widehat{\boldsymbol{z}}$ direction is negligible in comparison to diffusion of magnetic field due to gradients of the magnetic field in the $\widehat{\boldsymbol{x}}$ direction.

If one accepts these assumptions, the governing equation simplifies to (Clark, 1965)

$$U \sin kx \frac{dB}{dx} + (Uk \cos kx) B = \eta \frac{d^2 B}{dx^2}. \tag{8.54}$$

Since this involves only x derivatives and is exact, it can be rewritten in the form

$$\frac{d}{dx} \left(\frac{dB}{dx} - \frac{U}{\eta} \sin kx \, B \right) = 0. \tag{8.55}$$

[1] When $|U| < |c_{ph}|$ no steady state can be reached because the field constantly pulsates in amplitude, so no advection-diffusion balance is likely to be reached and this scenario is not studied. When $|U| > |c_{ph}|$ but of similar order of magnitude an advection-diffusion balance is likely to arise, but the physical mechanism of flow convergence causing field concentration balanced by advection then occurs in the drifting reference frame so the results of the present analysis should again be applicable.

Integrating with respect to x

$$\frac{\partial B}{\partial x} - \frac{U}{\eta}\sin kx\, B = C_1. \tag{8.56}$$

The advection-diffusion balance is therefore described by a 1st order ordinary differential equation. The arbitrary constant C_1 will be zero if when x=0, $\frac{dB}{dx} = 0$ also[2]. If this is the case then

$$\frac{\partial B}{\partial x} = \frac{U}{\eta}\sin kx\, B. \tag{8.57}$$

Separating the variables

$$\int \frac{dB}{B} = \int \frac{U}{\eta}\sin kx\, dx, \tag{8.58}$$

and then integrating

$$\ln B = -\frac{U}{k\eta}\cos kx + C_2, \tag{8.59}$$

so that

$$B(x,t)_{t\to\infty} = C_2 e^{-\frac{U}{k\eta}\cos kx}. \tag{8.60}$$

To determine the amplitude of this steady state magnetic field, the constant C_2 must be evaluated and the initial and steady state field strengths must be linked. This can be achieved following the approach adopted by Clark (1965) and considering the integrated magnetic field over one wavelength of the wave flow

$$\frac{d}{dt}\int_{-\frac{\pi}{k}}^{\frac{\pi}{k}} B(x,t)\, dx. \tag{8.61}$$

Since the velocity field u is periodic in x (wavelength $\frac{2\pi}{k}$), if the initial field B_0 is uniform, then the steady state field B and its derivatives with respect to x $\left(\frac{\partial B}{\partial x}$ and $\frac{\partial^2 B}{\partial x^2}\right)$ will also always be periodic with the same period as u and will integrate to zero over the interval $(\frac{-\pi}{k}, \frac{\pi}{k})$. Therefore, returning to the time dependent induction equation

$$\frac{\partial B}{\partial t} + U\sin kx\frac{\partial B}{\partial x} + Uk\cos kx B = \eta\frac{\partial^2 B}{\partial x^2}, \tag{8.62}$$

and integrating from $x = \frac{-\pi}{k}$ to $x = \frac{\pi}{k}$ leaves

$$\frac{d}{dt}\int_{-\frac{\pi}{k}}^{\frac{\pi}{k}} B(x,t)dx = 0. \tag{8.63}$$

Physically this says that the amount vertical magnetic flux within one wavelength of the stationary wave pattern is conserved. This property then allows the flux within a

[2]This cannot be rigorously established at this point. The analysis, however, proceeds on the assumption that C_1=0 and the assumption is justified a posteriori by the fact that the steady state solution found for B does indeed have this form.

wavelength of the flow in the steady state to be related to the flux within that wavelength of the flow initially when the magnetic field is assumed to be uniform

$$\int_{-\frac{\pi}{k}}^{\frac{\pi}{k}} C_2\, e^{-\frac{U}{k\eta}\cos kx}\, dx = \int_{-\frac{\pi}{k}}^{\frac{\pi}{k}} B_0\, dx, \tag{8.64}$$

or

$$C_2 \int_{-\frac{\pi}{k}}^{\frac{\pi}{k}} e^{-\frac{U}{k\eta}\cos kx}\, dx = \frac{2\pi B_0}{k}. \tag{8.65}$$

But using a standard integral for a zeroth order modified Bessel function (Abramowitz and Stegun, 1964)

$$\int_{-\frac{\pi}{k}}^{\frac{\pi}{k}} e^{-\frac{U}{k\eta}\cos kx}\, dx = 2\pi I_0\left(\frac{U}{k\eta}\right), \tag{8.66}$$

where I_0 is a zeroth order modified Bessel Function, so that

$$C_2 = \frac{B_0}{I_0(\frac{U}{k\eta})}. \tag{8.67}$$

Substituting back into equation (8.60) the steady state magnetic field profile is obtained

$$B(x,t)_{t\to\infty} = \frac{B_0}{I_0(\frac{U}{k\eta})} e^{-\frac{U}{k\eta}\cos kx}. \tag{8.68}$$

This result was first stated by Clark (1965). The non-dimensional parameter governing the amplitude of steady state magnetic field is a version of the magnetic Reynolds number of the wave flow that was defined by Clark (1965) and is here referred to as R_m^{cl}

$$R_m^{cl} = \frac{U}{k\eta}, \tag{8.69}$$

where $\frac{2\pi}{k}$ is the wavelength of the flow. The factor by which the initial magnetic field can be concentrated by is therefore $\frac{e^{R_m^{cl}}}{I_0(R_m^{cl})}$. Smaller scale, more intense magnetic field concentrations will be produced when the amplitude of the wave flow U is stronger, the length scale of the drifting wave flow $\frac{2\pi}{k}$ is larger and when the magnetic diffusivity η is smaller. In the limit of large R_m^{cl}, $I_0(R_m^{cl}) \to (2\pi R_m^{cl})^{1/2} e^{R_m^{cl}}$ so the maximum field amplitude will be $\sim B_0(2\pi R_m^{cl})^{1/2}$. In figure 8.5, equation (8.68) is plotted for a range of R_m^{cl} to illustrate the concentration achieved in this simple 1D model.

Applying the results of this model to estimate the amplitude of field concentrations produced by wave flows acting on B_r at Earth's core surface is difficult because the geometry there is 2D not 1D. Clark (1965) addressed this by analysing a 2D axisymmetric flow finding that for large R_m^{cl} in 2D the maximum field approached $B_0\,(R_m^{cl})^{1/2}$ rather than the 1D result of $B_0\,(2\pi R_m^{cl})^{1/2}$. The factor $(2\pi)^{1/2}$ means that the maximum concentration estimates obtained using the 1D model will be ~ 3 times too large.

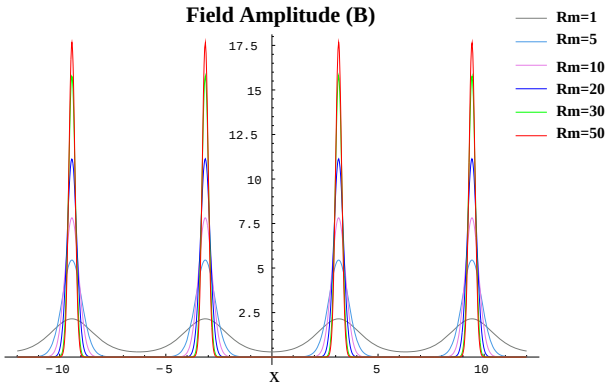

Figure 8.5: 1D advection-diffusion balance: Amplitude as a function of R_m^{cl}. Concentration of an initially uniform magnetic field, by a wave flow assuming a 1D advection-diffusion balance for R_m^{cl}=1, 5, 10, 20, 30, 40, 50. An estimate of the concentrations expected in a 2D geometry can be obtained by dividing the field amplitude by a factor of ~ 3.

Magnetic field features with amplitude at least 10 times that of the surrounding field have been inferred at the core surface (Jackson, 2003) from observations of the geomagnetic field and using maximum entropy regularisation methods that do not penalise large amplitudes. In the present model, taking into account 2D geometry this suggests $\frac{1}{3}\frac{e^{R_m^{cl}}}{I_0(R_m^{cl})} > 10$. When R_m^{cl}=150, $\frac{1}{3}\frac{e^{R_m^{cl}}}{I_0(R_m^{cl})} = 10.2$, so $R_m > 150$ seems to be the lower limit required by the observations. The observed features are of length scale $\sim 1800 \times 10^3$m, so with magnetic diffusivity $\sim 1\mathrm{m}^2\mathrm{s}^{-1}$ $R_m^{cl} > 150$ implies only rather low wave flow amplitudes $U > 3$ km yr^{-1} are required to produce field features with the observed concentration.

The shape and spatial extent of field concentrations produced as a result of a 1D advection-diffusion balance can be obtained by linearising the solution in equation (8.68) around $x_{\max} = \frac{(2n+1)\pi}{k}$. If δ represents a small displacement in $\widehat{\boldsymbol{x}}$ away from $x_{\max}$ then

$$\cos kx = \cos(kx_{\max} + k\delta) = \cos kx_{\max}\cos k\delta - \sin kx_{\max}\sin k\delta, \tag{8.70}$$

But $x_{\max} = \frac{(2n+1)\pi}{k}$ so then $\sin kx_{\max} = 0$ and $\cos kx_{\max} = -1$ and

$$\cos kx = -\cos k\delta. \tag{8.71}$$

Since δ is a small departure from $x_{\max}$ a reasonable first approximation is that

$$\cos k\delta = (1 - \frac{k^2\delta^2}{2}), \tag{8.72}$$

and the expression for B close to $x_{\max}$ is

$$B = B_0(x,0)e^{\frac{U}{k\eta}}e^{\frac{-Uk\delta^2}{2\eta}}. \tag{8.73}$$

Recognising that $B_0(x,0)e^{\frac{U}{k\eta}}$ is the maximum concentration reached by the field, and labelling it as $B_{\max}$, equation (8.73) becomes

$$B = B_{\max}e^{\frac{-Uk\delta^2}{2\eta}}. \tag{8.74}$$

Close to the maximum flux density at the position of flow convergence in a 1D advection-diffusion balance, the field profile will therefore be Gaussian, as previously noted through different analysis by Moffatt (1978) and Bloxham (1985). One might examine field concentrations at the core surface to determine whether they conformed to this profile, though it would also be necessary to take into account changes in morphology introduced by the regularisation applied during field modelling to eliminate contamination by crustal fields (see §8.3.6).

8.3 2D wave flow acting on a radial magnetic field at a spherical surface

The 1D model developed in the previous section has provided understanding of the physical mechanisms by which propagating wave flows can produce propagating concentrations of magnetic field. The geometry of this model is, however, very different from the scenario motivating this study: that at Earth's core surface. In the present section, a more complicated kinematic model in a spherical geometry that also includes horizontal magnetic diffusion is developed and solutions found numerically.

8.3.1 2D model equations and imposed flow

The magnetic induction equation is again used to determine the magnetic field evolution in this section. In spherical geometry at a rigid, insulating, boundary the radial component of the induction equation can be written following Gubbins and Bloxham (1985) as

$$\frac{\partial B_r}{\partial t} + \nabla_H \cdot (\boldsymbol{u} B_r) = \eta \left(\frac{\partial^2 B_r}{\partial r^2} + \frac{4}{r}\frac{\partial B_r}{\partial r} + \frac{2B_r}{r^2} + \frac{\Delta B_r}{r^2} \right), \tag{8.75}$$

where B_r is the radial component of the magnetic field at the core surface, $\boldsymbol{u}$ is the velocity field on the surface, $\nabla_H = \nabla - \frac{\partial}{\partial r}\widehat{\boldsymbol{r}}$ denotes the horizontal gradient, Δ denotes the angular part of $r^2\nabla^2$ and η is as before the magnetic diffusivity.

The following analysis proceeds on the assumption that the last two terms in equation (8.75) are the dominant magnetic diffusion terms because it is difficult to evaluate the other diffusion terms involving the radial derivatives from knowledge of only B_r at the core surface. This assumption will underestimate magnetic diffusion particularly if there are strong radial gradients of the B_r near the core surface, but has previously been employed by other authors Olson et al. (2002). The equation that will be solved numerically in this section is then

$$\frac{\partial B_r}{\partial t} + \nabla_H \cdot (\boldsymbol{u} B_r) = \frac{\eta}{r^2} \left(2B_r + \Delta B_r \right). \tag{8.76}$$

The imposed flows are chosen to have the same 2D spatial structure as simple, but dynamically plausible, wave flows close to the outer boundary in a rotating fluid sphere. Snapshots showing the morphology of the flows studied are presented in figure 8.6. These

(a) m=8, E^S, Zhang'00 inertial wave flow at outer spherical boundary

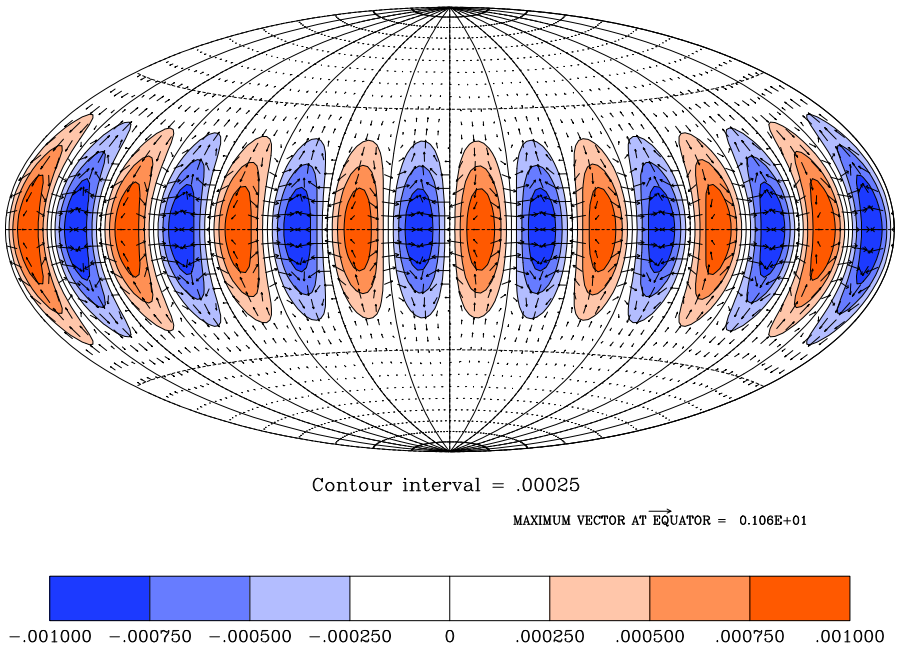

(b) m=8, E^A, Zhang'00 inertial wave flow at outer spherical boundary

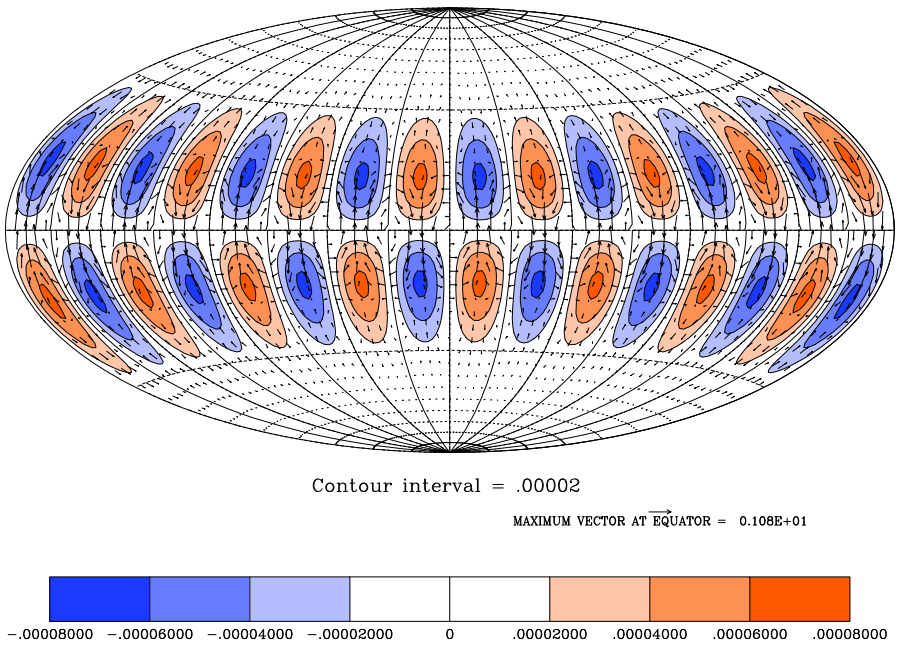

Figure 8.6: 2D wave flows on a spherical surface at an impenetrable boundary. Snapshots of (a) Equatorially symmetric (E^S) and (b) Equatorially antisymmetric (E^A) wave flows from Zhang et al. (2000) with $N_{\text{zhang}} = 1$, m=1, at the spherical outer boundary and with flow amplitude normalised to a maximum value of 1. Arrows show direction of the flow on the surface, with the size of the arrow proportional to the amplitude of the flow. Coloured contours show flow divergence, orange colours represent positive divergence, associated with upwelling, blue colours represent flow convergence associated with downwelling.

wave flows have a spatial structure[3] $U_{\text{zhang}}(\theta,\phi)$ that is the 2D structure at the outer boundary of the inertial wave[4] solutions in a sphere derived by Zhang et al. (2000)) The flow amplitude U, linear phase (drift) speed at the equator $c_{ph}=\frac{\omega c}{m}$ and azimuthal wavenumber m are taken to be free parameters with $\frac{2\pi}{\omega}$ the wave period, c the radius of the spherical surface and m the azimuthal wavenumber. Mathematically, the flow therefore has the form

$$\boldsymbol{u}=U\left[U_{\text{zhang}}(\theta,\phi)\sin(m\phi-\omega t)\right]. \tag{8.77}$$

Two different classes of U_{zhang} are considered: equatorially symmetric E^S flows (as defined in equations (2.15) and (4.1) of Zhang et al. (2000)) and equatorially antisymmetric E^A flows (as defined by equations (2.16) and (4.6) of Zhang et al. (2000)). Only modes with the simplest structure along the rotation axis (i.e. with N_{zhang}=1 where N_{zhang} is Zhang's N: a parameter determining the complexity of the solution in the direction parallel to the rotation axis). The azimuthal wavenumber was chosen to be m=8, matching that inferred from high resolution images of the core surface derived from satellite data (Jackson, 2003).

The Zhang inertial wave flows correctly capture the generic pattern of propagating regions of flow convergence (downwelling) and divergence (upwelling) associated with more complex thermally-driven hydromagnetic waves such as those studied in chapter 7, but are simpler to study because of their analytic form. Treating U as a free parameter can be justified because the amplitude U cannot be determined using the linear analytical approach of Zhang et al. (2000), because no dissipation or nonlinear energy transfer and saturation mechanisms are taken into account. Treating c_{ph} as a free parameter can be justified because following Malkus (1967) (see §6.5.2) and taking the inertial waves to be solutions of the hydromagnetic wave problem, the wave frequency and hence phase speed c_{ph} depend on the toroidal field strength inside Earth's core whose strength is not well constrained (Hide and Roberts, 1979). Studying the influence on B_r of wave flows of the form equation (8.77) while varying U and c_{ph} therefore allows a systematic investigation of the kinematic effects of hydromagnetic wave flows at the core surface.

8.3.2 Numerical solution of 2D wave flow model

To determine the evolution of a prescribed initial B_r produced by the wave flow defined in equation (8.77), equation (8.76) is numerically integrated (time-stepped) on a surface where r=c, with c=3485 km and the magnetic diffusivity η=1 $\text{m}^2\,\text{s}^{-1}$(=31.536 km^2 yr^{-1})

[3] $U_{\text{zhang}}(\theta,\phi)$ is normalised so that the maximum flow velocity within the wave on the surface has magnitude 1 $\text{km}\,\text{yr}^{-1}$.

[4] Although the solutions found by Zhang et al. (2000) were for inertial waves in a sphere, as described in §6.5.2, Malkus (1967) showed that such modes are also hydromagnetic wave solutions if the imposed magnetic field is of the form $\boldsymbol{B}=B_0 r\sin\theta\widehat{\boldsymbol{\phi}}$, with only the wave frequencies (and hence c_{ph}) modified in a manner depending on B_0 (see equation (6.45)).

to aid comparison with the situation at Earth's core surface. B_r and its time derivative are expanded in real, Schmidt quasi-normalised, spherical harmonic series. These involve utilising associated Legendre polynomials of degree l and order m (P_l^m), truncated at degree L and L_{sv} respectively (for an explanation of the properties of spherical harmonics, see Backus et al. (1996))

$$\begin{aligned}\frac{\partial B_r(\theta,\phi)}{\partial t} &= \sum_{l=1}^{l=L_{sv}}\sum_{m=0}^{m=l}(l+1)\left(\frac{a}{c}\right)^{l+2}(\gamma_l^{mc}\cos m\phi+\gamma_l^{ms}\sin m\phi)P_l^m(\cos\theta)\\ &= \sum_{i=1}^{i=L_{sv}(L_{sv}+2)}(l+1)\left(\frac{a}{c}\right)^{l+2}\gamma_i Y_i(\theta,\phi),\end{aligned} \tag{8.78}$$

$$\begin{aligned}B_r(\theta,\phi) &= \sum_{l=1}^{l=L}\sum_{m=0}^{m=l}(l+1)\left(\frac{a}{c}\right)^{l+2}(b_l^{mc}\cos m\phi+b_l^{ms}\sin m\phi)P_l^m(\cos\theta)\\ &= \sum_{j=1}^{j=L(L+2)}(l+1)\left(\frac{a}{c}\right)^{l+2}b_i Y_i(\theta,\phi),\end{aligned} \tag{8.79}$$

where

$$\int_0^{2\pi}\int_0^{\pi}P_l^m(\cos\theta)P_{l'}^{m'}(\cos\theta)\left\{\begin{array}{c}\cos m\phi\cos m'\phi\\ \sin m\phi\sin m'\phi\end{array}\right\}\sin\theta d\theta d\phi=\left\{\begin{array}{c}\frac{4\pi}{2l+1}\text{ if } l{=}l',\,m{=}m'\\ 0\text{ otherwise}\end{array}\right\}. \tag{8.80}$$

The notation involving the subscripts i and j (for γ_i or b_j) is convenient for representing numerical manipulations. These indices run sequentially over the $L_{sv}(L_{sv}+2)$ and $L(L+2)$ model parameters in the expansions of $\frac{\partial B_r}{\partial t}$ and B_r, incorporating both cosine coefficients (b_l^{mc} and γ_l^{mc}) and sine coefficients (b_l^{ms} and γ_l^{ms}). The notation $Y_i(\theta,\phi)$ is sensible because each i is associated with unique values of m, l and with either cos or sin, and therefore with a particular spherical harmonic coefficient.

The velocity field is expressed in terms of poloidal and toroidal scalars on a spherical surface[5]. The toroidal scalar T and the poloidal scalar on a surface S are related to the velocity field through the expression (Jackson, 1997)

$$\boldsymbol{u}(\theta,\phi)=\boldsymbol{u_T}+\boldsymbol{u_P}=\nabla\times(T\boldsymbol{r})+\nabla_H(rS). \tag{8.81}$$

The toroidal and poloidal scalars are then each expanded in terms of spherical harmonics, again using Schmidt quasi-normalised spherical harmonics, and truncated at degree L_u so that

$$\begin{aligned}T(\theta,\phi) &= \sum_{l=1}^{l=L_u}\sum_{m=0}^{m=l}(u_l^{Tmc}\cos m\phi+u_l^{Tms}\sin m\phi)P_l^m(\cos\theta)\\ &= \sum_{k=1}^{k=L_u(L_u+2)}u_k Y_k(\theta,\phi),\end{aligned} \tag{8.82}$$

[5]See chapter 7 for a general discussion of this representation and Bloxham and Jackson (1991) for its use with a surface vector field; the implementation used here is that described in Jackson et al. (1993) and Jackson (1997).

$$\begin{aligned} S(\theta,\phi) &= \sum_{l=1}^{l=L_u}\sum_{m=0}^{m=l}(u_l^{Smc}\cos m\phi + u_l^{Sms}\sin m\phi)P_l^m(\cos\theta) \\ &= \sum_{k=L_u(L_u+2)+1}^{k=2L_u(L_u+2)} u_k Y_k(\theta,\phi). \end{aligned} \tag{8.83}$$

The arrays of flow coefficients used in the numerical manipulations (labelled by the index k) comes in two parts; the first half of the array specifies the toroidal scalar T and the second half defines the poloidal scalar S. Note that because the wave flow is time dependent, the coefficients u_k are time dependent and must be recomputed at each time-step.

Substituting from equation (8.83) and equation (8.82) into equation (8.81), then from equations (8.81), (8.78) and (8.79) into equation (8.76) leads to the following expression for the secular variation model parameters γ_i

$$\gamma_i = \sum_{j,k} A_{ijk} b_j u_k - \frac{\eta(2-l(l+1))}{c^2} b_i, \tag{8.84}$$

where A_{ijk} is a matrix defining the secular variation for the spherical harmonic coefficient γ_i generated by a unit of the flow component u_k acting on a unit of the spherical harmonic of the magnetic field b_j. A_{ijk} is related to the matrix $\mathbf{A}(\mathbf{b})$ described by Jackson (1997) through the relation $A(b)_{ik} = \sum_j A_{ijk} b_j$ and is calculated using the efficient vector spherical transform method of Lloyd and Gubbins (1990), modified to treat Schmidt quasi-normalised spherical harmonics, as implemented by Jackson et al. (1993) and Jackson (1997).

Discretising time into intervals $(...q-1, q, q+1, ...)$ separated by equal steps of size δq, the system can be numerically integrated forward to determine the evolution of the field using knowledge of the field and flow at previous time-steps. A mixed implicit-explicit time stepping scheme was implemented, with the advection term treated explicitly using a second order Adams-Bashforth technique and the diffusion term treated implicitly using a second order Crank-Nicolson technique (see Fornberg (1998) p.204-206 for a detailed description of these methods), resulting in the time-stepping algorithm

$$\begin{aligned} b_i^{q+1} &= \left[\frac{1}{\delta q} - \frac{\eta(2-l(l+1))}{2c^2}\right]^{-1}\left[\frac{1}{\delta q} + \frac{\eta(2-l(l+1))}{2c^2}\right] b_i^q \\ &+ \frac{3}{2}\left(\sum_j\sum_k A_{ijk}u_k^q b_j^q\right) - \frac{1}{2}\left(\sum_j\sum_k A_{ijk}u_k^{q-1}b_j^{q-1}\right). \end{aligned} \tag{8.85}$$

The first term is the implicit Crank-Nicholson treatment of diffusion and the second term is the explicit Adams-Bashforth treatment of advection. Since the Adams-Bashforth scheme requires knowledge of the magnetic field at two previous time-steps it cannot be used for the first two time steps. A simple Euler method (again consult Fornberg (1998) for further details) was therefore used for the first two time-steps which were made shorter

than the other time-steps to limit the inaccuracies introduced by this crude approach. The size of time-step was chosen to always be much smaller than the length scale of the flow ($\frac{2\pi c}{m}$) divided by the fastest speed of information transport in the system (the larger of U and c_{ph}). The scheme was successfully benchmarked by considering the limiting cases of (i) pure diffusion of a m=4, l=4 field with no flow present, (ii) a simple, steady solid body flow acting on a simple l=2, m=2 (cos term only non-zero) initial field.

Trials showed that this numerical method permitted accurate time-stepping of the induction equation on a spherical surface, but it was rather slow and resolution was limited as the approach was very memory intensive. The source of inefficiency was that the velocity field u_q changes at each time step, so the $\sum_k A_{ijk}u_k$ had to be recomputed at each step. Also holding the large array A_{ijk} in memory limited the truncation of B_r that could be studied and hence the resolution of the solutions. Fortunately it proved possible to circumvent both these problems by making use of the constant propagation speed of the simple wave flows being investigated. By moving to a reference frame moving at the same speed as the phase speed of the wave flow (and carrying out the appropriate Galilean correction to the velocity), the wave flow in this reference frame becomes steady. Therefore $\sum_k A_{ijk}u_k$ is constant and need only be computed once at the start of the calculation, reducing the amount of memory required and greatly speeding up the calculations. The evolution of B_r in the results reported was therefore determined in a reference frame moving at phase speed of the wave flow.

The evolution of B_r in the stationary (mantle) reference frame was determined by coordinate transformations similar to those previously described by Holme and Whaler (2001). For a wave flow pattern drifting azimuthally at a constant angular rate $\dot{\Upsilon} = \frac{c_{ph}(\theta=90^\circ)}{c}$, then the accumulated drift angle Υ can be defined after time t to be

$$\Upsilon = \dot{\Upsilon} t = \frac{\omega}{m} t, \tag{8.86}$$

so for example, after a wave period ($t = \frac{2\pi}{\omega}$), the accumulated drift is $\Upsilon = \frac{2\pi}{m}$. The longitude coordinate in the original frame ϕ is then related to the longitude coordinate in the drifting reference frame ϕ' by

$$\phi' = \phi - \Upsilon. \tag{8.87}$$

The transformation of the velocity field in spherical polar co-ordinates to the drifting frame is then

$$\mathbf{u}'(\theta, \phi') = \mathbf{u}(\theta, \phi, t) - c_{ph} \sin\theta \, \hat{\boldsymbol{\phi}} \tag{8.88}$$

where $\hat{\boldsymbol{\phi}}$ is a unit vector in the eastward direction on the spherical surface. The transformations from the spherical harmonic representation of the magnetic field in the drifting frame to the spherical harmonics representation in stationary frame can be determined taking combinations of the expressions in equation (7) of Holme and Whaler (2001) (who use ψ rather than Υ to denote accumulated drift rate). Denoting real spherical harmonic

coefficients in the stationary frame by (b_l^{mc}, b_l^{ms}) and those in the drifting frame by ($b_l^{mc\prime}$, $b_l^{ms\prime}$) the required expressions are

$$b_l^{mc} = b_l^{mc\prime} \cos m\Upsilon - b_l^{ms\prime} \sin m\Upsilon, \tag{8.89}$$

$$b_l^{ms} = b_l^{mc\prime} \sin m\Upsilon + b_l^{ms\prime} \cos m\Upsilon. \tag{8.90}$$

The method of time-stepping in the drifting frame and then transforming back to the stationary frame was benchmarked against the original method of time-stepping in the stationary frame: the results in each case were found to agree very well, allowing confidence in the drifting reference frame methods which was, as expected, several of orders of magnitude faster and had smaller memory requirements.

The choice of the truncation level L of the spherical harmonic representations of the magnetic field and secular variation in both the stationary and drifting frame methods were limited by the memory capacity of the available computers and by the desire to produce accurately converged solutions within a sensible time period[6]. Typically, except for a few high resolution runs carried out when the chosen flows were particularly intense, truncation at spherical harmonic degree L=L_{sv} =40 was found to be sufficient to capture the evolution of the field over the range of parameter space explored.

Trials showed that when the flow possesses regions of strong convergence, the magnetic field eventually tends to become very localised and intense (as was earlier suggested the 1D model) in the absence of magnetic diffusion. It was therefore both numerically necessary and more physically realistic to include some magnetic diffusion (specifically, the terms $\frac{\eta}{r^2}(2B_r + \Delta B_r)$ that could be determined from knowledge of the field at the surface) at the level expected in Earth's core (η=1m^{2}s^{-1}). All results reported have been computed with this level of limited magnetic diffusion.

8.3.3 A parameter survey of results from the 2D wave flow model

Results reported in this section concern the action of the m=8 wave flows displayed in figure 8.6. The primary aims of this parameter survey were to determine whether the findings of the 1D model that different regimes of field evolution behaviour are possible depending on the relative amplitudes of c_{ph} and U carry over to a more Earth-like geometry and to to understand the influence of different equatorial flow symmetries on magnetic field evolution styles.

The simplest possible initial B_r approximating the scenario at Earth's core surface (an axial dipole[7], of amplitude -0.3×10^{5}nT) was chosen and its evolution calculated for a

[6] convergence was checked by examining the power spectra of the final magnetic field; if this decayed by several orders of magnitude prior to reaching the maximum spherical harmonic degree the solution was considered to be well converged.

[7] The axial dipole is actually a rather special case because azimuthal flows do not generate any secular variation when they act on it. To ensure that the results reported are not atypical, simple fields with m >0 are investigated in later.

suite of flow parameters with U varying between 0.01 km yr^{-1} and 10 km yr^{-1} and with c_{ph} varying between 0.01 km yr^{-1} and 100 km yr^{-1}). Both equatorially symmetric (E^S) and antisymmetric (E^A) flows were investigated for each choice of (U, c_{ph}) . The results were classified in terms of the regimes identified in the 1D model (either concentrating, pulsating or an intermediate regime called transition), by examining the time series for the evolution of the magnetic energy on the spherical surface. The results of the parameter survey are presented in figure 8.7.

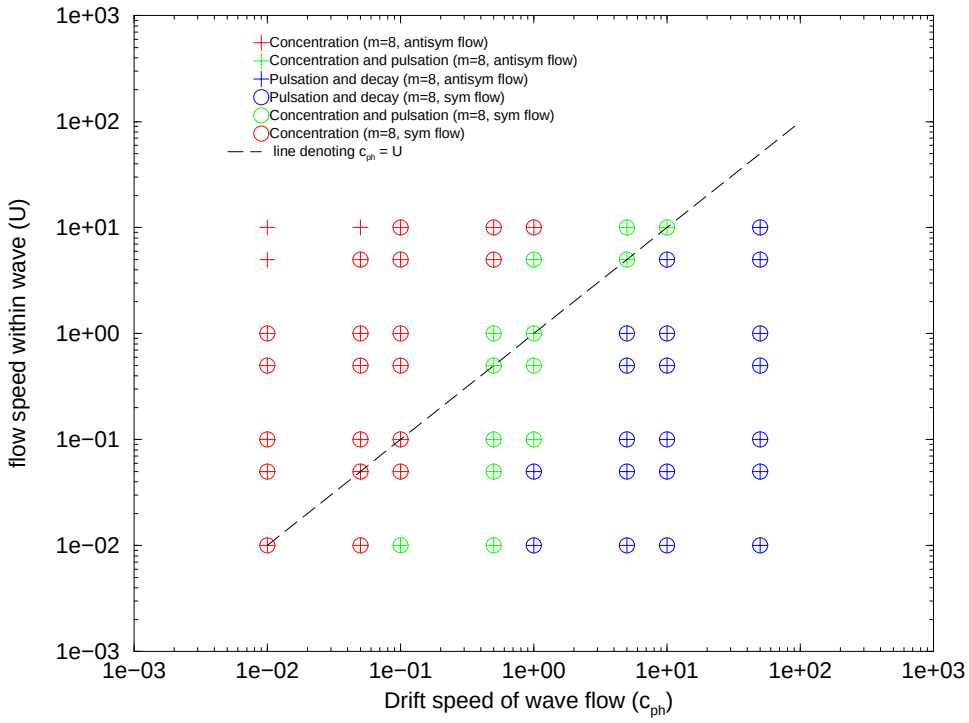

Figure 8.7: Action of 2D wave flow on a axial dipole initial magnetic field. Classification of the result of an m=8 wave flow from Zhang et al. (2000) acting at the outer boundary of a spherical container on an initially dipolar magnetic field, with limited magnetic diffusion present. c_{ph} was varied from 0.01 km yr^{-1} to 100 km yr^{-1} and U from 0.01 km yr^{-1} to 10 km yr^{-1}. Crosses represent the action of the E^A wave flows, circles represent E^S wave flows. Red represents concentration of magnetic field into drifting field maxima and minima; blue represents pulsation of amplitude of drifting field concentrations; green represents a transition between these two regimes with very slow pulsation of drifting field concentrations. The dashed line represents the boundary between the concentrating and pulsating regimes predicted to arise at $|c_{ph}| = |U|$ from a 1D analytic model which neglects diffusion. All speeds shown are measured in units of km yr^{-1}.

The spherical geometry, different equatorial symmetries of the flows and the presence of magnetic diffusion makes little difference to the qualitative character of the magnetic field evolution, which matched the predictions of the 1D model. Drifting field concentrations are obtained when $|U| >> |c_{ph}|$ and pulsating, drifting field concentrations are obtained when $|U| << |c_{ph}|$. In the region close to $|U| = |c_{ph}|$ some deviation from the predicted behaviour was observed, especially when c_{ph} was small, with more results being classified

as simple concentration than was expected. This is probably because the field pulsations were so long period (longer than the models were integrated for) that the associated pulsations were not observed. When c_{ph} was small and U was larger, is was not possible to follow the field evolution for long because field concentration was so much stronger than the horizontal diffusion that the resolution of the models was insufficient to capture the details of the very sharp field features formed. The major conclusion from the survey is clear: two distinct regimes of drifting concentrating field and drifting pulsating field are produced by the kinematic action of a wave flows on a spherical surface depending on whether U or c_{ph} is larger.

Time series from concentration and pulsation regimes

In figure 8.8 time series for 400 years of evolution of the maximum amplitude of the non-axial dipole radial magnetic field (B_r^{NAD}) are shown, in examples taken from the two regimes identified in the parameter survey. Each row documents a particular wave drift rate (c_{ph}), the right hand column is for E^S waves, the left hand column is for E^A waves and the different lines on each plot represent different magnitudes of fluid velocity (U) within the drifting wave.

When the drift speed is slow (c_{ph}=0.05 $\mathrm{km\,yr^{-1}}$) as shown in figure 8.8a,b, continuous growth in field amplitude is observed, with the highest amplitudes being obtained for the largest U. The maximum field amplitudes seem to be approaching a steady state, though this would require longer model runs for confirmation— the results shown are still slowly growing in amplitude after 400 years. Such an approach to a steady state of balance between field advection and horizontal diffusion in the drifting reference frame was anticipated in the modelling of §8.2.5. To compare to the analytic model of §8.2.5, it is worth noting that in the present model $R_m^{cl} = \frac{Uc}{m\eta} \sim 14U$. The 1D analytical model predicts field concentration factors in the advection-diffusion balance of $\frac{e^{14U}}{I_0(14U)}$ which translates into factors of 1.8, 2.6, 9.3, 20.9 respectively for U of 0.05, 0.1, 0.5, 1, and 5 $\mathrm{km\,yr^{-1}}$. Lower field concentrations are, however, expected in 2D (by about a factor for 3 in the high R_m limit) because the flows are not concentrating field in such a precise, symmetrical way as in the 1D model. Furthermore, the results shown have not yet reached the advection-diffusion balance so it may be premature to compare them to the 1D model where this is assumed to be the case. Bearing in mind these caveats the results shown in figure 8.8 seem compatible with the 1D analytic predictions of advection-diffusion balance.

E^S wave flows were found to be slightly more efficient at producing field concentrations than E^A flows, and flow amplitudes of $5\mathrm{km\,yr^{-1}}$ or greater were found to be required to produce field amplitudes 2 or more times stronger than the initial dipole field strength (i.e. for B_r^{NAD} to exceed 1×10^5nT). This is because there is more flow convergence and divergence in the E^S flow compared to the E^A flows (see figure 8.6).

(a) Max. of B_r^{NAD}, c_{ph}=0.05, E^S. **(b) Max. of B_r^{NAD}, c_{ph}=0.05, E^A.**

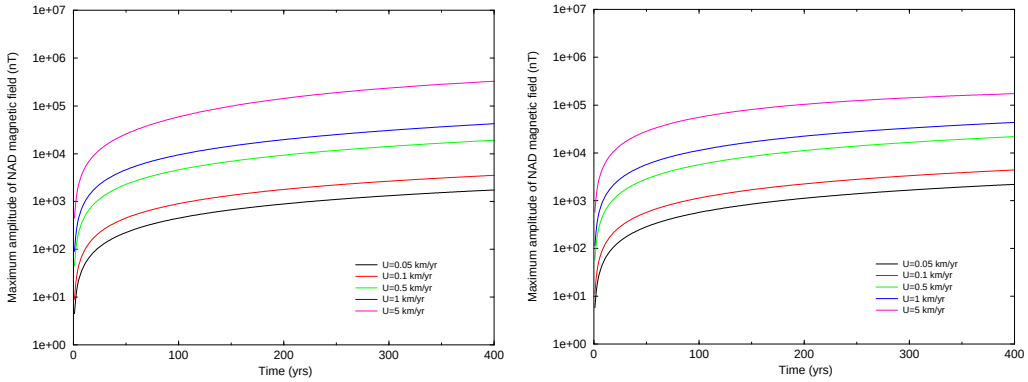

(c) Max. of B_r^{NAD}, c_{ph}=50, E^S. **(d) Max. of B_r^{NAD}, c_{ph}=50, E^A.**

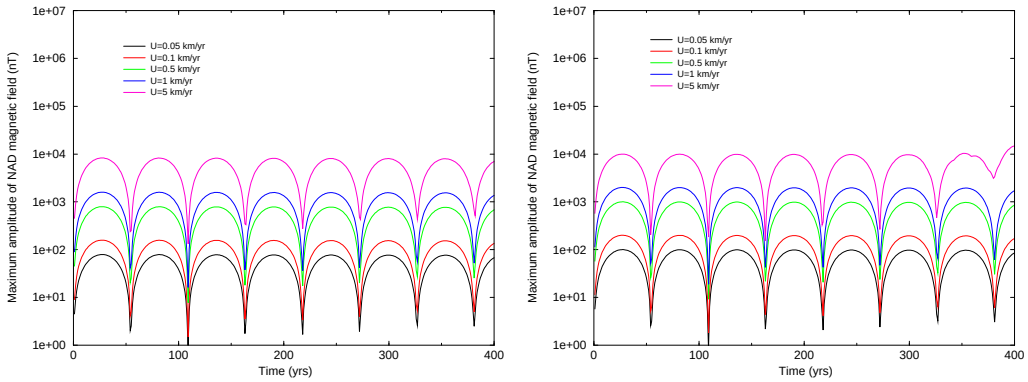

Figure 8.8: Time series of evolution of maximum amplitude of B_r^{NAD}. Time series of the evolution of the maximum amplitude of the non axial dipole (NAD) part of the radial magnetic field (B_r^{NAD}), obtained when an initial axial dipole radial magnetic field is acted on by an the m=8 wave of the form specified in equation (8.77). The left hand column shows the effect of E^S flows, the right hand column the effect of E^A flows. The top row is for $c_{ph} = 0.05\mathrm{km\,yr^{-1}}$ while the bottom row is for $c_{ph} = 50\mathrm{km\,yr^{-1}}$ and each plot illustrates the effect of 5 different wave flows with amplitudes U=0.05, 0.1, 0.5, 1.0, 5.0 $\mathrm{km\,yr^{-1}}$. Only the first 400 years of the field evolution is shown in each case, and the field amplitudes (B_r^{NAD}) are plotted on a log scale.

When $|U| << |c_{ph}|$ periodic pulsations in field amplitude were observed. One cycle of pulsation involves field amplitude growing (at a decaying rate) towards a maximum, then symmetrically decaying (at an increasing rate) to a low level, where there is a discontinuity in the growth rate and rapid growth in field amplitude begins again. The period of the pulsations is observed to be independent of U when $U << c_{ph}$, and matches the prediction of the time taken for the Galilean correction flow ($-c_{ph}$) in the drifting frame to travel one wavelength of the flow: $(\frac{2\pi c}{m}/c_{ph})$ ~54yrs. In figure 8.8d, for U=5$\mathrm{km\,yr^{-1}}$ close to the end of the time series, some deviation from simple periodic behaviour is observed. This is probably a numerical effect rather than a physical effect and occurs because the magnetic field produced by the strong wave flow in this case has become too

small scale to be followed with the resolution chosen. This does not however limit the applicability of the results reported.

8.3.4 Spatial characteristics of field evolution in the 2D wave flow model

The evolution of the morphology of B_r at the core surface provides one of the few constraints on the fluid motions inside of Earth's outer core. In this chapter the aim is to test the hypothesis that kinematic action of wave flows is capable of explaining some aspects of that magnetic field evolution. In this section the patterns of evolution of B_r produced by simple wave flows are described to enable comparison with the evolution found in geomagnetic field models as was described in chapters 3 and 4.

In figures 8.9 to 8.14 B_r resulting when an initial axial dipole is acted on by m=8, E^S and E^A flows for a range of choices of c_{ph} and U are presented. In each case (a) and (b) are B_r after 100 years and 300 years in the non-drifting (stationary) reference frame (SF), where the mean azimuthal flow is zero and the wave propagates with a phase speed c_{ph}; (c) is the velocity field in a drifting (rotating) reference frame (RF) where the wave flow is steady but there is an azimuthal Galilean correction flow. (d) is B_r^{NAD} (the radial magnetic field minus its axial dipole component) in the drifting (rotating) reference frame (RF) after 300 years. This plot can easily be compared with (c) and allows investigation of the relative positions of field concentrations and regions of flow convergence in the drifting (rotating) reference frame. The stationary field concentrations observed in the drifting frame of course move azimuthally with speed c_{ph} in the original reference frame.

Concentration regime

In figure 8.9 the field evolution produced by an E^S flow with $c_{ph} = 0.05$ km yr^{-1} and U=5 km yr^{-1} (so that U/c_{ph}=100: well inside the concentrating field regime) is presented. Associated animations of B_r and B_r^{NAD} are found in A8.1 and A8.2 respectively. As time goes on, field concentrations (of the same polarity as the initial field) are observed to form and become increasingly sharp and intense at locations of flow convergence in the drifting frame, which are almost identical to the positions of flow convergence in the stationary frame because c_{ph} is very small. The positions of strongest convergence (where largest arrows in the flow plot point towards each other) occur at regions of converging eastward and westward flow at the equator, but because the axial dipole initial B_r is weak there, highest concentrations of B_r develop at compromise latitudes close to 15 °N and 15°S. Because the flow is E^S and is acting on an E^A initial field, there is no distortion of the magnetic equator and B_r concentrations in one hemisphere occur at the same longitude as the concentrations in the opposite hemisphere. The whole pattern is observed to move slowly in the stationary frame of reference while the amplitude of field concentrations gradually increases.

(a)B_r in SF: c_{ph}=0.05, U=5, 100yrs. **(b)B_r in SF: c_{ph}=0.05, U=5, 300yrs.**

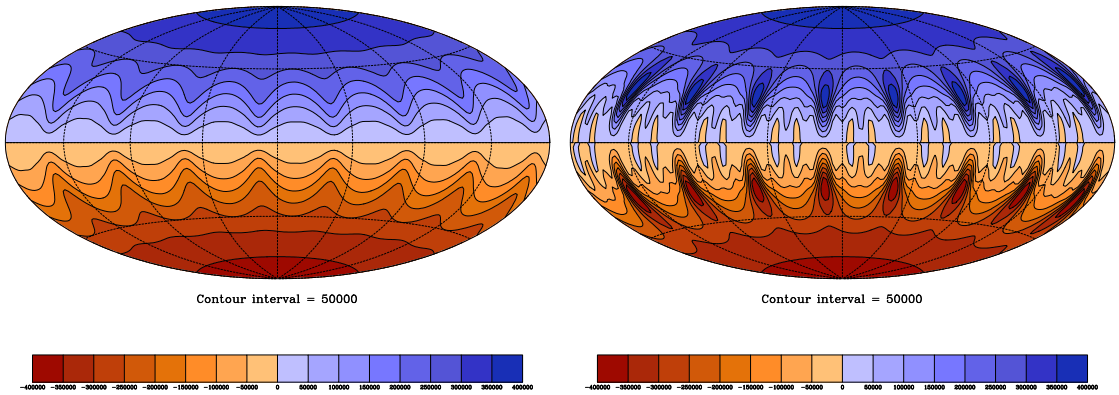

(c)u in RF: c_{ph}=0.05, U=5 . **(d)B_r^{NAD} in RF: c_{ph}=0.05, U=5, 300yrs.**

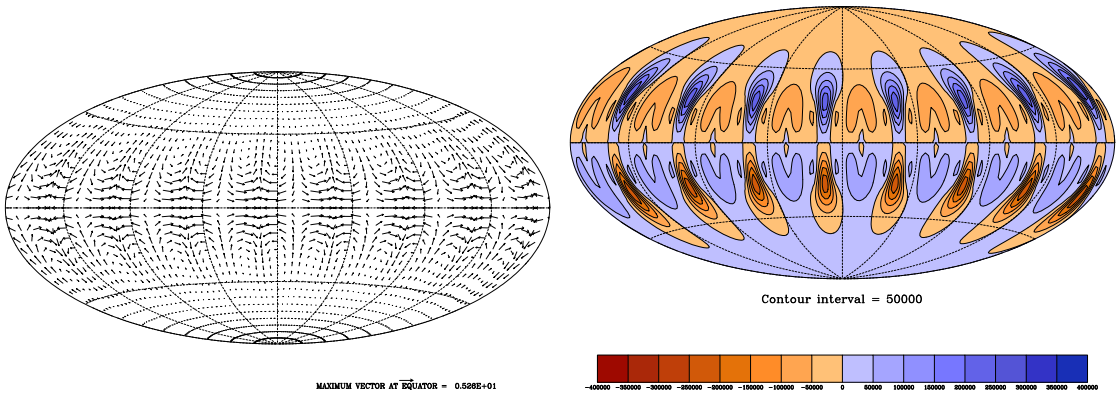

Figure 8.9: Axial dipole evolution for flow with m=8, E^S, c_{ph}=0.05, U=5. Drifting field concentrations produced from an initial axial dipole B_r for a m=8, E^S, c_{ph}=0.05 km yr^{-1}, U=5 km yr^{-1} flow. In (a) is a contour plot of B_r in units of nT after 100 yrs in a frame that is not drifting with the wave flow; (b) is the same after 300 years. (c) is a plot of the steady wave flow in a reference frame drifting (rotating) with the phase speed c_{ph} of the wave: arrows show the flow amplitude and direction on the spherical surface. (d) shows the non-axial dipole component of B_r in the reference frame moving along with the wave flow, after 300 years. Field concentrations occur at the positions of flow convergence in the drifting frame. These and all subsequent snapshots on a spherical surface in this chapter are in Mollewiede equal area map projection. The units of the contours of B_r are nT, while those for the flow vectors arekm yr^{-1}.

(a)B_r in SF: c_{ph}=0.05, U=5, 100yrs. **(b)B_r in SF: c_{ph}=0.05, U=5, 300yrs.**

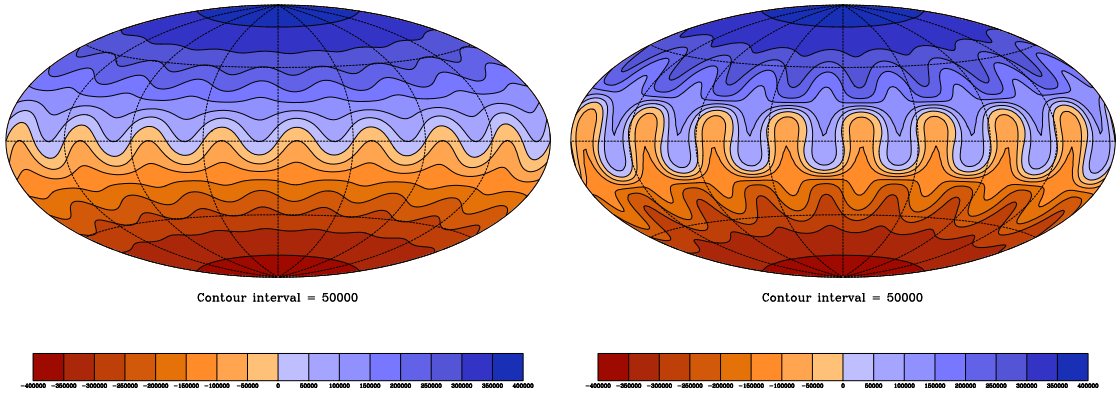

(c)u in RF: c_{ph}=0.05, U=5 . **(d)B_r^{NAD} in RF: c_{ph}=0.05, U=5, 300yrs.**

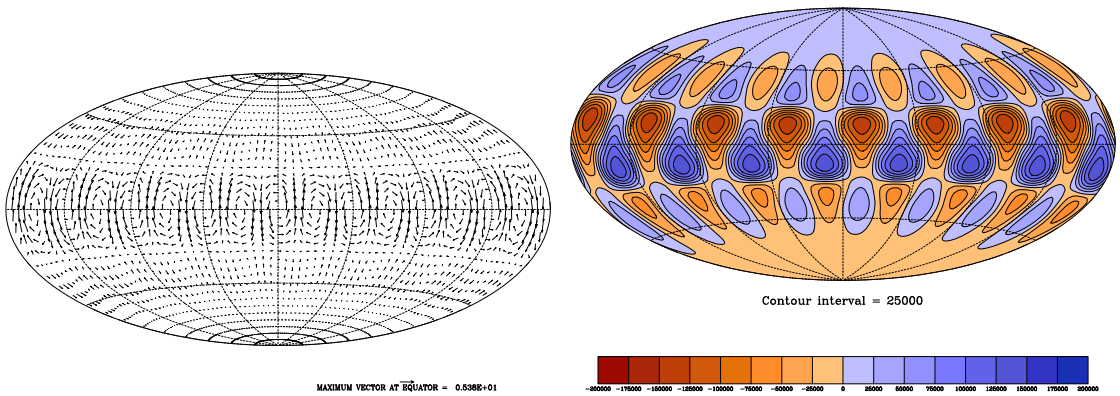

Figure 8.10: Axial dipole evolution for flow with m=8, E^A, c_{ph}=0.05, U=5. Drifting field concentrations produced from an initial axial dipole B_r for a m=8, E^A, c_{ph}=0.05 km yr^{-1}, U=5 km yr^{-1} flow. In (a) is a contour plot of B_r in units of nT after 100 yrs in a frame that is not drifting with the wave flow; (b) is the same after 300 years. (c) is a plot of the steady wave flow in a reference frame drifting (rotating) with the phase speed of the wave: arrows show the flow amplitude and direction on the spherical surface. (d) shows the non-axial dipole component of B_r in the reference frame moving with the wave, after 300 years. Field concentrations occur at the positions of flow convergence in the drifting frame.

(a)B_r in SF: c_{ph}=5, U=5, 100yrs. **(b)B_r in SF: c_{ph}=5, U=5, 300yrs.**

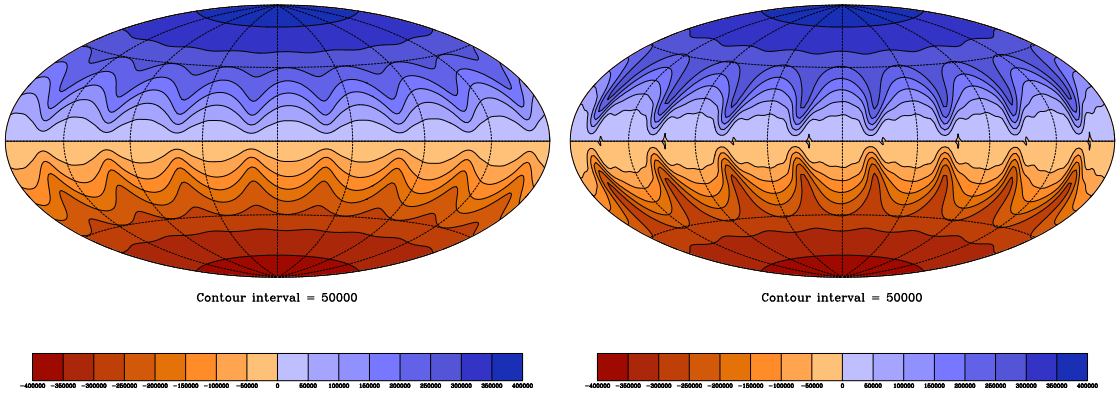

(c)u in RF: c_{ph}=5, U=5 . **(d)B_r^{NAD} in RF: c_{ph}=5, U=5, 300yrs.**

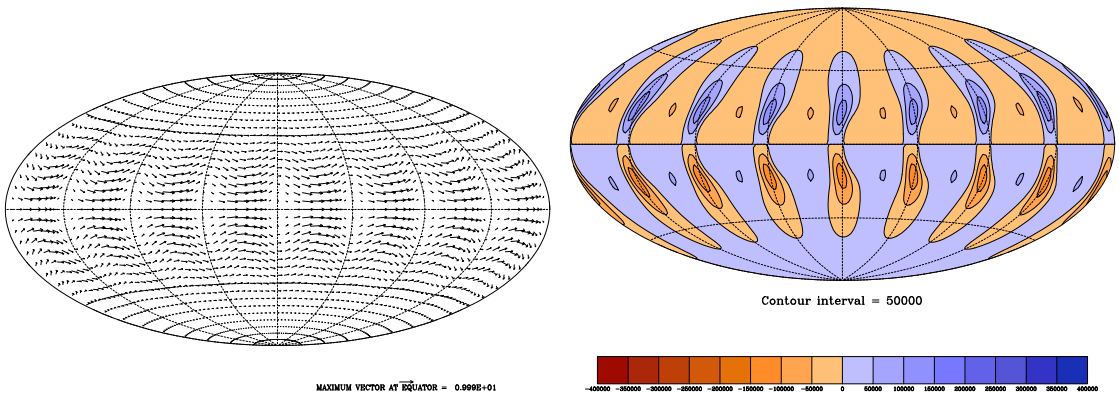

Figure 8.11: Axial dipole evolution for flow with m=8, E^S, c_{ph}=5, U=5. Drifting field concentrations produced from an initial axial dipole B_r for a m=8, E^S, c_{ph}=5 km yr^{-1}, U=5 km yr^{-1} flow. In (a) is a contour plot of B_r in units of nT after 100 yrs in a frame that is not drifting with the wave flow; (b) is the same after 300 years. (c) is a plot of the steady wave flow in a reference frame drifting (rotating) with the phase speed of the wave: arrows show flow amplitude and direction on the spherical surface. (d) shows the non-axial dipole parts of B_r in the reference frame moving with the wave, after 300 years. Field concentrations occur at the positions of flow convergence in the drifting frame.

(a)B_r in SF: c_{ph}=5, U=5, 100yrs. **(b)B_r in SF: c_{ph}=5, U=5, 300yrs.**

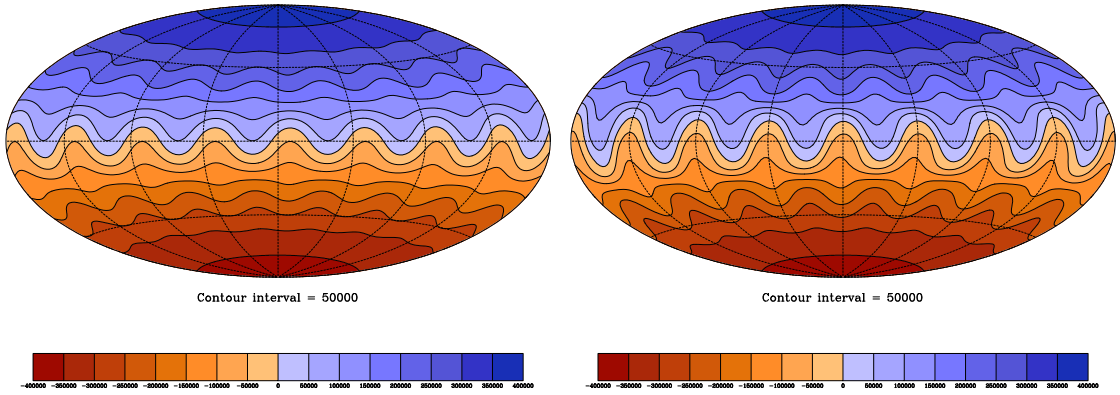

(c)u in RF: c_{ph}=5, U=5 . **(d)B_r^{NAD} in RF: c_{ph}=5, U=5, 300yrs.**

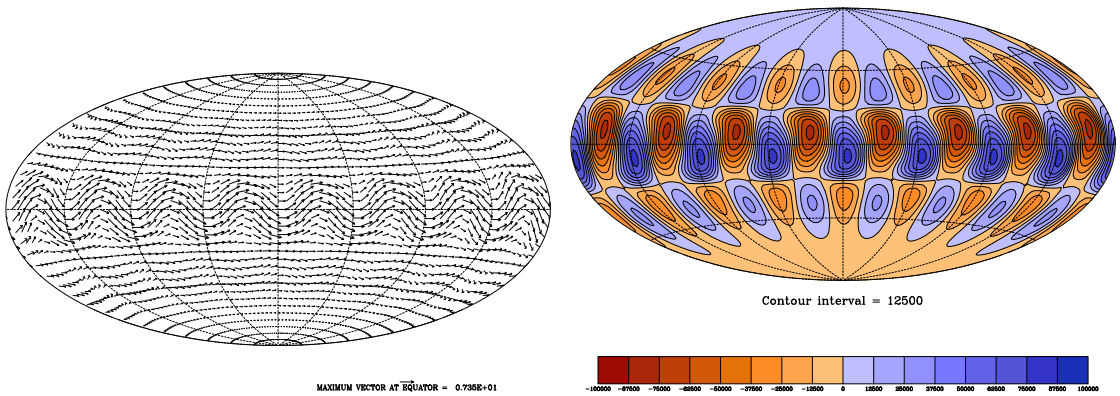

Figure 8.12: Axial dipole evolution for flow with m=8, E^A, c_{ph}=5, U=5. Drifting field concentrations produced from an initial axial dipole B_r for a m=8, E^A, c_{ph}=5 km yr^{-1}, U=5 km yr^{-1} flow. In (a) is a contour plot of B_r in units of nT after 100 yrs in a frame that is not drifting with the wave flow; (b) is the same after 300 years. (c) is a plot of the steady wave flow in a reference frame drifting (rotating) with the phase speed of the wave: arrows show the flow amplitude and direction on the spherical surface. (d) shows the non-axial dipole component of B_r in the frame rotating with the wave, after 300 years. Field concentrations occur at the positions of flow convergence in the drifting frame.

(a)B_r in SF: c_{ph}=50, U=5, 100yrs. **(b)B_r in SF: c_{ph}=50, U=5, 300yrs.**

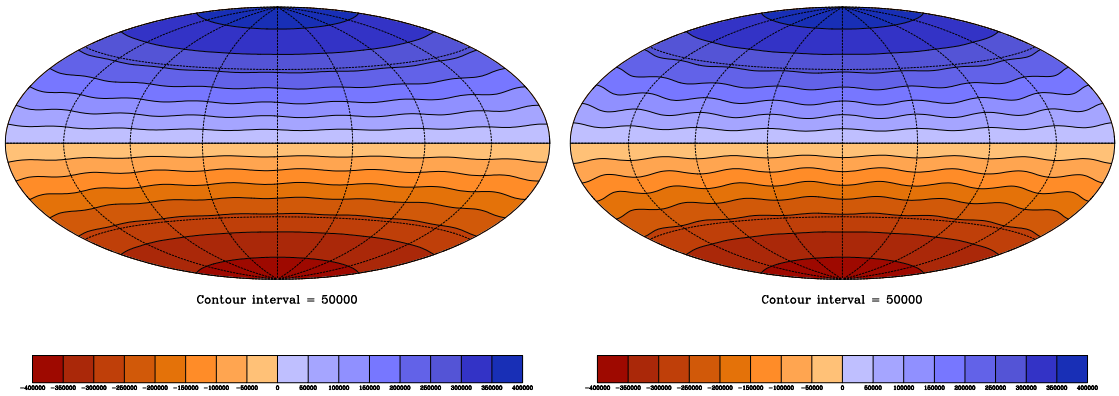

(c)u in RF: c_{ph}=50, U=5 . **(d)B_r^{NAD} in RF: c_{ph}=50, U=5, 300yrs.**

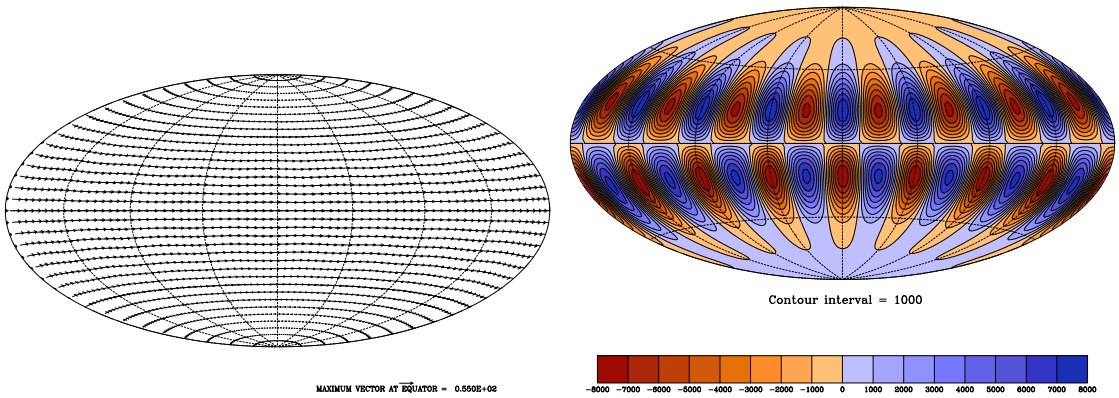

Figure 8.13: Axial dipole evolution for flow with m=8, E^S, c_{ph}=50, U=5. Drifting field concentrations produced from an initial axial dipole B_r for a m=8, E^S, c_{ph}=50 km yr^{-1}, U=5 km yr^{-1} flow. In (a) is a contour plot of B_r in units of nT after 100 yrs in a frame that is not drifting with the wave flow; (b) is the same after 300 years. (c) is a plot of the steady wave flow in a reference frame drifting (rotating) with the phase speed of the wave: arrows show the flow amplitude and direction on the spherical surface. (d) shows the non-axial dipole component of B_r in the reference frame moving with the wave, after 300 years. Field concentrations occur at the positions of flow convergence in the drifting frame.

(a)B_r in SF: c_{ph}=50, U=5, 100yrs. **(b)B_r in SF: c_{ph}=50, U=5, 300yrs.**

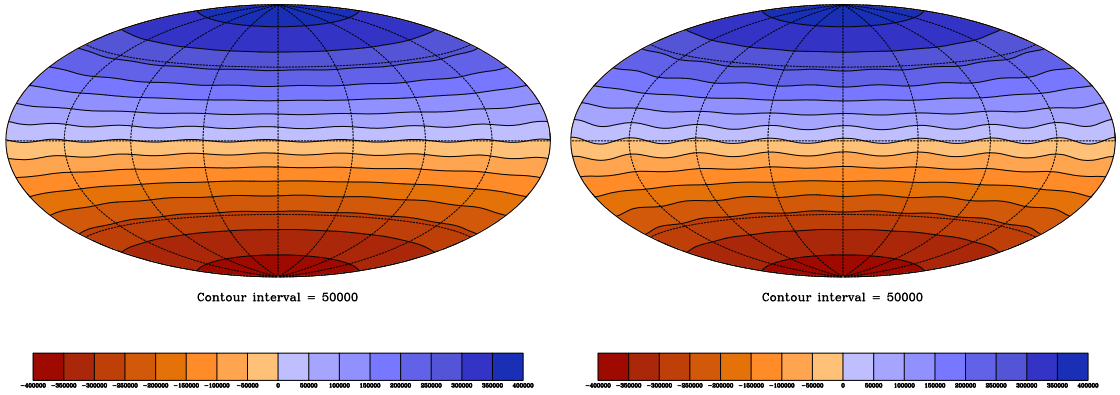

(c)u in RF: c_{ph}=50, U=5 . **(d)B_r^{NAD} in RF: c_{ph}=50, U=5, 300yrs.**

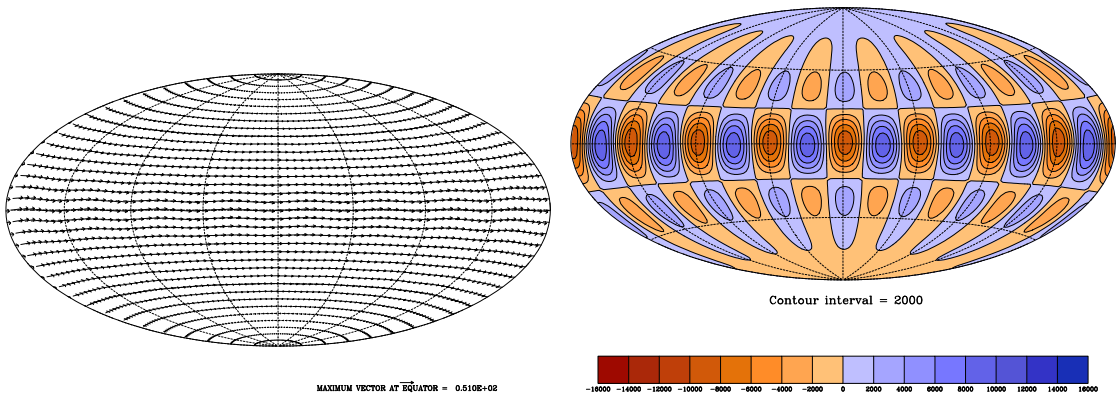

Figure 8.14: Axial dipole evolution for flow with m=8, E^A, c_{ph}=50, U=5. Drifting field concentrations produced from an initial axial dipole B_r for a m=8, E^A, c_{ph}=50 km yr^{-1}, U=5 km yr^{-1} flow. In (a) is a contour plot of B_r in units of nT after 100 yrs in a frame that is not drifting with the wave flow; (b) is the same after 300 years. (c) is a plot of the steady wave flow in a reference frame drifting (rotating) with the phase speed of the wave: arrows show the flow amplitude and direction on the spherical surface. (d) shows the non-axial dipole parts of B_r in the reference frame rotating with the wave, after 300 years. Field concentrations occur at the positions of flow convergence in the moving frame.

Figure 8.10 documents the field evolution produced by an E^A flow with the same parameters of $c_{ph} = 0.05$ km yr^{-1} and U=5 km yr^{-1}. Animations of the evolution of B_r and B_r^{NAD} are found in animations A7.3 and A7.4. In this case although less intense field concentrations are obtained, the major action of the wave flow is to produce oscillations of the magnetic equator. Field concentrations again arise at locations of flow convergence in the rotating reference frame: here these arise where poleward flow from low latitude meets equatorward flow from high latitudes, again near 15° north and south.

Transition Regime

Figures 8.11 and 8.12 along with animations A8.5 to A8.8 illustrate the properties of B_r evolution in the transition region between the concentration regime and the pulsation regime (when $c_{ph} = U =$ 5km yr^{-1}). Field morphologies in this case are similar to those found in the concentration regime, but the amplitude of the concentrations are smaller and have stopped growing, probably as part of some long period pulsation, by the end of the 300 year interval studied. Field concentrations once again appear at the positions of flow convergence in the rotating frame, but these are no longer the positions of flow convergence in the stationary frame (they are offset by a quarter of a cycle or $\frac{\pi}{2}$ radians described as previously in the 1D model). The drift in the field concentrations is observed very clearly in the animations in the stationary frame. This is unequivocal evidence that propagating wave flows can produce drifting magnetic field concentrations in a spherical geometry.

Pulsating regime

Figures 8.13 and 8.14 along with animations A8.9 to A8.12 illustrate the properties of B_r evolution in the pulsating regime when c_{ph}= 50km yr^{-1} and U= 5km yr^{-1}. For the same strength of U clear distortion of the initial field was observed in the concentrating regime; now only weak modulation of the initial field is seen. The perturbation to B_r has the same morphology as that found in the concentration and transition regimes, with field concentrations occurring at locations of flow convergence in the drifting reference frame. However, the flow in the drifting (rotating) reference frame is now dominated by the back-flow introduced by the Galilean change of reference frame, so no neutral points of flow exist and, in a manner similar to the 1D model, the field is advected over regions of net convergence and divergence causing the characteristic pulsations in amplitude. For the cases examined this pulsation manifests itself in intervals of growth of deviations of the contours of magnetic field from the axial dipole (either E^S or E^A depending on the parity of the wave flow), followed by a rapid decay back to the purely dipolar state, followed by another interval of rapid growth as the pulsation starts again. For sufficiently intense U (but it must be less than c_{ph} if pulsation is to occur) this regime can produce drifting concentrations of B_r that periodically pulsate in amplitude.

Effect of initial magnetic fields with $m > 0$

A possible objection to generalising the findings of the previous section might be that only the influence of the flow on an m=0, E^A, axial dipole initial B_r has been studied. To deal with this objection, initial fields with m=1 and 4 were also studied for the case when $c_{ph} = U = 5$ km yr^{-1}. The resulting B_r morphology after 300 years is shown in figure 8.15 and animations of the evolution can be found in animations A8.13 and A8.14.

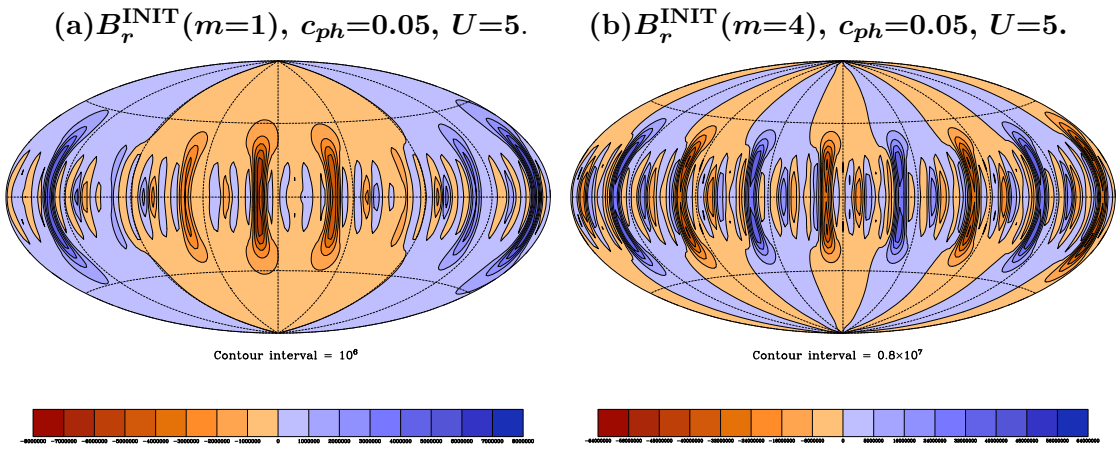

Figure 8.15: Evolution of initial B_r with m=1, 4.
Snapshots of the B_r, produced by after 300 years action by the m=8 E^S wave flow with c_{ph}=0.05 and U=5. In (a) the initial B_r was an equatorial dipole field ($m = 1$ while in (b) it was a l=4, m=4 (cosine term only) spherical harmonic.

The presence of an $m > 0$ initial field does not influence the number of strongest magnetic field concentrations obtained: this still matches the azimuthal wavenumber m of the wave flow. Field concentrations are coincident with the locations of the maxima of flow convergence at the geographical equator in the drifting (rotating) reference frame. The wavenumber of the initial field does however determine the polarity of the field concentrations. The field concentration will always be of the same polarity as the initial field at the location of the convergence of the flow in the drifting reference frame. When this flow convergence position occurs at a point where the magnetic field is close to zero, field concentrations of both polarities are obtained very close together.

8.3.5 Evolution of realistic magnetic fields produced by wave flows

Having established the influence of a wave flow on a variety of simple initial radial magnetic fields, the next logical step is to determine the effect such a flow would have on a more complex and realistic initial B_r. The 1590 B_r at the core surface from *gufm1* (see appendix A for a description of this model) shown in figure 8.16a was chosen for this purpose. Its observed evolution is illustrated by a snapshot of the field 200 years later in 1790 in figure 8.16b. A particularly notable feature is the westward motion of the B_r

concentration starting under India that finishes under the middle of the Indian ocean. It is the behaviour of such azimuthally drifting field features that the action of wave flows must be able to reproduce in order to be considered as a plausible mechanisms for the origin of azimuthal geomagnetic secular variation.

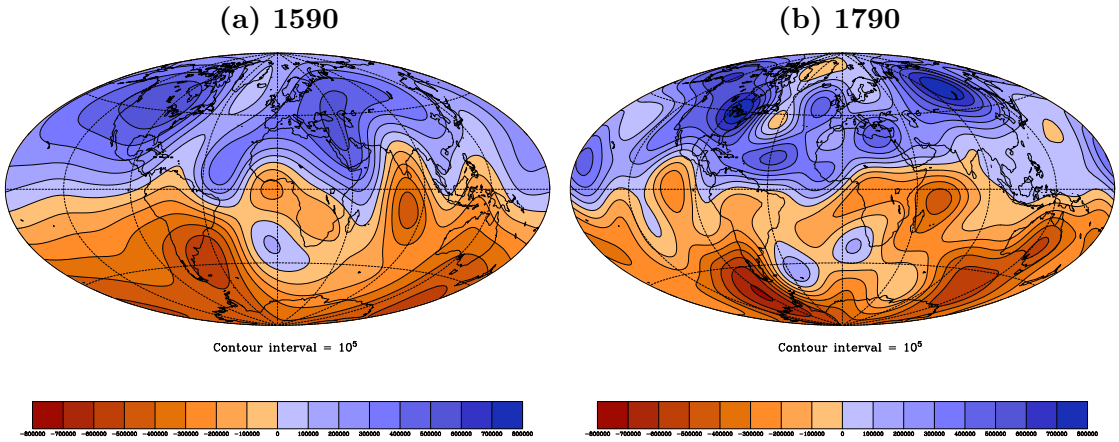

Figure 8.16: B_r from *gufm1* at core surface in 1590 and 1790.
Snapshots of B_r at the core surface, from the model *gufm1*, in 1590 in (a) and 200 years later in 1790 in (b).

The propagation speed c_{ph} of wave flows was chosen to match the observed westward drift speed of field features at the core surface (17 km yr^{-1})[8], magnetic diffusion was set to the expected core value of 1 m^{2}s^{-1} (31.5 km^{2}yr^{-1}) and the 1590 initial field was integrated forward for 200 years with both E^S and E^A wave flows with speeds within the wave (U) of 1, 5, 10, 15, 17 and 20 km yr^{-1}. Snapshots of the resulting B_r from E^S flows are presented in figure 8.17 and animations A8.15 to A8.20 and from E^A flows in figure 8.18 and animations A8.21 to A8.26 (further details of the animations can be found in appendix F).

The E^S flow is considered first. When U is 1 km yr^{-1} the influence of flow convergence is too weak to produce much observable effect on the field morphology and the resulting pulsations are too weak to be seen, except through tiny oscillations in the amplitude and positions of pre-existing low latitude field concentrations. When U=5 km yr^{-1}, the flow is strong enough to produce observable effects, but the positions and motions of field concentrations are still dominated by the initial field configuration. The animation A8.16 of field evolution in this case shows both growth and drift of field concentrations, but during the rapid decay phase of the pulsation the field returns back toward its initial configuration, and no consistent motions of field concentrations are achieved. For U=10 km yr^{-1}, the effects of field concentration and drift can be clearly seen, with field amplitudes several times that of the initial field are produced as the field is pulled

[8]This is an extreme scenario designed to highlight the effects of pure wave propagation. If azimuthal flows also contributed to the westward drift of B_r features as seems likely, then lower choices for c_{ph} could be envisaged.

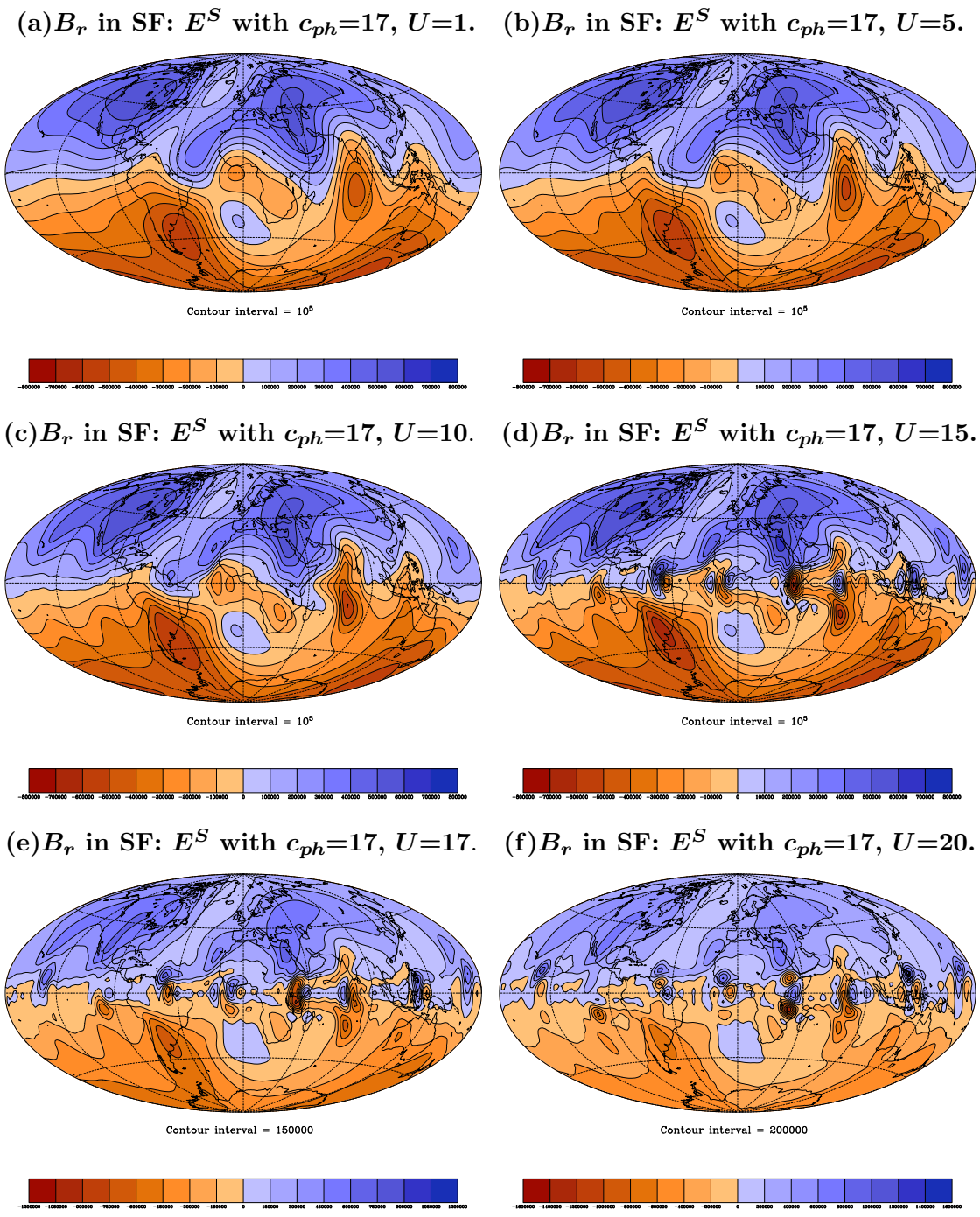

Figure 8.17: Action of E^S, m=8 flow on 1590 initial field after 200yrs. Result of 200 years of field evolution produced by E^S wave flows and weak magnetic diffusion starting from B_r at the core surface in 1590. The wave flows were chosen to have a propagation speed of c_{ph}= 17km yr^{-1} to match the observed westward drift speed and have wave amplitudes (U) of 1 km yr^{-1} in (a), 5 km yr^{-1} in (b), 10 km yr^{-1} in (c), 15 km yr^{-1} in (d), 17 km yr^{-1} in (e) and 20 km yr^{-1} in (f) (note the change in scale in (e) and (f)).

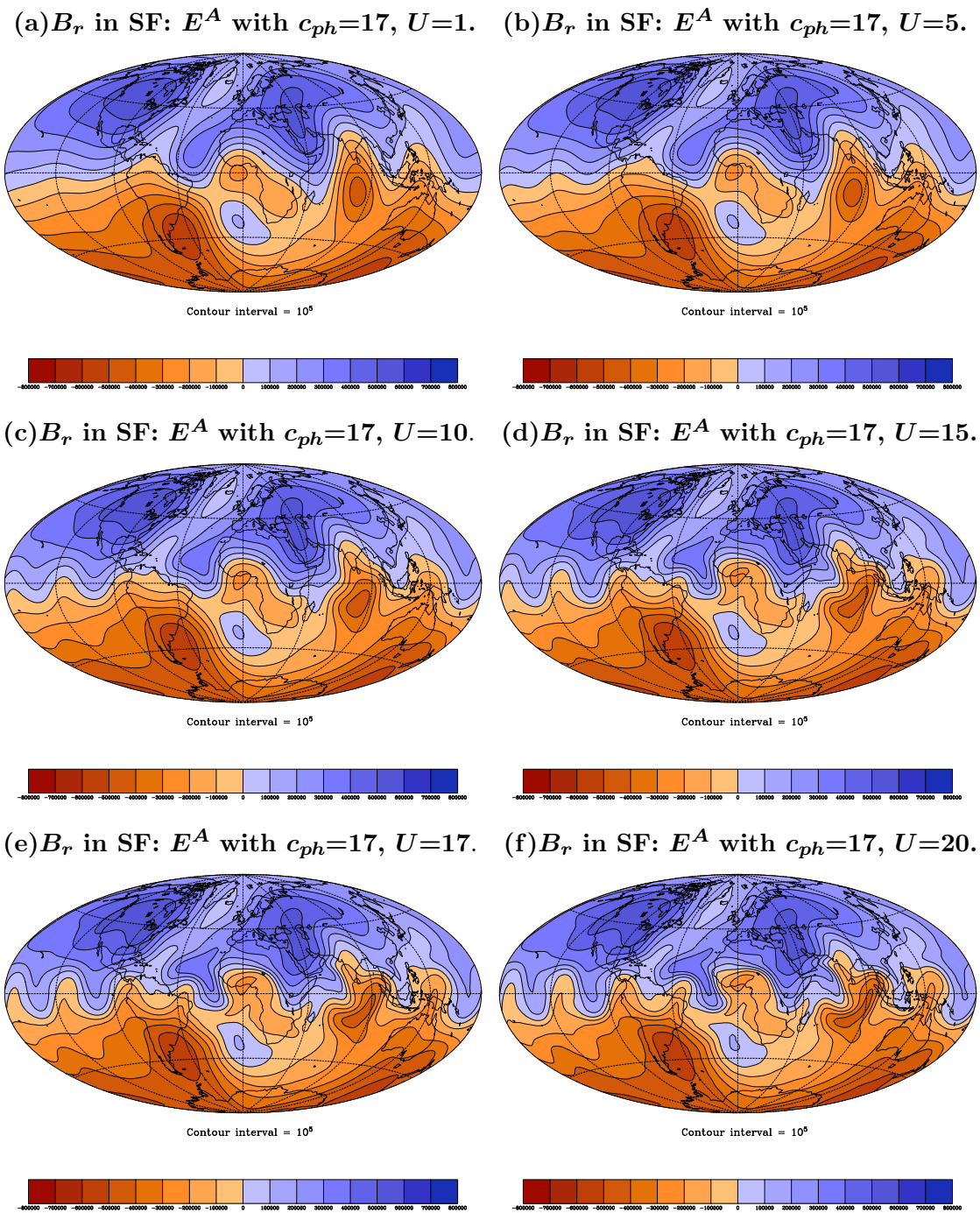

Figure 8.18: Action of E^A, m=8 flow on 1590 initial field after 200yrs. Result of 200 years of field evolution produced by E^A wave flows and magnetic diffusion on B_r at the core surface in 1590. The wave flows were chosen to have a drift speed of c_{ph}=17 km yr^{-1} to match the observed westward drift speed and have wave amplitudes (U) of 1 km yr^{-1} in (a), 5 km yr^{-1} in (b), 10 km yr^{-1} in (c), 15 km yr^{-1} in (d), 17 km yr^{-1} in (e) and 20 km yr^{-1} in (f).

towards the positions of flow convergence in the drifting (rotating) reference frame. However the field evolution is still in the pulsation regime and consistently propagating field features are still not observed. For example, the field concentration under India is initially intensified for the first 25 years of the wave flow action, then is observed to drift westward at speed c_{ph} for 75 years, but once the decay phase of the pulsation begins, the amplitude of the field perturbation decays and the field feature decays, even appearing to return towards its initial location.

When U=15 km yr^{-1} the field morphology becomes dominated by the positions of flow convergence, rather than by the initial magnetic field configuration. The feature under India can now be followed drifting as far as Africa, but has become much smaller scale. The pulsation phenomena is still evident, but now seems to have a longer period. When U=17 km yr^{-1} and U=20km yr^{-1} the field evolution is completely dominated by the positions of the flow convergence: clearly the simple wave flow chosen is not sufficiently complex to capture the detailed motions of field features at a range of latitudes. For an E^S wave flow acting on the 1590 initial field the field concentrations formed are E^S suggesting they result primarily from the action of the E^S wave flow on the E^S part of the 1590 field (that dominates the E^A component at low latitudes). Wave flows with large amplitudes are observed to produce field concentrations much more intense and smaller scale than those seen in observations (though the influence of crustal filtering has not yet been taken into account — see next section).

Moving on to consider the influence of E^A wave flows on the 1590 initial field shown in figure 8.18, the situation is similar to the E^S flow case with regard to little influence on the initial field when U is small (1 or 5 km yr^{-1}) while the influence of the flow again dominates field evolution when U is greater than 15 km yr^{-1}. The major impact of this flow on the field morphology is not to produce strong drifting field concentrations but to produces oscillations in the magnetic equator which drift westward. The observed field evolution with the E^A wave flows seems qualitatively different from that observed in the historical geomagnetic field model *gufm1*.

8.3.6 Impact of crustal filtering and sources of hemispherical asymmetry

Unfortunately, it is at present impossible to observe the small length scale ($l < 13$) details of the radial magnetic field at the core surface using observations made at Earth's surface because crustal magnetic fields contaminate measurements. This contamination means that in order to obtain converged images of the field at the core surface, regularisation must be applied during the inversion of observations for a field model. Details of the regularisation techniques can be found in appendix A or in Gubbins (2004). Field models obtained from regularised inversion (using quadratic norms, as is the case for *gufm1*) are therefore a smoothed image of the true core field. In order to determine whether the field morphologies produced by the action of wave flows bear any resemblance to the

observed field evolution, the calculated fields should be smoothed in the same manner as is the observed field.

A taper function which mimics the effect of field regularisation can be derived from the expression for the norm minimised on the core surface during the construction of field models. This involves differentiating the objective function (see appendix A) with respect to the gauss coefficients, setting the differential to zero and rearranging (For further details see Wardinski (2005), chapter 3, page 44). For the Ohmic heating norm minimised during the construction of *gufm1* the regularised (damped) gauss coefficients ${g_l^m}_{\mathrm{D}}$ are found to be related to the true coefficients g_l^m by the expression

$$ {g_l^m}_{\mathrm{D}} = \frac{g_l^m}{1 + \lambda_S \frac{4\pi(l+1)(2l+1)(2l+3)}{l} \left(\frac{a}{c}\right)^{2l+4}} \tag{8.91} $$

Using the same choice of the damping parameter as for *gufm1* ($\lambda_S = 1 \times 10^{-12}\mathrm{nT}^{-2}$), the results of the field evolution computations reported in the previous section can now be processed to mimic what would be observed in a regularised field model. Snapshots of the results of the application of such processing are shown in figure 8.19. Examples for E^S flows with $c_{ph} =$ 17km yr^{-1} and U=15, 17, 20 km yr^{-1} after 150 and 400 years of evolution from the 1590 *gufm1* field are presented. Animations of all 400 years of evolution for these 3 cases can be found in animations A8.27, A8.28 and A8.29.

Figure 8.19 clearly shows that even if the field at the core surface and is small scale and contains large amplitude features, then field models derived using quadratic regularisation techniques from observations at Earth's surface will be large scale and smooth. This makes it difficult to rule out particular core flows as unreasonable because of the high amplitude, sharp field features they would produce. Field concentrations in the damped models occur centred on the positions of field concentrations in the undamped case, but are of lower amplitude and larger spatial extent. As U becomes larger the initial field is more readily distorted, with field concentration forming at positions of drifting flow convergence, even in areas where the field initially has low amplitude and gradients. With the smoothing influence of regularisation taken into account, the field morphology produced when U is large is still rather different to that found in geomagnetic field models being very dominated by spatially periodic concentrations produced by the wave flow. It seems probable that whatever flows at the core surface are influencing the observed geomagnetic secular variation, they will be of magnitude less than 17 km yr^{-1}, otherwise core flow inversions (see, for example, Bloxham and Jackson (1991)) would be compelled to reproduce these large magnitudes.

The present experiments also give insight into the problem of whether the field structure in the Pacific means that the effects a global wave flow would be seen only weakly there (see §3.5). It is found that early in the experiments, when the field in the Pacific was low amplitude and featureless (similar to the 1590 *gufm1* field), that the wave flows produced high amplitude, drifting concentrations of field in the Atlantic hemisphere but

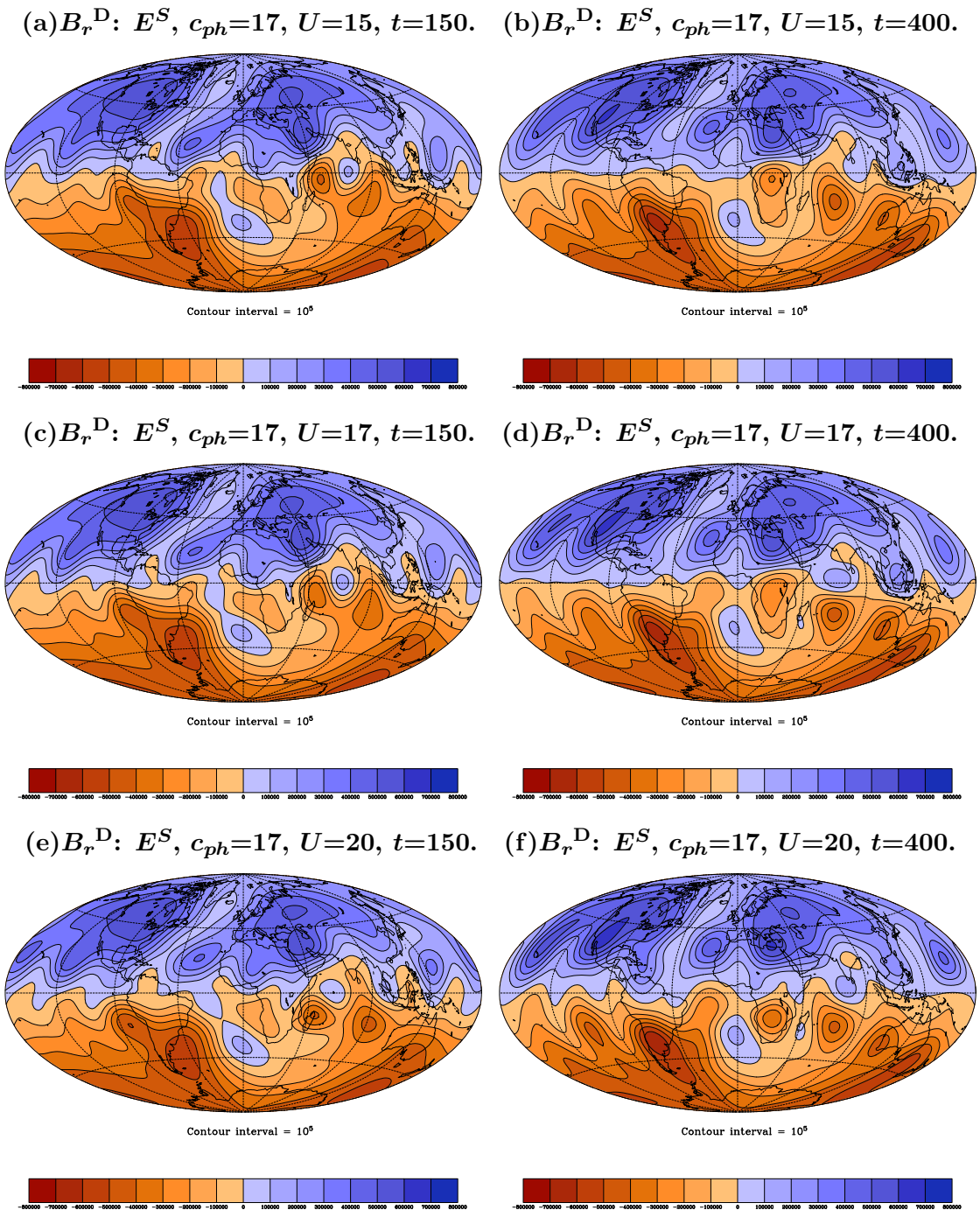

Figure 8.19: B_r^{D} due to E^S, m=8 flows acting on 1590 B_r for 150, 400 yrs. Result of 150 and 400 years of field evolution produced by E^S wave flows along with limited magnetic diffusion acting on B_r at the core surface starting with the 1590 *gufm1* field and with a synthetic crustal filtering applied. The wave flows were chosen to have a drift speed of c_{ph}=17 km yr^{-1} to match the observed westward drift speed and have wave amplitudes U of 15 km yr^{-1} in (a) and (b), 15 km yr^{-1} in (c) and (d), and 20 km yr^{-1} in (e), (f).

only weaker field evolution of a similar form in the Pacific hemisphere. However, after several hundred years, the global wave flow alters the background field in the Pacific sufficiently that high amplitude, drifting field concentrations are also observed there. Stronger flows (larger U) were found to produce stronger patterns of field evolution in the Pacific hemisphere after shorter amounts of time.

These results indicate that in order for the Pacific to have exhibited consistently weaker patterns of field evolution over the past 400 years, then the smooth field structure in the Pacific would need to maintained. One possible explanation consistent with these findings and with the results of chapters 3 and 4 is that a global wave flow is present, but there is a stratified layer close to the core surface at low and southern latitudes in the Pacific hemisphere. This layer would reduce the amplitude of the vertical fluid motion, and therefore the amplitude of associated flow convergence, making it more difficult to generate field concentrations and gradients in this region. The existence of such a layer could also explain why the wave flows are only seen weakly in the Pacific hemisphere over several centuries. Another, perhaps simpler, possibility is that the geodynamo mechanism operating with an inhomogeneous pattern of heat flow into the mantle tends to generate background fields in the Pacific that are consistently of the required low amplitudes and gradients.

8.3.7 Discussion of implications for mechanisms of geomagnetic secular variation and core flow inversion techniques

The purpose of this chapter was to test whether propagating wave flows were a reasonable model for the origin of azimuthally drifting, wave-like patterns in B_r observed at the core surface. The results from both the 1D and the 2D modelling have shown that wave flows can produce azimuthally drifting, spatially and temporally coherent, wave-like, magnetic field concentrations from an initially uniform field. The concentrations either grow in strength and sharpness until balanced by magnetic diffusion or undergo periodic pulsations in amplitude. It is therefore possible that the kinematic effect of propagating regions of convergence in wave flows close to the core surface could explain both the source of spatially and temporally coherent anomalies in B_r and their azimuthal motion.

However, for a simple m=8 wave flow propagating at the rate required to reproduce the observed westward drift of field concentrations ($c_{ph} = 17\mathrm{km\,yr^{-1}}$), there are difficulties in reproducing aspects of field evolution observed in historical geomagnetic field models. When the wave flow amplitude U is small, the resulting B_r morphology is dominated by that of the initial field and systematic pulsation prevents the generation of consistently drifting features. It should however be noted that there are indications of some pulsation-type behaviour of westward moving field features in *gufm1*, particularly of the field feature that starts in the Indian ocean in 1590. If $|c_{ph}| > |U|$, but U was large enough to produce field concentrations, the wave flow mechanism could perhaps account for both

the drift and the pulsation of this feature. However other systematically pulsing field features (not seen in *gufm1*) would also be expected to exist.

On the other hand, when the flow is strong enough so that pulsations are not observed ($U \geq 17\text{km}\,\text{yr}^{-1}$), positions of flow convergence dominate field evolution, with field observed being collected towards these locations into a series of intense, small scale drifting field features. Although these characteristics are smoothed when the effects of crustal filtering are taken into account, the domination of field morphology by the influence of the wave flow (overwhelming any memory the initial field configuration) suggests that such strong wave flows are unlikely.

In this chapter only the extreme case of azimuthal motion of field features being totally due to wave propagation was considered. If instead one admits the possibility that some (or most) of the observed westward drift is due to azimuthal flow, then large U are no longer required to avoid pulsation since c_{ph} is smaller and the domination of field morphology be the wave flows can be avoided. Such azimuthal flows are likely to exist in Earth's core due to thermal and magnetic winds in Earth's core (see, for example, Fearn et al., (1988) and Dumberry and Bloxham (2005)). If one imagines that c_{ph} is very small (as would be case for the convection-driven hydromagnetic waves studied in the previous chapter) then field concentrations could still be produced by the wave flows, and the whole pattern could move instead via advection by azimuthal flows. Perhaps the triple constraints of satisfying (i) the observed drift speed, (ii) the absence of systematic strong pulsation and (iii) absence of domination of field morphology by the wave flow pattern, may in the future prove useful in helping to quantify the relative proportion of wave propagation and bulk advection producing observed azimuthal field motions.

It should also be remarked that there are several deficiencies in the model presented in this chapter of how hydromagnetic wave flows produce patterns in B_r. These include that radial magnetic diffusion has been neglected; that the kinematic wave flows employed are dynamically over-simplified with no feedback from magnetic field concentrations (through the Lorentz force) on the flow; and that models ignore 3D aspects of field distortion which can produce B_r through the action of the flow on the unknown toroidal magnetic field. These limitations will result in field concentrations in these models prior to crustal filtering that are smaller scale and more intense than is actually likely to be the case.

The amplitude of U expected for hydromagnetic waves in the core is another important missing constraint that is crucial for assessing the relevance of the kinematic concentration by wave flow mechanism for producing geomagnetic secular variation. If U saturates at too small a value this mechanism will never be feasible. Knowledge of the amplitude of U from theory requires fully non-linear models of hydromagnetic waves including both saturation mechanisms and realistic toroidal fields in the parameter regime appropriate to Earth's core— such models do not yet exist (but see §9.3).

Hydromagnetic waves have however been found in geodynamo models (see chapter 5). These models include all the physical processes described above that have been neglected in the model of this chapter, though they are not in the correct dynamical regime for the Earth. In the geodynamo model DYN1 that was studied in chapter **??**, it was found that $|U| >> |c_{ph}|$ and observed that magnetic field concentrations (without pulsation in amplitude) were formed at and moved along with positions of flow convergence. These findings are in agreement with the results reported in this chapter and suggest that the 2D model presented here can correctly predict observable consequences, despite its simplicity. The magnetic field concentrations observed in the geodynamo model were less sharp than those found in the simple 2D model, suggesting that the presence of a Lorentz force and radial magnetic diffusion moderates the amplitude of field gradients that can develop. The non-linear interaction between the wave flow and other flows in DYN1 led to the break up of the field concentrations associated with the waves. This suggests that the long lived field concentrations found in the simple 2D model are unphysical and fits in well with the episodic evolution of azimuthally moving field patches observed in geomagnetic field models (see chapters 3 and 4).

The results reported in this chapter have implications for the inversion of geomagnetic field models to determine fluid motions at the core surface. If drifting B_r concentrations are (even partly) a result of a hydromagnetic wave propagation, and not just the bulk advection of magnetic field lines by a flow, then the strong westward flows inferred at low latitudes under the Atlantic hemisphere in many inversions (Bloxham and Jackson, 1991) may be quantitatively incorrect. This fact has already been noted by Love (1999) and Rau et al. (2000) where the flow calculated from the inversion of B_r evolution in a numerical dynamo model produced spurious equatorial jets where wave-related field drift was observed in the model. The results in this chapter suggest that the failure of the inversion technique was not due to the frozen flux assumption (the frozen flux assumption was made in the models used to demonstrate that drifting field concentration can be produced by propagating wave flows in §8.2). Instead it seem most likely that the regularisation applied during the inversion favours an incorrect explanation in terms of large scale flow rather than the small scale flows involved in a wave. Dynamical constraints that are instantaneously inconsistent with the wave flows may also play a part in such failures of flow inversions.

If drifting field concentrations are produced by a propagating wave flow, then carrying out a core flow inversion in a frame drifting along with the wave (Davis and Whaler, 1996; Holme and Whaler, 2001) should yield useful information. In the drifting frame, one could then recover the combination of the Galilean correction flow $-c_{ph}$ and the stationary wave flow U producing field concentrations. It might even be possible to simultaneously invert for several wave flows, each with an associated reference frame drifting at a different speed. However in order to have confidence in this procedure, it would be necessary that the flows in the drifting frame had a flow structure compatible

with wave propagation. It seems unlikely that this is the case in the studies that have been carried out to date.

If, as seems possible given the results in chapter 7, the distortion of the toroidal magnetic field by hydromagnetic wave flows contributes to the perturbations in B_r observed at the core surface, the interpretation of secular variation in terms core flow inversions is somewhat more difficult. For inversions involving a drifting reference frame, the speed of the drifting frame would yield information concerning the wave propagation speed (or the mean azimuthal flow speed advecting the wave). The flow inside the drifting reference frame would, however, not be that producing B_r concentrations, so the detailed wave flow patterns could not be retrieved. The fundamental limitation of core flow inversions is that they consider only the rearrangement of radial magnetic field lines as the origin of secular variation, so are unable to yield any useful information regarding radial field change resulting from distortion of the toroidal magnetic field. These limitations should be borne in mind by the practitioners of core flow modelling.

8.3.8 Summary

In this chapter the mechanism of magnetic field evolution produced by the kinematic action of a propagating wave flow has been investigated. A simplified 1D frozen flux model was developed and solved analytically to prove the existence of two distinct regimes of field evolution. Both involve the production of spatially periodic field concentrations that move along with the wave flow pattern in the absence of a mean flow. One regime involves steady growth in the amplitude of field concentrations while the other involves pulsation in amplitude. A more Earth-like model using wave flow patterns derived from models of hydromagnetic waves flows in spherical geometry, acting on realistic initial radial magnetic fields and including limited magnetic diffusion, demonstrated that similar regimes could exist at Earth's core surface. The geodynamo models analysed in chapter 5 are found to be consistent with the results of the simple models developed here, suggesting that despite the large number of assumptions made useful conclusions can be drawn. The 2D modelling results suggest that hydromagnetic wave flows could produce spatially and temporally coherent, azimuthally drifting, concentrations of B_r similar to those observed in geomagnetic field models, particularly if there is also some azimuthal flow that also contributes to the motion of the field features.

Chapter 9

Conclusions and suggestions for further research

9.1 A synthesis of results

In this concluding chapter results from the various avenues investigated during this thesis are collected and a self-consistent explanation is proposed. Answers are suggested to the questions posed in the introduction concerning the nature of hydromagnetic waves in Earth's core and their influence on geomagnetic secular variation.

Can hydromagnetic waves exist in Earth's outer core?

As was described in §6.3, hydromagnetic waves will exist when a magnetic field strong enough to influence flow dynamics is present. The properties of hydromagnetic waves will be strongly influenced by the rapid rotation of the fluid core. The elasticity imparted to the fluid by a latitude dependent Coriolis force in a spherical geometry and the resistance of strong toroidal magnetic fields to distortion provides the restoring forces for wave motion. A number of mechanisms that could excite hydromagnetic waves in Earth's outer core were discussed in §6.6. Although other excitation mechanisms cannot be ruled out, instability driven by convection requires the fewest additional assumptions and is entirely consistent with current understanding of core properties and motions. Of the different hydromagnetic wave types that can be driven by convection, magneto-Rossby waves (see §6.6.2 and §7.4.1) seem most compatible with the regime expected in Earth's core. Furthermore, as was shown in chapter 5, it is not necessary to have a steady background magnetic field in order to obtain hydromagnetic waves: they can exist in the presence of a time-dependent, dynamo generated magnetic field. It is therefore proposed that magneto-Rossby waves driven by convection will exist in Earth's core, and will involve distortion of the time-dependent, dynamo generated, magnetic field.

What would be the properties of hydromagnetic waves in Earth's core?

The properties of convection-driven hydromagnetic waves in a sphere and with no az-

imuthal flows present were investigated in chapter 7. Convection-driven, magneto-Rossby waves were found to be dispersive with higher wavenumbers propagating faster in the westward direction (see, for example, figure 7.9). The simple analytic model of these waves developed in §6.6.2 (see equation (6.67)) also suggests they will travel fastest at low latitudes. The time scale for the propagation of such waves was found to be the thermal diffusion time scale which is thought to be thousands to millions of years in Earth's core[1]. However as discussed in §6.6.2, the presence of azimuthal flows (likely for realistic magnetic and temperature fields in Earth's outer core — see Dumberry and Bloxham (2005)) will have a major impact on the properties of hydromagnetic waves (Fearn and Proctor, 1983), especially on their observed azimuthal speeds.

How would hydromagnetic waves in the core influence the evolution of B_r at the core surface and hence geomagnetic secular variation?

In this thesis it has been demonstrated that hydromagnetic waves in the core can influence B_r observed at the core surface in two ways:

The first mechanism involves hydromagnetic waves distorting toroidal magnetic fields in the core to generate spatially coherent, wave-like patterns in B_r at the core surface. This mechanism was demonstrated in a model of convection-driven hydromagnetic waves in a sphere in §7.4.1 (see, for example, figure 7.4). An example of the type of pattern in B_r at the outer boundary that can be produced by this mechanism is presented in figure 9.1. The details of the equatorial symmetry, latitudinal positioning and extent of such patterns in B_r will depend on both the toroidal magnetic field morphology and the azimuthal flow structure in the core (see §6.6.2).

A second possible mechanism by which hydromagnetic waves could influence B_r involves the action of wave flows close to the core surface. The wave flows consist of alternating regions of fluid convergence and divergence (see §7.4.1) and will act on pre-existing B_r to produce spatially coherent, wave-like patterns in B_r that propagate along with the wave flow. This mechanism was demonstrated using a kinematic model in chapter 8. Concentrations of B_r are produced at positions of flow convergence in a frame of reference drifting with the wave flow. These concentrations will pulsate in amplitude if the wave is propagating faster than the speed of the flows within the wave (see §8.2.4). The pulsation effect will, however, be avoided in Earth's core if propagation speeds are very slow.

Of these two mechanisms, the first seems certainly to operate because it is a fundamental aspect the hydromagnetic wave mechanism. The second mechanism is however also conceivable, particularly if a combination of hydromagnetic waves and strong azimuthal flows are present. Future tests using more realistic wave models will help resolve whether only one or both of these mechanisms operates in Earth's core (see §9.3 for further

[1] If convection is driven by buoyant light elements rather than by thermal effects, this time could be even longer because the diffusivities of light elements are expected to be smaller than that of heat.

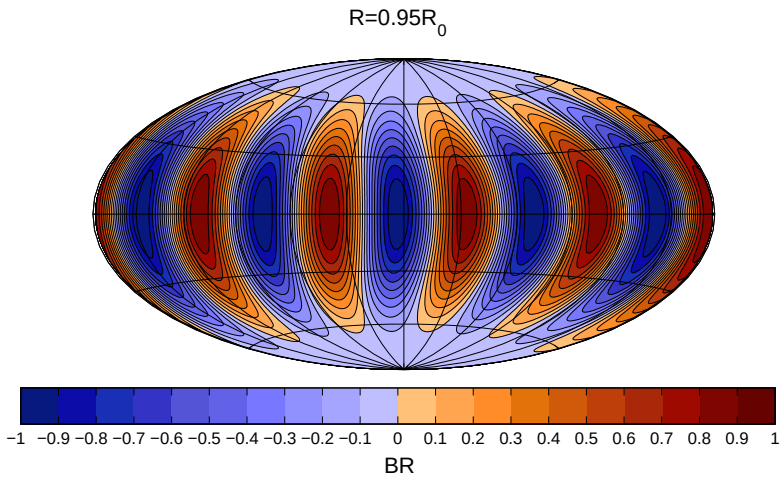

Figure 9.1: B_r perturbation caused by a m=5 hydromagnetic wave. Pattern in B_r at $r = 0.95r_0$ from the marginal mode of a thermal magneto-Rossby wave in a rotating spherical geometry where the imposed magnetic field is purely toroidal and $\Lambda = Pr = Pr_m = 1$, $E = 10^{-6}$. This shows how a toroidal magnetic field can be distorted into B_r by a hydromagnetic wave. Units are arbitrary because no nonlinear saturation mechanisms are included in this model.

details).

The temporally coherent motion of spatially periodic patterns in B_r at the core surface (a form of geomagnetic secular variation) could be produced either by wave propagation, by advection due to flows, or by a combination of these processes. The propagation speeds of convection-driven magneto-Rossby waves (the most likely type of wave to be excited in the core) are probably too slow (operating on the thermal diffusion time scale) to explain the observed azimuthal motions of B_r (see §7.5). This leaves the advection of the spatially coherent pattern in B_r by azimuthal flows as the most plausible mechanism producing azimuthal geomagnetic secular variation.

Is there any evidence supporting the existence of hydromagnetic waves in Earth's outer core?

Spatially and temporally coherent wave patterns consisting of positive and negative anomalies are observed in B_r at the core surface in the geomagnetic field model *gufm1*. The clearest signal found in §3.2.3 using the techniques described in chapter 2 has azimuthal wavenumber m=5, is equatorially symmetric and is centred on the geographical equator. Figure 9.2 shows a reconstruction of this m=5 signal in 1830 A.D.. The m=5 signal is not stationary, but moves westwards with a speed of $\sim$17 km yr^{-1} at the core surface.

In chapter 4, evidence was found for spatially and temporally coherent wave-like patterns in the archeomagnetic field model CALS7K.1. The patterns were observed to travel in both eastward and westward directions (sometimes simultaneously but at different

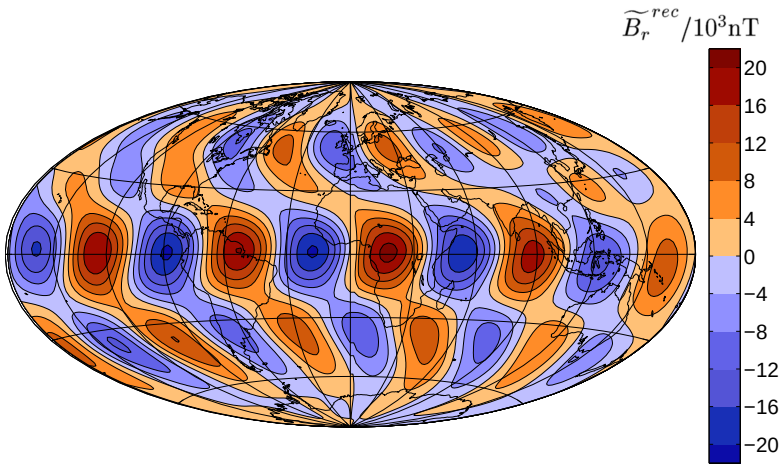

Figure 9.2: m=5 spatially coherent pattern in $\widetilde{B}_r^{rec}$ from *gufm1* in 1830. Wave-like pattern isolated in B_r at the core surface in 1830 from *gufm1*. The time-averaged axisymmetric field and changes occurring on time scales longer than 400 years have been removed. The signal has also been spatially filtered so only the strong m=5 signal remains. This spatially coherent, wave-like pattern in B_r is observed moving westwards from the 16th to the 20th century and is evidence for the influence of hydromagnetic waves in Earth's core on geomagnetic secular variation.

longitudes, see figure 4.9) on millennial time scales. Such simultaneous eastward and westward motion could arise from geographical variations in azimuthal flows but it is hard to envisage how it could result from wave propagation, unless the direction of propagation rests on a very delicate force balance.

It was shown in §3.4 and §3.7 that there is no evidence in *gufm1* for the dispersive effects or systematic geographical (latitudinal) trends in azimuthal speeds that are characteristic of hydromagnetic wave propagation in a rapidly rotating fluid. Neither of these phenomenon are expected to be present if advection by azimuthal flows were the primary mechanism producing motion of patterns in B_r. These findings lend further weight to the argument that azimuthal flows rather than wave propagation produce the observed motion of patterns in B_r at the core surface.

Can study of hydromagnetic wave motions in the core shed any light on the origin of hemispherical differences in magnetic field evolution at core surface?

It was shown in §3.5 that in the historical field model *gufm1* wave-like features in B_r at the core surface are strongest in the Atlantic hemisphere, but are also present in the Pacific hemisphere. Synthetic tests in §2.8 demonstrated that such signals in the Pacific hemisphere could not be aliased there from the Atlantic hemisphere, but are real. Study of the archeomagnetic field evolution over the past 3000 years using CALS7K.1 in §4.3.3 suggested that high amplitude, drifting, field features have been present at northern mid-latitudes in the Pacific hemisphere. The observed field evolution was much weaker and less coherent at low and southern latitudes in the Pacific hemisphere, though the

resolution of CALS7K.1 is likely insufficient to capture the weak wave-like signals that may be present there. Forward models of a global wave flow acting on the 1590 B_r from *gufm1* (with synthetic crustal damping applied) demonstrated that a low amplitude, featureless field in the Pacific was sufficient to ensure weak field evolution patterns there. However, in order for such a featureless field scenario to persist for several hundred years the mechanism producing this background field must involve persistent hemispherical differences.

A proposed scenario consistent with observations and theoretical models

The theoretical and observational results outlined above can be reconciled in the following scenario which is suggested here as a working model of azimuthal geomagnetic secular variation to be tested in the future:

East-west motions of the geomagnetic field can arise from azimuthal advection of spatially coherent patterns in the B_r at the core surface produced by convection-driven magneto-Rossby waves in the core. These patterns are produced by the distortion of underlying toroidal magnetic fields and modulation of existing B_r by wave flows. Hemispherical differences in the background magnetic field morphology result in such patterns having lower amplitudes under the Pacific hemisphere.

9.2 Summary of work carried out and main conclusions

· Development of tools for analysis of azimuthal evolution of scalar fields.

Codes carrying out space-time spectral analysis of a scalar field on a spherical surface and generating time-longitude plots, frequency-wavenumber power spectra and latitude-azimuthal speed plots have been developed and benchmarked using realistic synthetic examples.

· Detection of spatially and temporally coherent, azimuthally drifting, wave-like patterns in B_r.

Space-time spectral analysis tools have been applied to the historical geomagnetic field model *gufm1*. Removing the time-averaged axisymmetric field and field variations with time scales longer than 400 years, a strong m=5 signal was observed at low latitudes. This signal was shown to move westwards at $\sim$17 km yr^{-1}, consistent with the westward drift of the geomagnetic field observed at Earth's surface. The wave-like signal was found to be strongest in the Atlantic hemisphere, but also present in the Atlantic hemisphere.

· Observation of episodes of eastwards and westward motion in B_r.

Space-time spectral analysis tools have been applied to the archeomagnetic field model CALS7K.1. Problems in the accurate interpretation of precise wavenumbers and azimuthal speeds of field features were identified, but clear evidence for intervals of both

eastward and westward motions were found.

· Identification of hydromagnetic waves in geodynamo models.

Space-time spectral analysis tools have been applied to the magnetic and velocity fields from two convection-driven geodynamo models. The existence and propagation of hydromagnetic waves in the presence of a time varying, dynamo generated magnetic field was demonstrated.

· Review of the theory of hydromagnetic waves in rotating fluids.

A review of the physics of hydromagnetic waves has been carried out. Wave propagation mechanisms, time scales, effects of diffusion, spherical geometry, realistic imposed magnetic fields, azimuthal flows, nonlinear effects and stratification have been discussed. The role of azimuthal flows in determining wave properties has been emphasised.

· Documentation of parameter dependence of simple hydromagnetic waves.

An existing eigenvalue solver code has been extended to allow the study of simple hydromagnetic waves in the regime $\Lambda \sim 1$. The dependence of critical Ra, ω and the structure of the waves on m, Λ, E, Pr and Pr_m has been documented. The distortion of toroidal magnetic field into wave-like perturbations of B_r at the outer boundary was observed. Wave flow patterns were demonstrated to consist of alternating regions of convergence and divergence close to the outer boundary. Very slow wave propagation speeds were found in the absence of azimuthal flow.

· Deduction of the influence of hydromagnetic wave flows on B_r.

A simple analytic model of the action of a generic wave flow on a magnetic field was developed. This demonstrated that propagating concentrations of magnetic field are produced by the travelling wave flows. Field concentrations were found to pulsate when the wave phase speed was faster than the flow within the wave. A possible application of these results to Earth's core was demonstrated using a numerical model of advection of B_r by wave flows at a spherical surface.

· Proposal of a scenario consistent with theory and observations.

Hydromagnetic waves distort the magnetic field within the core to produce patterns in B_r that are subsequently advected by azimuthal flows, producing geomagnetic secular variation. It remains for this proposal to be tested in the future.

9.3 Suggestions of extensions and directions for future research

The scenario outlined above should certainly not be regarded as a rigorously proven theory, but rather as conjecture that provides a working model for a particular aspect of geomagnetic secular variation. Like any scientific hypothesis, it will only be of interest

so long as it is consistent with advances in observations and theoretical understanding. In this vein, future research directions that might help to support or falsify the proposed scenario are suggested in this section.

In the immediate future, much work can be carried out on improving models of hydromagnetic waves in Earth's core, building on the understanding gained in considering the simple model of chapter 7. Realistic background magnetic fields should be studied with self-consistent background azimuthal flows (magnetic winds) and full non-linear coupling to allow developed wave motions to be studied. Such models would permit tests of the hypothesis that azimuthal flows (rather than wave propagation) are responsible for the observed motion of wave patterns. Both poloidal and toroidal magnetic fields could be studied to determine whether distortion of the toroidal magnetic field into B_r (as suggested in chapter 7) or the concentration of existing B_r by the wave flows (as discussed in chapter 8) is primarily responsible for producing observed perturbations in B_r. A range of equatorial symmetries of imposed toroidal and poloidal fields could be studied to determine those combinations that can reproduce the observed equatorially focused patterns in B_r described in chapter 3. Finally, it would be interesting to study the effects of time-dependent background fields (mimicking dynamo generated fields) on the origin and lifetime of spatially and temporally coherent wave patterns. It is already possible to carry out all these proposed tests using a magnetoconvection version of the Leeds Spherical Dynamo code that was benchmarked against the eigenvalue solver code in chapter 7. This work is underway in collaboration with Nicolas Gillet and Ashley Willis at the University of Leeds and will hopefully yield answers to some of the theoretical issues left unresolved by this thesis.

Tests of the proposed scenario using currently available observational data are conceivable. In particular, given that azimuthal motion of the wave-like patterns in B_r is ascribed primarily to advection, it should be possible to perform a core flow inversion of *gufm1* specifically to retrieve these azimuthal flows (see, for example, the study by Dumberry and Bloxham (2005) of archeomagnetic field models). Unfortunately, the assumption of tangential geostrophy breaks down at the low latitudes of interest, so another dynamic assumption must be made if unique solutions are to be found (Backus, 1968; Bloxham and Jackson, 1991). Looking for flows consistent with theoretical models of magnetic and thermal winds might be a fruitful direction in this regard. It would be of interest to determine the latitudinal structure of the azimuthal flows and to consider the implications for the morphology of the underlying magnetic and temperature fields in the core.

Tests may also be envisaged using observational data that are not yet available, but which may be possible at some time in the future. The collection of many new measurements of the geomagnetic field over the past 7000 years (particularly at low latitudes and in the oceanic regions of the Southern hemisphere) and their incorporation into improved

geomagnetic field models would allow a more detailed study of the episodes of eastward and westward motion identified in chapter 4. An improved knowledge of the origin, spatial structure, evolution (including possible changes in direction) and eventual decay of wave patterns in B_r over this interval and a comparison of the results with more realistic theoretical models would enable a variety of tests of the proposed mechanism.

New, higher resolution, geomagnetic field models are capable of resolving sub-decadal geomagnetic field evolution over the past 20 years (see, for example, the recent study of Wardinski (2005)). In the near future these could be extended to include more data from past (POGO, Magsat), ongoing (Ørsted, CHAMP and SAC-C) and future (SWARM) satellite missions and resolution could be further improved by utilising new field modelling techniques such as the maximum entropy norm method of Jackson (2003). The resulting high quality images of field evolution at the core surface (suitably processed to focus on signals of interest) could be used to map the positions, amplitudes and motions of spatially coherent patterns in B_r at the core surface and to test whether azimuthal field evolution is dominated by particular wavenumbers.

Improvements in satellite monitoring of Earth's gravitational field, as showcased by the recent GRACE mission (Tapley et al., 2004), suggest the possibility of isolating time varying gravity signals caused by fluid motions in the outer core (Dumberry and Bloxham, 2004; Greff-Lefftz et al., 2004; Jiang et al., 2004). In principle, this could enable the mapping of motions of density anomalies in the core which could then be compared to theoretical predictions. In the present context, the relative positions of density anomalies and magnetic field concentrations in models of advected wave patterns in B_r produced by hydromagnetic waves could be compared to the observed gravity and magnetic fields.

Both observational and theoretical studies of the properties of hydromagnetic waves in Earth's core are still at a preliminary stage. More work, especially on possible excitation mechanisms (such as shear instability, topographic forcing and precessional driving) would be beneficial to the subject area. The current emphasis on modelling purely azimuthal toroidal magnetic fields (and hence azimuthally propagating waves) also seems rather restrictive; it would be of interest to use numerical models to test whether hydromagnetic wave propagation in north-south directions is also possible. Investigation of the motions of patterns in B_r arising in fully nonlinear models of hydromagnetic waves could also aid understanding of the relative importance of advection and magnetic diffusion in large scale magnetic field evolution. Combining such advances in theoretical understanding with improving observations and analysis methods would allow fresh insights into core dynamics and the mechanisms underlying variations in Earth's magnetic field.

Appendix A

Historical geomagnetic field model *gufm1*

A.1 Historical observations of Earth's magnetic field

Direct observations of the geomagnetic field with the extensive geographical coverage required for global field modelling exist from the 16th century onwards from a variety of sources:

(i) Maritime observations

(ii) Observatory measurements (after 1830)

(iii) Magnetic surveys (18th, 19th and 20th century)

(iv) Satellite magnetometer data (POGO late 1960s, Magsat 1980)

Jackson et al. (2000) constructed a time-dependent field model known as *gufm1* based on a new compilation of all suitable historical observations. Model *gufm1* represents a significant advance on previous historical models such as the *ufm* model of Bloxham and Jackson (1992), particularly in the number and spatial distribution of observations in the 18th and 19th centuries, though there are still changes in coverage with time (see figure A.1). The temporal change in the number of observations in each five year period between 1590 and 1990 is displayed in figure A.2.

A.2 Field modelling methodology

An outline of the inversion techniques used to construct the field model *gufm1* from historical observations is given here to aid understanding of the limitations of the model. The conclusions from the analysis in Chapter 3 of the properties of field features in *gufm1* are only trusted if the field features seen in the model can be considered robust.

Assuming the mantle to be an insulator, then the magnetic field outside the core can be expressed as the gradient of a scalar potential V that satisfies Laplace's equation and is

(a) Locations of declination observations from 1650-1699

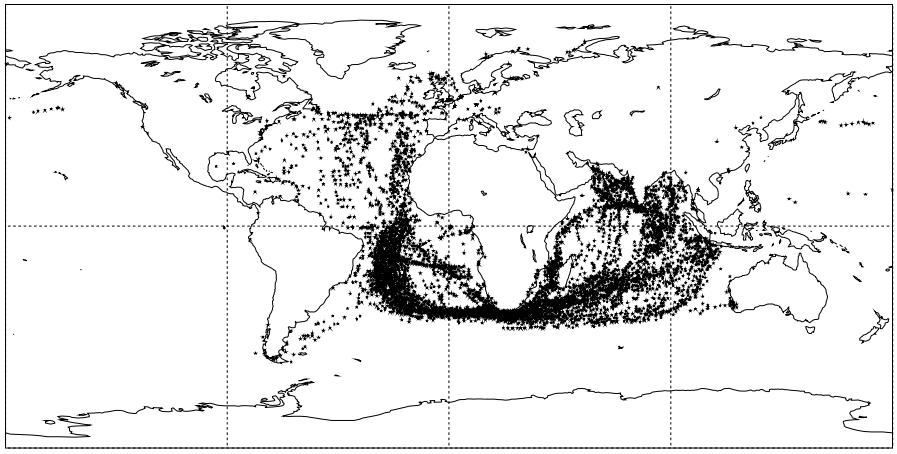

(b) Locations of declination observations from 1750-1799

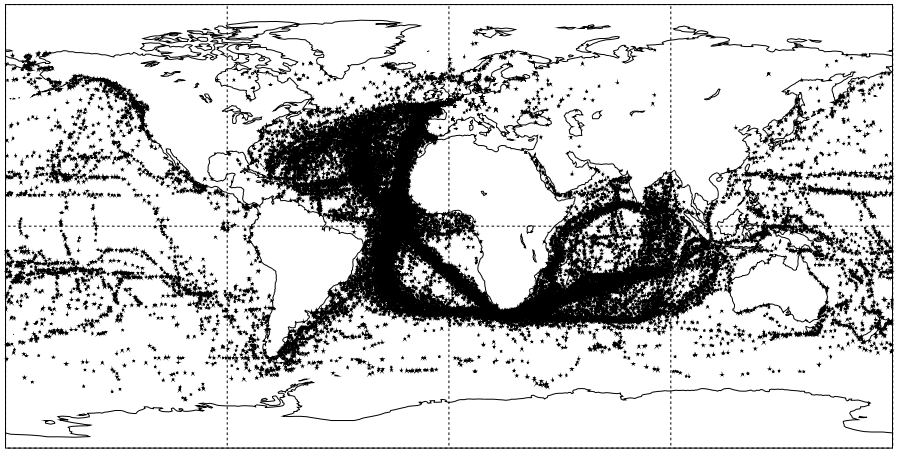

(c) Locations of all observations from 1850-1899

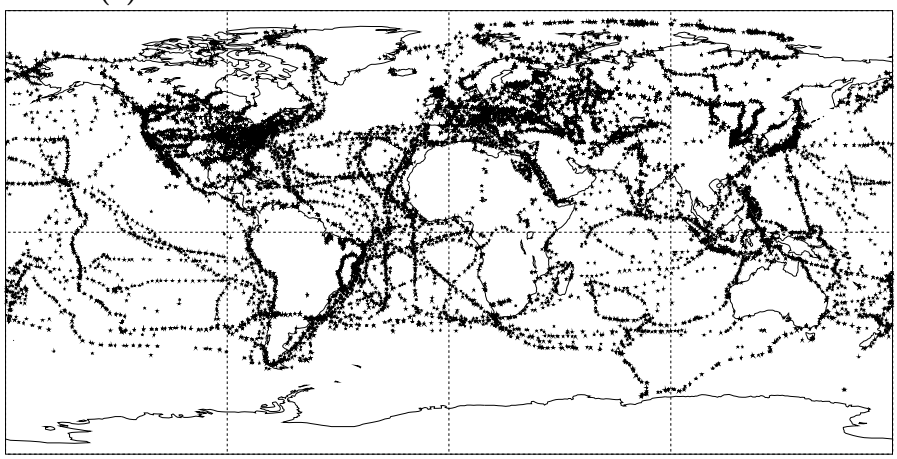

Figure A.1: Changes in spatial distribution of observations in *gufm1*.
Stars show the location of observations for the fifty year periods 1650-1699 in (a), 1750-1799 in (b), and 1850-1899 in (c). For further details see Jackson et al. (2000) and Jonkers et al. (2003)

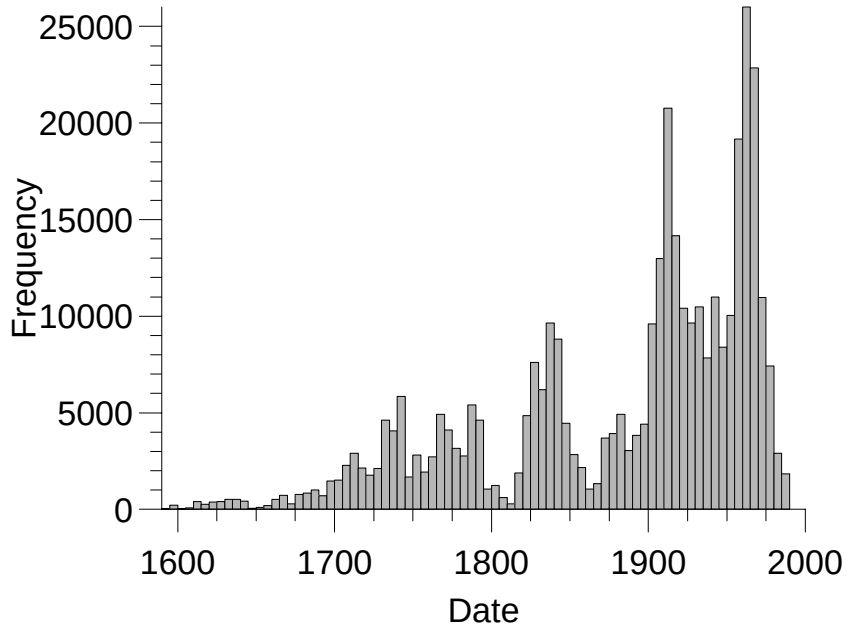

Figure A.2: Temporal distribution of *gufm1* observations.
The number of measurements used in constructing *gufm1* in five year intervals— for further details see Jackson et al. (2000) and Jonkers et al. (2003)

also a function of time

$$\mathbf{B} = -\nabla V, \tag{A.1}$$

$$\text{where } \nabla^2 V = 0, \tag{A.2}$$

$$\text{and} \qquad V \longrightarrow \frac{1}{r^2} \qquad \text{as} \qquad r \longrightarrow \infty, \tag{A.3}$$

where it has also been assumed that there are no field sources at infinity. Choosing a spherical polar co-ordinate system (r, θ, ϕ) the method of separation of variables is used to find a solution to Laplace's equation subject to these boundary conditions, in the form of a spherical harmonic expansion

$$V(t) = a \sum_{l=1}^{\infty} \sum_{m=0}^{l} \left(\frac{a}{r}\right)^{l+1} \left\{ g_l^m(t) \cos(m\phi) + h_l^m(t) \sin(m\phi) \right\} P_l^m(\cos\theta), \tag{A.4}$$

where only the solutions corresponding to internal field sources (found in modelling to be the dominant terms) have been retained, a=6371.2 km is Earth's mean radius and P_l^m are the Schmidt quasi-normalised associated Legendre functions of degree l and order m with normalisation defined as

$$\int_0^{2\pi} \int_0^{\pi} P_l^m(\cos\theta) P_{l'}^{m'}(\cos\theta) \left\{ \begin{array}{c} \cos m\phi \cos m'\phi \\ \sin m\phi \sin m'\phi \end{array} \right\} \sin\theta d\theta d\phi = \left\{ \begin{array}{c} \frac{4\pi}{2l+1} \text{ if } l{=}l', m{=}m' \\ 0 \text{ otherwise} \end{array} \right\}. \tag{A.5}$$

The constants $g_l^m(t)$, $h_l^m(t)$ are expanded in fourth order B-spline basis functions $M_n(t)$ erected on a series of knots such that

$$g_l^m(t) = \sum_n g_l^{mn} M_n(t), \tag{A.6}$$

$$h_l^m(t) = \sum_n h_l^{mn} M_n(t), \tag{A.7}$$

where $M_n(t) > 0$ if $t \epsilon \mid t_n, t_{n+4} \mid$ and is zero otherwise.Taking the gradient of equation ((A.4)) we obtain the following expressions for the spherical polar components of the magnetic field **B**: the radial magnetic field B_r, the southward magnetic field B_θ and the eastward magnetic field B_ϕ.

$$B_r = \sum_{l=1}^{\infty}\sum_{m=0}^{l}(l+1)\left(\frac{a}{r}\right)^{l+2}\left\{g_l^m(t)\cos(m\phi)+h_l^m(t)\sin(m\phi)\right\}P_l^m(\cos\theta) \tag{A.8}$$

$$B_\theta = -\sum_{l=1}^{\infty}\sum_{m=0}^{l}\left(\frac{a}{r}\right)^{l+2}\left\{g_l^m(t)\cos(m\phi)+h_l^m(t)\sin(m\phi)\right\}\frac{dP_l^m(\cos\theta)}{d\theta} \tag{A.9}$$

$$B_\phi = \frac{1}{\sin\theta}\sum_{l=1}^{\infty}\sum_{m=0}^{l} m\left(\frac{a}{r}\right)^{l+2}\left\{g_l^m(t)\sin(m\phi)-h_l^m(t)\cos(m\phi)\right\}P_l^m(\cos\theta) \tag{A.10}$$

The inverse problem of geomagnetic field modelling now involves finding the parameters g_l^{mn}, h_l^{mn} that determine the most reasonable (in a sense defined below) magnetic field at the core surface given geomagnetic observations and *a priori* information on the field structure. The prior information includes the fact that the mantle is approximately an insulator, that the internal field must originate in the core, the known core radius, and an upper limit on Ohmic heating from the magnetic field derived from the induction equation (Gubbins, 1975).

Spherical harmonic expansions were truncated at degree $l = L$ where $L = 14$ to obtain a finite representation of an otherwise infinite dimensional inverse problem. However, the favoured field models converge at $l < L$ thanks to the regularisation applied that penalises spatially complex field structures (see further discussion of regularisation below). 163 B-splines were employed to represent the time period 1590 to 1990, erected on $N = 167$ knots (spline end points) placed every 2.5 years. The total number of free parameters in the model is thus $P = N(L(L+2)) = 36512$.

The data in the inverse problem were magnetic field observations of various types: northward field component (X), eastward field component (Y), downward field component (Z), declination (D), inclination (I), horizontal field component (H) and total field (F). These are related to the spherical polar field components (B_r, B_θ, B_ϕ) and hence the model parameters by the relations

$$X = -B_\theta, \tag{A.11}$$

$$Y = B_\phi, \tag{A.12}$$

$$Z = -B_r, \tag{A.13}$$

$$H = \left(B_\theta^2 + B_\phi^2\right)^{\frac{1}{2}}, \tag{A.14}$$

$$F = \left(B_\theta^2 + B_\phi^2 + B_r^2\right)^{\frac{1}{2}}, \tag{A.15}$$

$$I = \text{Arctan}\left[\frac{-Br}{\left(B_\theta^2 + B_\phi^2\right)^{\frac{1}{2}}}\right] \text{ where } -\frac{\pi}{2} \leq I \leq \frac{\pi}{2}, \tag{A.16}$$

$$D = \text{Arctan}\left[\frac{B_\phi}{-B_\theta}\right] - \text{where } \pi \leq D \leq \pi, \tag{A.17}$$

Equations ((A.11)) to ((A.13)) are linear in the model coefficients $\{g_l^{mn}, h_l^{mn}\}$ while those in equations ((A.14)) to ((A.17)) are non-linear. This means the whole inverse problem must be solved iteratively if all the data types are to be included. If the observational data X, Y, Z, H, F, I, D are listed in a vector $\mathbf{d}$ of $\mathcal{D}$ observations ($\mathcal{D}$= 365 694 in *gufm1*), and the model coefficients are listed in a vector $\mathbf{m} = (g_1^{00}, g_1^{10}, h_1^{10}..)$ then the forward problem can be written in matrix form as

$$\mathbf{d} = \mathbf{f}(\mathbf{m}) + \mathbf{e}, \tag{A.18}$$

where $\mathbf{f}$ is the non-linear functional relating the data to the model and $\mathbf{e}$ is an error vector of length $\mathcal{D}$ which gives the error associated with each observation. Errors vary depending on the method of data acquisition.

The inverse problem of finding the model parameters (spherical harmonic coefficients) that best represent the core surface field, given geomagnetic measurements at Earth's surface is non-unique. The non-uniqueness arises due to the finite number of data (magnetic field observations at specific locations and times) being used to find a continuous function (the global, time-dependent magnetic field at the core surface). Geophysically plausible solutions can be found by using the method of regularised least squares inversion, that looks for solutions that both fit the data as well as possible in a least squares sense and minimise suitable model norms. Two model norms are employed in the construction of *gufm1*, one measuring roughness in the spatial domain and the other roughness in the temporal domain. The spatial norm is a quadratic norm that is physically associated with minimising Ohmic dissipation (Gubbins, 1975) and can be written as

$$\Psi = \frac{1}{t_e - t_s}\int_{t_s}^{t_e} \mathcal{F}(B_r)\mathrm{d}t = \mathbf{m}^T\mathbf{S}^{-1}\mathbf{m}, \tag{A.19}$$

$$\text{where} \quad \mathcal{F}(B_r) = 4\pi\sum_{l=1}^{L}\frac{(l+1)(2l+1)(2l+3)}{l}\left(\frac{a}{c}\right)^{2l+4}\sum_{m=0}^{l}\left[(g_l^m)^2 + (h_l^m)^2\right], \tag{A.20}$$

The temporal norm is

$$\Phi = \frac{1}{t_e - t_s}\int_{t_s}^{t_e}\oint_{CMB}(\partial_t^2 B_r)^2\mathrm{d}\Omega\mathrm{d}t = \mathbf{m}^T\mathbf{T}^{-1}\mathbf{m}, \tag{A.21}$$

Measurements (due to crustal fields, external fields, field measurement errors, mislocation errors) were estimated and assumed to be Gaussian (though this may not be totally

correct — see Walker and Jackson (2001) for a discussion), allowing the construction of the data covariance matrix $\mathbf{C}_e$. The model estimate is then that which minimises the objective function Θ

$$\Theta(\mathbf{m}) = [\mathbf{d} - \mathbf{f}(\mathbf{m})]^T \mathbf{C}_e^{-1} [\mathbf{d} - \mathbf{f}(\mathbf{m})] + \mathbf{m}^T \mathbf{C}_m^{-1} \mathbf{m}, \tag{A.22}$$

with the model covariance matrix being

$$\mathbf{C}_m^{-1} = \left(\lambda_S \mathbf{S}^{-1} + \lambda_T \mathbf{T}^{-1}\right) \tag{A.23}$$

where λ_S is the spatial damping parameter (chosen to be $1 \times 10^{-12}\mathrm{nT}^{-2}$) and λ_T is the temporal damping parameter (chosen to be $5 \times 10^{-4}\mathrm{nT}^{-2}\mathrm{yr}^{-4}$). The optimal solution is sought by iterating using the scheme in (A.24) below, until convergence on a model with minimum Θ. The scheme is derived by differentiating (A.22) with respect to $\mathbf{m}_i$, the ith model parameter, and using a first order approximation $\mathbf{f}(\mathbf{m} + \delta\mathbf{m}) = \mathbf{f}(\mathbf{m}) + \mathbf{A}\delta\mathbf{m}$ where $\mathbf{A}_{ij} = \frac{\partial f_i}{\partial m_j}$ and $\delta\mathbf{m}$ is the difference between the current approximation and the minimising model

$$\mathbf{m}_{i+1} = \mathbf{m}_i + (\mathbf{A}^T \mathbf{C}_e^{-1} \mathbf{A} + \mathbf{C}_m^{-1})^{-1} [\mathbf{A}^T \mathbf{C}_e^{-1} (\mathbf{d} - \mathbf{f}(\mathbf{m}_i)) - \mathbf{C}_m^{-1} \mathbf{m}_i]. \tag{A.24}$$

The regularisation ensures that expansions converge before the truncation levels are reached, so the solutions are insensitive to truncation. The procedure effectively damps out most power at degrees 12 and higher. The choice of damping parameters is however rather subjective—large differences in model complexity can be produced by varying them. The values used here were chosen to produce qualitatively similar maps to those of other authors at fixed epochs (refer e.g. Shure et al. (1985)) yielding a conservative picture of the field structures required to produce a normalised misfit $\chi = \sqrt{\frac{[\mathbf{d}-\mathbf{f}(\mathbf{m})]^T \mathbf{C}_e^{-1} [\mathbf{d}-\mathbf{f}(\mathbf{m})]}{D}}$, where D is the total number of data observations, as close to 1.0 as possible (i.e. fitting observations to within estimated errors). The preferred model *gufm1* actually has a normalised misfit of 1.16. More complex models with more power at higher spherical harmonic degree and larger time variations that fit observations better can be produced, but analysing field features from these models and basing interpretations on them increases the chances that the data are being over-fit or effects due to non-core fields erroneously included.

A.3 Comparison to observatory data

Perhaps the most rigorous test of the reliability of the model *gufm1* is how well it manages to fit main field and secular variation data recorded at observatories. Here the main field and secular variation from 5 observatories are plotted in figure (A.3) and figure (A.4) respectively. The main field component typically has little scatter and *gufm1* excellently fits the signal at all the observatories considered. There is considerably more scatter in

(a) Annual means at Fuquene (MF) **(b) Annual means at Mauritius (MF)**

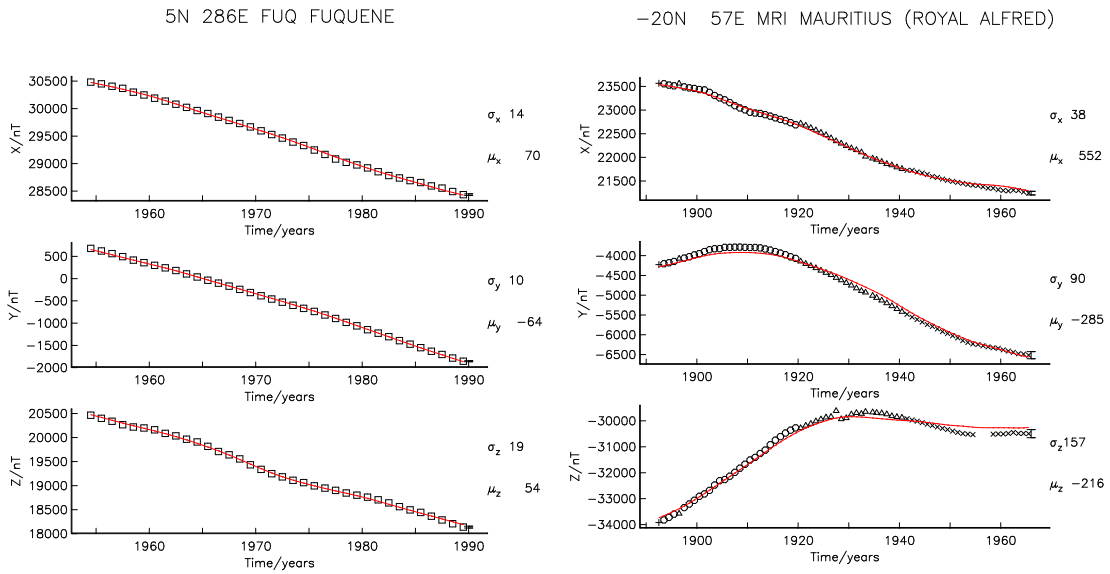

(c) Annual means at Niemegk (MF) **(d) Annual means at Tuscon (MF)**

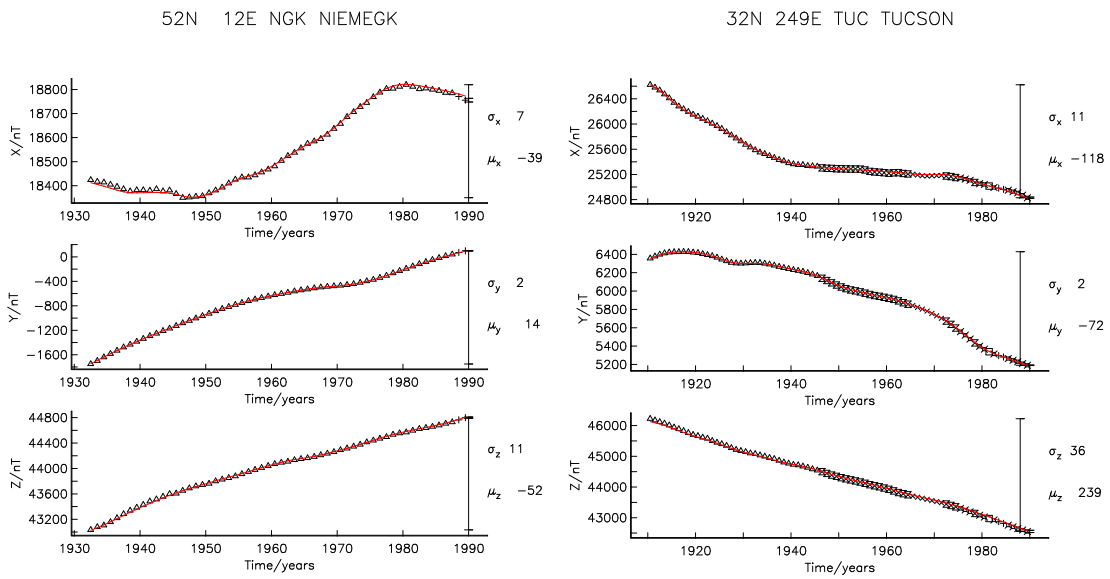

Figure A.3: Comparison of *gufm1* and observatory annual means (main field). Comparison of the main field predicted by the model *gufm1* and annual means of the main field components ($X = -B_\theta$, $Y = B_\phi$ and $Z = -B_r$) measured at observatories in different locations (Fuquene, Mauritius, Niemegk and Tuscon). Observatory data were obtained from the world data centre. The black squares, triangles and crosses are the observatory annual means and the red line is the prediction of *gufm1*. There was a site change in Mauritius in 1920, observatory results from both before and after the site change are presented in (b).

(a) Annual means at Fuquene (SV) **(b) Annual means at Mauritius (SV)**

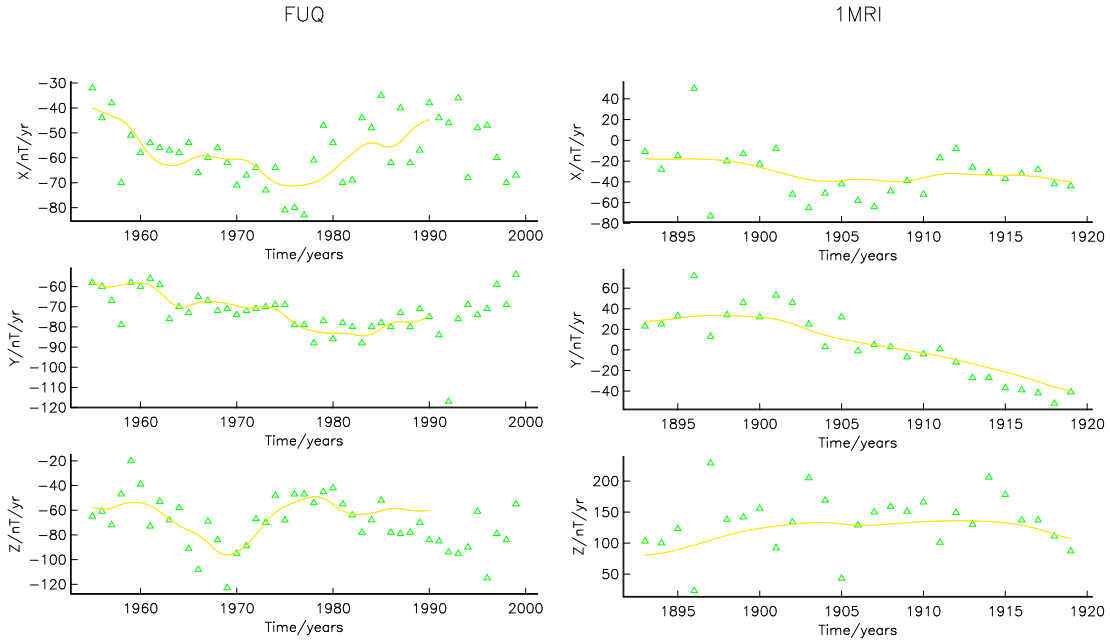

(c) Annual means at Niemegk (SV) **(d) Annual means at Tuscon (SV)**

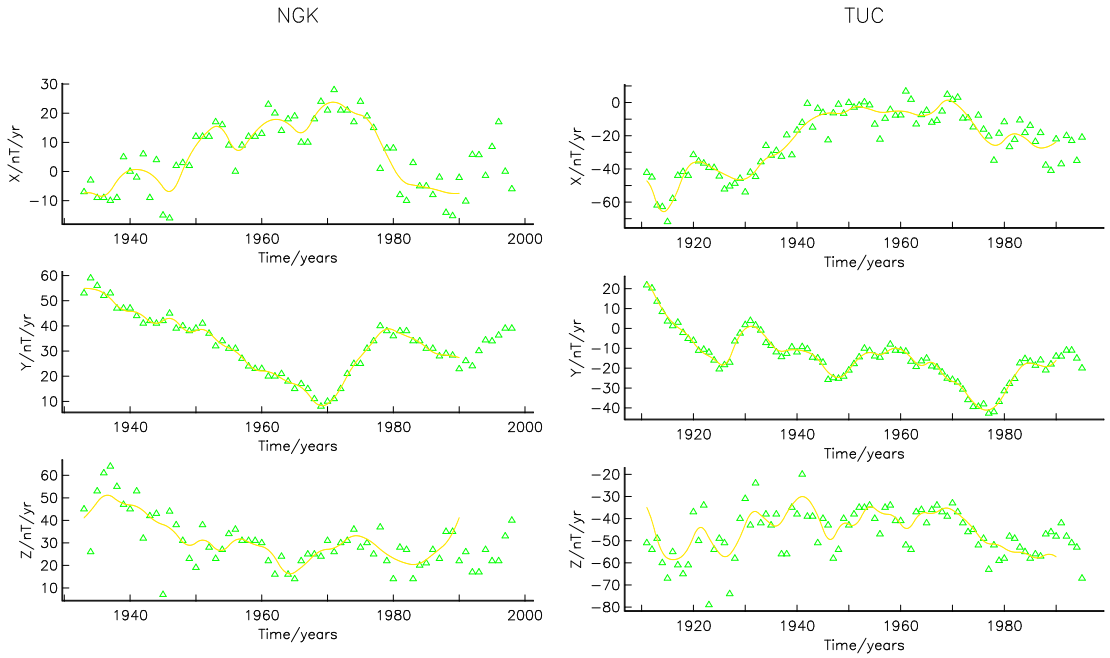

Figure A.4: Comparison of *gufm1* and observatory annual means (SV). Comparison of the secular variation (SV) predicted by the model *gufm1* and annual means of the secular variation components ($\dot{X} = -\frac{\partial B_\theta}{\partial t}$, $\dot{Y} = \frac{\partial B_\phi}{\partial t}$ and $\dot{Z} = -\frac{\partial B_r}{\partial t}$) measured at observatories in different locations (Fuquene, Mauritius, Niemegk and Tuscon). Observatory data were obtained from the world data centre. The green triangles are the observatory annual means of secular variation and the yellow line is the prediction of *gufm1*. Only results from the first observatory site on Mauritius are presented in (b).

the secular variation observations, but *gufm1* again does a good job of fitting the trend in these data.

Comparison with direct, high quality observations magnetic field measurements at Earth's surface shows that *gufm1* is an excellent description of the main field and its secular variation, giving confidence in its use in this thesis to analyse patterns of field evolution.

A.4 Limitations of *gufm1*

Although *gufm1* is our most detailed picture of how the geomagnetic field has varied in space and time over the past 400 years, it does have its limitations, in particular those due to the changing quality and distribution of the available observations with time.

The mapping of surface observations down to the core surface means this variability is manifested in the changing width of the resolving kernel (the filter through which we must view the field at the CMB) with space and time. Backus et al. (1996) discusses that inferences about the core field on spatial scales smaller than the area of averaging kernel peak are impossible, referring to this as the circle of confusion. Jackson (1989) has produced maps showing how the width of the averaging kernel varies with geographical position and finds it closely follows the density of observations, so for example in 1882.5 the width of the kernel varies from 11.5 degrees below Europe to 16.5 degrees in Antarctica where there were no measurements. Animations of *gufm1* show the field model becomes increasingly complex as time passes, indicating a decrease in the circle of confusion with time; the smallest features become visible especially in the last 20 years when satellite data has become available.

The model *gufm1* is ultimately constrained (even with perfect data coverage) by the limit placed on spatial resolution by crustal field contamination. Unless a sensible method of removing the crustal field from the signal can be found, our images of the magnetic field at the core surface will always be limited to less than spherical harmonic degree l=12 (around 1800 km at the equator of the core surface), at which point the crustal field begins to dominate, and where the field modelling strategy employed in *gufm1* means that regularisation rather than the fit to the data controls the field structure. In figure A.5 the spatial, spherical harmonic power spectra (as defined by Lowes (1974)) is plotted every 50 years to show how the information content of *gufm1* changes with time — at all epochs the power decays monotonically to less than 10^{-3}% of the total power by spherical harmonic degree 10. It is also clear that the more recent epochs contain more power at lower harmonics than the older epochs. This is because of the requirement that the models fit the data given the error estimates, therefore a larger misfit (hence smoother model) is permitted when data errors are larger at earlier epochs. The subject of absolute field amplitude errors inherent in the core surface field maps is troublesome. Gubbins and Bloxham (1985) produced variance estimates for their radial magnetic field

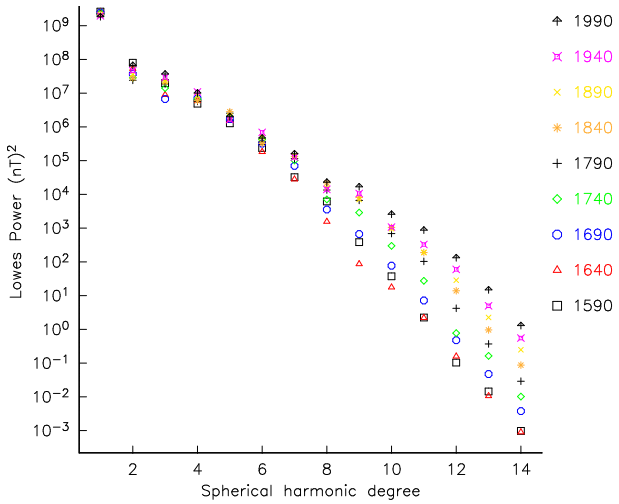

Figure A.5: Spherical harmonic power spectra from *gufm1*.
Lowes power spectra of gufm1 showing the change in spectral power at Earth's surface of the geomagnetic field field *gufm1* and illusstrates limits to resolution imposed by damping in order to prevent signal contamination by the crustal field.

models based on the error covariance matrix $\mathbf{C}_e$ and the asymptotic form of the model covariance matrix $\mathbf{C}_m$ (where $\mathbf{C}_m^{-1} = \lambda_S \mathbf{S}^{-1} + \lambda_T \mathbf{T}^{-1}$ in *gufm1*). Unfortunately, these error estimates depend on the choice of damping parameters for which at present there is no objective way of determining (the Ohmic heating bound suggests much weaker damping than is needed to suppress crustal fields — see Backus (1988)). The methodology employed here solves the existence problem but not the uniqueness problem: as such it appears difficult to place rigorous bounds on field amplitude errors.

Despite these limitations, *gufm1* is undoubtedly a good model of how the magnetic field at the core surface has changed over the past four hundred years. It is consistent with a huge number of measurements and shows the continuous changes in space and time expected of a real magnetic field. Core flow models derived from it can kinematically account for observed changes in the length of day in the 20th century (Jackson et al., 1993), an independent confirmation that the models are reasonable.

A.5 Griding of *gufm1* for analysis on core surface

In order to carry out a space-time analysis of the magnetic field features in *gufm1*, the spherical harmonic field model for V was used along with equation (A.8) to evaluate B_r on a regularly spaced grid in latitude, longitude and time on the core surface. The spatial grid was chosen to be 2 degrees in latitude and longitude and 2 years in time. These are both much finer scale then the original field model, ensuring that no information was lost as a result of the griding procedure.

Appendix B

The archeomagnetic field model CALS7K.1

B.1 Introduction

Knowledge of Earth's magnetic field prior to direct human measurements (such as those used to construct *gufm1*, see appendix A) comes from indirect sources, where the magnetic field in the past has been recorded either naturally during rock formation or accidentally as a by-product of early human activities such as pottery firing. CALS7K.1 (Korte and Constable, 2005; Korte et al., 2005) is a geomagnetic field model covering the past seven millennia from 5000 B.C to 1950 A.D. During this interval sufficient spatial and temporal coverage of indirect records exists to make feasible the construction of a global time-dependent field model. In this appendix a brief survey of the data compilation, the estimated data errors, field modelling assumptions and model characteristics are given. For further details the comprehensive papers of Korte et al. (2005) which describes the data compilation and Korte and Constable (2005) which describes the field model should be consulted.

B.2 Data sources

The records of Earth's magnetic field used to create CALS7K.1 come from,

- Detrital (depositional) Remanent Magnetization (DRM) of lake sediments (10637 declination, 12316 inclination)

- Thermal Remanent Magnetization (TRM) of archaeological artifacts and lavas (2443 declination, 3769 inclination, 3488 intensity).

For detailed discussions of DRM and TRM and the problems associated with determining the remanent magnetic field in each case, the reader should consult Butler (1992).

B.3 Spatial and temporal distribution of data

The spatial distribution of the records used in constructing CALS7K.1 are highly heterogeneous. The most serious shortcoming is the under-representation of the southern hemisphere, particularly in archeomagnetic and lava data constraining intensity (only 12738 measurements are from the southern hemisphere and only 228 of these are intensity measurements, of 64706 measurements in total of which 3188 are measurements of intensity). This is because there are very few records from Africa, South America and oceanic locations. In contrast, Europe is over-represented, especially in terms of archeomagnetic data. In figure B.1 the concentration of data as a function of position at Earth's surface is plotted along with the locations of the lakes and average locations of the archeomagnetic sites.

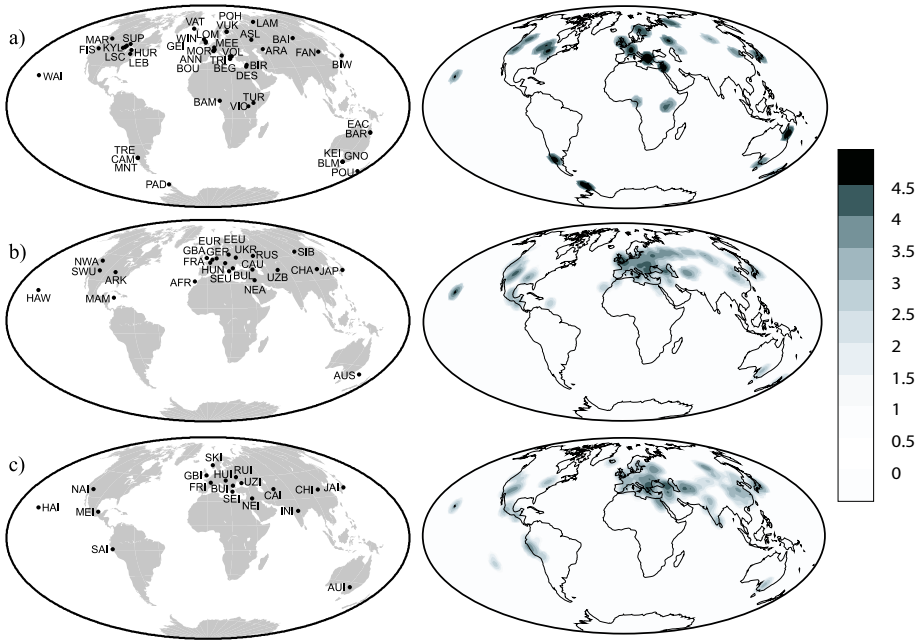

Figure B.1: Spatial locations and concentration of data in CALS7K.1. Locations of the global compilation of archeomagnetic and paleomagnetic data used in the construction of CALS7K.1 (from Korte et al. (2005)). Sites of lakes are shown in (a), of the archeomagnetic directional data in (b) and of the archeomagnetic intensity data in (c). In the left column the locations of lakes and average locations of the archeomagnetic regions are plotted, while on the right the log of the concentration of data is contoured (concentration is calculated by representing each datum location by a Fisherian probability density function centred on the data location with an angular standard deviation of 2.6 degrees; the integral of the concentration over the Earth's surface yields the total number of data points— see Korte et al. (2005) for further details.)

Temporal resolution and coverage of the data also varies greatly, with the archeomagnetic data worse at earlier times. As an illustration of the changes in the temporal distribution of data the number of lake sediment and archeomagnetic declination and inclination data per 100 years are plotted for different regions in figure B.2. The archeomagnetic intensity data follow similar trends. The increase in the number of European data as time goes on is particularly striking.

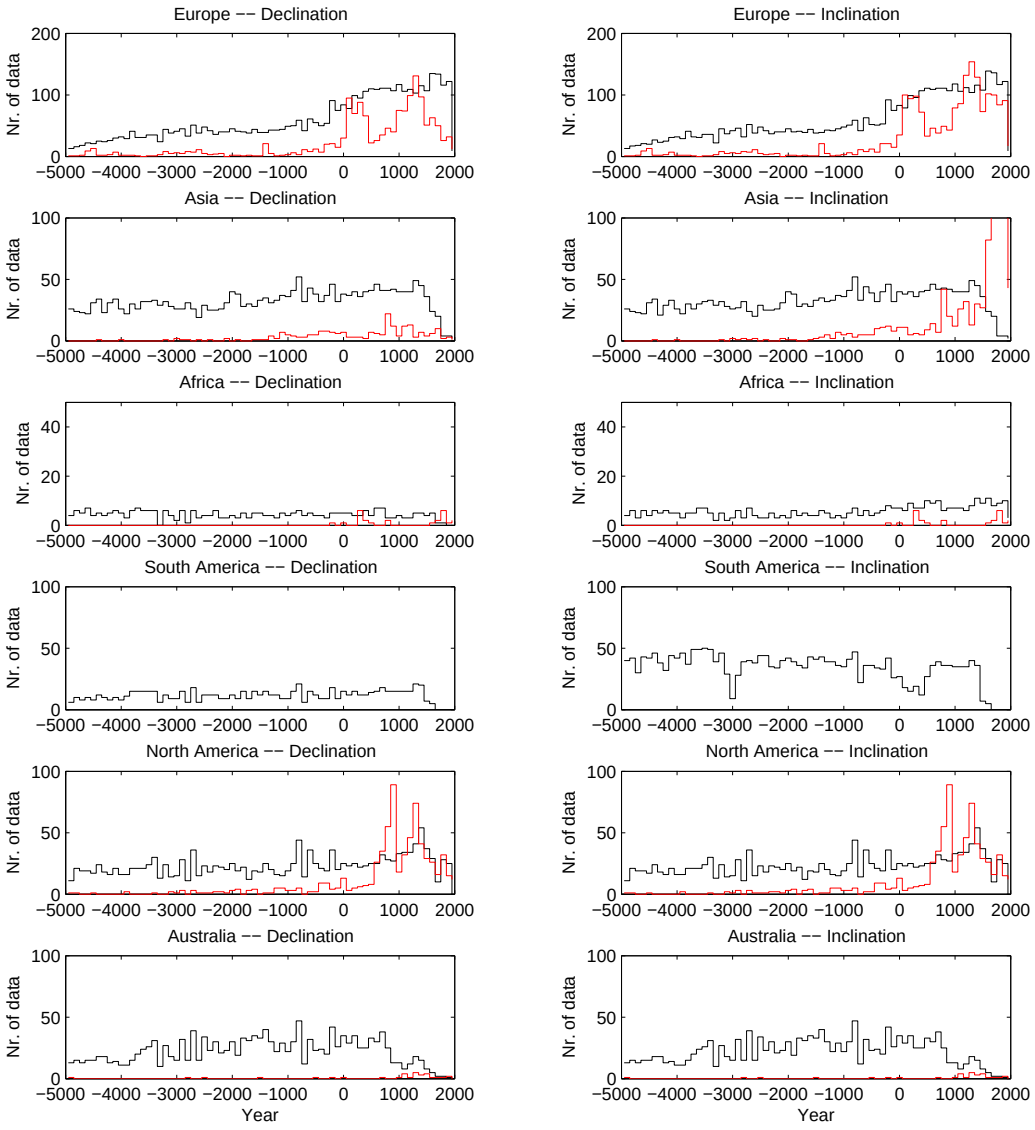

Figure B.2: Temporal distribution of declination, inclination in CALS7K.1. Histograms of declination (left) and inclination (right) data through time in 100 year bins. Black are lake sediment data, red are archeomagnetic data. Note the different scales on the y-axes (from Korte et al. (2005)).

B.4 Uncertainty estimates

To take into account the reliability of data when performing global geomagnetic field modelling it is necessary to weight data according to uncertainty estimates that are internally consistent within the dataset. Unfortunately the original error estimates of the data were not found to be consistent, so new criteria for determining errors were employed. Minimum directional uncertainty estimates of 2.5° for inclination and 3.5° for declination with archeomagnetic data and 3.5° for inclination and 5.0° for declination with lake sediment data were used because in previous studies (Constable et al., 2000; Korte and Constable, 2003) these uncertainties have allowed construction of smooth global models that satisfactorily fit the data. If original error estimates (often a 95 percent confidence cone calculated around a mean direction from independent measurements at a given site (α_{95}), rescaled to give standard deviations of the uncertainty (see Korte et al. (2005)) were greater than the minimum estimates then these were used instead. Error estimates for the archeomagnetic intensity data were assigned by allocating each measurement to a category based on a selection criteria that is a combination of the methodology employed, the dispersion of the mean and whether alteration tests were carried out. The classification and the associated errors estimates were then (i) reliable: 6 to 10 percent relative error, (ii) reliable but dispersed: original dispersion greater than 10 percent retained, (iii) less reliable: minimum relative error of 20 percent, or the original dispersion estimate if this was larger.

In addition, errors in dating were taken into account by increasing the data uncertainties by the measurement error that would result from the dating uncertainty as calculated using simple linear models of secular variation derived from recent global models. If dating uncertainty was estimated to be less than 10 years, then no additional error was added. If the dating uncertainty was 10 to 50 years an inclination error of 0.5° was added, a declination error of 1.5° was added and intensity error of $1.5\mu T$ was added. For age uncertainties of 50 to 100 years, 1° inclination, 3° declination and intensity $2.5\mu T$ errors were added. For age uncertainties of 100 to 500 years errors of 2° inclination, 6° declination and intensity $5\mu T$ were added. For dating errors estimated to be greater than 500 years, the data were rejected. Similarly, location uncertainties for sites of the archeomagnetic data from compilations were taken into account as additional measurement errors using a linear model for gradients of magnetic field elements, so each 1° latitude error corresponded to an additional error of 1° in inclination, 0.3° in declination and $0.5\mu T$ in intensity while each 1° longitude error corresponded to an additional error of 0.5° in inclination, 0.5° in declination and $0.25\mu T$ in intensity.

The resulting average error estimates calculated from all the data used in the modelling were 4.0° in inclination, 6.7° in declination and $11\mu T$ in intensity.

B.5 Field modelling methodology

The method of regularised inversion of geomagnetic observations to obtain a spatially and temporally smooth, continuous model of the global magnetic field at the core surface as applied by Bloxham and Jackson (1992) and Jackson et al. (2000) to historical data and by Korte and Constable (2003) to a preliminary archeomagnetic and lake sediment dataset was applied to the dataset described above in order to obtain the model CALS7K.1. A mathematical description of the methodology can be found in appendix A. The data are weighted by the error estimates described above and the RMS misfits of the model to the data (normalised by the errors and number of data) are calculated.

The model is a spherical harmonic expansion up to degree and order 10 in space and cubic B-splines in time, with node spacing of 60 years. The Ohmic heating bound of Gubbins (1975) is used for the spatial norm, while the temporal norm is the integral of the second derivative of B_r over the core surface. The lack of intensity data was compensated for by (i) the introduction of an artificial multiplicative weighting for the intensity data (ii) retaining an additional constraint (with an associated weighting factor) on the axial dipole by including a simple model for g_1^0 (see Korte and Constable (2003)) as additional data. These 4 parameters must be specified in such a way that the most geophysically reasonable model is arrived at. The spatial damping is chosen to be the minimum that gives a B_r that is predominantly dipolar, the temporal damping is chosen to be the lowest value which eliminates temporal variations on time scales shorter than 100 years. The weighting factor for the intensity data and the factor for the axial dipole constraint are picked so that all data types are fitted well within their estimated uncertainties. A weighting factor of 2 is found to minimise the total RMS misfit, while retaining the axial dipole constraint with low weighting factor of 0.001 can increase the overall misfit, and particularly the misfit to the intensity data.

The solution to the inverse problem obtained in this way is clearly non-unique, and relies upon the subjective choice of both the regularisation norms and the damping parameters. The strategy employed was to try to find the simplest possible model that fitted the data to its estimated accuracy. However, with the archeomagnetic and lake sediment data, the uncertainties in the data are very difficult to estimate accurately, and as a result the final models did not yield a misfit to within the desired tolerance. The model residuals from initial attempts at modelling were examined and it was found that compared to a normal distribution many of the data were not satisfactorily fit and outliers were present. The data that could not be fit by the initial model to within two times the average uncertainty of the original dataset were rejected and the model recalculated. After this procedure, the remaining data could be fitted to within the estimated tolerance by the new model, with the distribution of the residuals being much closer to a normal distribution. It was found at this stage that the use of an axial dipole constraint no longer influenced the model, so it was removed, yielding the final preferred model referred to as CALS7K.1.

B.6 Characteristics and evaluation of the model CALS7K.1

An RMS misfit of 1.00 was achieved for the model CALS7K.1 after data rejection, using a spatial damping parameter of $3 \times 10^{-7}\mathrm{nT}^{-2}$ (spatial norm was $40 \times 10^{9}\mathrm{nT}^{2}$) and a temporal damping parameter of $5 \times 10^{-1}\mathrm{nT}^{-2}\mathrm{yr}^{4}$ (temporal norm was $63 \times 10^{3}\mathrm{nT}^{2}\mathrm{yr}^{-4}$).

The best way of assessing the success of a model is to compare its predictions to the original data. This has been carried out by Korte and Constable (2005) with lake sediment data and archeomagnetic data at a number of sites. In general the fit of the model to the data was found to be good, though there are some discrepancies, for example in Lake Baikal in Japan where not even the trend was been well captured, suggesting that this record may have some serious errors. The good fit of the model to records in the Southern hemisphere was particularly encouraging, given the sparse nature of data coverage there.

B.7 Griding of CALS7K.1 for analysis on core surface

In order to carry out a space-time analysis of field features in CALS7K.1, the spherical harmonic field model for the magnetic potential V supplied by Monika Korte (personal communication July 2004) was used along with equations (A.8)-(A.17) to evaluate B_r on a regularly spaced grid in latitude, longitude and time at the core surface.

In all cases a grid of spacing 2 degrees in longitude by 2 degrees in latitude was used. This is considerably smaller then the resolution of a degree 10 spherical harmonic model, ensuring that no information was lost through the griding procedure.

For comparison to *gufm1* a subset of CALS7K.1 running from 1600A.D to 1950A.D (called CALS7K.1h) was gridded with a temporal spacing of 2 years. This is obviously much higher than the temporal resolution in CALS7K.1, but facilitates straightforward comparisons with the historical record. When studying the full span of CALS7K.1 a temporal spacing of 25 years was employed, again significantly less than the resolution of CALS7K.1. The study of the interval from 2000B.C to 1700A.D. employs a 25 year grid spacing.

Appendix C

A 3D, convection-driven, spherical shell dynamo model (MAGIC)

C.1 Introduction

In chapter 5 results from runs of the Wicht (2002) model of time dependent, 3D, Boussinesq thermal convection and magnetic field generation in an electrically conducting fluid contained in a spherical shell geometry (known as MAGIC) are analysed. MAGIC is designed to simulate as well as possible the geodynamo process thought to be operating in Earth's outer core given current computational limits. In this appendix, the model equations, boundary conditions and numerics of MAGIC are summarised, the parameters of the runs examined in this thesis are detailed, and possible scalings to Earth's core and the problems associated with such scalings are discussed.

C.2 Model equations and boundary conditions

MAGIC is described in detail by Wicht (2002), here the important details are collected for completeness. The non-dimensionalised equations of Boussinesq convection of an electrically conducting fluid in the presence of a magnetic field used in MAGIC are

$$E\left(\frac{\partial \boldsymbol{u}}{\partial t}+(\boldsymbol{u}\cdot\nabla)\boldsymbol{u}-\nabla^2\boldsymbol{u}\right)+2(\hat{\boldsymbol{z}}\times\boldsymbol{u})+\nabla P=\frac{1}{Pr_m}((\nabla\times\boldsymbol{B})\times\boldsymbol{B})+Ra_mT\frac{\boldsymbol{r}}{r_0}, \quad \text{(C.1)}$$

$$\frac{\partial \boldsymbol{B}}{\partial t}=\nabla\times(\boldsymbol{u}\times\boldsymbol{B})+\frac{1}{Pr_m}\nabla^2\boldsymbol{B}, \quad \text{(C.2)}$$

$$\frac{\partial T}{\partial t}=-(\boldsymbol{u}\cdot\nabla)T+\frac{1}{Pr}\nabla^2T, \quad \text{(C.3)}$$

$$\nabla\cdot\boldsymbol{u}=0, \qquad \nabla\cdot\boldsymbol{B}=0. \quad \text{(C.4)}$$

Non-dimensionalised was carried out using the viscous diffusion timescale of $\frac{D^2}{\nu}$ (where $D=r_0-r_i$ where r_0 is the radius of the outer shell and r_i is the radius of the inner shell), and measuring the magnetic field in units of $\left(\frac{\rho_0\Omega}{\sigma}\right)^{1/2}$ (where $\sigma=\mu_0\eta$ is the electrical

conductivity) and the temperature in units of the temperature difference across the spherical shell (ΔT). Detailed derivations of these governing equations and the meanings of the various symbols can be found in appendix D. When discussing MAGIC and the results obtained from it, the definitions of the non-dimensional numbers defined in Wicht (2002) will be employed

$$E = \frac{\nu}{\Omega D^2}, \qquad Pr = \frac{\nu}{\kappa}, \qquad Pr_m = \frac{\nu}{\eta}, \qquad Ra_m = \frac{\alpha g_0 \Delta T D}{\nu \Omega}, \tag{C.5}$$

where g_0 is the gravity field at the outer boundary. These are the same as those described in appendix D except that the Ekman number E is a factor 2 larger and Ra_m is a differential heating Rayleigh number that has been modified by multiplying by the Ekman number and dividing by the Prandtl number.

The governing equations are solved in the geometry of a rigid spherical fluid shell surrounding a solid inner core with the same electrical conductivity as the fluid. The inner core is free to rotate under mechanical and electrical torques (with no slip boundary conditions). The magnetic field in the inner core is determined by the diffusion of the time-dependent magnetic field from the fluid region. Rigid, no-slip boundary conditions are applied to the velocity field of the fluid at both boundaries and electrically insulating boundary conditions are applied to the magnetic field at the outer boundary. Both the inner and outer boundaries are held at fixed temperatures.

MAGIC does not use the controversial hyperdiffusion parameterisation of sub-grid scale effects (see Glatzmaier and Roberts (1995) and Zhang and Jones (1997) for discussions of this approach) and does not incorporate inhomogeneous thermal boundary conditions (see, for example, Gibbons and Gubbins (2000) or Christensen and Olson (2003)).

C.3 Numerical solution

The numerical method used to solve this system is based on the pseudo-spectral method in spherical coordinates developed by Glatzmaier (1984) that has been used in a number of recent 3D studies of the geodynamo (see, for example, Glatzmaier and Roberts (1995) or Olson et al. (1999)). The velocity and magnetic field are expressed in terms of poloidal and toroidal scalars, ensuring that the solenoidal conditions on $\boldsymbol{u}$ and $\boldsymbol{B}$ are automatically satisfied

$$\boldsymbol{u} = \nabla \times (\nabla \times f\widehat{\boldsymbol{r}}) + \nabla \times e\widehat{\boldsymbol{r}} \tag{C.6}$$

$$\boldsymbol{B} = \nabla \times (\nabla \times h\widehat{\boldsymbol{r}}) + \nabla \times g\widehat{\boldsymbol{r}} \tag{C.7}$$

The scalar fields are then expanded in terms of Chebyshev polynomials as a function of the transformed radial variable ($\frac{2(r-r_i)}{r_0-r_i} - 1$) and truncated at degree N_x, and in terms of complex surface spherical harmonics in co-latitude θ and longitude ϕ, truncated at degree L, so for example the toroidal scalar for the velocity field in the fluid spherical

shell is represented as

$$e(r,\theta,\phi) = \sum_{n=0}^{n=N} \sum_{l=0}^{l=L} \sum_{m=-l}^{m=l} e_{nlm} T_n\left(\frac{2(r-r_i)}{r_0-r_i} - 1\right) P_{lm}(\cos\theta) e^{im\phi}, \tag{C.8}$$

where T_n is a Chebyshev polynomial of degree n and P_{lm} is an associated Legendre function of degree l and order m. To ensure continuity and differentiability at the origin, fields in the inner core are represented instead by schemes such as

$$e^i(r,\theta,\phi) = \sum_{n=0}^{n=N^i} \sum_{l=0}^{l=L} \sum_{m=-l}^{m=l} e^i_{nlm} \left(\frac{r}{r_i}\right)^{l+1} T_{2n}\left(\frac{2(r-r_i)}{r_0-r_i} - 1\right) P_{lm}(\cos\theta) e^{im\phi}. \tag{C.9}$$

A mixed implicit/explicit algorithm is used to timestep the system of governing equations. Non-linear inertial terms and Coriolis terms are calculated explicitly by transforming from spectral to physical space and back using fast Fourier transforms for the azimuthal representation, Gauss-Legendre integration to deal with the latitude dependence and a fast cosine transform to transform the Chebyshev polynomials on a suitably chosen radial grid. Further details can be found in Wicht (2002), Glatzmaier (1984), Glatzmaier and Roberts (1995) and Christensen et al. (1999).

The MAGIC code has reproduced the numerical benchmark solution reported by Christensen et al. (2001) and the version with a finitely conducting, rotating inner core has been successful benchmarked against other schemes (A. Willis, personal communication, December 2004). The truncation parameters are chosen so that the magnetic and kinetic energy associated with the highest spherical harmonic degrees is several orders of magnitude lower than the peak energy in the spectrum (a good indicator of convergence) while the time-step is chosen adaptively to ensure optimal efficiency. The solutions for each set of parameters are determined after several magnetic diffusion times, after all transient effects have decayed. The initial conditions used are those of previous runs at nearby parameter values.

C.4 Parameters of models studied

Two solutions generated by Johannes Wicht using the model MAGIC (personal communications August 2004, November 2004) are analysed in Chapter 5 of this thesis. Model DYN1 is a high Ekman number case (E=2×10^{-2}) with relatively low magnetic Reynolds number $R_m = U_{RMS}D/\eta \sim 100$ (this non-dimensional number quantifies the ratio of the amount of magnetic field change caused by advection to the amount of magnetic field change caused by magnetic diffusion), while model DYN2 is a lower Ekman number case (E=3×10^{-4}) with larger $R_m \sim 500$. The precise parameter values and a comparison to the estimated parameters in Earth's core are listed in Table C.1.

In model DYN1 the length scales of convection and magnetic fields are relatively large so that when the model is truncated at degree L=32 little power is found spherical

Parameter	Model 1	Model 2	Earth(laminar)	Earth(turbulent)
Ekman No. (E)	2×10^{-2}	3×10^{-4}	10^{-16}	10^{-9}
Modified Rayleigh No. ($Ra_m = \frac{ERa}{Pr}$)	3×10^{2}	9×10^{2}	10^{15} (10^{24})	10^{3} (10^{6})
Prandtl No. (Pr)	1	1	0.1	1
Magnetic Prandtl No. (Pr_m)	10	3	10^{-6}	1
Magnetic Reynolds No. (R_m)	100	500	~ 1200	~ 1200

Table C.1: Parameters of dynamo models and estimates for Earth's core. The non-dimensional parameters specifying the regime of the 3D convective dynamo models whose output is analysed in Chapter 5 and estimated parameters for the Earth's liquid iron outer core using typical estimates of the molecular diffusivities at core pressures and temperatures from Table 1 of Gubbins (2000) ($\nu = 10^{-6}\ mboxm^2\,\mathrm{s}^{-1}, \kappa = 8.6\times10^{-6}\ \mathrm{m}^2\,\mathrm{s}^{-1}, \eta = 1.6\ \mathrm{m}^2\,\mathrm{s}^{-1}$) and the turbulent viscosity and thermal diffusivities $\nu_t = \kappa_t = \eta = 1.6\ \mathrm{m}^2\,\mathrm{s}^{-1}$. This crude parameterisation of the effect of small scale turbulent eddies on the thermal and viscous diffusion is discussed in detail by Roberts and Glatzmaier (2000a). Estimates for the modified Rayleigh number due to thermal convection also come from Gubbins (2000), estimates for the Rayleigh numbers appropriate for compositional convection are given in brackets. The estimates of the magnetic Reynolds number in the core are based on the estimates of Christensen and Tilgner (2004).

harmonic degrees greater than 10. In contrast for Model DYN2 the flow and magnetic field features are much smaller scale and a truncation level of L=85 is necessary for convergence. Since such small scales are masked by crustal effects (Langel and Hinze, 1998) when Earth's magnetic field is observed from its surface, a version of Model DYN2 (called Model DYN2d) that only includes the power up to spherical harmonic degree 14, (with degrees 13 and 14 progressively damped) was also studied.

C.5 Relating geodynamo model output to the Earth: problems with time scales

The convection driven geodynamo model MAGIC encapsulates the leading order physical processes believed to be operating in Earth's core and thought to be involved in generating Earth's magnetic field. Can it therefore be used to improve knowledge of the mechanisms underlying the observed magnetic field change at the core surface?

The first step towards answering this question involves determining whether the patterns of field change produced by the model have the same character as geomagnetic secular variation. In order to compare the form of observed secular variation to that seen in the model, the scales of length, time and magnetic field must be re-scaled from the non-dimensional numbers output by the model, to the scales appropriate for the Earth. This can be achieved by using estimates of the physical properties thought to be present in Earth's core to determine the relevant scales of shell thickness

$$D = r_0 - r_i = 3480\mathrm{km} - 1220\mathrm{km} \sim 2.3\times10^{6}\ \mathrm{m} \tag{C.10}$$

magnetic diffusion time

$$\tau_\eta = \frac{D^2}{\eta} = (2.3\times10^6)^2\ \mathrm{m}^2\cdot 4\pi\times10^{-7}\ \mathrm{T}^2\,\mathrm{m}^2\,\mathrm{kg}^{-1}\,\mathrm{s}^2\cdot 5\times10^5\ \mathrm{T}^{-2}\,\mathrm{kgs}^{-1} = 3.3\times10^{12}\mathrm{s}\sim10^5\ \mathrm{yrs}, \quad \text{(C.11)}$$

and magnetic field strength

$$\mathcal{B} = \left(\frac{\rho\Omega}{\sigma}\right)^{1/2} = \left(\frac{10^4\mathrm{kg}\cdot 7.3\times10^{-5}\ \mathrm{s}^{-1}}{5\times10^5\ \mathrm{T}^{-2}\,\mathrm{kgs}^{-1}}\right)^{1/2} \sim 1.2\times10^{-3}\ \mathrm{T}. \quad \text{(C.12)}$$

These factors can then be used to transform the model output to a dimensional form that can be compared and contrasted with observations as has been done by several previous workers (see for example Kuang and Bloxham (1998), Christensen and Olson (2003), Dumberry and Bloxham (2003) and Wicht and Olson (2004)).

Although a dimensionally correct approach, the results obtained using this procedure must be interpreted with care, and it should always be remembered that the time scales of dynamic processes in the model may not be comparable to those present in Earth's core. As discussed by Jones (2000), Dormy et al. (2000) and Hollerbach (2003), the problem in time scale interpretation arises because the non-dimensional parameters are ratios of the natural time scales of the system. In particular, E (the parameter that the model has most seriously wrong) can be interpreted as the ratio of the rotational to the viscous diffusion time scale. Therefore dynamic mechanisms associated with the rotation time scale in Earth's core will have very different time scales in redimensionalised model years. For example, inertial waves typically have periods on the order of a day in Earth's core but will have periods of around 100 re-dimensionalised years in the case of Model DYN2, because the ratio of the rotational time scale to the magnetic diffusion time scale (that equals the viscous diffusion time scale when Pr=1) is a factor of 10^5 too large in Model 2 compared to the Earth's core (turbulent case). Even worse, the dynamical balance producing fluid motions could be very different in the models than is the case in Earth's core (especially viscous effects will unrealistically large), again leading to changes in the characteristic time scales and damping of dynamics (Dumberry and Bloxham, 2003). Only if the models get the leading order force balance involved in a particular dynamic mechanism correct, and if the characteristic time scale of that mechanism is independent of the control parameters would direct comparisons of the space-time characteristics of geodynamo model output and the space-time characteristics of Earth's magnetic field be meaningful. It is for this reason that we prefer to leave the time scales in Chapter 5 in terms of the non-dimensional magnetic diffusion time scale.

Nonetheless, analysis of geodynamo model output provides invaluable information (especially regarding the mechanisms producing magnetic field evolution at the outer surface of its generation region inside a rotating fluid) that cannot be obtained from any other source. These models are potential very useful tools provided that their limitations are borne in mind.

Appendix D

Equations governing hydromagnetic waves in Earth's outer core

D.1 Boussinesq hydromagnetic equations for convection in a rotating fluid

Quantitative modelling of hydromagnetic waves in Earth's outer core requires equations encapsulating the physical laws governing the fluid dynamics of a rotating, electrical conducting liquid in a spherical container with a magnetic field present. The relevant laws are the conservation of mass, momentum and energy along with the principles of electromagnetism (for the background to these laws consult, for example, Feynman et al. (1963); Longair (2003)). A suitable system incorporating these principles but making reasonable simplifying assumptions[1] is the system of Boussinesq, hydromagnetic equations for a rotating fluid. A comprehensive and rigorous derivation of these equations detailing the assumptions involved can be found in Chandrasekhar (1961). A discussion of the applicability of this system to modelling the dynamics of Earth's core can be found in Gubbins and Roberts (1987).

In this thesis, ρ_0 is taken to represent the leading order, constant density of the fluid, $\boldsymbol{u}$ the velocity field, $\boldsymbol{\Omega}$ the angular rotation rate of the fluid, P the combined mechanical and centrifugal pressures, α the coefficient of volume expansion, T the temperature field, $\boldsymbol{g}$ the gravitational acceleration, μ_0 the magnetic permeability of a material that is not permanently magnetised, $\boldsymbol{B}$ the magnetic flux density (commonly called the magnetic field), ν the kinematic viscosity, κ the thermal diffusivity, $\epsilon = \frac{J_H}{\rho_0 C_p}$ where J_H is the internal heating rate per unit volume and C_p is the heat capacity at constant pressure, and η the magnetic diffusivity where $\eta = \frac{1}{\mu_0 \sigma}$ and σ is the electrical conductivity. The Boussi-

[1] These include assuming the fluid to be homogeneous, isotropic, incompressible except with regard to the action of the buoyancy force, and that it exhibits Newtonian viscosity. Motion is driven by uniform internal heating per unit volume and mechanical and joule heating effects are ignored in the heat equation. The MHD approximation is also made, neglecting relativistic effects and influence of displacement currents in Maxwell's equations, leading to the induction equation.

nesq hydromagnetic equations for a rotating fluid are then the Navier-Stokes equation expressing conservation of momentum

$$\rho_0 \left[\frac{\partial \boldsymbol{u}}{\partial t} + (\boldsymbol{u} \cdot \nabla)\boldsymbol{u} \right] + 2\rho_0(\boldsymbol{\Omega} \times \boldsymbol{u}) = -\nabla P - \rho_0 \alpha T \boldsymbol{g} + \frac{1}{\mu_0}(\nabla \times \boldsymbol{B}) \times \boldsymbol{B} + \rho_0 \nu \nabla^2 \boldsymbol{u}, \quad \text{(D.1)}$$

the Boussinesq heat equation expressing conservation of energy

$$\frac{\partial T}{\partial t} + (\boldsymbol{u} \cdot \nabla)T = \kappa \nabla^2 T + \epsilon, \quad \text{(D.2)}$$

the magnetic induction equation derived from Maxwell's equations

$$\frac{\partial \boldsymbol{B}}{\partial t} = \nabla \times (\boldsymbol{u} \times \boldsymbol{B}) + \eta \nabla^2 \boldsymbol{B}, \quad \text{(D.3)}$$

the incompressibility condition

$$\nabla \cdot \boldsymbol{u} = 0, \quad \text{(D.4)}$$

and the solenoidal condition for no magnetic monopoles

$$\nabla \cdot \boldsymbol{B} = 0. \quad \text{(D.5)}$$

D.2 Linearised governing equations

The properties of small, time dependent perturbations to a background state of this system (defined in terms of an imposed velocity field $\boldsymbol{U}_0$, temperature field T_0, magnetic field $\boldsymbol{B}_0$, and associated pressure field P_0) can be determined by substituting the expressions

$$\begin{aligned} \boldsymbol{u} &= \boldsymbol{U}_0 + \boldsymbol{u}' \quad \text{where} \quad |\boldsymbol{u}'| << |\boldsymbol{U}_0| \\ T &= T_0 + \Theta \quad \text{where} \quad |\Theta| << |T_0| \\ \boldsymbol{B} &= \boldsymbol{B}_0 + \boldsymbol{b}' \quad \text{where} \quad |\boldsymbol{b}'| << |\boldsymbol{B}_0| \\ P &= P_0 + P' \quad \text{where} \quad |P'| << |P_0| \end{aligned} \quad \text{(D.6)}$$

into equations (D.1) to (D.3). Retaining only the leading order terms, the equations determining the steady basic state are

$$\rho_0(\boldsymbol{U}_0 \cdot \nabla)\boldsymbol{U}_0 + 2\rho_0(\boldsymbol{\Omega} \times \boldsymbol{U}_0) = -\nabla P_0 - \alpha T_0 \boldsymbol{g} + \frac{1}{\mu_0}(\nabla \times \boldsymbol{B}_0) \times \boldsymbol{B}_0 + \rho_0 \nu \nabla^2 \boldsymbol{U}_0, \quad \text{(D.7)}$$

$$(\boldsymbol{U}_0 \cdot \nabla)T_0 = \kappa \nabla^2 T_0 + \epsilon, \quad \text{(D.8)}$$

$$\nabla \times (\boldsymbol{U}_0 \times \boldsymbol{B}_0) = -\eta \nabla^2 \boldsymbol{B}_0. \quad \text{(D.9)}$$

Subtracting this basic state and retaining only the remaining terms that are first order in the perturbation variables, the equations governing the evolution of small perturbations are

$$\begin{aligned} \rho_0 \frac{\partial \boldsymbol{u}'}{\partial t} &+ \rho_0(\boldsymbol{u}' \cdot \nabla)\boldsymbol{U}_0 + \rho_0(\boldsymbol{U}_0 \cdot \nabla)\boldsymbol{u}' + 2\rho_0(\boldsymbol{\Omega} \times \boldsymbol{u}') \\ = -\nabla P' - \rho_0 \alpha \Theta \boldsymbol{g} &+ \frac{1}{\mu_0}(\nabla \times \boldsymbol{b}') \times \boldsymbol{B}_0 + \frac{1}{\mu_0}(\nabla \times \boldsymbol{B}_0) \times \boldsymbol{b}' + \rho_0 \nu \nabla^2 \boldsymbol{u}', \end{aligned} \quad \text{(D.10)}$$

$$\frac{\partial \Theta}{\partial t} + (\boldsymbol{U}_0 \cdot \nabla)\Theta + (\boldsymbol{u}' \cdot \nabla)T_0 = \kappa \nabla^2 \Theta, \tag{D.11}$$

$$\frac{\partial \boldsymbol{b}'}{\partial t} = \nabla \times (\boldsymbol{U}_0 \times \boldsymbol{b}') + \nabla \times (\boldsymbol{u}' \times \boldsymbol{B}_0) + \eta \nabla^2 \boldsymbol{b}', \tag{D.12}$$

In the special case that $\boldsymbol{B}_0$ is a force free field (i.e. $(\nabla \times \boldsymbol{B}_0) \times \boldsymbol{B}_0 = 0$) then $\boldsymbol{U}_0 = 0$ is a solution to the steady state balance, $(\nabla \times \boldsymbol{b}') \times \boldsymbol{B}_0 + (\nabla \times \boldsymbol{B}_0) \times \boldsymbol{b}' = (\boldsymbol{B}_0 \cdot \nabla)\boldsymbol{b}' + (\boldsymbol{b}' \cdot \nabla)\boldsymbol{B}_0$ and the perturbation equations with ($\boldsymbol{u}'$, $\boldsymbol{b}'$, P') relabelled as ($\boldsymbol{u}$, $\boldsymbol{b}$, P) for notational convenience become

$$\rho_0 \frac{\partial \boldsymbol{u}}{\partial t} + 2\rho_0(\boldsymbol{\Omega} \times \boldsymbol{u}) = -\nabla P - \rho_0 \alpha \Theta \boldsymbol{g} + \frac{1}{\mu_0}\left[(\boldsymbol{B}_0 \cdot \nabla)\boldsymbol{b} + (\boldsymbol{b} \cdot \nabla)\boldsymbol{B}_0\right] + \rho_0 \nu \nabla^2 \boldsymbol{u}, \tag{D.13}$$

$$\frac{\partial \Theta}{\partial t} + (\boldsymbol{u} \cdot \nabla)T_0 = \kappa \nabla^2 \Theta, \tag{D.14}$$

$$\frac{\partial \boldsymbol{b}}{\partial t} = \nabla \times (\boldsymbol{u} \times \boldsymbol{B}_0) + \eta \nabla^2 \boldsymbol{b}, \tag{D.15}$$

$$\nabla \cdot \boldsymbol{u} = 0, \tag{D.16}$$

$$\nabla \cdot \boldsymbol{b} = 0. \tag{D.17}$$

D.3 Non-dimensionalisation using the viscous time scale

It is useful to group the physical parameters into a minimal number of non-dimensional quantities which then control the dynamics of the solution. In this thesis a non-dimensionalisation based on the viscous diffusion time scale ($\tau_\nu = \frac{d_0^2}{\nu}$) that facilitates straightforward comparison to non-magnetic convection is adopted. This requires that variables are re-scaled as follows

$$\nabla \rightarrow \frac{\nabla}{d_0}, \;\; t \rightarrow \frac{d_0^2}{\nu} t, \;\; \boldsymbol{u} \rightarrow \frac{\nu}{d_0}\boldsymbol{u}, \;\; \boldsymbol{b} \rightarrow \frac{B_0 \nu}{\eta}\boldsymbol{b}, \;\; \Theta \rightarrow \frac{|\nabla T_0| d_0 \nu}{\kappa}\Theta, \;\; p \rightarrow 2\Omega\nu p. \tag{D.18}$$

The governing equations then become

$$E\left(\frac{\partial}{\partial t} - \nabla^2\right)\boldsymbol{u} + (\widehat{\boldsymbol{\Omega}} \times \boldsymbol{u}) = -\nabla P - ERa\Theta\widehat{\boldsymbol{g}} + \Lambda\left[(\widehat{\boldsymbol{B}_0} \cdot \nabla)\boldsymbol{b} + (\boldsymbol{b} \cdot \nabla)\widehat{\boldsymbol{B}_0}\right], \tag{D.19}$$

$$\left(\nabla^2 - Pr\frac{\partial}{\partial t}\right)\Theta = \boldsymbol{u} \cdot \widehat{\nabla T_0}, \tag{D.20}$$

$$\left(\nabla^2 - Pr_m\frac{\partial}{\partial t}\right)\boldsymbol{b} = \nabla \times (\boldsymbol{u} \times \widehat{\boldsymbol{B}_0}). \tag{D.21}$$

along with the incompressibility condition on $\boldsymbol{u}$ and the solenoidal condition on $\boldsymbol{b}$ and where $\widehat{\boldsymbol{g}}$ is a unit vector in the direction of the gravitation acceleration (except in the case of a sphere[2]) and $\widehat{\boldsymbol{\Omega}}$ is a unit vector in the direction of the rotation axis, $\widehat{\boldsymbol{B}_0}$ is a

[2]The definition of the Rayleigh number used here (see equation (D.26)) is that of the conventional internal heating Rayleigh number which for a plane layer problem is $Ra = \frac{\gamma\alpha\beta' d_0^4}{\kappa\nu}$ (Chandrasekhar, 1961) with β' the magnitude of the temperature gradient ($|\nabla T_0| = \beta'$) and γ the magnitude of the gravitational force ($|g| = \gamma$). However, in a self-gravitating sphere ($d_0 = r_0$) with uniform internal heating per unit volume the expressions for the gravitational force and temperature gradient become $\boldsymbol{g} = \gamma r_0 \boldsymbol{r}$ and $\nabla T_0 = -\beta' r_0 \boldsymbol{r}$ where $\boldsymbol{r}$ varies between 0 and 1. Taking the magnitudes of the gravitational force and the temperature gradient appearing in Ra to be those at the outer boundary where $|\boldsymbol{r}|$=1, leads to a revised expression for the internal heating Rayleigh number containing an additional factor r_0^2 ($Ra = \frac{\gamma\alpha\beta' d_0^6}{\kappa\nu}$) which is used in chapter 7.

unit vector in the direction of the background magnetic field and $\widehat{\nabla T_0}$ is a unit vector in the direction of the background temperature gradient. The non dimensional control parameters are

$$\Lambda = \frac{B_0^2}{2\Omega\mu\rho_0\eta} = \frac{\text{Magnetic diffusion time scale}}{\text{MC timescale}} \qquad \text{(Elsasser No.)} \tag{D.22}$$

$$Pr = \frac{\nu}{\kappa} = \frac{\text{Thermal diffusion time scale}}{\text{Viscous diffusion time scale}} \qquad \text{(Prandtl No.)}, \tag{D.23}$$

$$Pr_m = \frac{\nu}{\eta} = \frac{\text{Magnetic diffusion time scale}}{\text{Viscous diffusion time scale}} \qquad \text{(Magnetic Prandtl No.)} \tag{D.24}$$

$$E = \frac{\nu}{2\Omega {d_0}^2} = \frac{\text{Rotational time scale}}{\text{Viscous diffusion time scale}} \qquad \text{(Ekman No.)}, \tag{D.25}$$

$$Ra = \frac{|\boldsymbol{g}|\,\alpha\,|\nabla T_0|\,d_0^4}{\kappa\nu} = \frac{\text{Time scale for buoyant motion of viscous fluid}}{\text{Thermal diffusion time scale}} \qquad \text{(Rayleigh No.)}, \tag{D.26}$$

The Prandtl number and the magnetic Prandtl number are material properties of the fluid (perhaps adjusted if turbulence dominates transport and eddy diffusion become important — see the discussion in (Roberts and Glatzmaier, 2000a)). For a particular fluid, the Ekman number is determined by the rotation rate of the fluid, the Elsasser number depends on the strength on the imposed magnetic field and the Rayleigh number depends on the temperature gradient driving convection.

Appendix E

Equatorial symmetry considerations in spherical geometry

E.1 Overview

In this appendix, the issue of equatorial symmetry in rotating spherical geometry is discussed following the notation of Gubbins and Zhang (1993) and Sarson (1994). The equatorial symmetries possible for linear hydromagnetic waves in this geometry are documented and the relationship between the equatorial symmetry of the B_r observed at Earth's core surface and the equatorial symmetry of flows within Earth's core is discussed.

E.2 Equatorial symmetry operations

The discussion here is based around spherical polar coordinates (r, θ, ϕ), with rotation understood to occur about the z axis where $\theta = 0$ and the x, y coordinates referring to positions the plane perpendicular to the rotation axis (see (Arfken, 1985) for a discussion of transformations between different coordinate systems).

Reflection in the equatorial (xy) plane in spherical polar coordinates (r, θ, ϕ) involves the transformation $\theta \to \pi - \theta$ and is denoted by the symbol E. E^S denotes symmetry[1] with respect to this operation while E^A denotes antisymmetry. Thus for a scalar field s

$$E^S \iff s(r, \theta, \phi) = s(r, \pi - \theta, \phi), \tag{E.1}$$

$$E^A \iff s(r, \theta, \phi) = -s(r, \pi - \theta, \phi), \tag{E.2}$$

[1]There has been some confusion over the definition of equatorial symmetry in the literature concerning thermal convection in rapidly rotating sphere because in the seminal paper of Busse (1970) vector velocity fields $\boldsymbol{u}$ with E^S symmetry are referred to as having 'odd' symmetry because $u_z(r, \theta, \phi) = -u_z(r, \pi - \theta, \phi)$. In this thesis such modes are referred to as equatorially symmetric.

while for a vector field $\mathbf{V} = (V_r, V_\theta, V_\phi)$

$$E^S \iff [V_r, V_\theta, V_\phi](r, \theta, \phi) = [V_r, -V_\theta, V_\phi](r, \pi - \theta, \phi), \tag{E.3}$$

$$E^A \iff [V_r, V_\theta, V_\phi](r, \theta, \phi) = [-V_r, V_\theta, -V_\phi](r, \pi - \theta, \phi). \tag{E.4}$$

The antisymmetric behaviour of the θ component arises from the inversion of the θ component during the E transformation, as can be seen by considering how the coordinate system changes under this transformation.

In order to determine allowed combinations of equatorial symmetries for fields in a system of interest (whose mathematical governing equations are known), it is necessary to determine how relevant combinations of differential operators, vector operators, scalar fields and vector fields behave under the equatorial symmetry transformation

The binary vector operators have the properties

$$\mathbf{a} \cdot \mathbf{b} = a_i b_i \quad \iff \quad E^S, \qquad \mathbf{a} \times \mathbf{b} = \epsilon_{ijk} a_j b_k \quad \iff \quad E^A, \tag{E.5}$$

where ϵ_{ijk} is the isotropic alternating tensor, itself reflectionally antisymmetric (see, for example, Arfken (1985)).

The operator E involves $\theta \to \pi - \theta$, so that $d\theta \to -d\theta$. Differential operators therefore have the symmetries

$$\frac{\partial}{\partial r} \quad \iff \quad E^S, \qquad \frac{\partial}{\partial \theta} \quad \iff \quad E^A, \qquad \frac{\partial}{\partial \phi} \quad \iff \quad E^S. \tag{E.6}$$

It is now also possible to establish the symmetry of vector differential operators

$$\nabla \iff E^S, \quad \nabla\cdot \iff E^S, \quad \nabla\times \iff E^A, \quad \nabla^2 \iff E^S. \tag{E.7}$$

The rules for calculating the symmetry of compounds of variables and operators is analogous to calculating the resultant parity of a product of algebraic terms, each of which is either positive or negative, but now the operator itself can have a parity, with the multiplication operator always positive. For example, considering an E^S scalar s, an E^A scalar a, an E^S vector $\mathbf{V_s}$ and an E^A vector $\mathbf{V_a}$ then

$$\mathbf{V_a} \cdot \mathbf{V_a} \iff E^S, \quad \mathbf{V_a} \cdot \mathbf{V_s} \iff E^A, \quad \mathbf{V_s} \times \mathbf{V_s} \iff E^A, \quad \mathbf{V_s} \times \mathbf{V_a} \iff E^S, \tag{E.8}$$

$$\text{and } \nabla \cdot \mathbf{V_a} \iff E^A, \quad \nabla s \iff E^S, \quad \nabla \times \mathbf{V_s} \iff E^A. \quad \nabla \times \mathbf{V_a} \iff E^S. \tag{E.9}$$

It should also be noted that any scalar or vector quantity can be decomposed into E^S and E^A parts: for an arbitrary vector $\mathbf{Q}$, if $\mathbf{Q}' = E^S\mathbf{Q}$ then the quantity $\mathbf{Q}^S = \frac{1}{2}(\mathbf{Q}+\mathbf{Q}')$ is E^S and $\mathbf{Q}^A = \frac{1}{2}(\mathbf{Q}-\mathbf{Q}')$ is E^A and $\mathbf{Q} = (\mathbf{Q}^A + \mathbf{Q}^S)$ is the required decomposition.

E.3 Symmetry in linear models of thermally-driven hydromagnetic waves

Having established the equatorial symmetry properties of the operators of interest, relations between the symmetries of the perturbations to the velocity field $\boldsymbol{u}$, the magnetic field $\boldsymbol{b}$ and the temperature field Θ associated with hydromagnetic waves can now be established. The linearised momentum, induction and heat equations (see appendix **??**) governing hydromagnetic waves are

$$E\left(\frac{\partial}{\partial t}-\nabla^2\right)\boldsymbol{u}+(\widehat{\boldsymbol{z}}\times\boldsymbol{u})=-\nabla P+ERa\Theta\boldsymbol{r}+\Lambda\left[(\widehat{\boldsymbol{B}_0}\cdot\nabla)\boldsymbol{b}+(\boldsymbol{b}\cdot\nabla)\widehat{\boldsymbol{B}_0}\right], \quad \text{(E.10)}$$

$$\left(\nabla^2-Pr_m\frac{\partial}{\partial t}\right)\boldsymbol{b}=\nabla\times(\boldsymbol{u}\times\widehat{\boldsymbol{B}_0}), \quad \text{(E.11)}$$

$$\left(\nabla^2-Pr\frac{\partial}{\partial t}\right)\Theta=-\boldsymbol{r}\cdot\boldsymbol{u}, \quad \text{(E.12)}$$

The link between the equatorial symmetry of $\boldsymbol{b}$ and $\boldsymbol{u}$ can be established by considering the induction equation (E.11). All terms in the equation must have the same equatorial symmetry. Therefore because $(\nabla^2-Pr_m\frac{\partial}{\partial t})$ is E^S, $\boldsymbol{b}$ must have the same symmetry as $\nabla\times(\boldsymbol{u}\times\widehat{\boldsymbol{B}_0})$. Since $\nabla\times$ and $\times$ are both E^A this means that $\boldsymbol{b}$ and the product of $\boldsymbol{u}$ and $\widehat{\boldsymbol{B}_0}$ will have the same equatorial symmetry. Therefore if $\widehat{\boldsymbol{B}_0}$ is E^S, $\boldsymbol{u}$ and $\boldsymbol{b}$ will have the same equatorial symmetry, while if $\widehat{\boldsymbol{B}_0}$ is E^A, $\boldsymbol{u}$ and $\boldsymbol{b}$ will have different equatorial symmetry.

A similar link between Θ and $\boldsymbol{u}$ can be found by considering the heat equation (E.12). Because $(\nabla^2-Pr\frac{\partial}{\partial t})$ is E^S, and $-\boldsymbol{r}\cdot$ is E^S, $\boldsymbol{u}$ and Θ will always have the same equatorial symmetry. The relation between the equatorial symmetry of Θ and $\boldsymbol{b}$ is therefore also that they will be the same symmetry if $\widehat{\boldsymbol{B}_0}$ is E^S and the opposite symmetry if $\widehat{\boldsymbol{B}_0}$ is E^A. Substituting these symmetry relations into the momentum equation (E.10) shows that these are indeed the required relations between the symmetries of the perturbation fields.

At the onset of thermal convection, magneto-convection or magnetic instability in a rapidly rotating sphere, wave flows $\boldsymbol{u}$ and the associated temperature perturbations Θ are always found to have E^S symmetry (Busse, 1970; Fearn, 1979b; Zhang and Fearn, 1995) as a result of the preference for fluid motions to be invariant parallel to the rotation axis in rapidly rotating fluid. The appropriate symmetries of $\boldsymbol{u}$ and Θ are then

$$[u_r,u_\theta,u_\phi](r,\theta,\phi)=[u_r,-u_\theta,u_\phi](r,\pi-\theta,\phi)\iff E^S, \quad \text{(E.13)}$$

$$\Theta(r,\theta,\phi)=\Theta(r,\pi-\theta,\phi)\iff E^S. \quad \text{(E.14)}$$

Assuming this is the case, there are two possible equatorial symmetries of the accompanying $\boldsymbol{b}$ depending on the choice of $\widehat{\boldsymbol{B}_0}$. If $\widehat{\boldsymbol{B}_0}$ is E^S (as is the Malkus field, see results in chapter 7) then

$$[b_r,b_\theta,b_\phi](r,\theta,\phi)=[b_r,-b_\theta,b_\phi](r,\pi-\theta,\phi)\iff E^S. \quad \text{(E.15)}$$

On the other hand if $\widehat{\boldsymbol{B}_0}$ is E^A as simple $\alpha\omega$ dynamo theory suggests should be the case to obtain an E^A poloidal magnetic field (see Fearn and Proctor (1983), Zhang (1995) and Longbottom et al. (1995)) then

$$[B_r, B_\theta, B_\phi](r,\theta,\phi) = [-B_r, B_\theta, -B_\phi](r,\pi-\theta,\phi) \iff E^A. \tag{E.16}$$

Attention in this thesis has focused on the simpler E^S symmetry of magnetic fields, future work should address the E^A symmetry in more detail.

As well as giving insight into the physical processes involved in pattern formation, knowledge of the symmetry properties of solutions can lead to substantial computational savings — this is because certain combinations of fields are disallowed, so need not be considered in the computations. In chapter 7 only E^S symmetry of $\boldsymbol{u}$, Θ and $\boldsymbol{b}$ is used in computations, which is consistent given the E^S imposed magnetic field and the knowledge that $\boldsymbol{u}$ and Θ will be E^S as the onset of convection.

E.4 Equatorial symmetry of B_r at the core surface and its relation to equatorial symmetry of flows at the core surface

The link between patterns of equatorial symmetry seen in the evolution of B_r at the core surface and the fluid flow there is determined by the magnetic induction equation (D.3). Considering only changes in B_r caused by advection of B_r by $\boldsymbol{u}$ and using the fact that at the core surface u_r=0, the magnetic induction equation reduces to the form (Backus, 1968)

$$\frac{\partial B_r}{\partial t} = -\nabla_H \cdot (\boldsymbol{u} B_r), \tag{E.17}$$

where $\nabla_H = \nabla - \frac{\partial}{\partial r}\widehat{\boldsymbol{r}}$. Writing $B_r = B_{r0} + B_r'$ with B_{r0} being a background radial magnetic field acted on by the flow and B_r' the perturbation produced, then equation (E.17) becomes

$$\frac{\partial B_r'}{\partial t} = -\nabla_H \cdot (\boldsymbol{u} B_{r0}) - \nabla_H \cdot (\boldsymbol{u} B_r'). \tag{E.18}$$

Assuming that $B_{r0} >> B_r'$ this simplifies to

$$\frac{\partial B_r'}{\partial t} = -\nabla_H \cdot (\boldsymbol{u} B_{r0}). \tag{E.19}$$

Therefore because $-\nabla_H \cdot$ has E^S symmetry the equatorial symmetry of B_r' will be the same as that of the product $\boldsymbol{u}$ and B_{r0}. So for example, if flows in the core are E^S, then B_r' and B_{r0} will have the same equatorial symmetry. This prediction has been confirmed by the numerical results reported reported in chapter 8.

It should be noted that the approach described in this section and also employed in chapter 8 implicitly assumes that changes in B_r can only be produced by rearrangements of B_r. This will not be true in general, because as described in chapter 7 fluid motions can distort toroidal magnetic fields in the core to produce new B_r.

Appendix F

Animations

F.1 Animations as a visualisation tool

It is rather difficult to appreciate how a time-dependent field on a surface evolves merely by looking at snapshots or space-time diagrams. Human visual perception has evolved to allow us to efficiently process changing images and to accurately interpret them. For example, most insight in studies of fluid dynamics often comes from watching the development of a particular flow pattern. It was therefore felt essential that animations of the magnetic field evolution at the core surface were produced and made available, in order that the field evolution modes being discussed were fully appreciated.

F.2 Construction of animations

The animations detailed in this appendix and referenced throughout the thesis were constructed by combining snapshots of the field at the core surface. These snapshots were chosen to be sufficiently closely spaced in time that whenever displayed sequentially the impression of a smooth evolution was conveyed to the viewer. The snapshots were created using the M—map freeware tool used with the MATLAB software package or the nview package developed by Nick Barber. The images were then combined to give animated gifs using the *gifsicle* freeware package.

F.3 Locations of animations

The animations can be found on the CD inside the back cover of this thesis. Animated gifs can be viewed by some web browsers (e.g. Netscape) and most media players. For best results the files should be copied onto the local hard disk. The tables below give the animation number, apage reference, the associated filename (preceding the .gif) and a brief description.

Reference	Filename Prefix	Page no.	Description
A3.1	Brg	55	B_r from *gufm1* unprocessed
A3.2	BrgZ	58	B_r from *gufm1* with time-averaged axisymmetric field removed
A3.3	BrgZT400	61	B_r from *gufm1* with time-averaged axisymmetric field removed and high pass filtered with t_c=400yrs
A3.4	BrgZT600	65	B_r from *gufm1* with time-averaged axisymmetric field removed and high pass filtered with t_c=600yrs
A3.5	BrgZT400F38K7	68	B_r from *gufm1* with time-averaged axisymmetric field removed and frequency-wavenumber filtered so only m=7 with periods 125 to 333 yrs remains
A3.6	BrgZT400F38K5	68	B_r from *gufm1* with time-averaged axisymmetric field removed and frequency-wavenumber filtered so only m=5 with periods 125 to 333 yrs remains
A3.7	BrgZT400F38K3	68	B_r from *gufm1* with time-averaged axisymmetric field removed and frequency-wavenumber filtered so only m=3 with periods 125 to 333 yrs remains

Table F.1: Animations from chapter 3.
References, the filename prefix (the full filenames are prefix.gif), page number where the animations are referenced, and a brief description of the field on the core surface from *gufm1* displayed in the animation. This table contains the animations referenced Chapter 3.

Reference	Filename Prefix	Page No.	Description
A4.1	Brarcheohist	81	B_r from CALS7K.1h , unprocessed from 1650 to 1950.
A4.2	Brgufmd	81	B_r from *gufm1d* (*gufm1* processed so power spectra matches that of CALS7K.1) from 1650 to 1950.
A4.3	Brarcheo	88	B_r from unprocessed CALS7K.1 , from 5000B.C. to 1950A.D.
A4.4	BrZT2500archeosub	91	$\widetilde{B}_r$ from CALS7K.1 over the interval 2000B.C. to 500A.D.

Table F.2: Animations from chapter 4.
References, the filename prefix (the full filenames are prefix.gif), page number where the animations are referenced, and a brief description of the field from CALS7K.1 displayed in the animations. This table contains the animations from chapter 4.

Reference	Filename Prefix	Page No.	Description
A5.1	Brd1	101	B_r from DYN1, unprocessed
A5.2	Urd1	108	u_r from DYN1, unprocessed
A5.3	Upd1	112	u_ϕ from DYN1, unprocessed
A5.4	Brd2HR	117	B_r from DYN2, unprocessed
A5.5	Brd2DAMP	122	B_r from DYN2, with spherical harmonic degrees l=13,15 damped, l> 15 set to zero
A5.6	Urd2HR	125	u_r from DYN2, unprocessed
A5.7	Upd2HR	128	u_r from DYN2, unprocessed

Table F.3: Animations from chapter 5.
References, the filename prefix (the full filenames are prefix.gif), page number where the animations are referenced, and a brief description of the field from DYN1 or DYN2 being displayed in the animations. This table contains the animations from chapter 5.

Reference	Filename Prefix	Page No.	Description
A8.1	mfzvS8C0.05U5	223	B_r evolution from an axial dipole due to m=8, E^S wave flow with c_{ph}=0.05 km yr^{-1} and U=5 km yr^{-1}.
A8.2	NDmfzvS8C0.05U5	223	B_r^{NAD} evolution from an axial dipole B_r due to m=8, E^S wave flow with c_{ph}=0.05 km yr^{-1} and U=5 km yr^{-1}.
A8.3	mfzvA8C0.05U5	230	B_r evolution from an axial dipole due to a m=8, E^A wave flow with c_{ph}=0.05 km yr^{-1} and U=5 km yr^{-1}.
A8.4	NDmfzvA8C0.05U5	230	B_r^{NAD} evolution from an axial dipole B_r due to a m=8, E^A wave flow with c_{ph}=0.05 km yr^{-1} and U=5 km yr^{-1}.
A8.5	mfzvS8C5U5	230	B_r evolution from an axial dipole due to a m=8, E^S wave flow with c_{ph}=5 km yr^{-1} and U=5 km yr^{-1}.
A8.6	NDmfzvS8C5U5	230	B_r^{NAD} evolution from an axial dipole B_r due to a m=8, E^S wave flow with c_{ph}=5 km yr^{-1} and U=5 km yr^{-1}.
A8.7	mfzvA8C5U5	230	B_r evolution from an axial dipole due to a m=8, E^A wave flow with c_{ph}=5 km yr^{-1} and U=5 km yr^{-1}.
A8.8	NDmfzvA8C5U5	230	B_r^{NAD} evolution from an axial dipole B_r due to a m=8, E^A wave flow with c_{ph}=5 km yr^{-1} and U=5 km yr^{-1}.
A8.9	mfzvS8C50U5	230	B_r evolution from an axial dipole due to a m=8, E^S wave flow with c_{ph}=5k0myr^{-1} and U=5 km yr^{-1}.
A8.10	NDmfzvS8C50U5	230	B_r^{NAD} evolution from an axial dipole B_r due to a m=8, E^S wave flow with c_{ph}=50 km yr^{-1} and U=5 km yr^{-1}.
A8.11	mfzvA8C50U5	230	B_r evolution from an axial dipole due to a m=8, E^A wave flow with c_{ph}=50 km yr^{-1} and U=5 km yr^{-1}.
A8.12	NDmfzvA8C50U5	230	B_r^{NAD} evolution from an axial dipole B_r due to a m=8, E^A wave flow with c_{ph}=50 km yr^{-1} and U=5 km yr^{-1}.
A8.13	Bm1C0.05U5m8S	231	B_r evolution from a m=1 E^S B_r due to a m=8, E^S wave flow with c_{ph}=0.05 km yr^{-1} and U=5 km yr^{-1}.
A8.14	Bm4C0.05U5m8S	231	B_r evolution from a m=4 E^S B_r due to a m=8, E^S wave flow with c_{ph}=0.05 km yr^{-1} and U=5 km yr^{-1}.
A8.15	1590C17U1ES	232	B_r evolution from the 1590 B_r due to a m=8, E^S wave flow with c_{ph}=17 km yr^{-1} and U=1 km yr^{-1}.

Table F.4: Animations from chapter 8 (Part i).
References, the filename prefix (the full filenames are prefix.gif), page number where the animations are referenced, and a brief description of the field model displayed in the animation. This table contains the first half of the animations from Chapter 8.

Reference	Filename Prefix	Page No.	Description
A8.16	1590C17U5ES	232	B_r evolution from the 1590 B_r due to a m=8, E^S wave flow with c_{ph}=17 km yr^{-1} and U=5 km yr^{-1}.
A8.17	1590C17U10ES	232	B_r evolution from the 1590 B_r due to a m=8, E^S wave flow with c_{ph}=17 km yr^{-1} and U=10 km yr^{-1}.
A8.18	1590C17U15ES	232	B_r evolution from the 1590 B_r due to a m=8, E^S wave flow with c_{ph}=17 km yr^{-1} and U=15 km yr^{-1}.
A8.19	1590C17U17ES	232	B_r evolution from the 1590 B_r due to a m=8, E^S wave flow with c_{ph}=17 km yr^{-1} and U=17 km yr^{-1}.
A8.20	1590C17U20ES	232	B_r evolution from the 1590 B_r due to a m=8, E^S wave flow with c_{ph}=17 km yr^{-1} and U=20 km yr^{-1}.
A8.21	1590C17U1EA	232	B_r evolution from the 1590 B_r due to a m=8, E^A wave flow with c_{ph}=17 km yr^{-1} and U=1 km yr^{-1}.
A8.23	1590C17U5EA	232	B_r evolution from the 1590 B_r due to a m=8, E^A wave flow with c_{ph}=17 km yr^{-1} and U=5 km yr^{-1}.
A8.23	1590C17U10EA	232	B_r evolution from the 1590 B_r due to a m=8, E^A wave flow with c_{ph}=17 km yr^{-1} and U=10 km yr^{-1}.
A8.24	1590C17U15EA	232	B_r evolution from the 1590 B_r due to a m=8, E^A wave flow with c_{ph}=17 km yr^{-1} and U=15 km yr^{-1}.
A8.25	1590C17U17EA	232	B_r evolution from the 1590 B_r due to a m=8, E^A wave flow with c_{ph}=17 km yr^{-1} and U=17 km yr^{-1}.
A8.26	1590C17U20EA	232	B_r evolution from the 1590 B_r due to a m=8, E^A wave flow with c_{ph}=17 km yr^{-1} and U=20 km yr^{-1}.
A8.27	1590C17U15ESTAPER	236	B_r evolution from the 1590 B_r due to a m=8, E^A wave flow with c_{ph}=17 km yr^{-1} and U=15 km yr^{-1}, with crustal filtering.
A8.28	1590C17U17ESTAPER	236	B_r evolution from the 1590 B_r due to a m=8, E^A wave flow with c_{ph}=17 km yr^{-1} and U=17 km yr^{-1}, with crustal filtering.
A8.29	1590C17U20ESTAPER	236	B_r evolution from the 1590 B_r due to a m=8, E^A wave flow with c_{ph}=17 km yr^{-1} and U=20 km yr^{-1}, with crustal filtering.

Table F.5: Animations from chapter 8 (Part (ii).
References, the filename prefix (the full filenames are prefix.gif), page number where the animations are referenced, and a brief description of the field model displayed in the animation. This table contains the second half of the animations from Chapter 8.

References

Abramowitz, M. and Stegun, I. A. *Handbook of mathematical functions.* Dover, 1964.

Acheson, D. J. On hydromagnetic stability of a rotating fluid annulus. *J. Fluid Mech.*, 52(3), 529–541, 1972.

Acheson, D. J. Hydromagnetic wavelike instabilies in a rapidly rotating stratified fluid. *J. Fluid Mech.*, 61(3), 609–624, 1973.

Acheson, D. J. Magnetohydrodynamic waves and instabilities in rotating fluids. *in Rotating fluids in geophysics Ed P. H. Roberts and A. M. Soward, Academic Press, London*, pages 315–349, 1978.

Acheson, D. J. Stable density stratification as a cataylst for instability. *J. Fluid Mech.*, 96, 723–733, 1980.

Acheson, D. J. Local analysis of thermal and magnetic instabilities in a rapidly rotating fluid. *Geophys. Astrophys. Fluid Dyn.*, 27, 123–136, 1983.

Acheson, D. J. and Hide, R. Hydromagnetics of rotating fluids. *Reports of Progress in Physics*, 36, 159–221, 1973.

Aldridge, K. D. Dynamics of the core at short periods. *Earthth's core and lower mantle,Ed. by Jones, C. A. and Soward, A. and Zhang, K., In series The Fluid Mechanics of Astrophysics and Geophysics*, pages 180–210, 2003.

Alexandrescu, M., Gibert, D., Hulot, G., LeMouël, J. L., and Saracco, G. Worldwide wavelet analysis of geomagnetic jerks. *J. Geophys. Res.*, 101(B10), 21975–21994, 1996.

Alfé, D., Gillan, M.J., Vočadlo, L., J., Brodholt, and D., Price G. The ab-initio simulation of the Earth's core. *Phil. Trans. R. Soc. Lond. A*, 360, 1227–1224, 2002.

Alfvén, H. Existence of EM-hydrodynamic waves. *Nature*, 150, 405–406, 1942.

Allan, D.W. and Bullard, E.C. The secular variation of the Earth's magnetic field. *Proc. Camb. Phil. Soc.*, 62(3), 783–809, 1966.

Allègre, C. J., Poirier, J. P., Humler, E., and Hofmann, A. W. The chemical composition of the Earth. *Earth Planet. Sci. Lett.*, 134, 515–526, 1995.

Andrews, D. G. *An introduction to Atmospheric Physics.* Cambridge Univeristy Press, 2000.

Ardes, M., Busse, F. H., and Wicht, J. Thermal convection in rotating spherical shells. *Phys. Earth Planet. Int.*, 99, 55–67, 1997.

Arfken, G. *Mathematical Methods for Physicists.* Academic Press, Orlando, 1985.

Aubert, J., Gillet, N., and Cardin, P. Quasigeostrophic models of convection in rotating spherical shells. *Geochem. Geophys. Geosyst.*, 4, doi:10.1029/2002GC000456, 2003.

Backus, G. A class of self-sustaining dissipative spherical dynamos. *Ann. Phys.*, 4, 372–447, 1958.

Backus, G. Kinematics of geomagnetic secular variation in a perfectly conducting core. *Phil. Trans. R. Soc. Lond. A*, 263, 239–266, 1968.

Backus, G. Bayesian inference in geomagnetism. *Geophys. J. R. Astr. Soc.*, 92, 125–142, 1988.

Backus, G., Parker, R., and Constable, C. *Foundations of geomagnetism*. Cambridge Univeristy Press, 1996.

Batchelor, G. K. *An introduction to fluid mechanics*. Cambridge Univeristy Press, 1967.

Bell, P. I. and Soward, A. M. The influence of surface-topography on rotating convection. *J. Fluid Mech.*, 313, 147–180, 1996.

Bergman, M. I. Magnetic Rossby waves in a stably stratified layer near the surface of Earth's outer core. *Geophys. Astrophys. Fluid Dyn.*, 68, 151–176, 1993.

Birch, F. Density and composition of mantle and core. *J. Geophys. Res.*, 69, 4377–4388, 1964.

Bloxham, J. *Geomagnetic secular variation*. Ph. D. Thesis, University of Cambridge, 1985.

Bloxham, J. The expulsion of magnetic flux from the Earth's core. *Geophys. J. R. Astr. Soc.*, 87, 669–678, 1986.

Bloxham, J. Global magnetic field. *Global Earth Physics: A Handbook of Physical Constants*, pages 47–65, 1995.

Bloxham, J. Dynamics of angular momentum in the Earth's core. *Annu. Rev. Earth Planet. Sci.*, 26, 501–517, 1998.

Bloxham, J. Time-independent and time-dependent behaviour of high-latitude flux bundles at the core-mantle boundary. *Geophys. Res. Lett.*, 29(18), 1854–1858, 2002.

Bloxham, J. and Gubbins, D. The secular variation of Earth's magnetic field. *Nature*, 317, 777–781, 1985.

Bloxham, J. and Gubbins, D. Geomagnetic field analysis IV - Testing the frozen flux hypothesis. *Geophys. J. R. Astr. Soc.*, 84, 139–152, 1986.

Bloxham, J. and Gubbins, D. Thermal core-mantle interactions. *Nature*, 325, 511–513, 1987.

Bloxham, J., Gubbins, D., and Jackson, A. Geomagnetic secular variation. *Phil. Trans. R. Soc. Lond. A*, 329(1606), 415–502, November 1989.

Bloxham, J. and Jackson, A. Fluid flow near the surface of the Earth's outer core. *Rev. Geophys.*, 29, 97–120, 1991.

Bloxham, J. and Jackson, A. Time-dependent mapping of the magnetic field at the core-mantle boundary. *J. Geophys. Res.*, 97(B13), 19537–19563, 1992.

Bloxham, J., Zatman, S., and Dumberry, M.. The origin of geomagnetic jerks. *Nature*, 420, 685–687, 2002.

Boulanger, J.-P. and Menkes, C. Long equatorial wave reflection in th Pacific ocean from TOPEX/POSEDIDON data during the 1992-1998 period. *Climate Dynamics*, 15, 205–225, 1999.

Boyd, J.P. *Chebyshev and Fourier Spectral Methods*. Dover, 2001.

Braginsky, S. I. Magnetohydrodynamics of the Earth's core. *Geomagnetism and Aeronomy*, 7, 698–712, 1964.

Braginsky, S. I. Magnetic waves in the Earth's core. *Geomagnetism and Aeronomy*, 7, 851–859, 1967.

Braginsky, S. I. Torsional magnetohydrodynamic vibrations in the Earth's core and variations in day length. *Geomagnetism and Aeronomy*, 10, 1–8, 1970.

Braginsky, S. I. Analytic description of the geomagnetic field of past epochs and determination of the spectrum of magnetic waves in the core of the Earth I. *Geomagnetism and Aeronomy*, 12, 947–957, 1972.

Braginsky, S. I. Analytic description of the geomagnetic field of past epochs and determination of the spectrum of magnetic waves in the core of the Earth II. *Geomagnetism and Aeronomy*, 14, 441–447, 1974.

Braginsky, S. I. Magnetic waves in the Earth's core II. *Geophys. Astrophys. Fluid Dyn.*, 14, 189–208, 1980.

Braginsky, S. I. Waves in a stably stratified layer on the surface of the terrestrial core. *Geomagnetism and Aeronomy*, 27, 410–414, 1987.

Braginsky, S. I. Magnetohydrodynamic waves within the Earth. *Encyclopedia of solid Earth geophysics*, 1989.

Braginsky, S. I. MAC oscillations of the hidden ocean of the core. *J. Geomagn. Geoelectr.*, 45, 1517–1538, 1993.

Braginsky, S. I. Dynamics of the stably stratified ocean at the top of the core. *Phys. Earth Planet. Int.*, 111, 21–34, 1999.

Braginsky, S. I. and Roberts, P. H. Magnetic field generation by baroclinic waves. *Proc. R. Soc. Lond. A*, 347, 125–140, 1975.

Brito, D., Arnou, J., and Cardin, P. Turbulent viscosity measurements relevant to planetary core-mantle dynamics. *Phys. Earth Planet. Int.*, 141, 3–8, 2004.

Buffett, B. A. Gravitaional oscillations in the length of day. *Geophys. Res. Lett.*, 23, 2279–2282, 1996a.

Buffett, B. A. A mechanism for decade fluctuations in the length of day. *Geophys. Res. Lett.*, 23, 3803–3806, 1996b.

Buffett, B. A. Geodynamic estimates for the viscosity of Earth's inner core. *Nature*, 388, 571–573, 1997.

Buffett, B. A. and Glatzmaier, G. A. Gravitational braking of inner core rotation in geodynamo simulations. *Geophys. Res. Lett.*, 27, 3125–3128, 2000.

Bullard, E. C. The magnetic field within the Earth. *Proc. R. Soc. Lond. A*, 197, 433–453, 1949.

Bullard, E. C., Freedman, C., Gellman, H., and Nixon, J. The westward drift of Earth's magnetic field. *Phil. Trans. R. Soc. Lond. A*, 243, 67–92, 1950.

Bullard, E. C. and Gellman, H. Homogeneous dynamos and terrestrial magnetism. *Phil. Trans. R. Soc. Lond. A*, 247, 213–278, 1954.

Busse, F. H. Thermal instabilities in rapidly rotating systems. *J. Fluid Mech.*, 44, 441–460, 1970.

Busse, F. H. Generation of planetary magnetism by convection. *Phys. Earth Planet. Int.*, 12, 350–358, 1976.

Busse, F. H. Asymptotic theory of convection in a rotating, cylindrical annulus. *J. Fluid Mech.*, 173, 545–556, 1986.

Busse, F. H. Convective flows in rapidly rotating spheres and their dynamo action. *Prog. Ocean.*, 14(4), 1301–1314, 2002.

Busse, F. H. and Or, A. C. Convection in a rotating cylindrical annulus I: Thermal rossby waves. *J. Fluid Mech.*, 166(4), 173–187, 1986.

Butler, R. F. *Paleomagnetism: Magnetic domains to geological terranes*. Blackwell, 1992.

Buttkus, B. *Spectral analysis and filter theory in applied geophysics*. Springer-Verlag, Berlin, 2000.

Canuto, C., Hussaini, M. Y., Quarteroni, A., and Zang, T. A. *Spectral Methods in Fluid Mechanics*. Dover, 2001.

Cardin, P. and Olson, P. Chaotic thermal convection in a rapidly rotating spherical shell: consequences for flow in the outer core. *Phys. Earth Planet. Int.*, 82, 235–259, 1994.

Cardin, P. and Olson, P. The influence of the toroidal magnetic field on convection in the core. *Earth Planet. Sci. Lett.*, 132, 167–181, 1995.

Chandrasekhar, S. *Hydrodynamic and hydromagnetic stability*. Clarendon Press, 1961.

Chelton, B. C. and Schlax, M. G. Global observations of oceanic Rossby waves. *Science*, 272, 234–238, 1996.

Chelton, B. C., Schlax, M. G., Lyman, J. M., and Johnson, G. C. Equatorially trapped Rossby waves in the presence of meridionally sheared baroclinic flow in the Pacific ocean. *Progress in Oceanography*, 56, 323–380, 2003.

Christensen, J.,U. R.and Aubert, Dormy, E., Gibbons, S., Glatzmaier, G. A., Grote, E., Honkura, Y., Jones, C., Kono, M., Matsushima, M., Sakuraba, A., Tabahashi, F., Tilgner, A., Wicht, J., and Zhang, K. A numerical dynamo benchmark. *Phys. Earth Planet. Int.*, 128, 25–34, 2001.

Christensen, U. R. and Olson, P. Secular variation in numerical geodynamo models with lateral variations of boundary heat flow. *Phys. Earth Planet. Int.*, 138, 39–54, 2003.

Christensen, U. R., Olson, P., and Glatzmaier, G. A dynamo model interpretation of geomagnetic field structures. *Geophys. Res. Lett.*, 25, 1565–1568, 1998.

Christensen, U. R, Olson, P., and Glatzmaier, G. Numerical modeling of the geodynamo. *Geophys. J. Int.*, 138, 393–409, 1999.

Christensen, U. R. and Tilgner, A. Power requirement of the geodynamo from Ohmic losses in numerical and laboratory dynamos. *Nature*, 429, 169–171, 2004.

Cipollini, P., Cromwell, D., Challenor, P. G., and Raffaglio, S. Rossby waves detected in global ocean data. *Geophys. Res. Lett.*, 28, 323–326, 2001.

Cipollini, P., Cromwell, D., Jones, M. S., Quartly, D., and Challenor, P. G. Concurrent altimeter and infrared observations of Rossby wave propagation near 34N in the Northeast Atlantic. *Geophys. Res. Lett.*, 24, 889–892, 1997.

Cipollini, P., Quartly, D., Challenor, P. G., Cromwell, D., and Robinson, I. S. Remote sensing of extra-equatorial planetary waves in the oceans. *Manual of remote sensing*, page Submitted, 2004.

Clark, A. Some exact solutions in magnetohydrodynamics with astrophysical applications. *Phys. Fluids*, 8, 644–649, 1965.

Clement, B. Dependence of the duration of geomagnetic polarity reversals on site latitide. *Nature*, 428, 637–640, 2004.

Constable, C. G., Johnson, C. L., and .P., Lund S. Global geomagnetic field models for the past 3000 years: transient or permanent flux lobes? *Phil. Trans. R. Soc. Lond. A*, 358, 991–1008, 2000.

Courtillot, V., Ducruix, J., and Le Mouël, J. L. Sur une acceleration recente de la variation seculaire du champ magnetique terrestre. *C. R. Acad. Sci. Paris*, D287, 1095–1098, 1978.

Courtillot, V. and Le Mouël, J. L. Geomagnetic secular variation impulses. *Nature*, 311, 709–716, 1984.

Cowling, T.G. The magnetic field of sunspots. *Mon. Not. R. Astr. Soc.*, 94, 39–48, 1934.

Davidson, P.A. *An introduction to magnetohydrodynamics.* Cambridge Univeristy Press, 2001.

Davis, R.G and Whaler, K. Determination of a steady velocity field in a rotating frame of reference at the surface of Earth's core. *Geophys. J. Int.*, 1126, 92–100, 1996.

Deans, S. R. *The Radon transform and some of its applications.* John Wiley, New York, 1988.

deWijs, G. A., Kresse, G., Vočadlo, L., D., Dobson, Alfeé, D., J., Gillan M., and D., Price G. The viscosity of liquid iron at the physical conditions of the Earth's core. *Nature*, 392, 805–808, 1998.

Dickinson, R. E. Rossby waves— long-period oscillations of oceans and atmospheres. *Annu. Rev. Fluid Mech.*, 10, 159–195, 1978.

Doell, R. R. and Cox, A. *J. Geophys. Res.*, 70, 3377–3405, 1965.

Doell, R. R. and Cox, A. Pacific Geomagnetic Secular Variation. *Science*, 171, 248–254, 1971.

Dormy, E., Soward, A. M., Jones, C.A., Jault, D., and Cardin, P. The onset of thermal convection in rotating spherical shells. *J. Fluid Mech.*, 501, 43–70, 2004.

Dormy, E., Valet, J.-P., and Courtillot, V. Numerical models of the geodynamo and observational constraints. *Geochem. Geophys. Geosyst.*, 1, 1–42, October 2000.

Drazin, P. G. *Introduction to hydrodynamic instability.* Cambridge Univeristy Press, 2002.

Drew, S. The effect of a stable layer at the core-mantle boundary on thermal convection. *Geophys. Astrophys. Fluid Dyn.*, 65, 173–182, 1992.

Drew, S. Magnetic field line expulsion into a conducting mantle. *Geophys. J. Int.*, 115, 303–312, 1993.

Dumberry, M. and Bloxham, J. Torque balance, Taylor's constraint and torsional oscillations in a numerical model of the geodynamo. *Phys. Earth Planet. Int.*, 140, 29–51, 2003.

Dumberry, M. and Bloxham, J. Variations in Earth's gravity field caused by torsional oscillations in the core. *Geophys. J. Int.*, 159, 417–434, 2004.

Dumberry, M. and Bloxham, J. Azimuthal flows in the Earth's core and changes in the length of day on millennial timescales. *Geophys. J. Int.*, page submitted, 2005.

Dziewonski, A. M. and Anderson, D. L. Preliminary reference Earth model. *Phys. Earth Planet. Int.*, 25, 297–356, 1981.

El Sawi, M. and Eltayeb, I. A. Wave action and critcial surfaces for hydromagnetic-inertial-gravity waves. *Quart. App. Math.*, 34, 187–202, 1981.

Elsasser, W.M. Induction effects in terrestrial magnetism I. *Phys. Rev.*, 69(3-4), 106–116, 1946.

Eltayeb, I. A. Hydromagnetic convection in a rapidly rotating fluid layer. *Proc. R. Soc. Lond.*, 326, 229–254, 1972.

Eltayeb, I. A. Propagation and stability of wave motions in rotating magnetic systems. *Phys. Earth Planet. Int.*, 24, 259–271, 1981.

Eltayeb, I. A. The propagation and stability of linear wave motions in rapidly rotating spherical shells: weak magnetic fields. *Geophys. Astrophys. Fluid Dyn.*, 67, 211–239, 1992.

Eltayeb, I. A. and Kumar, S. Hydromagnetic convective instability of a rotating, self-gravitating fluid sphere containing a uniform distribution of heat sources. *Proc. R. Soc. Lond.*, 353, 145–162, 1977.

Ewen, S. A. and Soward, A. M. Phase mixed rotating magnetoconvection and Taylor's condition I. Amplitide equations. *Geophys. Astrophys. Fluid Dyn.*, 77, 209–230, 1994a.

Ewen, S. A. and Soward, A. M. Phase mixed rotating magnetoconvection and Taylor's condition II. Travelling pulses. *Geophys. Astrophys. Fluid Dyn.*, 77, 231–262, 1994b.

Ewen, S. A. and Soward, A. M. Phase mixed rotating magnetoconvection and Taylor's condition III. Wave trains. *Geophys. Astrophys. Fluid Dyn.*, 77, 263–283, 1994c.

Farrell, B. and Ioannou, P.J. Generalized stability theory, part i: Autonomous operators. *J. Atmos. Sci.*, 53, 2025–2040, 1996.

Fearn, D. R. Thermally-driven hydromagnetic convection in a rapidly rotating sphere. *Proc. R. Soc. Lond.*, 369, 227–242, 1979a.

Fearn, D. R. Thermal and magnetic instabilities in a rapidly rotating fluid sphere. *Geophys. Astrophys. Fluid Dyn.*, 14, 102–126, 1979b.

Fearn, D. R. Hydromagnetic waves in a differentially rotating annulus I: A test of local stability analysis. *Geophys. Astrophys. Fluid Dyn.*, 27, 137–162, 1983.

Fearn, D. R. Hydromagnetic waves in a differentially rotating annulus II. resistive instabilities. *Geophys. Astrophys. Fluid Dyn.*, 30, 227–239, 1984.

Fearn, D. R. Hydromagnetic waves in a differentially rotating annulus IV. insulating boundaries. *Geophys. Astrophys. Fluid Dyn.*, 44, 55–75, 1988.

Fearn, D. R. Differential rotation and thermal convection in a rapidly rotating hydromagnetic system. *Geophys. Astrophys. Fluid Dyn.*, 49, 173–193, 1989.

Fearn, D. R. Magnetic instabilities in rapidly rotating systems. *Theory of solar and planetary dynamos, Edited by Proctor, M. R. E., Matthews, P. C. and Rucklidge, A. M.*, pages 59–68, 1993.

Fearn, D. R. Hydromagnetic flow in planetary cores. *Rep. Prog. Phys.*, 61, 175–235, 1998.

Fearn, D. R. and Loper, D. E. Compositional convection and stratification of earth's core. *Nature*, 289, 393–394, Jan 1981.

Fearn, D. R. and Proctor, M. R. E. Hydromagnetic waves in a differentially rotating sphere. *J. Fluid Mech.*, 128, 1–20, 1983.

Fearn, D. R., Proctor, M. R. E., and Sellar, C. C. Non-linear magnetoconvection in a rapidly rotating sphere and Taylor's constraint. *Geophys. Astrophys. Fluid Dyn.*, 77, 111–132, 1994.

Fearn, D. R., Roberts, P. H., and Soward, A. M. Convection, stability and the dynamo. *Pitman Research notes in Mathematics Series*, 168, 60–324, 1988.

Feynman, R. P., Leighton, R. B., and Sands, M. *The Feynman Lectures on Physics, Volume 1.* Addison-Wesley, 1963.

Finlay, C. C. and Jackson, A. Equatorially dominated magnetic field change at the surface of Earth's core. *Science*, 300, 2084–2086, 2003.

Fisk, H. W. Isopors and isoporic movements. *Intern. Geodet. Geophys. Union, Section Terrest. Magnet. Elec. Bull. Stockholm*, 8, 280–292, 1931.

Forbes, A. J. General Instrumentation. *Geomagnetism, Ed. Jacobs, J.A.*, 1, 51–142, 1987.

Fornberg, B. *A practical guide to pseudosectral methods.* Cambridge Univeristy Press, 1998.

Gibbons, S. J. and Gubbins, D. Convection in the Earth's core driven by lateral variations in the core-mantle boundary heat flux. *Geophys. J. Int.*, 142, 631–642, 2000.

Gill, A. E. *Atmosphere-Ocean dynamics.* Cambridge Univeristy Press, 1982.

Gillet, N., Brito, D., Jault, D., and Masson, J.-P. Developed magnetoconvection in a rapidly rotating sphere: Experimental study versus quasi-geostrophic modelling. *J. Fluid Mech. (submitted)*, 2005.

Glatzmaier, G. A. Numerical simulations of stellar convective dynamos I. the model and methods. *J. Comp. Phys.*, 55, 461–484, 1984.

Glatzmaier, G. A. and Olson, P. Probing the geodynamo. *Scientific American*, 292(4), 33–39, 2005.

Glatzmaier, G. A. and Roberts, P. H. A three-dimensional convective dynamo with rotating and finitely conducting inner core and mantle. *Phys. Earth Planet. Int.*, 91, 63–75, 1995.

Glatzmaier, G. A. and Roberts, P. H. Simulating the geodynamo. *Contemp. Physics*, 38(4), 269–288, 1997.

Golub, G. H. and Van Loan, C. F. *Matrix Computations.* John Hopkins Press, 1996.

Greenspan, H. P. *The theory of rotating fluids.* Cambridge Univeristy Press, 1968.

Greff-Lefftz, M., Pais, M. A., and LeMouël, J.-L. Surface gravitational field and topography induced by the Earth's fluid core motions. *Journal of Geodesy*, 78, 386–392, 2004.

Gubbins, D. Can the Earth's magnetic field be sustained by core oscillations? *Geophys. Res. Lett.*, 2(9), 409–512, 1975.

Gubbins, D. Mechanism for geomagnetic polarity reversals. *Nature*, 326, 167–169, 1987.

Gubbins, D. Geomagnetic polarity reversals: a connection with secular variation and core-mantle interaction. *Rev. Geophys.*, 32(1), 61–83, 1994.

Gubbins, D. A formalism for the inversion of geomagnetic data for core motions with diffusion. *Phys. Earth Planet. Int.*, 98, 193–206, 1996.

Gubbins, D. The distinction between geomagnetic excursions and reversals. *Geophys. J. Int.*, 173, F1–F3, 1999.

Gubbins, D. The Rayleigh number for convection in the Earth's core. *Phys. Earth Planet. Int.*, 128, 3–12, 2000.

Gubbins, D. *Time series analysis and inverse theory for geophysicists*. Cambridge Univeristy Press, 2004.

Gubbins, D., Alfe, D., Masters, G., Price, D., and M., Gillan. Can the Earth's dynamo run on heat alone? *Geophys. J. Int.*, 155, 609–622, 2003.

Gubbins, D., Alfe, D., Masters, G., Price, D., and M., Gillan. Gross thermodynamics of 2-component core convection. *Geophys. J. Int.*, 157, 1407–1414, 2004.

Gubbins, D., Barber, C. N, Gibbons, S., and Love, J.J. Kinematic dynamo action in a sphere: I Effects of diferential roation and meridional circulation on solutions with axial dipole symmetry. *Proc. R. Soc. Lond. A*, 456, 1333–1353, 2000.

Gubbins, D. and Bloxham, J. Geomagnetic field analysis- III. Magnetic fields on the core-mantle boundary. *Geophys. J. R. Astr. Soc.*, 80, 695–713, 1985.

Gubbins, D. and Gibbons, S. Low Pacific Secular Variation. *Timescales of the Paleomagnetic field, Geophysical Monograph Series*, 145, 279–286, 2004.

Gubbins, D. and Kelly, P. A difficulty with using the frozen flux hypothesis to find steady core motions. *Geophys. Res. Lett.*, 23, 1825–1828, 1996.

Gubbins, D. and Masters, T. G. Driving mechanism for the Earth's dynamo. *Advances in Geophysics*, 21, 1–50, 1979.

Gubbins, D. and Roberts, P. H. Magnetohydrodynamics of the Earth's core. *Geomagnetism, Ed. Jacobs, J.A.*, 2, 1–183, 1987.

Gubbins, D., Thompson, C.J., and Whaler, K.A. Stable regions in the Earth's liquid core. *Geophys. J. R. Astr. Soc.*, 68, 241–251, 1982.

Gubbins, D. and Zhang, K. Symmetry properties of the dynamo equations for paleomagnetism and geomagnetism. *Phys. Earth Planet. Int.*, 75, 225–241, 1993.

Hale, C. J. New paleomagnetic data suggest a link between the archean-proterozoic boundary and nucleation of the inner core. *Nature*, 329, 233–237, 1987.

Halley, E. On the cause of the change in the variation of the magnetic needle, with a hypothesis of the structure of the internal parts of the Earth. *Phil. Trans. R. Soc. Lond.*, 17, 470–478, 1692.

Hayashi, Y. Spectral analysis of tropical disturbances appearing in a GFDL general circulation model. *J. Atmos. Sci.*, 31, 180–218, 1974.

Hayashi, Y. and Golder, D. G. Tropical intraseasonal oscillations appearing in a GFDL general circulation model and FGGE data. Part I: Phase propagation. *J. Atmos. Sci.*, 43, 3058–3067, 1986.

Hayashi, Y. and Golder, D. G. Kelvin and mixed Rossby-gravity waves appearing in the GFDL 'SKYHI' general circulation model and the fgge dataset: Implications for their generation mechanism and role in QBO. *J. Atmos. Sci.*, 72, 901–934, 1994.

Helffrich, G. and Kaneshima, S. Seismological constraints on core composition from Fe-O-S liquid immiscibility. *Science*, 306, 2239–2242, 2004.

Herzenberg, A. Geomagnetic dynamos. *Phil. Trans. R. Soc. Lond. A*, 250, 543–583, 1958.

Hide, R. Free hydromagnetic oscillations of the Earth's core and the theory of geomagnetic secular variation. *Phil. Trans. R. Soc. Lond. A*, 259, 615–647, 1966.

Hide, R. Motions of the Earth's core and mantle and variations in the main geomagnetic field. *Science*, 157, 55–56, 1967.

Hide, R. Fluctuations in the Earth's rotation and topography of the core-mantle interface. *Phil. Trans. R. Soc. Lond. A*, 259, 351–363, 1989.

Hide, R. Generic nonlinear processes in self-exciting dynamos and the long-term behaviour of the main geomagnetic field, including superchrons. *Phil. Trans. R. Soc. Lond. A*, 358, 943–955, 2000.

Hide, R. and Malin, S. R. C. On the determination of the size of the Earth's core from observations of geomgnetic secular variation. *Proc. R. Soc. Lond. A*, 374, 15–33, 1981.

Hide, R. and Roberts, P. H. How strong is the magnetic field in earth's liquid core? *Phys. Earth Planet. Int.*, 20, 124–126, 1979.

Hide, R. and Stewartson, K. Hydromagnetic oscillations of the Earth's core. *Rev. Geophys.*, 10 (2), 579–598, 1973.

Hill, K. L., Robinson, I. S., and Cipollini, P. Propagation characteristics of extratropical plaentary waves observed in the ATSR global sea surface temperature record. *J. Geophys. Res.*, 105(C9), 21927–21945, 2000.

Hilst, R. D., Widiyantoro, S., Creager, K. C., and McSweeney, T. J. Deep subduction and aspherical variations in P-wavespeed at the base of Earth's mantle. *The Core-Mantle Boundary Region, AGU Geodynamics Monograph*, 28, 5–20, 1998.

Hollerbach, R. A spectral solution of the magneto-convection equations in spherical geometry. *Int. J. Numer. Meth. Fluids*, 32, 773–797, 2000.

Hollerbach, R. The range of timescales on which the geodynamo operates. *The core-mantle boundary region, AGU geodynamic monograph*, 31, 181–192, 2003.

Holme, R. Electromagnetic core-mantle coupling I: Explaining decadal changes in the length of day. *Geophys. J. Int.*, 132, 167–180, 1998a.

Holme, R. Electromagnetic core-mantle coupling II: Probing deep mantle conductance. *The Core-Mantle Boundary Region, Ed. Gurnis, M. and Wysession, M. E. and Knittle, E. and Buffett, B. A., AGU Geodynamics series*, 1998b.

Holme, R. Electromagnetic core-mantle coupling III: Laterally varying mantle conductance. *Phys. Earth Planet. Int.*, 117, 329–344, 2000.

Holme, R. and deViron, O. Geomagnetic jerks and a high resolution length-of-day profile for core studies. *Geophys. J. Int.*, 160, 435–439, 2005.

Holme, R. and Whaler, K. A. Steady core flow in an azimuthally drifting reference frame. *Geophys. J. Int.*, 145, 560–569, 2001.

Hovmöller, E. The trough and ridge diagram. *Tellus*, 1(2), 62–66, 1949.

Jackson, A. *The Earth's Magnetic Field at the Core-Mantle Boundary*. Ph. D Thesis, University of Cambridge, 1989.

Jackson, A. Time-dependency of tangentially geostrophic core surface motions. *Phys. Earth Planet. Int.*, 103, 293–311, 1997.

Jackson, A. Intense equatorial flux spots on the surface of Earth's core. *Nature*, 424, 760–763, 2003.

Jackson, A., Bloxham, J., and Gubbins, D. Time-dependent flow at the core suface and conservation of angular momentum in the coupled core-mantle system. *Dynamics of Earth's Deep Interior and Earth Rotation, Geophysical Monograph*, 72, 97–107, 1993.

Jackson, A., Constable, C. G., Walker, M. R., and Parker, R.L. Models of Earth's main magnetic field incorporating flux and radial vorticity constraints. *Geophys. J. Int.*, page In Press, 2005.

Jackson, A., Jonkers, A. R. T., and Walker, M. R. Four centuries of geomagnetic secular variation from historical records. *Phil. Trans. R. Soc. Lond. A*, 358, 957–990, 2000.

Jacobs, J. A. *A textbook on geonomy*. Adam Hilger, 1974.

Jacobs, J. A. *Reversals of the Earth's magnetic field*. Cambridge University Press, 2nd edition, 1994.

James, I. N. *Introduction to circulating atmospheres*. Cambridge Univeristy Press, 1994.

Jault, D., Gire, C., and LeMouël, J. L. Westward drift, core motions and exchanges of angular momentum between core and mantle. *Nature*, 333, 353–356, 1988.

Jault, D. and LeMouël, J. L. The topographic torque associated with a tangentially geostrophic motion at the core surface and inferences on the flow inside the core. *Geophys. Astrophys. Fluid Dyn.*, 48, 273–296, 1989.

Jiang, W., Kuang, W., Chao, B. F., and Fang, M. Time-variable gravity anomaly arising from dynamical mass transport in the outer core and core-mantle interaction. *Eos Trans. AGU*, 85 (47), G31C–0809, Fall Meet. Suppl. 2004.

Johnson, C. L. and Constable, C. G. Persistently anomalous pacific geomagnetic fields. *Geophys. Res. Lett.*, 25, 1011–10114, 1998.

Jones, C. A. Convection-driven geodynamo models. *Phil. Trans. R. Soc. Lond. A*, 358, 873–897, 2000.

Jones, C. A., Soward, A. M., and Mussa, A. I. Thermal convection in a rapidly rotating sphere. *J. Fluid Mech.*, 405, 157–179, 2000.

Jones, C.A., Mussa, A. I., and Worland, S. J. Magnetoconvection in a rapidly rotating sphere: the weak field case. *Proc. R. Soc. Lond.*, 429, 773–797, 2003.

Jonkers, A. R. T., Jackson, A., and Murray, A. Four centuries of geomagnetic data from historical records. *Rev. Geophys.*, 41, 1006 doi:10.1029/2002RG000115, 2003.

Kageyama, A., Sato, T., and the Complexity Simulation Group. Computer simulation of a magnetohydrodynamic dynamo. II. *Phys. Plasmas*, 2, 1421–1431, 1995.

Kerswell, R. R. Tidal excitation of hydromagnetic waves and their damping in the Earth. *J. Fluid Mech.*, 274, 219–241, 1994.

Kerswell, R. R. and Davey, A. On the linear instability of elliptic pipe flow. *J. Fluid Mech.*, 316, 307–324, 1996.

Killworth, P.D., Chelton, D.B., and Szoekede, R.A. The speed of observed and theoretical long extratropical planetary waves. *J. Phys. Oceanogr.*, 27, 1946–1966, 1997.

Kivelson, M. G. and Russell, C. T. *Introduction to space physics.* Cambridge Univeristy Press, 1995.

Kono, M. and Roberts, P. H. Recent geodynamo simulations and observations of the geomagnetic field. *Rev. Geophys.*, 40, 1013, doi:10.1029/2000RG00102, 2003.

Kono, M., Sakuraba, A., and Ishida, M. Dynamo simulation and paleosecular variation models. *Phil. Trans. R. Soc. Lond. A*, 358, 1123–1139, 2000.

Korte, M. and Constable, C. Continuous global geomagnetic field models for the past 3000 years. *Phys. Earth Planet. Int.*, 140, 73–89, 2003.

Korte, M. and Constable, C. Continuous geomagnetic field models for the past 7 millennia II: CALS7K.1. *Geochem. Geophys. Geosyst.*, 6(1), Q02H16,doi:10.1029/2004GC000801, 2005.

Korte, M., Genevey, A., Constable, C., Frank, U., and Schnepp, E. Continuous geomagnetic field models for the 7 millennia I: A new global data compilation. *Geochem. Geophys. Geosyst.*, 6 (2), Q02H15,doi:10.1029/2004GC000800, 2005.

Kuang, W. and Bloxham, J. On the effect of boundary topography on flow in the Earth's core. *Geophys. Astrophys. Fluid Dyn.*, 72, 161–195, 1993.

Kuang, W. and Bloxham, J. Numerical dynamo modelling: Comparison with the Earth's magnetic field. *The Core-Mantle Boundary Region, AGU Geodynamics*, 28, 197–209, 1998.

Kuang, W. and Chao, B. F. Topographic core-mantle coupling in geodynamo modeling. *Geophys. Res. Lett.*, 28(9), 1871–1874, 2001.

Langel, R. A. The Main Field. *Geomagnetism, Ed. Jacobs, J.A.*, 2, 1987.

Langel, R. A. and Hinze, W. J. *The magnetic field of Earth's lithosphere. The planetary perspective.* Cambridge Univeristy Press, 1998.

Larmor, J. How could a rotating body such as the Sun become a magnet? *Rept. Brit. Assoc. Adv. Sci.*, pages 159–160, 1919.

Lay, T., Williams, Q., Garnero, E. J., Kellogg, L., and Wysession, M. E. Seismic wave anisotropy in the D″ region and its implications. *The Core-Mantle Boundary Region, AGU Geodynamics Monograph*, 28, 97–118, 1998.

Layer, P., Kröner, A., and McWilliams, M. An Archean geomagnetic reversal in the Kaap Valley pluton, South Africa. *Science*, 273, 943–946, 1996.

Lehnert, B. Magnetohydrodynamic waves under the action of the coriolis force. *Astrophysical Journal*, 119, 647–654, 1954.

Lehoucq, R. B., C., Sorensen D., and Yang, C. *ARPACK Users' Guide: Solution of Large-Scale Eigenvalue Problems with Implicitly Restarted Arnoldi Methods*. Society for Industrial and Applied Mathematics, 1998.

LeMouël, J. L. Outer core geostrophic flow and secular variation of Earth's magnetic field. *Nature*, 311, 734–735, 1984.

Lighthill, M. J. Dynamics of rotating fluids: a survey. *J. Fluid Mech.*, 26, 411–431, 1966.

Lighthill, M. J. *Waves in fluids*. Cambridge University Press, 1978.

Lister, J.R. and Buffett, B.A. Stratification of the outer core at the core-mantle boundary. *Phys. Earth Planet. Int.*, 105, 5–19, 1998.

Livermore, P. W. *Magnetic stability analysis for the geodynamo*. Ph.D Thesis, University of Leeds, 2003.

Livermore, P. W. and Jackson, A. On magnetic energy instability in spherical stationary flows. *Proc. R. Soc. Lond. A*, 460(2045), 1453–1476, 2004.

Lloyd, D. and Gubbins, D. Toroidal fluid motion at the top of the Earth's core. *Geophys. J. Int.*, 100, 455–467, 1990.

Longair, M. *Theoretical concepts in Physics*. Cambridge Univeristy Press, 2003.

Longbottom, A. W., Jones, C. A., and R., Hollerbach. Linear magnetoconvection in a rotating spherical shell incorporating a finitely conducting inner core. *Geophys. Astrophys. Fluid Dyn.*, 80, 205–227, 1995.

Longuet-Higgins, M. S. Planetary waves on a rotating sphere. *Proc. R. Soc. Lond.*, 279, 446–73, 1964.

Love, J. J. A critique of frozen-flux inverse modelling of a nearly steady geodynamo. *Geophys. J. Int.*, 138, 353–365, 1999.

Lowes, F. J. Spatial power spectrum of the main geomagnetic field, and extrapolation to the core. *Geophys. J. R. Astr. Soc.*, 36, 717–730, 1974.

Malin, S. R. C. and Hodder, B. M. Was the 1970 geomagnetic jerk of internal or external origin? *Nature*, 296, 726–728, 1982.

Malkus, W. V. R. Hydromagnetic planetary waves. *J. Fluid Mech.*, 28(4), 793–802, 1967.

Malkus, W. V. R. Energy sources for planetary dynamos. *Lectures on Solar and Planetary Dynamos, (Ed. M. R. E. Proctor and A.D. Gilbert)*, pages 161–179, 1994.

Mandea, M. and Macmillan, S. Internation Geomagnetic Reference Field— the eighth generation. *Earth, Planets, Space*, 52, 1119–1124, 2000.

Masters, T. G. and Shearer, P. M. Summary of the seismological constraints on the structure of Earth's core. *J. Geophys. Res.*, 95, 21691–21695, 1990.

McDonough, W. F. and Sun, S.-S. The composition of the Earth. *Chemical Geology*, 120, 223–253, 1995.

McElhinny, M. W. and McFadden, P. L. *Paleomagnetism*. Academic Press, 2000.

McFadden, P. L. and Merrill, R. T. Lower mantle convection and geomagnetism. *J. Geophys. Res.*, 89, 3345–3362, 1984.

McIntyre, M. E. On global scale atmospheric circulations. *in Perspectives in fluids dynamics ed G. K. Batchelor, H. K. Moffatt, and M. G. Worster*, pages 557–624, 2000.

Melchoir, P. *Physics of the Earth's core*. Pergamon Press, 1986.

Merrill, R. T. and McFadden, P .L. Geomagnetic polarity transition. *Rev. Geophys.*, 37, 201–226, 1999.

Mete Uz, B., Yoder, J. A., and Osychny, V. Pumping of nutrients to ocean surface waters by the action of propagating planetary waves. *Nature*, 409, 597–600, 2001.

Moffatt, H. K. *Magnetic field generation in electrically conducting fluids.* Cambridge Univeristy Press, 1978.

Mound, J. E. and Buffett, B. A. Interannual oscillations in length of day: Implications for the structure of the mantle and core. *J. Geophys. Res.*, 108(B7), 2334, doi:10.1029/2002/JB002054, 2003.

Mound, J. E. and Buffett, B. A. Mechanisms of core-mantle angular momentum exchange and the observed spectral properties of torsional oscillations. *J. Geophys. Res.*, 110, B08103, 2005.

Needham, J. *Science and civilisation in China*, Volume 4. Cambridge University Press, 1962.

Ockendon, J., Howison, S., A., Lacey, and A., Movchan. *Applied Partial Differential Equations.* Oxford University Press, 2nd edition, 2003.

Olson, P., Christensen, U., and Glatzmaier, G.A. Numerical modelling of the geodynamo; Mechanisms of field generation and equilibriation. *J. Geophys. Res.*, 104(B5), 10383–10404, 1999.

Olson, P. and Glatzmaier, G. A. Magnetoconvection in a rotating spherical shell: structure of flow in the outer core. *Phys. Earth Planet. Int.*, 92, 109–118, 1995.

Olson, P., Sumita, I., and Aurnou, J. Diffusive magnetic images of core upwellings. *J. Geophys. Res.*, 107, 10.1029/JB000384, 2002.

Parker, E. N. Kinematic hydromagnetic theory and its application to the low solar photosphere. *Astr. J.*, 138, 552–578, 1963.

Parker, R. L. *Geophysical inverse theory.* Princeton Univeristy Press, 1994.

Pawlowski, R. S. Use of the slant stack for geologic or geophysical map lineament analysis. *Geophysics*, 62(6), 1774–1778, 1997.

Pedlosky, J. *Geophysical fluid dynamics.* Cambridge Univeristy Press, 1987.

Percival, D. B. and Walden, A. T. *Spectral analysis for physical applications.* Cambridge Univeristy Press, 1993.

Poirier, J. P. Physical properties of the Earth's core. *C. R. Acad. Sci. Paris*, 318, 341–350, 1994.

Press, W. H., Teukolsky, S. A., Vetterling, W. T., and Flannery, B.P. *Numerical Recipies in Fortran 77.* Cambridge Univeristy Press, 2nd edition, 1992.

Priestley, M. B. *Spectral Analysis and Time Series.* Academic Press, 1981.

Proctor, M. R. E. Convection and magnetoconvection in a rapidly rotating sphere. *Lectures on Solar and Planetary Dynamos, Edited by Proctor, M. R.E. and Gilbert, A. D.*, pages 97–115, 1994.

Quartly, G. D., Cipollini, P., Cromwell, D., and Challenor, P. G. Synergistic observations of Rossby waves. *Phil. Trans. R. Soc. Lond. A*, 361, 57–63, 2003.

Rau, S., Christensen, U., Jackson, A., and Wicht, J. Core flow inversion tested with numerical dynamo models. *Geophys. J. Int.*, 141, 484–497, 2000.

Riley, K. F., Hobson, M. P., and Bence, S. J. *Mathematical methods for physics and engineering.* Cambridge Univeristy Press, 2nd edition, 2002.

Roberts, P. H. On the thermal instability of a rapidly rotating fluid sphere containing heat sources. *Phil. Trans. R. Soc. Lond. A*, 263, 93–117, 1968.

Roberts, P. H. Mac waves. *Geofluiddynamical Wave Mechanics Research, ed W. Criminale. Publ. of Appl. Math. Dept. Univ. of Wash., Seattle*, pages 218–225, (reprinted in Magnetohydrodynamics and Earth's core: Selected works of Paul Roberts ed A. M. Soward, Taylor and Francis, 2003, pp 261–263), 1977.

Roberts, P. H. Magnetoconvection in a rapidly roataing fluid. *in Rotating fluids in geophysics ed P. H. Roberts and A. M. Soward, Academic Press, London*, pages 421–435, 1978.

Roberts, P. H. Fundamentals of dynamo theroy. *Lectures on Solar and Planetary Dynamos, Edited by Proctor, M. R. E. and Gilbert, A. D.*, pages 1–58, 1994.

Roberts, P. H. and Glatzmaier, G. A. Geodynamo theory and simulations. *Rev. Mod. Phys.*, 72 (4), 1081–1123, 2000a.

Roberts, P. H. and Glatzmaier, G. A. A test of the frozen flux approximation using a new geodynamo model. *Phil. Trans. R. Soc. Lond. A*, 358, 1109–1121, 2000b.

Roberts, P. H. and Jones, C. A. The onset of magnetoconvection at large Prandtl number in a rotating layer I. Finite magnetic diffusion. *Geophys. Astrophys. Fluid Dyn.*, 92, 289–325, 2000.

Roberts, P. H., Jones, C. A., and Calderwood, A. R. Energy fluxes and Ohmic dissipation. *In Earth's core and lower mantle, Ed. Jones, C. A. and Soward, A. and Zhang, K.*, pages 100–129, 2003.

Roberts, P. H. and Loper, D. E. On the diffusive instability of some simple, steady magnetohydrodynamic flows. *J. Fluid Mech.*, 90, 641–668, 1979.

Roberts, P. H. and Scott, S. On the analysis of the secular variation — 1 : A hydromagnetic constraint. *J. Geomagn. Geoelectr.*, 17(2), 137–151, 1965.

Roberts, P. H. and Soward, A. M. Magnetohydrodynamics of the Earth's core. *Annu. Rev. Fluid Mech.*, 4, 117–153, 1972.

Roberts, P. H. and Stewartson, K. On finite amplitude convection in a rotating magnetic system. *Phil. Trans. R. Soc. Lond.*, 277, 287–315, 1974.

Romanowicz, B. Inversion of surface waves: a review. *IASPEI Handbook (W. Lee Editor)*, 1, 1–26, 2002.

Rossby, C.-G. Relation between variations in the intensity of the zonal circulation of the atmosphere and the displacements of the semi-permanent centres of action. *J.Mar. Res.*, 2(0), 33–55, 1939.

Rotvig, J. and Jones, C. A. Rotating convection driven dynamos at low Ekman number. *Phys. Rev. E*, 66, 056308, 2002.

Rüdiger, G. and Hollerbach, R. *The magnetic universe.* Wiley-VCH, 2004.

Sabaka, T. J., Olsen, N., and Langel, R. A. A comprehensive model of the quiet-time, near-earth magnetic field: phase 3. *Geophys. J. Int.*, 151, 32–68, 2002.

Sabaka, T. J., Olsen, N., and Purucker, M. E. Extending comprehensive models of the Earth's magnetic field with Oersted and CHAMP data. *Geophys. J. Int.*, 159, 521–547, 2004.

Sakuraba, A. and Kono, M. Effect of a uniform magnetic field on nonlinear magnetoconvection in a rotating fluid spherical shell. *Geophys. Astrophys. Fluid Dyn.*, 92, 255–287, 2000.

Sarson, G. R. *Kinematic dynamo calculations for geomagnetism.* Ph. D. Thesis, University of Leeds, 1994.

Secco, R. A. and Schloessin, H. H. The electrical reistivity of solid and liquid Fe at pressures up to 7 GPa. *J. Geophys. Res.*, 94, 5887–5894, 1989.

Shankland, T. J., Peyronneau, J., and Poirier, J.-P. Electrical conductivity of the Earth's lower mantle. *Nature*, 366, 453–455, 1993.

Shearer, P. M. *Introduction to Seismology.* Cambridge Univeristy Press, 2001.

Shepp, K. L. and Kruskal, J. B. Computerised tomography: The new medical X-Ray technology. *Amer. Math. Monthly*, 85, 420–439, 1978.

Shure, L., Parker, R. L., and Langel, R. A. A preliminary harmonic spline model from Magsat data. *J. Geophys. Res.*, 90(B13), 11505–11512, 1985.

Simons, F. J., Dahlen, F. A., and Wieczorek, M. A. Spatiospectral concentration on a sphere. *SIAM Review (submitted)*, 2005.

Smith, S. W. *The Scientist and Engineer's Guide to Digital Signal Processing.* California Technical Publishing, 1997.

Soward, A. M. Convection driven dynamos. *Phys. Earth Planet. Int.*, 20, 134–151, 1979a.

Soward, A. M. Thermally and magnetically driven convection in a rapidly rotating fluid layer. *J. Fluid Mech.*, 90, 669–684, 1979b.

Soward, A. M. and Dormy, E. Dynamics in rotating spheres: Boundary layers and waves. *Mathematical Aspects of Natural Dynamos (Ed. E. Dormy)*, 2005.

Stellmach, S. and Hansen, U. Cartesian convection driven dynamos at low Ekman number. *Phys. Rev. E*, 70, 056312, 2004.

Stewartson, K. Slow oscillations in a rotating cavity in the presence of a toroidal magnetic field. *Proc. R. Soc. Lond.*, 299, 173–187, 1967.

Stewartson, K. Waves in homogeneous fluids. *Rotating fluids in geophysics, Ed. Roberts, P.H. and Soward, A.M.*, pages 67–103, 1978.

Stewartson, K. and Rickard, J. A. Pathological oscillations of a rotating fluid. *J. Fluid Mech.*, 35, 759–773, 1969.

Sutton, R. R. and Allen, M. R. Decadal predictability of North Atlantic sea surface temperature and climate. *Nature*, 388, 563–567, 1997.

Tackley, P. J. Three-dimensional simulations of mantle convection with a thermo-chemical basal boundary layer: D"? 1998.

Tapley, B. D., Bettadpur, S., Ries, J. C., Thompson, P. F., and Watkins, M. M. GRACE measurements of mass variability in the Earth system. *Science*, 305, 502–505, 2004.

Taylor, J.B. The magneto-hydrodynamics of a rotating fluid and the Earth's dynamo problem. *Proc. R. Soc. Lond. A*, 9, 274–283, 1963.

Tritton, D. J. *Physical fluid dynamics*. Oxford University Press, 1987.

Valet, J.-P. Time variations in geomagnetic intensity. *Rev. Geophys.*, 41, 1004, doi:10.1029/2001RG000104, 2003.

Valet, J.-P., Meynadier, L., and Guyodo, Y. Geomagnetic dipole strength and reversal rate over the past two million years. *Nature*, 435, 802–805, 2005.

Vestine, E. H. and Kahle, E. The small amplitude of magnetic secular change in the pacific area. *J. Geophys. Res.*, 71(2), 527–530, 1966.

Vestine, E. H. and Kahle, E. The weswtard drift and the geomagnetic secular change. *Geophys. J. R. Astr. Soc.*, 15, 29–37, 1968.

Voorhies, C. V. and Backus, G. E. Steady flows at the top of the core from geomagnetic field models. *Geophys. Astrophys. Fluid Dyn.*, 32, 163–173, 1985.

Walker, A. D. and Backus, G. E. On the difference between the average values of B_r^2 in the atlantic and pacific hemipheres. *Geophys. Res. Lett.*, 23, 1965–1968, 1996.

Walker, M. R. and Barenghi, C. F. Magnetoconvection in a rapidly rotating sphere. *Geophys. Astrophys. Fluid Dyn.*, 85, 129–162, 1997.

Walker, M. R. and Barenghi, C. F. Nonlinear magnetoconvection and the geostrophic flow. *Phys. Earth Planet. Int.*, 111, 35–46, 1999.

Walker, M. R., Barenghi, C. F., and Jones, C. A. A note on dynamo action at asymptotically small Ekman number. *Geophys. Astrophys. Fluid Dyn.*, 88, 261–275, 1998.

Walker, M. R. and Jackson, A. Robust modelling of the Earth's magnetic field. *Geophys. J. Int.*, 143, 799–808, 2001.

Wardinski, I. *Core flow models from decadal and sub-decadal secular variation of the main geomagnetic field*. Ph.D. Thesis, Der Freien Universität Berlin, 2005.

Wheeler, M. and Kiladis, G. N. Convectively coupled equatorial waves: Analysis of clouds and temperature in the wavenumber-frequency domain. *J. Atmos. Sci.*, 56, 374–399, 1999.

Whitham, K. The relationships between the secular change and the non-dipole fields. *Can. J. Phys.,*, 36, 1372–1396, 1958.

Wicht, J. Inner-core conductivity in numerical dynamo simulations. *Phys. Earth Planet. Int.*, 132, 281–302, 2002.

Wicht, J. and Olson, P. A detailed study of the polarity reversal mechanism in a numerical dynamo model. *Geochem. Geophys. Geosyst.*, 5, Q03H10, doi:10.1029/2003GC000602, 2004.

Worland, S. J. *Magnetoconvection in rapidly rotating spheres.* Ph.D Thesis, University of Exeter, 2004.

Wysession, M. E., Lay, T., Revenaugh, J., Williams, Q., Garnero, E. J., Jeanloz, R., and Kellogg, L. H. The D″ discontinuity and its implications. *The Core-Mantle Boundary Region, AGU Geodynamics Monograph*, 28, 273–297, 1998.

Yano, J.-I., Talagrand, O., and Drossart, P. Outer planets: Origins of atmospheric zonal winds. *Nature*, 421, 36, doi:10.1038/421036a, 2003.

Yokoyama, Y. and Yukutake, T. Sixty year variation in a time series of geomagnetic gauss coefficients between 1910 and 1983. *J. Geomagn. Geoelectr.*, 43, 563–584, 1991.

Zhang, K. Spiralling columnar convection in rapidly rotating spherical fluid shells. *J. Fluid Mech.*, 236, 535–556, 1992.

Zhang, K. On equatorially trapped boundary inertial waves. *J. Fluid Mech.*, 248, 203–217, 1993.

Zhang, K. On coupling between the poincare equation and the heat equation. *J. Fluid Mech.*, 268, 211–229, 1994a.

Zhang, K. On coupling between the poincare equation and the heat equation: no slip boundary conditions. *J. Fluid Mech.*, 284, 239–256, 1994b.

Zhang, K. Spherical shell rotating convection in the presence of a toroidal magnetic field. *Proc. R. Soc. Lond.*, 448, 245–268, 1995.

Zhang, K. Nonlinear magnetohydrodynamic convective flows in earth's fluid core. *Phys. Earth Planet. Int.*, 111, 93–103, 1999.

Zhang, K. and Busse, F. H. On the onset of convection in rotating spherical shells. *Geophys. Astrophys. Fluid Dyn.*, 39, 119–147, 1987.

Zhang, K. and Busse, F. H. On hydromagnetic instabilities driven by the hartmann boundary layer in a rapidly rotating sphere. *J. Fluid Mech.*, 304, 363–283, 1995.

Zhang, K., Earnshaw, P., Liao, X., and Busse, F.H. On inertial waves in a rotating fluid sphere. *J. Fluid Mech.*, 437, 103–119, 2000.

Zhang, K. and Fearn, D. R. How strong is the invisible component of the magnetic field in the earth's core. *Geophys. Res. Lett.*, 20(19), 2083–2086, 1993.

Zhang, K. and Fearn, D. R. Hydromagnetic waves in rapidly rotating spherical shells, generated by magnetic toroidal decay modes. *Geophys. Astrophys. Fluid Dyn.*, 77, 133–157, 1994.

Zhang, K. and Fearn, D. R. Hydromagnetic waves in rapidly rotating spherical shells, generated by magnetic poloidal decay modes. *Geophys. Astrophys. Fluid Dyn.*, 81, 193–209, 1995.

Zhang, K. and Gubbins, D. Convection in a rotating spherical fluid shell with inhomogeneous temperature boundary conditions at infinite Prandtl number. *J. Fluid Mech.*, 250, 209–232, 1993.

Zhang, K. and Gubbins, D. Is the geodynamo process intrinsically unstable? *Geophys. J. Int.*, 140, F1–F4, 2000a.

Zhang, K. and Gubbins, D. Scale disparities and magnetohydrodynamics in the Earth's core. *Phil. Trans. R. Soc. Lond. A*, 358, 899–920, 2000b.

Zhang, K. and Gubbins, D. Convection driven hydromagnetic waves in planetary fluid cores. *Mathematical and Computer Modelling*, 36, 389–401, 2002.

Zhang, K. and Jones, C. A. The influence of Ekman boundary layers on rotating convection. *Geophys. Astrophys. Fluid Dyn.*, 71, 145–162, 1993.

Zhang, K. and Jones, C. A. On small roberts number magnetoconvection in rapidly rotating systems. *Proc. R. Soc. Lond. A*, 452, 981–995, 1996.

Zhang, K. and Jones, C. A. The effect of hyperviscosity on geodynamo models. *Geophys. Res. Lett.*, 24, 2869–2872, 1997.

Zhang, K. and Liao, X. A new asymptotic method for the analysis of convection in a rapidly rotating sphere. *J. Fluid Mech.*, 518, 319–346, 2004.

Zhang, K., Liao, X., and Schubert, G. Non-axisymmetric instabilities of a torioidal magnetic field in a rotating sphere. *Astr. J.*, 585, 1124–1137, 2003.

Zhang, K. and Schubert, G.. Magnetohydrodynamics in rapidly rotating spherical systems. *Annu. Rev. Fluid Mech.*, 32, 409–443, 2000.